Mechanical Engineering Series

P. A. Lakshminarayanan
Yogesh V. Aghav

Modelling Diesel Combustion

Second Edition

Springer

Mechanical Engineering Series

Series Editor

Francis A. Kulacki, Department of Mechanical Engineering, University of Minnesota, Minneapolis, MN, USA

The Mechanical Engineering Series presents advanced level treatment of topics on the cutting edge of mechanical engineering. Designed for use by students, researchers and practicing engineers, the series presents modern developments in mechanical engineering and its innovative applications in applied mechanics, bioengineering, dynamic systems and control, energy, energy conversion and energy systems, fluid mechanics and fluid machinery, heat and mass transfer, manufacturing science and technology, mechanical design, mechanics of materials, micro- and nano-science technology, thermal physics, tribology, and vibration and acoustics. The series features graduate-level texts, professional books, and research monographs in key engineering science concentrations.

More information about this series at https://link.springer.com/bookseries/1161

P. A. Lakshminarayanan · Yogesh V. Aghav

Modelling Diesel Combustion

Second Edition

Springer

P. A. Lakshminarayanan
Indian Institute of Technology Kanpur
Kanpur, India

Yogesh V. Aghav
Kirloskar Oil Engines Limited
Pune, India

With Contributions by
Rolf Reitz
Department of Mechanical Engineering,
Engine Research Center
University of Wisconsin-Madison
Madison, WI, USA

Haiwen Ge
Department of Mechanical Engineering
Texas Tech University
Lubbock, TX, USA

Yu Shi
Phillips 66 Company
Houston, TX, USA

Anirudh Jaipuria
Formerly with Ashok Leyland
Chennai, India

ISSN 0941-5122 ISSN 2192-063X (electronic)
Mechanical Engineering Series
ISBN 978-981-16-6741-1 ISBN 978-981-16-6742-8 (eBook)
https://doi.org/10.1007/978-981-16-6742-8

This Springer imprint is published by the registered company Springer Nature Singapore Pte Ltd.
The registered company address is: 152 Beach Road, #21-01/04 Gateway East, Singapore 189721, Singapore

Preface

Phenomenology of Diesel Combustion and Modelling

Diesel is the most efficient combustion engine today, and it plays an important role in the transport of goods and passengers on land and on high seas. The emissions must be controlled as stipulated by society without sacrificing the legendary fuel economy of diesel engines. These important drivers caused innovations in diesel engineering like re-entrant combustion chambers in the piston, lower swirl support, and high-pressure injection, in turn reducing the ignition delay and hence the nitric oxides. The limits on emissions are being continually reduced. Therefore, the required accuracy of the models to predict the emissions and efficiency of the engines is high. The phenomenological combustion models based on the physical and chemical description of the processes in the engine are practical to describe diesel engine combustion and to carry out parametric studies. This is because the injection process, which can be relatively well predicted, has the dominant effect on mixture formation and subsequent course of combustion. The need for improving these models by incorporating new developments in engine designs is explained in Chap. 2. With "model-based control programs" used in the electronic control units (ECUs) of the engines, phenomenological models are assuming importance now because the detailed CFD-based models are too slow to be handled by the ECU.

Experimental work is necessary to develop a basic understanding of the processes. Chapter 3 describes the experimental set-up of the bomb for interferometry and real engine studies for validation of the phenomenological models. This chapter also includes the details of the measurement techniques for obtaining the experimental data needed for validating the phenomenology. Empirical relations have been obtained in Chap. 4 to describe the axial and radial variations of fuel concentration in the vaporizing and burning sprays, and to evaluate penetration and air entrainment of the free and wall jet regions. The movement of the "tail" of the spray in the post-injection period has been studied. These equations form the basis for building the phenomenological models of ignition delay, emissions, and heat release rate in subsequent chapters.

The norms for NO_x and HC emissions are so tight that the prediction of ignition delay has become necessary. In Chap. 5, phenomenological calculations of the cooling of spray surface have shown that the physical parameters and fuel type influence the temperature of the mixture of air and the fuel vapour throughout its life up to the end of ignition delay. A model is proposed in Chap. 6 to predict rapid convective heat transfer between spray and wall by extending the analogy by Woschni.

The rate of heat release in an indirect injection engine is modelled on the lines of its observed rate in a direct injection engine. The diffusion combustion is modelled as proportional to the available fuel and rate of air entrainment in Chap. 7. Chapter 8 introduces the concept of air useful for combustion. The ratio of momentum of the useful air to the total momentum of injected fuel near TDC at the end of the ignition delay period is found to bear a universal relationship with the indicated efficiency and dry soot emissions in the case of combustion chambers supported by air swirl. In Chap. 9, the combustion rate is precisely described using the concept developed in Chap. 7 by relating the fuel–air mixing rate to the turbulent energy created at the exit of the nozzle as a function of the injection velocity and by considering the dissipation of energy in free air and along the wall. The absence of adjustable constants distinguishes the model from the other zero-dimensional or pseudo-multi-dimensional models. The success of the model is demonstrated by applying the technique to engines widely varying in bore size with single-shot fuel injection.

The almost infinite ability of the common rail diesel injection system spawned multiple injections, currently up to nine shots per cycle. It enables containing nitric oxide and particulate emissions as much as possible within the cylinder and very little treatment after the engine to meet some of the tightest emission standards. The model detailed in Chap. 9 has been morphed successfully to accept multiple injections in Chap. 10. Examples of predictions of heat release rate are provided for a commercial truck engine with pilot, main, and post-injections.

Hydrocarbon (HC) emissions from direct injection diesel engines are mainly due to fuel injected and mixed beyond lean combustion limit during ignition delay and fuel effusing from the nozzle sac at low pressure. The concept has been developed in Chap. 11 to provide an elegant model to predict HC emissions. To contrast the phenomenon of HC formation in a diesel and a spark-ignition engine, Chap. 12 is included. The absorption and desorption of fuel by cylinder lubricating oil films have been modelled using principles of mass transfer.

A new model for smoke explained in Chap. 13 characterizes the smoke emitted at higher loads from the wall–spray formed after impingement. The smoke has been treated by ignoring the fast chemistry, as the slow physical mixing seems to be controlling. A new phenomenological model for NOx emission is developed based on mixing-controlled combustion incorporating localized wall heat transfer in Chap. 14. Based on the smoke formation and oil consumption, an estimate of the particulate matter is made in Chap. 15. In this chapter, some of the intricate relationships between smoke and soot are explored. Also, smoke, as measured by filter paper method and opacity, is compared and the usefulness of the different methods for the development engineer is explained.

Chapter 16 reviews the basic approach of multi-dimensional CFD modelling of diesel combustion, focusing on the advanced turbulence and combustion models. Recent efforts for reducing the computational expense of multi-dimensional CFD modelling are also discussed. CFD tools reveal details about invisible or technically difficult or costly to measure in-cylinder processes of diesel combustion so that guidance can be provided to improve engine designs in terms of emission reduction and fuel economy; innovative combustion concepts can be evaluated numerically before experimental tests to reduce the number of investigated parameters and thus costs; important design parameters can be discovered by modelling engines of different sizes to establish engine size-scaling relationships and thus non-dimensionalizing engine designs; by integration with optimization methodologies, CFD tools can also directly impact the design of optimum engine systems, such as piston geometry and injection parameters. Each of these aspects is described by relevant case studies in Chap. 17.

Even though the direct simulation of turbulence may be attractive, the cost and time of computation are prohibitive. Therefore, the closure of turbulence equations by RANS as explained in Chaps. 16 and 17 is used to obtain useful results. With the advent of faster computers, it is possible to graduate to the next step of simulating large eddies. Large eddy simulation (LES) gives insight into engine emissions that might be missed by RANS. Chapter 18 opens the door to the vista of LES with all the attendant equations and examples.

The appendix is numbered as a chapter in the second edition. Also, at the end of chapters, relevant nomenclatures are appended as suggested by the series editor of the Springer Mechanical Engineering Series.

Kanpur, India — P. A. Lakshminarayanan
Pune, India — Yogesh V. Aghav

Acknowledgments

Our work at the Indian Institute of Technology Madras, Indian Institute of Technology Delhi, and Loughborough University, and later at the industrial R&Ds of Ashok Leyland Ltd., Kirloskar Oil Engines Ltd., and Simpson & Co. Ltd. for the last five decades forms the basis of the phenomenological models presented in the book. We are grateful to these great institutions for the constant encouragement and guidance we received. We express our thanks to FEV, India, for their kind support during the preparation of the book.

In the second edition, we enhanced the chapter on PM emissions bringing in recent publications on the subject. We hope it will enable developers to estimate the particulate mass during the development process.

The common rail fuel injection system made a direct injection diesel engine highly adaptable, offering a variety of combustion and emission solutions. Multiple injections of chosen durations with predetermined separation are the basis for the versatility. In this book, the heat release rate in a diesel engine is treated as the transformation of the rate of injection. This concept is developed successfully for engines of widely varying bores with single-shot injection. Then, a chapter is dedicated to extending the idea for multiple injections and authenticated. A good prediction of heat release leads to predicting many thermodynamic parameters of an engine.

The book is complete only with the two chapters on the reviews and applications of modern methods of simulating diesel engines by Dr. Yu Shi and Prof. Dr. Rolf Reitz of Engine Research Centre at the University of Wisconsin-Madison. They acceded to our request spontaneously and gracefully to provide the material. We express our gratitude to them for showing magnanimity. Large eddy simulation as an elegant closure for the turbulence flow equations helps in modelling combustion and emissions better with the help of new generation computers. Through Dr. Shi and Prof. Reitz, we were introduced to Dr. Haiwen Ge of Texas Tech University who could offer an excellent chapter on the subject.

We thank Mr. R. Seshsayee, Ashok Leyland, and Mr. R. R. Deshpande, Kirloskar Oil Engines Ltd., for encouraging us to write this book.

We express a deep sense of gratitude to Prof. Dent, Prof M. K. Gajendra Babu, Prof. U. P. Nagpukar, and Dr. Nagaraj Nayak for their valuable contributions.

We thank the Society of Automotive Engineers (SAE), American Society of Mechanical Engineers (ASME), and Institute of Mechanical Engineers, London (IMechE), for allowing us to use the figures and other material published by us in their learned journals. We thank the publisher Springer for giving us a chance to write this book.

We are thankful to our families for their support and understanding throughout the research work and the preparation of the book.

P. A. Lakshminarayanan
Yogesh V. Aghav

Contents

Authors and Contributors

About the Authors

Dr. P. A. Lakshminarayanan (born 1950) studied at Indian Institute of Technology Madras for his B.Tech, M.S. and Ph.D. degrees. He worked at Loughborough University of Technology and Kirloskar Oil Engines Ltd. for about 5 and 20 years, respectively, before moving to Ashok Leyland in 2002 to head the Engine R&D. From 2011 till 2019, he was the CTO, and the Technical Adviser at Simpson and Co. Ltd. Now, he is an adjunct professor at IIT Kanpur.

With his teams, he has developed more than eight diesel and CNG engine platforms and 150 engine types commercially successful for efficiency and cost effectiveness. Two engine designs received prizes from the Institute of Directors (India). Twelve ideas were patented during the development of engines over 40 years. He has authored 54 research papers in journals and conferences of international repute. Four of them received the prizes for integrity and quality of contents from the SAE (Arch Colwell Award), Combustion Society (India), AVL (Graz) and AVL (India) in 1983, 1993, 2005 and 2011, respectively. He has coauthored two books titled *Modeling Diesel Combustion* (Springer 2010) and *Critical Component Wear of Parts in heavy Duty Engines* (John Wiley 2011). He has coedited a handbook *Design and Development of Heavy Duty Diesel Engines*(Springer, 2020). Now, he is editing his fourth book *Thermal Management of Engines for Performance and Emissions* which is due in 2021. He is elected to the fellowships of SAE (2009), INAE (2013) and ISEES (2018).

Dr. Yogesh V. Aghav received B.E. and M.Tech. degrees from VIT Pune and IIT Madras, respectively. His Doctoral degree is from IIT Delhi for his research work on heat release in diesel engines. Currently, he is the associate vice president of the corporate Research and Engineering, Kirloskar Oil Engines Ltd., Pune, with responsibilities for the performance, emissions, NVH, and development of internal combustion engines running on diesel and alternative fuels like natural gas and biodiesel. For two years, he served FEV, Pune, and helped to found the organization. For the last 25

years, he has lead teams to develop many engines of swept volumes ranging from 300 c.c. to 32-litre applied to agriculture, off-highway, power generation, construction equipment, marine, and defense.

He has published more than 50 research papers in ASME, SAE, and IMechE journals. He is associated with the boards of studies of VIT and MITADT, Pune. He advises the Universities and takes part in faculty development. He is a member of the SAE India.

Contributors

Prof. Rolf Reitz's research interests include internal combustion engines and sprays. He is Former Director of the Engine Research Center and is Emeritus Wisconsin Distinguished Professor of Mechanical Engineering at the University of Wisconsin-Madison. Before joining UW-Madison, he spent six years at the GM Research Laboratories, three years as Research Staff Member at Princeton University, and 2 years as Research Scientist at the Courant Institute of Mathematical Sciences, New York University. He received his Ph.D. in mechanical and aerospace engineering from Princeton University in 1978. He is Fellow Member of SAE and ASME, and he serves as a consultant to many industries through his consulting company, Wisconsin Engine Research Consultants. He is Editor (Americas) and Co-founder of the *International Journal of Engine Research* and is past Chairman of the Institute of Liquid Atomization and Spraying Systems—North and South America. He and his group have won major research awards, and he has co-authored over 550 technical papers on engine research.

Yu Shi received his Ph.D. in mechanical engineering from the Engine Research Center at the University of Wisconsin-Madison, where he specialized in computational optimization of internal combustion engines. After finishing his Ph.D. in 2009, he worked as a postdoctoral associate in the Department of Chemical Engineering at the Massachusetts Institute of Technology, where he contributed to the field of accelerated reactive flow computations using heterogeneous computational architectures. He is currently Senior Data Scientist with the Phillips 66 Company based in Houston, Texas, where he applies advanced machine learning to business analytics.

Dr. Haiwen Ge received B.Eng. and M.Eng. in engineering thermophysics from the University of Science and Technology of China in 1999 and 2002, respectively. In 2006, he received Doctor of Science in Physical Chemistry from the University of Heidelberg, Germany. He joined the Engine Research Center, University of Wisconsin-Madison, as a postdoctoral fellow in 2006. Since 2010, he worked for the Ford Motor Company as Resident Engineer. In 2013, he joined the Fiat Chrysler Automobiles (FCA), where he was Senior Technical Specialist in Combustion Development and Technical Lead in 3-D Combustion CFD. In 2016–2017, he was Senior Combustion CFD Engineer of John Deere. In 2017, he joined the Department of Mechanical Engineering, Texas Tech University, as an instructor. He has published

one monograph, two chapters, 68 peer-reviewed publications, and 67 conference papers.

Mr. Anirudh Jaipuria completed his B.Tech. in mechanical engineering from the National Institute of Technology Surat, India, after which he joined Ashok Leyland Ltd. as Deputy Manager where he led the development of the BS-IV heavy-duty diesel engine family. Following that, he completed his master's in combustion engines from RWTH Aachen, Germany. In 2012, he joined MAN Diesel & Turbo as Simulation Engineer responsible for valvetrain development for 4-stroke large diesel engines. Since 2015, he has been with BMW M-GmbH, Munich, as SE-Team Leader and technical specialist responsible for all dynamic simulations and drivetrain development for high-performance sports cars. He has five publications and has been a speaker at two international conferences.

Chapter 1
Introduction

Role of Internal Combustion Engines

Rapid increase in pollution levels, escalation of fuel prices, and depletion of hydrocarbon reserves of the world have forced the engineers to look for appropriate technology and alternative fuels to cater to the ever-increasing demands of energy. The internal combustion (IC) engines form an indispensable part of industrial growth. IC engines play a dominant role in the fields of propulsion, power, and energy. They also contribute to our modernized agricultural sector and the transportation of goods and passengers. It is impossible to do without the IC engines and hence means must be sought to improve the designs.

It has been estimated that the present fossil fuel demand is expected to double between now and 2050. At present, about two-thirds of world energy demand is met by fluid fossil fuels because of their availability and convenience of use in the existing design of several prime movers such as internal combustion engines. In the future, the energy scenario is likely to be several times worse than the two oil crises of the 1970s. The second predicament involving fossil fuels is the environmental damage caused by the combustion of fossil fuels. Technologies for fossil fuel extraction, transportation, processing, and particularly their combustion have harmful impacts on the environment. The fossil fuels which constitute carbon and hydrogen in addition to traces of sulphur and quality enhancer additives like oxygenates produce various gases, soot, ash, and other organic compounds during combustion and when released into the atmosphere cause degradation of air quality [1, 2]. These pollutants when mixed with water and other atmospheric compounds or triggered by sunlight change their form and become pollutants like ozone, aerosols, peroxyacetyl nitrates, various acids causing damage to the aquatic and terrestrial ecosystem, affecting humans, animals, vegetation, and structure.

In IC engines, the chemical energy of the fuel is released inside the cylinder to produce mechanical power. Spark-ignited (SI) gasoline and compression-ignited (CI) diesel engines are the main types of IC engines. In 1876, Otto invented the SI engine, and later in 1892 Diesel developed the CI engine. Traditionally, SI gasoline engines

P. A. Lakshminarayanan and Y. V. Aghav, *Modelling Diesel Combustion*,
Mechanical Engineering Series, https://doi.org/10.1007/978-981-16-6742-8_1

are employed for light-duty applications, as they are compact with a simple construction for a lower power range. On the other hand, CI diesel engines are for heavy-duty usage as they can develop more power at lesser fuel consumption. Different methods of fuel supply are used for CI engines, namely indirect and direct types. Out of these different types of engines, the direct injection (DI) diesel engine exhibits the best fuel economy along with the lowest engine-out emissions. Therefore, it is emerging as the engine of the future. The packing of higher power also improves the power-to-weight ratio to make the engine more compact. Traditionally, considered heavy-duty, the DI diesel engines are also popular in the passenger car market. The best fuel economy car consuming only three litres of fuel for 100 km is developed with the modern DI diesel engine. This trend is facilitated by the development of contemporary injection systems that are more flexible and generate higher injection pressures for better spray atomisation and combustion characteristics than their predecessors. The modern DI diesel engines satisfy stringent emission norms of Euro III without after-treatment. The DI diesel engine is now recognized as environmentally friendly, powerful, and smooth running [3].

Developments in DI Diesel Engines

In DI diesel engines, the fuel is sprayed at higher pressure directly into the main combustion chamber where it ignites by mixing with hot air produced by isentropic compression. The stoichiometric air-to-fuel ratio is 14.7 for diesel fuel. However, the diesel engines work satisfactorily above the air-to-fuel ratio of 19, i.e. always with some excess air. As the fuel is directly sprayed into the cylinder, sufficient time is not available for mixing, which results in smoke in zones of lower air-to-fuel ratios. The higher compression ratio helps improve the efficiency of diesel engines at higher loads. They are also more economical than gasoline engines at lower loads because they can work at very lean mixtures avoiding throttling losses of charge air. Due to their lower heat losses, diesel engines have a lower risk of gradually over-heating if left idling for long periods. In many applications, such as marine, agriculture, and railways, diesel is left idling unattended for many hours. These advantages are especially attractive in locomotives.

A naturally aspirated diesel engine produces less power density, i.e., power in a given volume, compared to gasoline engines. The power of the diesel engine is always limited by the air available. Therefore, they are often turbocharged to improve power density. The turbocharged versions can produce more power than petrol engines, limited by mechanical capability. The diesel engines do not face knocking problems. A turbocharger consists of a turbine and a compressor linked by a shared axle. The turbine inlet receives exhaust gases from the engine exhaust manifold causing the turbine wheel to rotate. This rotation drives the compressor, compressing ambient air, and delivering it to the intake of the engine; this allows more fuel to burn in the cylinder. At a higher boost, the benefit of more air mass diminishes as the density drops substantially. Inter-cooling by using atmospheric air

or engine jacket water helps to recover the density by bringing down the temperature of the charge. The charge air is not throttled in diesel engines; therefore, a governor is used to control fuel supply quantity. A sophisticated fuel supply system consisting of a pumping unit, multi-hole injector, and governor are employed in DI diesel engines to inject the correct amount of fuel at the required time under favourable conditions for combustion.

Early DI diesel engines operated at relatively low compression ratios and low injection pressures. Hence, they demanded very advanced injection timings commensurate with the large ignition delay. During the ignition delay period at the beginning of combustion, up to about 20% of the injected fuel is prepared to stoichiometric proportion. Due to high flame speed, the prepared mixture burns at high temperatures to produce nitrogen oxides and explosive noise characteristic of a diesel engine, Fig. 1.1. This period of combustion is said to be the premixed phase governed by chemical kinetics. On the other hand, the rest of the fuel burns as and when the mixture is prepared because the delay is absent with hot gases and radicals available in the vicinity, a remnant of the fuel burnt earlier. This second part is called the diffusive phase, and the rate of combustion of the majority of fuel is controlled by the physical mixing processes in the spray. The third or the last stage corresponds to the tail of the heat release diagram in which a small but distinguishable rate of heat release persists late into the expansion stroke [4]. Such a design was the result of the available technology and lack of norms for noise and emissions.

During the last 50 years, the design of DI engines has undergone a sea change because of social and economic aspects [5]. With the advent of new emission norms, reduction in ignition delay held the key to solve twin problems of NO_x emission and noise. The higher temperature at the beginning of injection by increased compression ratio reduced the delay period and subsequent premixed combustion phase substantially. Higher injection pressures and turbulence were introduced to improve the mixing rate and hence to maintain the combustion duration within a reasonable limit, in spite of the loss of the fast-burning premixed combustion process. User demands of improving fuel economy and legal requirement of reduction in emissions are driving the engine development persistently. The advancements in the design are summarized in Table 1.1.

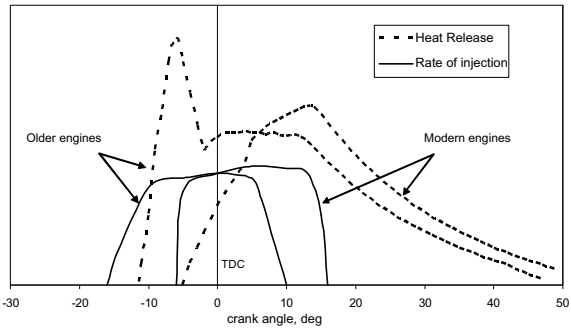

Fig. 1.1 Combustion in DI diesel engine

Table 1.1 Advancements in DI diesel engines

Period	Advancements	Events
The early 1970s	The main problems were the life of an engine and visible smoke	Improve design engine components, avoid secondary injection
The late 1970s to early 1980s	Improve fuel economy	Improved design of the combustion chamber, valve train
The mid-1980s to early 1990s	Reduction in noise Reduction in NOx, HC, CO	Improved compression ratios Very low nozzle sac volumes or valve-closed orifice (VCO) nozzles Increase injection pressure capability even more, especially at a lower speed Increase injection timing flexibility
1990–2000	Reduction in particulate Improving power packing	Turbo-charging, electronic control of injection rate, injection timing
2000–2006	Stricter emission laws, rapid escalation, and shortages of fuel	Heavy boosting and inter-cooling, higher injection pressure, oxygenated fuels

The DI diesel engines are regulated by government laws for gaseous emissions like HC, CO, and NO_x as well as for solid emissions known as particulate matter and smoke. In diesel engines, both HC and CO emissions are a small fraction of those found in a gasoline engine. Even engine-out NO_x emissions in a diesel engine are less than their corresponding gasoline emissions. However, modern gasoline engines operate at a stoichiometric ratio where the three-way catalyst performs at its highest conversion efficiency resulting in extremely low HC, CO, and NOx emissions. Unfortunately, diesel exhaust is very lean, and reducing NO_x in an oxygen-rich environment is a very challenging task. The catalyst industry is developing solutions like DeNOx catalyst or selective catalytic reduction (SCR) for the diesel NO_x problem. Another problematic pollutant associated with diesel engines is particulate matter. The casual observer is made aware of this pollutant in the form of black smoke or soot emitted from either the tailpipes of many diesel-equipped passenger cars or the stacks of diesel-powered heavy-duty vehicles. Emission of soot is also accompanied by other matter suspended in the exhaust, such as unburned lube oil, unburned fuel, trace metals, and sulphur by-products. Emission of soot in particulate matter results from the nature of the heterogeneous combustion process or diffusion-type combustion that is prevalent in diesel engines. The preparation of fuel and air mixture in modern diesel engines has greatly reduced this problem. The development of diesel particulate filters promises to eliminate it.

There are several serious reasons for considering biofuels like vegetable oil-based biodiesel, alcohols, as alternatives for petroleum-based diesel fuel, e.g. expected

growth of prices of fossil liquid fuels soon and gradual exhaustion of crude oil sources in the next 80–100 years. Governments of many countries have started thinking that biofuels will provide a boost to the agricultural industry. Also, oxygenated fuels have attracted increasing attention in engine development owing to their excellent combustion characteristics in reducing emissions [6, 7]. Therefore, oxygenated fuels would find a way as a supplement and substitute for diesel fuels for regular usage.

Heavy turbocharging along with inter-cooling, higher injection pressures with finer sprays, flexible injection timing, exhaust gas recirculation, and electronic control unit are the main features of modern DI diesel engines. The modern DI diesel engines are compact, smooth, reliable, and sturdy as shown in Fig. 1.2. To accomplish improved air–fuel mixing, reduced premixed phase of combustion, and minimize the tail in the heat release diagram modern DI diesel engine employ:

- Higher compression ratios
- Turbocharging and inter-cooling
- Down-sizing and up-rating
- Smaller fuel orifice sizes and sac volume
- Oxygenated fuels.

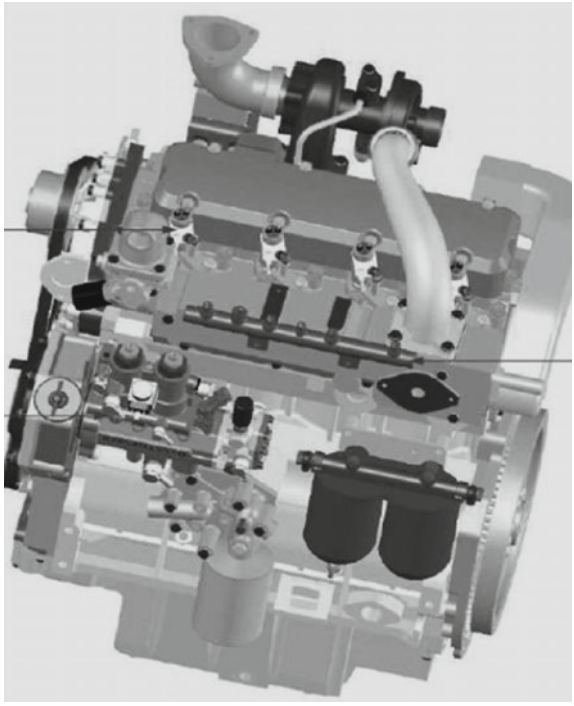

Fig. 1.2 Modern DI diesel engine

Modelling of Combustion in DI Diesel Engines

The complex task of improving IC engines, which have reached a higher degree of sophistication, can be achieved by a combination of advanced experiments and computational studies. Despite the quantitative uncertainties of numerical simulations, which are often greater than those of experiments, the modelling of combustion engine processes has some significant advantages that make its utilization in engine development a necessity. In this regard, it is obvious that numerical simulations are especially suited to carry out extensive parametric studies since they are more effective than the alternative construction and investigation of numerous prototypes [8].

The advantages of engine modelling are: (a) parametric studies of each variable can be done, (b) a wide range of boundary conditions can be analysed, (c) separation of each sub-process from other, (d) detailed information is available as output, and (e) effective in terms of time and cost.

Depending on the various possible applications, different types of models for engine combustion processes have been developed. Three different model categories are typically distinguished. In an order of increasing complexity and increasing requirements of computing power, these are zero-dimensional thermodynamic models, quasi-dimensional phenomenological models, and multi-dimensional computational fluid dynamics (CFD) models.

In thermodynamic models, the heat released by combustion cannot be easily derived by detailed modelling of physical and chemical sub-processes, because these processes are strongly affected by the distribution of unresolved spatial temperature and composition. Because the combustion chamber is taken as zero-dimensional, it is mandatory to model the heat release rate by empirical sub-models using simple mathematical equations. On the other hand, the multi-dimensional CFD models are based on the locally resolved solution of conservation of mass, energy, momentum, and include detailed sub-models for spray and combustion phenomena. With these models, the gas flow patterns can be predicted best and the prediction of fuel spray is less complete, and combustion calculations present considerable difficulties. The CFD models are of immense use to appreciate the inner mechanism of diesel sprays but are very difficult to comprehend during the complete simulation of a diesel engine. Therefore, there is a need for a third category of the model that allows executing efficient, fast, and economic preliminary calculations of heat release models and exhaust emissions as a function of important engine parameters like injection pressure, injection timing, swirl ratio, and boost pressure. These models based on physical and chemical sub-models, for local processes like spray formation, air–fuel mixing, ignition, and combustion including emission formation are termed phenomenological models. These models are more comprehensive compared to thermodynamic models and consume less computational resources compared to CFD models. It should be noted that phenomenological models are the most practical to describe diesel engine combustion [8]. This is because the injection process, which can be relatively well predicted with the phenomenological approach, has the dominant

effect on mixture formation and subsequent course of combustion. Therefore, these models are widely used as predictive tools for carrying out parametric studies during engine development.

Many experimental investigations are also being carried out to provide a better insight into the combustion process happening under the engine environment. More recently, the development of laser-based diagnostics has provided a means for making detailed in situ measurements of the processes occurring inside a reacting diesel fuel jet. These diagnostics allow specific species within the reacting jet to be measured at multiple points simultaneously with high spatial and temporal resolution.

Even though the IC engine was invented a century ago, its development is continuing, as new technology is available and new demands are arising. Although the DI diesel engine is a better choice among different types of IC engines as a prime mover considering fuel economy and exhaust emissions, efforts are being put to improve them further to meet future stringent demands of fuel economy and pollution. Alternative technologies and fuels are being implemented in these engines. Therefore, theoretical and applied understanding of the engine processes is also developing at a faster rate.

References

1. Walsh MP (2000) Global trends in motor vehicle pollution control, accomplishments to date and challenges for new millennium. Paper No. F2000PH02, Proceedings of FISITA-2000, Seoul, Korea
2. Fiaz A, Sturm PJ (2000) New directions, road traffic in developing countries. J Atmos Environ 34:4745–4746
3. Krieger K, Hummel HG, Naik LM (2000) Diesel fuel injection technology: an essential contribution towards an environment-friendly powerful diesel engine. SAE 2000-01-1429
4. Heywood JB (1988) A textbook on internal combustion engine fundamentals. McGraw-Hill International edition
5. Bosch Automotive Handbook (2000) Bosch, 5th edn
6. Miyamoto N, Ogawa H, Nurun NM, Obata K, Arimes T (1998) Smokeless, low NOx, high thermal efficiency, and low noise diesel combustion with oxygenated agents as the main fuel. SAE 980506
7. Xiao Z, Ladommatos N, Zhao H (2000) The effect of aromatic hydrocarbon and oxygenates on diesel engine emissions. IMechE 214, Part D
8. Stiesch G (2003) Modelling engine spray and combustion processes. Springer

Chapter 2
Phenomenology of Diesel Combustion and Modelling

The phenomenological combustion models are very practical to describe diesel combustion and to carry out parametric studies. This is because of the injection process. The models are improved by incorporating new developments in engine designs.

The combustion in modern DI diesel engines is mainly divided into two phases (a) a small ignition delay event in which preflame activities take place followed by (b) the main heat release event in which actual combustion happens. These events are modelled differently considering the prominent role of chemical kinetics during ignition and physical mixing rate during heat release. This approach is described in detail in the following sections. This chapter summarizes different types of models along with a description of popular models.

Combustion Model

The combustion starts almost at the onset of fuel injection because the ignition delay in modern DI diesel engines is very small with a high compression ratio and highly retarded injection timing enabling a substantial reduction in noise, $NO_{x,}$ and HC. The heat release estimated with this assumption predicts satisfactorily the important instantaneous parameters used by a designer, e.g. heat transfer, fuel consumption, and the performance turbocharger and piston. In the same tenor, ignition delay cannot be neglected while estimating emissions however small it may be.

Ignition Delay

In direct injection diesel engines, estimation of ignition delay is of great importance because of its effect on startability, noise, and formation of NO_x. The ignition delay

P. A. Lakshminarayanan and Y. V. Aghav, *Modelling Diesel Combustion*,
Mechanical Engineering Series, https://doi.org/10.1007/978-981-16-6742-8_2

in a diesel engine is defined as the time interval between the start of injection and the start of combustion. This delay period consists of (a) physical delay, wherein atomization, vaporization, and mixing of air–fuel occur and (b) chemical delay attributed to precombustion reactions. Both physical and chemical delays occur simultaneously. Early DI diesel engines operated at relatively low compression ratios and low injection pressures with very advanced injection timings commensurate with the large ignition delay [35]. Reduction in ignition delay held the key to solving emission and noise problems. The higher temperature at the beginning of injection by increased compression ratio reduces the delay period substantially.

Numerous ignition delay correlations have been proposed based on experiments carried out in constant volume bombs, steady-state reactors, rapid compression machines, and engines. Wolfer [54] developed the earliest correlation for predicting ignition delay. The equation was in the form of an Arrhenius expression representing a single-stage reaction. Kadota et al. [29] related results of combustion bomb experiments to an Arrhenius-type expression by introducing dependence of equivalence ratio. Lahiri et al. [34] modified this equivalence ratio to fuel–oxygen ratio, attempting to make it suitable for oxygenated fuels. However, these correlations fail to predict the ignition delay under unsteady diesel engine conditions as they are based on experiments conducted in a constant volume bomb. On the other hand, a few correlations have been developed considering engine data [21, 53]. These correlations also were not successful in yields, satisfactory predictions under widely varying operating conditions as they have ignored the effect of mixture quality. Recently Assanis et al. [4] have compared these correlations and found better predictability using the Watson correlation (1980). They improved the correlation by introducing the equivalence ratio and tuning the empirical constants. They postulated that the introduction of the dependency of ignition delay on the overall equivalence ratio makes the correlation more dynamic.

The time taken for the visible fire to appear in the premixed zone of spray is a strong function of pressure and temperature of the ambient. Also, the physical properties such as Cetane number, the viscosity of fuel, nozzle hole size, injected quantity, and injection pressure contribute to the delay phenomenon in diesel engines [11].

Heat Release

The shaft work by a diesel engine is the sum of work on the piston by the pressure produced by the heat released by combustion and the losses due to pumping, heat transfer, and friction. While the flow losses and friction work could be reasonably comprehended, the heat release is dependent on the complex turbulent mixing of fuel and air at high temperatures after compression. The variety of combustion chambers and types of fuel injection equipment influence the heat release rate characteristically.

Models Based on Fluid Dynamics

These types of models are often called multi-dimensional models due to their inherent ability to provide detailed geometric information on the flow field based on the solution of the governing equations. In the numerical calculations of reacting flows, computer time and storage constraints severely restrict the complexity of the reaction mechanism that can be incorporated. They use a simplified model for predicting combustion, which is mixing controlled and kinetically controlled [33]. The choice between these two models is made by the ratio of the chemical reaction time to the turbulent mixing time. Several three-dimensional simulation models of injection, mixing, and burning in diesel engines exist [6, 19, 40] described various phenomena in the engine and providing possibilities of understanding the inner mechanism of diesel sprays. However, the volume of computation in multi-dimensional models is too prohibitive to carry out many parametric studies. Also, their sub-models require a thorough validation with detailed experiments before employing them confidently in engine design work [13, 14, 49].

Phenomenological Models

In these types of models, details of different phenomenon happening during combustion are added to the basic equation of energy conservation. In the simplest approach, Rife and Heywood [45] assumed the growth and motion of the spray within the chamber and analysed it as a quasi-steady one-dimensional turbulent gaseous jet. Shahed et al. [46], Dent and Mehta [16] and Hiroyasu et al. [24] found that the spray structure offered the clue to better heat release predictions. In these investigations, detailed two-dimensional axisymmetric spray calculations are attempted using the mixing of the injected fuel with the surrounding air-entrained due to the high shear velocity of the jet as shown in Fig. 2.1. A criterion of stoichiometric burning of the fuel in ignitable elements has been used in these models by spray-mixing approach.

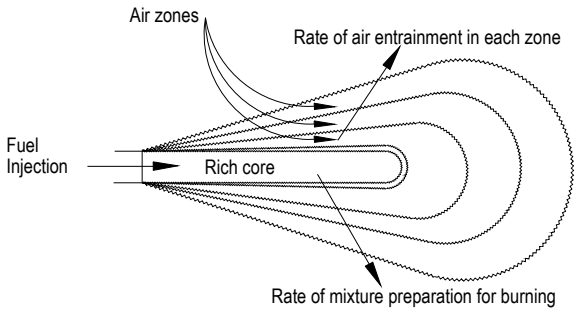

Fig. 2.1 Multi-zone spray model

Zero-Dimensional Models

This type of models is more attractive due to their simplicity as they use simple algebraic equations to describe the heat release rate. Lyn's work [5] is the earliest in identifying a strong relationship between fuel injection and heat release rates. The rate of injection diagram was subdivided into elemental fuel packets emanating as rectangular pulses, which results in exponentially decaying heat energy function. The convolution integral of the heat release from the individual packets summed neatly to the net heat release rate, Fig. 2.2. Due to the absence of universal decay constants for elemental heat release rates in different types of engines and their operating conditions, the application of this elegant idea posed difficulty.

In this regard, the global heat release rate function of Vibe [51] earned much wider acceptance in diesel engine simulation for several years now as shown in Fig. 2.3. The Vibe's function, however, requires two adjustable constants for a given engine type and even then fails to explain the effects of speed and load. Also, this function does not reflect the effects of the shape of the combustion chamber and the fuel injection rate on the history of heat release as desired in current engine development.

The limitations of Vibe's function to predict the rate of heat release during the early premixed period were somewhat overcome by Watson et al. [53] through the concept of double Vibe function. This, however, added more adjustable constants that are dependent on the engine type. While such algebraic functions are easy to compute, there are various other complex models as shown in Table 2.1.

In a simpler approach, avoiding the necessity of engine-dependant tuning constants, Chmela et al. [12] proposed an innovative model on the premise that the fuel–air mixing, and hence the burning in diesel engines, is proportional to the

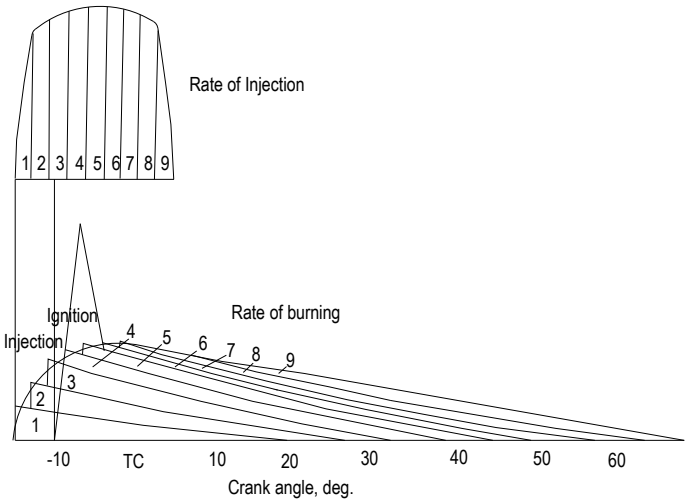

Fig. 2.2 Relation between rate of injection and rate of burning

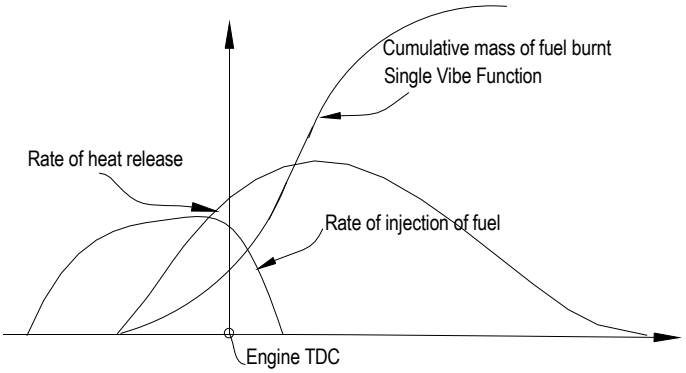

Fig. 2.3 Vibe's model

Table 2.1 Combustion models

Author (year)	Specialty of model	Remark
Austen et al. (1960) [5]	The direct relation between the fuel injection pump and heat release rate	Absence of universal constants
Vibe [51]	Exponential decay function with empirical constants	No effect of injection rate and combustion chamber
Shahed et al. [46] Dent and Mehta [16] Hiroyasu et al. [24]	Detailed computation of two-dimensional axisymmetric spray	Engine-dependant constant No effect of load and speed
Cartillieri et al. (1983) [6] Gosman and Watkins (1985) [19]	Three-dimensional finite volume technique	A large volume of calculation
Chmela et al. [12]	Mixing-controlled combustion	No effect of wall impingement

average turbulent kinetic energy associated with the fuel injection rate. Also, the turbulent energy decay in time is proportional to the total kinetic energy of the injected fuel itself. It is observed that this model predicts the trend of heat release quite closely if only there is no impingement of sprays on the piston. A comparison of the predicted and the experimental results is not satisfactory in the case of spray impinging on the wall. This situation arises in engines of capacities less than 2 L per cylinder operating at more than half load, where the majority of diesel engines belong. Therefore, an attempt has been made in this book to enhance this model by encompassing the phenomena at the wall and the instantaneous injection rate derived from the indicated performance of fuel injection equipment [36].

Emission Models

DI diesel engines emit smoke, hydrocarbons, nitric oxides, carbon monoxide, and particulate matter which are mainly regulated. They are formed in different phases of combustion as described below.

Hydrocarbons

The fuel leaned beyond flammability limits [20], bulk quenching during expansion, fuel effusing from nozzle sac after completion of injection [57] are the most important reasons for hydrocarbon (HC) emissions. A semi-empirical phenomenological model was successfully made for HC emissions considering the fuel-injected and mixed beyond the lean combustion limit during ignition delay and fuel effusing from the nozzle sac at low pressure [36]. Exhaust gas recirculation (EGR), a well-accepted method of NO_x reduction, alters ignition delay and HC emissions. The oxygen-enriched fuels that attract great attention worldwide owing to their excellent combustion characteristics exhibit different behaviour especially in case of ignition delay and HC emissions.

Oxides of Nitrogen

Considering the heterogeneous nature of fuel–air mixture in diesel engines, NO_x and particulate matter (PM) are important emissions. Continuous efforts are being made to minimize the quantities of these two pollutants from the diesel engine exhaust. Vioculescu and Borman [52] carried out gas sampling from within the cylinder of a naturally aspirated direct injection (DI) diesel engine using a rapid-acting sampling valve. This resulted in a plot showing the time history of the ratio of the average cylinder NO_x concentration in the exhaust during the combustion process. Similar modelling and gas sampling studies have been done with indirect injection (IDI) diesel engines, which suggest that the prechamber is the prominent location for the formation of nitrogen oxides [39]. Duggal et al. [17] plotted the NO concentrations and equivalence ratios as a function of crank angle using a rapid-acting sampling valve at different locations within the prechamber of a swirl chamber IDI engine. There are many potential mechanisms responsible for NO in combustion processes. The relative importance of these different mechanisms is strongly affected by the temperature, fuel–air equivalence ratio, pressure, flame conditions, residence time, and concentrations of key reacting species. Rapid NO_x formation begins after the start of heat release. Shortly after the end of heat release, the period of rapid NO_x formation ends because of temperatures of the burned gases decrease due to mixing with cool bulk gas and expansion of the charge [31]. The fuel–air equivalence ratio is another

important factor influencing NO_x formation. As the equivalence ratio becomes leaner, NO and NO_x decrease significantly as expected. NO_2 however shows an opposite trend to that of NO that causes the NO_2/NO_x ratio to increase at leaner conditions. The NO_2 peaks at an equivalence ratio near 0.25. The leaner equivalence ratio is indicative of lower loads and lower bulk gas temperatures that are conducive to the formation of NO_2 [42].

Advancing injection timing or increasing injection pressure improves combustion efficiency and raises combustion temperature. In general, higher combustion temperatures lead to higher NO_x formation [22]. The addition of diluents to the engine intake air is considered as an effective means to reduce the NO formation rate and hence the exhaust NO_x levels. The effect is primarily one of reducing the peak flame temperature, which is the driving factor for NO_x formation. Diluents such as N_2, CO_2, and exhaust gas were added to the intake air of the direct injection (DI) engine to study their effect on NO_x reduction [10]. Similar studies on indirect injection (IDI) engines showed similar trends [56]. Plee et al. [43, 44] established a correlation showing the effect of changes in intake air composition and temperature on NO_x emissions.

NO_x emissions comprise NO and NO_2. The NO_2 is formed via the NO molecule. Therefore, the modelling of NO_x formation is most often reduced to studying the formation of NO. It is widely accepted that in diesel engines the major portion of NO is formed via thermal path [1]. Many multi-dimensional and multi-zone phenomenological models use the extended Zeldovich mechanism [23]. This mechanism was postulated by Zeldovich [58] and improved by Lavoie et al. [37]. Khan et al. [30] related FIE and engine operating conditions to NO formation and developed a method of calculation for emissions [30]. They concluded that an increased rate of injection or increased air swirl reduces the amount of exhaust smoke and increases NO_x.

All these models utilize empirical heat transfer correlation, which is mass averaged. During combustion, the heat loss is caused partly by convection from burned gases at high temperatures and partly by radiation from soot particles formed during the diffusion flame [18, 25]. Due to the short distance between the nozzle and the combustion chamber wall under typical operating conditions, diesel fuel impinges on the wall in the form of liquid followed by fuel vapour and flame after the onset of auto-ignition. The peak radiant heat flux is always less than 20% total heat flux confirming the dominant role of spray and flame interaction with piston bowl [2].

The contribution of the convective mode of heat transfer is about 80% to total engine heat transfer [23, 47]. However, it is known that in diesel engines radiative heat transfer may have a significant contribution in addition to convective heat transfer. The radiative heat transfer in diesel engines is caused by both radiations of hot gases and by soot particles within the diffusion flame. It is agreed in the literature that the latter has a significantly greater impact on the radiative heat flux, and thus most heat transfer models concentrate on the radiation of soot only. It should be noted though, that the general difficulty in the evaluation of soot radiation exists in that the prediction of the soot concentration itself is typically subject to significant uncertainties [47]. Therefore, the empirical heat transfer correlations focused mainly on convective mode.

The heat transfer coefficient has been derived by many researchers by assuming an analogy with a steady turbulent flow over a solid wall. The colour pyrometer and fast response thermocouples were employed for experimental investigations. Annand and later Arcoumanis et al. [2, 3] developed a correlation for convective heat transfer, but it was based on experiments conducted on the only cylinder head. Probably, the most widely used approach in this category is the one suggested by Woschni [55]. Hohenberg [26] improved the above correlation by using a length based on instantaneous cylinder volume and exponent of the temperature term. This approach gives an estimate of the surface-averaged heat transfer coefficient history in terms of the bulk gas temperature and a surface-averaged or total heat flux [27, 41]. However, this approach cannot give the kind of information necessary to design modern engines. The empirical correlations underestimate to varying degrees, the heat transfer during combustion. The investigations have revealed that during the combustion period, the wall heat flux is substantial locally in space and time, due to the transient nature of the flame propagation. In particular, during combustion, the heat flux increases rapidly after impingement on the wall [32]. The characteristics of injected spray and its interaction with the swirling air and the wall of the combustion chamber determine the efficiency and the exhaust emissions. In Chap. 14, a phenomenological model for NO_x prediction is proposed based on spray combustion incorporating the localized effect of heat transfer from wall–spray and exhaust gas recirculation.

Smoke and Particulate Matter

Diesel particulates consist principally of carbonaceous material (soot from smoke) generated by combustion on which some organic compounds have become absorbed. Most of the particulate material results from incomplete combustion of fuel hydrocarbons [14, 15, 38]; some are contributed by the lubricating oil [23]. Diesel particulate matter is therefore a complex mixture of organic and inorganic compounds in solid and liquid phases [28]. The basic measurement of particulate matter is by its mass, and it can be described as any exhaust components other than uncombined water that collects on a filter in a dilution tunnel at a temperature less than 53 °C. In the standard procedure of measurement of mass emission, dilution tunnels are used to simulate the physical and chemical processes the particulate emissions undergo in the atmosphere. In the dilution tunnel, the raw exhaust gases are diluted with the ambient air to 53 °C or less and the sample stream from the diluted exhaust is filtered to remove the particulate matter. The mathematical modelling of particulate matter is always concentrated around soot because of its complex nature. Different studies have been carried out to establish contributions of soot, unburnt HC from fuel and lubricating oil [7–9]. Most of the PM correlations consider only soot to estimate particulate matter. Recently, one phenomenological model is proposed for PM based on soot and unburnt HC from fuel [48]. However, this model requires tuning of the engine and load-dependent constants. It does not account for SOF from lubricating oil and IOF from sulphates.

Theme of the Book

The literature survey highlighted some of the limitations of present phenomenological models for application to modern engines. The available models require many engine-dependent empirical constants, and consideration is given to neither spray–wall interaction nor the effect of oxygenated fuels. The book presents the results of the research work based on comprehensive experimental work undertaken for improving phenomenological modelling of combustion in modern engines.

The highlights of the phenomenology of diesel combustion considered in the following chapters are as follows:

- Analysis of modern in-cylinder emission control technologies
- Turbulence structure for engine sprays
- Spray–wall interaction and its effect
- Mixing-controlled combustion
- Localized heat transfer
- Quasi one-dimensional approach to the heat release in DI engines
- Consideration to fuel-bound oxygen
- Avoid engine-dependent constants
- Sub-model for prediction of combustion
- Sub-models for important exhaust emissions.

About 16 modern engines from six different engine families with widely varying features like bore sizes, aspiration, and cooling systems are selected for experimental work. These engines meet current emission norms and are capable of upgrading to the next stage with minor changes. Observations about fuel injection, emissions, and engine performance were collected simultaneously using the experimental setup specially developed. Additional experiments were also carried out to study the effect of oxygenated fuels and exhaust gas recirculation on a few engines. The new models are thoroughly validated by using a large number of data collected from many experimental data. Also, the results of new models are compared with 1-D engine cycle simulation tools like AVL Boost [50] which are being extensively used for engine development. The objectives of the research work are:

- To improve understanding of ignition delay and mixing-controlled combustion
- Develop turbulence structure for engine spray
- Estimation of combustion cavity–spray interaction
- Wall impingement of sprays causing loss of kinetic energy and intense heat transfer
- Effect of exhaust gas recirculation, EGR on combustion
- Effect of fuel-bound oxygen on combustion and emission
- Effect of injection characteristics and nozzle features.

To meet the above objectives, a research scheme was developed as shown schematically in Fig. 2.4.

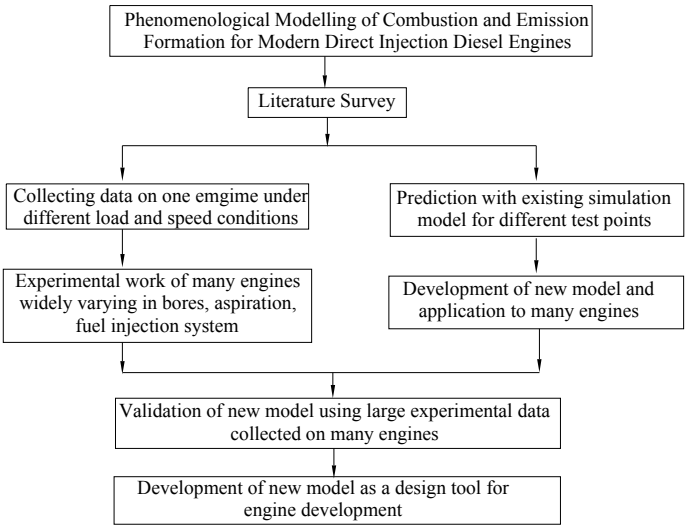

Fig. 2.4 Book scheme

References

1. Ahmed T, Plee SL (1983) Application of flame temperature correlations to emissions from a direct-injection diesel engine. SAE paper 831734
2. Annand WJD (1963) Heat transfer in the cylinders of reciprocating internal combustion engines. Proc IMechE 177:973990
3. Arcoumenis C, Cuter P, Whitelaw DS (1998) Heat transfer process in diesel engines. IChemE, 176, Part A
4. Assanis DN, Filipi ZS, Fiveland SB, Syrimis M (1999) A predictive ignition delay correlation under steady-state and transient operation of a direct injection diesel engine. In: ASME-ICE fall technical conference
5. Austen AEW, Lyn WT (1960) Relation between fuel injection and heat release in a direct-injection engine and the nature of the combustion process. Proc IMechE
6. Cartillieri W, Johns RJR (1983) Multidimensional modelling of engine processes: progress and prospects. Fifteenth CIMAC Congress, Paris
7. Cartillieri W, Wachter WF (1987) Status report on a preliminary survey of strategies to meet US-1991 HD diesel emission standards without exhaust gas after-treatment. SAE 870342
8. Cartillieri W, Herzog PL (1988) Swirl supported of quiescent combustion for 1990's heavy-duty DI diesel engines—an analysis. SAE 880342
9. Cartillieri W, Trittari P (1984) Particulate Analysis of light-duty diesel engines [IDI and DI] with particular reference to lubricating oil particulate fraction. SAE 840418
10. Challen B, Baranescu R (1999) Diesel Engine reference book, 2nd ed. SAE, Warrendale, PA
11. Chandorkar SB, Dani AD, Lakshminarayanan PA (1988) Effects of injection parameters, fuel quality, and ambient on the ignition delay and the location of the flame Kernel in a diesel spray in a quiescent chamber. SAE 881227
12. Chmela FG, Orthaber GC (1999) Rate of heat release prediction for a direct injection diesel engine based on purely mixing controlled combustion. SAE 99010186
13. Dec JE (1997) A conceptual model of DI diesel combustion based on laser sheet imaging. SAE 970873

14. Dec JE, Tree DR (2001) Diffusion-flame wall interactions in a heavy-duty DI diesel engine. SAE 2001-01-1295
15. Dent JC (1980) Turbulent mixing rate—its effect on smoke and hydrocarbon emissions from diesel engines. SAE 800092
16. Dent JC, Mehta PS (1981) Phenomenological combustion model for a quiescent chamber diesel engine. SAE 811235
17. Duggal VK, Priede T, Khan IM (1978) A study of pollutant formation within the combustion space of a diesel engine. SAE paper 780227
18. Fusco A, Knox-Kelecy AL, Foster DE (1994) Application of a phenomenological soot model to diesel engine combustion. In: 3rd international symposium, COMODIA
19. Gosman AD, Tsui YY, Watkins AP (1985) Calculation of unsteady three-dimensional flow in a model motored reciprocating engine and comparison with experiment. In: Fifth international turbulent shear flow meeting, Cornell University
20. Greeves G, Khan IM, Wang CTH, Fenne I (1977) Origins of hydrocarbon emissions from diesel engines. SAE 770259
21. Hardenberg HO, Hase FW (1979) An empirical formula for computing the pressure rise delay of a fuel from its cetane number and the relevant parameters of direct-injection diesel engines. SAE 790493
22. Henein NA, Patterson DJ (1972) Emissions from combustion engines and their control. Ann Arbor Science Publishers
23. Heywood JB (1988) A textbook on internal combustion engine fundamentals. McGraw-Hill Int ed
24. Hiroyasu H et al (1983) Development and use of spray combustion modelling to predict diesel engine efficiency and pollutant emissions. Bull JSME 26:214
25. Hiroyasu, Kadota (1976) Models for combustion and formation of nitric oxide and soot in direct injection diesel engines. SAE 760129
26. Hohenberg GF (1979) Advanced approaches for heat transfer calculations. SAE 790825
27. Ikegami M, Kidoguchi Y, Nishiwaki K (1986) A multidimensional model prediction of heat transfer in non-fired engines. SAE 860467
28. Johnson JH, Bagley ST, Gratz LD, Leddy DG (1994) A review of diesel particulate control technology and emission effects. SAE 940233
29. Kadota T, Hiroyasu H, Oya H (1976) Spontaneous ignition delay of a fuel droplet in high-pressure high-temperature gaseous environments. Bull. JSME, 19~130, Paper No. 536.46, pp. 437–445
30. Khan IM, Greeves G, Wang CHT (1973) Factors affecting smoke and gaseous emissions from direct injection diesel engines and a method of calculation. SAE 730169
31. Kitamura Y, Mohammadi A, Ishiyama T, Shioji M (2005) Fundamental investigation of NO_x formation in diesel combustion under supercharged and EGR conditions. SAE 2005-01-0364
32. Kleemann AP, Gosman AD, Binder KB (2001) Heat transfer in diesel engines: a CFD evaluation study. In: COMODIA 2001, Nagoya, pp 123–134
33. Kurtz, EM, Foster DE (2004) Identifying a critical time for mixing in a direct injection diesel engine through the study of increased in-cylinder mixing and its effect on emissions through a study of increased in-cylinder mixing and its effects on emissions. Int J Eng Res IMechE 5
34. Lahiri D, Mehta P, Poola R, Sekar R (1997) Utilization of oxygen-enriched air in diesel engines: fundamental considerations. ASME Paper No. 97-ICE-72, New York
35. Lakshminarayanan PA, Aghav YV, Dani AD, Mehta PS (2002) Accurate prediction of the rate of heat release in a modern direct injection diesel engine. J Auto Eng IMechE 216
36. Lakshminarayanan PA, Nayak N, Dingre SV, Dani AD (2002) Predicting hydrocarbon emissions from direct injection diesel engine. ASME J Power Gas Turbine 124
37. Lavoie GA, Heywood JB, Keck JC (1970) Experimental and theoretical investigation of nitric oxide formation in an internal combustion engine. Combust Sci Tech 1
38. Magnussen BF, Hjertager BH (1976) On mathematical modelling of turbulent combustion with special emphasis on soot formation and combustion. In: International symposium on combustion

39. Mansouri SH, Heywood JB, Radhakrishnan K (1982) Divided-chamber diesel engine, part i: cycle-simulation which predicts performance and emissions. SAE 820273
40. Nishida K, Hiroyasu H (1989) Simplified three-dimensional modelling of mixture formation and combustion in a DI diesel engine. SAE 890269
41. Nishiwaki K (1998) Modeling engine heat transfer and flame-wall interaction. Proc COMODIA 98:35–44
42. Pipho MJ et al (1991) NO_2 formation in a diesel engine. SAE 910231
43. Plee SL, Ahmed T, Myers JP (1983) Diesel NO_x emissions—a simple correlation technique for intake air effects. In: Proceedings nineteenth international symposium on combustion, The Combustion Institute, Pittsburgh, pp 1495–1502
44. Plee SL, Myers JP, Ahmed T (1981) Flame temperature correlation for the effects of exhaust gas recirculation on diesel particulate and NO_x emissions. SAE 811195
45. Rife JM, Heywood JB (1974) Photographic and performance studies of diesel combustion with a rapid combustion machine. SAE 740948
46. Shahed SM, Chiu WS, Yumlu VS (1973) A preliminary model for the formation of nitric oxides in D I diesel engine and its application in parametric studies. SAE 730083
47. Stiesch G (2003) Modelling engine spray and combustion processes. Springer
48. Tan PQ, Hu ZY, Deng KY, Lu JX, Lou DM, Wan G (2007) Particulate matter emission modelling based on soot and SOF from direct injection diesel engines. Int J Energ Convers Manag 48:510–518
49. Tree DR, Dec JE (2001) Extinction diesel combustion: an integrated view combining laser diagnostics, chemical kinetics, and empirical validation. SAE 2001-01-1296
50. Guide U (2005) AVL Boost 4:1
51. Vibe II (1970) Brennverlauf und Kreisprozeb von Verbrennungsmotoren. VEB VerlagTechnik, Berlin
52. Vioculescu IA, Borman GL (1978) An experimental study of diesel engine cylinder-averaged NO_x histories. SAE 780228
53. Watson N, Pilley AD, Marzouk M (1980) A combustion correlation for diesel engine simulation. SAE 800029
54. Wolfer, HH (1938) Ignition lag in diesel engines. VDI-Forschungsheft 392, translated by Royal Aircraft Establishment, Aug. 1959, Farnborough Library No. 358, UDC 621-436.047
55. Woschni G (1967) A universally applicable equation for the instantaneous heat transfer coefficient in the internal combustion engine. SAE 670931
56. Yu RC, Shahed SM (1981) Effects of injection timing and exhaust gas recirculation on emissions from a D.I. diesel engine. SAE 811234
57. Yu RC, Wong VW, Shahed SM (1980) Sources of hydrocarbon emissions from direct injection diesel engines. SAE 800048
58. Zeldovich YB (1946) The oxidation of nitrogen in combustion and explosions. Acta Physicochimica, USSR, 21

Chapter 3
Experiments

Nomenclature

B	Spalding's mass transfer number (−)
BSU	Bosch smoke unit (−)
$C_{f,r}$	Concentration of fuel at a radius of an axisymmetric evaporating, non-burning spray of the mixture of fuel vapour and air (−)
$C_{i,r}$	Concentration of various species, i at radius r of an axisymmetric burning spray jet at radius r (−)
C_p	Specific heat at constant pressure [J/(kg·K)]
d_0	Nozzle hole diameter (m)
d_e	Equivalent diameter of the nozzle hole, do [density of fuel/density of combustion products at flame temperature]½ (m)
FID	Flame ionization detector (−)
h	Planck's constant (m kg s)
k	Conductivity (W/m K)
K_i	Gladstone–Dale constant for a species, i (m^3/kg)
L	Characteristic engine size (e.g., bore) (m)
M	Molecular weight (kg/kmol)
n	Refractive index (−)
r	Radius of the jet spray measured from the axis of the axisymmetric jet spray (m)
T	Temperature (K)
U_j	Velocity of the jet at the nozzle hole exit (m/s)
μ	Dynamic viscosity (Pa s)
ν	Frequency of the radiation (Hz)
ρ	Density (kg/m^3)
ρ_{rg}	Density of the products (kg/m^3)
Φ	Equivalence ratio (−)

P. A. Lakshminarayanan and Y. V. Aghav, *Modelling Diesel Combustion*,
Mechanical Engineering Series, https://doi.org/10.1007/978-981-16-6742-8_3

Subscripts

∞	Bulk air far away from the combustion and sprays (−)
air	Air (−)
f	Fuel (−)
i	Specie i (−)
mix	Mixture of fuel vapour and air (−)
r	Mixture of fuel and air in an axisymmetric evaporating, non-burning spray (−)
r_B	Mixture of burned products and unburned fuel + air (−)
s	Saturated vapour (−)

The phenomenological models [10] are based on the physical and chemical description of the processes in the engine. Experimental work helps in collecting some data used as input for the phenomenological model and validating them. This chapter describes the set-up of the bomb and engines for developing the phenomenology of combustion.

Studies in a Bomb

Holographic interferometry is attractive as the concentration and temperature fields within a transient vapourizing fuel spray with or without combustion can be obtained in principle [5, 6]. Using a double exposure pulsed laser technique, the transient development of the injected fuel spray and its combustion can be frozen at any instant and recorded on a holographic plate as a two-dimensional interference frinsge field, which is a result of refractive index changes arising from optical path length variation through the spray. Later analysis and inversion of the interference fringe field yield the local refractive index within the spray plume.

The refractive index is dependent on both species concentration and temperature. The decoupling of these individual contributions to the absolute value of the refractive index is used to obtain the concentration and temperature fields within the spray [5, 6]. The schematic of the experimental set-up is shown in Fig. 3.1.

The experimental study in the bomb is considered in two parts [7]. The first deals with vaporizing sprays in the absence of combustion establish equations for the description of concentration and temperature fields within a transient spray, particularly the behaviour following detachment of the jet from the injector nozzle at the end of injection. The data reduction procedure for the evaluation of concentration and temperature from the refractive index field is discussed in references [5].

The second part of the study deals with auto-ignited sprays of injected fuel into high-temperature air. In decoupling the contributions of species concentration and temperature to the refractive index field, the equations obtained in the first phase of the work are used to determine local stoichiometry within the spray. During the

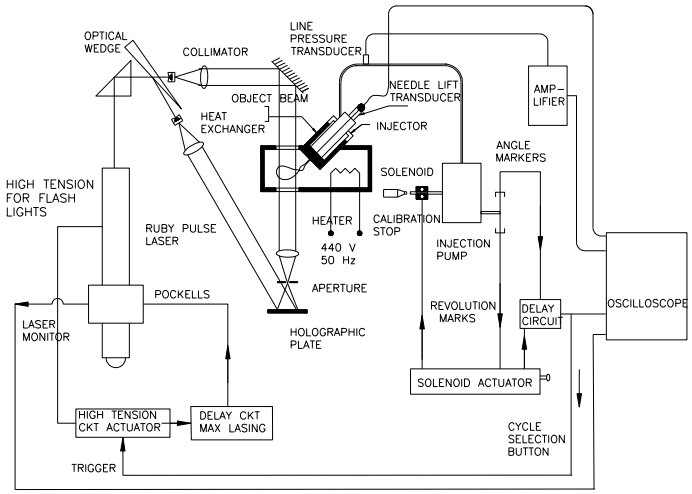

Fig. 3.1 Test set-up for bomb experiments

evaluation of local species concentration and burned gas temperature, the chemical equilibrium of the combustion reaction is assumed.

Attractive as holographic interferometry is, it suffers from disadvantages if applied directly to a typical Diesel engine. High interference fringe density at high compression ratios coupled with laser speckle noise makes fringe interpretation difficult. The problem is compounded if the gas motion within the engine is highly turbulent, due to high swirl and squish. This causes corruption of the background fringe field.

A quiescent chamber diesel engine is simulated. A suitable set of scaling parameters has been used to relate the fuel–air mixing process in a constant volume bomb to those within an actual engine cylinder.

To initiate auto-ignition and combustion in the bomb with ignition delay typically observed in engines, diethyl ether doped with an ignition improver was used as the injected fuel. The experimental rig—Fig. 3.1—consisted of a stainless steel bomb [3] with good optical access (70 mm thick quartz windows), the centrally mounted injector with a single-hole nozzle produced a spray plume directed radially across the bomb within the full view of the windows. A flat impingement surface was provided at a distance of 60 mm from the nozzle to enable the study of transient wall jet behaviour following jet impingement. An electronically controlled jerk pump system enabled single injections of fuel to be achieved with good repeatability.

The beam from a 300 mJ pulsed ruby laser was split with an optical wedge and the two resultant beams collimated to the size of the optical windows. The object beam was transmitted through the bomb, a condensing lens, and aperture, and finally combined with the reference beam at the holographic plate. Because of the transmission optical arrangement used, a dark field interferogram [9] is obtained, which improves fringe contrast and resolution.

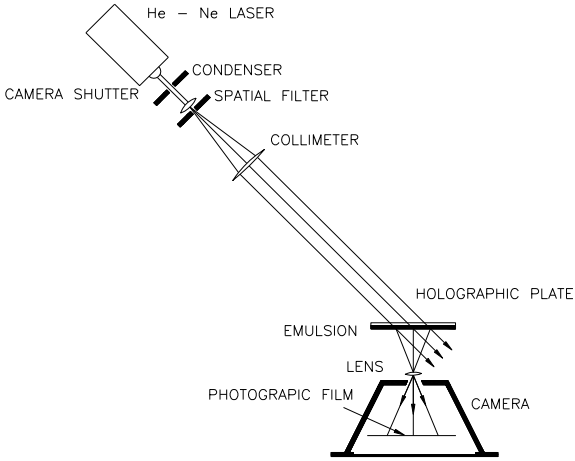

Fig. 3.2 Reconstruction of hologram

The air to the bomb was from the laboratory supply at a pressure of 7-bar. For the vaporization studies, the air was preheated in an electric furnace and bled slowly through the bomb, this produced a quiescent condition in the bomb with air temperatures reaching about 420 K. The combustion studies required modification to the bomb to incorporate a 2.5 kW heating element within the cavity, this enabled the air temperature to be increased to 720 K. However, the presence of strong free convective flows was observed in the cavity. Double exposure holographic interferometry was used; image reconstruction and photography are indicated schematically in Fig. 3.2.

Engine—Bomb Similarity

It has been shown [5, 6] that similarity between a quiescent chamber engine and its simulation is achieved when the two parameters below are equal for the engine and the simulation.

$$\text{Fuel injection Engine Scale} = \frac{U_j d_e}{L} \tag{3.1}$$

$$\text{Fuel vaporisation} = \left(\frac{k}{c_p}\right)_{\text{mix}} \left(\frac{\rho^{0.69}}{\mu^{0.63}}\right) \frac{B}{1+B}(1+d_e) \tag{3.2}$$

Assuming a naturally aspirated engine and an injection timing of 20° bTDC, Fig. 3.3 shows the fuel vaporization parameter plotted against engine compression ratio. The experimental points for the vaporization and combustion studies are (*A*, *B*, *C*, *D*, *E*, *G*) and (*K*, *J*) respectively.

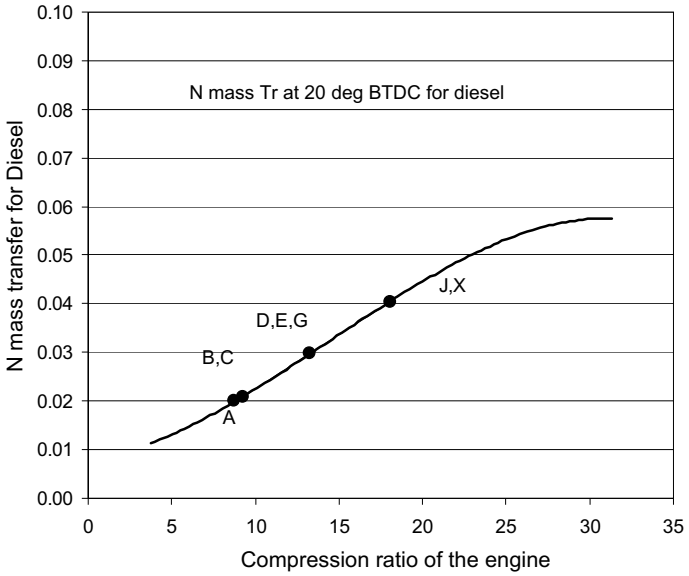

Fig. 3.3 Similarity between bomb and engine experiments

Vaporization Studies

n-Pentane was used because of its low boiling point. The experimental conditions were (*A*, *B*, *C*, *D*, *E*, and *G*) as listed in Table 3.1. Typical interferograms obtained at different instants at experimental condition *E* are shown in Fig. 3.4. Enlarged photographic prints of the interferograms were used for fringe counting, from the periphery of the jet to its axis. The inversion of the fringe count data to yield local refractive index difference $(n_r - n_m)$ relative to the air reference state refractive index n_r, n_m, and the derivation of the local fuel vapour concentration C_f which is

$$C_{f_r} = \frac{\left(\frac{T_\infty}{T_r} - 1\right) - \frac{n_r - n_m}{\rho_\infty K_\infty}}{\left(\frac{M_\infty}{M_f} - 1\right)\frac{(n_r - n_\infty)}{(\rho_\infty K_\infty + 1)} - \frac{T_\infty}{T_r}\left(\frac{K_f}{K_m} - 1\right)} \tag{3.3}$$

follow directly from references [5, 7]. The local temperature T_r can be expressed as:

$$T_r = C_{f_r} T_s + \left(1 - C_{f_r}\right) T_\infty \tag{3.4}$$

Here, T_s is the saturated vapour temperature. For every point r, Eqs. (3.3) and (3.4) were solved using a predictor–corrector iteration procedure to obtain C_{fr} and T_r. Typical contour plots of $C_{f\,r}$ and T_r are shown in Fig. 3.5a, b.

Table 3.1 Experimental conditions, nozzle (single) hole diameter = 0.21 mm

					Bomb conditions			Similar engine conditions 100 mm bore at 20 deg BTDC			
Study code	Fuel	Nozzle opening pressure	Injection quantity /nozzle hole, mm^3	Injection duration, ms	Pressure, bar	Temperature, K	Density, kg/m^3	Pressure, bars	Temperature, K	Density kg/m^3	Compression ratio
A	n-Pentane	110	7	1.2	3	433	2.36	15.0	651	7.87	10
B	n-Pentane	110	7	1.2	3	403	2.54	12.4	618	6.85	9
C	n-Pentane	110	11	1.5	3	403	2.54	12.4	618	6.85	9
D	n-Pentane	110	11	1.5	6	403	5.08	20.0	703	9.72	15
E	n-Pentane	110	7	1.2	6	403	5.08	20.0	703	9.72	15
G	n-Pentane	165	11	1.5	6	403	3.08	20.0	703	9.72	15
J	Diethyl ether*	130	10	1.5	7	723	3.08	25.0	736	12.0	20
K	Diethyl ether*	130	7	1.5	7	723	3.08	25.0	736	12.0	20

1.5% nitromethane is added to reduce delay to 0.75 ms

Fig. 3.4 Interferogram for Data *E*, at 1.5 ms after the start of injection

Combustion Studies

In a real engine, a jet of diesel fuel burns in an atmosphere of varying pressure. In the interferometric technique described earlier, the condition of the surroundings should be the same in the two exposures. Therefore, a constant pressure burning jet was studied. Also, the ignition delay should be of the order of 1 ms as in a real engine. To achieve this, a fuel mixture of diethyl ether and 1.5% nitromethane was added. Initial studies of high-speed movies of a combusting jet confirmed a small ignition delay. Data J and K in Table 3.1 correspond to the combustion studies. Interferograms of the burning jet were analysed as follows.

The bomb reference state condition was considered when the air temperature in the bomb had stabilized before injection. The object state condition was taken at times after ignition delay. Because of the large capacity of the bomb and the small quantity of fuel injected, the pressure change due to combustion was of the order of 0.01-bar.

The value of equivalent diameter d_e is given [1] by

$$d_e = d_0 \left(\frac{\text{density of fuel}}{\text{density of combustion products at flame temperature}} \right)^{\frac{1}{2}} \tag{3.5}$$

To find the temperature using the fringe count data a chart of T, $n-1$, Φ (temperature, refractivity, and equivalence ratio) was prepared (Fig. 3.6) using the following principle [5] With combustion present, in a burning air fuel vapour region at the outer edge of the spray at radius r, the products of combustion are assumed to be in equilibrium. The major species present are CO_2, CO, H_2O, N_2, O_2, and H_2. The reactions [8] considered are

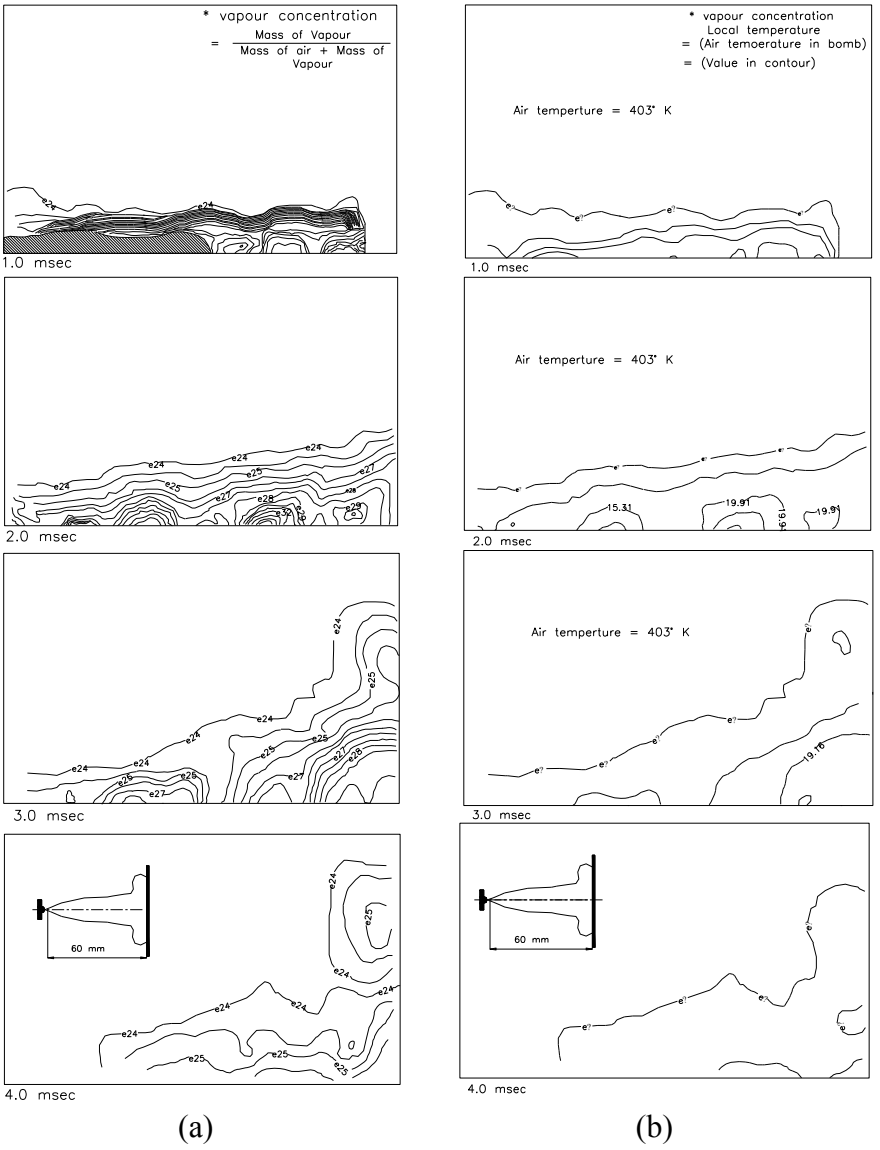

Fig. 3.5 **a** Concentration contours. **b** Concentration contours

$$\begin{aligned} &C_xH_yO_z + q(O_2 + 3.76N_2) \rightarrow uCO_2 + (x-u)CO \\ &+\nu H_2O + \left(\frac{y}{2} - \nu\right)H_2 + \left[q + \frac{1}{2}z - \frac{1}{2}(x+y+\nu)\right]O_2 + 3.76qN_2 \end{aligned} \tag{3.6}$$

$$CO_2 \leftrightarrow CO + O_2 \tag{3.7}$$

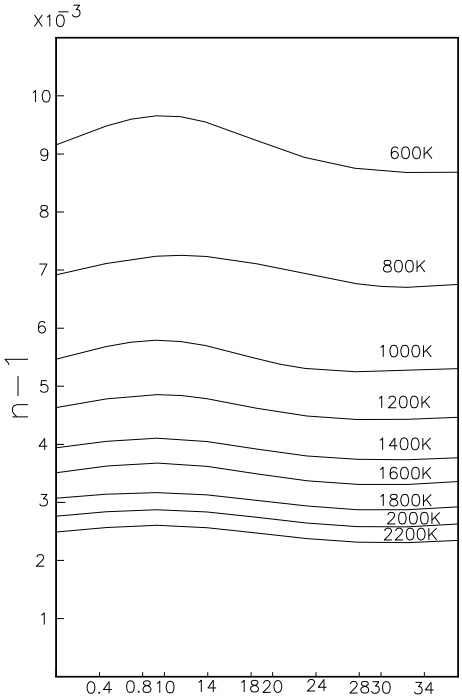

Fig. 3.6 $\Phi, n-1, T$ chart

$$H_2O \leftrightarrow H_2 + \frac{1}{2}O_2$$

In the products of reaction with an equivalence ratio greater than 1.5, CO_2 is absent. Also, beyond the rich limit of combustion (equivalence ratio 3 for diethyl ether), fuel vapour coexists with the products of combustion at the rich limit [2]. For a given equivalence ratio, Φ, temperature, T, and type of fuel using Eqs. (3.6) and (3.7) the concentration $C_{i,r}$, of various species, i, and the density of the products ρ_{rg} can be calculated. The refractive index, n_{r_B} is given by:

$$n_{r_B} = \rho_{r_B} \sum C_{i,r} K_i + 1 \tag{3.7}$$

Here K_i [11] is the Gladstone–Dale constant for a species, i. Thus, a table or a chart of T, $n-1$, Φ (Fig. 3.6) can be prepared. Table 3.1 gives a complete listing of the experimental conditions. It should be noted that the fuel injection—engine scale parameter was approximately satisfied in all tests.

Real Engine Studies

The newly developed phenomenological models were applied to many modern DI diesel engines to predict the rate of heat release and exhaust emissions. Experimental results were also collected from these engines using the experimental set-up compliant with ISO 8178. Then, the predicted and experimental values are compared and analysed to understand the process of combustion and the formation of pollutants. This helped in assessing and improving predictability by the models.

Engines A9 to E10 and A10 to G10, Table 3.2 are of a modern type designed for low emissions of NOx and hydrocarbons. The compression ratio was relatively higher to enable injection delayed with respect to the previous generation of engines to which engine G10 belongs. The decrease in ignition delay in such engines resulted in a lower premixed burning fraction and hence the sharp first peak is missing in the heat release diagrams [4]. These engines used a Bosch jerk-type fuel injection system. To cover a wide range of engines in the study of HC emissions, the engine, E10 used by [4] and engine, H10 (PT-fuel Injection system) used by [12] are also studied using the integrated parameters such as ignition delay, nozzle hole size, and injected quantity.

The cylinder pressure was measured using an uncooled AVL piezoelectric pressure transducer of type GM11D or AVL cooled pressure transducer of type GM12D in engines. Here the length of the duct leading the pressure from the cylinder to the transducer was very short. In the engines was used. The line pressure was measured using a strain gauge-type pressure transducer from AVL of type 31DP2000-2.0, GG0443. The needle lift was measured using by building in a linearly variable differential transformer. The crank angle position was sensed using an angle encoder. The engine is loaded using an eddy current brake. All the transient signals from different transducers and the encoder are fed into an indicating system. Here, there are signal conditioners and amplifiers and a computer to process all the signals for calculating thermodynamics like heat release rate and other details like the duration of injection, ignition delay, and peak values of various pressures.

Injection Characteristics and the Indicated Diagrams

A schematic diagram of the experimental set-up is shown in Fig. 3.7. Further, to filter out the fluctuations in pressure due to physical effects in the cylinder, and the duct leading the pressure to the transducer, a moderate smoothening of the pressure diagram is optionally carried out using the moving average software of the indicating system. However, since the smoothening was done for the 2-degree crank angle the missing of the first peak is more due to higher compression ratio and delayed fuel injection than due to smoothening.

Figure 3.8 shows typical traces of line pressure, cylinder pressure, needle lift, and apparent heat release of the turbocharged engine, B10 at 90% load.

Table 3.2 Specifications of engines used in the book. Number suffix of engine type refers to the chapter

Engine type	Aspiration	Cylinders	Bore, mm	Stroke, mm	Rated speed, rpm/1000	Nozzle holes	Hole diameter, μm	Sac volume, mm^3	Injection pressure press	Injection quantity, mm^3/str	Fuel pump
A6	NA	1	130.0	150.0	1.4	8	–	–	1000	96	–
RE7	NA	4	90.0	94.0	3.5	1	P	–	180	32	A
A8	NA	1	75.0	76.0	2.2	4	220	1.37	500	17	Q
B8	NA	6	100.0	120.0	2.3	4	280	0.30	450	60	E
C8	NA	4	110.0	116.0	2	4	280	1.37	550	77	E
D8	NA	3	100.0	110.0	2	5	250	1.37	450	36	E
E8	NA	1	68.0	76.0	3	1	P	–	180	14	A
F8	NA	1	80.0	95.0	1.5	3	286	1.69	200	26	A
G8	NA	4	100.0	120.0	2	4	280	0.30	400	50	E
H8	TA	9	280.0	290.0	1	9	450	m	1000	2250	A
J8	TA	6	175.0	220.0	1	8	330	m	800	570	Z
K8	NA	1	80.0	110.0	1.5	3	286	1.69	300	29	A
L8	NA	4	100.0	120.0	1.5	4	280	0.30	400	48	E
M8	NA	3	110.0	116.0	2	5	280	0.30	450	44	E
N8	NA	1	87.5	110.0	1.5	3	286	1.69	200	35	A
R	NA	1	88.0	85.5	2.4	5	220	–	–	–	A
S1	NA	1	88.0	85.5	2.4	5	220	–	–	–	A
S2	NA	1	88.0	85.5	2.4	5	220	–	–	–	A
A9	NA	4	105.0	120.0	2.7	5	200	1.37	800	55	V
B9	T	4	105.0	120.0	2.5	5	240	1.37	600	75	E

(continued)

Table 3.2 (continued)

Engine type	Aspiration	Cylinders	Bore, mm	Stroke, mm	Rated speed, rpm/1000	Nozzle holes	Hole diameter, µm	Sac volume, mm^3	Injection pressure press	Injection quantity, mm^3/str	Fuel pump
C9	TA	6	175.0	220.0	1.5	8	330	m	800	600	Z
D9	TA	8	280.0	320.0	0.8	8	550	m	700	3200	A
E9	TA	1	124.0	165.0	1	8	240	–	800	255	C
A10	NA	4	105.0	120.0	2.2	5	200	0.59	680	60	E
C10	TA	4	110.0	116.0	2.2	5	200	1.37	650	65	E
D10	TA	9	280.0	320.0	1	8	550	m	1000	2350	A
E10	TA	6	118.0	135.0	1.5	4	350	0.60	600	105	E
F10	NA	6	100.0	120.0	2.5	4	290	0.59	600	57	E
G10	TA	6	102.0	120.0	2.5	6	260	1.37	600	85	E
H10	NA	1	140.0	152.0	1.5	8	203	0.62	p	p	T
B10	T	4	105.0	120.0	2.2	5	240	0.38	485	75	E
A11	NA	1	82.5	114.3	1.3	–	–	–	–	–	–
C12	NA	4	105.0	120.0	1.5	5	200	0.59	600	58	E
D12	T	4	105.0	120.0	1.5	5	240	0.38	650	88	E
E12	NA	6	100.0	120.0	1.5	5	180	z	550	57	E
F12	NA	1	124.0	130.0	2.3	5	226	z	675	80	F
G12	T	4	105.0	125.0	2.5	5	240	0.38	700	72	E
H12	TA	4	105.0	125.0	2.5	5	240	0.38	725	75	E
I12	TA	4	105.0	125.0	2.5	5	250	0.38	725	75	E
K12	TA	4	105.0	120.0	1.5	5	240	0.38	525	112	E

(continued)

Table 3.2 (continued)

Engine type	Aspiration	Cylinders	Bore, mm	Stroke, mm	Rated speed, rpm/1000	Nozzle holes	Hole diameter, μm	Sac volume, mm^3	Injection pressure press	Injection quantity, mm^3/str	Fuel pump
L12	TA	6	104.0	113.0	2.4	5	225	z	463	61	V
M12	TA	6	104.0	113.0	2.4	5	228	z	775	76	V
N12	TA	6	104.0	113.0	2.4	5	228	z	834	82	V
O12	TA	6	107.3	121.0	2.4	6	175	z	802	64	V
P12	TA	6	107.3	121.0	2.4	6	190	z	812	76	V
L16	TA	1	137.2	165.1	2.1	6	158	m	1500	114	C
M16	TA	1	82.0	90.4	4	7	141	m	860	16	C
S16	TA	1	82.0	90.4	4	8	133	m	1600	22	C
H16	TA	1	137.2	165.1	2.1	8	217	m	1600	274	C

Fuel timing, deg bTDC	Combustion chamber (Fig. no)	Piston cavity diameter, mm	Impingement distance	Boost ratio	Swirl number	No. of valves	Emission norms	Compression ratio	Bmep, bar
9	–	88	45	2.9	–	4	–	17.3	19.0
	SC	–	–	1.0	–	2	–	22.0	5.1
	8.7a	–	–	1.0	2.70	2	–	18.0	6.1
32	8.7b	55	30	1.0	2.70	2	–	17.5	7.8
28	8.7c	74	42	1.8	2.20	2	–	17.5	9.2
R	8.7d	60	33	1.0	2.50	2	–	17.5	5.6
	S	–	–	1.0	–	2	–	19.0	5.4
24	8.7c	45	24	1.0	3.30	2	–	17.0	6.3

(continued)

Table 3.2 (continued)

Fuel timing, deg bTDC	Combustion chamber (Fig. no)	Piston cavity diameter, mm	Impingement distance	Boost ratio	Swirl number	No. of valves	Emission norms	Compression ratio	Bmep, bar
28	8.7b	55	–	1.0	2.70	2	–	17.5	7.2
	9.9	220	120	4.0	0.80	4	–	12.0	20.2
	9.9	130	70	2.5	1.00	4	–	13.5	17.0
	8.7c	45	24	1.0	3.30	2	–	17.0	6.3
20	8.7b	55	30	1.0	2.70	2	–	17.5	7.2
24	8.7c	74	42	1.0	1.80	2	–	17.5	5.6
	8.7c	48	25	1.0	3.30	2	–	17.0	6.3
	8.1	44	23	1.0	3.30	2	e	17.0	–
	8.1	44	23	1.0	3.30	2	e	17.0	–
	8.1	44	23	1.0	3.30	2	e	17.0	–
Q	9.9	60	33	1.0	2.10	2	–	18.0	7.0
T	9.9	62	36	1.8	2.10	2	–	18.0	9.5
	9.9	130	70	2.5	1.00	4	–	14.5	17.0
	9.9	220	120	4.0	0.80	4	–	11.0	24.4
	–	100	55	2.5	1.80	4	–	18.0	22.0
T	9.9	60	33	1.0	2.10	2	–	18.0	7.5
28	8.7c	74	42	1.5	1.80	2	–	17.0	8.3
	9.9	220	120	4.0	0.80	4	–	12.0	18.3
18	-	63	34	2.0	2.20	2	–	17.0	10.2
32	8.7b	55	30	1.0	2.70	2	–	17.5	7.1

(continued)

Table 3.2 (continued)

Fuel timing, deg bTDC	Combustion chamber (Fig. no)	Piston cavity diameter, mm	Impingement distance	Boost ratio	Swirl number	No. of valves	Emission norms	Compression ratio	Bmep, bar
	8.7b	56	30	1.8	–	2	–	17.5	9.8
	–	–		1.0	–	2	e	14.1	–
T	9.9, 12.3	62	36	2.0	2.50	2	TI	18.0	10.3
35*	SI	–	–	–	–	–	e	7.0	3.8**
18	12.3	60	33	1.0	2.50	2	TI	18.0	8.1
22	12.3	62	36	2.0	2.50	2	TI	18.0	12.0
10	12.3	55	30	1.0	2.70	2	TII	17.5	8.1
11	12.3	74	40	1.0	2.70	2	TII	18.0	6.4
22	12.3	62	36	2.0	2.50	2	TI	18.0	8.7
22	12.3	62	36	2.1	2.50	2	TI	18.0	9.1
22	12.3	62	36	2.3	2.50	2	TI	18.0	9.1
15	12.3	62	36	2.3	2.50	2	TI	18.0	15.2
12	12.3	62	27	2.1	2.30	2	EII	17.5	8.6
12	12.3	62	27	1.9	2.30	2	EII	17.5	10.8
12	12.3	62	27	1.9	2.30	2	EII	17.5	11.7
11	12.3	64	28	2.0	2.50	2	EII	17.5	7.8
11	12.3	64	28	2.2	2.50	2	EII	17.5	9.2
X	16.13	98	e	e	0.50	4	e	15.5	–
Y	16.1	46	e	e	2.2	4	e	16.6	–
Z	16.13	51.3	e	e	vs	4	e	14.3	–

(continued)

Table 3.2 (continued)

Fuel timing, deg bTDC	Combustion chamber (Fig. no)	Piston cavity diameter, mm	Impingement distance	Boost ratio	Swirl number	No. of valves	Emission norms	Compression ratio	Bmep, bar
W	16.13	97.8	e	e	0.5	4	e	16.1	–

Varied swirl vs: 2.2–5.6
Emission norms: EII—Euro-2 on road; TI—US Tier-1 off-road; TII—US Tier-2 off-road
Engine: e—Experimental engine
Fuel pump: V—Rotary distributor type pump, VE; E—inline-block pump, PE-A; Q—Individual fuel pump submerged in the crankcase, PF-Q; A—Individual fuel pump above the crankcase, PF-A; Z—large Individual fuel pump above the crankcase, PF-Z; C—common rail system, CRS; T—Cummins PT injection system
Nozzle: m—mini sac; z—zero sac, with 10% hydro eroded holes; P—Pintle type
Fuel timing: x—−35 to −5; y—−39 to −21; z—−35 to −5; w—−10 to 10; t—15–22; q—10–12; r—13–20; *—spark ignition timing
Valves: 4—For engine typesH8, J8, C9, D9, D10; 2—rest of the engines
Aspiration: NA—Naturally aspirated; T—Turbocharged; TA—Turbocharged aftercooled
Combustion chamber: SC—Prechamber type with swirl chamber, IDI; S—Saurer combustion chamber in the piston with pintle nozzle; SI—Spark Ignition; others—direct injection type with a combustion chamber in the piston
General: -----Not relevant for analysis or not applicable; p—variable; **—imep

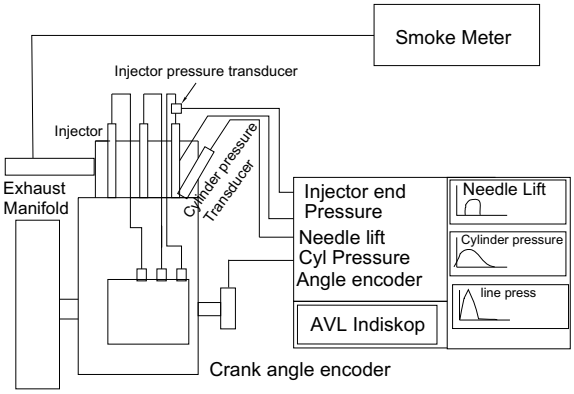

Fig. 3.7 Experimental set-up

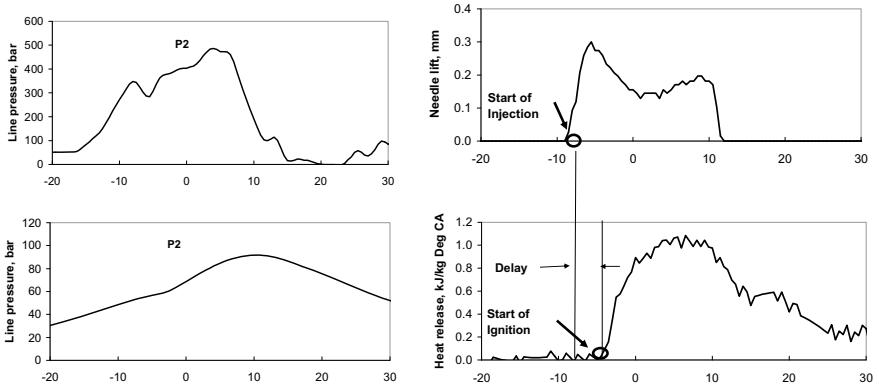

Fig. 3.8 Injector and in-cylinder characteristics of a turbocharged engine, B10 at 90% load

Exhaust Raw Gas Analysis

The gaseous emissions, smoke, and particulate sampling probes were fitted at least 0.5 m or 3 times the diameter of the exhaust pipe to ensure an exhaust gas temperature of at least 343 K (70 °C) at the probe. In the case of a multi-cylinder engine with a branched exhaust manifold, the inlet of the probe was located sufficiently far downstream to ensure that the sample is representative of the average exhaust emissions from all cylinders. The test set-up meets the requirements of ISO 8178 for intake air, fuel, and emission measurements. Commercially available gas analysers were used.

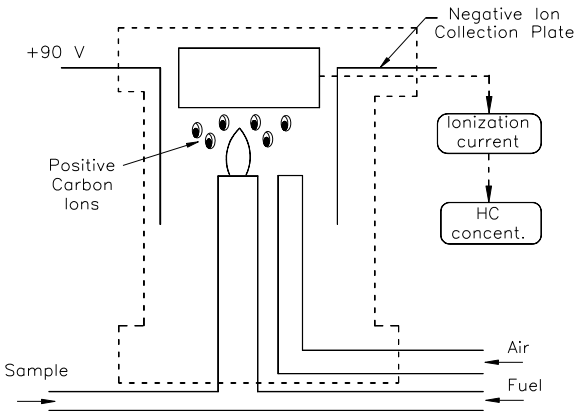

Fig. 3.9 Flame ionization detector for HC measurement

Hydrocarbon (HC) Measurement

Gaseous HC emissions from diesel engines are measured using a hot particulate filter at 190 °C and a heated FID. Thus, the HC constituents varying from methane to the heaviest hydrocarbons remain in the vapour phase in the heated sampling line which is also maintained at about 190 °C. Any hydrocarbons heavier than this are therefore condensed and with the solid phase soot, are filtered from the exhaust gas stream upstream of the detector. Figure 3.9 shows the heated Flame ionization detector used for the analysis of HC emission. The flame in an FID instrument is usually generated by combusting a 40% H_2/60% He mixture in air. Any oxygen present in the sample influences the FID analyser. To minimize this effect, zero and reference gases are used with O_2 content close to that of the gas to be measured. FID instruments are unaffected by the water vapour in the analysed gas.

Oxides of Nitrogen (NO_x) Measurement

$$NO + O_3 \rightarrow NO_2^* + O_2$$

where NO_2* represents the excited state molecule.

Only about 20% of the NO_2 that is formed is in the excited state. This NO_2* reverts to the ground state while emitting electromagnetic radiation.

$$NO_2^* \rightarrow NO_2 + h\nu$$

The $h\nu$ represents the radiated electromagnetic emission, which is in the wavelength range between 600 and 3000 nm, with an intensity maximum at approximately 1200 nm. The light emission is filtered to eliminate interference from other gases, such as CO, SO_2, and unsaturated hydrocarbons. This chemiluminescence signal is detected photoelectrically by a photomultiplier tube. This signal is proportional to

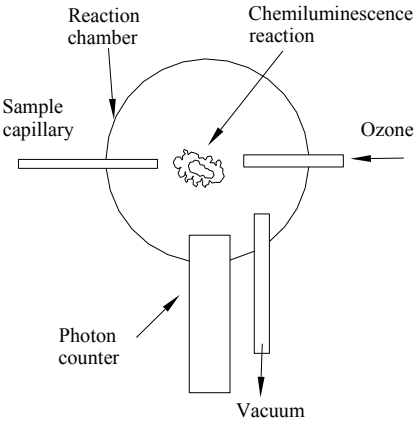

Fig. 3.10 Principle of chemiluminescence

the NO concentration in the sample gas. When NO_x measurement is to be done, the exhaust sample is first rooted through a converter heated to a specific temperature. The temperature of the converter is typically between 350 and 650 °C. The converter reduces NO_2 present in the exhaust to NO. Then the exhaust containing only NO is rooted in the reaction chamber, and measurement is done as explained earlier. Figure 3.10 shows the schematic diagram of a typical NO_x analyser used for the measurement of emissions.

Smoke Evaluation

Smoke is evaluated by using the opacity principle as well as the filtering method. In the current study, AVL Opacimeter-439 and Bosch smoke gun were used to collect smoke data. Opacimeter measures the opacity of a sample of the exhaust gas extracted from the exhaust pipe and passed through a heated measurement chamber. Since condensation of hydrocarbon and water is avoided, due to heating of the exhaust the measured opacity is only by black carbon. Figure 3.11 illustrates the operating principle, which involves measuring the opacity of a portion of exhaust gas continuously flowing through the sample tube. Zero reference is achieved by a switching arrangement utilizing a second tube containing clean air, free of smoke. An internal electric fan purges the instrument case and clears soot from the light source and photocell. The calibrated ammeter reads in units from 0 (clear) to 100 (opaque). Since the length of the smoke tube is fixed and known, these readings can be related to measurements made with other instruments using the Beer–Lambert law. The smoke reading is not affected by the exhaust pipe diameter. Transient response is limited to the time required to fill the sampling tube.

Bosch smoke gun, on the other hand, works on the filtering principle wherein soot particles are collected on a filter medium from a known volume of the exhaust. The

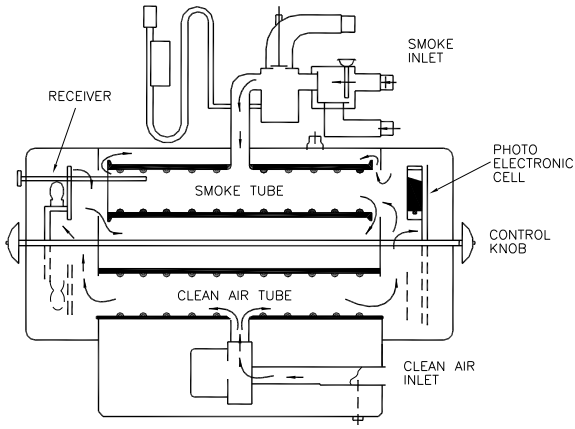

Fig. 3.11 Operating principle opacity meter

filter is evaluated by comparison with standards using the photoelectric reflectance method. Both the methods mentioned above are partial flow systems having a maximum error of 0.2 BSU, which is the uncertainty in the experiments. The average of three readings was acquired for exhaust smoke data. An example of the filtering type system is a portable Bosch smoke gun shown in Fig. 3.12. A spring-operated sampling pump draws a fixed volume of exhaust gas from the exhaust stream through a controlled density paper filter disc.

Soot particles from the sample are deposited on the filter disc, causing it to darken in proportion to soot particle concentration. A separate 110 V AC or battery-powered photoelectric device measures the light reflected from the darkened filter disc. The readout is calibrated in 0 to 10 Bosch Smoke Units (BSU). Figure 3.13 shows the operating principle of the photoelectric evaluation system. The calibration of the photoelectric readout consists of zero adjustment with the detector exposed to a clean filter and full-scale reading with the switched off.

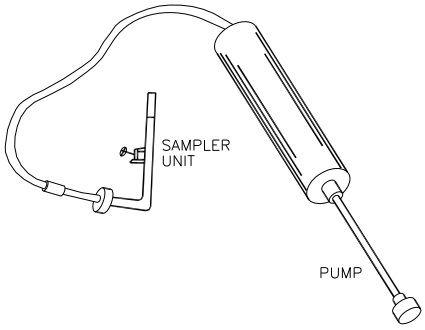

Fig. 3.12 Portable Bosch smoke gun

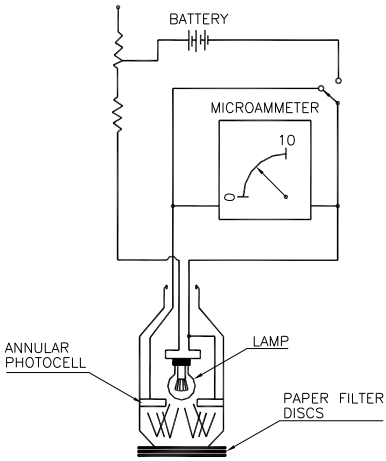

Fig. 3.13 Photoelectric evaluation system

References

1. Beer JM, Chigier NA (1972) Combustion aerodynamics. Applied Science Publishers
2. Bradshaw P, Cebeci T, Whitelaw JH (1981) Eng calculations for turbulence flow. Academic Press
3. Chiu WS (1973) The experimental set-up for basic diesel spray mixing and combustion studies. Cummins Tech Report doc 3534
4. Chmela FG, Orthaber GC (1986) Rate of heat release prediction for a direct injection diesel engine based on purely mixing controlled combustion. SAE 99010186
5. Dent JC (1980) Potential applications of holographic interferometry to engine combustion. In: Combustion modelling in reciprocating engines. Plenum, New York
6. Dent JC, Keightley JD, DeBoer CD (1977) Application of interferometry to air-fuel measurements. SAE 770825
7. Lakshminarayanan PA, Dent JC (1983) Interferometric studies of vapourising and combusting sprays. SAE 830244
8. Martin MK, Heywood JB (1977) Approximate relationship for the thermodynamic properties of hydrocarbon-air combustion products. Combus Sci Technol
9. Matulka RD (1970) The application of holographic interferometry to the determination of asymmetric 3-dimensional density fields in free jet flows. Ph.D. thesis, US Naval Postgraduate School
10. Shahed SM, Chiu WS, Lyn WT (1975) A mathematical model of diesel combustion. Proc. IMechE C94/75
11. Tennent RM (1971) Science data book. Oliver and Boyd
12. Yu RC, Wong VW, Shahed SM (1980) Sources of hydrocarbon emissions from direct injection diesel engines. SAE 800048

Chapter 4
Turbulent Structure of the Diesel Spray

Nomenclature

A_f	= 0.5 (experimental), the proportionality constant of Ricou-Spalding relation of the ratio of air entrainment rate to fuel injection rate with the ratio of axial distance to equivalence diameter of the nozzle hole whereas proposed by Spalding was 0.32 (−)
A_w	similar to the A_f proposed by Ricou and Spalding for free spray, a constant for spray along the wall, 0.95 (−)
C	concentration (−)
C_f	concentration of fuel (−)
$C_{f_{\max}}$	concentration with axial distance, x (−)
$C_{R,L.}$	refers to the mixture fraction at rich limit combustion (−)
d_e	orifice equivalent diameter and for the non-burning jet is defined as d_o × [density of injected fuel/density of air in Bomb]$^{1/2}$ (m)
de	equivalent diameter of the nozzle hole (m)
H	distance from the nozzle hole to the plate on which the spray impinges at a right angle (normally) (m)
K_b	combined Gladstone-Dale constant for burned products (m^3/kg)
m	mass entrained (kg)
m'_a and m'_o	rate of air mass entrained into the jet, and the rate of mass flow of the jet fluid through the orifice respectively (kg/s)
M_b	average molecular weight of the products of combustion at the rich limit (kg/kmol)
M_f	molecular weight of fuel (kg/kmol)
n	refractive index (−)
p	pressure (Pa)
r	radius at any x position from the nozzle hole (m)
$R_{0.5}$	radius at which the concentration has half its maximum value (m)
$r_{0.5}$	radius at which concentration of fuel drops 50%, used for non-dimensionalizing r (m)

P. A. Lakshminarayanan and Y. V. Aghav, *Modelling Diesel Combustion*,
Mechanical Engineering Series, https://doi.org/10.1007/978-981-16-6742-8_4

S	penetration along the wall (m)
s	distance of the wall jet from the point of impingement (m)
t	time (s)
T	temperature (K)
t_{imp}	time after jet impingement (s)
t_{inj}	injection period (s)
U_j	velocity of fuel at the nozzle hole (m/s)
w	radius of the free jet at $x = H$ (m)
x	axial distance in the free spray along the centre line of the nozzle hole from the nozzle hole (m)
x_o	distance from the orifice beyond which $C_{f_{\max}}$ with the axial position is decaying (m)
y	distance perpendicular to the impingement plate (m)
y	height of wall jet (m)
y	height in the free spray at a radial distance of s from the point of impingement (m)
$y_{0.5}$	height at which concentration of fuel drops 50%, used for non-dimensionalizing y (m)
z	constant of proportionality in equation (4–7) =0.75
δ	location of the virtual source inside the nozzle at $\delta/d_e = 2.3$ (m)
$\theta_{\text{cone}}/2$	half jet angle, tan(cone angle/2) = 0.22 (°)
ρ_a	density of air (kg/m^3)
ρ_f	density of fuel (kg/m^3)
Φ	mixture fraction (−)

Subscripts

∞	surroundings
r	considered a point in the jet
f	fuel vapour
a	air
f	free jet
f	fuel
imp	impingement time
inj	end of injection
max	maximum of the variation, for example, of the concentration profile of fuel over a section at an axial distance x or distance along the wall, s
r	any point in burning spray
w	wall jet

Superscripts

·	rate with respect to time
’	rate with respect to time

Combustion in a diesel engine involves the transient injection of a finely atomized liquid fuel into the air at high temperature and pressure. Auto-ignition of these regions and progressive diffusive burning of the remainder of the spray follow rapid vaporization at the edges of the spray.

The ability to study the processes of vaporization and combustion in the injected fuel spray to obtain quantitative information on the spatial and temporal distribution of air, fuel vapour, combustion products, and the temperature is of importance in gaining a better understanding of these basic processes and in providing data for computer modelling and engine development studies [27]. Based on the study in a bomb [8, 13], a full description of the penetration of the spray when it is free, and later when it impinges on the wall and finally detaches from the nozzle tip, is made. The distribution of concentration of fuel vapour in the free and wall jets and description of the liquid core [18] and additionally, the flame structure of a transient burning diesel spray are described.

Vaporizing Spray

Free Jet Region

The free portion of the jet was nearly conical, subtending a half cone angle of approximately 13°, at a virtual source lying upstream of the orifice. To establish the similarity characteristics of the jet vapour concentration profiles, the ratio of the concentration at any radial position (for a given axial distance from the jet orifice) to the maximum concentration at the same axial position was plotted against the radius, non-dimensionalized with respect to the radius at which the concentration has half its maximum value $R_{0.5}$ Fig. 4.1.

The variation of $R_{0.5}$ was plotted against axial distance from the orifice, x—Fig. 4.2. The results show considerable scatter particularly after the termination of injection. To completely describe the jet behaviour, we need to know the decay in concentration with axial distance, x. The literature [29] for steady-state jets suggests

$$\frac{1}{C_{f_{\max}}} = \text{const}\left(\frac{x}{d_e}\right) \tag{4.1}$$

where d_e is the orifice equivalent diameter, and for the non-burning jet, it is defined as $d_o \times$ [Density of injected fuel/Density of air in Bomb]$^{1/2}$. Equation (4.1) is valid for

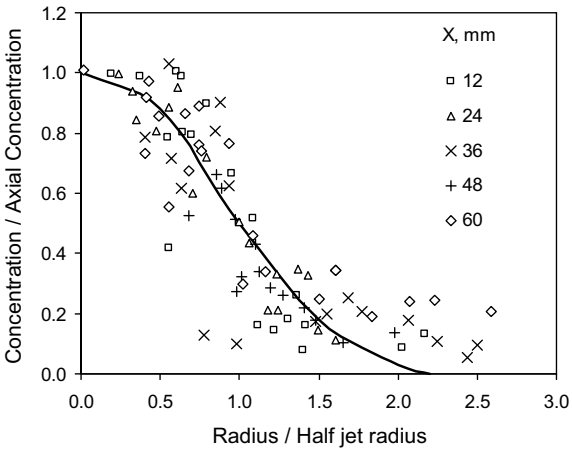

Fig. 4.1 Radial variation of concentration for a typical vaporizing free jet (Data *B*)

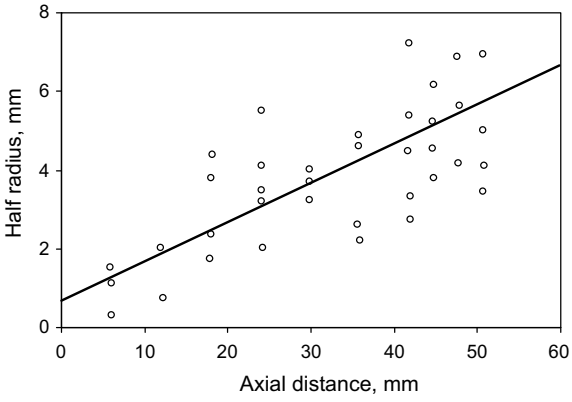

Fig. 4.2 Axial variation of half radius for a typical vaporizing jet (Data *B*)

the region beyond the liquid (potential) core of the jet, which extends from between 4 and 6 times (x/d_e) from the nozzle exit plane.

The vaporization history during the injection process is built up from a sequence of individual interferograms, which represent particular instants in time of the jet's development, as shown in Fig. 4.4 In analysing the variation of $C_{f_{\max}}$ with x/d_e from individual interferograms, it was found as expected that vaporization and hence $C_{f_{\max}}$ increased progressively with distance, x/d_e from the nozzle orifice. This variation was found to be nearly linear with (x/d_e) and intersected the curve described by Eq. (4.1) at a value of x/d_e

$$\frac{x}{d_e} = 7.5 \text{ for time } t < t_{\text{inj}} \tag{4.2}$$

where t_{inj} = The injection period.

x_o defines the distance from the orifice beyond which the variation of $C_{f_{max}}$ with the axial position, x follows Eq. (4.1).

When $t > t_{inj}$, *the* injection has ceased, yet a jet-like structure is observed as shown in Fig. 4.4. It would be expected that under these conditions, $C_{f_{max}}$ would be lower than indicated by Eq. (4.1). In fact, analysis of interferograms showed that $C_{f_{max}}$ follows a linear variation with (x/d_e) when $t > t_{inj}$ and intersects the steady-state $C_{f_{max}}$ curve (Eq. (4.1)) at values of (x_o/d_e) progressively larger than 7.5.

A schematic summarizing the probable behaviour of the transient vaporizing jet is shown in Fig. 4.3. From Fig. 4.3, the transient evaporating fuel injection process can be considered as the introduction of successive packets of fuel along a steam line coincident with the jet axis. Each packet is made up of many elemental sub-packets. If it is assumed that the injection period is 5 Δt say, then 0, 1, 2, …, 5 in Fig. 4.3a represent the distribution of mixture packets injected at times 0, Δt, $2\Delta t$, …, $5\Delta t$. Because of shear and turbulent diffusion, the sub-packets and the vaporizing droplets and vapour have the distribution as shown in Fig. 4.3a. Packet 4 say, had at $t - \Delta t$, the same state as packet 5 at t. The change in concentration of vapour in packet 4 in the time interval Δt from $t - \Delta t$ to t is due to the combined effects of

- Dilution due to entrained air (B).
- Vaporization of liquid (C).

The time history of packet 4 between $t - \Delta t$ and t is shown by ABC in Fig. 4.3a. Point 3 on Fig. 4.3a represents the packet with the maximum vapour concentration.

For instants in time greater than the injection period, $(t > 5\Delta t)$ represented schematically in Fig. 4.3b. While the jet-like structure is still maintained, turbulent mixing occurs entraining air into the jet-like plume, but packets of fuel are not replenished by the nozzle. Therefore, regions near the nozzle tip will be leaner than at the instant injection was complete $(5\Delta t)$. Sub-packets on the centreline will still

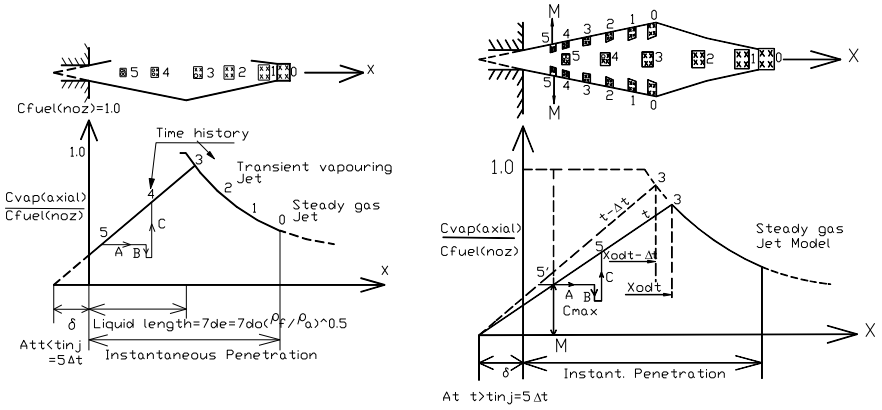

Fig. 4.3 Scheme of Jet detachment and vaporization

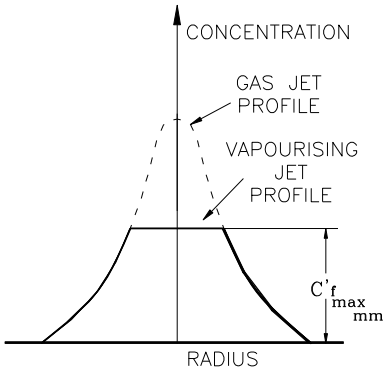

Fig. 4.4 Radial profile of concentration in a vaporzing jet

move downstream at a faster rate than those near the edges of the plume. Furthermore, no appreciable increase in jet width is observed. Therefore, the concentration profile across the plume near the nozzle tip is likely to be very flat in the central regions as shown in Fig. 4.4.

The concentration at $6\Delta t$ of the central region of the plume at plane MM is $C_{f_{\max},M}$ and is shown in Fig. 4.3b. Figure 4.5 is a plot of the experimental data. Projection of the linear variation of $C_{f_{\max}}$ with x/d_e to a common origin yields the virtual source of the nozzle, at a distance, δ from the exit plane of the orifice. The decrease in $C_{f_{\max}}$ and jet centreline velocity $U_{C.L}$ following the end of injection will be governed by equations having the form of Eq. (4.1). The variation of x/d_e will follow the penetration relationship derived in reference [10] and is given by

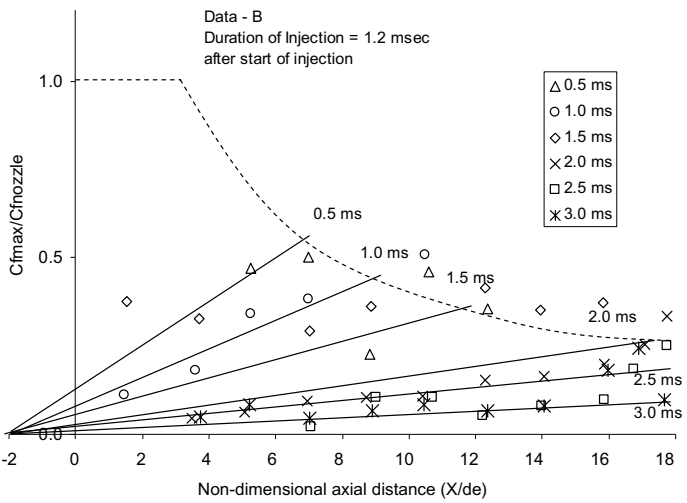

Fig. 4.5 Axial decay of concentration, after the end of injection

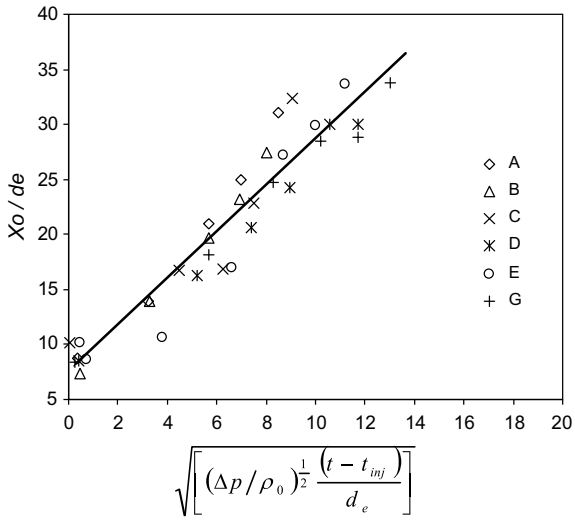

Fig. 4.6 Jet detachment studies

$$\frac{x_0}{d_e} \propto \sqrt{\left(\frac{\Delta p}{\rho_0}\right)^{\frac{1}{2}} \frac{(t - t_{\text{inj}})}{d_e}} \tag{4.3}$$

Figure 4.6 is a plot of experimental data using Eq. (4.3) with the assumption of constant fuel density (ρ_f). The intercept gives the characteristic value of $x_o/d_e = 7.5$ for the transient vaporizing fuel spray during the period of injection. From the foregoing discussion, the vapour concentration at a particular instant and any location within the injected spray can be determined as follows.

Equation -4

$$\text{Half jet angle} \tan(\text{cone angle}/2) = 0.22.$$

$$\text{Variation of } x_0 : \frac{x_0}{d_e} = 7.5 + 1.71\sqrt{\left(\frac{\Delta p}{\rho_l}\right)^{0.5} \frac{(t - t_{\text{inj}})}{d_e}}.$$

$$\text{Virtual source, } \delta \text{is given by} \frac{\delta}{d_e} = 2.3$$

Variation of $C_{f_{\max}}$ (Fig. 4.13)

$$\text{If} \frac{x}{d_e} > \frac{x_0}{d_e}, C_{f_{\max}}(x) = 5.2 C_{f_{\max}}(x_0)\left[\frac{d_e}{x + \delta}\right]$$

$$\text{If} \frac{x}{d_e} < \frac{x_0}{d_e}, C_{f_{\max}}(x) = C_{f_{\max}}(x_0)\left[\frac{x + \delta}{x_0 + \delta}\right],$$

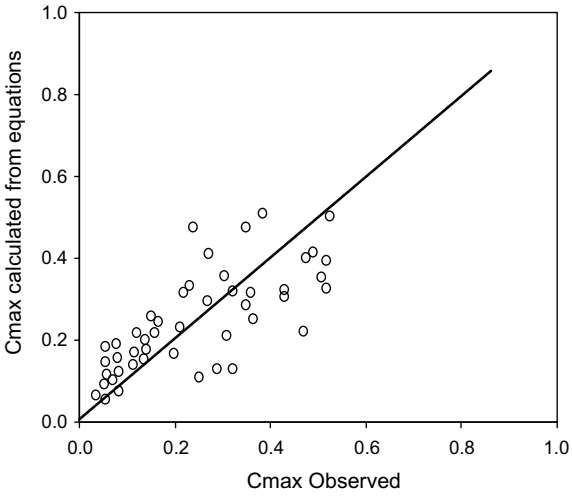

Fig. 4.7 Axial concentration in free jet (Data B)

Variation of C_f with radius, r and axial distance, x (Fig. 4.14)

$$\text{For} \frac{x}{d_e} > \frac{x_0}{d_e}$$

$$C_f(r, x) = C_{f_{\max}}(x) \exp\left[-203\left(\frac{r}{x+\delta}\right)^{2.5}\right] \tag{4.4}$$

or $= C'_{f_{\max}}$ whichever is smaller (Fig. 4.4).

The variation between computed results using the set of Eqs. (4.4) to evaluate $C_{f_{\max}}(x)$ and C_f (r, x) and experimental data are shown in Figs. 4.7, 4.13 and 4.14 respectively.

Wall Jet Region

Figure 4.15 shows a schematic of the wall jet and the notation used. Experimental data for the variation of C_f $(y, s)/C_{f_{\max}}(s)$ with $(y/y_{0.5})$ is shown in Fig. 4.8, where $y_{0.5}$ is the distance at which the vapour concentration is half its maximum value. Figure 4.9 shows the variation of y with the thickness (y) of the wall jet, as obtained from the experiment. The variation of $C_{f_{\max}}$ with distance, s along the wall was found to follow a hyperbolic relationship approximately Fig. 4.10.

The following relationships were established for the wall jet.

For $S > 0.2(x+\delta)\text{and}(x+\delta) > 0.9(H+\delta)$

$$C_{f_{w(\max)}} = 0.5\frac{d_e}{s} \tag{4.5}$$

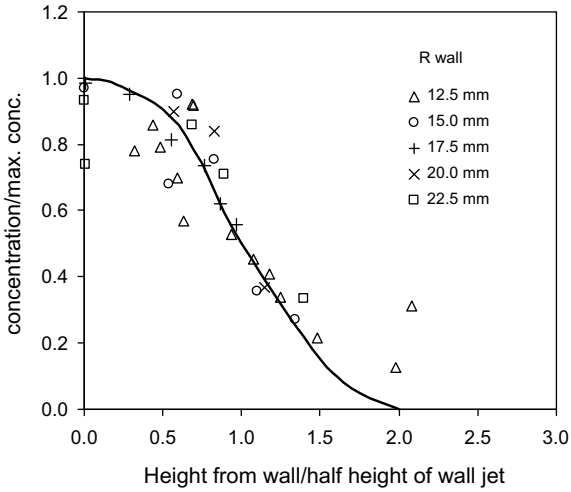

Fig. 4.8 Variation of concentration at any radius of wall jet (Data B)

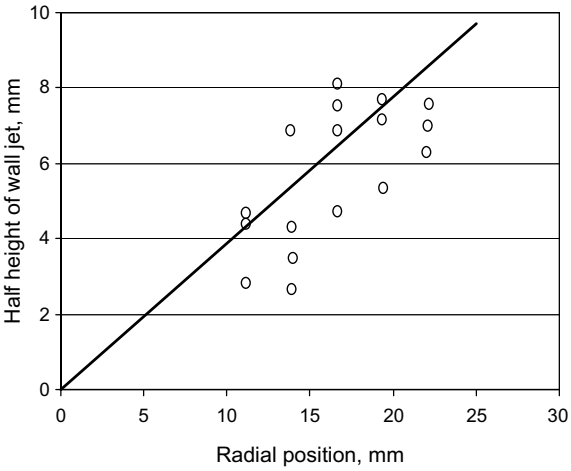

Fig. 4.9 Variation of the height of wall jet (Data C)

$$C_{f_{w,y}} = C_{f_{\max}} \exp\left[-16.5\left(\frac{y}{s}\right)^{2.9}\right]$$

Figures 4.11 and 4.12 show the comparison between calculated and experimental values of $C_{f_{w(\max)}}$ and $C_{f_{w,y}}$, respectively.

Using Eqs. (4.4) and (4.5) and a modified value of d_e, the values of mixture fraction during combustion were calculated at every point in the jet. Justification for use of Eqs. (4.4) and (4.5) derived from experiments with Pentane, for prediction of mixture fraction of diethyl ether, can be made on the basis that the equations are non-dimensional. This is illustrated in Figs. 4.13 and 4.14 where the comparison of results obtained with Eqs. (4.4) and (4.5) in this study is plotted with results

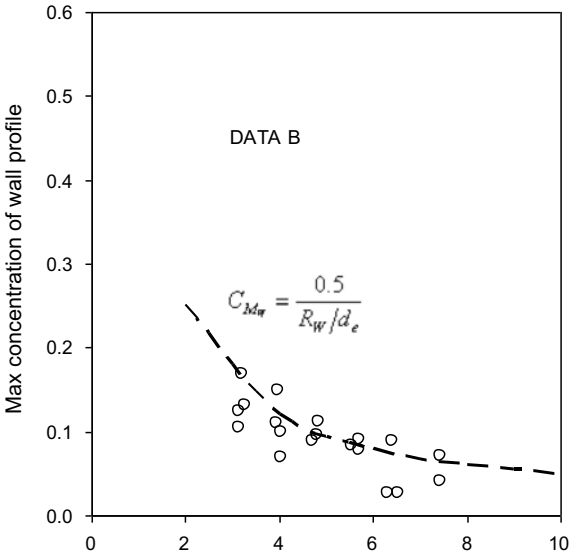

Fig. 4.10 Maximum concentrations in the wall jet along the non-dimensional length along the all

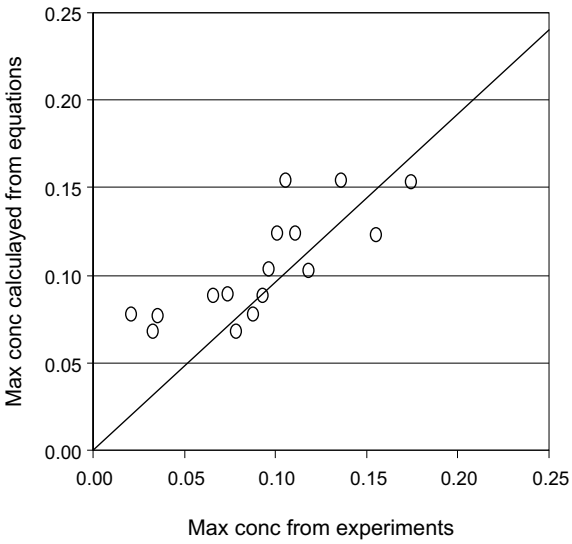

Fig. 4.11 Comparison of maximum concentration calculated using Eq. 8 and experiments for a typical wall jet (Data B)

obtained by Steward and Guruz [29] for compressed air jets with CO_2 tracer. In the transition region where the jet commences spreading into a wall jet flow (Fig. 4.15), the concentration in the jet can be reasonably described using the expressions derived for a free jet, Eq. (4.4).

On completion of the injection, the Eq. (4.5) slightly overestimates the actual concentrations. With the limited experimental data, an explanation can be provided using a diagram similar to Fig. 4.3b. The point which separates the hyperbolic curve

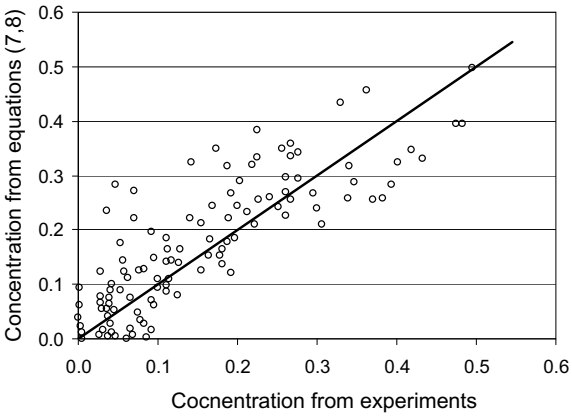

Fig. 4.12 Comparison of the calculated concentration of many vaporizing jets (free and wall) at many points with the values observed (Data B)

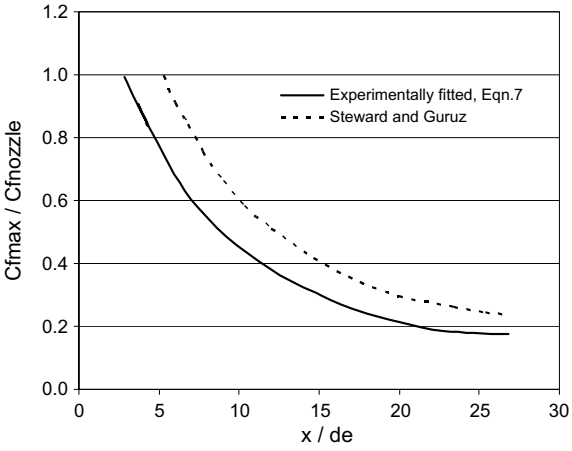

Fig. 4.13 Comparison of axial concentration decay of a transient and a steady jet

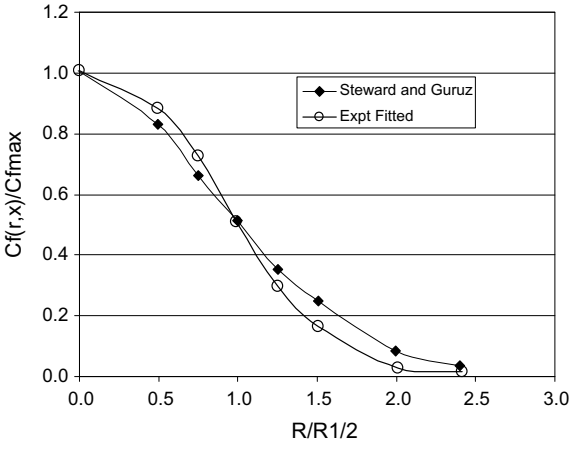

Fig. 4.14 Comparison of radial concentration profiles (fitted from experiments, Steward and Guruz)

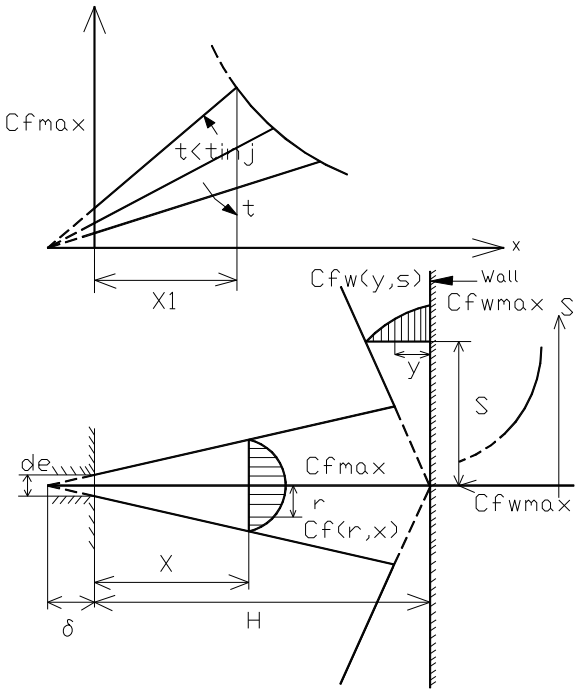

Fig. 4.15 Notations used in the text

(representing the steady-state behaviour of the wall jet) and the straight line (representing the transition developing phase of the wall jet flow) moves continuously away from the stagnation point with time. Extending the argument presented for the case of detaching free jets, the maximum concentration along the radius, *s* (Fig. 4.15) falls approximately on a straight line joining the maximum concentrations at the impingement point and the point separating the steady and transition portions of the wall jet. As the difference between the two values is not large, the assumption that the separating point lies on the radius where the steady wall jet maximum concentration is equal to the concentration at the point of impingement produced reasonable results, for the present set of conditions.

Jet Penetration and Entrainment of Air

The penetration of the jet with time and the rate of air entrainment into it are two important characteristics that need to be known. Comparison of experimental data on jet penetration was made with the relationship obtained by Dent [10], and the results shown in Fig. 4.16, where agreement is seen to be reasonable. The penetration of the wall jet was investigated similarly and is plotted against

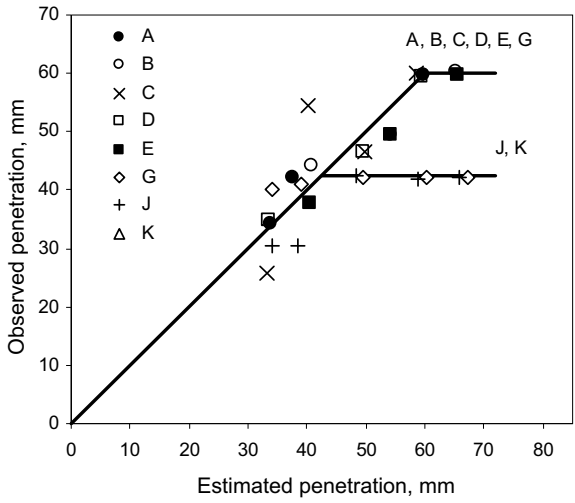

Fig. 4.16 Penetration of free jets

$$\sqrt{\left(\frac{2\Delta p}{\rho_f}\right)^{\frac{1}{2}} d_e t_{\text{imp}}} \tag{4.6}$$

Here, t_{imp} is the time following jet impingement. The results are shown in Fig. 4.17, from which the wall jet penetration s is

$$s = 0.75\sqrt{\left(\frac{2\Delta p}{\rho_f}\right)^{\frac{1}{2}} d_e t_{\text{imp}}} \tag{4.7}$$

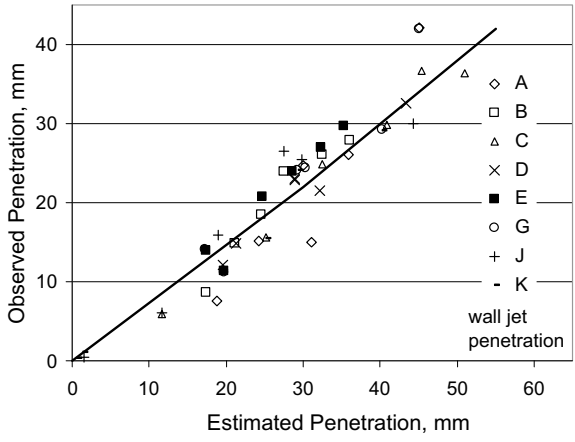

Fig. 4.17 Penetration of wall jets

For a steady-state free jet, the entrainment relationship of Ricou and Spalding [24] has the form

$$\frac{\dot{m}_a}{\dot{m}_0} = 0.32\frac{x}{d_e} - 1 \tag{4.8}$$

Here, m'_a and m'_o are the rate of air mass entrained into the jet and the rate of mass flow of the jet fluid through the orifice, respectively. Rewriting Eq. (4.8) as

$$\frac{\dot{m}_a}{\dot{m}_0} = A_f\frac{x}{d_e} - 1 \tag{4.9}$$

and integrating with respect to time, t results in

$$\dot{m}_a = \dot{m}_0 \int_0^t A_f\frac{x}{d_e} - 1 \tag{4.10}$$

Here, t_o = time taken by the jet to penetrate a distance equal to the potential core. From Ricou and Spalding [24]

$$\frac{dx}{dt} = 4U_j\frac{d_e}{x} \tag{4.11}$$

$$\dot{m}_0 = \frac{\pi}{4}d_0^2\rho_f U_j = \frac{\pi}{4}d_e^2\rho_a U_j \tag{4.12}$$

$$\dot{m}_a = \frac{\pi}{16}d_e^2\rho_a\left[\frac{A_f}{3}\left(\frac{x}{d_e}\right)^3 - \frac{1}{2}\left(\frac{x}{d_e}\right)^2\right]_{x_0(t)}^{x(t)} \tag{4.13}$$

Here, $x_o(t) = d_e/A_f$ is the distance below which are entrainment is absent. Substituting the limits and simplifying yields

$$\frac{\dot{m}_a}{\frac{\pi}{16}d_e^3\rho_a} = \frac{A_f}{3}\left(\frac{x}{d_e}\right)^3 - \frac{1}{2}\left(\frac{x}{d_e}\right)^2 + \frac{1}{6}\left(\frac{1}{A_f}\right)^2 \tag{4.14}$$

A plot [4] of the left-hand term of (4.14) obtained experimentally against the right-hand term calculated for various X and A_f values is shown in Fig. 4.18. It can be seen that a value of 0.32 for A_f underestimates the experimentally observed entrainment, and that a value around 0.5 is reasonable and is close to the value of 0.45 observed by Bremhorst and Watson [5] in their study of air entrainment into pulsed jets.

Extending the above idea for a wall jet as shown in Fig. 4.15, the total rate of air entrainment into the free and wall jets is given by

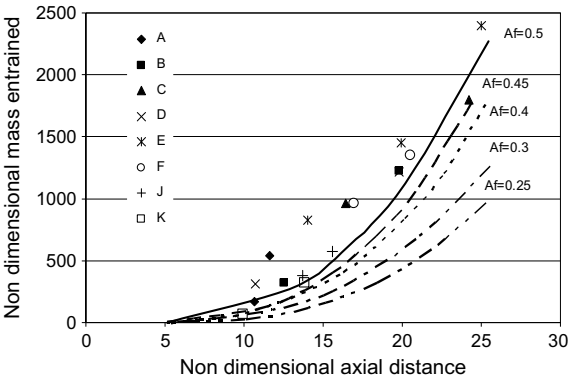

Fig. 4.18 Air entrainment in a free jet

$$\frac{\dot{m}_a}{\dot{m}_0} = A_f \frac{H}{d_e} + A_w \frac{s}{d_e}, \text{ where } A_f = 0.5 \tag{4.15}$$

Using Eq. (4.7) in Eq. (4.15) and integrating, the mass of air in the wall jet portion alone results in

$$m_{a_w} = \frac{\pi}{4z^2} \rho_\infty \left[A_f H s^2 + \frac{2}{3} A_w \left(s^3 - w^3 \right) \right] \tag{4.16}$$

Here, z is the constant of proportionality (0, 0.75) in Eq. (4.7), and w is the radius of the free jet at $x = H$. The agreement between computed values of maw with experimental data was obtained for $A_w = 0.95$. This is shown in Fig. 4.19. This value of A_w is close to the value of 0.86 given by Hartel [14].

Equations (4.5) and (4.7) were compared with wall jet data observed for an impinging steady-state jet on a flat surface [23]. It was found that wall jet penetration and thickness differed substantially from the data in the penetration rate being nearly

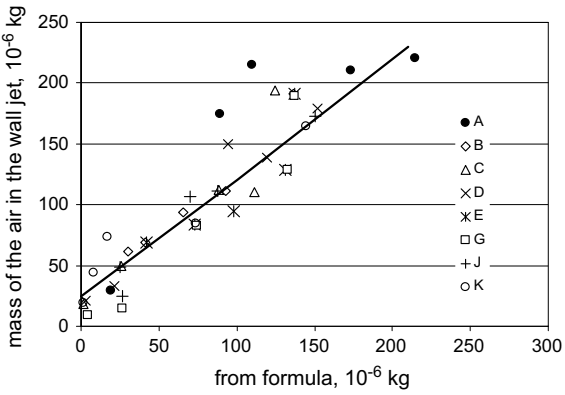

Fig. 4.19 Entrainment of air in a wall jet

half and the half-thickness about three times that observed in the above reference [23].

Combusting Sprays

The refractive index at every point in the jet is calculated from the fringe counts using the procedure as by Dent et al. [12] and Dent [11]. The fringe counts were assumed to decrease up to the radius where the refractive index calculated would be such that the temperature of the products of combustion would correspond to the adiabatic flame temperature for the mixture fraction, beyond this point and up to the axis of the jet the fringe count increases (Fig. 4.20). The refractive index and mixture fraction at any point are used to find the temperature from the chart of T, $n-1$, Φ (Fig. 3.6), up to the rich limit. Beyond the rich limit, fuel vapour and products of combustion at the rich limit are present. The concentration of the fuel vapour is given by (Appendix I) the following equation.

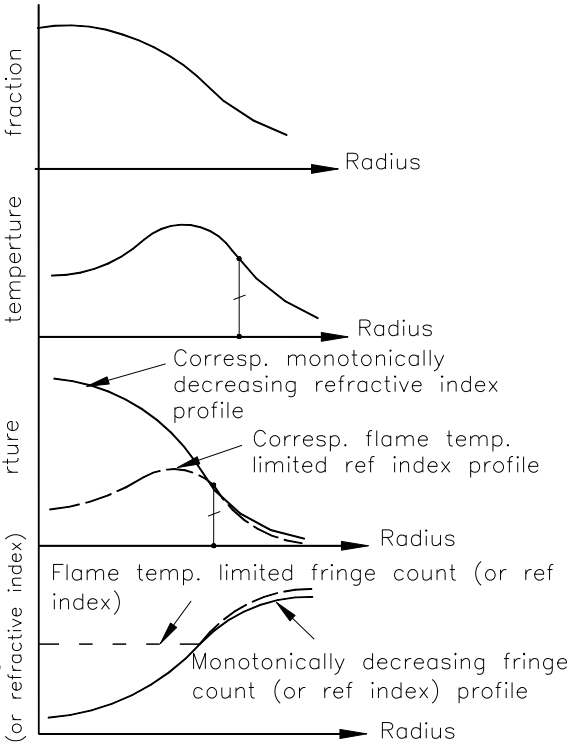

Fig. 4.20 Counting fringes in a burning jet

$$C_f = \frac{C_{(r,x)} - C_{R,L}}{1 - C_{R,L}} \tag{4.17}$$

Here, $C_{R,L}$. refers to the mixture fraction at rich limit combustion. If the combined Gladstone–Dale constant and average molecular weight of the products of combustion at the rich limit are K_b and M_b, respectively (Appendix II), the temperature at any point in the jet can be calculated as

$$T_r = \frac{T_\infty}{M_\infty} \frac{C_f K_f + (1 - C_f) K_b}{\left(K_\infty + \frac{n_r - n_\infty}{\rho_\infty}\right)\left(\frac{C_f}{M_f} + \frac{(1-C_f)}{M_b}\right)} \tag{4.18}$$

Here, ∞, r, and f refer to the surroundings, considered point in the jet and fuel vapour. The entire scheme of calculation is summarized in Fig. 4.21.

Figure 4.23 shows the radial variation of temperature at various axial stations from the orifice. Near the nozzle axis, the temperature is high, and away from it, the temperature drops. For a time 1.5 ms after the start of injection, the temperatures along the axis of the jet are low and remain so along the whole length of the jet indicating

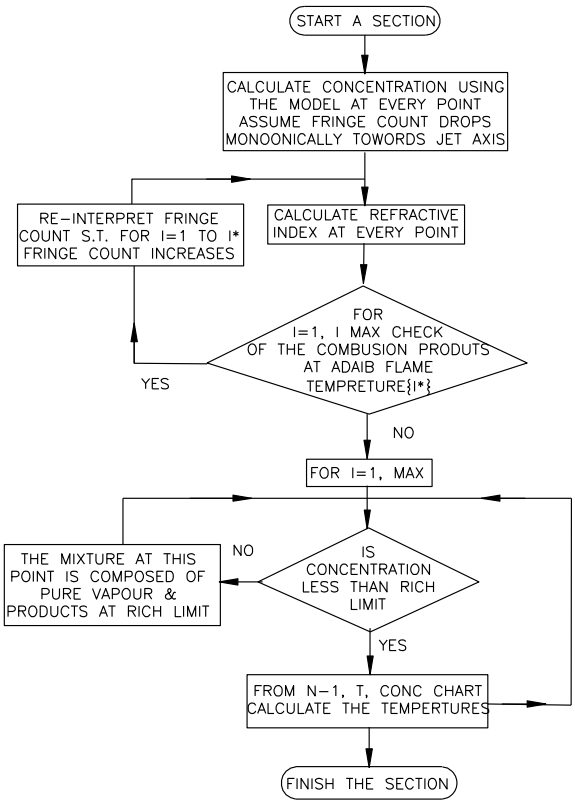

Fig. 4.21 Computational flow chart

a cool central core region. The temperature increases in the radial direction to reach a peak and then decreases sharply towards the edge of the jet. By 2.5 ms after injection, the central regions of the jet have reached temperatures of the order of the adiabatic flame temperature along the length of the jet. This indicates that strong air entrainment into the tail and central regions must occur. By 3.5 ms, this entrainment appears to have caused a decrease in the temperature of the central regions of the jet from about half the jet length to the tip, the presence of the deflection plate causing a considerable drop in temperature. The tail half of the jet remains at remarkably high temperatures indicating a reduction in entrainment (Figs. 4.22 and 4.24).

The concentrations of water vapour, CO_2, and CO vary according to the completion of combustion (Figs. 4.25, 4.26 and 4.27). For example, at a distance of 19.5 mm from the nozzle, H_2O and CO_2 increase and then decrease from the periphery to the axis of the jet. The maximum is reached when the mixture fraction is stoichiometric. This peak in the profile disappears at larger intervals of time (e.g. −2.5 ms) due to mixing and entrainment of air. The concentration of oxygen decreases from the periphery towards the axis and is absent near the axis, during the initial period just after the start of combustion. As time progresses, due to further dilution, the concentration of oxygen near the axis increases. Very near the wall, the concentrations of

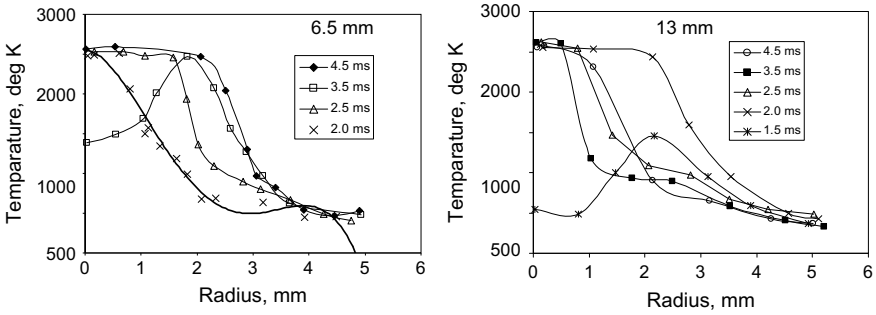

Fig. 4.22 Radial temperature profiles

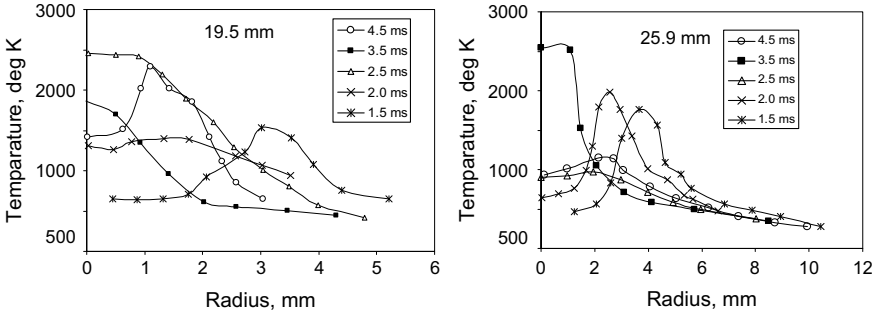

Fig. 4.23 Radial temperature profiles

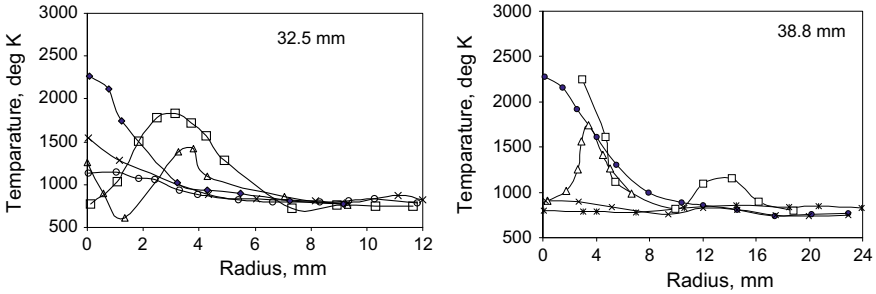

Fig. 4.24 Radial temperature profiles

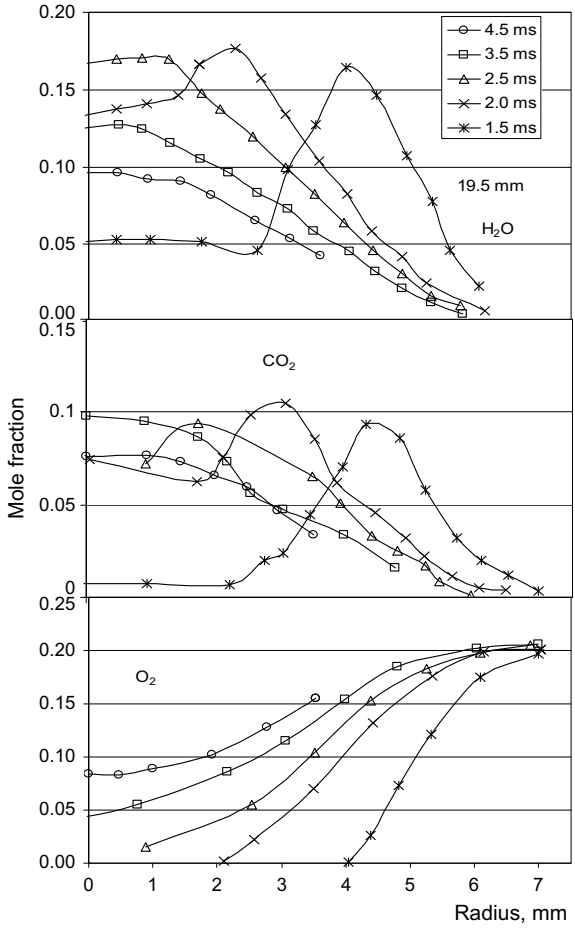

Fig. 4.25 H_2O, CO_2, and O_2 at 19.5 mm from the nozzle

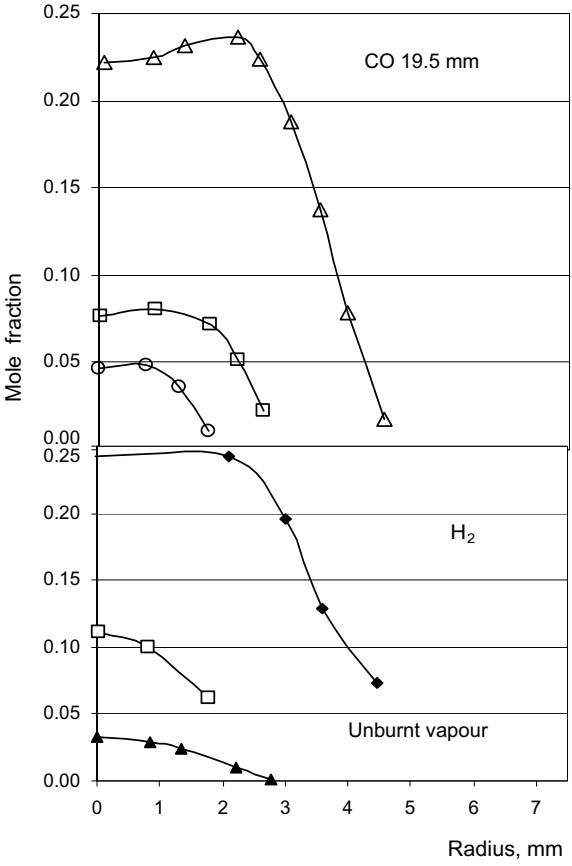

Fig. 4.26 CO, H_2, and fuel vapour at 19.5 mm from the nozzle

H_2O and CO_2 are high for times as large as 4.5 ms, suggesting that combustion is complete. The trends and the values of concentrations of various products and temperatures are similar to those reported by Chigier and Strokin [7] and Chigier and Apak [6]. Figure 4.27 shows the axial variation of the mass-averaged (radial) temperature. Although the peripheral regions of the jet reduce this temperature, a fair idea of vaporization, combustion, and dilution histories can be obtained. These variations of mass-averaged temperature and the products of combustion for the whole jet are shown in Fig. 4.28. The notable features are the maximum reached by the temperature and fraction of carbon monoxide and fuel vapour.

Finally, the entrainment of air into the free and wall jet was studied identically to the case of vaporizing jets, except for the definition of the equivalent diameter [2] as given in Eq. (3.5).

It can be seen in Fig. 4.18 that the entrainment of air in the transient burning jet tends to follow that of a transient vaporizing spray. As a check on the calculation procedure, the total amount of fuel vapour at any instant (burned or unburned) in the jet was calculated and was found to give the total amount of fuel injected, at times

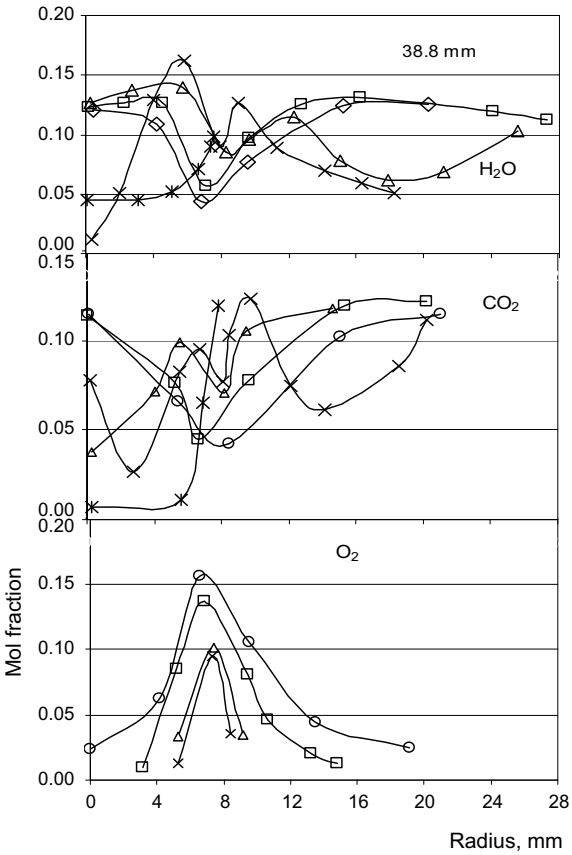

Fig. 4.27 H_2O, CO_2, and O_2 at 4 mm from the impingement plane

(Fig. 4.30) sufficiently long after the end of injection (2 ms). This is similar to the observation made for purely vaporizing jets (Fig. 4.31).

Summary of the Model for Vapourizing and Combusting Sprays

A holographic interferometric technique has been applied to study the concentration and temperature distributions in transient vaporizing and combusting jet sprays with the inherent advantage of mapping the whole field at an instant. Suitable assumptions were made based on the theories of vaporization and combustion to decouple the effects of temperature and concentration on the interference pattern. While concentration had a dominating effect on the fringe spacing in a vaporizing spray, temperature influenced this spacing in a burning spray.

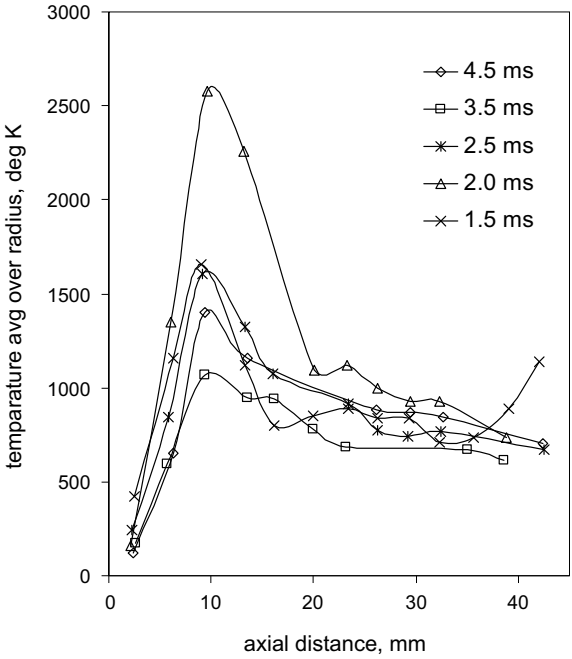

Fig. 4.28 Mass-averaged temperature along the axis in a burning jet

The vaporizing jet was studied by simple mathematical functions, and the radial and axial variations of concentrations of the fuel vapour are described. It was found that the central regions of the transient vaporizing jet are comparable to a steady-state jet. At the nozzle, for about six (equivalent) nozzle diameters, the vapour concentration increases monotonically from a virtual source point. The detachment of the jet from the nozzle, at the end of injection, was explained by observing the extent of departure from steady-state behaviour. Impingement of the jet causes a loss of momentum and growth (thickening) of the wall jet and as a result slower penetration along the wall.

In the case of a burning jet, it was assumed that the distribution of concentration of fuel vapour would be the same as in a vaporizing jet. Assuming equilibrium between reactants and products [21], the temperature and molar concentrations of species were calculated. From the axis of the jet, a thick envelope of gases where combustion is complete is found. At the core close to the nozzle, fuel vapour is present along with some products of incomplete combustion. At the jet boundaries and the jet tip, the products of complete combustion diluted by fresh air are present showing very little heat release. At times sufficiently long after injection, all the fuel is consumed, and the temperature is lowered due to dilution by the surroundings (Fig. 4.29).

Holographic interferometry is not devoid of its difficulties. The post-experiment analysis of the fringe count is time-consuming. The fringes in a turbulent jet submerged in not so quiescent surroundings are corrupted. The averaging of fringes on either side of the axis of symmetry solved this problem in part. In regions where

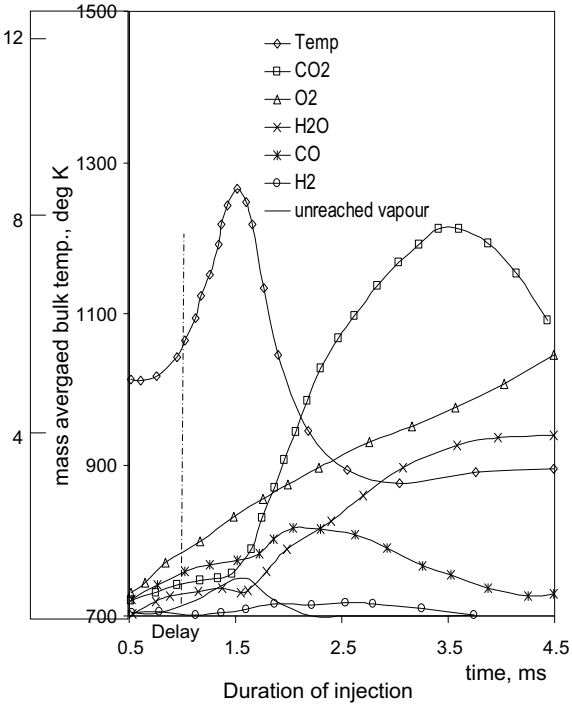

Fig. 4.29 Masses of various components and mass-averaged temperature in a transient burning spray

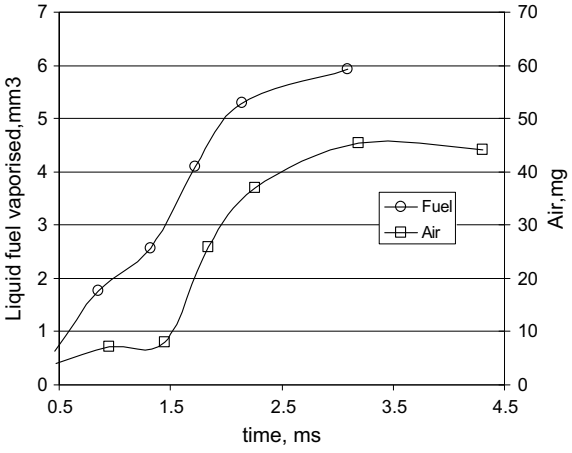

Fig. 4.30 Quantity of fuel vapour and air entrained in a burning jet

the fringe density is very high (up to 6 per mm), errors can be introduced in the fringe count. The maximum error in obtaining the fringe count versus radius profile is very much smaller than the error introduced by the thermal noise in the surroundings. This noise is one of the reasons for the deviations in the experimental data from average

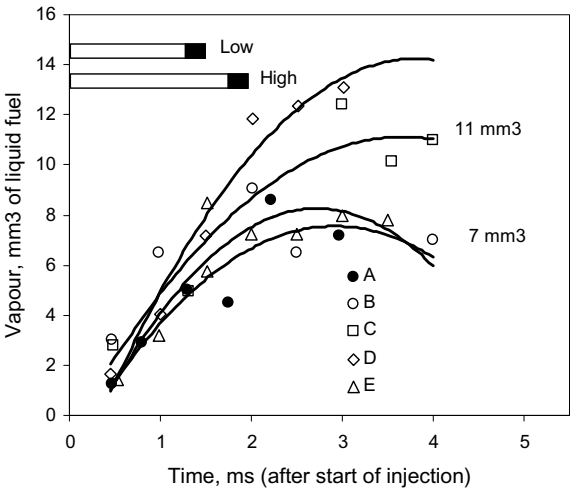

Fig. 4.31 Quantity of fuel vapour in vaporizing jet

behaviour (Fig. 4.16); turbulence introduced by the jet causing pockets of concentration is another reason. It is extremely difficult to quantify the accuracy of the technique in absolute terms about the experimental results presented here. Besides the problems of high fringe density and background thermal noise mentioned above, the fact that vaporization and combustion "histories" of the jet are not built up from a single injection event, but rather from a series of injections at the same test condition, results in the inevitable variation between injection events being reflected in the final results. Furthermore, the method of decoupling concentration and temperature effects on the refractive index are themselves approximate.

While being aware of the limitations of the technique as listed above, valuable observations on the spatial variation of concentration distributions within the transient vaporizing and burning jet during the injection and post-injection periods have been highlighted and described through generalized equations. Similarly, the penetration behaviour of the free and wall jet flow has been described for vaporizing burning and non-burning sprays.

Finally, experimental results for the distribution of fuel vapour, air, and other equilibrium reaction species and temperature within the burning transient jet have been presented.

A Modern View of the Vaporizing and Burning Spray

Diesel combustion is a complex, turbulent, three-dimensional, multi-phase process that occurs under conditions of high pressure and temperature. In the absence of detailed measurements within the reacting fuel jet, early attempts to describe diesel combustion were based on studies of steady spray combustion in furnaces and gas

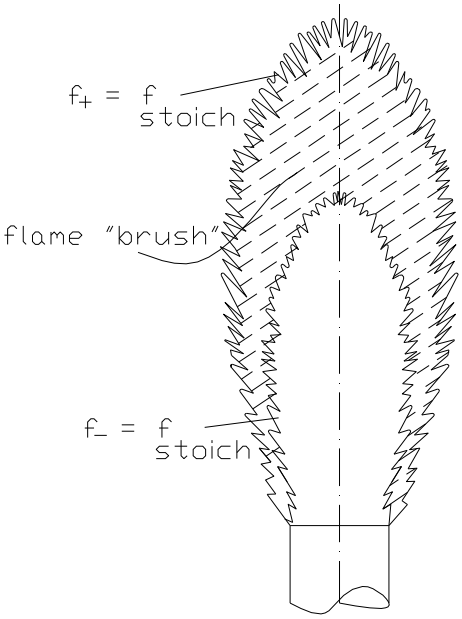

Fig. 4.32 Turbulent flame structure with brush

turbines. The luminous combustion in a diesel engine is essentially a diffusion flame. Spalding [28] described this flame as thick and unsteady with instantaneous tattered shape in violent motion. In the brush like portion at the periphery, the mixture fraction, f is at stoichiometric proportion on the curve edge as shown in Fig. 4.32. The reaction zone will be a definite volume, enclosed by surfaces on which f_- and f_+ equal to the flammability limits in a turbulent flame.

Subsequently, direct measurements were carried out using flame luminosity detection, interferometry, high-speed backlight, Schlieren, cinematography or sampling probe data to study time histories and spatial distribution of various species [1, 16, 19, 22]. These experimental works have concluded that soot emissions were elemental carbon that contributed to visible smoke and particulate emissions. Soot concentrations rise rapidly soon after injection starts. High local fuel carbon has also been found in fuel-rich cores of high-pressure liquid-fuelled turbulent diffusion flames. Pyrolysis of fuel is, therefore, the most important source of soot. These high local soot concentrations decrease rapidly as the fuel injection ceases and the rich core mixes to leaner equivalence ratios [15]. On the other hand, soot concentrations rise in the spray close to the piston bowl outer radius and at the cylinder wall later that are an order magnitude less and decay more slowly. Away from the fuel spray core, with increasing distance from the centre line, soot concentrations decrease rapidly.

In the last decade, detailed in situ measurement of the process occurring inside a reacting diesel fuel jet has been carried out using advanced laser-based diagnostics [9]. An integrated view of DI diesel combustion was derived from this and other optical data [9]. The combustion was summarized in a series of idealized schematics

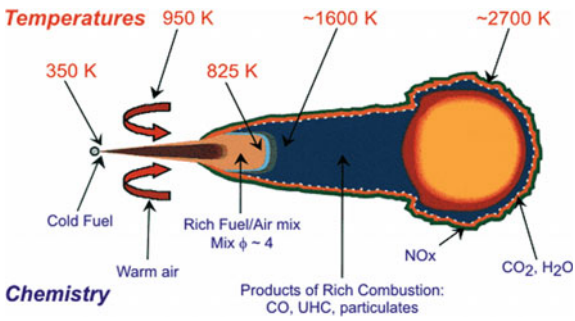

Fig. 4.33 Modern view of a vaporizing and burning spray jet

that depicted the combustion process as shown in Fig. 4.33. The soot formation starts just downstream of the liquid fuel region and grows in size and volume fraction, as it flows downstream, eventually being oxidized at the diffusion flame. Soot occurs throughout the jet cross section, and diffusion flame appears mainly around the jet periphery.

The cause of exhaust smoke and its reduction methods in a small DI diesel engine with a nozzle of small orifice diameter and common rail fuel injection equipment were investigated undeombr high speed and high load conditions using both in-cylinder observations and three-dimensional numerical analysis by Yoshihiro et al. [17]. These studies revealed that fuel sprays were easily pushed away by a strong swirl and that the air–fuel mixture immediately flows out to the squish area by a strong reverse squish. Therefore, the air in the cavity is not effectively used. Suppressing the airflow in a cavity using such ideas as enlarging the piston cavity diameter or reducing the port swirl ratio decreases the excessive outflow of the fuel–air mixture into the squish area and allows the full use of air in the whole cavity. Hence, exhaust smoke reduces.

Lyu and Shin [20] investigated the effect of nozzle characteristics on the performance of a small-bore high-speed DI diesel engine. The volume between the needle tip and seat in the nozzle is referred to as the sac. The fuel in this volume contributes to HC emissions. Therefore, valve closed orifice (VCO) type of nozzles was developed wherein the sac is absent. These VCO nozzles resulted in higher smoke due to poorer fuel atomization than sac type nozzles. They concluded that swirl and spray penetration should be carefully optimized, and higher injection pressure is not always advantageous.

Benajas et al. [3] analysed the effect of swirl on combustion and exhaust emissions. They concluded that there is no single optimum value of swirl ratio for the whole operating range of the engine and that matching the level of swirl with other parameters depends on the combustion chamber geometry and injection characteristics. Nevertheless, the results obtained shed light on the swirl effect on diesel engine combustion and exhaust emissions over a wide range of operating conditions. They observed that NO_x is formed very early in the combustion process and that it depends on the temperature reached during premixed combustion while soot emissions are dependent on oxidation during the late combustion phase which is mixing-controlled. A theoretical investigation on the effect of combustion chamber geometry and the

engine speed on the emissions of soot and NO_x was carried out by Risi et al. [26]. The bowl re-entrance, the spray angle, and the injection timing were the critical parameters that had to be optimized. Subsequently, new methodologies for the design of the combustion chamber shape and the injection strategy were developed aiming at the reduction in emissions without deteriorating engine performance [25].

Kurtz and Foster [18] identified a critical time for mixing in a direct injection diesel engine through the study of increased in-cylinder mixing and its effect on emissions. The results suggested that the fuel injected at the tail end of the fuel injection event had difficulty in mixing and caused large quantities of soot. An innovative method of secondary injection was used to reduce exhaust emissions by a substantial amount.

References

1. Aoyagi Y et al (1980) A gas sampling study on the formation process of soot and NO in a DI engine. SAE 800254
2. Beer JM, Chigier NA (1972) Combustion aerodynamics. Applied Science Publishers
3. Benajes J, Molina S, Garcia JM, Riesco JM (2004) The effect of swirl on combustion and exhaust emissions. J Auto Eng IMechE 218
4. Bradshaw P, Cebeci T, Whitelaw JH (1981) Engineering calculations for turbulence flow. Academic Press
5. Bremhorst K, Watson RD (1981) Velocity field and entrainment of a pulse cored jet. J Fluid Eng Trans ASME 103
6. Chigier NA, Apak G (1975) Interaction of multiple turbulent diffusion flames. Combust Sci Technol 10:219–231
7. Chigier NA, Strokin V (1974) Mixing processes in a turbulent diffusion flame. Combust Sci Technol 9:111–118
8. Chiu WS (1973) The experimental set up for basic diesel, spray mixing and combustion studies. Cummins Tech Report doc 3534
9. Dec JE, Westbrook C (1999) Diesel combustion: an integrated view combining laser diagnostics, chemical kinetics and empirical validation. SAE 1999-01-0509
10. Dent JC (1971) Basis for comparison of various experimental methods for studying penetration. SAE Trans 710571
11. Dent JC (1980) Potential applications of holographic interferometry to engine combustion. Combustion modeling in reciprocating engines. Plenum, New York
12. Dent JC, Keightley JD, DeBoer CD (1977) Application of interferometry to air-fuel measurements. SAE Paper No. 770825
13. Guruz AG, Guruz HK, Osuwan S, Steward RF Aerodynamics of a confined burning jet. Combust Sci Technol 9:103–110
14. Hartel H (1962) Stromongsorgange beim Freien Huberstrahler Luftfahrtechnik, 8
15. Heywood JB (2018) Internal combustion engine fundamentals. McGraw-Hill Education
16. Hiroyasu H, Arai M, Nakanishi K (1980) Soot formation and oxidation in diesel engines. SAE 800252
17. Yoshihiro H, Kiyomi N, Takayuki F, Minaji I, Kiyoshi F, Ichiro S (2002) The cause of exhaust smoke and its reduction methods in an HSDI diesel engine under high speed and high load conditions. SAE Transactions, pp 2064–2074, 2002-01-1160
18. Kurtz EM, Foster DE (2004) Identifying a critical time for mixing in a direct injection diesel engine through the study of increased in-cylinder mixing and its effect on emissions through the study of increased in-cylinder mixing and its effects on emissions. Int J Eng Res IMechE 5(3)

19. Lakshminarayanan PA, Dent JC (1983) Interferometric studies of vapourising and combusting sprays. SAE 830244
20. Lyu MS, Shin BS (2002) Study of nozzle characteristics on the performance of a small-bore high-speed D. I. engine. Int J Eng Res IMechE 3
21. Martin MK, Heywood JB (1977) Approximate relationship for the thermodynamic properties of hydrocarbon-air combustion products. Combus Sci Technol
22. Matsui Y, Kamimoto T, Matsuoka S (1982) Formation and oxidation processes of soot particulates in a D. I diesel engine—an experimental study via the two-colour method. SAE paper 820464
23. Rajaratnam N (1976) Turbulent jets. Elsevier
24. Ricou FP, Spalding DB (1961) Measurement of entrainment by axisymmetrical turbulent jets. J Fluid Mech 11:21–23
25. De Risi A, Donabeo T, Laforgia D (2005) An innovative methodology to improve the design and the performance of direct injection diesel engine. Int. J. Eng. Res. IMechE 5(5)
26. De Risi A, Manieri D, Laforgia D (1999) A theoretical investigation on the effects of combustion chamber geometry and engine speed on soot and NO_x emissions. ASME-ICE, Paper No. 99-ICE-207, vol 33-1
27. Shahed SM, Chiu WS, Lyn WT (1975) A mathematical model of diesel combustion. Proc IMechE C94/75
28. Spalding DB (1979) Combustion and mass transfer. Cox and Wyna Ltd., London
29. Steward FR, Guruz AG (1977) Aerodynamics of a confined jet with variable density. Combust Sci Technol 16:20–45

Chapter 5
Ignition Delay in a Diesel Engine

Nomenclature

$r_a\ (t)$	Mean radius of the cylinder (m)
$(T\text{-}T_0)$	Temperature difference between the liquid surface and the bulk at (r, x) (K)
Δp	Differential pressure (N/m^2)
Δt	Time interval (s)
a, k^* and n^*	Empirical constants (–)
B	Spalding's mass transfer number (–)
B	A constant used in the formula for finding activation energy from Cetane number, 450E4 (kJ/mol)
c	Polytropic constant (–)
C	Mass concentration defined as the ratio of the mass of an injected substance to the total mass at any (r, x)
C_D	Coefficient of discharge of the orifice (–)
CN	Cetane number (–)
C_p	Specific heat (J kg^{-1} K^{-1})
D	Local Sauter mean diameter/Sauter mean diameter of the whole spray near the orifice (m)
d	Droplet diameter (m)
d_0	Nozzle hole diameter (m)
d_e	Equivalent diameter of the orifice (m)
dV	Volume of the annular cylinder (m^3)
E_a	Activation energy (kJ/mol)
E_a/R	Activation energy/gas constant (K)
F	Equivalence ratio (–)
f	Constant 1.1, used in the formula for polytropic constant
$r_{½}$	Half radius = 0.0846 x (m)
ID	Ignition delay (degree, s)

P. A. Lakshminarayanan and Y. V. Aghav, *Modelling Diesel Combustion*,
Mechanical Engineering Series, https://doi.org/10.1007/978-981-16-6742-8_5

K	$\left(\frac{\pi d_0^2}{4}\right) u_f \rho_f \Delta t$, An intermediate variable to avoid carrying heavy expression in subsequent equations (–)
k	Conductivity of the ambient air (W/m–K)
$k+$	Ratio of specific heats, $c_p / c_v = 1.4$ (–)
L	Latent heat of evaporation (J/kg)
L'	Latent heat + sensible heat to convert liquid to saturated vapour, (J/kg)
m	Mass of fuel (kg)
m''	Mass transfer per unit area (kg/s/m^2)
Nu	Nusselt number (–)
P_{cyl}	Cylinder charge pressure (bar)
P_m	Charge pressure at the manifold (bar)
p_m	Mean pressure of the ambient (N/m^2)
Q	Rate of injection (kg/s)
r	Radius (m)
Re	Reynolds number of relative flow based on relative velocity, (–)
R_u	Universal gas constant (JK^{-1} mol^{-1})
SMD	Sauter mean diameter (m)
T	Temperature of the mixture (K)
T_{cyl}	Cylinder charge temperature (K)
T_m	Charge temperature at the manifold (K)
T_m	Mean temperature of the ambient (K)
u	Velocity at (r, x) (m/s)
u_f	Velocity of fuel (m/s)
U_j	Velocity of fuel at the orifice, (m/s)
u_p	Mean piston velocity (m/s)
V	Volume (m^3)
V_{disp}	Cylinder volume displaced (m^3)
V_{soi}	Cylinder volume at the start of injection (m^3)
W	Mass concentration (–)
$W(D)$	Cumulative volume versus drop size distribution
W_{air}	Mass concentration of air (kg/m^3)
W_{fuel}	Mass concentration of fuel vapour, (kg/m^3)
x	Axial distance (m)
ε_{eff}	Effective compression ratio
θ	Crank angle (degree)
μ	Dynamic viscosity (kg m^{-1} s^{-1})
ρ_f	Density of fuel (kg/m^3)
τ_{id}	Ignition delay (s)

Ignition delay of a fuel, in the context of diesel engines, is the period from the time the first parcel of fuel enters the chamber to the point when the first flame is observed in the spray. This is different from the combustion performance of the fuel, which

influences the efficiency of the engine. The ignition delay of a diesel spray is important from the viewpoint of preparing the fuel before injecting in the engine as well as selecting optimum injection timing. The delay is primarily dependent on the ambient temperature. This has been shown by Wolfer [23]. His correlation showed exponential dependence on temperature as in Arrhenius' equation for the rate of reaction. Pischinger et al. [13] have experimentally shown the strong influence of the injection parameters like the hole size, injection pressure, and types of fuel and hence quality of fuel on the measured delay. The physical parameters mentioned above are normally lumped as physical delay [19, 22]. This is either a constant or variable according to the characteristics of the injector and has a form of Wolfer's correlation. Ahmed [2] and Tsao et al. [20] related physical delay to engine operating conditions. Thelliez and Ji [19] attempted to incorporate a constant physical delay. It was explained as the time taken for the fuel to reach the length at which ignition occurs. This characteristic length was assumed to depend only on the chamber pressure and temperature at the start of injection contrary to the experimental results [13], which show its dependence on injection parameters as well. This period is about 0.5 ms for the injection systems that are encountered. Andree and Paschernegg [3] emphasized the importance of basic research to investigate the physical and chemical complexities involved in igniting and burning hydrocarbon fuels. Since conclusive information was not available, a combination of empirical observations with modified working theories was used to fill the gap in understanding this persistent problem of diesel combustion. An integral of the difference between the temperature of the gases in the engine and the ignition temperature of the fuel over time, from the time of the start of injection till the end of ignition delay, was found to be nearly a constant irrespective of fuel or engine speed [3]. The present work describes an attempt to incorporate the effects of injection parameters, dimensions of the nozzle orifice, fuel type, and ambient conditions into a comprehensive ignition delay model [6].

Definition and Measurement of Ignition Delay

The definition of ignition delay is the time lag between the start of injection to the start of the combustion when the air–fuel mixture is ignited. In a diesel engine, it can be determined experimentally as the time interval between the start of injection and the start of combustion as shown in Fig. 3.8. Due to vaporization effects, the apparent heat release curve will typically exhibit negative values before combustion for direct injection diesel engines. The start of combustion is taken as the angle value at which the rate of apparent heat release changes from negative to positive. The start of injection is defined as the crank angle at which the needle of nozzle lifts by 5%. The time difference between the start of injection and the start of combustion is called ignition delay. The Arrhenius type of equation to describe ignition delay,

$$\tau_{\mathrm{id}} = a\Phi^{-k}P^{-n}\exp\left(\frac{E_a}{R_u T_{\mathrm{cyl}}}\right) \tag{5.1}$$

where τ_{id} = Ignition delay.
Φ = Equivalence ratio.
E_a = Activation energy.
T_{cyl} = Cylinder charge temperature.
R_u = Gas constant.
$a, k^* and n^*$ = Empirical constants.

The Classical Model for Ignition Delay and Its Extension to Other Fuels

The time taken for the visible fire to appear in the premixed zone of spray is a strong function of pressure and temperature in the ambient. Also, the physical properties such as the Cetane number, viscosity of fuel, nozzle hole size, injected quantity, and injection pressure contribute to the delay phenomenon in diesel engines. In the original work of Assanis [4], the measured values of pressure and temperature are necessary to predict ignition delay. If this equation has to be developed as a design tool, then it is necessary to predict pressure and temperature precisely for required engine operating condition. Considering pressure and temperature at TDC position will ignore the effect of injection timing. Therefore, it is necessary to estimate pressure and temperature at the start of injection by using the following equations.

$$T_{\text{cyl}} = T_m \varepsilon_{\text{eff}}^{c-1} \tag{5.2}$$

$$P_{\text{cyl}} = P_m \varepsilon_{\text{eff}}^{c} \tag{5.3}$$

where $\varepsilon_{\text{eff}} = \dfrac{V_{\text{disp}}}{V_{\text{SOI}}}$ = Effective compression ratio.
c = Polytropic constant.
P_{cyl} = Cylinder charge pressure.
P_m = Charge pressure at the manifold.
T_{cyl} = Cylinder charge temperature.
T_m = Charge temperature at the manifold.
V_{disp} = Cylinder volume displaced.
V_{soi} = Cylinder volume at the start of injection.

Here, the fact that must be considered is at lower piston speeds achievable pressure and temperature under compression decrease under engine conditions. This is due to higher heat transfer and blow-by as more absolute time is available per cycle. An expression developed by Hardenberg and Hase [8] can be used to describe polytropic exponent.

$$c = k^{+} - \frac{k^{+} - 1}{f u_p + 1} \tag{5.4}$$

where k^{+} = Ratio of specific heats, $c_p/c_v = 1.4$.
f = Constant 1.1.
u_p = Mean piston velocity.

In the above correlation of ignition delay, oxygenated fuel is not accounted for. Lahiri et al. [12] introduced fuel to oxygen ratio in place of equivalence ratio. This makes ignition delay a function of the oxygen content in the fuel. The ignition delay increases with the addition of alcohols [9] because alcohols have a very low Cetane number. The reduction in ignition delay has been observed with biodiesel, another oxygen-containing fuel described in the literature [18]. The Cetane number of biodiesel is better than that of diesel. Therefore, the Cetane number truly represents the compression ignition quality of fuel. Therefore, this parameter needs to be incorporated while developing a new model for predicting the ignition delay especially with fuels containing oxygen. Here, the correlation developed by Hardenberg and Hase [8] can be employed.

$$E_A = \frac{B}{\mathrm{CN} + 25} \tag{5.5}$$

where B = A constant.
CN = Cetane number.

Watson [21] and Assanis [4] proposed a value of $E_a/R_u = 2100$ for diesel D_2. Therefore, the value of constant B needs to be modified from the original value of 618,840–1,310,000 [1] a value in line with observation by Watson [21] and Assanis [4].

Validation of Classical Model

The time taken for the visible fire to appear in the premixed zone of spray is a strong function of pressure and temperature of the ambient. Also, the physical properties such as Cetane number, the viscosity of fuel, nozzle hole size, injected quantity, and injection pressure contribute to the delay phenomenon in diesel engines [6]. However, for diesel fuels, a reasonable estimate of the delay, ID is achieved by Wolfer [23].

$$ID = 3.45 exp(2100/T_m) p_m^{-1.02} \tag{5.6}$$

Here, T_m and p_m are the mean temperature and pressure of the ambient during ignition delay.

Initially, the prediction model was applied to engine C12. Experimental work was also carried out on the engine with different blends of biodiesel and exhaust gas recirculation on different engines (A12, C12, E12, and B10) listed in Table 3.2. The conditions at rated power and speed were considered for this study. The predicted and

observed values compared favourably for this engine at different operating conditions in terms of absolute value as well as trend as shown in Fig. 5.1. Then, the model was applied to other engines namely A12, C12, E12, and B10. The older generation of engines E12 and B12 was also considered for model evaluation. The results and predictions are plotted in Fig. 5.2. The new correlation has better predictability compared to the best model available in the literature [10]. The newer engine designs have remarkably lesser ignition delay compare to the older generation. The predictions with the new model are favourable for both old and modern designs with a regression coefficient of 0.97 with a slope close to one as shown in Fig. 5.2.

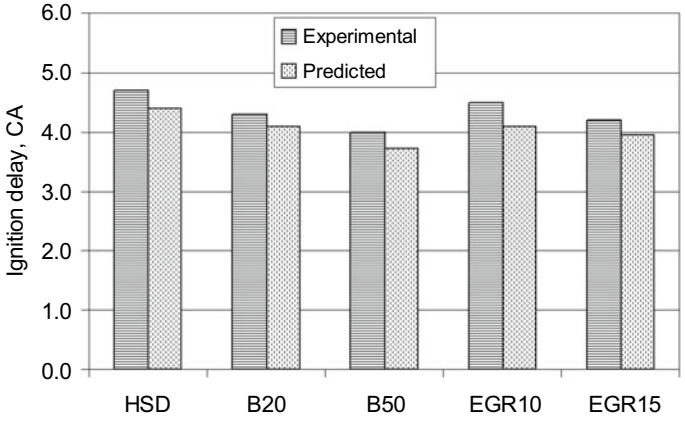

Fig. 5.1 Prediction of ignition delay at rated conditions for engine C12

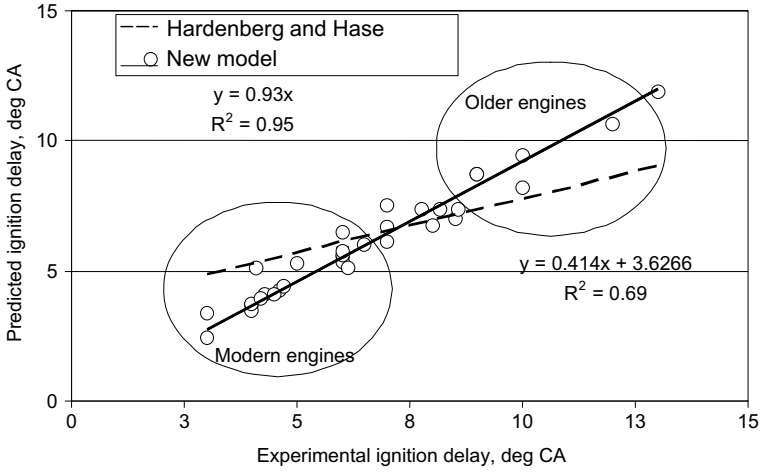

Fig. 5.2 Prediction of ignition delay for A12, C12, E12 and B10 engines

Phenomenological Model of Ignition Delay

Mechanism of Ignition Delay

The physical preparation of fuel is considered hand in and with the chemical reaction. The formation of drops, evaporation, and chemical reaction are phenomenologically modelled to explain the total delay. The end of the ignition delay period is defined in this model as the state in which a very fast rate of exothermic reaction of fuel particles occurs producing a distinct emission of visible light from the spray surface. The vapour envelope [3] emanating from the liquid surface depends on its chemical composition and the boiling curve of the fuel. Perceptible ignition will occur with a lower fraction of distillation. The group of molecules that ignites early can transfer energy to adjacent and more stable molecules. Oxidation does not occur on intact hydrocarbons, but it does on intermediate substances formed during the delay time, such as hydrocarbon radicals and peroxides. Due to non-homogeneity of the fuel–air mixture in the spray, the local air–fuel ratio is extremely high in the areas where vapour emanates from liquid fuel. Initial ignition has the advantage of high oxygen concentration around the fuel. This non-homogeneity persists even after the ignition delay.

Spray Formation

Diesel fuel as it emerges out of the nozzle orifice is in the shape of a sphere whose diameter is nearly equal to the orifice diameter. Every droplet is assumed to go along a line radiating from an origin at δ (virtual source, see Eq. (4.4)). Therefore, the problem simplifies to enable concentrating our attention on the drops inside an annular cone (shown by dotted lines in Fig. 5.3). Subsequently, the drop breaks into smaller droplets due to the combined tearing action of the dense ambient and the instability of large drops. In high-pressure sprays, encountered in diesel engines, the tearing action is very important. This is proportional to the velocity of injection, injection pressure, coefficient of discharge of the orifice and fuel viscosity [11], Reitz and Diwaker 1977]. According to Knight [11], the Sauter mean diameter of droplets,

$$\text{SMD} = 1.58 \frac{Q^{0.21}}{\Delta P^{0.5}} \nu^{0.2} C_D^{0.9} \tag{5.7}$$

Here SMD = Sauter mean diameter m.
Q = Rate of injection, m/s.
Δp = Differential pressure, N/m^2
ν = Kinematic viscosity, m^2/s.
C_D = Coefficient of discharge of the orifice.

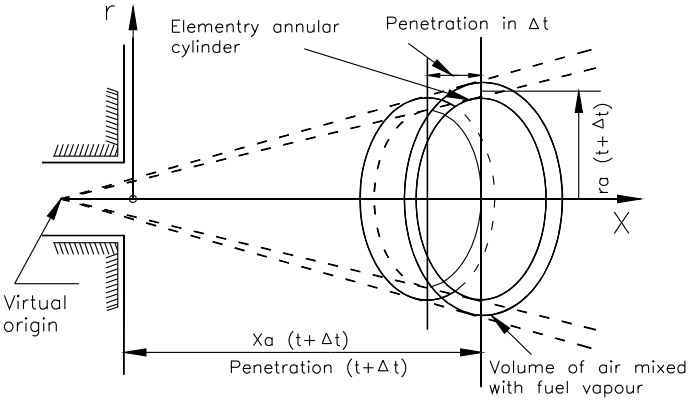

Fig. 5.3 Control volume in the shape of an annular cone

The SMD given above is characteristic of the whole fuel as soon as it is injected. In reality, there is a typical distribution of drop size decreasing, away from the centre line of the spray. This is calculated as follows. Spalding [17] gives the distribution of velocity and concentration in a turbulent jet in a quiescent chamber as,

$$\frac{u}{u_{C.L}} = \frac{1}{\left[1 + 0.414\left(\frac{r}{r_{1/2}}\right)^2\right]^2} \tag{5.8}$$

$$\frac{u}{u_{C.L}} = \left(\frac{C}{C_{C.L}}\right)^{0.7} \tag{5.9}$$

Here *Half radius*, $r_{1/2} = 0.0846x$.

r = Radius.

x = Axial distance.

u = Velocity at (r, x).

C = Mass concentration defined as the ratio of the mass of an injected substance to the total mass at any (r, x).

Subscript C.L. *indicates* Centre line value at x.

The velocity of the fuel decreases axially due to loss of momentum to the entrained air. The penetration of fuel along the centre line [7],

$$x = \sqrt{8u_j d_e t} \tag{5.10}$$

Here, uj = The velocity of fuel at the orifice.

d_e = The equivalent diameter of the orifice.

The velocity of fuel along the centre line is obtained by differentiation of Eq. (5.10) with respect to t. At any other radius, the velocity is obtained by using Eq. (5.8) and the derivative of Eq. (5.10) with respect to t.

The volume of the elementary annular cylinder (Fig. 5.3), which contains the first parcel of fuel injected between times 0 and Δt,

$$dV = 2\pi r_a x_a u \Delta t d\theta \tag{5.11}$$

This volume increases with time, t, due to air entrainment. The amount of fuel injected into this volume in a time interval, Δt,

$$dm = \rho c dV \tag{5.12}$$

Here, ρ = mean density of the fuel, air, and products at (r, x).

Substituting Eq. (5.8) and (5.9) in Eq. (5.12),

$$dm = \text{function of } \theta \text{ only} = \text{dm}(\theta) = f(\theta)d\theta \tag{5.13}$$

The distribution of mass, $f(\theta)$ with respect to angle, θ, calculated using Eq. (5.8), (5.9), (5.11) and (5.12), is as shown in Fig. 5.4. The cumulative volume versus drop size distribution of a diesel spray is as follows [16],

$$W(D) = \exp\left(0.0532D - 0.5417D^2\right) \tag{5.14}$$

where D = (local Sauter mean diameter/Sauter mean diameter of the whole spray near orifice).

The volume fraction of fuel with a relative diameter in the range D to $D + dD$,

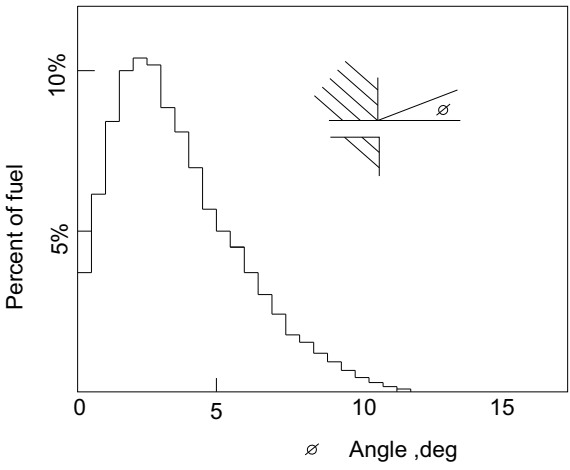

Fig. 5.4 Dispersion of fuel

$$dw = \frac{dw}{dD} dD \tag{5.15}$$

The mass of fuel in this range is,

$$dm = \left[\left(\frac{\pi d_0^2}{4} \right) u_f \rho_f \Delta t \right] dW$$

$$dm = K dW \tag{5.16}$$

Here, the first term refers to the total mass of fuel injected in Δt. Equating masses in Eq. (5.12) and (5.16)

$$f(\theta) d\theta = dm(\theta) = K dW$$

Integrating, after rearrangement of the equations given above,

$$D = \int_{\theta_{max}}^{\theta} \frac{f(\theta) d\theta}{K \frac{dW}{dD}} + D_0 \tag{5.17}$$

Here, is the SMD ratio at the outer envelope of the spray and is assumed to be equal to 0.086. The radial distribution of droplet diameter calculated using Eq. (5.14) is shown in Fig. 5.5. For purposes of calculations, a linear approximation as shown in Fig. 5.5 is helpful. The fuel droplet traces a nearly linear path from the time of formation, often breaking and coalescing with other drops in the neighbourhood. This important phenomenon is however not applicable to the drops on the outer surface of a spray because they are formed first and hence do not interact with other droplets. The breakup of these drops is negligible if the drops are small as in high-pressure sprays. Thus, these droplets on the spray surface can be said to reduce in size only by

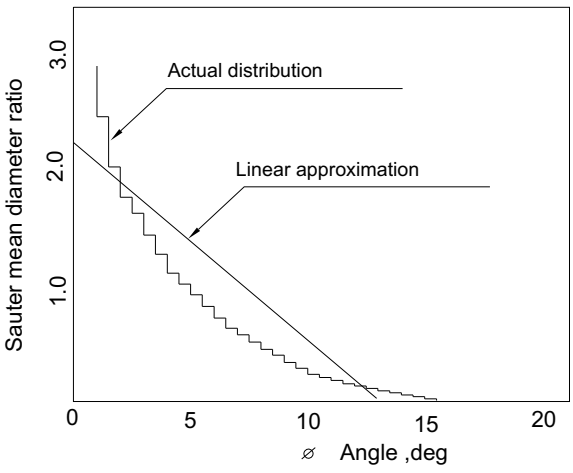

Fig. 5.5 Mean diameter of fuel at different angular positions just after injection

vaporization. Evaporation of fuel depends on the relative velocity of the surrounding medium.

Mass Transfer

The relative velocity of drops with respect to the surroundings is 10–20% of the mean velocity at any point [14, 15]. The mass transfer from the surface of the liquid drop to the ambient is analogous to the heat transfer. Figure 5.6 schematically shows the evaporation process. From the bulk surroundings, air flows towards the liquid surface. This hot air warms up the liquid layer (where the concentration of vapour = 1) and evaporation takes place. Since it is not soluble in liquid, the air returns to the bulk flow carrying the fresh vapour along with it. The boundary layer between the bulk and the liquid surface is similar to the heat transfer boundary layer. In general, the bulk flow contains vapour apart from the main constituent, air. However, mass transfer increases the boundary layer thickness. This effect is equal to ln *(1 + B)* where B is Spalding's mass transfer number (Appendix-III), [17].

Thus, the rate of mass transfer per unit area of the droplet,

$$\frac{dm''}{dt} = Nu\left(\frac{k}{D}\right)\frac{ln(1+B)}{L'}(T - T_0) \tag{5.18}$$

where $(T - T_0)$ = Temperature difference between the liquid surface and the bulk at(r, x).

Nu = Nusselt number.

L' = Latent heat + sensible heat to convert liquid to saturated vapour.

Re = Reynolds number of relative flow based on relative velocity.

d = Droplet diameter.

k = Conductivity of the ambient.

The radius of the drop decreases due to evaporation. As the radius reaches zero, the mass transfer stops.

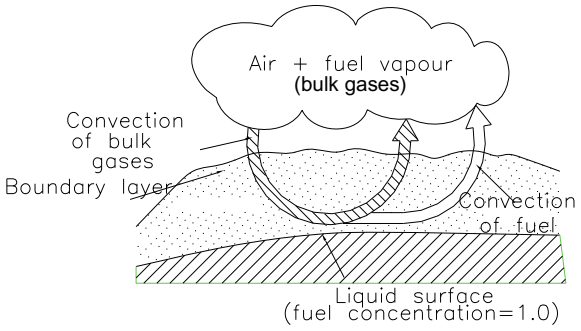

Fig. 5.6 Mechanism of fuel vaporization from droplet surface

Reactions

The nascent drop as soon as formed starts evaporating and is surrounded by a cloud of the vapour–air mixture. The concentration of the fuel vapour, w_{fuel} (kg/m^3) is the ratio of the mass evaporated (until time = t) from drops injected (during time = 0–Δt) into the annular conical control volume to the volume of the annular cylinder shown in Fig. 5.3 The length of the cylinder is the penetration of the spray at angle θ from t to $t + \Delta t$. The mean radius of the cylinder is r_a *(t)*. The concentration, W_{air} of air is similarly defined. It should be noted here that the definition of W_{fuel} is different from that of C_{fuel} given in Eq. (5.9). The temperature of the mixture is a function of the latent heat of vaporization, specific heats of vapour, and liquid and the temperatures of air and liquid. The temperature, T at r_a *(t)*, x_a *(t)* is obtained by solving the heat balance equation,

$$W_{\text{air}} C_{p,\,\text{air}}(T_\infty - T) = W_{\text{fuel}} C_{p,\,\text{air}}(T - T_s) + L + C_{\text{liq}}(T_s - T_0) \tag{5.19}$$

Here W = Mass concentration.
C_p = Specific heat.
T = Temperature.
and L = Latent heat of evaporation.
subscript w = Ambient.
vap = Vapour.
liq = Liquid.
s = Saturation conditions.
and o = Conditions at the liquid surface.

Since the injected fuel is sub-cooled during the initial stages of evaporation, the mass transfer number calculations show that the conditions at the liquid surface can be sub-cooled. However, most of the time saturation conditions are reached at the surface.

The evaporated fuel instantly starts reacting according to the Arrhenius equation Assuming a bimolecular reaction (Spalding 1077), the global rate of change of concentration of fuel,

$$\frac{dW_{\text{fuel}}}{dt} = 0.847 \times 10^9 W_{\text{fuel}} W_{\text{air}} exp(-E_a/RT) \tag{5.20}$$

Here, W_{fuel} = Mass concentration of fuel vapour, kg/m3.
W_{air} = Mass concentration of air, kg/m3.
E_a/R = Activation energy/gas constant, K.
= $450 \times 10^4/(\text{CN} + 400)$ (Eq. 5.24).
T = Temperature of the mixture, K.
CN = Cetane number.

$$\text{The rate of increase of mass of products} = -\left(\frac{dW_{\text{fuel}}}{dt}\right)dV \tag{5.21}$$

Here, dV is the volume of the annular cylinder (Fig. 5.3, Eq. (5.11)) containing the first parcel of fuel injected. Integrating Eq. (5.21) from time = *0–t*, the total mass of products at the desired point in time can be obtained. The mass concentration of products is the ratio of the mass of products in the elementary annular cylinder (Fig. 5.3) obtained by integration, as mentioned above to the total mass of air, fuel vapour, and products in the elementary annular cylinder. The temperature of the elementary cylinder is proportional to the mass concentration of products. The preexponential constant in Eq. (5.20) is calibrated, such that at the ignition distance and time for arbitrarily selected spray (data for which is given below), the mass concentration of products has a value of 100. Therefore, the unit of mass concentration is mentioned in the text as arbitrary units.

$$\begin{aligned}
\text{Spray hole diameter} &= 0.27\ \text{mm}.\\
\text{Ambient pressure} &= 45\ \text{bar}.\\
\text{Ambient temperature} &= 500\ ^{\circ}\text{C}.\\
\text{Injection quantity} &= 14\ \text{mm}^3/\text{stroke}.\\
\text{Fuel} &= \text{Diesel}.
\end{aligned}$$

Ignition Delay

Until the end of the ignition delay period, the increase in the concentration of fuel is too small to cause any substantial change in mixture temperature compared to the cooling due to evaporation. This is observed normally in preflame reactions, Fig. 5.7. However, near the end of the ignition delay period, the temperature rises rapidly. Curve *a* shows the case when the effect of heat release due to preflame reactions is neglected. Curves *b* consider the heat release. It is shown in the figure that until the end of ignition delay, it is justified to omit the increase in temperature due to preflame combustion. Practically, at a typical concentration of products, the temperature rise is high to cause a high rate of reaction. This typical concentration (100 arbitrary units) according to the integral of Eq. (5.21) is termed as the critical extent of reaction in this chapter.

The Extent of Reaction Within the Spray

The extent of reaction is defined as the integral over path line of the droplet (on the outer surface of the spray) per unit mass of the air–fuel mixture. It can be seen that the integral increases monotonically along the path line since the combustion reaction is irreversible. However, the temperatures along the outer path lines are more, and

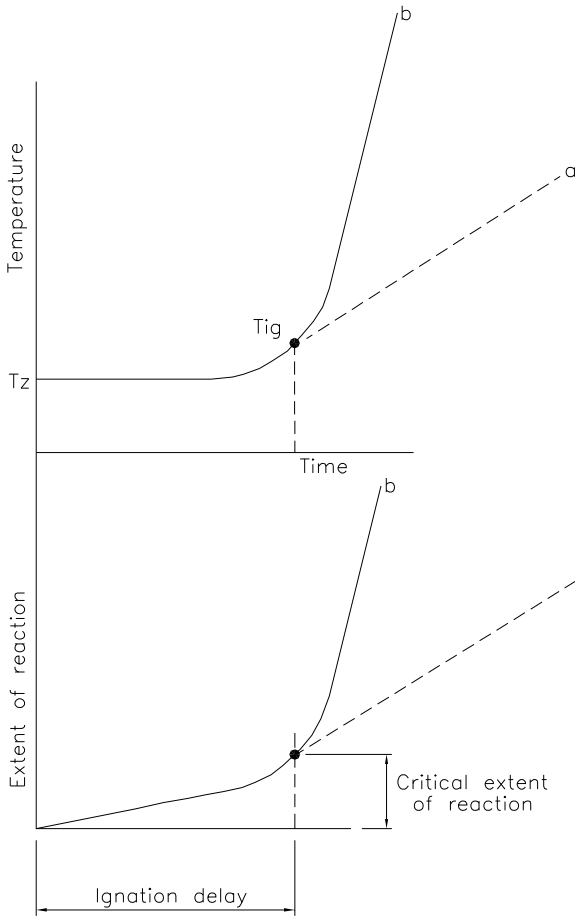

Fig. 5.7 Schematic representation of temperature and extent of reaction against time

the concentration of fuel vapour is less than temperatures along the path lines close to the centre line, Fig. 5.9. These two contradictory trends result in a definite peak in the plot of the extent of reaction against radius. The effect of prolonged stay of fuel on the outer periphery though helps in increasing the integral of Eq. (5.21); the concentration on the outer periphery is too small to result in a higher extent of reaction. In the top half of Fig. 5.8, the extent of reactions along the radius at different axial distance X_0, X_1, X_2, and X_3 are shown. It takes times, t_1, t_2, and t_3 for the spray to penetrate distances of X_1, X_2, and X_3. The extent of the reaction on the outer surface of the transient spray is shown at the bottom of Fig. 5.8.

When the maximum of this extent reaches the critical level at any time, ignition takes place at that location. Such a critical value will be reached on the spray surface later as well. However, since the ignition has already taken place, these locations are irrelevant. This critical value will not be reached before this time because of the

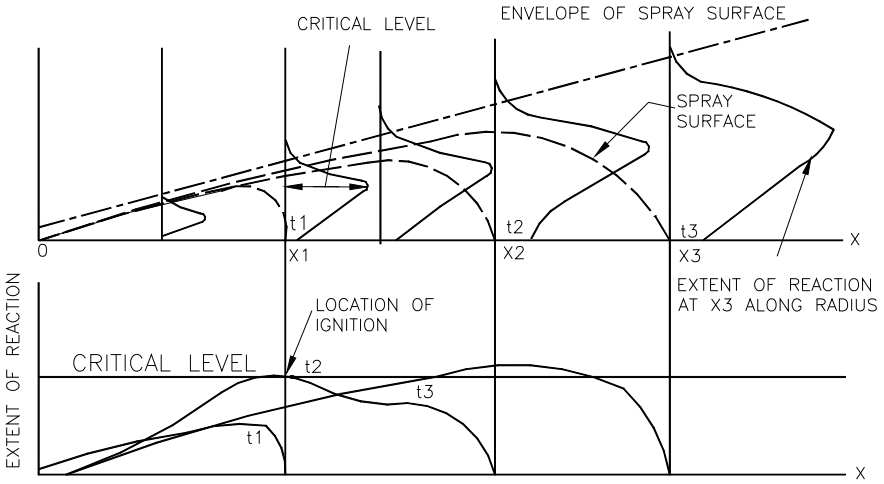

Fig. 5.8 Ignition model

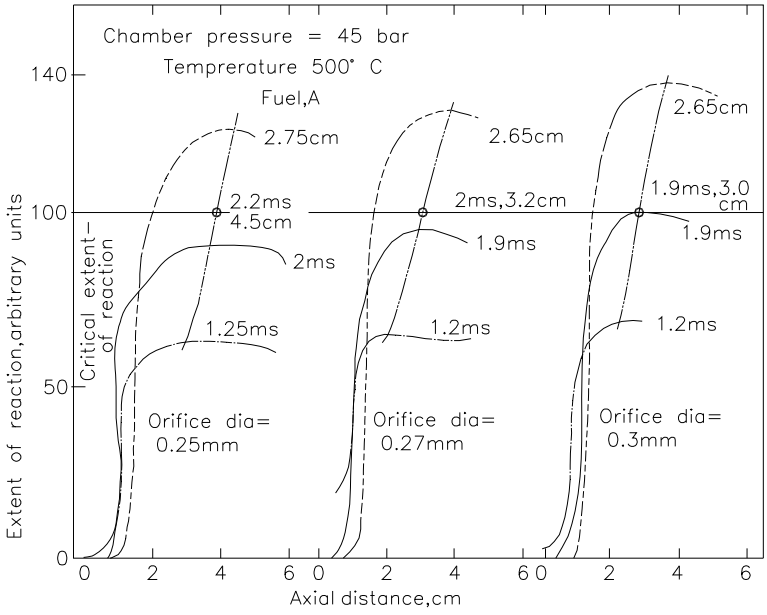

Fig. 5.9 Calculation of ignition model, effect of injector nozzle hole-size

monotonic curves along any path line. For the same reason, ignition does not take place inside a spray.

Thus, according to this model, the ignition zone is an infinitesimally thin ring on the spray surface. The nature of variation of the extent of reaction, explained

now, is a necessary condition to obtain unique ignition delay and location of the ring. Figure 5.9 shows the calculated extent of the reaction on the spray surface at different times (1.25 ms, 2 ms, and 2.75 ms) after injection for different injector hole sizes for the experiments given in by [13]. The locii of the maxima are shown by double chain dotted lines. The distance and time at which the locus reaches the critical value (=100 arbitrary units) are the ignition point. It could be seen that with the increase in hole size, ignition delay decreases arid the location of ignition moves towards the nozzle. This phenomenon is discussed in depth later, in another section.

Turbulence

Photographic evidence of spray ignition shows that the ignition occurs apparently in small zones at any radius below the surface [13]. This can be explained using Fig. 5.10. It shows the polar plot of the extent of reaction at any axial section. The calculations explained earlier in this paper implicitly assume axisymmetric sprays. In practice, turbulence in sprays causes random fluctuations in the extent of reaction, resulting in critical values at only a few points on the surface, near the thin ring at MM, postulated earlier. The distance of these points from the ring is of the order of turbulence small scale at the point. The photographic projection of a point on the surface of the spray is however seen as if the ignition point is at a radius less than the maximum. The probable ring zone of ignition is schematically shown in Fig. 5.10.

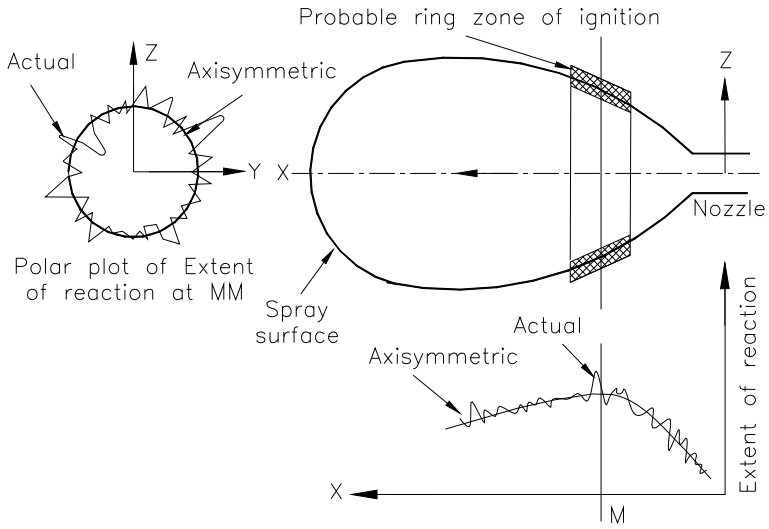

Fig. 5.10 Model of ignition delay

Computations

The mechanism of the ignition delay is easily calculated over the entire spray. The first occurrence of the critical extent of reaction is noted for the estimation of ignition delay and the location of the ignition point.

Validation of the Model

Results from highly controlled experiments reported by [13] were used to validate the calculations of the effects of injection parameters and ambient on ignition delay. Fuels (Table 5.1) of viscosity varying from 4 to 60.5 mm^2 /s, different boiling ranges, and of Cetane numbers were sprayed into a quiescent chamber charged to 45 bar at 450, 500, 550, and 600° C. Orifice hole size was varied from 0.2 to 0.3 mm, keeping injection quantity at 14 mm^3 per stroke and injection duration at 1.8-ms. It was possible by varying injection pressures. Later, the quantity of injection was varied from 7 mm^3 to 28 mm^3 keeping the orifice size fixed at 0.3 mm. Based on the data reported, the mean injection pressure differential necessary to inject the fuel could be calculated. In general, the pressure during injection rate against time is triangular. The mean pressure estimated from the flow is:

$$P_{\text{injection}} = \left(\frac{1}{T} \int_0^T \sqrt{\Delta p} dt \right)^2 + P_{cyl} \tag{5.22}$$

where P_{cyl} = combustion chamber pressure.

The Sauter mean diameter is dependent more on the arithmetic mean of the injection pressure.

Table 5.1 Experimental data from Pischinger et al. [13]

Fuel	A	B	B*	G
Cetane number	50.6	39.1	50.6	45
Density at 15 °C, kg/m^3	847	875	875	930
Distillation, 5% recovery, °C	205.5	207.0	207.0	350.0
90% recovery	341	342	342	450
Kinematic viscosity at 20 °C, mm^2/s	5.0	4.7	4.7	60.5

Note B* = B + Ignition Improver

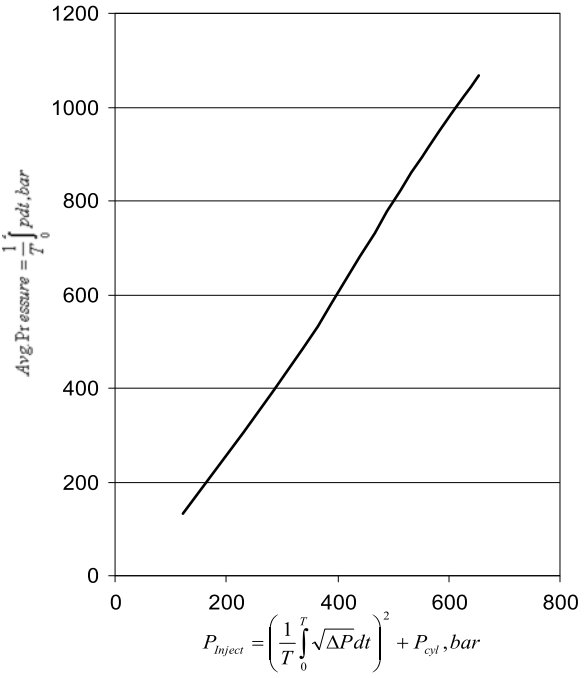

Fig. 5.11 Mean injection pressures for SMD and flow for a triangular injection pressure history

$$P_{\text{average}} = \frac{1}{T}\int_0^T P dt \tag{5.23}$$

Assuming a triangular shape of pressure history and needle closing pressure as equal to 0.8 times needle opening pressure, a plot of $P_{\text{injection}}$ against P_{average} was made as shown in Fig. 5.11. Thus for any injection condition given in ref [13], an average pressure can be estimated. The results of the model and experiments are compared in Figs. 5.12, 5.13, 5.14, and 5.15.

Effect of Orifice Size

In Fig. 5.12, the delay is plotted against injector hole size when injection quantity and duration were kept constant at 14 mm^3 and 1.8 ms. With a decrease in hole size, atomization is finer due to high-pressure injection, and hence, evaporation of fuel is intense to cool the air–fuel mixture. Lower temperature results in a very slow rate of conversion of fuel to products of combustion, i.e. very slow preflame reaction. Therefore, a decrease in hole size increases the time to reach the critical extent of reaction along the path of drops and hence increase the delay. This effect

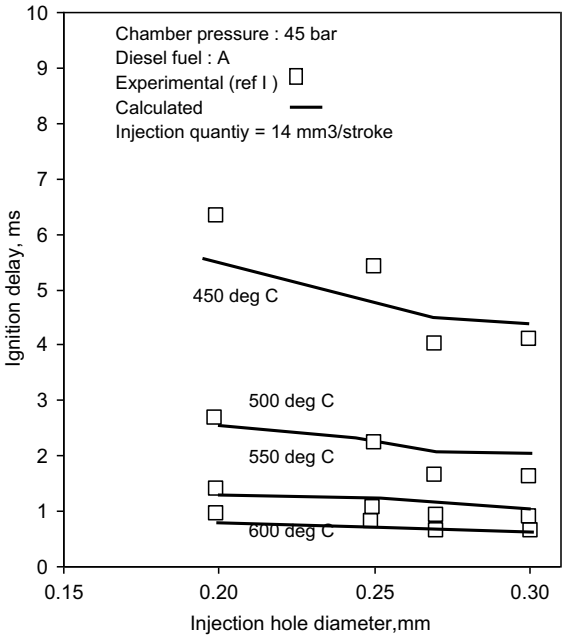

Fig. 5.12 Effect of injection hole diameter on injection delay

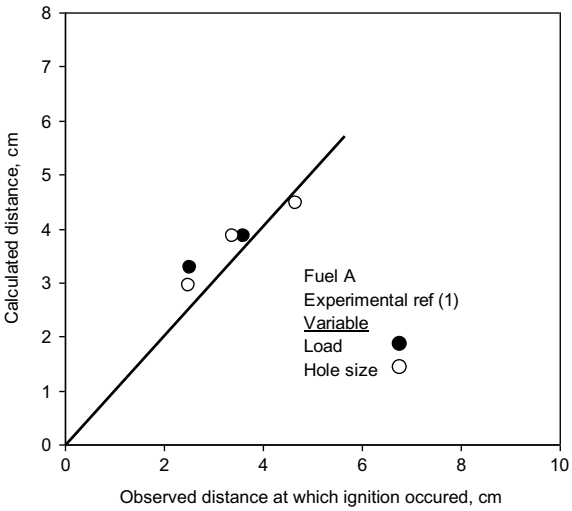

Fig. 5.13 Location of ignition

is pronounced when the hole size is between 0.2 and 0.27 mm. As the hole size is increased above 0.27 mm, the injection pressure varies very little. Hence, it does not affect the cooling rate and hence the ignition delay. The longer the delay, the longer is the distances over which the rate equation is integrated to reach the critical extent of reaction. This results in the location of ignition occurring far away from the nozzle.

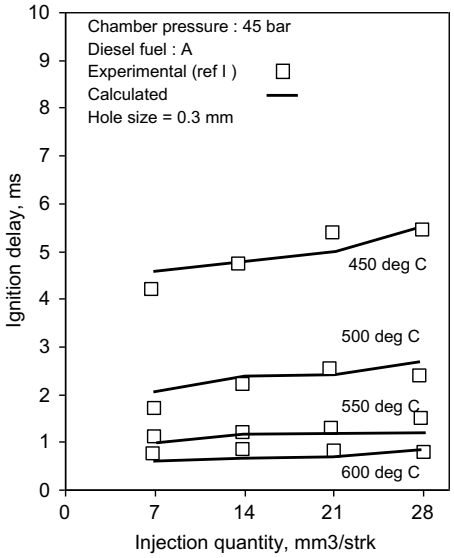

Fig. 5.14 Effect of injection quantity on ignition delay

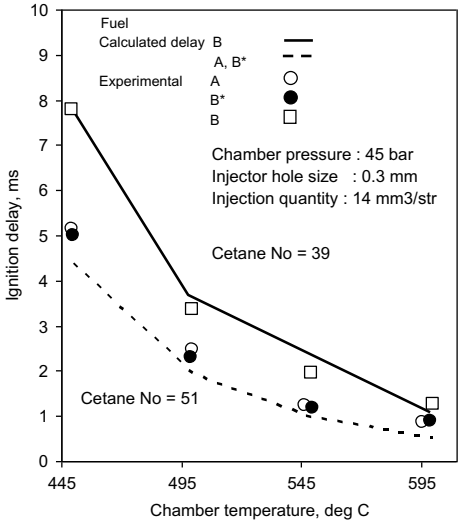

Fig. 5.15 Effect of Cetane number on ignition delay

Figure 5.13 shows the comparison of computed and experimental distances at which ignition occurred. The trends and values compare well.

Effect of Injection Quantity

Figure 5.14 shows the influence of injection quantity on the ignition delay. With the increase in injection quantity, the injection pressure increases. This results in smaller drop sizes that evaporate quickly and hence in low temperatures. The rate of preflame reactions decreases. Thus, the critical value of the extent of reaction is reached late to increase the ignition delay. The location of the ignition also moves farther from the nozzle. Pischinger et al. [13] have explained this differently as a phenomenon due to continued injection at high load, which cools the ignition site. However, in a spray, the vapour–air mixture has a high mean velocity compared to the fluctuations. Therefore, the reacting mixture does not stay at a point, and hence, it may not be cooled by the fuel that follows it. The method described here can predict the observed delay, even though it does not consider the explanation given in [13]. Figure 5.13 shows that the observed distances of ignition are predicted well.

Effect of Cetane Number

Cetane number of a fuel is determined by the structure of the hydrocarbon [5]. From the experimental data given in Ref. [13] a correlation similar to that given in Hardenberg, Hase (1979) [8] was derived.

$$\frac{E_a}{R} = \frac{450 \times 10^4}{\mathrm{CN} + 400} \tag{5.24}$$

Here, E_a = Activation energy.
R = Gas constant.
CN = Cetane number.

The effect of the Cetane number is given in Fig. 5.15. With the decrease in Cetane number from 56 to 39, the increase in activation energy decreases the rate of reaction (Eq. (5.11)) and hence the integral along the path of droplets. This results in a longer delay to obtain the critical level of the extent of reaction. The increase in delay at low temperatures is predicted to be very high as observed experimentally.

Effect of Volatility

The vapour pressure of less volatile fuels is very low, and the latent heat of vaporization is high. Hence, these fuels, when sprayed in a chamber, produce very little vapour cloud. Also, less volatile fuels are thicker or more viscous. Increased viscosity results in large drop sizes. The net effect is to decrease fuel vapour concentration on the right-hand side of Eq. (5.12). However, due to reduced evaporation, the cooling effect is less. Two fuels (Table 5.1) A and G [13] are compared in Fig. 5.16. Even though the fuels are mixtures with definite boiling curves, for simplicity, they are

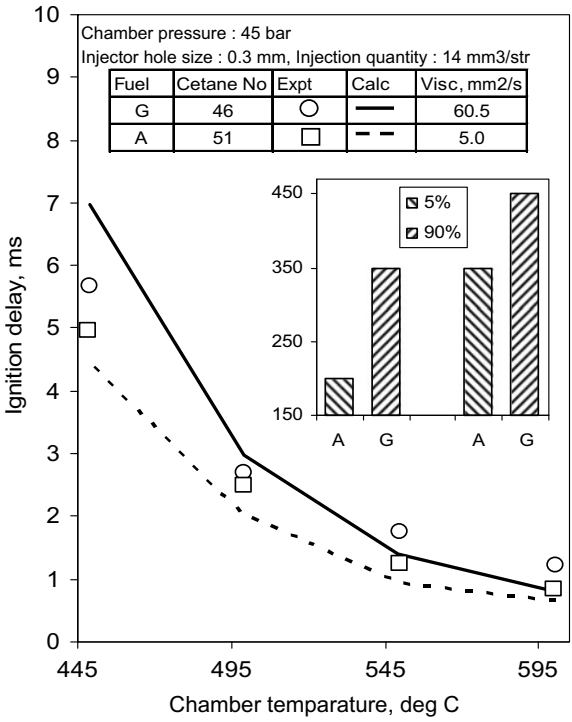

Fig. 5.16 Effect of volatility and viscosity on ignition delay

assumed to be pure fuels with typical boiling points for a given saturation pressure. The input data is given in Appendix-IV and Table 5.1. The trends of calculated delay match with experimental results. Heavier fuel has a higher ignition delay at all temperatures.

Summary

When diesel is injected through an orifice, larger drops are formed near the core and finer droplets at the periphery. Smaller drops evaporate faster and cool the spray zone. However, near the outer periphery of the spray, the concentration of fuel and hence vapour is low to allow the slow preflame reaction. At the centre, temperatures are low because fuel concentration is high. In the middle zone, the peak reaction rates are observed. The extent of completion of reaction per unit mass of air–fuel mixture along a path line increases monotonically. This reaches a critical level at the end of the ignition delay along a thin ring-like zone on the surface of the spray. Beyond this level, the reaction is accelerated, and spray is covered by premixed flame. In practice due to turbulence, the spray is not axisymmetric. The critical level is reached only at a few points about the thin zone. The time to reach the critical level is a strong function

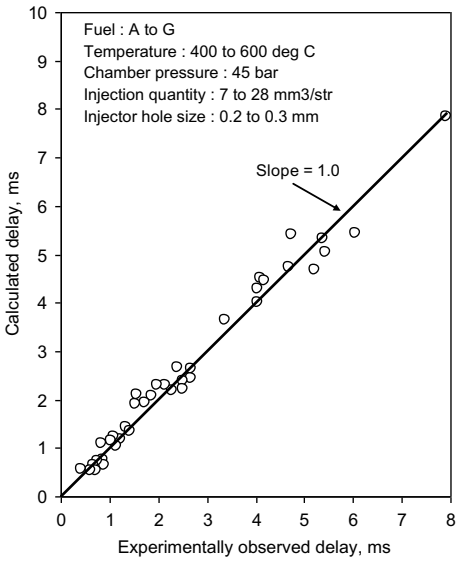

Fig. 5.17 Comparison of predicted and observed ignition delay for different cases and ambient conditions

of the cooling rate of the spray, temperature, and chemical activation energy of the fuel. The cooling rate is found to be a function of the vaporization characteristics of the fuel and the injection parameters only. The activation energy is correlated to the reciprocal of the Cetane number of the fuel. Thus, the effects of fuel types, injection parameters, and ambient conditions on ignition delay could be explained. An increase in injection pressure due to a decrease in injector hole size or due to the increase in the load increases the cooling rate and hence slows down the preflame reactions. Also, the decrease in Cetane number increases the activation energy to decrease the rate of reactions. The decrease in volatility reduces the formation of vapours to decelerate the conversion of fuel to products.

The ignition delay and location of ignition obtained experimentally compare favourably with the theoretically calculated values to reach the critical level of extent of reaction, for different experimental parameters like hole size and injection quantity for different fuel characteristics like volatility, viscosity, and Cetane number and different ambient conditions like temperature (Fig. 5.17).

References

1. Aghav YV, Lakshminarayanan PA, Sujeet V, Kumar MN, Kumar C, Babu MKG (2008) Predicting ignition delay and HC emission for DI diesel engines encompassing oxygenated fuels. SAE international mobility conference

2. Ahmed A (1980) Etude analitique et modelisation correlative de la phase de combustion dans les moteurs allumage par compression surralirmentes, a injection directe, Doctoral Thesis, University Pierre et Marie Curies (Paris VI)
3. Andrea A, Paschernegg SJ (1969) Ignition conditions in diesel engines, SAE 690253
4. Assanis DN, Filipi ZS, Fiveland SB, Syrimis M (1999) A predictive ignition delay correlation under steady-state and transient operation of a direct injection diesel engine. ASME-ICE fall technical conference
5. Bailey BK, Russell JA, Wimer WW, Buckingham JP (1986) Cetane number prediction from proton-type distribution and relative hydrogen population. SAE 861521
6. Chandorkar SB, Dani AD, Lakshminarayanan PA (1988) Effects of injection parameters, fuel quality and ambient on the ignition delay and the location of the flame kernel in a diesel spray in a Quiescent Chamber. SAE 881227
7. Dent JC (1971) A basis for comparison of various experimental methods for studying penetration. SAE Transaction 710571
8. Hardenberg HO, Hase W (1979) An empirical formula for computing the pressure rise delay of a fuel from its Cetane number and relevant parameters of direct injection diesel engines. SAE 790493
9. Huang Z, Lu H, Jiang D, Zeng K, Liu B, Zhang J, Wang X (2004) Combustion behaviours of a compression-ignition engine fuelled with diesel/methanol blends under various fuel delivery advance angles. Bio-resource technology 95:331–341
10. Ikegami M, Kidoguchi Y, Nishiwaki K (1986) A multidimensional model prediction of heat transfer in non-fired engines. SAE 860467
11. Knight BE (1955) Communication on the performance of a type of swirl atomizer. Proc Inst Mech Eng 169
12. Lahiri D, Mehta P, Poola R, Sekar R (1997) Utilization of oxygen-enriched air in diesel engines: fundamental considerations. Paper No. 97-ICE-72, New York
13. Pischinger F, Scheid E, Reuter U (1987) Influences of fuel quality and injection parameters on self-ignition of sprays. CIMAC, D-112, Warsaw
14. Ranz WE, Marshall WR (1952) Evaporation from drops Part-2. Chem Eng Prog 48
15. Reitz RD, Diwaker R (1987)Structure of high-pressure fuel sprays. SAE 870598
16. Simmons HC (1977) The correlation of drop-size distribution in fuel nozzle sprays, Part I, drop size volume fraction distribution. J Eng Power
17. Spalding DB (1977) Combustion and mass transfer. Pergamon Press, Oxford, chapters 4,6,11
18. Szybist JP, Boehman AL, Taylor JD, McCormick RL (2005) Evaluation of formulation strategies to eliminate the biodiesel NOx effect. Fuel Process Technol 86(10):1109–112
19. Thelliez M, Ji ZM (1987) Reflexion sur la modelisation du delai d' inflammation dans les moteurs dieselm. Entropie, 134
20. Tsao KC, Myers PS, Uyehara OA (1962) Gas temperature during compression in motored and fired diesel engines. SAE Transactions
21. Watson N, Pilley AD, Marzouk M (1980) A combustion correlation for diesel engine simulation. SAE Paper No. 800029
22. Woschni G, Anisits F (1974) Experimental investigation and mathematical representation of the rate of heat release in diesel engines dependent upon engine operating conditions, SAE 740086
23. Wolfer HH (1950) Ignition lag in diesel engines, Translation Royal Aircraft Est, 358

Chapter 6
Heat Transfer

Nomenclature

A_{ring}	Area of an annular division (m^2)
A_s	Instantaneous surface area (m^2)
$C*$	A dimensional constant
$dh_t/d\theta$	Rate of heat transfer (J/degree)
$dQ/d\theta$	Rate of heat release (J/degree)
h_c	Heat transfer coefficient ($W/(m^2K)$)
$h_{f,\text{ring}}$	Average heat flux for an annular division (W/m^2)
$h_{t,\text{ring}}$	Average heat transfer for an annular division (W)
L	Characteristic length, wall spray diameter, mean diameter of the ring (m)
P_{cyl}	Cylinder pressure (bar)
T_{cyl}	Temperature of the cylinder charge (K)
T_m	Mean temperature of outer and inner boundaries of circular regions (K)
T_p	Piston temperature (K)
T_w	Wall temperature (K)
u_p	Piston velocity (m/s)
u_{wall}	Wall spray velocity (m/s)
V_{inst}	Instantaneous cylinder volume (m^3)

A large surface area of the combustion chamber is exposed to gases in the later part of the combustion and heat transfer. Therefore, the heat transfer rate must be estimated accurately enough, while experimentally obtaining the heat release rate during this period.

P. A. Lakshminarayanan and Y. V. Aghav, *Modelling Diesel Combustion*,
Mechanical Engineering Series, https://doi.org/10.1007/978-981-16-6742-8_6

Heat Transfer Across the Walls

Hohenberg's correlation [4] for the instantaneous heat transfer considers truly the conditions present in a DI diesel engine. This correlation is based on extensive experiments done on DI diesel engines. The instantaneous heat transfer across the walls for engines A12 to D12 mentioned in Table 3.2 is estimated using the following equation.

$$h_c = \frac{130 P_{\text{cyl}}^{0.8} \cdot \left(u_p + 1.4\right)^{0.8}}{V_{\text{inst}}^{0.06} \cdot T_{\text{cyl}}^{0.4}} \tag{6.1}$$

where h_c = Heat transfer coefficient.
u_p = Piston velocity.
V_{inst} = Instantaneous cylinder volume.
T_{cyl} = Temperature of the cylinder charge.

The cycle-averaged heat transfer coefficient for individual surfaces can be used in the network of resistances to iteratively obtain different surface temperatures of the combustion chamber enabling precise estimation of instantaneous heat transfer [3].

$$\frac{\mathrm{d}Q_{\text{ht}}}{\mathrm{d}\theta} = h_c A_s \left(T_{\text{cyl}} - T_w\right) \cdot \left(\frac{1}{6N}\right) \tag{6.2}$$

where A_s = Instantaneous surface area.
T_w = Wall temperature.

Heat Transfer Coefficient at the Wall Where the Spray Impinges

An analogy between the in-cylinder flow and the steady-state turbulent flow through a circular tube is used by Woschni [8] to estimate the heat transfer coefficient. The spray properties and wall impingement were predicted by earlier work of authors [1, 2, 6]. The analogy adopted by Woschni [8] is applied for the spray impinging on the combustion chamber walls.

$$h_c = C^* L^{-0.2} P_{\text{cyl}}^{0.8} u_{\text{wall}}^{0.8} T_m^{-0.35} \tag{6.3}$$

where h_c = Heat transfer coefficient
C^* = A constant
L = Characteristic length, wall spray diameter, mean diameter of the ring
P_{cyl} = Cylinder pressure, bar

u_{wall} = Wall spray velocity, m/s
T_m = Mean temperature of outer and inner boundaries of circular regions

The wall jet portion of the engine spray is divided into five annular rings, Fig. 6.2. The annular divisions grow every time step as per wall spray growth. For every division, the mean spray temperature, area, and heat flux are predicted and finally integrated to get the heat flux (Fig. 6.1).

$$h_{f_{\text{ring}}} = h_c\left(T_m - T_p\right) \tag{6.4}$$

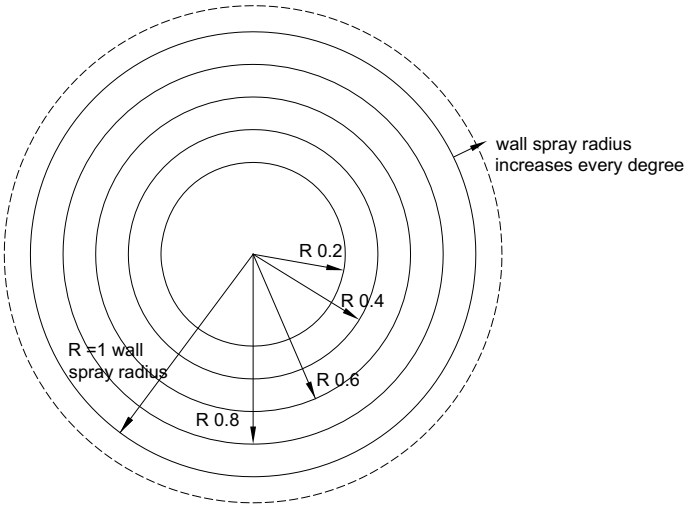

Fig. 6.1 Section of wall spray divided into annular rings

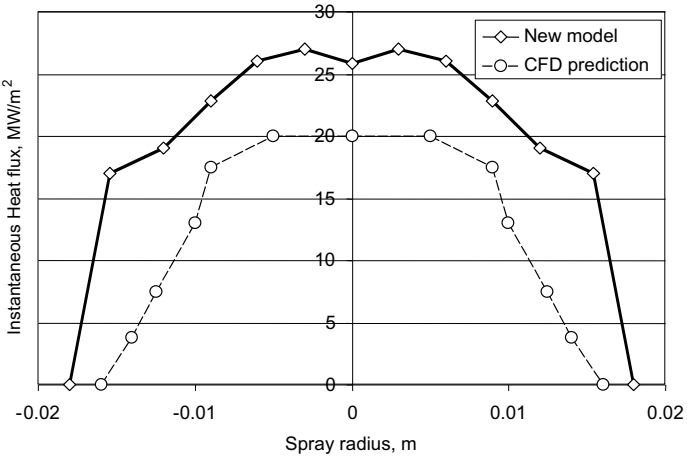

Fig. 6.2 Heat flux profiles along spray cross section at piston wall

$$h_{t_{\text{ring}}} = \sum h_{f_{\text{ring}}} A_{\text{ring}} \tag{6.5}$$

where $h_{f,\text{ ring}}$ = Average heat flux for an annular division.
T_p = Piston temperature, K
$h_{t,\text{ ring}}$ = Average heat transfer for an annular division.
A_{ring} = Area of an annular division.

The mixing-controlled combustion model proposed by Lakshminarayanan et al [6] with the introduction of wall impingement is employed for the prediction of heat release. The rate of burning is proportional to the available fuel and the rate of entrainment of air. The temperatures and equivalence ratios in wall–spray are also corrected by the ratio of net heat release to gross heat release rate.

$$t_{\text{corr}} = \left(\frac{\frac{\mathrm{d}Q}{\mathrm{d}\theta} - \frac{\mathrm{d}h_t}{\mathrm{d}\theta}}{\frac{\mathrm{d}Q}{\mathrm{d}\theta}} \right) \cdot t \tag{6.6}$$

$$\Phi_{\text{corr}} = \left(\frac{\frac{\mathrm{d}Q}{\mathrm{d}\theta} - \frac{\mathrm{d}h_t}{\mathrm{d}\theta}}{\frac{\mathrm{d}Q}{\mathrm{d}\theta}} \right) \cdot \Phi \tag{6.7}$$

where $\frac{\mathrm{d}Q}{\mathrm{d}\theta}$ = Rate of heat release.
$\frac{\mathrm{d}h_t}{\mathrm{d}\theta}$ = Rate of heat transfer.

Heat Transfer from Spray to the Wall

A phenomenology for heat transfer arising out of interactions between spray and combustion cavity is developed during modelling for the NO_x model. A CFD study of non-fired engine was developed by Ikegami et al [5]. Later the study was extended to a fired engine by Nishiwaki [7]. The CFD study and measurements for a heavy-duty engine described in reference [7] were considered for model validation. The details of the engine as well as the assumed data are given in Table 6.1.

Initially, the geometric spray properties like penetration and impingement are predicted. Then physical properties like vapour concentration are predicted for different annular zones of the spray (Chap. 4). Finally, after impingement, the convective heat transfer is considered and heat fluxes from different divisions of wall spray are predicted.

The heat flux predicted by the new model is compared with CFD results at spray and wall interaction section, Fig. 6.2. This shows the new model predicts a slightly higher radius as well as heat flux, but the overall trend matches with CFD results. Then average heat flux at different crank angle positions is compared for predictions with the new model, CFD, and experimental value, Fig. 6.3. Predictions with the new model are done with a different number of divisions to study the model sensitivity. With 10 annular divisions, the predicted values match CFD results. The predictions

Table 6.1 Details of engine, A6 for heat transfer St

Bore × stroke, mm	130 × 150 mm
Connecting rod length	273 mm
Compression ratio	17.25
Boost pressure	2.85 bar
Boost temperature	315 K
Engine speed	1420 RPM
Nozzle	8 hole
Fuel mass injected	80.38 g
Start of injection	351.2 CA
Spray cone angle	150° (assumed)
Duration of injection	27°CA (assumed)

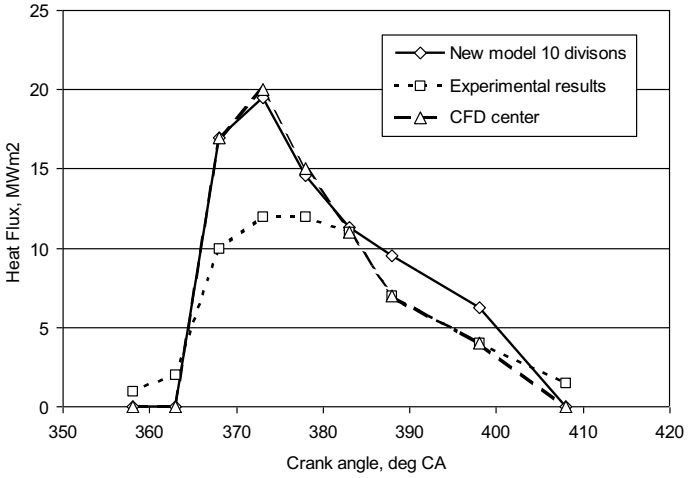

Fig. 6.3 Heat flux data at various crank positions

with CFD and the new model are similar, however; both are higher than experimental values especially during the initial period after impingement. The reason could be the numerical approach followed by the simulation models and errors in instruments to measure the sudden rise in temperature.

References

1. Aghav YV, Lakshminarayanan PA, Babu MKG, Azimuddin, Dani AD (2007) Validating newly evolved smoke model at widely varying operating conditions of DI diesel engine. GTP-06.1096, ASME J Eng Gas Turbines Power

2. Aghav YV, Lakshminarayanan PA, Babu MKG, Nayak NS, Dani AD (2005) Phenomenology of smoke from direct injection diesel engines. In: Paper No. 1350, Proceedings of ICEF2005. ASME
3. Gajendra Babu MK, Murthy BS (1976) Simulation and evaluation of exhaust and Intake system of a 4-stroke spark-ignition Engine SAE 760763
4. Hohenberg GF (1979) Advanced approaches for heat transfer calculations. SAE 790825
5. Ikegami M, Kidoguchi Y, Nishiwaki K (1986) A multidimensional model prediction of heat transfer in non-fired engines. SAE \ 860467
6. Lakshminarayanan PA, Aghav YV, Dani AD, Mehta PS (2002) Accurate prediction of the rate of heat release in a modern direct injection diesel engine. J Automobile Eng IMechE 216
7. Nishiwaki K (1998) Modelling engine heat transfer and flame-wall interaction. Proc COMODIA 98:35–44
8. Woschni G (1967) A universally applicable equation for the instantaneous heat transfer coefficient in the internal combustion engine. SAE 670931

Chapter 7
Heat Release in Indirect Injection Engines

Nomenclature

A	A coefficient in expression for fmep, 0.06898 (bar)
A	Geometrical area of the orifice (m^2)
A	Arrhenius pre-exponent, 2.58×10^{-4} (–)
B	A coefficient in expression for fmep, 0.02897 (bar/rps)
C	A coefficient in expression for fmep, 4.008×10^{-3} (bar/(m/s)^2
C	Concentration of fuel in the chamber from which the mass transport takes place (–)
C_{D1}, C_{D2}	Constants describing the rate of diffused combustion (–)
C_m	Mean piston speed (m/s)
C_{P1}	A constant dependent on the delay period describing premixed combustion (–)
C_{P2}	A constant for all engines, describing premixed combustion, 5000 (–)
D_c	Discharge coefficient of the orifice (–)
$dm_d/d\tau$	Rate of diffusion burning (kg/non-dimensional time)
$dm_{dx}/d\tau$	Rate of diffusive burning in chamber X (kg/non-dimensional time)
$dm_P/d\tau$	Rate of the burning of premixed fuel (kg/non-dimensional time)
$dm_x/d\tau$	Rate of transport of gases to the chamber from the adjoining chamber (kg/non-dimensional time)
E	Arrhenius pseudo activation energy 38,689 (kJ/mol)
fmep	Friction mean effective pressure (bar)
m	−0.293, a constant in Eqs. (7.11, 7.12)
$m_d(t)$	Fuel quantity that would burn diffusively after t seconds (kg)
m_f	Total injected fuel. (kg)
N	Engine speed (rpm)
n	A constant in Eqs. (7.11, 7.12), −0.25
p	A constant in Eqs. (7.11, 7.12), −0.25
P_1	Upstream pressure (Pa)
P_2	Downstream pressure (Pa)

P. A. Lakshminarayanan and Y. V. Aghav, *Modelling Diesel Combustion*,
Mechanical Engineering Series, https://doi.org/10.1007/978-981-16-6742-8_7

P_I	Prechamber pressure (bar)
q	A constant in Eq. (7.11) (–)
q, m, n, p	Constants for a given engine (–)
r	A constant in Eq. (7.12) (–)
R_u	Universal gas constant, 8.32 (kJ/kmol K)
T_1	Upstream temperature (Pa)
T_I	Prechamber temperature (K)
U_p	Crank speed (rev/s)
x	I refers to the auxiliary chamber, II refers to the main chamber (–)
β	Premixed fuel fraction (fraction of fuel mixed with air during the delay) (–)
δ	Ignition delay (ms)
λ	Relative air–fuel ratio (–)
τ	Time, non-dimensionalized with respect to nominal combustion duration (–)

High-speed indirect injection (IDI) ENGINES produce less nitric oxides and particulate emissions than similar automotive direct injection (DI) engines. Also, high-speed DI engines require high-pressure fuel injection equipment, which is expensive and fine nozzle orifices, which are difficult to maintain. On the other hand, IDI engines are less fuel efficient due to large pumping losses in the auxiliary chamber. The disadvantages of DI engines have caused a revival of interest in improving the fuel economy of IDI engines [5, 11]. The effect of changes in the geometry and assembly parameters on the engine performance could be studied if a simple representative model is available. The combustion model is an important part of this. In this paper, an attempt is made to describe the combustion process in the two chambers of an IDI engine.

A wealth of literature is available on the modelling of IDI engines [3, 4, 6, 8, 12]. Most of them fall in the category of incomplete models [2], which require certain parameters empirically adjusted for the specific system being modelled which require only fundamental data or correlations of a general nature and not specific to the system being modelled is not available. Of the former type, quasi-dimensional and zero-dimensional models are popular. The model discussed in the present work is zero dimensional and of incomplete type.

Bowden et al. [3] synthesized the heat release rate from the fuel injection pressure diagram. The magnitude of heat release in the auxiliary chamber was modelled to depend on the total amount of injected fuel and the ratio of the volume of this chamber to the total clearance volume. The portion of the fuel injected early was assumed to burn in the auxiliary chamber. An element of fuel was assumed to burn according to two laws in the shape of triangles [1], exclusively in one of the two chambers. The heat release in the main chamber was modelled delayed by 10º crank angles. Brandstetter [4] has reported calculations for a spark-ignition IDI engine. In this model, two Vibe's constants were used for the two chambers. During combustion, fuel exchange was allowed to take place through the connecting throat. The fuel was assumed to

have a memory of the chamber in which it was before combustion and hence of the Vibe's constant. Also, the combustion in the main chamber was assumed delayed by a definite crank angular time after it started in the prechamber. Miyamoto et al. [8] used a single Vibe's function. There was no distinction between the temperature and pressures in the two chambers. The total heat release due to premixed combustion was found to be 88% of the energy injected during the ignition delay. The combustion duration was correlated to the total fuel that would burn diffusively. Smoke was found to be dependent on this duration. Mansouri et al. [6] used a stochastic mixing approach during the combustion and expansion processes to describe the non-uniform distribution of fuel–air ratio in an IDI engine. Most of the discussions were written at 1500 rpm. About 3% reduction in the efficiency was calculated for a 70% reduction in the effective area of the throat. The difference between the pressures in the two chambers was small as the speed was very low. Terada [12] neglected the pressure difference between the two chambers. The experimentally obtained heat release rates and the time difference between the start of combustion in the two chambers were input to a thermodynamic simulation programme to calculate the temperatures and the formation of nitric oxides.

Description of the Phenomenological Model

The experimental heat release rates in the two chambers of the IDI engine under study (RET7, Table 3.2) were analysed, and it was found that they were similar to that shown in Terada [12]. The rate in the prechamber was very high in the beginning and was tapering off later. The heat release starts later in the main chamber and is comparatively slower. The ignition delay was slightly lower than that was observed in a DI engine of equivalent geometry. Based on these observations a model, which is closely related to a DI engine combustion heat release, was developed. The main features of the present model are as follows [5].

- It clearly shows the difference in pressures and temperatures in the two chambers and hence is useful in calculating emissions.
- It does not assume a definite crank angular delay between the start of combustion in the two chambers.
- Combustion in the prechamber is completely stopped after all the air is utilized.
- It reacts well with the changes in injected fuel and speed.
- It is zero dimensional and simple to apply.

Combustion Model

Let us consider the fuel injected in the form of a transient spray into an infinite surrounding after the ignition delay is over, as shown in Fig. 7.1. The air is entrained in the spray to vaporize the liquid fuel and mix with the vapour. The rate of the

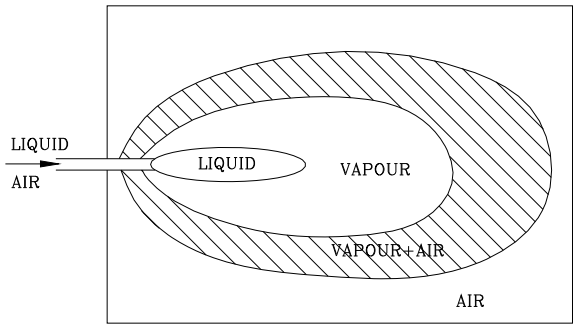

Fig. 7.1 Typical vaporizing spray

chemical reaction is very high, compared with the rate at which the fuel mixes with air [9]. Thus, the rate of burning is controlled by the rate of diffusion of air or the mixing rate. Figure 7.2 shows the rate of formation of the vapour–air mixture. If the fuel available for diffused burning is known,

$$\text{Rate of burning} = \text{Available fuel} \times \text{Rate of mixing with air} \tag{7.1}$$

Figure 7.3 shows the amount of air entrained by a transient spray and the rate of fuel injected. In the case of a diesel engine, the surrounding is finite, and the maximum air is limited. The time scale in the diagram is non-dimensionalized with

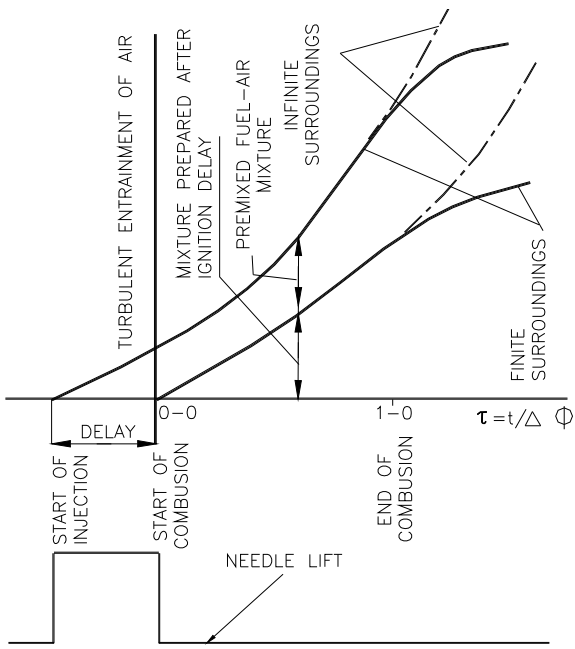

Fig. 7.2 Rate of formation of the vapour–air mixture

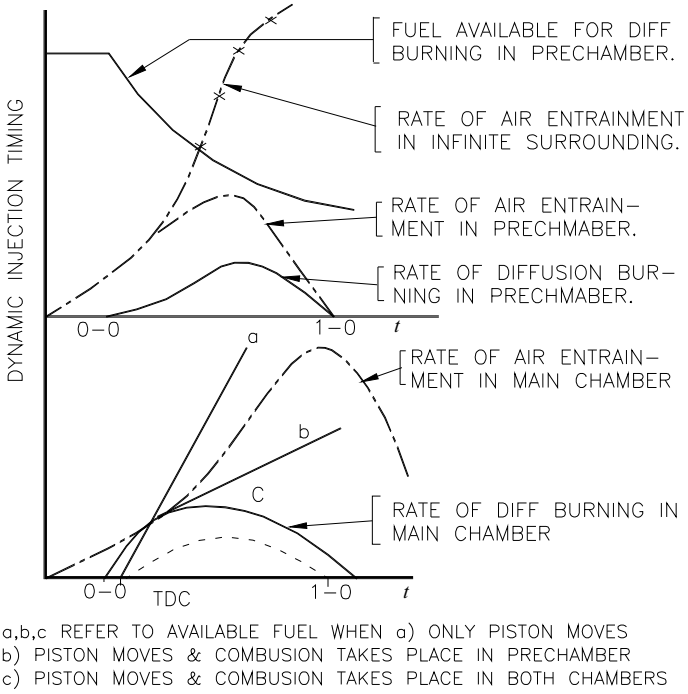

Fig. 7.3 Rate of diffusion burning

respect to combustion duration for convenience. Any fuel that mixed with air during ignition delay is termed premixed fuel, and it burns at a rate determined mostly by the chemical kinetics and engine turbulence. In Fig. 7.3, the rate of diffusion of air is plotted. The fuel available for burning decreases because of burning itself. Applying Eq. (7.1), the rate of diffusion burning could be obtained. For DI engines, Watson et al. [13] have shown that the two rates of burning discussed above could be written as below. The second equation is the well-known Vibe law of burning (1956).

$$\dot{m}_p(\tau) = \beta m_f C_{P_1} C_{P_2} \tau^{C_{P_1}-1} \times \left(1 - \tau^{C_{P_1}}\right)^{C_{P_2}-1} \tag{7.2}$$

$$\dot{m}_\tau = (1-\beta) m_f C_{d_1} C_{d_2} \tau^{C_{d_2}-1} \exp\left(-C_{d_1} \tau^{C_{d_2}}\right) \tag{7.3}$$

Here,

β = The amount of fuel mixed with air during the delay.
C_{P1} = A constant dependent on the delay period.
C_{P2} = *Nearly a constant (*=5000*) for all engines.*
C_{D1}, C_{D2} = Constants describing the rate of diffused combustion.
$\dot{m}_P(\tau) = \frac{dm_P}{d\tau}$ = Rate of the burning of premixed fuel.
$\dot{m}_d(\tau) = \frac{dm_d}{d\tau}$ = Rate of diffusion burning.

τ = Time, non-dimensionalized with respect to nominal combustion duration.

Equation (7.3) could be explained using Figs. 7.2 and 7.3. Integrating (7.3), we get

$$m_d(\tau) = (1-\beta)m_f\left[1-\exp\left(-C_{d_1}\tau^{C_{d_2}}\right)\right] \tag{7.4}$$

Substituting $m_{d_u}(\tau) = (1-\beta)m_f \exp\left(-C_{d_1}\tau^{C_{d_2}}\right)$ in Eq. (7.3), we get

I II

$$m_d(\tau) = \left[m_{d_u}(\tau)\right]\cdot\left[C_{d_1}C_{d_2}\tau^{C_{d_2}-1}\right] \tag{7.5}$$

Here, $m_d(\tau)$ = fuel quantity that would bum diffusively after τ.

The first term on the right refers to fuel available for diffusion burning, and the second term describes the rate of air entrained into the spray, or mixedness. An equation similar to (7.5) could be derived from the Vibe function also. Thus, Eqs. (7.5) and (7.1) have the same meaning. This idea was extended to an IDI engine (RET7, Table 3.2). In this type of engines, let us assume, for convenience, that all the fuel is injected within the delay period. Figure 7.4a shows the rates of diffusion burning in both the main and auxiliary chambers. The size of the auxiliary chamber limits the rate of entrainment of air. Thus, only part of the available fuel is burnt in the prechamber, and the rest flows to the main chamber along with burned gases in the form of a torch. Line "a" represents the fuel available in the main chamber if there is no burning in the auxiliary chamber. The amount of fuel increases due to the piston action. Line "b" will be the case if there is piston movement, and there is burning in the auxiliary chamber only. If burning takes place in both chambers, the available fuel is represented by line "c". Using Eq. (7.1), the rate of diffusion burning could be obtained. The fuel and air premixed during the delay period burns at a rate

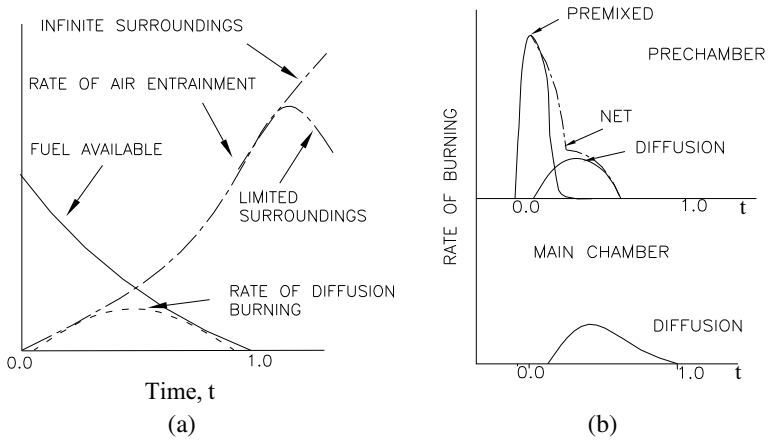

Fig. 7.4 Rates of burning in an IDI engine

determined by kinetics and turbulence only. Since it occurs very fast, we model it as a phenomenon happening only in the auxiliary chamber. Figure 7.4b shows the net burning rates in the two chambers derived from this model. Swirl chamber engines are over-swirled at high speeds and under-swirled at lower speeds [11]. Therefore, the preparation rate during the delay period decreases with speed. The mixing of fuel and air in the two chambers, their conversion to products, and the exchange of gases between the two chambers are schematically shown in Fig. 7.5.

The equation for the model could be written as follows.

Rate of the appearance of unprepared fuel in a chamber,

$$x = \frac{\mathrm{d}m_{\mathrm{ux}}}{\mathrm{d}\tau} = c\frac{\mathrm{d}m_{\mathrm{ux}}}{\mathrm{d}\tau} - \frac{\mathrm{d}m_{\mathrm{dx}}}{\mathrm{d}\tau} \tag{7.6}$$

Here, $x =$ I refers to auxiliary chamber.

$=$ II refers to the main chamber.

$\frac{\mathrm{d}m_x}{\mathrm{d}\tau}$ = Rate of transport of gases to the chamber from the adjoining chamber.

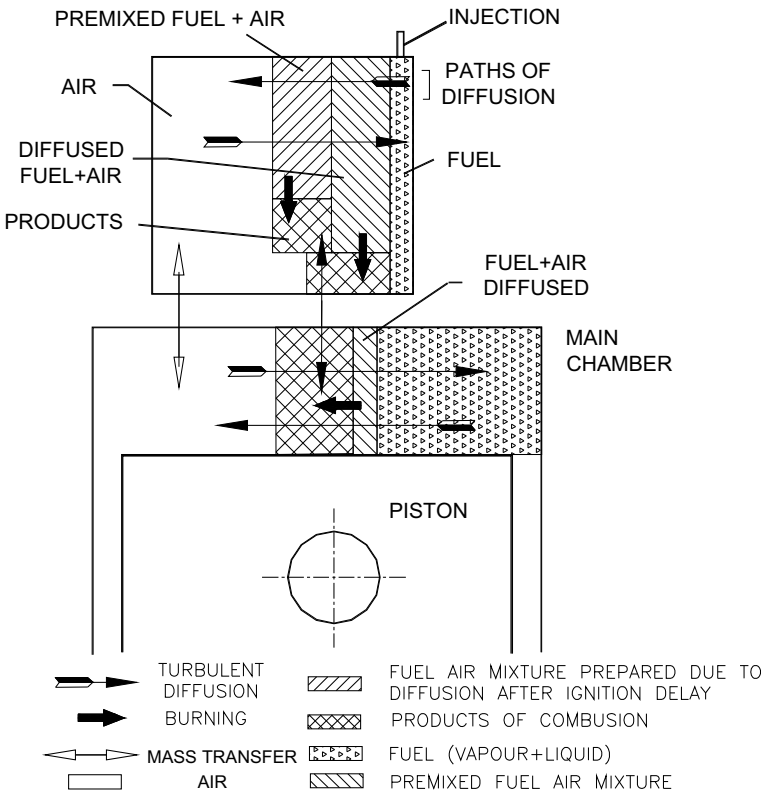

Fig. 7.5 Schematic of combustion mode1

C = Concentration of fuel in the chamber from which the above transport takes place.
$\frac{dm_{dx}}{d\tau}$ = Rate of diffusive burning in chamber X.
The flow rate is given by the equation for flow through an orifice.

$$\frac{dm_x}{dt} = f(T_1, P_1, P_2, A, D_c) \tag{7.7}$$

Here, T_1, P_1 = Upstream temperature and pressure.
P_2 = Downstream pressure.
A = Geometrical area.
D_c = Discharge coefficient of the orifice.

$$\text{Rate of diffused burning} = \frac{dm_{dx}}{d\tau} = m_{ux} g(\tau) \tag{7.8}$$

Here,

$$g(\tau) = \text{rate of mixing} = C_{d_1} C_{d_2} \tau^{C_{d_2}-1} \tag{7.9}$$

$$\begin{aligned}\text{Rate of burning of premixed fuel} &= \frac{dm_{P_1}}{d\tau} = (1-\beta) m_f C_{P_1} C_{P_2} \tau^{C_{P_1}-1} \\ &= \left(1 - \tau^{C_{P_1}}\right)^{C_{P_2}-1}\end{aligned} \tag{7.10}$$

Here, m_f = total injected fuel.
Premixed fuel fraction,

$$\beta = 1 - q\lambda^m \delta^n N^p \tag{7.11}$$

where λ = Relative air–fuel ratio.
δ = Ignition delay in milliseconds.
N = Engine speed, rev/min.
q, m, n, p = Constants for a given engine.

The ignition delay expressed in an equation similar to Wolfer [15] is given by

$$\delta = \mathrm{AP}_I^r \exp\left(\frac{E}{R_u T_I}\right) \tag{7.12}$$

Here T_I, P_I = Prechamber temperature, K, pressure, bar, respectively.
A, E = Arrhenius pre-exponent and pseudo activation energy.
R_u = Gas constant.

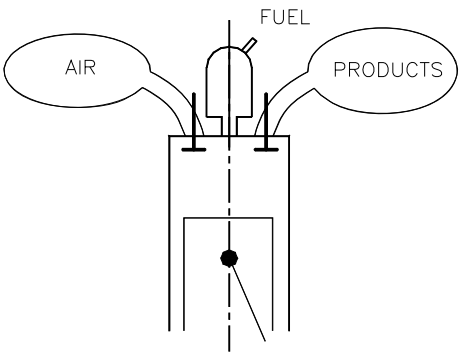

Fig. 7.6 Gas exchange model

Heat Transfer

The heat transfer coefficient in the two chambers was assumed the same and calculated using Woschni's formula [16], Eqs. (6.3) and (A.32).

Gas Exchange Model

The gas exchange process was modelled [4] as simple filling and emptying of the engine cylinder as shown in Fig. 7.6.

Friction Power

Millington and Hartles [7] give two different formulae for calculating friction power for DI and IDI engines. The extra pumping loss encountered by the flow between the auxiliary and main chamber accounts for the difference. Since in the present model, the indicated work is calculated using the pressure in the main chamber, and the formula given for a DI engine is applicable.

$$\text{fmep (bar)} = A + \text{BU}_p + \text{C C}_m^2 \tag{7.13}$$

$A = 0.06898 (\text{Compression ratio} = 4)$
$B = 0.02897$
$C = 4.008 \times 10^{-3}$,
$C_m = \text{mean piston speed, ms}^{-1}$.

Calculation Procedure

Applying the first law of thermodynamics, the models mentioned above were solved to obtain the state of gases in the two chambers. The fourth-order Runge–Kutta method was used to solve all the first-order ordinary differential equations. Step sizes of 5°, 0.1°, and 1° were used during gas exchange, ignition delay, and combustion, respectively, to avoid instabilities in the results.

Experimental Technique

The steady-state parameters were measured using conventional techniques. The measurement of differential pressure, however, needed some care. The two piezoelectric transducers, whose sensitivities are close to each other, were calibrated using a calibrating unit where hydraulic pressure was created by placing accurate weights on a standard piston. The electrical charge amplifiers were set according to the calibration constants obtained above. The outputs of the two amplifiers were fed to a subtracting amplifier, to obtain the difference. Since the pressure difference during the gas exchange is very small, the nearly horizontal line during this period was taken as the zero reference.

Results and Discussions

The parameters C_{P1}, C_{P2}, C_{D1}, *and* C_{D2} in Eqs. (7.2, 7.3 and 7.11) were correlated to the relative air–fuel ratio (λ), delay (δ ms), and speed [10] for the engine under consideration.

$$C_{P_1} = 3 + 3.9 \times 10^{-4}(\delta N)^{1.05}$$

$$C_{P_2} = 5000$$

$$C_{d_1} = 13.9\lambda^{0.64}$$

$$C_{d_2} = 1.14C_{d_1}^{0.26}$$

$$C_{d_2} = 1 - 5.5\lambda^{-0.293}(\delta N)^{-0.25}$$

The other constants in Eqs. (7.11) and (7.12) are as follows:

$q = 5.5$	$r = -1.19$
$m = -0.293$	$A = 2.58$ e-4
$n = -0.25$	$R_u = 8.32$ kJ/kmol K
$p = -0.25$	$E = 38{,}689$ kJ/kmol

Using these parameters, simulation of 1/4, 3/4, and full loads at 1500, 2000, 2500, 3000, and 3500 rpm was made, and the base condition of this was a full load at 2500 rpm. Comparison of transient absolute pressures and differential pressures obtained experimentally and by calculations is shown in Fig. 7.7. In general, the comparison is favourable. At very low loads, the model predicts a slightly earlier pressure rise in the swirl chamber. This is because the effect of low loads on delay was not taken into account. At 2000 rpm, the experimental pressure difference is higher than the predicted value. It was observed during experiments that the pressure in the swirl chamber was cyclically varying as in the case of spark-ignition (SI) engines. The origins of these variations may be similar to those in an SI engine. It was also observed that at high speeds and high loads, the differential pressure was a clear smooth curve, superimposed by high-frequency fluctuations. Similar disturbances were noticed by Mansouri et al. [6] at 1500 rpm. It was also observed that these disturbances increased with speed and load, and these may be due to the

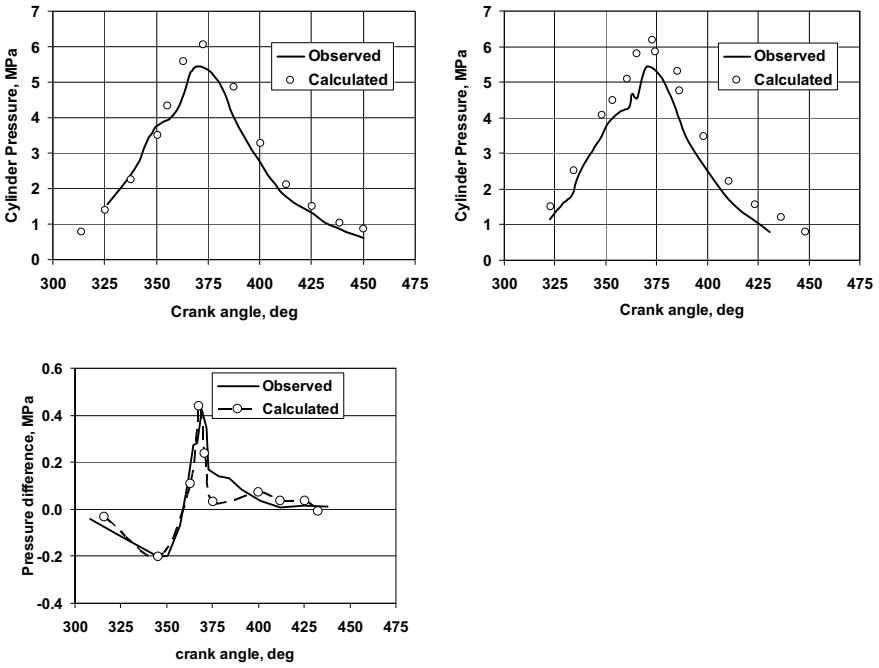

Fig. 7.7 Pressure in prechamber, main chamber and pressure difference—Crank Angle Diagrams

vortices produced at the sharp edges of the throat, resonating in the swirl chamber cavity. The pressure in the swirl chamber is low during compression stroke due to throttling. Then the pressure rises quickly due to the heat released by premixed burning. At some loads and speeds, a second peak in the differential pressure could be observed. This is due to diffusion burning in the swirl chamber.

Figures 7.8, 7.9, 7.10, and 7.11 show some parameters at the base condition. Flow through the throat is shown in Fig. 7.8. The concentration of unprepared fuel in the two chambers is shown in Fig. 7.9. Only a part of the fuel is completely burned in the prechamber, and the rest flows to the main chamber. Figure 7.10 shows the heat release rate in the two chambers. They are similar to the results reported by [12] and as discussed in Sect. 2.1. The time lag in starting combustion in the main chamber could be seen.

The mean temperatures in the two chambers are shown in Fig. 7.10. In Fig. 7.11, smoke is correlated with the duration of diffusion combustion defined as the time between 5 and 95% of the net heat release in the main chamber [8]. Two data points,

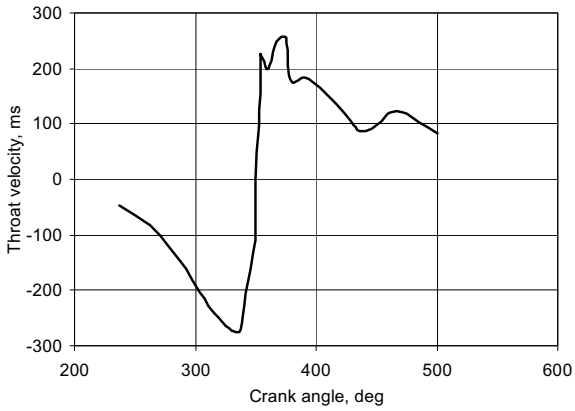

Fig. 7.8 Flow velocity through the throat

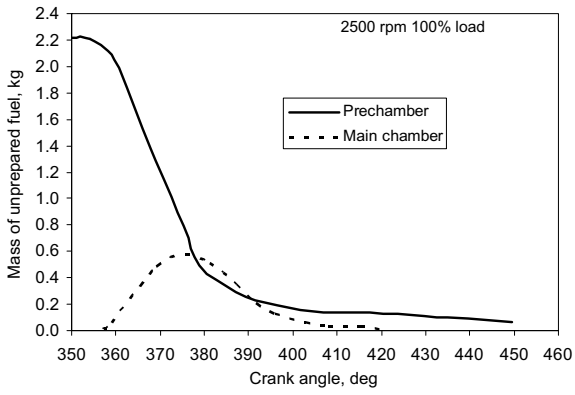

Fig. 7.9 Mass of unprepared fuel

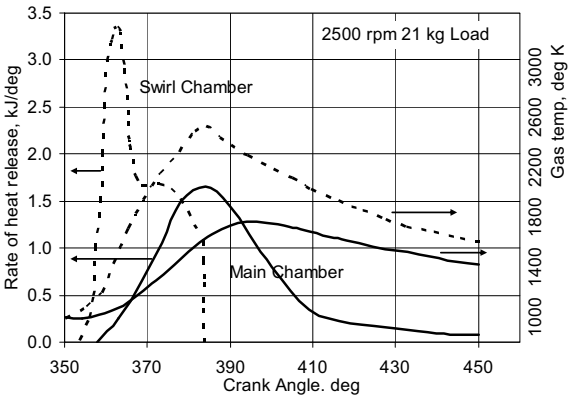

Fig. 7.10 Heat release rates in the swirl chamber and the main combustion chamber

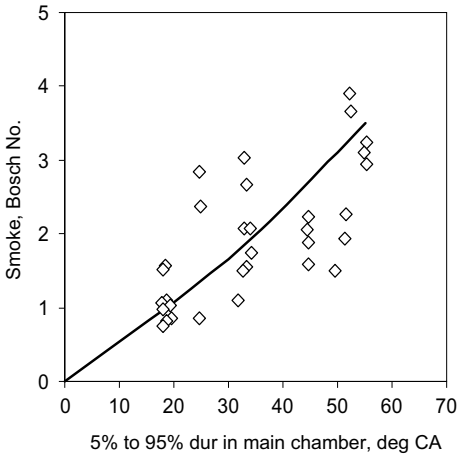

Fig. 7.11 Correlation of smoke and diffusion combustion duration

which were far away from the mean curve, were omitted. In this graph, a wide range of speed and load is covered.

Figures 7.12, 7.13, 7.14, and 7.15 show the results of some parametric studies made using the combustion model. In Fig. 7.12, the sensitivity of the model to changes in the value of nominal combustion duration (input to the model) is shown. The peak pressures and exhaust temperature are affected more by this parameter. The change in indicated mean effective pressure (i.m.e.p.) is small. Figure 7.13 shows the effect of change in volume of prechamber keeping the compression ratio constant. With the increase in volume, the mean gas temperature during injection increases as the heat transfer and throttling losses decrease. Consequently, the delay decreases. However, if the volume is very high, the burned gases at high pressure are throttled during expansion and the i.m.e.p decreases. Therefore, there is a clear optimum volume of the swirl chamber.

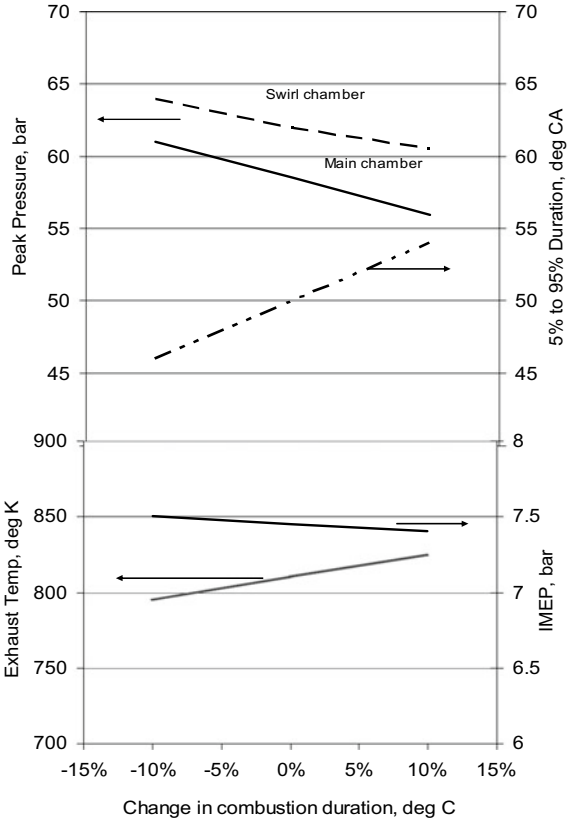

Fig. 7.12 Effect of change of combustion duration on engine performance

Peak pressures in the two chambers are affected very little. In Fig. 7.14 the effect of change in fuel, timing is shown. The peak pressure increases with negligible change in i.m.e.p. as the timing is changed. This is due to the complementary roles of both throttling and heat transfer. This tolerance to timing helps design a simple mechanism for advancing the timing with speed. The duration of combustion in the main chamber and the temperature of the exhaust gases decrease as expected. Figure 7.15 shows the effect of insulation on engine performance. The full lines show the engine behaviour for constant dynamic injection timing. The flow pattern and, hence, the convective heat transfer coefficient are affected very little when the engine is insulated. However, since the wall temperatures are nearly constant, heating of the gases during the intake stroke reduces the volumetric efficiency. This increases the duration of diffusion burning as the overall air–fuel ratio reduces, leading to lesser i.m.e.p. Since the average gas temperatures are higher, the ignition delay decreases with increased insulation. Consequently, the premixed burning is less.

The maximum pressures in the two chambers decrease, and the i.m.e.p. is affected very little if for a given insulation the timing was changed (dashed lines in Fig. 7.15) to obtain constant start of combustion. Figure 7.16 shows the engine behaviour if

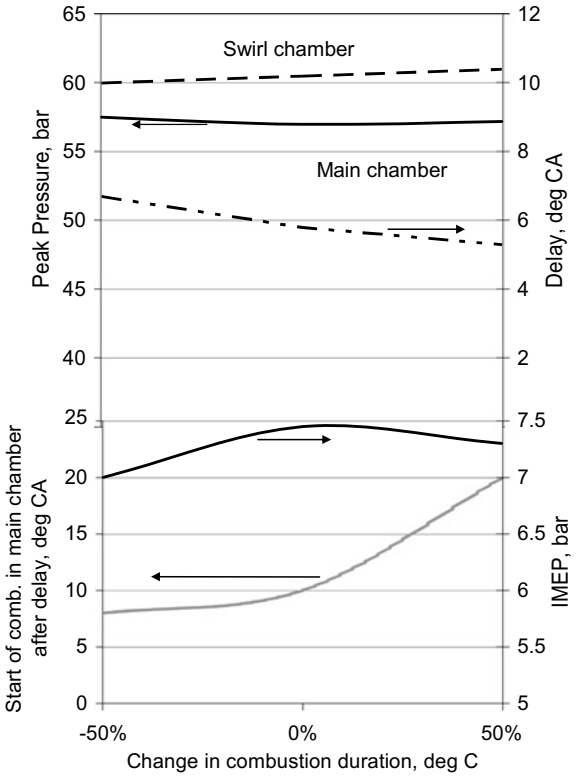

Fig. 7.13 Effect of the change of swirl chamber volume on engine performance

the swirl chamber alone was insulated. The trends are the same as in the case of complete insulation. The effect of compression ratio keeping the ratio of volumes of prechamber to the main chamber constant is shown in Fig. 7.17. Since the expansion ratio increases, there is an increase in i.m.e.p. Optimization of throat area and timing would lead to further increase in i.m.e.p. The effect of changing the throat area is shown in Fig. 7.18. With the increase in throat area from 0.5 to 1.5 times the base value, there is a 10% increase in indicated mean effective pressure mainly due to reduced throttling [6, 11]. This study assumed that the rate of air entrainment was unaffected by the change in the throat area.

Conclusions

1. A physical explanation was provided for the available heat release correlations for DI engines.

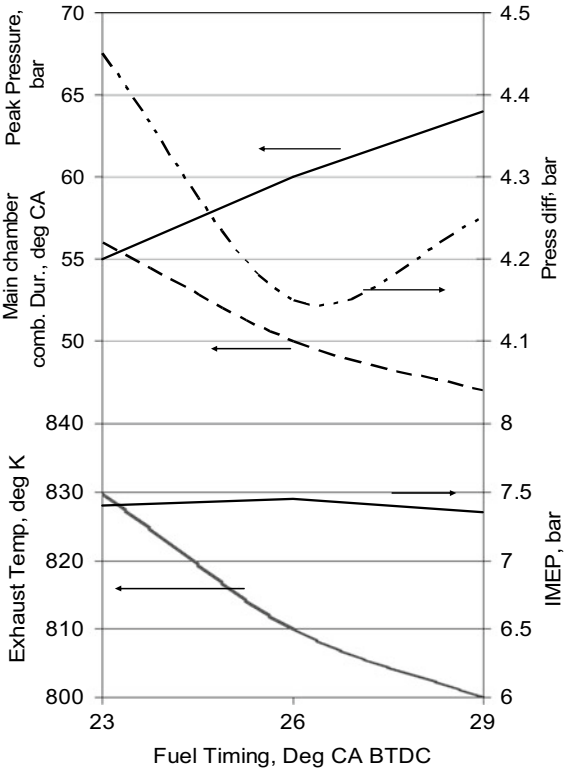

Fig. 7.14 Effect of change of fuel timing on engine performance

2. One such correlation [16] was extended to IDI engines. It was written as rate of diffusion burning proportional to rate of air entrainment × available fuel for diffusive burning [11].
3. Constants in the correlation were tuned using experimental data over wide ranges of speed and load. Swirl chamber pressure and the differential pressure were predicted reasonably well.
4. Smoke was correlated with the duration of diffusion burning in the main chamber.
5. Parametric studies were made to describe the effect of changes in the volume of the swirl chamber, throat area, heat transfer, compression ratio, fuel timing, and duration of combustion. In general, the results reflected the observed trends in a real engine.
6. Bmep, temperature, heat transfer, and airflow obtained by integration over the cycle are predicted to an accuracy of about 5% over the entire speed load range. Measured values of instantaneous pressures in the two chambers are within 7% of predicted results above 50% full load. At lower loads, the predicted pressures are higher.

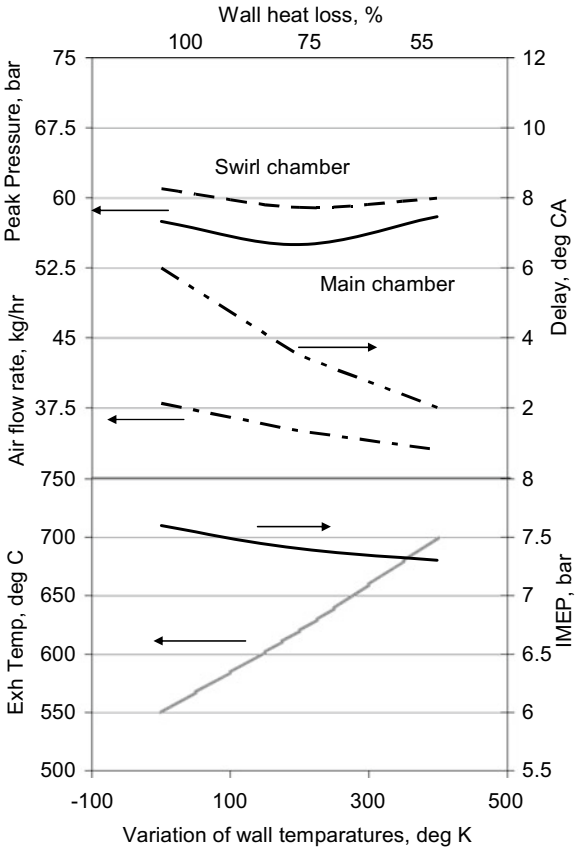

Fig. 7.15 Effect of insulation on engine performance

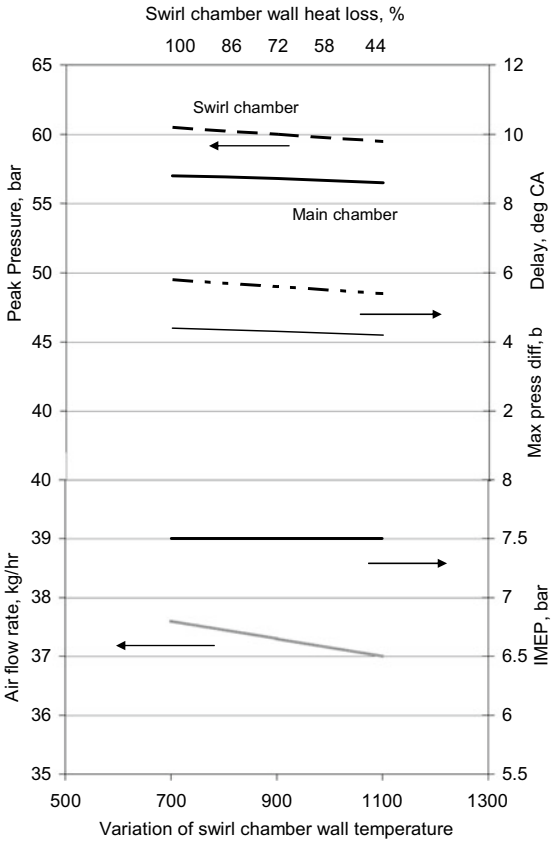

Fig. 7.16 Effect of insulation of swirl chamber on engine performance

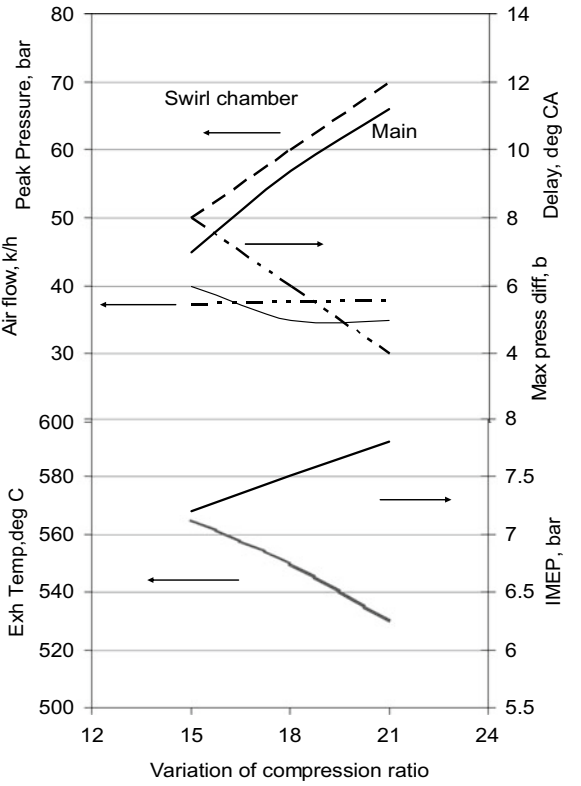

Fig. 7.17 Effect of variation of compression ratio on engine performance

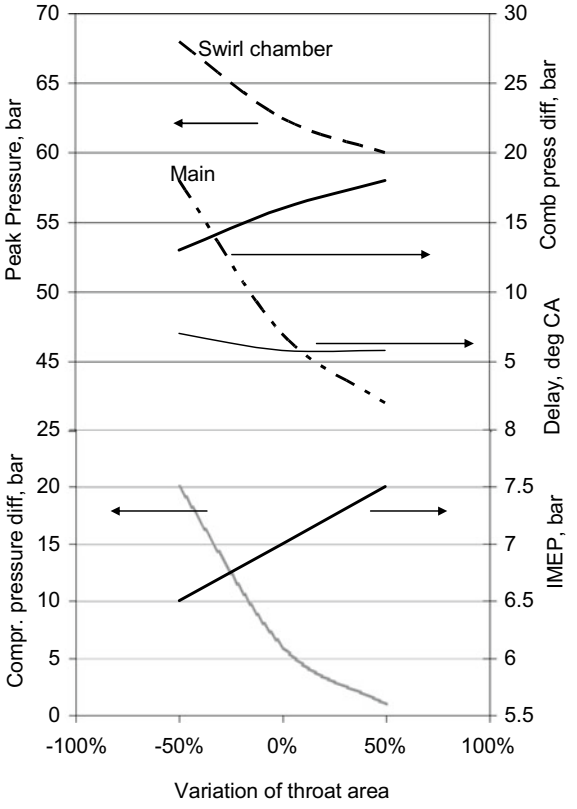

Fig. 7.18 Effect of variation of throat area on engine performance

References

1. Austen AEW, Lyn WT (1962) The application of heat release analysis to engine combustion study. CIMAC, Copenhagen
2. Borman GL (1980) Modelling flame propagation and heat release in engines. In: Mattavi JN, Amann CA (eds) Combustion modelling in reciprocating engines. Plenum, New York
3. Bowden CM, Samaga BS, Lyn WT (1969) Rate of heat release in high-speed induction ignition engines. In: Proceeding Swirl chamber wall heat loss Main chamber variation of swirl chamber wall temperature—IMechE 1969–70 184 1. Part 3
4. Brandstetter WR (1980) Modelling of a stratified charge engine with an unscavenged prechamber. In: Mattavi JN, Amann CA (eds) Combustion modelling in reciprocating engines. Plenum, New York
5. Lakshminarayanan PA, Nagpurkar UP (1986) Rate of heat release for the divided combustion chamber. SAE 860084
6. Mansouri SH, Heywood JB, Radhakrishnan K (1982) Undivided chamber engine Part I: a cycle simulation, which predicts and emissions. SAE 820273, Detroit, February
7. Millington BW, Hartles ER (1968) Frictional losses in diesel engines, SAE 680590
8. Miyamoto N, Cnikahisa T, Murayama, Sawyer TR (1985) Description of diesel engine rate of combustion and performance using Vibe's functions. SAE 850107
9. Plee SL, Ahmad T (1983) Relative roles of premixed and diffusion burning in diesel combustion, SAE 831733

10. SAE Handbook (1984) 3, pp 24.01
11. Scott J (1985) Giving the IDI diesel a fresh start, SAE 850452
12. Terada K (1981) Ermittlung der Gastemperaturen in beiden Brennraumen eines viirbelkammer dieselmotors. Motortechnische Zeitschrift (MTZ), 42
13. Watson N, Pilley AD, Marzouk M (1980) A combustion correlation for diesel engine simulation, SAE 800029
14. Wiebe I (1956) Halbempirische Formel fur die Verbrennungsgeschwindigkeit. Verlag der Akademie der Wissenschaften der UdsSR, Moscow
15. Wolfer HH (1938) Ignition lag in diesel engines, VDI-Forschungsheft No. 392
16. Woschni G (1961) A universally applicable equation for the instantaneous heat transfer coefficient in the internal combustion engine SAE 675931

Chapter 8
Mixing Correlations for Smoke and Fuel Consumption of Direct Injection Engines

Nomenclature

B	Distance from the nozzle to the bowl (m)
C_d	Coefficient of discharge (–)
D	Geometrical diameter of the orifice (m)
d_e	Equivalent spray orifice diameter (m)
l	Length of the potential and liquid core (m)
t	Time from the start of injection and (s)
u_j	Fuel velocity at the nozzle tip (m/s)
ρ_a	Density of air (kg/m^3)
ρ_f	Density of the fuel (kg/m^3)
x	Spray penetration (m)

The adaptation of diesel fuel to direct injection engine necessitates the understanding of mixing of fuel with air. All direct injection (DI) diesel engines are generically the same with the following features to achieve optimum mixing of fuel. (a) High-pressure injection of diesel fuel through fine nozzle holes, (b) momentum incorporated to air during the inlet stroke by the inlet port, and (c) a bowl in the piston which amplifies the inlet-swirl and contains the majority of combustion. A variety of synergistic designs of these three processes has been successful. Before self-ignition of fuel, the reaction rate is slow and found to be dependent on rates of turbulent mixing and chemical reactions [5]. At the end of the delay period, the concentration of products of combustion reaches a critical level to initiate uncontrolled premixed combustion. Subsequently, diffusion-controlled main combustion takes place. The rate of combustion in this period is exactly equal to the rate at which air is mixed with fuel. In the pockets where ignition occurs, the fuel and air are mixed in stoichiometric proportion. If the delay period to form the critical concentration of precursors is zero, then no fuel could be mixed leaner than stoichiometric burning. In this case, there would be no hydrocarbon emission. However, since the delay is finite, there could be pockets diluted by air to proportions less than the lean flammability limit, before

P. A. Lakshminarayanan and Y. V. Aghav, *Modelling Diesel Combustion*,
Mechanical Engineering Series, https://doi.org/10.1007/978-981-16-6742-8_8

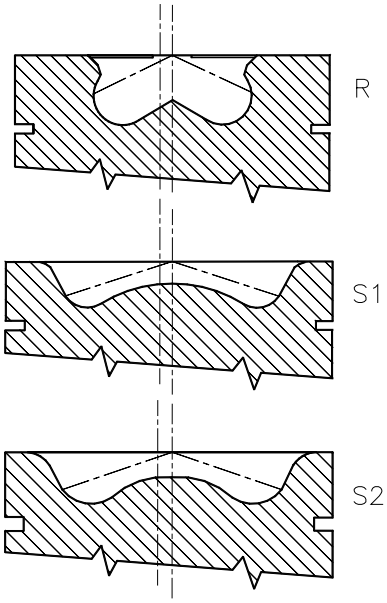

Fig. 8.1 Three piston cavities used for evaluating air–fuel momentum correlations Kuo et al. [12, 13]

auto-ignition occurs in several pockets. Thus, this fuel does not burn and contributes to emissions. Dent [7] correlated the emission of aldehydes and soot with mixing rate calculated from a mixing parameter, Taylor's microscale. Morris and Dent [16] and Bassoli et al. [3] correlated fuel consumption and soot emission with the ratio of the total air momentum at TDC to the total momentum of injected fuel with some success. Ball [2] related the performance to the ratio of penetration of fuel spray at the end of ignition delay to the penetration up to impingement against the wall. Timoney [19] correlated the engine performance with the crosswind velocity. Wakuri et al. [21] have attempted to correlate the angular spray dispersion with the engine behaviour. Ishida et al. [10] reported improvement in performance proportional to a K-factor, defined as the ratio of the piston cavity volume to the total volume at TDC including the piston land and groove crevices. Munro [17], and McLean [15] have reported performance and emissions benefits when the piston top land is reduced. In this paper, an attempt is made to explain the indicated behaviour and emissions of all the direct injection diesel engines. Kuo et al. [12] thoroughly evaluated the correlations mentioned above. They had presented detailed experimental and calculated data on three types of cavities, namely re-entrant type (R) and two shallow cavities (S1, S2), Fig. 8.1. The data consisted of injection duration, injection velocity, the total momentum of air, total momentum of fuel injected, distribution of radial velocity in the piston cavity, amount of air inhaled, and quantity of injected fuel. All the experiments were designed to study the effects of variation in speed, air–fuel ratio, and shapes of piston bowl on the indicated specific fuel consumption (ISFC) and dry Soot in the exhaust. After evaluating the correlations of the data mentioned above, they concluded that although the correlations seem to have potential in specific

cases as interpretive tools, the lack of generality limited their usefulness for the design engineer (Kuo et al. [12, 13]). In this chapter, the performance and emissions were successfully related to the characteristic ratio of the momenta of air useful to combustion and the injected fuel [6].

Characteristic Parameter for Air–Fuel Mixing in a Crossflow

A correlation between ISFC and the product of swirl number of airflow (Appendix V) at the end of the inlet stroke, as measured in a steady flow rig according to von Thien [20], and the number of spray orifices was developed by the authors for engines A8, D8, F8, G8, H8, K8, N8, C9, C10, Table 3.2. When the product attains a value between 10 and 12, the ISFC is the minimum (Fig. 8.2). This relationship is akin to the work of Wakuri et al. [21] but does not indicate the type and shape of the combustion chamber and injection parameters except the number of spray orifices. At higher engine speeds, the injection velocity increases to improve the atomisation of fuel and hence combustion efficiency. Therefore at higher speeds, the ISFC for the same swirl number and the number of sprays is lesser. Abramovitch [1], Ramsey and Goldstein [18] and Kamotani and Greber [11] studied the trajectory of steady gas jets in a uniform crossflow. The ratio of jet momentum fluxes of air and fuel was the major correlating parameter. Morris and Dent [16] encountered difficulty in using this parameter and hence considered the measured air–fuel ratio inside the

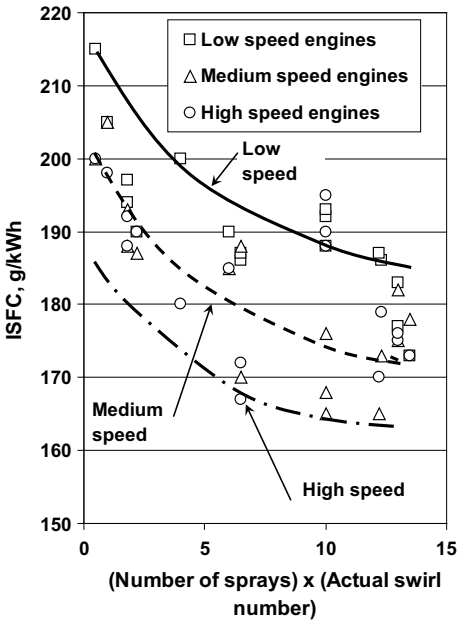

Fig. 8.2 Correlation of product of the number of sprays

gas jet to correct the parameter. The correlation implied that it applies to combustion chamber supported by swirl, and the effect of fuelling on the air–fuel mixing rate is to be considered. In this chapter, the dilution of fuel is appropriately taken into account as only the air, which is taking part in the main combustion, is considered. In a transient jet, the flux of fuel is not continuous. Over fuelling and under fuelling could be considered by the integrated momentum of injected fuel. Instead of the ratio of momentum fluxes considered by Abramovitch [1], the ratio of the momentum of air useful to combustion and the integrated momentum of injected fuel is considered along the lines of Bassoli et al. [3], at a characteristic instant in time.

The Concept of Useful Air

Air, which is available during the main period of combustion for mixing with fuel, is termed useful. Its description involved understanding of air volumes, spray pattern, and transients after injection is completed [6].

(A) The e*ngine size*

There are two cases to be distinguished. (1) When the bumping (squish) clearance above the squish area is small and (2) when the clearance is very large, of the order of the depth of the bowl in piston. Figure 8.3 shows these two cases schematically.

Case (1): Small squish clearance: In engines of bore less than 120 mm, the air swirl at BDC is high (swirl number 1.5–3.5) and is further enhanced at TDC due to the reduction in moment of inertia of the air. The sprays are designed to remain within the cavity during a substantial period of combustion. Therefore, the air in the squish gap remains fairly unmixed with the fuel. Thus, the air in this gap is not useful.

Case (2): Large squish clearance: In large engines of bore greater than 120 mm, the swirl level is low (swirl number less than 1.5) and the bowl in the piston is shallow. Also, the squish clearance is of the order of the bowl depth. Hence, about a third of the spray is designed to penetrate up to the cylinder wall. The air above the squish gap is useful as the fuel mixes with it during the period of combustion. In both cases, the zone of air in the piston land and ring groove crevices remains unavailable and

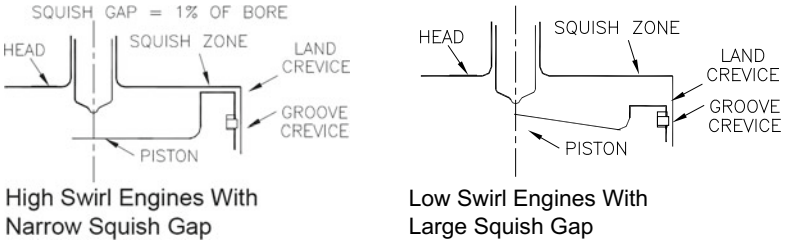

Fig. 8.3 Effect of engine size on useful air

hence not useful [15, 18]. The concept of unavailability of air in squish gap in small engines is very closely related to the K-factor [10].

(B) *Potential core of the spray*

In the potential core of a turbulent jet, the concentration of fuel [14] is very high. Downstream of this core intense mixing with the air entrained due to shear flow takes place. In the case of liquid sprays, even when the chamber is above critical pressure and temperature of the fuel, the liquid core is observed within the potential core to slightly increase the unmixed length of the potential core. The length of the potential and liquid core [14] is given in Eq. 8.1 as

$$l = 7.5 d_e \tag{8.1}$$

Here, d_e = equivalent spray orifice diameter $= d\sqrt{\frac{\rho_f}{\rho_a}}$.

D = geometrical diameter of the orifice.

ρ_f = density of the fuel.

ρ_a = density of air.

Figure 8.4a and b show the liquid core in different cases. The volume of air in the zone defined by the radius, corresponding to the length of the liquid core is unavailable for combustion, in large or small engines.

(C) *Characteristic time*

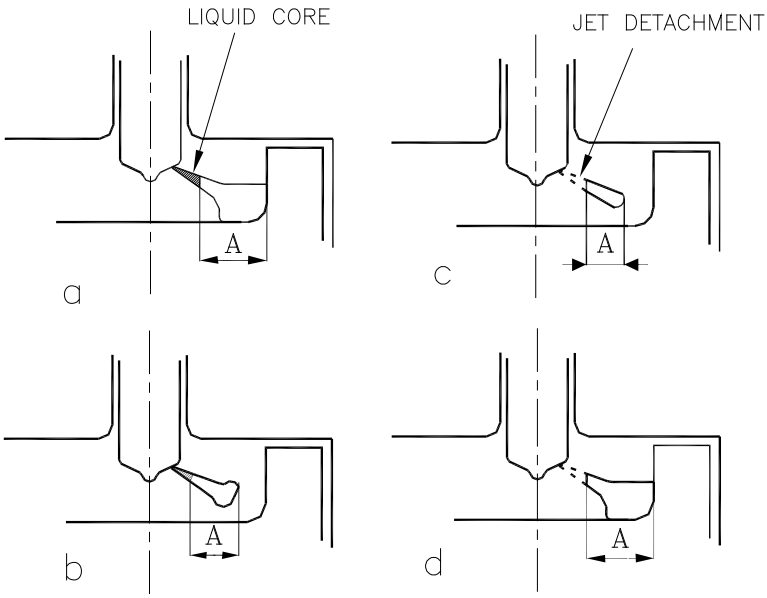

Fig. 8.4 Schematic of fuel spray showing positions of liquid core and detachment

When the fuel enters the combustion chamber and mixes with air during the ignition delay period, the mixtures that are too lean or too rich to burn (equivalence ratio outside the range of 0.5–3) give the trend of variation of HC emission [9]. Also, penetration is important from the viewpoint of understanding HC emissions and ISFC [14]. The end of the ignition delay period is the characteristic time at which all the parameters of the correlation are evaluated. At or about the maximum engine load, the fuel spray penetrates almost up to the wall of the piston bowl or the cylinder wall at the end of the ignition delay depending upon the design of the cavity and the size of the engine bore. Figure 8.4a shows this case. However, at part loads, the penetration at the characteristic time falls short of the distance to the wall of the combustion chamber. The air in the zone between the spray tip and the combustion chamber wall remains unavailable for combustion. Figure 8.4b shows schematically the part-load cases.

(D) *Spray detachment*

At the end of the injection, the spray detaches from the nozzle. The detached zone still contains traces of fuel and the mixture in it is too lean to burn effectively. Figure 8.4c shows the spray detachment schematically at the end of the delay period. The penetration of the detached portion of the jet is calculated using Eq. (4.7) as shown in Fig. 8.3. The air in the radius corresponding to the detachment is not useful for effective combustion.

In all cases shown in Fig. 8.4a–d, the air in the annular ring of radial width A is useful. Therefore, the proportion of useful air is less than that given by the *K*-factor, by the amount corresponding to the initial thick spray or detached tip and the non-penetrated distance.

Calculation of Momentum of Injected Fuel

The integration of the instantaneous product of injected fuel quantity and the fuel velocity at the nozzle tip gives the total momentum of injected fuel. However, measurement of the instantaneous fuel flow and the velocity is tedious in commercial engines. Assuming the coefficient of discharge, C_d as 0.8, and coefficient of velocity, C_v as 0.9 the momentum could be calculated from the pressure–time diagram measured at the inlet to the injector. For a quick estimate, the average pressure determined by the area under the diagram during the injection period may be used. The average velocity calculated using the average pressure mentioned above, however, results in a higher estimate of average velocity because of the nonlinear relationship.

$$\text{velocity} \propto \sqrt{\text{pressure difference}} \tag{8.2}$$

The estimate is correct only when the pressure difference is constant during the needle open period. Assuming a parabolic variation of pressure from needle opening

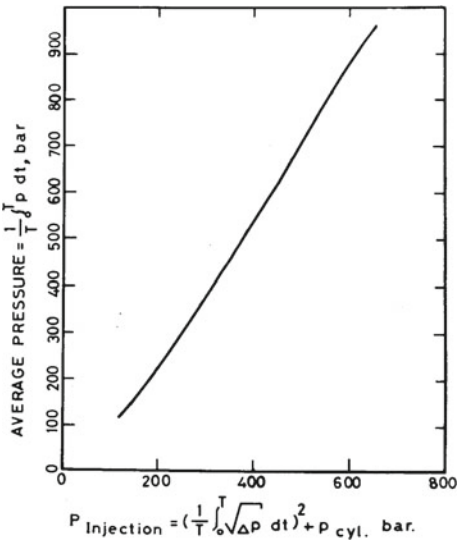

Fig. 8.5 Relationship between average pressure and corrected injection pressure

pressure to needle closing pressure, the average pressure that will yield the correct average velocity could be obtained. In Fig. 8.5, the average is shown along the *y*-axis and the correct pressure for velocity calculation is read along the *x*-axis. By using this help-graph for any average nozzle pressure, average velocity could be easily calculated. The total momentum of the injected fuel could then be calculated as the product of fuel mass injected per cycle and the average velocity. The penetration of the spray at the end of the ignition delay is appropriately calculated using the average velocity at the nozzle tip during this period. The penetration,

$$x = \min\left(C_d\sqrt{8u_j d_e t}, B\right) \tag{8.3}$$

Here,

u_j = Fuel velocity at the nozzle tip,
d_e = Equivalent orifice diameter,
t = Time from the start of injection and
B = Distance from the nozzle to the bowl
C_d = Coefficient of discharge of the nozzle hole

There are special cases when the injected quantity is so low that the spray detachment calculated from Eq. (8.2) is larger than the bowl radius, B at the characteristic time. Near the wall, the fuel collects like a cloud [22] and swirls along the wall (Fig. 8.4d). A reasonable estimate for the maximum detachment is assumed as 70% of the bowl radius which means that the thickness of the cloud is about twice the radial distance from the point of maximum velocity to the wall (Fig. 8.6).

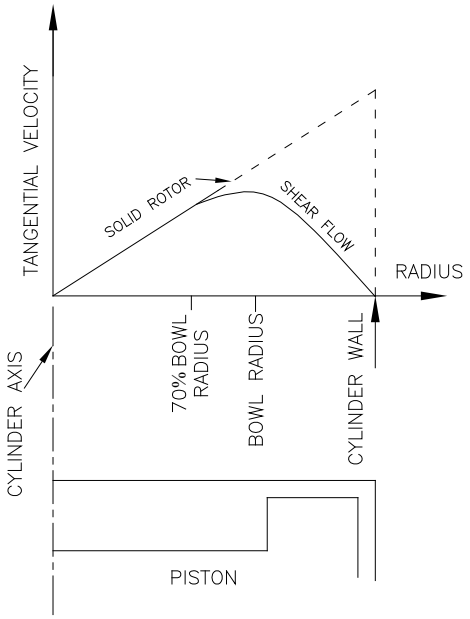

Fig. 8.6 Variation of tangential velocity of air in the radial direction

Calculation of Momentum of Useful Air

At TDC, the tangential velocity of the air in the cup and squish gap is as shown in Fig. 8.6. The linear variation of velocity suggests strong solid-body rotation above the cylinder axis. Due to the wall drag, the velocity falls off close to the wall. The linear relationship is assumed valid in the squish gap also. The total air momentum in the annular ring of radial width A as shown in Fig. 8.4 could be calculated from the velocity profile. Results of thorough analytical flow calculations using finite difference techniques are given in Kuo et al. [12, 13] for different types of combustion chambers (R, S1, and S2) (Fig. 8.7).

In case such calculations are not possible, a reasonable estimation of the air momentum could be made by assuming,

- Solid-body rotation of air during piston travel from BDC to TDC.
- Air density as a function of compression ratio with respect to inlet valve closing time.
- End of ignition close to TDC.
- The total angular momentum is retarded by about 25% during the compression stroke, due to friction in the squish gap.
- The spray reaches the walls of the piston bowl by the end of the ignition delay period.
- The velocity profile, in general, is as shown in Fig. 8.6 [4]. Using this profile and assuming the momentum loss due to friction, the angular momentum could be easily calculated.

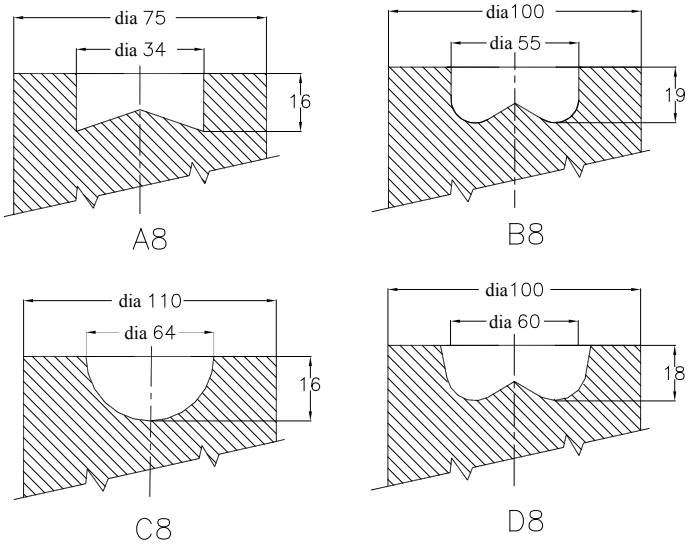

Fig. 8.7 Types of piston cavities used for correlation validation A8, B8, C8, and D8

Characteristic Mixing Parameter of an Engine

The ratio of the momentum of air useful to combustion at TDC as explained above to the integrated momentum of fuel is defined as the parameter characteristic of the engine design and operating conditions. This factor will cover the principles envisaged by various investigators in the following manner (Table 8.1).

Since the principal direction of air, movement is tangential and that of the fuel is radial, the crosswind velocity concept is in the calculation of the momentum of air. The basis of the present work is an improved definition of the ratio of the momentum of air to the momentum of injected fuel. Depending upon the ignition delay, the

Table 8.1 Introduction of different facts in a single correlation

Feature	Figure showing the concept of useful air	Ref
Momentum ratio and crosswind velocity	Figure 8.4a–d	Morris et al. [16], Bassoli et al. [3], Timoney [19]
Penetration at the end of ignition delay	Figure 8.4a–d	Ball [2]
Swirling angle	Figure 8.4d	Wakuri [21]
K-factor	Figure 8.3a, b	Ishida et al. [10]
Exclusion of dead volumes	Figure 8.3a, b	Ishida et al. [10], McLean [15], Munro [17]

outer radius of the typical annular volume changes. The outer radius is nearly equal to the penetration of fuel in a swirling flow. For medium-size engines, as already described, we are excluding squish volume and hence K-factor is considered. Since the land and groove crevices are not considered the dead volumes are excluded. The swirling angle is dependent on the strength with which airflow deflects fuel spray. This is dependent on the momentum ratio. Thus, the new definition of momentum ratio in this paper seems to cover wide-ranging observations and concepts of previous workers.

The indicated performance is not only a function of fuel–air mixing and hence rate of burning but also a function of the heat transfer, especially about compression TDC. Therefore, while attempting to derive a universal relationship of the performance and emissions with fuel–air mixing the factor of engine surface to volume ratio (proportional to engine bore) must be kept in mind. Since the heat transfer at TDC is fairly well understood, it may not be difficult to incorporate this effect while estimating ISFC. However, the authors have refrained from doing this for reasons of brevity and hence assumed that for the popular bores in the range of 70–125 mm the heat transfer phenomenon is similar. The combustion behaviour of the direct injection open chamber diesel engine with swirl-supported combustion was found strongly related to the characteristic parameter. This was validated over a wide range of diesel engines.

Validation of the Mixing Parameter

Input Data

For a part of the validation of this correlation, the data of Kuo et al. [12, 13] for chamber shapes (Engines R1, S1, S2 in Table 3.2) shown in Fig. 8.1 were extensively used. The engine data are given in the following table.

Bore × stroke	88 × 85.5 mm
Fuel injection system	Rotary pump, 5 holes × 0.22 mm, 150 deg. spray angle, 33.9 MPa opening pressure

Instead of the value of fuel momentum as given by Kuo et al. [12, 13], the momentum calculated by the product of mean fuel velocity and the injected quantity given in Kuo et al. [12, 13] was used. Assuming a coefficient of discharge of the orifice in the nozzle as 0.8, the average injection pressure difference is calculated from the published injection velocity 11 [12, 13]. This pressure difference was used in Eq. (8.2) to calculate the detachment at the end of the ignition delay. Results of these calculations are tabulated in Appendix VI.

The correlation worked even when the air and fuel momenta are obtained by simplified calculations assuming solid-body rotation with a 25% loss in momentum

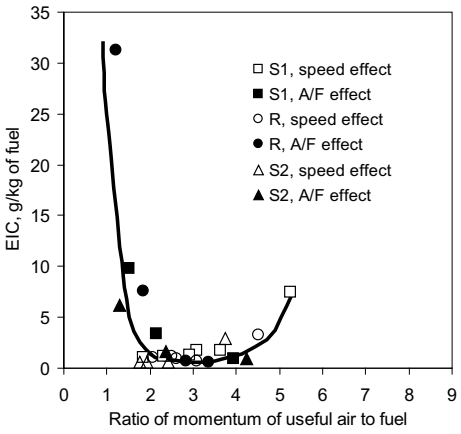

Fig. 8.8 Measured exhaust soot exhaust indicated carbon as a function of the ratio of momentum of useful air to total fuel momentum

during the compression stroke. The authors collected extensive data on four of the engines. The types of combustion chambers and operating speeds are mentioned in the following table.

Engine type	Bore, stroke, mm	Speed, rpm	Piston cavity
A8	75, 76	2200	Figure 8.8b toroid
B8	100,120	1500, 2000, 2300	Figure 8.8b toroid
C8	110, 116	1200, 1500, 1800,2000	Figure 8.8c hemisphere
D8	100, 110	1200,1600,1800, 2000	Figure 8.8d toroid

Results

Figure 8.8 shows the major exhaust soot exhaust indicated carbon (EIC defined as dry soot emitted per unit of energy produced at the engine shaft, g/kWh) of combustion chambers R, S1, and S2 plotted against the characteristic ratio of the momentum of useful air to the total momentum of fuel. There is a unique optimum range of the characteristic ratio for both re-entrant and shallow type piston bowls. Therefore, independent of the shape of the piston cavity and air–fuel ratio, the spray pattern can be matched with the piston bowl by designing the proper dimensions.

This is in contrast with the conclusion of Bassoli et al. [3] and Kuo et al. [12, 13] where the optimum range varied with the piston cavity shape lacking in generality, as the parameter identified by them did not capture exactly the air–fuel mixing phenomenon and the factors affecting them. Above a certain value of momentum ratio, excessive mixing causes too much dilution resulting in poor quality lean

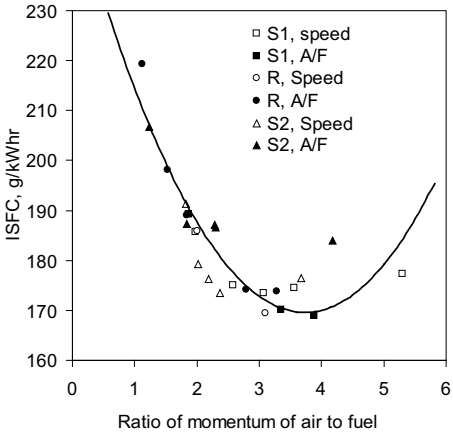

Fig. 8.9 Indicated specific fuel consumption as a function of the characteristic mixing parameter

burning. When the air momentum is very less, rich burning causes excessive emission of carbon. Carbon emission increases at a lesser rate when the mixing parameter is above the optimum range than when it is below the optimum.

Similarly, Fig. 8.9 shows the effect of the characteristic mixing parameter on the indicated specific fuel consumption (ISFC) of chambers R, S1, and S2. A thick line shows the relationship. There is a definite optimum range of the characteristic ratio for ISFC as well. Nevertheless, this range is narrower than that for EIC. Also, it lies within the optimum range for EIC.

The data of engines A8, B8, C8, and D8 covered wide ranges of operating speed, bore sizes, and spray arrangement. The shapes of the piston cavities were hemispherical and toroidal type. Thus, the most popular range of direct injection diesel engines was considered. The ratio of the momentum of useful air to the fuel momentum is calculated using the simplified method, as explained earlier. The indicated performance, the estimated air momentum at TDC from the steady flow rig data, the total momentum of the injected fuel consumption, and other data of these engines are tabulated in Appendix VII. In Fig. 8.10, the indicated specific fuel consumption is plotted against the characteristic mixing parameter. For comparison, the relationship in Fig. 8.9 is transcribed as a thick line in Fig. 8.10. The correlations of engines A8, B8, C8, and D8 could be seen to coincide with the relationship observed for types R, S1, and S2 in Fig. 8.1.

The carbon emissions of engines A8, B8, C8, and D8 were measured using a Bosch smoke meter in Bosch smoke number. The smoke values were converted to carbon particulate concentration using the correlation of Hardenberg and Albrecht [8]. Figure 8.11 shows the correlation curve transcribed from Fig. 8.8 against the backdrop of the exhaust carbon of the commercial engines namely A8, B8, C8, and D8. The favourable comparison of the correlations shown in Figs. 8.8, 8.9, 8.10 and 8.11 with measured data of fuel consumption performance and smoke emissions of various commercial and experimental diesel engines validates the universality of the correlation. The optimum range of mixing parameter for the performance and

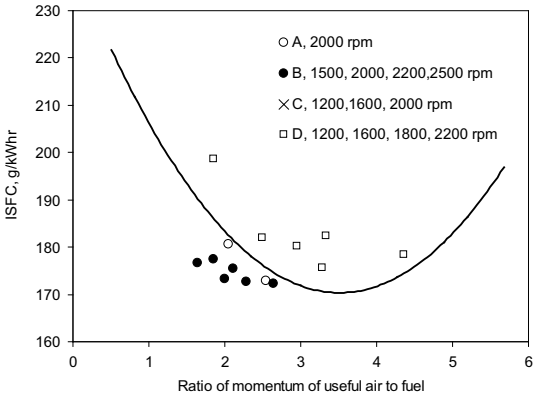

Fig. 8.10 Indicated specific fuel consumption as a function of the characteristic mixing parameter

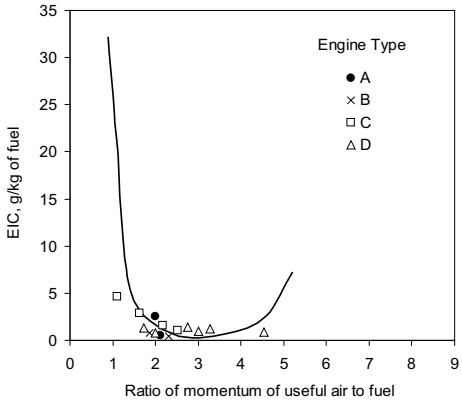

Fig. 8.11 Exhaust soot exhaust indicated carbon as a function of the characteristic mixing parameter

emission is irrespective of the shape of the piston cavity, type of engine, size, and speed for all direct injection diesel engines.

Conclusion

After the study and evaluation of various mixing correlations, a new concept of useful air was introduced. This is the air in the annular zone, where the fuel spray excluding liquid core is present at the end of the ignition delay period. The ratio of the momentum of the useful air to the total momentum on the total injected fuel is defined as the characteristic parameter. The mixing parameter is found strongly correlated with the indicated performance and dry soot emissions of direct injection engines. The correlation has been validated by using seven types of combustion chambers in pistons of size from 75 to 110 mm running at speeds from 2500 to 1200 rpm and at wide-ranging air-to-fuel ratios.

References

1. Abramovitch GN (1963) The theory of turbulent jets. MIT Press
2. Ball WF (1980) A practical approach to the combustion modelling of a direct injection diesel engine. In: Conference on recent progress in automobile engine and emissions. La Sociéte' des 1' automobile, Paris, April 2–3
3. Bassoli C, Bodritti G, Cornetti GM (1985) Optimum air motion and spray formation for D.I. Diesel. SAE Paper 850501
4. Borgnakke C, Davis GC, Tabaczynski RJ (1981) Prediction of in-cylinder swirl velocity and turbulence intensity for an open chamber cup in the piston. SAE 810224
5. Chandorkar SB, Dani AD, Lakshminarayanan PA (1988) Effects of injection parameters, fuel quality, and ambient on the ignition delay and the location of the flame kernel in a diesel spray in a quiescent chamber. SAE Transactions, SAE 881227
6. Dani AD, Nagpurkar UP, Lakshminarayanan PA (1990) Universal mixing correlations for the performance and emission of open chamber diesel combustion supported by Air Swirl. SAE 900446
7. Dent JC (1980) Turbulent mixing rate—its effect on smoke and hydrocarbon emission from diesel engines. SAE 800092, Diesel combustion and emissions, SAE Proceedings, P-86
8. Hardenberg H, Albrecht H (1987) Limits of soot determination from optical measurements (in German). Motoren Techniche Zeitschrift MTZ 48:2
9. Henningsen S (1984) Hydrocarbon emission from the ignition delay period in a D.I. diesel engine. SAE Trans 93(6):28–40
10. Ishida, Kihara, Furubayashi (1985) Development of direct Injection diesel engines. SAE 850068
11. Kamotani Y, Greber I (1972) Experiments on a turbulent jet in a crossflow. AIAA J 10(11)
12. Kuo TW, Henningsen S, Wu KJ (1988a) Evaluation of four mixing correlations for performance and soot emission characteristic of a small open chamber diesel engine. SAE 880599
13. Kuo TW, Wu KJ, Henningsen (1988b) Effects of fuel over-penetration and over-mixing during the ignition delay period on hydrocarbon emissions from a small open chamber diesel engine. In: Proceeding of international symposium on basic processes in I.C. engines III. ASME
14. Lakshminarayanan PA, Dent JC (1983) Interferometric studies of evaporating and combusting diesel sprays. SAE Trans SAE830244
15. McLean DH, Bremfoerder FW, Hamelink JC (1986) Development of headland ring and piston for a four-stroke direct injection diesel engine. SAE 860164
16. Morris CJ, Dent JC (1976) The simulation of air-fuel mixing in high swirl open chamber diesel engines. Proc I Mech E 190:47–76
17. Munro R (1979) Some diesel piston features in design analysis and experiment. SAE 790858, Diesel engine thermal cooling. SP-449
18. Ramsey JW, Goldstein RJ (1971) Interaction of a heated jet with a deflecting stream, J Heat Transfer, ASME, Sec. C, 93, No. 4
19. Timoney DJ (1985) A simple technique for predicting optimum fuel-air mixing conditions in a direct injection diesel engine with swirl. SAE paper 851543
20. von Thien (1965) Entwicklungsarbeiten an Ventilkanalen von Viertakt Dieselmotoren. In: Osterreichen Ingenieur Zeitschrift, Heft 9, Jg 8, Springer
21. Wakuri V, Ono S, Takasaki K (1985) Influences of air swirl on fuel spray combustion in a marine diesel engine. In: International symposium on flows in I.C. engines. ASME, FED. 28, pp 47–55
22. Whitehouse ND, Way RJB (1969–1970) Rate of heat release in diesel engines and its correlation with fuel injection data. In: Diesel Engine Combustion, The IMechE Proc. 184, part 3J

Chapter 9
Heat Release in Direct Injection Engines

Abbreviations

n	Engine speed (rpm)
$1/\rho_f \; dm_f/d\theta$	Volumetric injection rate injection of fuel (m^3/crank degree)
a and b	Engine-specific constants for the rate of burning (−)
AFR_{stoich}	Air–fuel ratio for the stoichiometric combustion of diesel (−)
A_n	Area of nozzle holes (m^2)
A_s	Instantaneous surface area (m^2)
C_d	Coefficient of discharge of the nozzle (−)
C_{diss}	Dissipation constant = 0.01 (s^{-1})
C_{model}	A model constant, 1000 (kJ/kg/deg)
C_{rate}	Constant for mixing rate, 0.002 (s)
C_{turb}	Efficiency of conversion of kinetic energy to turbulence energy in free jet = 0.2 (−)
d_e	Equivalent diameter of the orifice (m)
$dE_{diss}/d\theta$	Rate of energy dissipation across the control surface (J/s)
$dE_i/d\theta$	Rate of the generation of the kinetic energy of fuel jet into the cylinder (J/s)
dm_b/dt	Rate of burning (kg/s)
$dQ/d\theta$	Rate of heat release (J/s)
E_u	Total turbulent kinetic energy of fuel jet at a given crank angle instant (J)
f_1	A function of fuel availability (−)
f_2	A function of fuel–air mixing (−)
h_c	Heat transfer coefficient ($W/(m^2K)$)
k	Density of turbulent kinetic energy (J/m^3)
LCV	Lower calorific value of fuel (J/kg)
m_b	Cumulative mass of fuel burnt (kg)
m_f	Cumulative mass of fuel injected (kg)
n_p	Piston velocity (m/s)

P. A. Lakshminarayanan and Y. V. Aghav, *Modelling Diesel Combustion*,
Mechanical Engineering Series, https://doi.org/10.1007/978-981-16-6742-8_9

Q	Cumulative heat release (J)
s	Penetration of spray (m)
t	Time after the start of injection (s)
T_g	Cylinder charge temperature (K)
T_o	Reference temperature, 294 (K)
T_{surr}	Surrounding temperature (K)
T_w	Wall temperature (K)
U_j	Velocity of fuel jet at the exit of the nozzle (m/s)
V	Instantaneous cylinder volume (m^3)
V	Instantaneous cylinder volume (m^3)
λ_{diff}	Air excess ratio for diffusion combustion (−)
ρ_f	Density of fuel (kg/m^3)

Early DI diesel engines operated at relatively low compression ratios and low injection pressures. They, hence, demanded very advanced injection timings commensurate with the large ignition delay. Such a design was the result of the available technology and lack of norms for noise and emissions.

During the ignition delay period at the beginning of combustion, up to about 20% of the injected fuel is prepared to stoichiometric proportion. Due to high flame speed, the prepared mixture burns at high temperatures to produce nitric oxides and explosive noise characteristics of a diesel engine. This troublesome period of combustion is kinetically controlled. On the other hand, the rest of the fuel burns as and when the mixture is prepared because the delay is absent with hot gases and radicals available in the vicinity, a remnant of the fuel burnt earlier. This second part is diffusive, and the rate of combustion of the majority of fuel is controlled by the physical mixing processes in the spray.

With the advent of new norms, reduction in ignition delay held the key to solving emission and noise problems. The higher temperature at the beginning of injection by increased compression ratio reduced the delay period so substantially that the delay could be ignored. Higher injection pressures and higher turbulence were introduced to improve the mixing rate and hence to maintain the combustion duration within a reasonable limit, despite the loss of the fast-burning premixed combustion regime.

Heat Release Rate in Diesel Engines

Single-Dimensional Models

Probably, Austen and Lyn's work [1] is the earliest in identifying the strong relationship between the injection rate and the heat release rate. The rate of injection diagram was subdivided into elemental fuel packets emitted in the form of rectangular pulses. Each pulse is converted to heat according to an exponentially decaying function. The convolution integral of the heat release from individual packets is summed neatly to

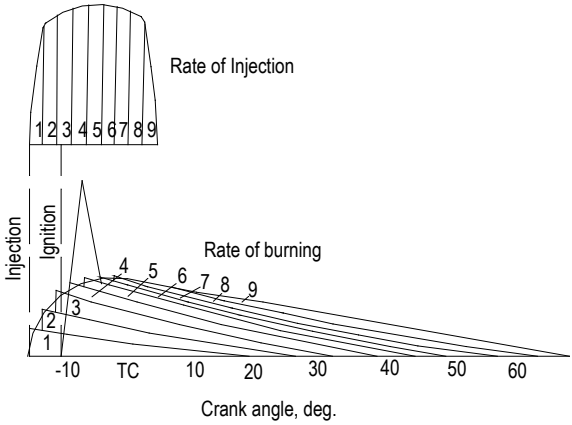

Fig. 9.1 Lyn's model

the net heat release rate. See Fig. 9.1. However, the application of this elegant idea was fraught with complexity, as the decay constants for elemental heat release rates were not available for a general engine. Therefore, the global heat release rate function of Vibe Weibe [16] ruled the world of diesel engine simulation for many years. The function has two engine-dependent constants to be tuned for a given engine type. The function could not explain the effect of speed and load easily. Further, it could not reflect the effects of the shape of the combustion chamber and the fuel injection rate on the history of heat release. The engine simulation was carried out using this function with a vast data bank of tuneable constants. Since a single Weibe function could not predict the rate of early premixed burning, [2] introduced the concept of double Weibe function. This needed more number of constants adjusted for a given engine type. While such algebraic functions were easy to compute, very complex multi-dimensional models were proposed at the other end of the spectrum.

Multi-dimensional Models

Shahed et al. [3], Dent and Mehta [4], and Hiroyasu [5] found that the understanding of the spray structure offered the clue to heat release rate. Essentially, they were a detailed 2-dimensional description of axisymmetric sprays. The mixing of the fuel with the ambient air entrained due to the high shear velocity of the jet was studied. A stoichiometric switch was devised that will completely burn the fuel in an element when the fuel–air mixture is chemically correct. Depending upon the coarseness of the division of spray for calculations, a highly fluctuating heat release rate was obtained. Smoothening of the curves was resorted to match with the experimental data.

The 3-dimensional simulation of the injection, mixing, and burning [6, 7] describes in full various phenomena in the engine. The chamber is divided into

finite volumes with moving boundaries. In principle, the airflow past the valves, the breakup of fuel into tiny droplets, vaporization, and combustion up to the formation of pollutants could be studied. Nevertheless, the volume of computation is too prohibitive to carry out many parametric studies. Though the trends could be obtained, the sub-models must be validated thoroughly by experiments for using the output for design work. The three-dimensional models were of immense use to appreciate the inner mechanism of diesel sprays, but very difficult to comprehend during the full simulation of a diesel engine.

Mixing-Controlled Combustion

In simplicity, avoidance of engine-dependent tuning constants, and easy application, the work of Chmela et al. [8] was an innovation. The burn rate is described as strictly proportional to the mixing rate which in turn is determined by the average turbulent kinetic energy of the sprays. In turn, the turbulent energy decays at any time proportional to the energy itself. The work predicted the trend of heat release successfully if there was little impingement of sprays on the piston. However, the calculated and experimental courses of heat release fell apart after the spray reached the walls. The deviation in the character of calculated heat release was obvious in engines of capacities less than 2-L and at more than half load. The majority of diesel engines belong to this category. An attempt has been made in the present work to enhance this model by encompassing the phenomena at the wall and the instantaneous injection rate derived from the indicated performance of fuel injection equipment [9].

Rate of Mixing and Burning in a Fuel Spray

Let us consider the fuel injected in the form of a transient spray into an infinite surrounding, Fig. 9.2. The air in the ambient entrains in the spray due to the turbulent shear between the ambient air and the fuel emanating from the nozzle at high velocity.

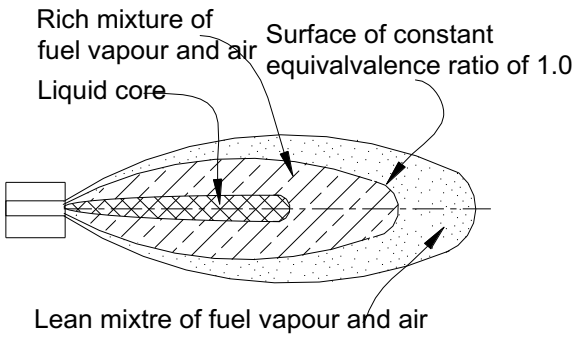

Fig. 9.2 Vaporizing spray

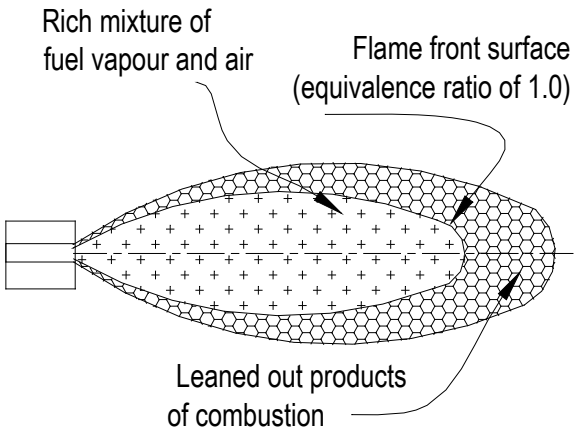

Fig. 9.3 Combusting spray

This figure shows the diffusion of air in the fuel spray to prepare a thin mantle of fuel to stoichiometric proportions somewhere in the middle of the spray. The simplest description for a burning spray is the model where products of combustion exist outside this mantle and fuel-rich mixture remains unburned inside it, Fig. 9.3. When compared with the slow mixing rate of fuel with the air, the rate of a chemical reaction is too large to determine the rate of combustion. Thus, the availability of fuel in the chemically correct proportion (by turbulent mixing) determines the burn rate and not the speed of reaction.

Lakshminarayanan and Nagpurkar [10], and later Chmela et al. [8] have shown that the rate of burning is proportional to the available fuel and the rate of entrainment of air. See Chap. 7.

Rate of burning $\propto$ Rate of air entrainment $\times$ Fuel available

$$\frac{\mathrm{d}Q}{\mathrm{d}\theta} = C_{\text{model}} f_1(\text{fuel availability})\, f_2(\text{mixing}) \tag{9.1}$$

Here, $\frac{\mathrm{d}Q}{\mathrm{d}\theta}$ = Rate of heat release.
C_{model} = A model constant = 1000 kJ/kg/deg.
f_1 and f_2 = Functions.

The same conclusion could be arrived at from the well-known empirical relation for burning by Weibe [16] as well.

The analogy of the rate of mixing-controlled combustion with Weibe function.

The cumulative fuel burnt, m_b at any time, t is given by an exponential Weibe function, Eq. (9.2), where m_f is the total injected fuel.

$$m_b = m_f\left(1 - e^{-at^b}\right) \tag{9.2}$$

The deceleration of combustion with time is emphasized by the exponent t^b. Differentiating Eq. (9.2) on either side, we obtain the rate of burning, Eq. (9.3).

$$\frac{dm_b}{dt} = \left(m_f e^{-at^b}\right)\left(abt^{b-1}\right) \tag{9.3}$$

$$\frac{dm_b}{dt} = \text{factor}_1 \times \text{factor}_2$$

where m_b = Cumulative mass of fuel burnt.
m_f = Cumulative mass of fuel injected.

$$\frac{dm_b}{dt} = \text{Rate of burning}$$

a and b = Engine specific constants.

The first factor on the right-hand side of Eq. (9.3) corresponds to the fuel remaining unburnt, and the second represents the rate of mixing due to entrainment of air. In Fig. 9.4, these two terms are shown graphically. By converting the fuel spray in Fig. 9.2 to a simple two-dimensional cone, we can transform the penetration distance to time coordinate as shown in Fig. 9.4. The rate of entrainment increases, and the available fuel decreases with time or analogously with the penetration distance. The simple product of these two curves is in the form of a hump representing the rate of diffusive burning of a diesel spray as shown in the lower part of Fig. 9.4.

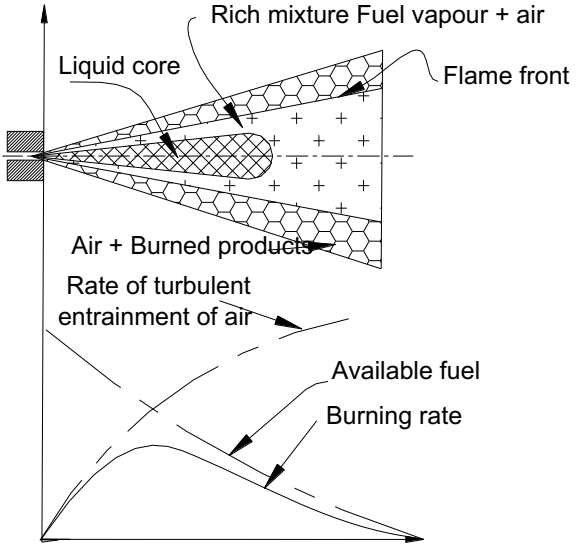

Fig. 9.4 Rate of mixing, available fuel, and combustion rate

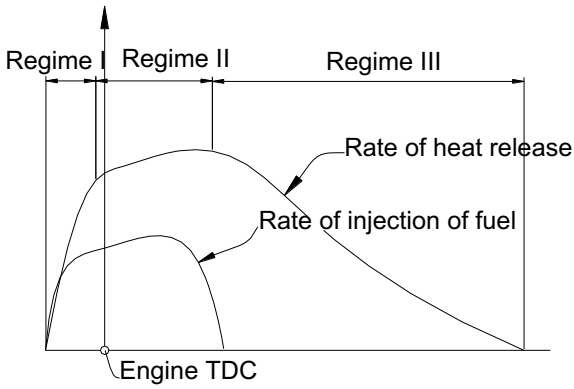

Fig. 9.5 Three regimes of diffusive combustion of a modern diesel engine

Model for Mixing-Controlled Combustion

Regimes of Combustion in a Modern DI Diesel Engine

The rate of heat release of diffusive combustion in a modern DI diesel engine has three characteristic regimes of combustion, Fig. 9.5. In the first, the early stage of combustion starts almost along with the beginning of the injection of fuel. Here, the rate of rise of the heat release rate is at its highest in its entire history and proportional to the turbulent kinetic energy produced at the nozzle as very little time has elapsed for any substantial decay of the energy. In the second distinctive part, the combusting spray has impinged on the piston wall, Fig. 9.6. There is a sudden loss of kinetic energy to slow down the rate of mixing and hence combustion. The spray continues to burn at a nearly constant rate until the injection is on.

In the third regime after the injection ends, the combustion rate decays asymptotically as fresh energy input to turbulence in the fuel spray has stopped. The fuel continues to burn until too little diesel is left to burn. The mixing rates in the three regimes could be quantified by using the turbulent kinetic energy of the spray.

Two Factors Affecting the Heat Release Rate

Available fuel factor, f_1.

At any instant, the fuel available for burning is the portion of the fuel so far still left unburnt.

Available fuel = cumulative fuel injected – fuel burnt

$$f_1(\text{fuel availability}) = m_f - \frac{Q}{\text{LCV}} \tag{9.4}$$

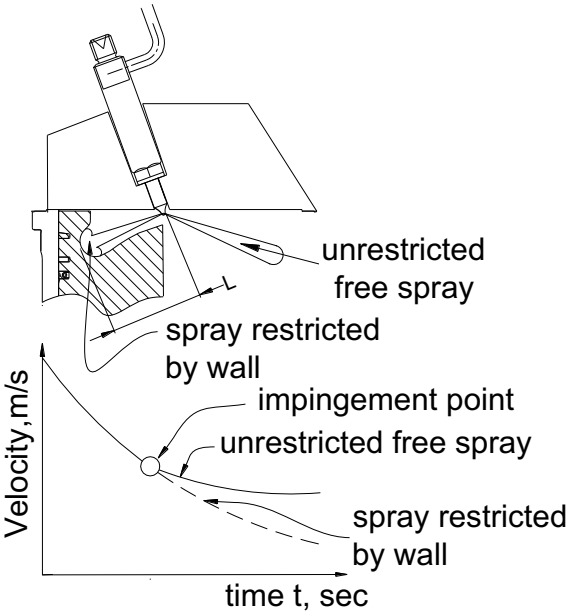

Fig. 9.6 Loss of velocity after impact against the wall, due to the finite size of the combustion chamber

Here, m_f = Cumulative mass of fuel injected.
Q = Cumulative heat release.
LCV = Lower calorific value of fuel.

Mixing rate factor, f_2.

The rate of mixing of fuel vapour and air depends on the local density of turbulent kinetic energy. Three sources of kinetic energy are there in a diesel engine, namely swirl, squish, and injection velocity of fuel, Fig. 9.7. The contribution of each source to total kinetic energy for a typical modern engine was summarized by Chmela et al. [8], for example, as in Table 9.1. Since the major portion of kinetic energy comes

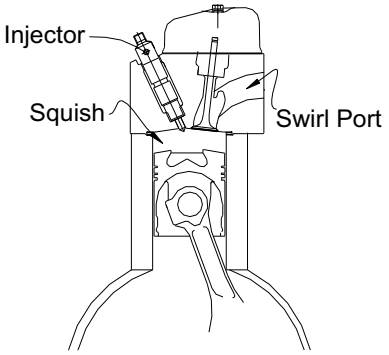

Fig. 9.7 Sources of kinetic energy

Table 9.1 Contribution of different sources to the turbulent kinetic energy of the spray [8]

Source	Contribution to total kinetic energy (%)
Swirl flow	2.0
Squish flow	1.5
Fuel injection	96.5

from the injection of fuel, other sources of kinetic energy are neglected. A part of this kinetic energy is converted into turbulence that is responsible for the mixing process.

k-ε Theory

In zero-dimensional combustion models, it is not easy to apply Magnussen's k-ε theory of turbulent burning [11], where the ratio of kinetic energy to dissipation rate, k/ε, determines the rate of mixing and hence the rate of burning. Chmela et al. [8] postulated a modified turbulent mixing rate, which is akin to the k-ε model.

Modified k-ε Model

The rate parameter for the combustion controlled by mixing, k/ε, is substituted by the ratio of turbulence intensity to a distance characteristic of the transport of momentum in the combustion chamber of volume, V.

Turbulence Intensity $\propto \sqrt{k}$ and

$$\text{Mixing distance for momentum transport} \propto \sqrt[3]{V}$$

$$\text{Mixing parameter} \propto \frac{\sqrt{k}}{\sqrt[3]{V}}$$

Even at a low turbulence level, the combustion rate will not become zero in engine conditions. Hence, it was proposed that the mixing rate is an exponential function of the mixing parameter.

$$f_2(\text{mixing}) = e^{C_{\text{rate}} \frac{\sqrt{k}}{\sqrt[3]{V}}} \tag{9.5}$$

where C_{rate} = Constant for mixing rate = 0.002 s.
K = Density of turbulent kinetic energy.
V = Instantaneous cylinder volume.

Input rate and dissipation rate of the turbulent kinetic energy of fuel spray

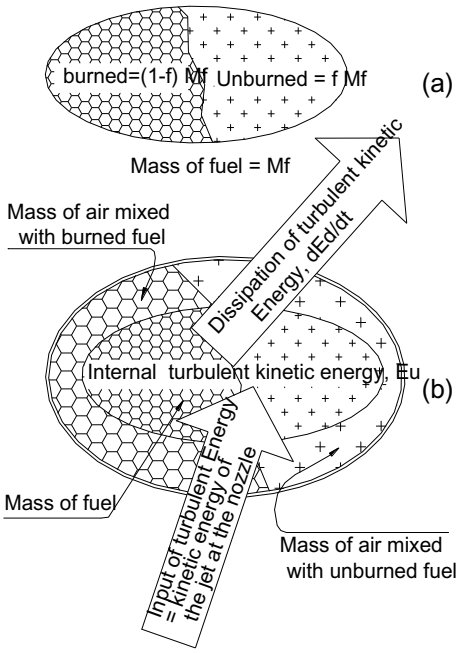

Fig. 9.8 **a** Burned and unburned fuel, **b** air mixed with fuel and flow of turbulent kinetic energy across the control surface of the spray and its decay

At any instant, the spray contains an unburned fraction, f, and correspondingly a burned fraction of $(1 - f)$, of the cumulative fuel-injected until then, m_f, Fig. 9.8a.

Figure 9.8b shows the rate of turbulent energy input, $\frac{dE_i}{d\theta}$, and its dissipation rate, $\frac{dE_{diss}}{d\theta}$, depicted as energy exchanges across the control surface enveloping the injected fuel and the air mixed with it, where θ is the crank angle in degree. The energy balance is given by the differential Eq. (9.6).

$$\frac{dE_u}{d\theta} = \frac{dE_i}{d\theta} - \frac{dE_{diss}}{d\theta} \tag{9.6}$$

where E_u = Total turbulent kinetic energy of fuel jet at a given crank angle instant.

θ

$\frac{dE_{diss}}{d\theta}$ = Rate of energy dissipation across the control surface.

C_{diss} = Dissipation constant = 0.01 s^{-1}.

Energy Input

The kinetic energy created by the injection at high velocity degenerates to random turbulence determined by the conversion efficiency C_{turb}. The value of C_{turb} is 0.2 for all the direct injection studies in this work. The injection velocity of an elemental mass dm_f is v. Then, the input turbulent energy to the spray would be given by Eq. 9.5.

$$\mathrm{d}E_i = C_{\text{turb}} \frac{1}{2} \mathrm{d}m_f v^2 \tag{9.7}$$

We can rewrite the equation as follows

$$\frac{\mathrm{d}E_i}{\mathrm{d}\theta} = C_{\text{turb}} 18 \rho_f \left(\frac{n}{C_d A_n} \right)^2 \left(\frac{1}{\rho_f} \frac{\mathrm{d}m_f}{\mathrm{d}\theta} \right) \tag{9.8}$$

Here, $\frac{\mathrm{d}E_i}{\mathrm{d}\theta}$ = Rate of the generation of the kinetic energy of fuel jet into the cylinder.
C_{turb} = Efficiency of conversion of kinetic energy to turbulence energy in free jet = 0.2.
n = Engine speed.
ρ_f = Density of fuel.
C_d = Coefficient of discharge of the nozzle.
A_n = Area of nozzle holes.
$\frac{1}{\rho_f} \frac{\mathrm{d}m_f}{\mathrm{d}\theta}$ = Volumetric injection rate of fuel.

Calculation of Fuel Injection Rate

The rate of injection can be obtained by simulation of the fuel injection equipment. Alternatively, it can be obtained from experimental data if available, as in the case of engines studied in the present work. The instantaneous flow area around the needle seat obtained from the measured needle lift and the total area of the spray holes are considered as two orifices in series. The rate of fuel injection at any instant is calculated using the effective area, A_n, of flow through the two orifices and the measured pressures at the injector entry, p_f, and in the cylinder p_c. A flow coefficient, C_d, of 0.8 is reasonable for the spray holes. See Appendix IX.

The instantaneous injection rate,

$$\frac{\mathrm{d}m_f}{\mathrm{d}\theta} = c_d \rho_f A_n \sqrt{\frac{2(p_f - p_c)}{\rho_f}} \tag{9.9}$$

In the present work, the heat release rate is modelled as a strong function of the rate of fuel injection [9]. Therefore, the accuracy of estimation of the fuel injection rate is important, especially in the first regime of combustion.

Energy Dissipation

With time, the turbulent kinetic energy of the spray dissipates to heat as the size of eddies reduces to a level too low to maintain the turbulent kinetic energy. The rate

of loss $\frac{dE_{diss}}{d\theta}$ is proportional to the internal turbulent energy of the spray, E_u at the given instant. It could be treated as a transfer of energy across the control surface, Fig. 9.8b.

$$\frac{dE_{diss}}{d\theta} = -\frac{C_{diss}}{6n} E_u \tag{9.10}$$

where

E_u = Total turbulence energy of fuel jet at the instant.
$\frac{dE_{diss}}{d\theta}$ = Rate of energy dissipation across the control surface.
C_{diss} = Dissipation constant = 0.01 s^{-1}.

The turbulent internal energy-specific per unit mass of mixture determines the combustion rate. The total mass of the air in the fuel–air mixture is estimated as follows. Here,

Air mass = air–fuel ratio in the burning part of the mixture × fuel injected so far = Air excess ratio for diffusion combustion × stoichiometric air–fuel ratio × fuel mass = $\lambda_{diff}\ AFR_{stoich} m_f$.

m_f = Cumulative mass of fuel injected, $\int_0^t \frac{dm_f}{dt} dt$.
λ_{diff} = Air excess ratio for diffusion burning = 1.4.
AFR_{stoich} = Air–fuel ratio for the stoichiometric combustion of diesel.

The Density of Turbulent Energy

At any instant during combustion, the density of turbulent kinetic energy is obtained by dividing the total turbulent energy of the spray by the total mass of the air–fuel mixture in the spray.

$$k = \frac{E_u}{m_f(1 + \lambda_{diff} AFR_{stoich})} \tag{9.11}$$

The turbulent intensity characterized by the root mean square of the deviation of velocity from the mean can be expressed proportionally to the square root of the density of the kinetic energy.

Modelling Three Regimes of Heat Release Rate

The first regime of burning dependent on turbulence energy in the free jet: During this early period, the spray is in the free air, Fig. 9.6. The increase in the mass of the spray due to air entrainment allows the rate of penetration of the spray to decelerate with time [15], Eq. (9.12).

$$s = \sqrt{8C_d U_j d_e t}\left[\frac{T_0}{T}\right]^{\frac{1}{4}} \tag{9.12}$$

where s = Penetration of spray.
U_j = Velocity of fuel jet at the exit of the nozzle.
d_e = Equivalent diameter of orifice.
t = Time after the start of injection.
T_o = Reference temperature, 294 K.
T_{surr} = Surrounding temperature.
C_d = Coefficient of discharge of the nozzle.

Differentiating Eq. (9.12), we obtain the velocity of penetration of the free jet in the air, V_{free}.

$$V_{\text{free}} = \sqrt{8C_d U_j d_e}\frac{1}{2\sqrt{t}}\left[\frac{T_0}{T_{\text{surr}}}\right]^{\frac{1}{4}} \tag{9.13}$$

During this period, the combustion accelerates at the highest rate in its entire history with increasing turbulence intensity due to continuous input of kinetic energy from the injected fuel. Also, the efficiency of transformation of normal kinetic energy to turbulence, C_{turb}, is high at 0.2, as the spray has not yet reached the wall to lose momentum to the wall, Eqs. (9.6) and (9.7). Considering the rate of dissipation of energy, the turbulence energy at any instant can be calculated to predict the rate of combustion by integrating the differential Eq. (9.6).

The second regime of combustion: It is influenced by the energy in the wall jet and input of energy from the spray. In engines of smaller bore sizes, combustion decelerates after the spray reaches the wall at a distance, L from the injector tip, Fig. 9.6. It starts at a time when $L = s$ in Eq. (9.12). During this intermediate period of combustion, there is a continuous loss of momentum to the wall. The growth of the spray, V_{wall}, along the wall is sluggish [15]. Here, the effect of temperature of the surrounding air is taken into account as in Eq. (9.13).

$$V_{\text{wall}} = 0.75\sqrt{U_j d_e}\frac{1}{2\sqrt{t}}\left[\frac{T_0}{T_{\text{surr}}}\right]^{\frac{1}{4}} \tag{9.14}$$

In other words, the kinetic energy input to the portion of the fuel in the wall jet is less by a factor, C_{wall}, given by the ratio of the kinetic energy of the spray along the wall and the free spray.

$$C_{\text{wall}} = \left[\frac{V_{\text{wall}}}{V_{\text{free}}}\right]^2 \tag{9.15}$$

Hence, the right-hand side of Eq. (9.8) is moderated by multiplying by the factor C_{wall} to obtain the energy input to the wall jet. Since the total turbulent energy in the fuel is nearly equal to that contained in the static conical portion of the spray in the

air from the injector the wall, the energy in the spray is approximately static and so is the rate of heat release. With increasing volume of the wall jet, the energy density drops slightly and hence the mixing rate or the combustion velocity.

The third decaying part of combustion:

With no more fresh input of energy to the spray after the end of injection, the average turbulence intensity of the spray degenerates monotonically, according to the differential Eqs. (9.6) and (9.10). The exponential term in Eq. (9.5) for the rate of combustion reflects the pattern of decaying heat release rate.

Steps to Calculate Heat Release Rate Using the New Model

Step 1: Prediction of Impingement and Loss in Kinetic Energy

In the first step of calculations, the instance of wall impingement and loss in velocity is computed by using average injection pressure, nozzle hole size, compression ratio, and impingement distance by using Eq. (9.12), when the penetration of spray s is equal to impingement distance L. If injection duration is more than the time for impingement, then instantaneous velocities of unrestricted and restricted sprays are calculated using Eqs. (9.13) and (9.14). The ratio of these velocities gives C_{wall} at different times after impingement.

Step 2: Computation of Factors of Rate of Heat Release

In the second step of calculations, the two factors affecting the rate of heat release are calculated at an interval of one degree of crank angle. The first factor of available fuel is calculated from the cumulative mass of fuel injected and cumulative heat release using Eq. (9.4). The second factor of mixing rate is computed from the injection trace, the cylinder volume, and the nozzle details using Eq. (9.5). The useful kinetic energy is calculated by using Eqs. (9.6), (9.8), and (9.10), considering the effect of wall impingement.

Step 3: Resultant Rate of Heat Release

The product of two factors along with the model constant, C_{model}, gives the rate of heat release at different time intervals.

Experimental Validation

Engines Under Study

Five direct injection diesel engines differing widely in swept volumes, rated speeds, methods of aspiration, and injection systems were selected for validation studies. The engine details are summarized in Tables 9.2 and 3.2. The results of engine E9 are from Chmela et al. [8]. The shapes of cavities for engines A9, B9, C9, and D9 are shown in Fig. 9.9.

Table 9.2 Details of engines studied

Engine	A9	B9	C9	D9	E9 [8]
Bore, mm	105	105	175	280	124
Stroke, mm	120	120	220	320	165
Compression ratio	18:1	18:1	14.5:1	11:1	18:1
Number of valves	2	2	2	4	4
Swirl number	2.1	2.1	1.0	0.8	1.8
Impingement distance, L, mm	32.5	36	70	120	*55
Aspiration	NA	T	TA	TA	*TA
Boost ratio	1	1.8	2.5	4	*2.5
Fuel pump	Rotary	Inline	Individual	Individual	Common rail
Injection pressure, bar	800	600	800	700	*800
Injected qty, mm^3/str	55	75	600	3200	255
Number of holes in the injector × hole size	5 × 0.2	5 × 0.24	8 × 0.33	8 × 0.55	*8 × 0.24
Speed, rpm	2700	2500	1500	750	1000
Bmep, bar	7	10	17	24.5	22
Cavity dia, mm	60	62	130	220	*100

TA—Turbocharged and after-cooled; T—turbocharged; NA—naturally aspirated
*Data assumed for computation

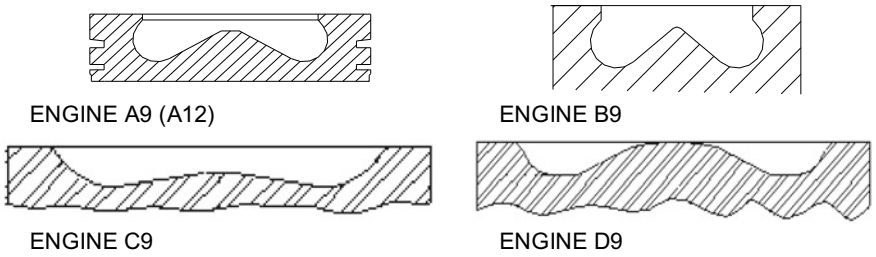

Fig. 9.9 Engine cavities studied

Heat Release Rate from the Experiments

The net heat release is calculated by applying the first law of thermodynamics [12] to the pressure crank angle diagram. The instantaneous heat transfer rate across the walls to the cooling medium is added to the net rate to obtain the gross heat release rate.

The heat release rate for engine E9 is straight available in the literature without any need to process the experimental pressure diagram.

The Net Heat Release Rate

Engines A9, B9, and C9

The indicated pressure diagrams and the injection traces were collected in the computer during the experiment. From the pressure diagram and the engine bore and stroke, the rate of net heat release was calculated by using the first law of thermodynamics with the help of the internal computer resident in the *AVL Indiskop*. The calculation of the net rate of heat release does not consider the heat transfer across the walls of the combustion chamber.

Engine D9

The available indicated pressure diagrams were manually digitized after smoothening by 2-point moving average method. The first law of thermodynamics was used to calculate the net heat release rate [12].

Estimation of Heat Transfer Across the Walls

Large surface area is exposed to gases in the later part of the combustion and hence for heat transfer. Therefore, the heat transfer rate must be estimated accurately enough, while obtaining the heat release rate during this period, experimentally. Hohenberg's correlation [13] for the instantaneous heat transfer considers truly the conditions present in a DI diesel engine. This correlation is based on extensive experiments done on a DI diesel engine. The instantaneous heat transfer across the walls for engines A9 to D9 was estimated using the following equation.

$$h_c = \frac{130 p_c^{0.8} \left(v_p + 1.4\right)^{0.8}}{V^{0.06} T_g^{0.4}} \tag{9.16}$$

Here, h_c = Heat transfer coefficient.
v_p = Piston velocity.
V = Instantaneous cylinder volume.
T_g = Cylinder charge temperature.

The cyclic-averaged heat transfer coefficient for individual surfaces can be used in the network of heat resistances to iteratively obtain different surface temperatures of the combustion chamber enabling precise estimation of the instantaneous heat transfer [14].

$$\frac{\mathrm{d}Q_{ht}}{\mathrm{d}\theta} = h_c A_s \left(T_g - T_w\right)\left(\frac{1}{6n}\right) \tag{9.17}$$

Here, A_s = Instantaneous surface area.
T_w = Wall temperature.

Results

Parametric Studies of Engine A9

The naturally aspirated engine A9 was selected for detailed study to validate the new model for different operating parameters of load and speed. The swept volume per cylinder is about 1 L, and it was rated at 2700 rpm and 80 hp. The experimental data were collected at six different points, Table 9.3. The main inputs to the calculation are the injection trace shown in Fig. 9.5, impingement distance of 32.5 mm computed from the geometry of the combustion chamber, and the conditions in the chamber at the start of injection (Fig. 9.10; Table 9.4).

Table 9.3 Data points of engine A9

Data point	Speed (rpm)	Load (Nm)	%	Injection pressure (bar)	Fuelling (mm^3/str)
1	2700	55	100	800	54
2	2700	41	75	800	43
3	2700	28	50	800	34
4	2700	14	25	800	26
5	1400	67	100	600	63
6	750	0	0	400	7

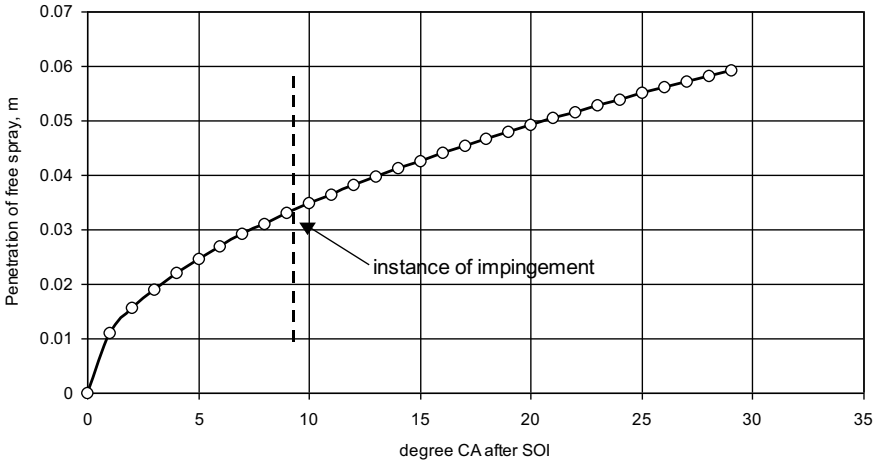

Fig. 9.10 Spray penetration in free air—engine A9, 2700 rpm and 100% load

Table 9.4 Data points of other engines B9, C9, D9, and E9

Engine	Speed (rpm)	Load (Nm)	%	Injection pressure (bar)	Fuelling (mm^3/str)
B9	2500	65	100	600	75
C9	1500	700	100	700	480
D9	750	3750	100	800	3200
E9	1000	350	100	800	255

Base Data at Rated 100% Load and 2700 rpm

At 2700 rpm, and 100% load, the spray reached the wall at about 9 deg after the start of injection, Fig. 9.11. This can be obtained from Eq. (9.12) for spray penetration. The velocities of penetration of the spray tip along the wall and if it were unrestricted can be seen in Fig. 9.12. The instantaneous ratio of the square of the two velocities is used in calculating C_{wall} and the kinetic energy in the spray along the wall.

Next, the entire heat release history is calculated in steps of 1-degree crank angle. The rate of injection is calculated using the needle lift, the instantaneous geometric area of flow, and the flow coefficient of the nozzle, Fig. 9.13. Using Eqs. (9.4) and (9.5), the available fuel and the mixing rate are calculated. The two factors are shown in arbitrary units in Fig. 9.14. After the impingement on the wall, the conversion efficiency of kinetic energy to turbulence sharply drops. After the end of injection, the degeneration of turbulence without any fresh addition of energy dictates the heat release rate. The calculated heat release rate is shown in Fig. 9.15 with the experimentally obtained burn rate in the backdrop. A very satisfactory comparison between the experiment and the present model could be seen. Also, the results from the earlier successful mixing-controlled combustion model [8] are superimposed

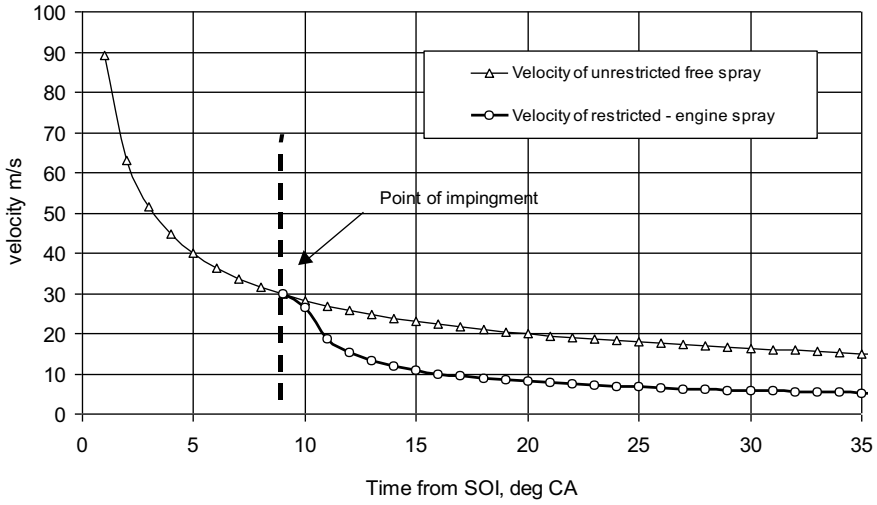

Fig. 9.11 Spray penetration velocities in free air and along the wall—engine A9, 2700-rpm and 100% load

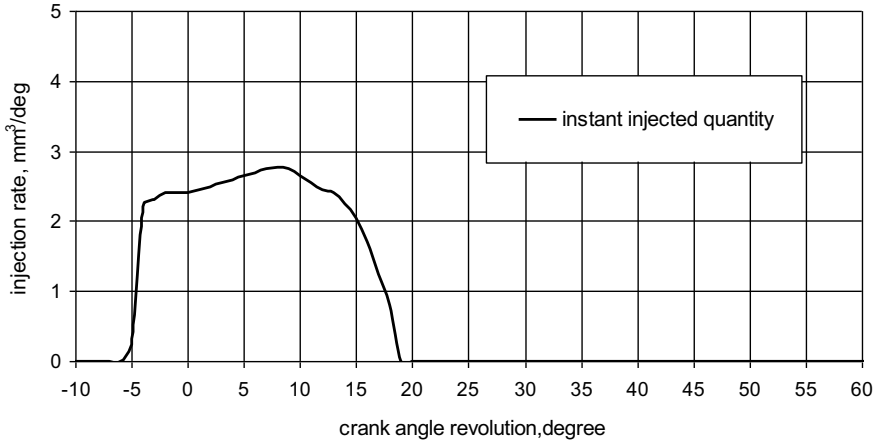

Fig. 9.12 Rate of injection derived from the needle lift diagram, instantaneous geometric flow area, and the flow coefficient of the nozzle holes

for comparison. The deviation from the experiment is obvious beyond the point of impingement against the wall.

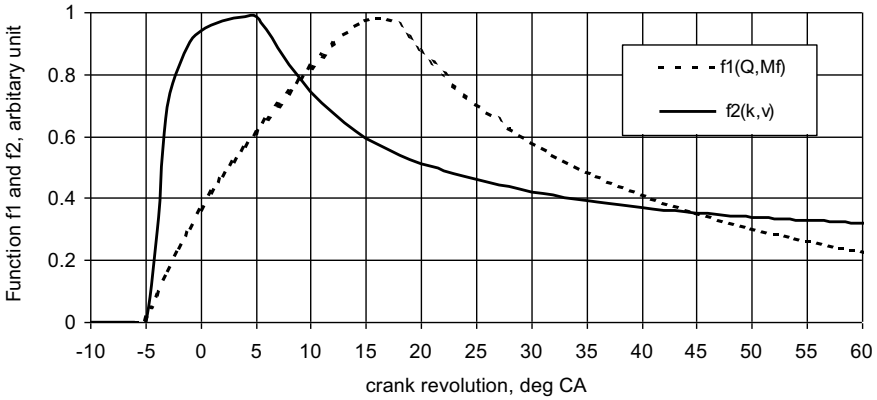

Fig. 9.13 Mixing rate, f2, and available fuel, f1—engine A9, 2700-rpm and 100% load

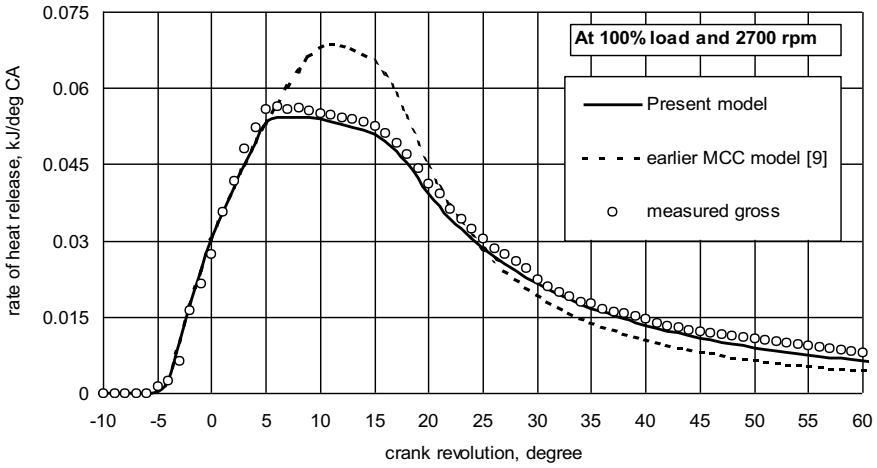

Fig. 9.14 ROHR, engine A9, 100% load, 2700 rpm

Other Loads and Speeds

Similarly, the rate of heat release (ROHR) was calculated for 75%, 50%, and 25% load at 2700 rpm. See Figs. 9.16, 9.17, and 9.18. The instance of impingement was approximately the same at all loads for the given engine speed. At 1400 rpm, the wall impingement occurred at about 8 degree after the start of injection, which is reflected in the ROHR curve in Fig. 9.19. At 750 rpm and low idle, there was no impingement. See Fig. 9.20. In the background, for every case, the burn rate obtained experimentally and that calculated using the earlier mixing-controlled combustion (MCC) model [8] are shown for comparison.

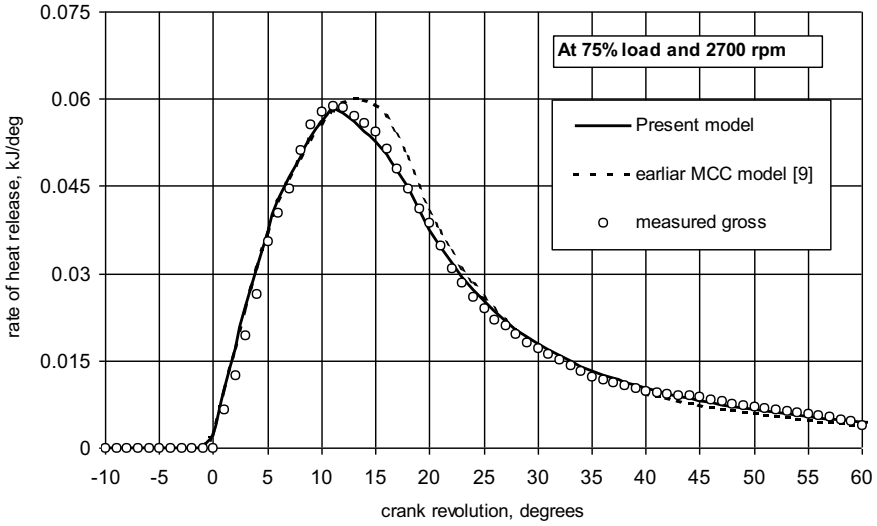

Fig. 9.15 ROHR, engine A9, 75% load, 2700 rpm

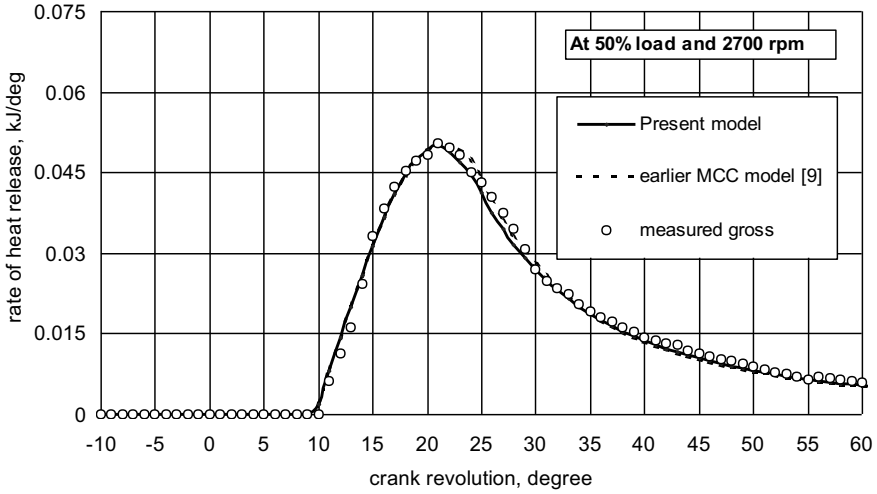

Fig. 9.16 ROHR, engine A9, 50% load, 2700 rpm

Study of Engine B9

The engine B9 was a turbocharged version of engine A9 with a compression ratio of 17.0. Here, the comparison between the experiment and model is still better because the ignition delay is lesser than in the case of the naturally aspirated version, Fig. 9.21.

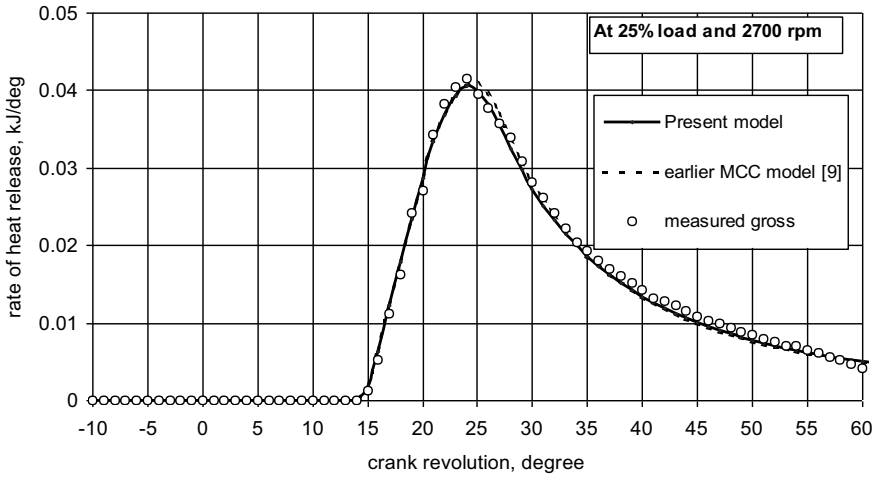

Fig. 9.17 ROHR, engine A9, 25% load, 2700 rpm

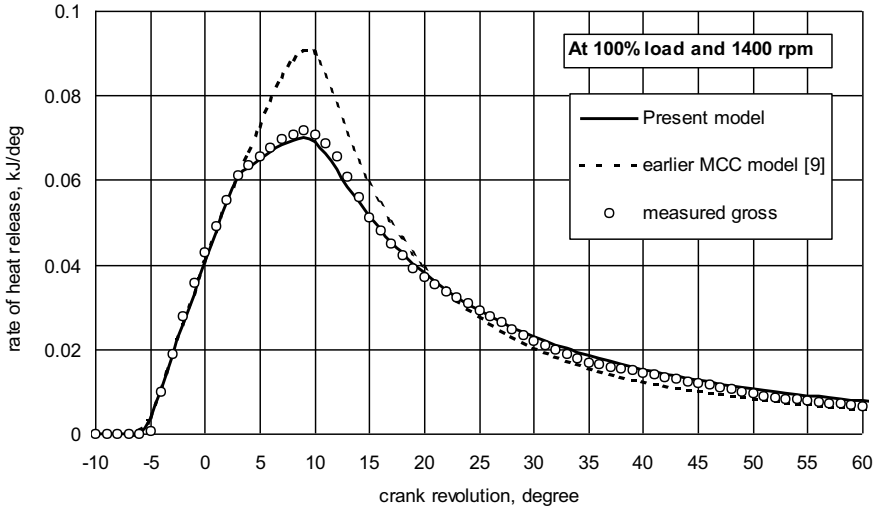

Fig. 9.18 ROHR, engine A9, 100% load, 1400 rpm

As the impingement is not taken into account, the earlier mixing-controlled model overestimates the heat release rate and hence thermal efficiency.

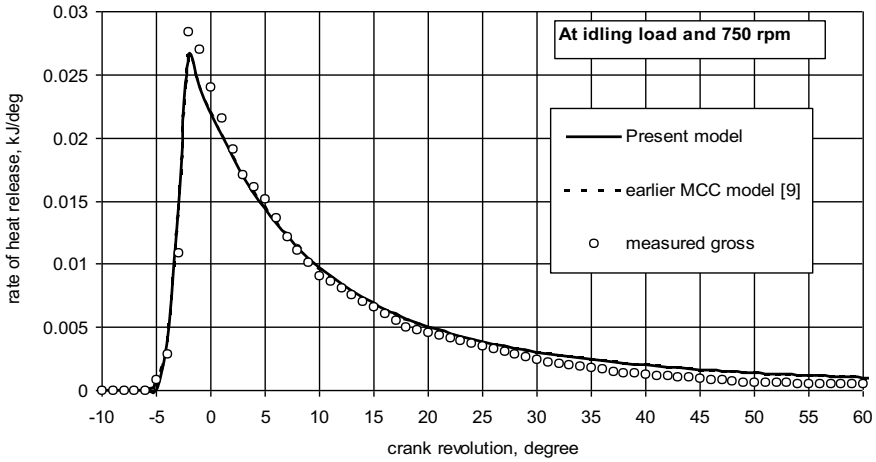

Fig. 9.19 ROHR, engine A9, idling load, 750 rpm

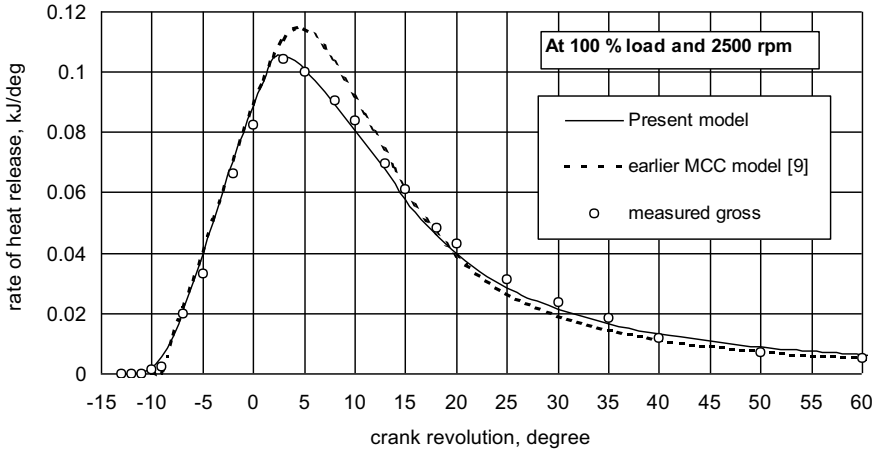

Fig. 9.20 ROHR, engine B9, 100% load, 2500 rpm

Engine C9 and Engine D9

Engine C9 and engine D9 are of bores 175 mm and 280 mm, respectively, running at high brake mean effective pressure of 17 and 24.5. The engines are rated at 1500 and 750 rpm; however, the corresponding piston speeds are of state of the art. Again, the effectiveness of the new mixing-controlled model is demonstrated in Figs. 9.22 and 9.23.

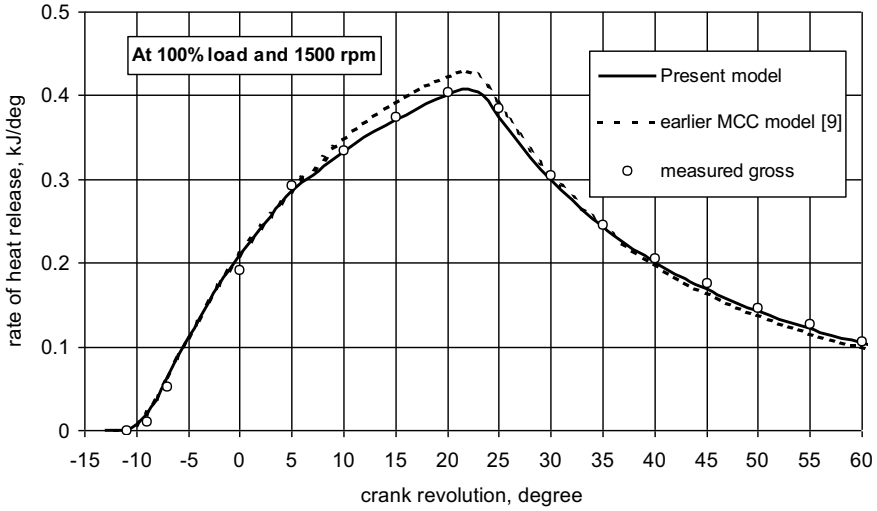

Fig. 9.21 ROHR, engine C9, 100% load, 1500 rpm

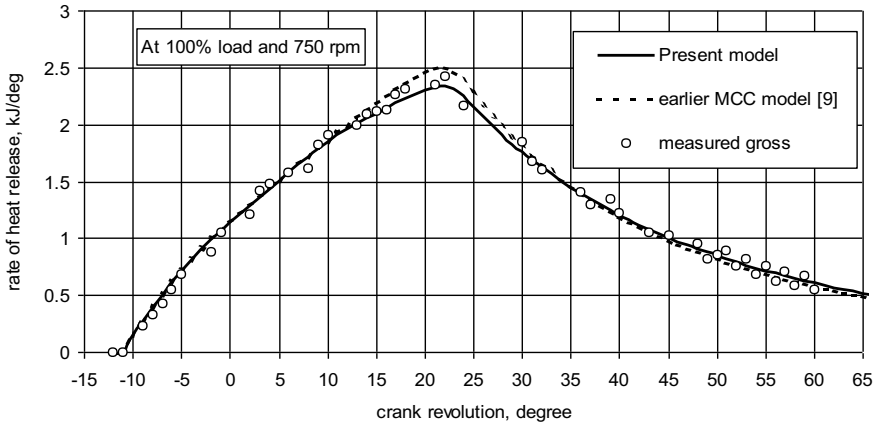

Fig. 9.22 ROHR, engine D9, 100% load, 750 rpm

Engine E9

The engine E9 [8] was studied at the rated conditions of the engine, namely 1000 rpm and 22 bar using the new model and that presented in the same reference. Since the dimensions of the combustion cavity were not explicitly available, a probable impingement distance was obtained from data on engines of similar bores, Fig. 9.24. The experimentally obtained heat release rate compared more favourably with the

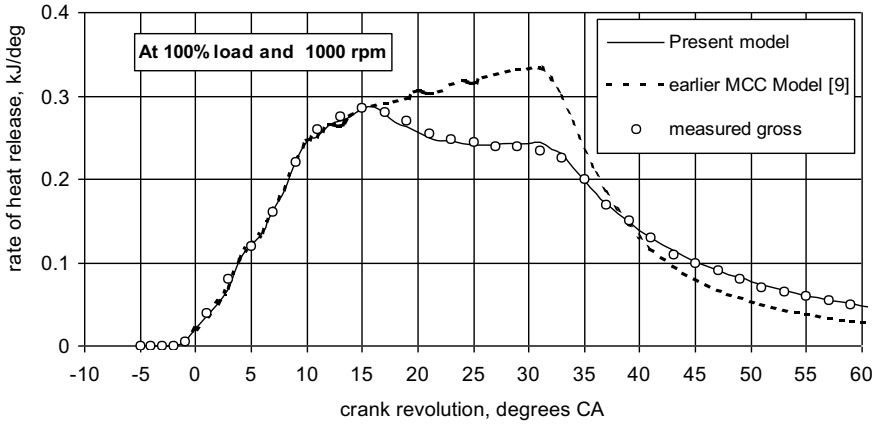

Fig. 9.23 ROHR, engine E9, 100% load, 1000 rpm (Chmela, Orthaber 1999)

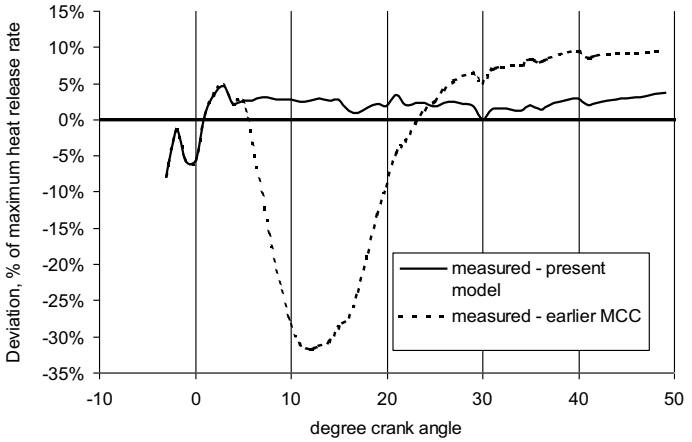

Fig. 9.24 Deviation of the models from the measured heat release for engine A9 at 100% load and 2700 rpm

new model than the known models. The observation is similar to cases of other engines.

Discussion

To appreciate the accuracy of the models a typical data of 100% load and 2700 rpm for engine A9 is studied in Fig. 9.25. The deviation of the heat release predicted using the present and the earlier models from the measured is plotted. The deviation

is significantly less in the case of the present work after the wall impingement. The relatively low error in the third regime of combustion in the present work validated the accuracy of the dissipation model proposed by Chmela et al. [8] for turbulent energy, Eq. 9.10. This was not obvious in his work as it was camouflaged, unfortunately, by the large error integrated during the second part of combustion.

To study the overall accuracy, the root-mean-square (RMS) deviation is evaluated. It is obtained at a 1-degree crank interval during the 5% to 95% of cumulative heat release, by calculating the square of the deviation of the predicted rates from the measured. Then, the square root of the sum of squares is divided by the maximum of the measured heat release, to obtain the percentage RMS of the deviation. Table 9.5 compares the five different engines at various operating conditions. The overall accuracy of the new model stands out in comparison at 1.5%. The new model has improved prediction substantially for engines with smaller bore sizes and at loads higher than 25%. The deviation is relatively five times better than the best available mixing-controlled combustion model, as shown in Table 9.5.

Chemical kinetics may not be fast enough at cold starting conditions. Further, during transient conditions, the characteristic air excess ratio may be less than 1.4. This is so because the injected quantity exceeds the steady-state requirements, or in the case of turbocharged engines, the familiar turbo-lag does not allow the air commensurate with the injected fuel. In such cases, the predicted and actual heat release rate histories may diverge. Except for these operating conditions on the fringe, the new model is probably the first satisfactory tool for design work and predicting the engine performance accurately at different speeds and loads in steady state.

Table 9.5 Accuracy of prediction of heat release rates using the new model

Engine	Speed (rpm)	Load (%)		Deviation (%)
			Present model	MCC model (Chmela 1999)
A9	2700	100	2.1	14.5
	2700	75	1.0	5.3
	2700	50	1.2	2.5
	2700	25	1.5	1.6
	1400	100	1.5	9.8
	750	0	1.4	1.4
B9	2500	100	1.3	6.2
C9	1500	100	1.5	2.8
D9	750	100	1.8	3.0
E9	1000	100	1.5	16.0
Average			1.5	6.4

Summary

Emissions of nitric oxides and noise are primarily attributed to the combustion of fuel premixed during the ignition delay. To reduce the delay and hence solve the twin problems, the high compression ratio is designed in modern diesel engines. The kinetically controlled premixed combustion is almost absent in these engines, and most of the combustion is diffusive. The diffusive heat release rate in diesel engines is proportional to the fuel not yet burned and the turbulent mixing rate. Turbulence is generated in the spray by the shear velocity at the exit of the nozzle, and its decay rate is a linear function of the kinetic energy of the spray. The mixing length is postulated as a function of the volume of the combustion chamber. The mixing rate is an exponential function of the ratio of turbulence intensity to the mixing length. To predict the heat release rate, the study of mixing rate in free air is enough, if the injected quantity is sufficiently low to avoid wall impingement. However, at higher loads, the drop in turbulent energy due to collision against the walls of the combustion chamber must be necessarily considered in order not to overestimate the thermal efficiency. The new model enhances the known mixing-controlled combustion model. Since it considers the wall impingement, it is a single-dimensional model with the simplicity and ease of application of a zero-dimensional model. The new model was thoroughly validated as a valuable tool by comparing the predicted heat release rates with the measured in five engines of widely varying bore sizes. The accuracy was demonstrated at different conditions of loads and speeds in steady state.

References

1. Austen AEW, Lyn WT (1960) Relation between fuel injection and heat release in a direct-injection engine and the nature of the combustion process. In: Proceedings of the Institute of Mechanical Engineers
2. Watson N, Pilley AD, Marzauk M (1980) A combustion correlation for diesel engine simulation. SAE 800029
3. Shahed SM, Chiu WS, Yumlu VS (1978) A preliminary model for the formation of nitric oxides in DI diesel engine and its application in parametric studies. SAE 730083
4. Dent JC, Mehta PS (1981) Phenomenological combustion model for a quiescent chamber diesel engine. SAE 811235
5. Hiroyasu H et al (1983) Development and use of spray combustion modelling to predict diesel engine efficiency and pollutant emissions. Bull JSME 26(214)
6. Cartillieri W, Johns RJR (1983) Multidimensional modeling of engine processes: progress and prospects. Fifteenth CIMAC Congress, Paris
7. Gosman AD, Tsui YY, Watkins AP (1985) calculation of unsteady three-dimensional flow in a model motored reciprocating engine and comparison with experiment. In: Fifth International Turbulent Shear Flow Meeting, Cornell University
8. Chmela FG, Orthaber GC (1999) Rate of heat release prediction for a direct injection diesel engine based on purely mixing controlled combustion. SAE 99010186
9. Lakshminarayanan PA, Aghav YV, Dani AD Mehta PS (2002) Accurate prediction of the rate of heat release in a modern direct injection diesel engine. IMechE, 216, J Automobile

10. Lakshminarayanan PA, Nagpurkar UP (1986) Rate of heat release for the divided combustion chamber. SAE 860084
11. Magnussen BF and Hjertager BH (1976) On mathematical modelling of turbulent combustion with special emphasis on soot formation and combustion. In: International symposium on combustion
12. Heywood JB (1988) A textbook on Internal Combustion engine fundamentals. McGraw-Hill International Edition
13. Hohenberg GH (1979) Advance approach for heat transfer calculation. SAE 790825
14. Gajendra Babu MK, Murthy BS (1976) Simulation and evaluation of Exhaust and Intake system of a 4-stroke spark-ignition Engine. SAE 760:763
15. Lakshminarayanan PA, Dent JC (1983) Interferometric studies of vapourising and combusting sprays. SAE 830244
16. Weibe II (1970) Brennverlauf und Kreisprozeb von Verbrennungsmotoren. VEB Verlag Technik, Berlin

Chapter 10
Prediction of the Rate of Heat Release of Mixing-Controlled Combustion in a Common-Rail Engine with Pilot and Post Injections

Anirudh Jaipuria and P. A. Lakshminarayanan

Nomenclature

A_h	Area of the nozzle hole (m^2)
C_d	Nozzle discharge coefficient (–)
C_{diss}	Constant for dissipation of the turbulence energy = 0.01 (s^{-1})
C_{model}	Model constant = 1000 (kJ/kg)
C_{rate}	Constant for the rate of mixing = 0.002 (s)
C_{turb}	Efficiency of conversion of the kinetic energy to the turbulence energy (–)
C_{wall}	Ratio of the kinetic energy of the spray along the wall to the kinetic energy of the free spray (–)
$(dQ/dh)_{MI}$	Quantity of heat released during the main injection for the corresponding crank angle of the post-injection (kJ/deg)
d	Diameter of the nozzle hole (m)
d_e	Effective diameter of the nozzle hole (m)
d_{scone}	Radius of the spray cone on the piston-bowl wall (m)
E_{diss}	Dissipation turbulence kinetic energy (J)
$E_{k,\,i}$	Input kinetic energy of the jet (J)
$E_{t,\,k,\,i}$	Turbulence kinetic energy of the jet (J)
E_{total}	Total turbulence kinetic energy (J)
f_1	Function representing the availability of fuel for combustion (–)
f_2	Function representing the rate of mixing of the fuel (–)
k	Density of the turbulence kinetic energy (J/kg)

A. Jaipuria
Formerly with Ashok Leyland, Chennai, India

P. A. Lakshminarayanan (✉)
IIT Kanpur, Kanpur, India
e-mail: lakshminarayananloganayagi@gmail.com

P. A. Lakshminarayanan and Y. V. Aghav, *Modelling Diesel Combustion*,
Mechanical Engineering Series, https://doi.org/10.1007/978-981-16-6742-8_10

l_{impg}	Impingement distance, the minimum distance between the nozzle hole and the bowl wall (m)
LCV	Lower calorific value of the fuel (kJ/kg)
M_a	Mass of charge air per cylinder per stroke (kg)
M_f	Cumulative mass of fuel injected up to a given crank angle (kg)
n_h	Number of injector holes (–)
N	Engine speeda (r/min)
P_c	Combustion pressure (bar)
P_r	Rail pressure (bar)
Q	Cumulative heat release (J)
s	Penetration distance of the spray jet (m)
s_{wall}	Growth of the wall spray (m)
t_{impg}	Time after the start of spray impingement on the wall (s)
t_{inj}	Time after the start of injection (s)
T_{surr}	Temperature of the mixture in the combustion chamber(K)
T_0	Reference temperature = 294 (K)
V	Instantaneous cylinder volume (m^3)
V_{free}	Velocity of the spray jet through the charged air in the combustion chamber (m/s)
V_j	Velocity of the spray jet (m/s)
V_{wall}	Velocity of the spray jet along the combustion bowl wall (m/s)
θ	Crank angle (deg)
θ_{cone}	Cone angle of the spray cone (deg)
ε	Rate of dissipation of the turbulence kinetic energy (s^{-1})
k	Polytropic coefficient, the ratio of specific heats (–)
λ	Excess air ratio
r_f	Density of the diesel fuel ($kg/m^{3)}$
r_g	Density of charge air inside the cylinder (kg/m^3)

A thermodynamic analysis before prototyping reduces the time required for the optimization of performance and emissions later during the development of a new engine. The rate of heat release (ROHR) is probably at the heart of the engine performance, like the power, specific fuel consumption, peak combustion pressure, and emissions [10]. Several advances have taken place in the last five decades to predict the ROHR using zero-dimensional, one-dimensional, and three-dimensional models [2, 10, 16, 18].

The single-zone Vibe [18] model has been successfully used to predict the ROHR and the burn rate. However, the model was limited in application and could be used for engines with one main injection. The two-zone Vibe model [2] was an improvement over its predecessor as it was successful in modelling premixed combustion. The single-and two-zone models are phenomenological and use parameters tuned for a given engine type. These parameters are often difficult to obtain for a new engine. Importantly, these models do not characterize the fuel injection that controls fuel–air mixing and decisively influences the ROHR and emissions.

The mixing-controlled combustion (MCC) model developed by Chmela and Orthaber [4] was successful in predicting the ROHR in direct-injection diesel engines. However, the model overestimated the ROHR at full-load conditions. Lakshminarayanan et al. [12] refined the MCC model to predict accurately the heat release histories at high loads, by estimating the reduction in the turbulence kinetic energy of the spray after wall impingement. The model does not use any constant dependent on the engine type and was validated on many engines including a common-rail engine with one main injection at 800 bar injection pressure. The one-dimensional approach of this refined model provides results more quickly, which are sufficiently accurate for most design work. In contrast, the three-dimensional computational fluid dynamics model yields many details accompanied by computational intensity and time, with limited use in iterative work during design and development [10].

Incorporating newer technologies of fuel injection and airflow into the phenomenological ROHR models is, therefore, a continuous effort. For example, modern diesel engines are equipped with common rail fuel injection technology with flexibility, first, to change electronically the injection pressure, timing, and fuel quantity and, second, to have up to five injections per engine cycle. The pilot injection of a small quantity of fuel before the main injection makes the combustion smooth and the pressure rises steadily, reducing the combustion noise and emissions of nitrogen oxides (NOx). A post-injection at about 20–40u crank angle after top dead centre (ATDC) with or without exhaust gas recirculation (EGR) increases the temperature and hence burns the soot to reduce particulate matter [5]. In this chapter, steps are described to refine the MCC model proposed by Chmela and Orthaber [4] and later by Lakshminarayanan et al. [12] and to consider the pilot and post injections [9].

Description of the Model

MCC Model

The MCC model [4, 12] is based on the theory of MCC. The ROHR is considered to be a function of two parameters, namely the availability f_1 of fuel for combustion and the rate f_2 of mixing of fuel with the incoming charge air, according to

$$\frac{dQ}{d\theta} = C_{\text{model}} f_1 f_2 \tag{10.1}$$

The fuel available for burning at any instant is equal to the difference between the cumulative fuel injected and the total fuel burned until that instant. The total fuel burned, denoted Q, is the ratio of the heat energy released to the calorific value of the fuel, and thus

$$f_1 = M_f - \frac{Q}{LCV} \tag{10.2}$$

The injection velocity of fuel at each crank angle is calculated using the Bernoulli flow equation

$$V_j = \sqrt{\frac{2 \times 10^5 (P_r - P_c)}{\rho_f}} \tag{10.3}$$

The quantity of fuel injected at each crank angle is calculated from the injection velocity V_j, the engine speed N (r/min), the number of holes, $n_{h,}$ and the area A_h of each nozzle hole according to

$$\frac{dM_f}{d\theta} = \frac{C_d \rho_f n_h A_h V_j}{6N} \tag{10.4}$$

the rate of mixing of fuel is strongly dependent on the turbulence kinetic energy of the spray. The total kinetic energy input is a summation of the energy due to swirl, the energy due to squish, and the kinetic energy of the spray. As the contributions of swirl and squish to the total kinetic energy are less than 4%, they were neglected to simplify the model [4]. The input kinetic energy is equal to the kinetic energy of the spray. Knowing the amount of fuel injected at each crank angle and the injection velocity, the input kinetic energy can be calculated as

$$\frac{dE_{k,i}}{d\theta} = \frac{1}{2}\frac{dM_f}{d\theta} V_j^2 \tag{10.5}$$

The turbulence kinetic energy k produced is less than the input kinetic energy by a factor equal to C_{turb}. The constant C_{turb} considers the efficiency of the transformation from kinetic energy into turbulence kinetic energy according to

$$\frac{dE_{t,k,i}}{d\theta} = C_{\text{turb}} \frac{dE_{k,i}}{d\theta} \tag{10.6}$$

The rate parameter k/e (where e is the rate of dissipation of turbulence kinetic energy) for the combustion controlled by mixing is replaced by the ratio of the turbulence intensity to a distance characteristic of the transport of momentum in a combustion chamber of volume V, with

$$\text{Turbulence intensity} \propto \sqrt{k}$$

$$\text{Mixing distance for momentum transpport} \propto \sqrt[3]{V}$$

$$\text{Mixing parameter} \propto \frac{\sqrt{k}}{\sqrt[3]{V}}$$

Even at low turbulence levels, the combustion rate will not become zero in engine conditions. Hence, the mixing rate was proposed as an exponential function of the mixing parameter as in the modified k–e theory suggested by Chmela and Orthaber [4] according to

$$f_2 = \exp\left(C_{\text{rate}} \frac{\sqrt{k}}{\sqrt[3]{V}}\right) \tag{10.7}$$

As the rate of energy dissipation of the turbulent kinetic energy is proportional to the turbulence kinetic energy at each instant, it can be expressed as

$$\frac{dE_{\text{diss}}}{d\theta} = \frac{C_{\text{diss}}}{6N} E_{\text{total}} \tag{10.8}$$

At any instance, the spray contained an unburned fraction f, and correspondingly a burned fraction 1-f of the cumulative mass M_f of fuel injected until then. The total turbulence kinetic energy at each instant is the difference between the input turbulence kinetic energy and the energy dissipated as given by

$$\frac{dE_{\text{total}}}{d\theta} = \frac{dE_{t,k,i}}{d\theta} - \frac{dE_{\text{diss}}}{d\theta} \tag{10.9}$$

The local density of turbulence kinetic energy is defined as the ratio of the total turbulence kinetic energy to the total mass of mixture present at each instant. The local turbulence kinetic energy density k is given by the ratio of E_{total} to the sum of the instantaneous mass M_f of fuel and the mass M_a of fresh air necessary for combustion according to

$$k = \frac{E_{\text{total}}}{M_f + M_a} \tag{10.10}$$

Modelling Three Regimes for a Single Injection

A typical ROHR trace can be studied by splitting the trace into three regimes. The first regime is where the spray grows in free air. The spray penetrates the combustion bowl until the penetration distance of the spray is equal to the minimum impingement distance at each crank angle. During the early period, the spray is in the free air. The increase in the mass of the spray by air entrainment allows the rate of penetration of the spray to decelerate with time [11]. The instantaneous penetration distance s and velocity V_{free} of free spray through the charge air in the combustion chamber in this regime can be calculated as

$$s = \sqrt{8C_d V_j d_e t_{\text{inj}}} \left(\frac{T_0}{T_{\text{surr}}} \right)^{1/4} \tag{10.11}$$

where

$$d_e = d\sqrt{\frac{\rho_f}{\rho_g}}$$

$$V_{\text{free}} = \frac{\sqrt{8C_d V_j d_e}}{2\sqrt{t_{\text{inj}}}} \left(\frac{T_0}{T_{\text{surr}}} \right)^{1/4} \tag{10.12}$$

$$\frac{dE_{k,i}}{d\theta} = \frac{1}{2} \frac{dM_f}{d\theta} V_{\text{free}}^2 \tag{10.13}$$

The second regime begins after the impingement of spray on the bowl wall. In reference [12] the spray is described as growing sluggishly along the wall in the second regime. The spray is modelled to impinge on the wall of the bowl when the spray penetration length is just greater than the impingement distance ($s > l_{impg}$). Immediately after impingement, the input kinetic energy of the spray is reduced by a factor C_{wall} which depends on the ratio of the kinetic energy of the spray along the wall to the kinetic energy of the free spray. The reduction in the input kinetic energy accounts for the momentum transfer to the wall [4,12, 1]. Also

$$V_{\text{wall}} = \frac{0.75\sqrt{V_j d_e}}{2\sqrt{t_{\text{impg}}}} \left(\frac{T_0}{T_{\text{surr}}} \right)^{1/4} \tag{10.14}$$

$$C_{\text{wall}} = \left(\frac{V_{\text{wall}}}{V_{\text{free}}} \right)^2 \tag{10.15}$$

However, considering C_{wall} from the instant of impingement, the rate of decay of the ROHR curve in the second regime is underestimated, as is evident in Figs. 10.1 and 10.2. The modified model in Figs. 10.1 and 10.2 refers to the model in reference [12]. After the total injected quantity has been completed, there is no further input from the fresh kinetic energy of the spray. This indicates the beginning of the third regime. In this regime, the ROHR curve is purely a function of the energy dissipated. The total energy in this regime can be expressed as

$$\frac{dE_{\text{total}}}{d\theta} = -\frac{dE_{\text{diss}}}{d\theta}$$

The negative sign in the above expression shows the continuous decay of energy in the third regime until the ROHR curve becomes asymptotic to the time axis.

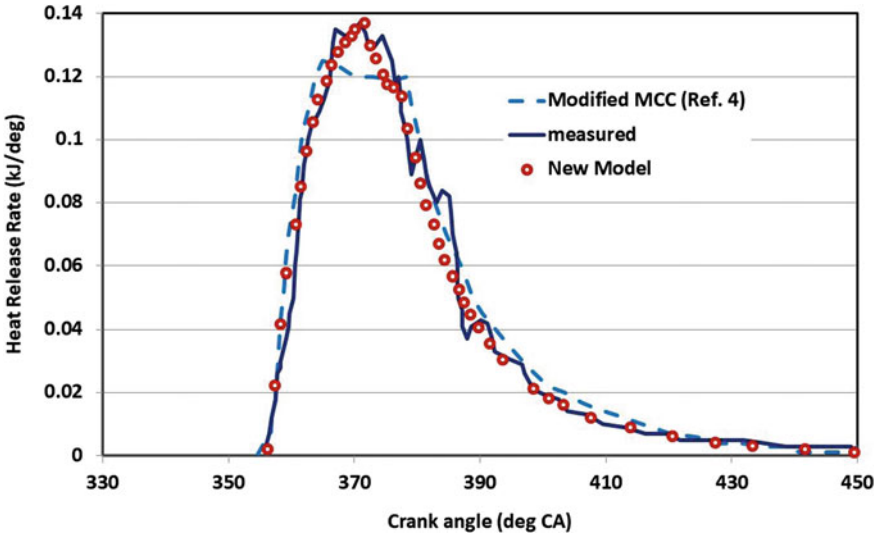

Fig. 10.1 Comparison of the measured and calculated ROHR histories at 1700 r/min, full load, and 1310 bar injection pressure

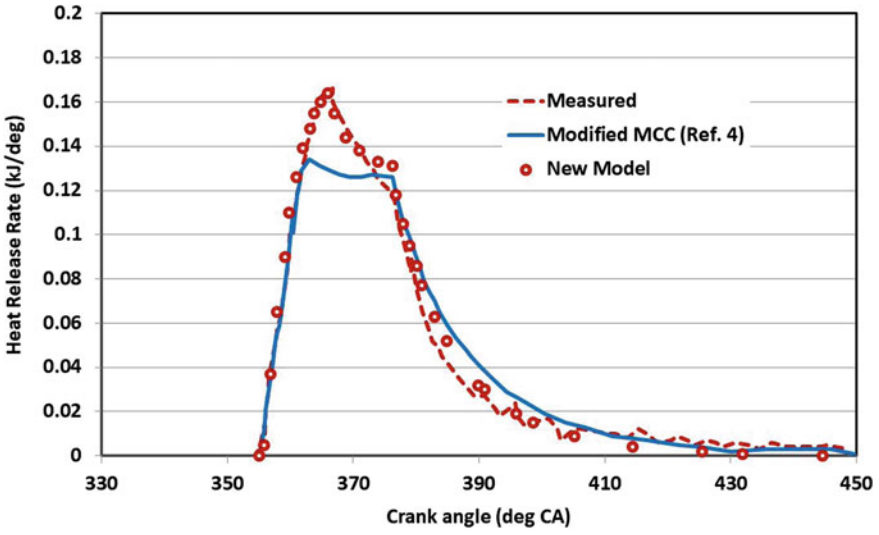

Fig. 10.2 Comparison of the measured and calculated ROHR histories at 1500 r/min, full load, and 1230 bar injection pressure

Refining the Model in the Second Regime

To model the decay rate of the ROHR curve, the concept of delaying the effect of impingement was introduced. Since V_{wall} is modelled as inversely proportional to the square root of t_{impg}, V_{wall} mathematically tends to infinity as t_{impg} tends to zero. The retardation of the wall jet is hypothesized to commence only when the wall jet grows to the diameter d_{scone} of the spray cone at the wall. See Eq. (10.16).

The correlation of Ranz [15] was used to determine the half cone-angle of the spray. The value of the parameter A in the correlation given by

$$\tan\left(\frac{\theta_{\text{cone}}}{2}\right) = \frac{4\pi}{A}\left(\frac{\rho_g}{\rho_f}\right)^{1/2}\frac{\sqrt{3}}{6}$$

was considered to be variable and a function of the injection pressure [3]. The diameter of the spray cone at the wall is calculated based on the penetration of the free spray and spray cone angle as

$$d_{\text{scone}} = 2s\tan\left(\frac{\theta_{\text{cone}}}{2}\right)$$

The growth of the wall spray was determined by integrating Eq. (10.14) to give

$$s_{\text{wall}} = 0.75\sqrt{V_j d_e t_{\text{impg}}}\left(\frac{T_0}{T_{\text{surr}}}\right)^{1/4}$$

The effect of C_{wall} is taken into account in the second regime if $s_{\text{wall}}. > d_{\text{scone}}$

$$\frac{dE_{k,i}}{d\theta} = C_{\text{wall}}\frac{1}{2}\frac{dM_f}{d\theta}V_{\text{free}}^2 \tag{10.16}$$

The results containing the improvement in the second regime are shown in Figs. 10.1 and 10.2 as open circles (labelled New Model).

Modelling the Pilot and Main Injections

The heat release curve is split into three sections for the pilot injection, main injection, and post-injection. Each section is considered to have three regimes. Usually, the pilot injection and post-injection have only the first regime and the third regime respectively as the spray in most cases does not reach the bowl since the piston is usually far away from the top dead centre (TDC) at the crank angles at which the pilot and post injections are used.

At the start of the pilot injection, the input turbulence kinetic energy is zero and the ROHR is determined as for the first regime. Usually, the injected quantity in the pilot injection is 2–6 mg/stroke and this is the reason why there is usually no spray impingement on the wall. However, in certain cases, if spray impingement does occur, then the second regime is incorporated. When the pilot injection has been completed, the ROHR is calculated in the same way as for the third regime with only dissipation taking place.

For the main injection, the first regime is modelled with the total turbulence kinetic energy equal to the total energy of the pilot injection in the third regime, after its decay in the time elapsed between the end of the pilot injection and the start of the main injection. The second and third regimes discussed earlier in the paper are determined as usual.

Modelling the Post-Injection

For the post-injection, the first regime starts with the total turbulence kinetic energy equal to the total energy of the main injection in the third regime at that crank angle. The functions f_1 and f_2 are calculated from Eqs. (10.2–10.10). The heat release due to the post-injection is then added to the heat released during the third regime of the main injection for the same crank angle.

The ROHR per crank angle is then calculated as

$$\frac{dQ}{d\theta} = C_{\text{model}} f_1 f_2 + \left(\frac{dQ}{d\theta}\right)_{MI}$$

Similar to the pilot injection, the second and third regimes can be calculated for the post-injection.

Experimental Validation

The model is validated by comparing the ROHR histories with the measured values. Figure 10.3 shows the schematic layout of the engine test bench and Table 10.1 shows the specifications of the experimental engine and the instruments used for the study. Figure 10.4 shows the piston bowl cavity of the test engine.

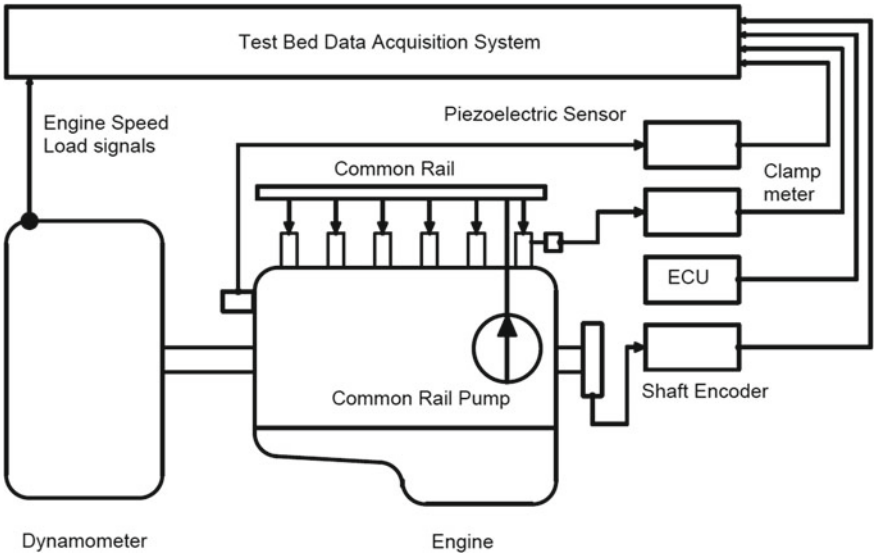

Fig. 10.3 Schematic test-bench layout

Table 10.1 Specifications for the engine and equipment

Engine type	Six cylinders inline direct-injection turbocharged intercooled
Bore	104 mm
Stroke	113 mm
Compression ratio	17.5
Number of valves per cylinder	2
Swirl number	1.8
Maximum power	165 kW at 2500 r/min
Maximum torque	800Nm at 1400–1900 r/min
Fuel injection system	Common rail, 1600 bar, electronically controlled solenoid injectors
Nozzle specification	Seven holes, hydraulic through-flow at 1680cm^3/ min, 0.141 mm diameter, k-factor nozzle
Emission compliance	Euro 4 with selective catalytic reduction after-treatment
Engine dynamometer	330 kW transient dynamometer
In-cylinder pressure measurement	Piezoelectric sensor, indicating system
Shaft encoder	Shaft encoder, accuracy, 0.1u crank angle

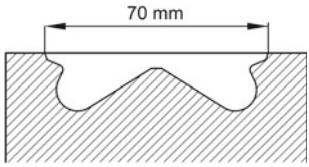

Fig. 10.4 Piston bowl cavity of the test engine

Characteristics of the Common-Rail Injector

The common-rail injector is electronically controlled. The injection timing is calibrated in the corresponding timing map in the engine's electronic control unit (ECU) software window viewed via the calibration hardware INCA [6].

Based on the injection timing calibrated in the INCA window, the armature of the injector is energized to lift the needle of the injector. The time delay between the timing set in the INCA window and the physical lifting of the needle is added to the injection timing to obtain the physical injection timing. In the past decade, the ignition delay in diesel engines (the period between the start of injection and the start of combustion) is reduced to minimize the premixed combustion and hence to reduce NOx, thus changing the character of the ROHR. This development was possible by the steady increase in the injection pressure, which in turn reduces soot. Thus, in modern diesel engines, the shortening of the ignition delay also implies that injection and combustion are better correlated. In this paper, the ignition delay is considered negligible [4] and hence the premixed combustion is omitted in the heat release model.

The quantity of fuel injected is governed by the duration for which the injector needle remains lifted. This is calibrated in the energizing time map of the engine's ECU. The time taken for the calculated injected quantity by Eq. (10.4) agreed well with the energizing time for that fuel quantity. The coefficient of discharge of the nozzle is a function of the coefficient of velocity and the area contraction coefficient. During the pilot injection, the needle lift is less than that during the main injection; hence the area of contraction changes according to the simple rule of orifices in series [21]. This reduces the overall discharge coefficient of the injector during the pilot phase. A similar phenomenon applies to post-injection.

Experimental Measurement of the ROHR and the Effect of TDC Determination

Experimentally the ROHR is obtained from the cylinder pressure curve based on a physical model of the phenomena in the cylinder by taking into account the volume work transferred by the piston, the energy released during combustion, the wall heat loss, and the pressure loss due to blow-by. The ROHR history is determined using the continuity equation, the first law of thermodynamics, and the equation for ideal gases.

During the high-pressure phase, the ports are closed by valves. The start of the high-pressure part of the thermodynamic cycle is from when the intake valve closes until when the exhaust valve opens. The mass in the cylinder changes owing to the blow-by past the piston rings and the fuel-injected during the internal mixture preparation. The temperature curve and the energy are determined from the pressure curve using the ideal-gas equation. Blow-by is determined from the pressure difference between the cylinder and the closed gap of the piston ring. The crankcase and the wall heat losses are determined by the Hohenberg [8] equation [7]. The alternative approach employed by Woschni [19, 20] can be used to consider the wall heat losses.

The physical model utilized is sensitive to the instantaneous cylinder volume, which is a function of the crank angle. If the TDC location obtained by the measurement instrument is not accurate, then an error is introduced into the calculated ROHR.

Figure 10.5 shows the variation in the ROHR for an error of 0.5º crank angle in the determination of the TDC. To reduce the error in the TDC, it was determined by the motoring cylinder pressure curve with the engine motored at fly-up speed. Theoretically, the peak pressure during motoring should occur at the TDC. However, owing to heat losses the crank angle at which the peak pressure occurs is offset. A correction for the thermodynamic loss angle was applied to the measured TDC. For other methods of determining the TDC, references [13, 14, 17] should be consulted.

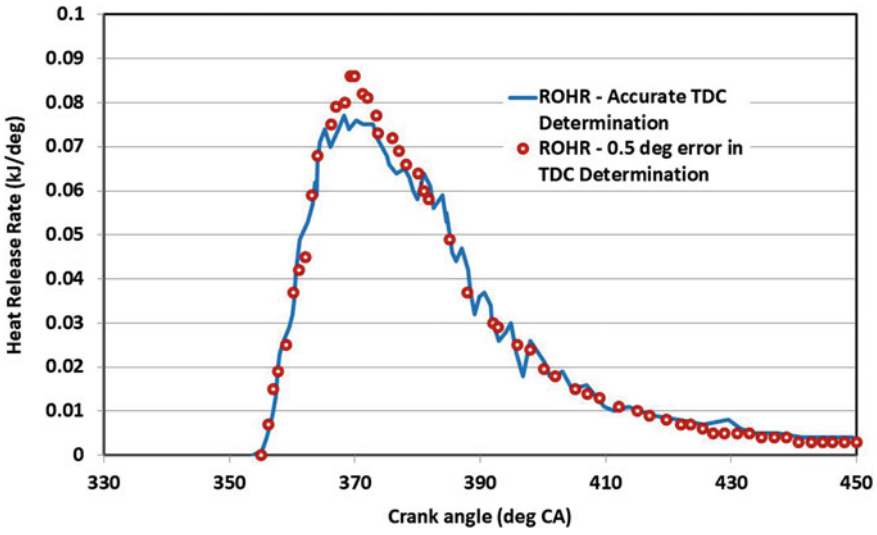

Fig. 10.5 Effect of the TDC determination on the ROHR histories

Results and Discussion

The experimental and theoretical results are compared at different speeds, different loads, and different injection pressures. The improvement proposed in the second regime of the ROHR curve was validated at full-load speeds in which the spray jet impinges the wall. Figures 10.6 and 10.7 show the calculated results for speeds corresponding to the maximum torque and maximum power for the engine under study. At maximum torque, tests were carried out with two different injection pressures. The results show that the new model is successful in accurately capturing the decay in the second regime.

At part-load conditions where spray penetration is not sufficient to wet the bowl wall, the new model is similar to the original MCC model as proposed by Chmela and Orthaber [4]. Figures 10.8 and 10.9 show the result at part-loads at the rated speed and the maximum torque speed respectively. The model is in good agreement with the measured traces. However, the peak due to premixed combustion is not captured in this simulation as the model neglects the ignition delay.

Figures 10.10, 10.11 and 10.12 show the results obtained for multiple injections with one pilot injection and one main injection. The energizing current is plotted to depict the start of the energizing crank angle for the pilot injection and the main injection. It can be observed that there is a delay between the start of the energizing current and the release of the heat. This delay is caused by the injector needle lift characteristics, as explained in the previous section. The pilot injection is typically used either in a small quantity at 5–10º before the top dead centre (BTDC) to reduce

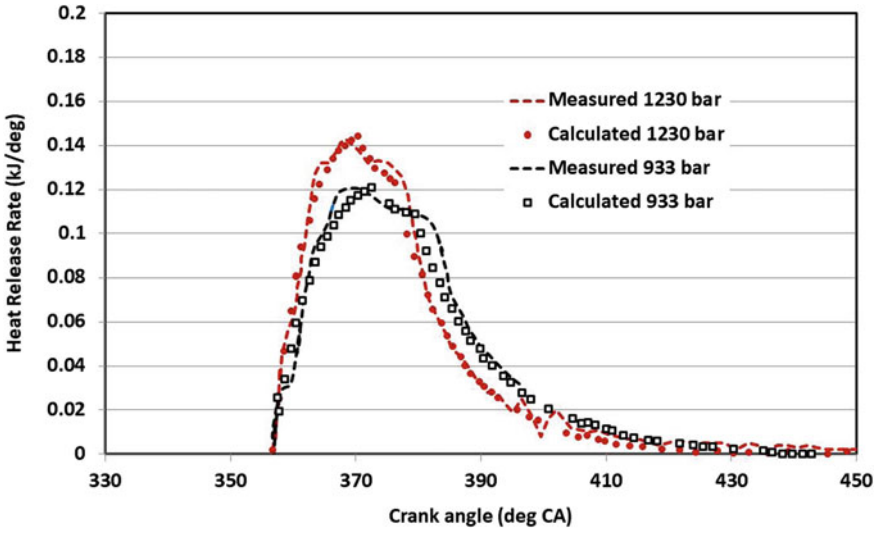

Fig. 10.6 Comparison of the measured and calculated ROHR histories at 1500 r/min, full load, and 1230 bar and 933 bar injection pressures

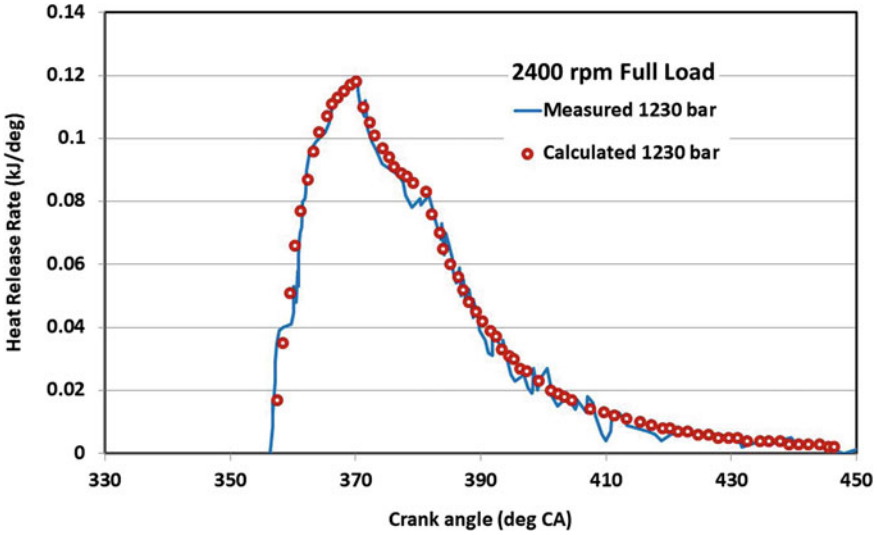

Fig. 10.7 Comparison of the measured and calculated ROHR histories at 2400 r/min, full load, and 1600 bar injection pressure

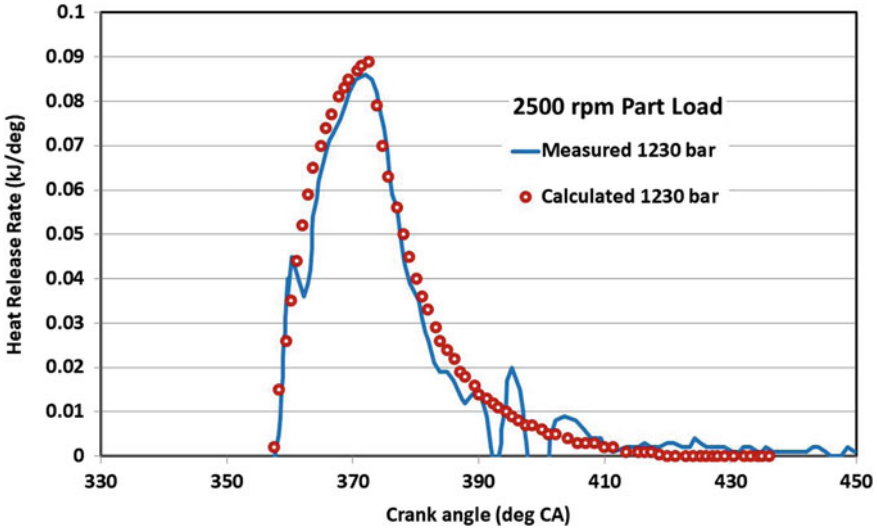

Fig. 10.8 Comparison of the measured and calculated ROHR histories at 2500 r/min, 50% load, and 1200 bar injection pressure

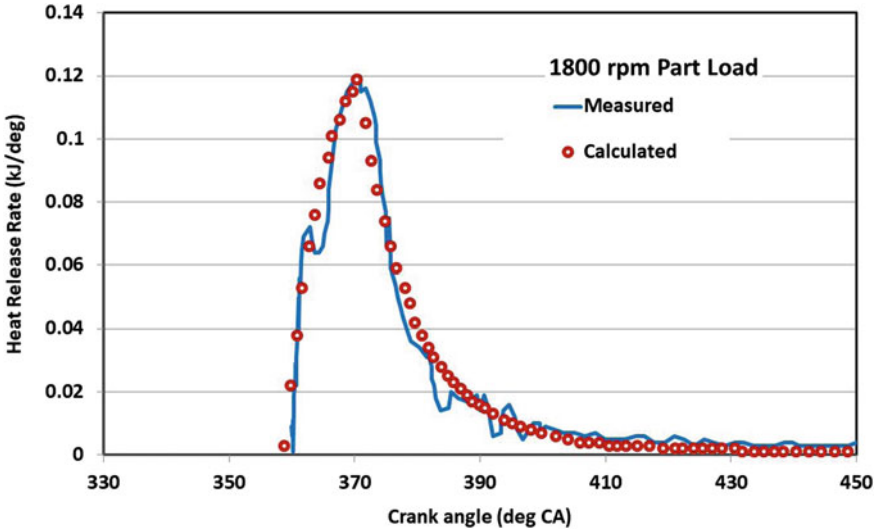

Fig. 10.9 Comparison of the measured and calculated ROHR histories at 1800 r/min, 50% road, and 1240 bar injection pressure

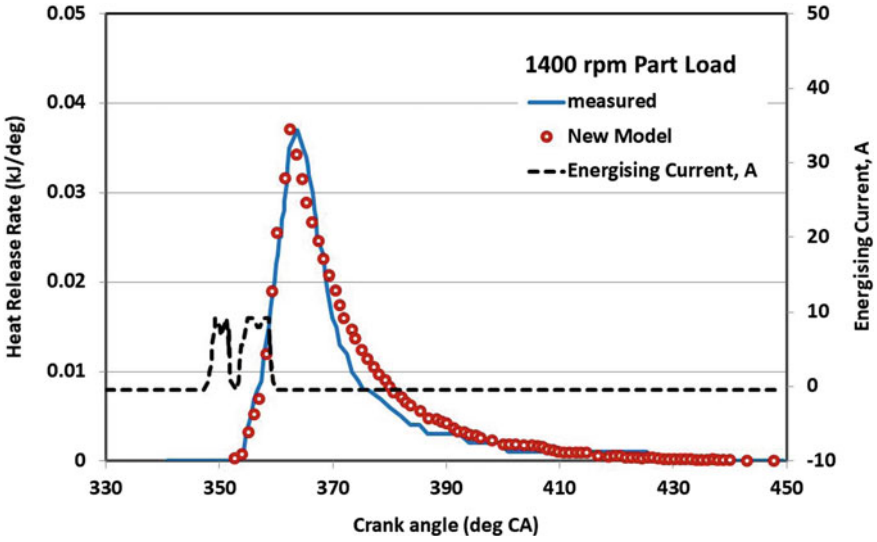

Fig. 10.10 Comparison of the measured and calculated ROHR histories at 1400 r/min, 20% load, and 580 bar injection pressure with a pilot injection of 2 mg

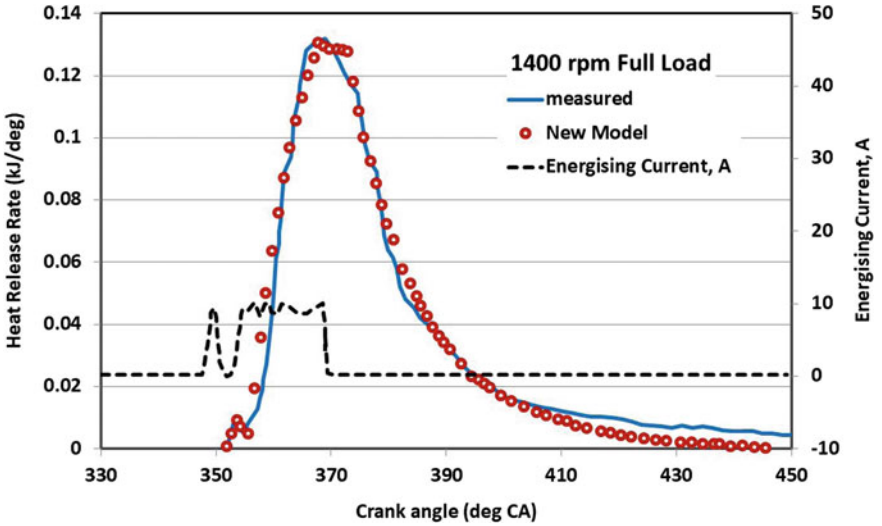

Fig. 10.11 Comparison of the measured and calculated ROHR histories at 1400 r/min, full load, and 1205 bar injection pressure with a pilot injection of 3 mg

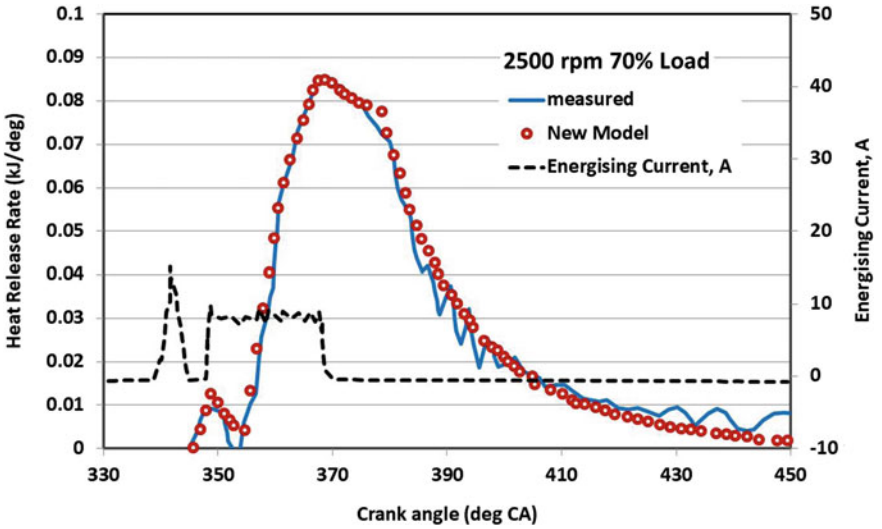

Fig. 10.12 Comparison of the measured and calculated ROHR histories at 2500 r/min, 70% load, and1600 bar injection pressure with a pilot injection of 5 mg

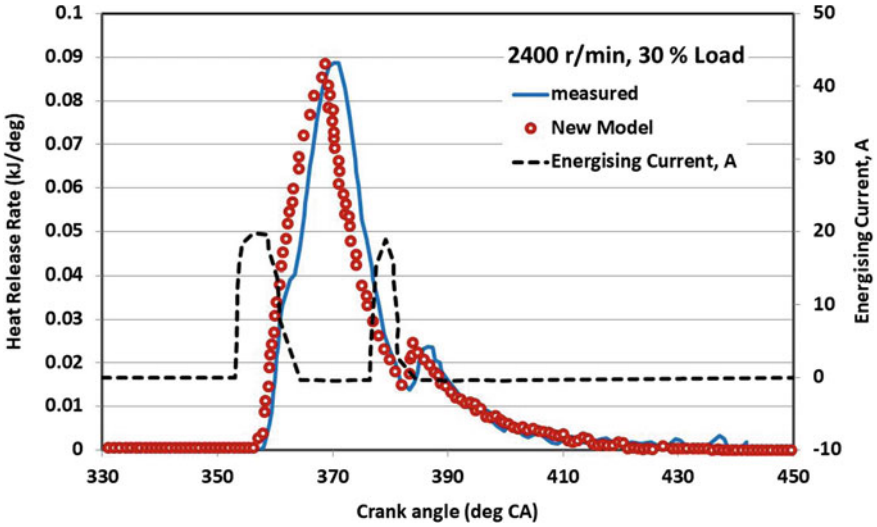

Fig. 10.13 Comparison of the measured and calculated ROHR histories at 2400 r/min, 30% load, and 1305 bar injection pressure with one pilot injection, one main injection, and one post-injection

the premixed combustion peak or in a larger quantity at 20–30º BTDC to smooth the pressure curve as a measure to reduce combustion noise. Figures 10.10 and10.11 show the results obtained for injection close to the TDC. Figure 10.12 shows the case of an early pilot injection in which a larger quantity of fuel is injected. From the three figures, it can be seen that the pilot plateau in the ROHR is accurately captured at various loads, injection pressures, and speeds.

Figures 10.13 and 10.14 show the results for a combination of the pilot, main, and post injections. The calculated and measured histories for post-injection agreed both qualitatively and quantitatively.

Discussion on the Model Constants

The new model is primarily based on the extended MCC model and the four constants in the empirical relations, namely C_{turb}, C_{diss}, C_{model}, and C_{rate} are the same as in reference [12]: $C_{\text{turb}} = 0.2$; $C_{\text{diss}} = 0.01\ \text{s}^{-1}$; $C_{\text{rate}} = 0.002$ s; $C_{\text{model}} = 1000$ kJ/kg. However, a value of 0.23 for C_{turb} was found to yield good results for most cases as against the value of 0.2 reported in reference [12]. Table 10.2 shows the best values of the constant C_{turb} for different conditions for the test engine.

From the data presented in Table 10.2 and the other data collected for different engine conditions, a distinct trend for the constant C_{turb} could not be arrived at. However, apart from a few outliers, the range for the constant is between 0.18 and

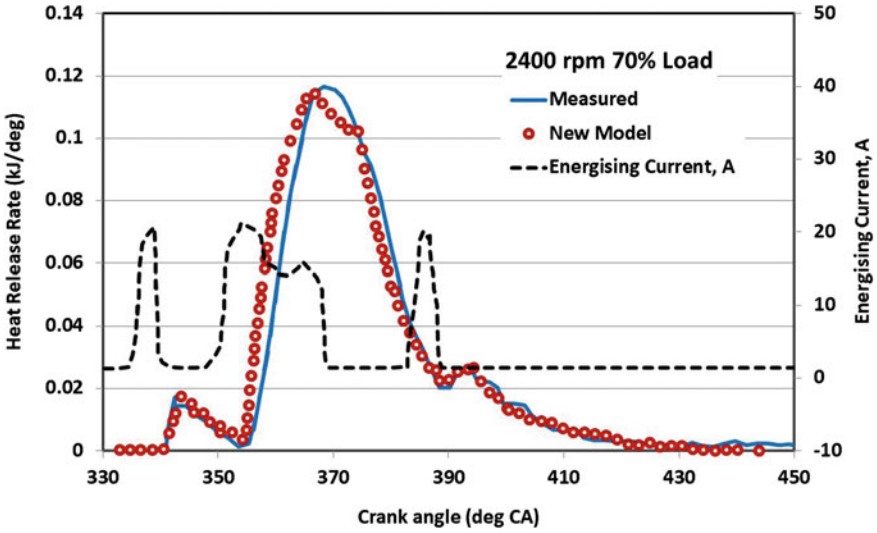

Fig. 10.14 Comparison of the measured and calculated ROHR histories at 2400 r/min, 70% load, and 1592 bar injection pressure with one pilot injection, one main injection, and one post-injection

0.25. The sensitivity of results to the value of C_{turb} for the pilot injection and the post-injection was less than for the main injection, as the quantity for the pilot injection and the post-injection is less than the quantity for the main injection.

Summary

The prediction of the ROHR of the MCC with the effect of a wall jet was improved in the second regime of heat release by hypothesizing that the wall jet effect starts when the wall jet grows to the diameter of the spray cone at the wall. The effect of the pilot and post injections on the ROHR was included in the new model and the measured data agreed well with the model. The inputs to the model, e.g. the injection pressure, timing, and quantity, are the same as those used in the actual engine during optimization of the common-rail engine. However, the model can be implemented for engines with mechanical jerk-type piston pumps as well. The ROHR is an important input for emission models used for predicting the formation of pollutants such as NOx and. smoke during combustion. The pilot and post-injection traces can be utilized to estimate NOx and the reduction in smoke due to diffusion burning in smoke models [1]. The key to accurately predicting the ROHR with the MCC model lies in estimating the constant C_{turb}. More investigations for engines with different bores, strokes, and aspiration methods are required to understand the parameters affecting C_{turb}. A further improvement in the predictions can be achieved

Table 10.2 Best values of the constant C_{turb} for different speeds, loads, and injection pressures

Test	C_{turb}	Speed (r/min)	Load (%)	Rail pressure	Figure	Pilot injection	Post injection
1	0.23	1000	100	1000	–	–	–
2	0.28	1300	20	605	–	✓	–
3	0.23	1400	20	580	10,8	✓	–
4	0.23	1400	100	1204	10.9	✓	–
5	0.23	1400	100	1206	–	–	–
6	0.23	1400	100	1230	10.2	–	–
7	0.25	1500	50	680	–	–	–
8	0.22	1500	50	827	–	–	–
9	0.25	1500	50	974	–	–	–
10	0.23	1500	100	930	10.4	–	–
11	0.18	1500	100	1080	–	–	–
12	0.23	1500	100	1230	10.4	–	–
13	0.13	1600	50	950	–	✓	✓
14	0.3	1600	100	1275	–	–	–
15	0.23	1700	100	1312	10.1		
16	0.23	1800	50	940	–	–	–
17	0.23	1800	50	1090	–	–	–
18	0.23	1800	50	1240	10.7		
19	0.25	1800	100	1065	–	–	–
20	0.22	1800	100	1215	–	–	–
21	0.3	1800	100	1290	–	–	–
22	0.23	1800	100	1363	–	–	–
23	0.23	2400	30	1305	10.11	✓	✓
24	0.23	2400	70	1592	10.12	✓	✓
25	0.23	2400	100	1600	10.5	–	–
26	0.18	2500	50	1000	–	–	–
27	0.23	2500	50	1200	10.6	–	–
28	0.23	2500	70	1600	10.10	✓	–
29	0.14	2500	100	1600	–	–	–

by incorporating the effect of cooling due to the vaporization of fuel from the liquid state, the injector needle lift characteristics, and the effects of swirl and squish.

Acknowledgements The authors thank Mr Prasann Deshpande and the testing team of Engine R&D, Ashok Leyland, Hosur, Tamil Nadu, India, for their help to write the computer program and analyzing the data.

This chapter is based on the paper, "Prediction of the Rate of Heat Release of Mixing-Controlled Combustion in a Common-Rail Engine with Pilot and Post Injections" published in the Proceedings of the Institution of Mechanical Engineers, Part D: Journal of Automobile Engineering 225,

References

1. Aghav YV, Lakshminarayanan PA, Babu MKG (2008) Validating the phenomenological smoke model at different operating conditions of DI diesel engines. Trans ASME J Eng Gas Turbines Power 130(1):012803
2. AVLB (2008) User's guide, version 5.1, 2008 (AVL List GmbH, Graz)
3. Chang CT, Farrell PV (1998) Spray characteristics and near injector tip effects of injection pressure and ambient density. In: Proceedings of the fourth international symposium on the diagnostics and modeling of combustion in internal combustion engines (COMODIA '98), Kyoto, Japan, 20–23 July 1998, Japan Society of Mechanical Engineers, Tokyo, pp 465–470
4. Chmela FG, Orthaber GC (1999) Rate of heat release prediction for direct injection diesel engines based on purely mixing controlled combustion. SAE paper 1999–01–0186
5. Dronniou N, Lejeune M, Balloul I, Higelin P (2005) Combination of high EGR rates and multiple injection strategies to reduce pollutant emissions. SAE paper 2005–01–3726
6. ETAS (2010) INCA software products, ETAS Group, Stuttgart. Available from http://www.etas.com/en/products/inca_software_products.php
7. Heywood JB (1988) In: Internal combustion engine fundamentals, McGraw-Hill, New York
8. Hohenberg GH (1979) Advance approach for heat transfer calculation. SAE paper 790825
9. Jaipuria A, Lakshminarayanan PA (2011) Prediction of the rate of heat release of mixing-controlled combustion in a common-rail engine with pilot and post injections. Proc Instit Mech Eng Part D: J Automobile Eng 225(2):246–259. https://doi.org/10.1243/09544070JAUTO1615
10. Lakshminarayanan PA, Aghav YV (2010) Modelling diesel combustion. Springer Science + Business Media, Dordrecht, pp 213–254
11. Lakshminarayanan PA, Dent JC (1983) Interferometric studies on vaporizing and combusting spray. SAE paper 830244
12. Lakshminarayanan PA, Aghav YV, Dani AD, Mehta PS (2002) Accurate prediction of the rate of heat release in a modern direct injection diesel engine. Proc IMechE, Part D: J Automobile Eng 216(8):663–675
13. Marek SJ (1996) Thermodynamic determination of T.D.C. in piston combustion engines. SAE paper 960610
14. Nilsson Y, Eriksson L (2004) Determining TDC position using symmetry and other methods. SAE paper 2004–01–1458
15. Ranz WE (1958) Some experiments on orifice sprays. Can J Chem Eng 36(4):175–181
16. Tatschi R, Pachler K, Fuchs H (1995) Multidimensional simulation of diesel engine combustion process—modeling and experimental validation. In: Proceedings of the fifth symposium on the working process of the internal combustion engine, Graz, Austria, September, Technische Universitat Graz, Graz
17. Tazerout M, Le Corre O, Rousseau S (1999) TDC determination in IC engines based on the thermodynamic analysis of the temperature–entropy diagram. SAE paper 1999–01–1489
18. Vibe II (1970) Brennverlauf und Kreisprozess von Verbennungsmotoren, VEB Verlag Technik, Berlin
19. Woschni G (1967) A universally applicable equation for the instantaneous heat transfer coefficient in the internal combustion engine. SAE paper 670931

20. Woschni G (1991) Einfluß von Rußablagerungen auf den Wa¨rmeu¨bergang zwischen Arbeitsgas und Wand im Dieselmotor. In 3. Tagung Der Arbeitsprozess des Verbrennungsmotors, Mitteilungen des Instituts fur Verbrennungskraftmaschinen und Thermodynamik, Graz, Austria, 20–21 September 1991, (Instituts fur Verbrennungskraftmaschinen und Thermodynamik, Graz), pp 149–169
21. Zinner K (1978) Supercharging of internal combustion engines—fundamental; calculations; examples. Springer, Berlin

Chapter 11
Hydrocarbons from DI Diesel Engines

Nomenclature

m	Exponent of fuel concentration in Arrhenius equation = 1 (–)
n	Exponent of air concentration in Arrhenius equation = 18 (–)
A	Instantaneous flow area (m^2)
A	Pre-exponent factor of Arrhenius equation, 150 to 210 (Dimensional constant)
C_a	Mean concentration of air in the lean zone-1, approximately (–)
C_d	Flow coefficient for the spray holes = 0.8 (–)
C_f	Mean concentration of fuel leaned out and effused from the sac (–)
dq/dt	Instantaneous injection rate (kg/s)
E/R	Ratio of activation energy to gas constant = 2100 (K)
Φ_L	Lean combustion limit of the relative air–fuel ratio (–)
HCv	Hydrocarbon emission, due to sac volume (kg)
ID	Ignition delay (degree, s)
m_{cal}	fuel injected during delay $\times$ fuel overleaning factor $+$ sac volume $-$ yield $-$ slow burnt fuel (kg)
m_f	Injected fuel (kg)
p_1	Pressure in the cylinder (bar)
p_2	Pressure before the nozzle (bar)
p_m	Mean pressure of the ambient during the ignition delay (bar)
Q_{del}	Fuel injected during the delay period of the combustion process (kg)
ρ_f	Density of fuel (kg/m^3)
T_m	Mean temperature of the ambient during the ignition delay (K)
V_s	Sac of volume (m^3)
y	Yield or the fraction of fuel evaporated from the sac of volume (–)

HC emissions from diesel engines are due to several factors. The fuel leaned beyond flammability limits [5], bulk quenching during expansion, and fuel effusing from nozzle sac after completion of injection [12] are the most important reasons. Only

P. A. Lakshminarayanan and Y. V. Aghav, *Modelling Diesel Combustion*,
Mechanical Engineering Series, https://doi.org/10.1007/978-981-16-6742-8_11

under extreme operating conditions like long idling or cold starting, wall wetting, cyclic misfire, and local under-mixing influence the HC [3]. On the other hand, in spark-ignition engines, the emission of HC [3] is mainly due to quenching near the cylinder walls and crevices like adsorption and desorption by oil film on the cylinder walls and quenching. The detailed work of Yu et al. [12] on diesel engines dealt with design parameters that have a decisive influence on the HC. HC formation was studied by looking at the structure of spray, in an engine with a bore of 140 mm. Except for the effect of engine speed, the influence of all the operating parameters was satisfactorily explained. The temporal factor due to speed was not having any effect in the model as opposed to the experimental results because the reaction of over-mixed fuel was not considered. Ikegami et al. [7] carried out a schematic study of particulate and hydrocarbon from a direct injection diesel engine by sampling from a mini dilution tunnel. HC concentrations were found affected by ignition delay or by temperature in the engine cylinder. Nakayama et al. [9] studied the effects of valve timings and valve lift systems on HC in cold start conditions on an engine of bore 85 mm. Tsunemoto et al. [10] studied the effects of combustion and injection systems on HC and particulate emissions on an engine of a bore 102 mm. Parametric studies were made by varying aspect ratio of piston cavity, swirl at TDC, the start of injection, and excess air–fuel ratio. HC emissions were found invariant for swirl and the shapes of the cavity if they were optimized for smoke and fuel consumption. A good empirical correlation was arrived at between the particulate matter and Bosch smoke number. Dent [2] considered the influence of the mixing scale of the shear flow generated by the spray, on HC emissions. All the above work showed that for the usual operating conditions of speed and load, HC emission from a reasonably optimized engine depends on the fuel injected and over-mixed during ignition delay. The fuel evaporating from the sac [5] after injection and reacting slowly during expansion stroke adds to the HC emissions.

In this chapter, a phenomenological model is successfully made for HC emissions from direct injection diesel engines. The unburned HC was correlated with the over-mixed fuel during the ignition delay and the fuel effusing from the sac that undergoes slow burning in the expansion stroke. The over-mixed fuel is calculated from the measured instantaneous pressures in the nozzle and the cylinder in conjunction with the effective flow area derived from the measured needle lift. The slow reaction of the over-leaned fuel was considered during the characteristic time of ignition delay. The ratio of observed raw HC emissions in the exhaust to the total quantity of fuel injected is defined as the exhaust indicated hydrocarbons, EIHC or specific hydrocarbon, SHC.

Injection Characteristics and the Indicated Diagrams

Engines A10 to G10 in Table 3.2 were fully instrumented for needle lift and pressures in the injection line and cylinder. Table 3.2 explains the details of FIE used on the engine. To cover a wide range of engines in the study of HC emissions, the engine used

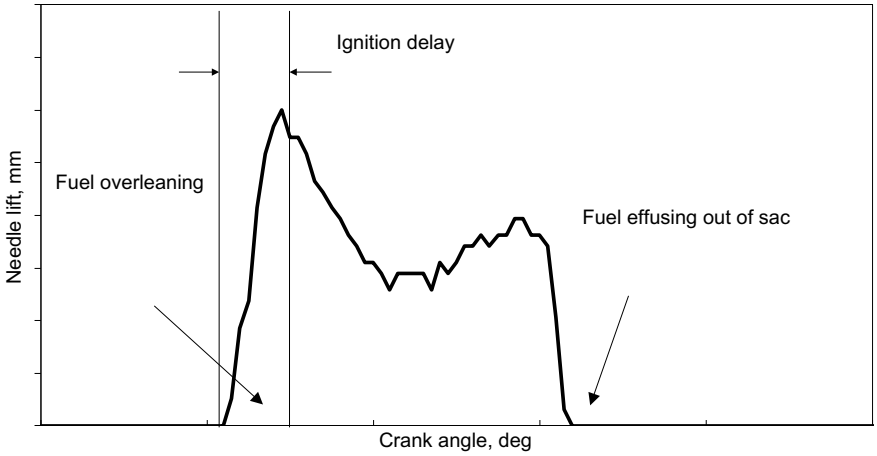

Fig. 11.1 A typical trace of needle lift with regions of over-leaning and effusing of fuel to contribute to hydrocarbon emissions

by Yu et al. [12] was also studied using integrated parameters such as ignition delay, nozzle hole size, and injected quantity. See Table 3.2 and Appendix-XV (engine H10). Figure 11.1 shows a typical trace of needle lift, of the turbocharged engine, B10 at 90% load indicating the times when fuel over-leaning and effusing takes place. All the engines from A10 to G10 were of the modern type designed for low emissions of NO_x and hydrocarbons. The compression ratio was relatively higher to enable injection delayed with respect to the previous generation of engines to which engine G10 belongs. The decrease in ignition delay in such engines resulted in a lower premixed burning fraction and hence the sharp first peak is missing in the heat release diagrams [4]. Further, to filter out the fluctuations in pressure due to physical effects in the cylinder, and the duct leading the pressure to the transducer, a moderate smoothening of the pressure diagram is optionally carried out using the moving average software of the AVL Indiskop. However, since the smoothening was done over a duration of 2-degree crank angle, the missing of the first peak is more due to higher compression ratio and delayed fuel injection than due to smoothening.

HC Model

In the theoretical approach of Yu et al. [12], the effects of fuel–air mixing are isolated from the effect of injection system characteristics, misfire, and other sources. The contribution to hydrocarbon emissions from fuel–air mixing is calculated using a transient spray model. The spray structure in different types of engines (A10 to G10,

Table 3.2) was found similar during the small period of ignition delay, and hence, they could be represented by simple numbers.

Spray structure

The spray mixing model and spray characteristics are determined by equations of spray penetration and growth of spray width. A schematic behaviour of the transient vaporizing spray is shown in Fig. 4.3 before a detachment of the spray and after detachment [3]. The transient evaporating process can be considered as the introduction of successive packets of fuel along many streamlines radiating from a virtual origin of the spray located inside the nozzle at a distance from the mouth.

Ignition delay

Theoretical estimation:

Ignition delay (*ID*) is the time lag between the start of injection to the ignition. The time taken for visible fire to appear in the premixed zone of spray is a strong function of pressure and temperature of the ambient. In addition, the physical properties such as Cetane number, the viscosity of fuel, nozzle hole size, injected quantity, and injection pressure contribute to the delay phenomenon in diesel engines [1]. However, for diesel fuels, a reasonable estimate of the delay ID is achieved by Wolfer [11].

$$ID = 3.45 \cdot \exp\left(\frac{2100}{T_m}\right) \cdot p_m^{-1.02} \tag{11.1}$$

Here T_m and p_m are the mean temperature and pressure of the ambient during the ignition delay.

Experimental estimation:

Alternatively, the delay could be measured using the experimental pressure and needle lift traces, as shown in Fig11.1. Using the first law of thermodynamics, the apparent heat release rate could be calculated from the pressure crank angle diagram. The ignition delay is measured as the time from the point of needle lift to the start of heat release. However, the measurement noise does not allow us to pick the two points from experimental data. Therefore, as the needle opening is assumed to be at a threshold of 10% of the maximum lift and the time when 5% of cumulative heat release is reached is considered the start of burning. The ignition delay of engines A10 to G10 was satisfactorily predicted using Eq. 10.1, and the results matched with the delay obtained from the pressure and needle lift traces.

Fuel injected during delay

The flow area of the nozzle holes, *A*, is calculated using the series of resistances, namely the gap between the needle seat, seat in the needle, and spray holes by treating them as a series of orifices. A flow coefficient C_d of 0.8 is reasonable for the spray holes. The instantaneous injection rate *dq/dt* is given by the pressures before the nozzle, $p_{2,}$ and in the cylinder, $p_{1,}$ and instantaneous flow area A (see Appendix IX).

$$\frac{dq}{dt} = C_f \rho_f A \sqrt{\frac{2(p_2 - p_1)}{\rho_f}} \tag{11.2}$$

Here, ρ_f = density of fuel.

Since the value of p_1 and p_2 changes during the delay period, their mean values are considered in the equation. The amount of fuel injected during the delay period of the combustion process Q_{del}, is obtained from the delay period and the rate of injection.

$$Q_{\text{del}} = \text{ID}\frac{dq}{dt} \tag{11.3}$$

Over-leaned fuel–air mixture

Considering the structure of the nascent spray during the ignition delay, the fuel–air mixture beyond the lean combustion limit of relative air–fuel ratio, Φ_L, will not burn efficiently, as it is over-leaned. It will be emitted as unburned HC by the engine. The value of Φ_L lies between 3.0 and 5.0, for most of the operating and injection parameters [12]. In the present work, a lean limit of 5.0 is used. The concentration profiles along the axis and radius of conical spray are self-preserving except for the rich core containing liquid spray [8]. The zone of lean fuel–air mixture lies on the periphery of the cone, and hence, the simplified laws of similarity for concentration profiles are valid. Hence, in principle, with the help of Eqs. (4.1–4.5), it is possible to estimate the fuel mass leaned beyond the flammability limit, ΦL. Equations (4.1–4.5) and those given in the reference [8] allow calculation of over-leaned fuel at the end of ignition. The fuel integrated over the spray volume using Eq. (11.6) is not finite. Therefore, the over-leaned fuel is calculated as the difference between the fuel injected during the delay using Eq. (11.9) and that integrated from zero radius to the radius of Φ_L.

Over-leaning factor:

The detailed calculations of several cases given in appendix-XVI for various engines showed that the over-leaned fuel could be expressed as a fraction of the fuel injected during the delay period and that the fraction is a constant. The value of the fraction was roughly equal to 0.01 if either the delay or the injected quantity during the delay is not large and dealt with in detail later in the chapter. The fraction is defined as the over-leaning factor.

Fuel effusing the injector sac

The liquid fuel remaining in the sac after the needle closed is at a pressure equal to that in the engine cylinder. The heat transferred from the hot combustion gases to the sac vaporizes a part of the fuel components. The vapour comes through the holes at velocities too low to mix sufficiently with air and burn in the short period available during the expansion. The residue remains in the sac to be injected normally in the next cycle. The actual formation of hydrocarbons from the fuel in the sac is a

function of the time and the rate at which the fuel discharges from the sac volume, [5]. Therefore, the hydrocarbon emission, *HCv,* due to sac volume is

$$HCv = V_s \rho_f y \tag{11.4}$$

Here, y refers to the yield or the fraction of fuel evaporated from the sac of volume, $V_{s,}$ and ρ_f is the density of the fuel.

Other sources of Hydrocarbons

The engine coolant temperature and lubricating oil could influence hydrocarbon emissions as well. However, in the present model, the engine is considered warmed up sufficiently so that the two factors have a negligible effect on HC emissions.

Formation of Unburned Hydrocarbons

After the ignition delay, the combustible mixture of air and fuel within limits of combustion burns explosively to form equilibrium combustion products. The fuel beyond the lean limit of combustion burns slowly or partially decomposes to lighter fractions or recombines to heavier hydrocarbon molecules resulting in exhaust hydrocarbons. This phenomenon is modelled according to a global slow burning rate.

Global slow burning rate:

The diesel combustion is heterogeneous in nature, where the fuel evaporates, and the burned and unburned gases mix during expansion. Hence, many processes contribute to hydrocarbon emissions from a diesel engine. Greeves et al [5] and Yu et al [12] explain the phenomenon of bulk quenching as a physical process, related to the incomplete combustion of the combustible mixture due to volume expansion. The leaned-out fuel finds it difficult to support a propagating flame in the expansion stroke, as the reaction rate is very slow by the low concentration of fuel. In the present work, quenching is modelled using a global slow rate of reaction.

$$\text{Diesel} + 18\ \text{Air} \rightarrow \text{Products of combustion} \tag{11.5}$$

$$\text{Mean reaction rate} = \text{A}C_a^n C_f^m \cdot \exp\left(\frac{E}{RT}\right) \tag{11.6}$$

where

$A = 150$ to 210
$Ca =$ Mean concentration of air in the lean zone-1, approximately
$C_f =$ Mean concentration of fuel leaned out and effused from the sac
$n = 18$
$m = 1$
$E/R = 2100$ K.

The equation for the slow reaction is validated for the ignition delay period in an earlier work of Chandorkar et al. [1]. The dilution of the leaned-out fuel after a characteristic period will be too low even to continue the slow reaction. The typical period scales with the delay period. The quantity of slow burnt fuel is given by the mean reaction rate and a characteristic ignition delay.

$$\text{slow burnt fuel} = \text{reaction rate} \times \text{Ignition delay} \tag{11.7}$$

Predicting HC in the Exhaust

Relating HC to ignition delay:

The measured specific HC is plotted against the ignition delay as given by Greeves et al. [5], Fig. 11.2. Their correlation seems to be valid for a given engine and at one condition of speed and load. For a wide variety of engines and operating conditions, the correlation coefficient is as low as 0.3.

Relationship of HC emissions and sac volume:

Figure 11.3 shows [5] the effect of sac volume alone on HC at a particular condition

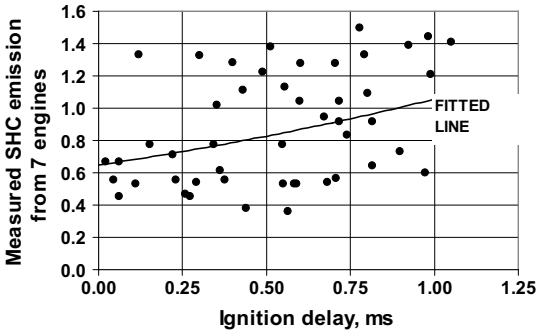

Fig. 11.2 Correlation of exhaust indicated hydrocarbon with ignition delay

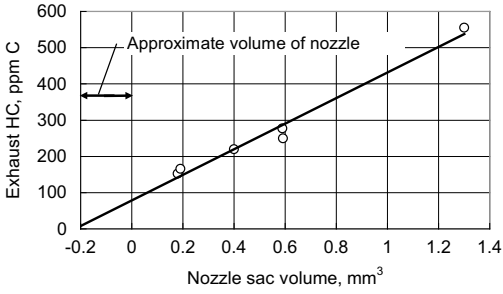

Fig. 11.3 Effect of nozzle sac volume on HC concentrations and yield [5]

of load and speed for the engine studied. The negative intercept on the horizontal axis corresponds to the volume of holes. The yield value could be estimated as 0.21.

On the other hand, an insignificant correlation was found between the observed mass of HC emissions and the sac volume for various engines at different operating conditions, as shown in Fig. 11.4.

HC and fuel injected during the delay

As a first step, the observed HC was plotted against the ratio of fuel injected during ignition delay to the total fuel injected in Fig. 11.5, without considering the emissions from the sac. The regression coefficient was 0.93 showing the important effect of the quantity of fuel injected during ignition delay, Q_{del} on HC emissions from a diesel engine. The straight line relationship in a semi-log plot showed that with an increasing amount of fuel injected during the delay, the emissions increased exponentially, as shown in Fig. 11.5. Figure 11.6 shows a good nonlinear relationship in a Cartesian coordinate system. However, the fuel injected during the delay period is many times higher than the observed HC emissions. Further, the exponential relationship suggests that more time is available for the fuel to lean out when the delay increases. Therefore, considering an over-leaning factor and the effect of sac volume will improve the correlation quantitatively.

$$\frac{HC}{m_f} = 0.0012 \cdot \exp\left(2.86 \frac{Q_{\text{del}}}{\text{total fuel injected}}\right) \tag{11.8}$$

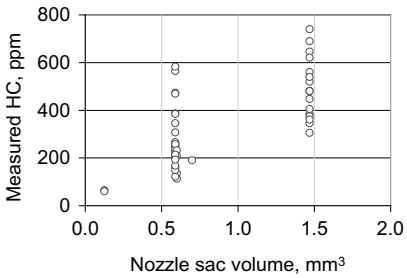

Fig. 11.4 Effect of nozzle sac volume on HC for many engines

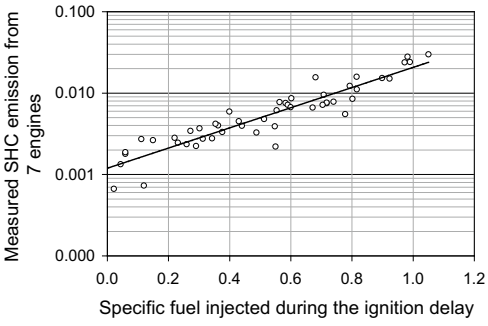

Fig. 11.5 Semi-log plot of specific mass of fuel injected during the ignition delay and HC

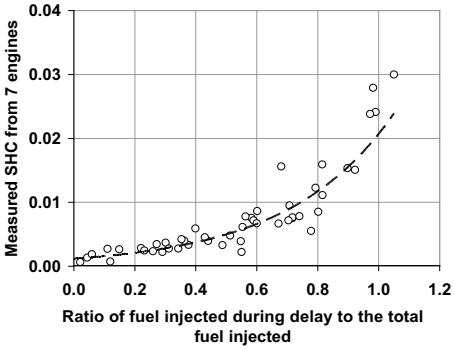

Fig. 11.6 Specific fuel injected during the ignition delay period

Specific HC in the exhaust

Specific HC in the exhaust is defined as the ratio of HC emissions in the exhaust to the quantity of fuel injected during the delay. Thus, the specific HC could be modelled using the expression given below.

$$\text{EIHC in exhaust} \propto \frac{1}{m_f}$$

$$(\text{fuel injected during delay} \times \text{fuel over leaning factor} + \text{sac volume} \times \text{yield}) - \text{slow burnt fuel}) = \frac{m_{\text{cal}}}{m_f} \tag{11.9}$$

Phenomenological Model

The relationships with important parameters, namely the sac volume and fuel injected during the delay, suggest that the correlation will not predict HC if the two parameters are considered individually. The over-leaning factor and the unburnt fuel yielded by the sac volume when incorporated lead to a phenomenological model. The suitable yield from the sac was found to be 12%.

An average over-leaning factor of 0.008 could be obtained from the thick jet structure of a diesel spray given in Eqs. (4.1–4.5), during the ignition delay period. The measured specific HC was plotted against the EIHC calculated using this factor in Eq. 10.9 on a semi-log paper in Fig. 11.7 and on a linear graph paper in Fig. 11.8. Here, the coefficient of the fit was better than 0.9 validating the proposed model for predicting HC emissions, quantitatively.

Discussions

The fuel injected during the ignition delay is cold and is dispersed into various packets of different air–fuel ratios. The fuel leaned beyond an air excess ratio of 5.0 exits

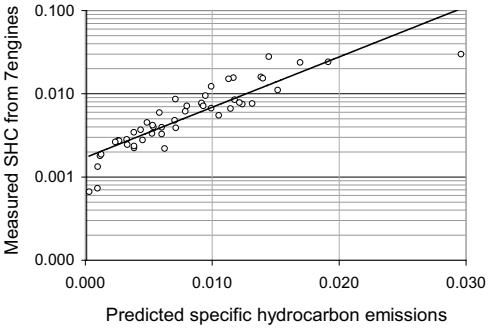

Fig. 11.7 Semi-log plot of specific mass of fuel and HC considering sac and an over-leaning factor was 0.008

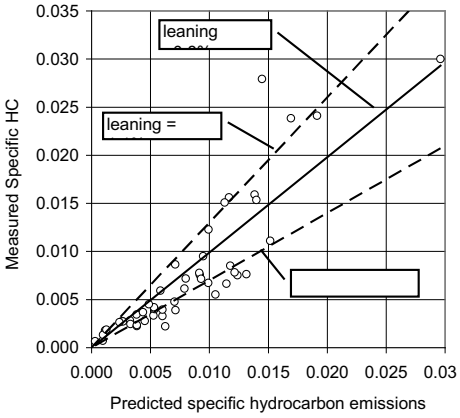

Fig. 11.8 Specific mass HC considering over-leaning and sac

the engine as unburned hydrocarbon emissions. By studying the spray structure, the over-mixed fuel is estimated to lie between 0.007 and 0.011 of the fuel injected during the delay period in case of direct injection diesel engines, as shown in Fig. 11.8. The lower value of the leaning factor is valid when the ignition delay is relatively less. The HC emissions are augmented by fuel effusing from the sac. The yield from the sac is about 0.12. The over-leaned fuel–air mixture burns slowly along with the fuel leaked from the sac during a characteristic period. The reaction rate could be described by the Arrhenius type relationship. The ignition delay correlation (ch-5 Eq. 5.1) was applied to predict ignition delay. On engine C10, detailed experiments were carried out with oxygenated fuels and exhaust gas recirculation, EGR at rated conditions. The predictions were in agreement with observed values, Fig. 11.9.

Then, a similar prediction methodology was applied to different engines widely varying in dimensions, methods of aspiration, and rated speeds. Older versions of engine E10 and B10 were also considered for model evaluation where a larger amount of HC was observed. The satisfactory comparison of predicted and experimental values of HC emission under different operating conditions proved the validity of the new correlation, Fig. 11.10.

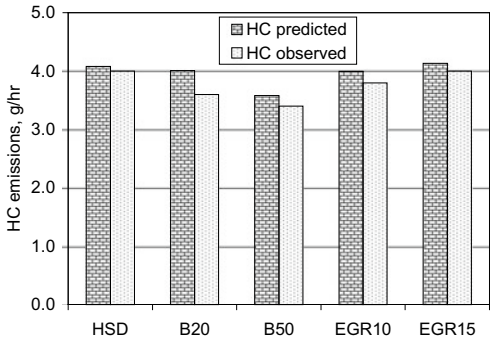

Fig. 11.9 Prediction of HC emissions at rated conditions for engine C10

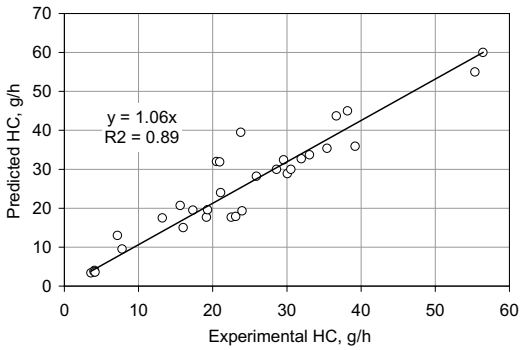

Fig. 11.10 Prediction of HC emissions for many engines

Summary

A strong relationship of HC exists with the sum of leaned-out fuel during the ignition delay and fuel yielded by the sac. Detailed consideration of over-leaning factor enables prediction of exhaust indicated HC for any DI diesel engine over a wide range of speeds and loads irrespective of the nature of aspiration, after a reasonable warm-up of the engine. The model considers the chemical effect of fuel on HC emissions indirectly in the ignition delay term.

References

1. Chandorkar SB, Dani AD, Lakshminarayanan PA (1988) Effects of injection parameters, fuel quality and ambient on the ignition delay and the location of the flame Kernel in a diesel spray in a quiescent chamber. SAE 881227
2. Dent JC (1980) Turbulent mixing rate- its effect on smoke and hydrocarbon emissions from diesel engines. SAE800092
3. Dent JC, Lakshminarayanan PA (1983) A model for absorption and desorption of fuel vapour by cylinder lubricating oil films and its contribution to hydrocarbon emissions. SAE 830652

4. Franz G, Chmela, Orthaber GC, (1999) Rate of heat release prediction for direct injection diesel engines based on purely mixing controlled combustion. SAE 1999–01–0186
5. Greeves G, Khan IM, Wang CTH, Fenne I (1977) Origins of Hydrocarbon emissions from diesel engines. SAE 770259
6. Heywood JB (1988) A textbook on Internal Combustion engine fundamentals. McGraw-Hill International editions
7. Ikegami M, Xin-he Li, Nakayama Y, Keimiwa (1983) Trend and origins of Particulate and Hydrocarbon emission from a direct injection diesel engine. SAE 831290
8. Lakshminarayanan PA, Dent JC (1983) Interferometric studies of vapourising and combusting sprays. SAE 830244
9. Nakayama Y, Maruya T, Oikawa T, Fujiwara M, Kawamata M (1994) Reduction of HC emission from VTEC engine during cold start condition. SAE 940481
10. Tsunemoto H, Ishitani H, Konno A (1992) The increase of HC emissions from a direct injection diesel engine during long idling operation. SAE 922227
11. Watson N, Pilley AD (1980) A Combustion correlation for diesel engine simulation SAE 800029
12. Yu RC, Wong VW and Shahed SM (1980) Sources of hydrocarbon emissions from direct injection diesel engines. SAE 800048

Chapter 12
Hydrocarbon Emissions from Spark-Ignition Engines

Abbreviations

A	Surface area of the region (m^2)
A_v	Flow area (m^2)
C	Bulk gas state; charge condition at any instant (–)
C_d	Coefficient of discharge (–)
D	Molecular diffusion coefficient for the oil film (m^2/s)
dA_{ij}/dt	Rate of change in the area of the region i due to changes in the boundaries of adjacent regions. (m^2/s)
dm_i/dt	Rate of change of the fuel content of region i (kg/s)
Δt	Time interval (s)
e *and* v	Specific internal energy and volume (J/kg, m^3/kg)
E_σ	Instantaneous internal energy of the cylinder contents (J)
F	Bulk of the oil film (–)
f_i	Mass fraction of specie i (–)
G	Bulk gas state (–)
g_F*	Liquid-phase mass transfer conductance (kg/(m^2 s))
g_G*	Gas-phase mass transfer conductance (kg/(m^2 s))
H_C	Henry constant (–)
m_σ	Instantaneous mass of the cylinder contents (kg)
$\dot{m}\prime$	Convective mass flux (kg/(m^2s))
$-\dot{m}\prime$	Desorption results (kg/(m^2s))
L	Liquid side of the interface (–)
m_c	Mass of gas trapped (kg)
m_{fFi}	Mass fraction of fuel in oil in the region i (–)
m_{fg} and m_{fs}	Mass concentrations of fuel vapour in the bulk gas state (G) and on the gas side of the interface (S) (–)
m_{fL} and m_{fF}	Mass concentrations of the dissolved fuel on the liquid side of the interface (L) and in the bulk of the oil film (F) (–)

P. A. Lakshminarayanan and Y. V. Aghav, *Modelling Diesel Combustion*,
Mechanical Engineering Series, https://doi.org/10.1007/978-981-16-6742-8_12

m_{fs} and m_{fL}	Mass fractions of fuel vapour in the gas phase and dissolved into the oil layer, respectively (–)
m_i and h_i	Mass and specific enthalpy of specie i, (fuel, air, or burned gas) ()
M_O	Molecular weights of oil and the charge gas mixture (kg/kmol)
N	Engine speed (rpm)
n_{fL}	Mole fraction of the fuel dissolved in the oil film (–)
N_{Hc}	Henry number (–)
P	Prevailing pressure in a cylinder (Pa)
P_{fs}	Partial pressure of the fuel vapour in the gas phase adjacent to the interface S state (Pa)
P_{tot}	Total instantaneous cylinder pressure (bar)
P_v	Density (kg/m^3)
θ	Crank angle (degree)
Q	Heat transfer (J)
ρ_o	Density of the oil layer (kg/m^3)
Z_o	Thickness of the oil layer (m)
S	Gas side of the interface (–)
S	Oil film gas-phase interface (–)
T_w	Temperature of the wall (K)
U_v	Velocity the valve, a function of the pressure drop across the valve and upstream pressure (m/s)
V	Crevice volume, calculated from the crevice gap, x (x assumed to be constant) (m^3)
w	Work transfer (J)
x	Crevice gap (m)
δ	Fuel penetration depth of in a semi-infinite slab of oil (m

The literature of unburned hydrocarbon emissions (HC) from spark ignition (SI) engines is comprehensively cited by Lavoie and Blumberg [23]. The HC emissions phenomenon is different from that in a diesel engine, where it is generated by the fuel over-leaned at the surface of the sprays and by the fuel effusing from the nozzle sac. Four sources of unburned hydrocarbon generation have been identified for SI engines.

- Quenching of the propagating flame at the cold wall surfaces in the combustion space.
- Unburned fuel–air mixture trapped in the piston top land and ring crevices.
- Gas-phase quenching when the engine is operating under extreme conditions of stoichiometry.
- Absorption/desorption processes by cylinder lubricating oil films and deposits, which is identified as one of the major phenomena.

Daniel [5] identified the existence of cylinder quench layers and their relationship with the engine stoichiometry and showed a correlation with quench layer thickness established from burner studies. Daniel concluded that the observed quench

distances were of the right order of magnitude to account for HC emissions. An extensive sampling valve study by Daniel [6] identified the major engine-operating variables controlling HC emissions. From his measurements, Daniel also concluded that post-quench mixing and oxidation of the quench mass were taking place during the expansion and exhaust strokes of the engine cycle.

Lavoie and Blumberg [23], and Lavoie [22] based on the observations of Daniel considered a model for diffusion and oxidation of the quench mass in the turbulent thermal boundary layer separating the cylinder wall from the burned gas region formed behind the propagation flame front. The model indicated that oxidation of the diffused HC was rapid, and any remaining wall quenched HC was in low-temperature regions of the thermal boundary layer (below about 1100 K).

An in-cylinder sampling valve study by Locusso et al. [24] indicated rapid and extensive burn-up of quench layer hydrocarbons, upper limit calculations showing that less than 10% of exhaust HC originates from the quench mass. Fundamental experimental studies by Blint and Bechtel [2] corroborate the findings of Locusso et al. [24].

Unburned mixture trapped in the piston top land and ring crevices during the compression and combustion phases of the engine cycle, and which later in the expansion process expand into the combustion space, is known to be a major contributor to exhaust hydrocarbons [34, 28].

Gas-phase quenching when chemical reaction rates are low compared with turbulent mixing rates, occurs under extremely unfavourable engine stoichiometry [10] and excessive combustion chamber turbulence [4].

Unburned fuel absorption/desorption processes by lubricating oil films contributing to exhaust HC emissions have been identified by Kaiser et al from bomb and engine studies [12, 13]. Support for this mechanism has been provided by the modelling study of Carrier et al [3] which has shown the variation of HC emissions with engine speed and cooling water temperature to follow observed experimental trends more closely than the comprehensive model of Lavoie and co-workers [22, 23].

From the foregoing discussion, the major sources of HC emission from homogeneous spark-ignited engines operating under normal conditions are those due to crevice volumes and absorption/desorption of unburned fuel by lubricating oil films and deposits.

A model for HC emission based upon a consideration of the contribution from crevice volumes and the cyclic adsorption/desorption phenomenon due to the lubricating oil film [8] is presented in this chapter. The absorption/desorption process is considered to be controlled by both gas and liquid-phase conductances, unlike Carrier et al. [3] who consider the liquid (lubricating oil film) phase to be controlling. The model is compared with the extensive experimental data of Lavoie and Blumberg [23] obtained in a low turbulence engine with disc-shaped combustion chamber geometry. The effects of engine speed, load, equivalence ratio, exhaust gas circulation (EGR), and spark timing are compared with the experiment. Parametric studies to investigate the effects of compression ratio, lubricating oil film thickness, and cylinder charge turbulence are also presented and discussed.

Description of the Engine Model

- The engine model is considered in three subsections:
- Breathing.
- Combustion.
- HC emissions.

Breathing

Detailed dynamics of flow through the engine [16–20] can be considered for evaluating breathing by the engine. However, for most of the model-based controls of modern engines, a filling and emptying model is used. Here, the engine intake is considered a pipe with two resistances—the carburettor and the intake valve. Ahead of the carburettor resistance, a plenum at ambient conditions is assumed. The engine exhaust flow is considered through a resistance—the exhaust valve—into a plenum, which is at exhaust manifold pressure and temperature. Figure 12.1 shows a schematic of the induction exhaust configuration.

The flow across the valves and throttle is quasi-steady and depends on effective flow areas and discharge coefficients, which have been taken from Sherman and Blumberg [26]. The model is of the "filling and emptying" type without the effects of wave action—energy and mass conservation about an open system are applied. EGR is considered a diluent present in the air with the composition of the exhaust gases. Considering the instantaneous cylinder volume as the system control volume (σ) energy and mass conservation equations can be written as follows:

$$\mathrm{d}E_\sigma = \sum_{\text{all } i} h_i \mathrm{d}m_i + \delta Q - \delta W \tag{12.1}$$

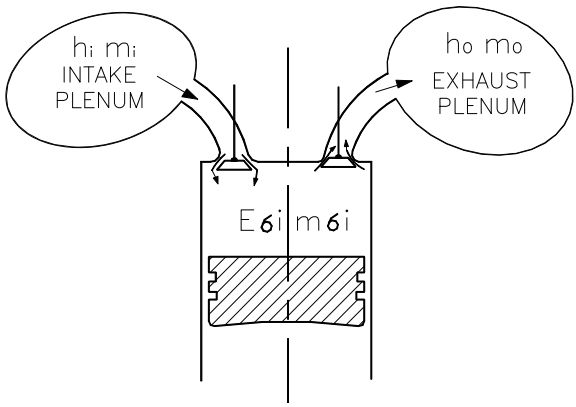

Fig. 12.1 Schematic diagram of engine and surroundings

$$dm_\sigma = \sum_{\text{all}i} dm_i \tag{12.2}$$

E_σ and m_σ are the instantaneous internal energy and mass of the cylinder contents, m_i and h_i are mass and specific enthalpy of species i, (fuel, air or burned gas) entering or leaving the control volume. Q and w are heat and work transfer.

$$dm_i = f_i dm_V = f_i \rho_V C_d A_V U_V dt \tag{12.3}$$

Here, f_i is the mass fraction of specie i, ρ_v the density, A_v the flow area, U_v the velocity at the valve, and C_d the coefficient of discharge. U_v is a function of the pressure drop across the valve and upstream pressure.

Backflow into the induction system is accounted for in the following manner. The inlet valve closes after the bottom dead centre; hence, a quantity of the cylinder charge is forced back into the inlet port and the induction manifold as the piston moves towards TDC on the compression stroke; this mass is assumed to reside as a plug inside the inlet tract. Late in the exhaust stroke of the inlet tract, plug flow is again considered, and no mixing with the plug of induction charge residing in the inlet tract is assumed. As the next induction stroke commences, these two plugs of burned gas and fresh charge are drawn into the engine cylinder. The computation scheme keeps track of these plugs for use in the energy and mass conservation Eqs. (12.1 and 12.2).

Combustion

The air–fuel mixture induced into the cylinder mixes with the residual fraction with EGR, and the effective residual increases. The gaseous mixture is compressed, heat transfer with the cylinder walls being calculated from Woschni's correlation [29].

Following the ignition process, the burned and unburned gases in the cylinder are considered separated by a thin flame front. Heat transfer to the cylinder walls is considered independently from these two zones using Woschni's correlation. The ignition delay is an input parameter to the computation, the data being taken from reference [23]. A cosine burning "law" [23] is used for the calculation of the mass burning rate. The burned mass fraction α at any crank angle during the burn period is defined by

$$\alpha = 0.5\left[1 - \cos\left\{\frac{\pi}{1.16} \cdot \frac{\theta - \theta_{0.05}}{\theta_{0.95} - \theta_{0.05}}\right\}\right] \tag{12.4}$$

Here, θ is crank angle, and subscripts 0.05 and 0.95 refer to the position when 5 and 95% of the charge has been burned.

Use of the cosine burning "law" in preference to the phenomenological models described in references [7, 11] enables comparison of the results obtained with the

HC emission model developed here with that presented by Lavoie and Blumberg [23]. During the combustion process, the contributions of the unburned mixture and burned products to total internal energy E and volume V are as follows:

$$m_b e_b + m_u e_u = E \tag{12.5}$$

$$m_b v_b + m_u v_u = V \tag{12.6}$$

Here, e and v are specific internal energy and volume, and suffices u and b refer to the unburned mixture and burned products. The set of Eqs. (12.1)–(12.6) are used in the evaluation of cylinder pressure and burned and unburned gas temperatures. A schematic of the solution procedure is shown in Fig. 12.2.

HC Emissions

The piston motion exposes the cylinder liner and oil film to the charge gases at various times during the engine cycle. The lubricating oil film is assumed to be of a uniform thickness on the liner surface, and its total area can be considered as made up of four regions.

Region (1) in contact with unburned gases.
Region (2) that was in contact with unburned gases and is presently covered by the piston.
Region (3) in contact with burned gases.
Region (4) that was in contact with the burned gases and is presently covered by the piston.

The sum of the areas of these four regions is invariant, but individual areas increase or decrease at the expense of their neighbours. This is summarized schematically in Fig. 12.3.

The following mechanism is considered to apply for the transfer phenomenon of fuel vapour between the gas and liquid (oil film) phases.

Between the bulk gas state (C) (charge condition at any instant) and the oil film gas-phase interface (S), vapour transport is by convective mass transfer through the burned and unburned gas turbulent boundary layers.

Henry's law is assumed to hold for the absorption of the vapour by the oil film, and the partial pressure of the fuel vapour (P_{fs}) in the gas phase adjacent to the interface S state is related to the mole fraction of the fuel dissolved in the oil film (n_{fL}) by the Henry constant (H_C) where

$$H_C = \frac{P_{f_s}}{n_{f_L}} \tag{12.7}$$

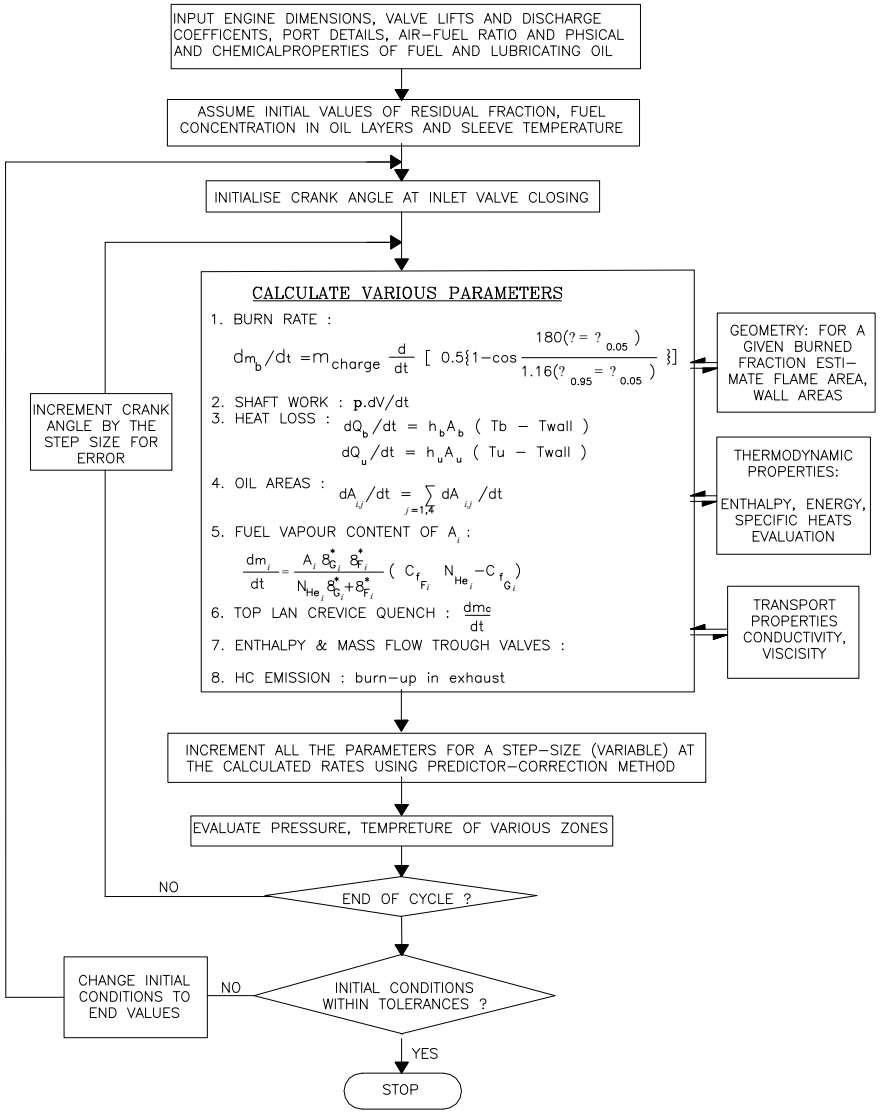

Fig. 12.2 Model

A *Henry* number N_{Hc} is defined (12.17) as follows:

$$m_b v_b + m_u v_u = V \tag{12.8}$$

Here, m_{fs} and m_{fL} are the mass fractions of fuel vapour in the gas phase and dissolved into the oil layer, respectively. Equations (12.7) and (12.8) are combined to yield.

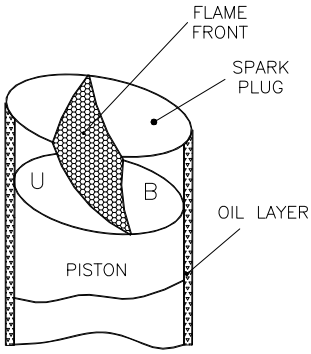

Fig. 12.3 Schematic diagram of oil layers, flame front, unburned zone (U), and burned gas zone (B)

$$N_{\mathrm{HC}} = \left(\frac{H_c}{P_{\mathrm{tot}}}\right)\left(\frac{M_0}{M}\right) \tag{12.9}$$

Here, P_{tot} is the total instantaneous cylinder pressure, and M_O and $\overline{M}$ are the molecular weights of oil and the charge gas mixture—here assumed air. The evaluation of the Henry constant for the oil film is discussed in Appendix XI.

The transfer of the dissolved fuel across the oil film is assumed to occur by molecular diffusion. A linear concentration gradient in the oil film is assumed. To accommodate the effects of engine speed on the diffusion process, a penetration depth (δ) is assumed over which the concentration gradient is effective. This procedure is similar to that adopted in transient heat conduction [14] where for the fast transients a finite body can be assumed to be semi-infinite in behaviour. From Kreith [14], the penetration depth can be expressed as

$$\delta = \sqrt{\frac{\pi D}{N}}. \tag{12.10}$$

Here D is the molecular diffusion coefficient for the oil film and N is engine speed. Figure 12.4 shows a schematic of the ideas discussed above. For a dilute mixture of fuel in the air, the convective mass flux ($\dot{m}''$) across the gas-phase boundary layer can be expressed as [27]

$$\dot{m}'' = g_G^*\left(m_{f_G} - m_{f_s}\right) \tag{12.11}$$

Here g_G* is the gas-phase mass transfer conductance and is evaluated in Appendix XII, m_{fG} and m_{fs} are the mass concentrations of fuel vapour in the bulk gas state (G) and on the gas side of the interface (S). Across the penetration depth, $\dot{m}''$ can be written as

$$\dot{m}'' = g_F^*\left(m_{f_L} - m_{f_F}\right) \tag{12.12}$$

Here,

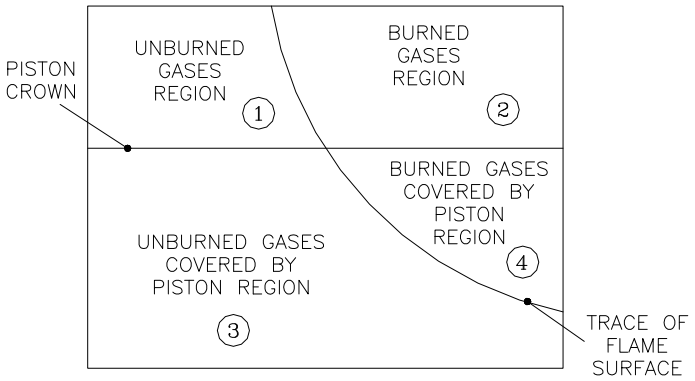

Fig. 12.4 Schematic of oil regions participating in absorption and desorption

$g_F{}^*$ = Liquid-phase mass transfer conductance (and is evaluated in Appendix XII).

m_{fL} and m_{fF} = Mass concentrations of the dissolved fuel on the liquid side of the interface (L) and in the bulk of the oil film (F).

Equating (12.11) and (12.12) and using Eq. (12.8) along with algebraic rearrangement and the definition of $\dot{m}''$ in Eq. (12.12) results in

$$\dot{m}'' = \frac{g_G^* g_F^*}{N_{Hc} g_G^* + g_F^*} \left[m_{f_G} - m_{f_F} N_{Hc} \right] \tag{12.13}$$

The desorption results in a change of sign in $\dot{m}''$ in Eqs. (12.11)–(12.13). The mass transfer flux ($\dot{m}''$) from Eq. (12.13) multiplied by the surface areas of the cylinder liner in contact with unburned or burned gases gives the rate of absorption of desorption of fuel vapour by the oil film (Fig. 12.5).

As pointed out earlier, the dissolved fuel content of the four regions changes due to mass transfer and also because of changes in regional surface areas due to flame propagation and piston movement see Fig. 12.6. This is expressed mathematically for the region i as follows:

$$\frac{\mathrm{d}m_i}{\mathrm{d}t} = \dot{m}'' A_i + \rho_0 Z_0 \sum_{\substack{j=1,4 \\ i \neq j}} m_{f_{F_i}} \frac{\mathrm{d}A_{i,j}}{\mathrm{d}t} \tag{12.14}$$

Here, $\mathrm{d}m_i/\mathrm{d}t$ = Rate of change of the fuel content of i.

A = Surface area of the region.

ρ_o and Z_o = Density and thickness of the oil layer, respectively.

m_{fFi} = Mass fraction of fuel in oil in the region i.

$\mathrm{d}A_{ij}/\mathrm{d}t$ = Rate of change in the area of the region (i) due to changes in the boundaries of adjacent regions.

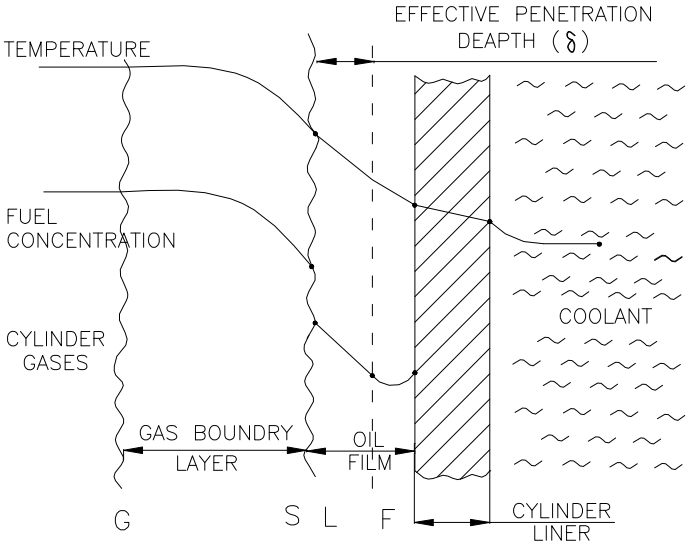

Fig. 12.5 Temperature and concentration gradients within the engine

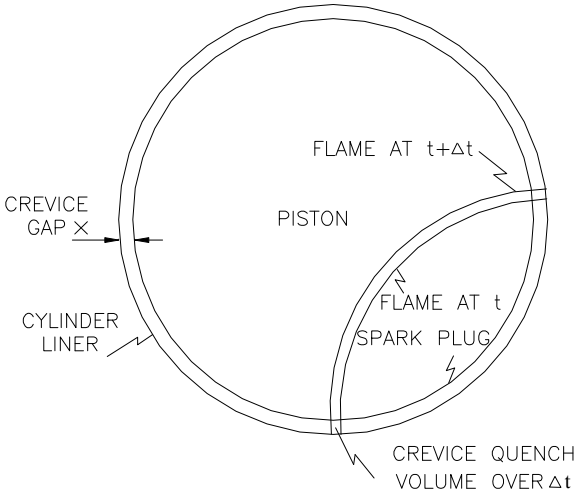

Fig. 12.6 Interaction of flame and top land crevice

Complete oxidation of desorbed fuel into the burned gases was assumed if the arithmetic mean of the burned gas and oil film temperature is above 1100 K. At lower temperatures, the desorbed fuel is integrated and considered to contribute to HC emitted during blowdown, and justification for this is given in appendix XIII.

The Contribution of Ring Crevice to HC Emission

As the propagating flame front passes over the piston, crown fuel–air mixture is trapped in the top land crevice where it is assumed to region unreacted. Considering the flame propagate over the time interval Δt (Fig. 12.6), the hatched crevice volume v traps the unreacted fuel–air mixture. The mass of gas (m_c) trapped is determined by the prevailing pressure P in a cylinder and the temperature of the walls T_w and can be expressed as follows:

$$\frac{\mathrm{d}m_c}{\mathrm{d}t} = \left[\frac{P}{\mathrm{RT}_w}\right]\left[\frac{\mathrm{d}v}{\mathrm{d}t}\right] \tag{12.15}$$

The crevice volume, V, is calculated from the crevice gap, x, which is here assumed to be constant. In actual conditions, however, the gap varies with piston material, construction details, and its temperature under varying conditions of operation. m_c is assumed to undergo no reaction in the cylinder and contributes to the total HC emission at the exhaust valve. It is assumed that the crevice mass discharged is in proportion to the mass of burned gas discharged over any time interval.

Oxidation of HC During the Exhaust

The hydrocarbons emitted from the engine are assumed to be uniformly mixed with the products of combustion and any remaining air in the cylinder. The process of exhaust flow, oxidation of the emitted HC, and heat transfer to the port follow [23]. However, after the exhaust valve closure, the exhausted gases are assumed to continue flowing through the exhaust port and pipe at a progressively diminishing velocity. This requires a change in the flow regime from turbulent to laminar and an appropriate change in the friction factor for use with the Reynolds analogy relationship.

Solution Procedure

The sub-models—breathing, combustion, and HC emissions—are used in a thermodynamic cycle simulation programme [9] to evaluate the HC emission behaviour of the engine. Transport and thermodynamic properties of unburned mixture and burned products are available from the various subroutines of the simulation programme. The rate of change of heat loss, work output, combustion, relevant surface areas, fuel vapour absorbed and desorbed from the oil film, crevice mass trapped, and inducted and exhausted masses from the cylinder are used in an interactive integration scheme of the predictor–corrector type which is part of the cycle simulation programme. The complete computation scheme is shown in Fig. 12.2.

Initially, the oil film contains no absorbed fuel, and during the desorption process not all the fuel vapour is desorbed. Hence, there is a progressive accumulation of fuel in the oil film, until a steady mean concentration is reached, with further absorption and description occurring about the mean. It was found that the number of engine cycles to reach this mean value was dependent on wall temperature, engine speed, and oil film thickness. With the range of these parameters investigated here, it was found that when wall temperature is low, or engine speed is high or oil film thickness is large, about ten cycles were necessary to achieve the steady value, while at the other extreme of these parameters, steady oil film concentration was achieved within two cycles. This point is dealt with further in the discussion of results.

Comparison of the Model Prediction with Engine Experiments

The results obtained with the model described were compared against the experimental data of Lavoie and Blumberg [23] and Lavoie et al. [22] obtained on a CFR engine. The engine details and operating conditions are given in reference [23] where engine speed, load, equivalence ratio, EGR, and timing were varied relative to a baseline condition, which is listed here in Table 12.1.

The effects of compression ratio and wall temperature were evaluated against the data of reference [22]. The effects of turbulence of intake charge were evaluated using the model and the operating conditions of references [22, 23] over a range of engine speed. Direct comparison with experimental data was not possible. The gas exchange and combustion sub-models were tested for accuracy against mass flow data provided by Lavoie [21] and IMEP data of Lavoie, Blumberg [23]. At their worst, computed airflow was within 2% and IMEP within 8% of the experimental values. The deviation in IMEP could be due to the use of Woschni's equations [29] for heat transfer, which was not modified in any way for the present study.

Figure 12.7 shows the variation of HC (fuel vapour) in the oil layer with the crank angle for the first cycle of the computation at the engine baseline condition. The mass

Table 12.1 Basic engine-operating parameters

Base point engine conditions	Ref. Lavoie and Blumberg [23]
RPM	1250
IMEP	380 kPa (55 psi)
A/F	16.0 ($\Phi = 0.9$)
Compression ratio	7.1 (8.65 for EGR runs)
Spark timing	MBT (35° BTC)
EGR	0%
Burning interval	(−14°, 34°)
ISFC	240 g/kW-h(0.395 lb/hp-hr)

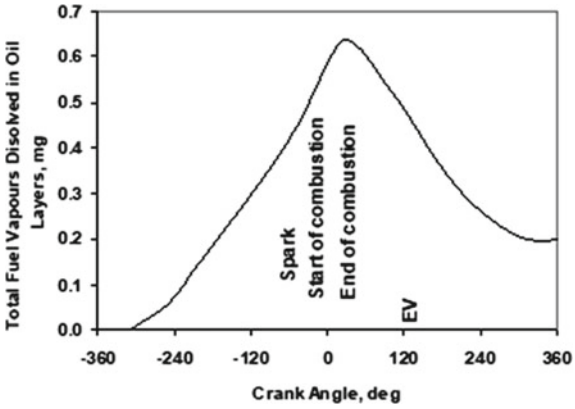

Fig. 12.7 Fuel content of oil layers variation with crank angle

of HC is zero initially and then follows a trend similar to cylinder pressure as it then increases and decreases to a value of approximately 0.2 mg at the end 720° CA. The trend with cylinder pressure is to be expected because absorption and desorption are related directly to the Henry constant (Eq. 12.7) and the mass transfer conductance g_G* (Eq. 12.11). Because of the finite engine cycle time, there is some fuel remaining within the oil layer at the end of the engine cycle (720° CA), the quantity depending on engine speed and oil film thickness (wall temperature variation). The quantity of fuel remaining in the oil film at the end of the first cycle provides the initial condition for the second cycle where once again there is a residual of fuel at the end of the cycle, and hence, there is a build-up of fuel mass in the oil film until a steady level is reached about which there is a periodic variation due to absorption and desorption.

This point is emphasized in Figs. 12.8 and 12.9, where variation mass desorbed with crank angle and cycle number is also shown. It is seen from Fig. 12.8 (a) that the

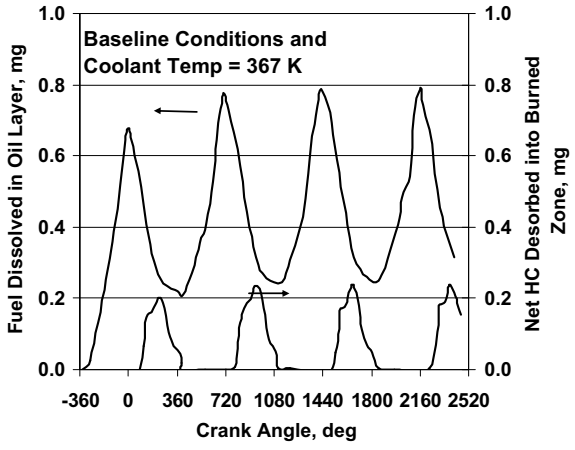

Fig. 12.8 Stabilization of fuel quantity in oil layers at 367 K coolant temperature

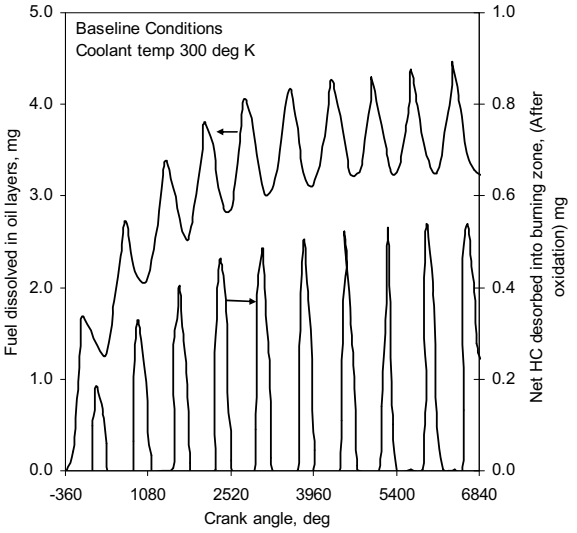

Fig. 12.9 Stabilization of fuel quantity in oil layers at 300 deg K coolant temperature

net HC absorbed into the burned gas commences about 90° ATDC on the expansion stroke and increases rapidly as the expansion proceeds. This is due to three factors. The boundary layer film temperatures are below 1100 K (see Appendix XIII and Fig. 17.9); therefore, oxidation of the desorbed HC is negligible. Secondly, the surface area for desorption increases as the expansion proceeds, and thirdly the decrease in-cylinder pressure during expansion causes an increase in the Henry number N_{Hc}, which from Eq. (12.13) results in an increased desorption rate $\dot{m}''$. A further increase in the desorbed mass of hydrocarbons occurs following exhaust valve opening for the three reasons just discussed above. During the exhaust stroke beyond the bottom dead centre, the desorbed hydrocarbons decrease because of the reducing surface area for desorption. The decrease in cylinder pressure with inlet valve opening reduces this trend for a moment, but the admission of fresh charge increases the concentration of fuel vapour m_{fG} Eq. (12.13). This coupled with minimal desorption areas around TDC causes the desorption of hydrocarbons to fall rapidly to zero. It should be noted that in all comparisons with experimental data, the results for absorption and desorption were considered after the steady-state value had been reached.

Figure 12.10 shows the variation with the crank angle in integrated HC (fuel) desorbed before oxidation—curve (*A*)—the integrated desorbed HC remaining after in-cylinder oxidation—curve (*B*)—and the integrated desorbed HC remaining in the cylinder after exhaust valve opening—curve (*C*). It should be noted that oxidation of the desorbed HC ceases after about 80° ATDC because the gas temperature has fallen below 1100 K, hence the constant difference between curves (*A*) and (*B*). The difference between curves (*B*) and (*C*) is the integrated mass of HC desorbed which is discharged to the exhaust port along with the appropriately integrated mass of the crevice contribution, and this is shown as curve (*D*).

Figure 12.11 shows the variation in exhaust HC concentration and gas velocity at

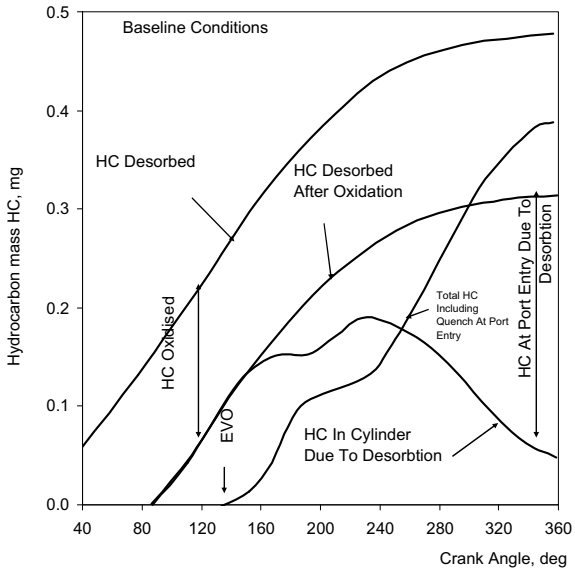

Fig. 12.10 Variation of integrated hydrocarbons with crank angle

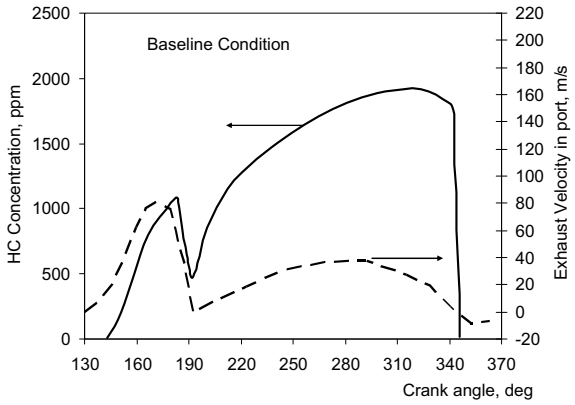

Fig. 12.11 Variation in the HC emission at the exhaust port with crank angle

the exhaust port with crank angle. The HC concentration follows the exhaust velocity, as the velocity drops after the blowdown period, the HC concentration falls since the crevice mass flow rate discharged in the exhaust flow is proportional to the mass flow rate of burned gases exhausted. Following blowdown, the HC concentration follows the exhaust flow until valve closure.

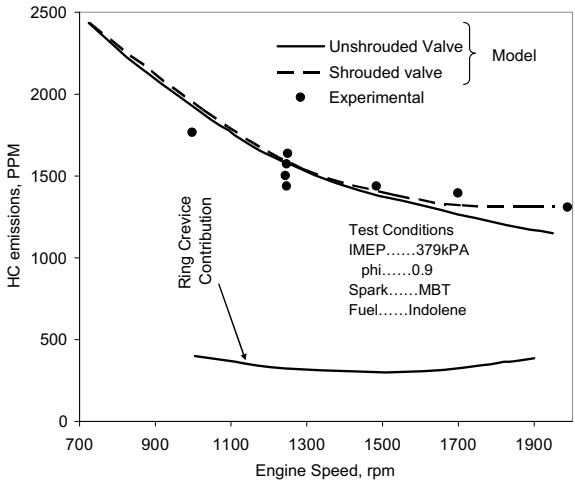

Fig. 12.12 Effect of engine speed on HC emissions

Effect of Engine Speed

Figure 12.12 considers the effect of engine speed on HC emission, where the agreement with experimental data is good. The computed ring crevice contribution is approximately constant. This follows from the condition of the test where engine stoichiometry and IMEP were held constant. The decrease in HC emitted with speed is due to the reduced engine cycle time allowing lower absorption and desorption to occur, higher cylinder wall temperatures at the higher speeds result in reduced oil film thickness due to reduced viscosity and also an increase in Henry's constant which reduces the fuel vapour absorbed. It should be noted that while the change in mean wall temperature over the speed range is small (approximately 16 K), Henry's constant varies by a factor of 2—see appendix XI.

Effect of IMEP

Figure 12.13 shows the effect of load (IMEP) on exhaust HC at fixed engine speed, equivalence ratio, and MBT timing. The crevice contribution to exhaust HC is again approximately constant following Lavoie et al. [22]. The decrease in the desorbed HC mass fraction (ppm) emitted with the increase in engine load is due to increased wall temperature—from 400 to 455 K—as the load is increased from 240 to 655 kPa, and the increased post-desorption oxidation due to higher burned gas temperatures with increasing load.

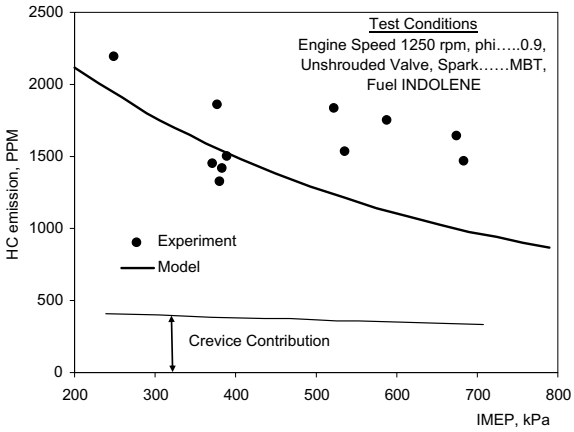

Fig. 12.13 Effect of IMEP

Effects of Equivalence Ratio and Timing

The effects of equivalence ratio at the baseline operating condition are shown in Fig. 12.14, while Fig. 12.15 shows the effect of spark retard to produce a 10% fuel economy penalty (ISFC). Increasing equivalence ratio [Φ] increases the concentration of fuel vapour in the bulk gas state m_{fG}, which increases the absorption and hence desorption from the oil layer. In addition, the higher cylinder pressures with increasing Φ promotes higher absorption. The crevice mass contribution increases progressively with the increase in Φ.

Retarded timing (Fig. 12.15) produces a reduced level of HC emission due to lower cylinder peak pressures, producing lower fuel absorption and higher expansion temperatures which in turn results in higher HC oxidation. The increase in HC emission when $\Phi < 0.7$ is attributed to higher cyclic variability because of the low

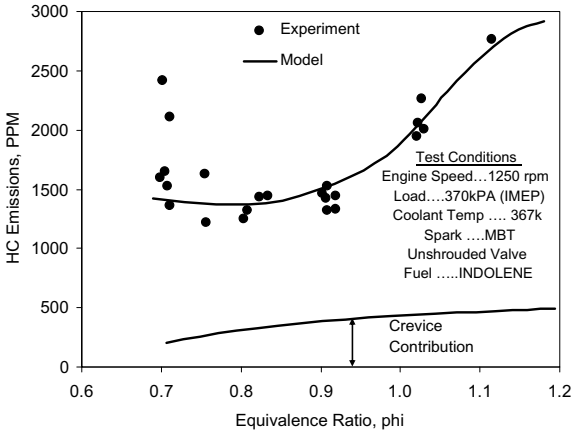

Fig. 12.14 Effect of equivalence ratio

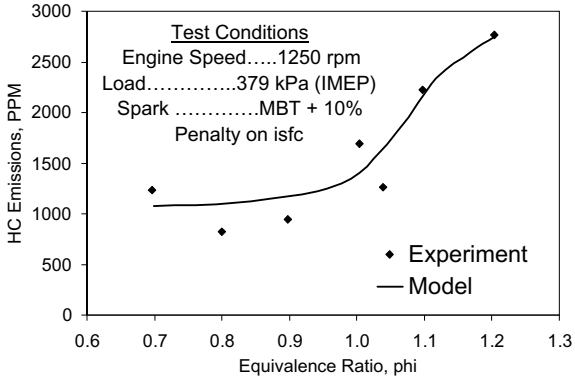

Fig. 12.15 Effect of spark retard

compression ratio (7.1:1) and quiescent nature of the combustion chambering of the CFR engine. This point is corroborated by the lower scatter of experimental data for the retarded timing—Fig. 12.15—where higher temperatures at ignition would contribute to better ignition of the lean mixture.

Effect of EGR

Figure 12.16 shows the effect of EGR at fixed engine speed, load, equivalence ratio, and MBT timing, but with engine compression ratio increased to 8.65:1. The comparison with experimental data is not adequate, prediction indicating a smaller increase in exhaust HC with increasing EGR. The absorption/desorption mechanism contributes a decreasing amount of HC with the increase in EGR due to reduced cylinder pressure levels, while the small decrease in wall temperature—8 K—as the EGR increases causes an increase in HC absorption and desorption. The lower burned gas temperatures with increasing EGR result in a lower oxidation rate. The model described

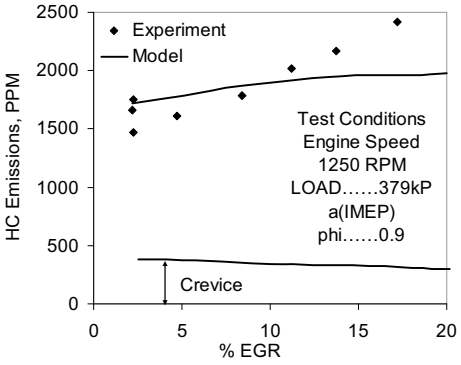

Fig. 12.16 Effect of EGR

here does not account for wall quenching. However, wall quenching as indicated by Lavoie and Blumberg [23] is likely to be a major contribution to HC emissions with increasing EGR. The wall quenching is as important as bulk gas quenching and cyclic variability due to poor combustion.

Effect of Indicated Specific Fuel Consumption

Figure 12.17 shows the variation of HC emission with indicated specific fuel consumption (ISFC), and the experimental data was obtained at a constant equivalence ratio, speed, IMEP, and compression ratio of 6.92. The ISFC variation was achieved by spark retardation. The agreement shown in Fig. 12.17 between prediction and experiment is fair. The decrease in the crevice contribution with increasing ISFC follows directly from the reduced cylinder pressure levels as ISFC increases with spark retard. This reduction of cylinder pressure also results in a small HC contribution from the absorption/desorption mechanism. Finally, oxidation of the desorbed HC increases with spark retard. It should be emphasized that the oil film thickness on which the foregoing computations were made was assumed to be a constant 5 μm at the baseline condition—Table 12.1; this appeared to be a reasonable mean between maximum and minimum values computed for the thickness of the oil film on the cylinder bore of a petrol engine at the top ring reversal [1] and gave a reasonable level of HC emission when compared with the baseline experimental data. The oil film thickness was considered to vary in proportion with the square root of the oil film kinematic viscosity [25]. Hence, from the baseline conditions, variation in oil film thickness could be computed with changes in engine variables that altered the cylinder wall temperature. The procedure used for wall temperature evaluation is given in appendix XIV.

In making the comparison with the engine data of Lavoie et al. [22], it should be noted that the CFR engine used in the test reported by Lavoie and Blumberg [23] was

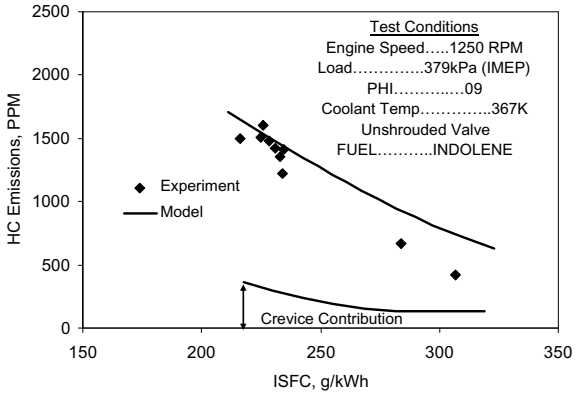

Fig. 12.17 Effect of timing

modified in several ways: a masked inlet valve was used to create higher in-cylinder air motion, the ring pack was altered to give better oil control and less blowby, and the exhaust port was longer. The tests by Lavoie et al. [22] were run on iso-octane rather than the Indolene-clear used by Lavoie and Blumberg [23]. The variation of the ignition timing and $\theta_{0.05}$ and $\theta_{0.95}$ with compression ratio were provided by Lavoie [21] for use in the comparison with the data of Lavoie et al. [22]. To accommodate the better oil control with the new ring pack, model predictions for the data used from the above reference were made with a baseline oil film thickness of 2 μm, which appears to be reasonable for current engine practice.

Effect of Compression Ratio

Figure 12.18 shows the variation of HC emission with compression ratio while Fig. 12.19 shows HC variation with change in wall temperature. In both the figures, the agreement between predictions with the 2 μm (base line) film thickness and experiment appears reasonable. While the crevice contribution increases with compression ratio—Fig. 12.18—because of the increased cylinder pressure, increase in compression ratio also increases the HC contribution from the absorption/desorption mechanism. The HC oxidation level falls with an increase in compression ratio because the IMEP has been maintained constant during the test, and therefore, expansion pressures and temperatures reduce.

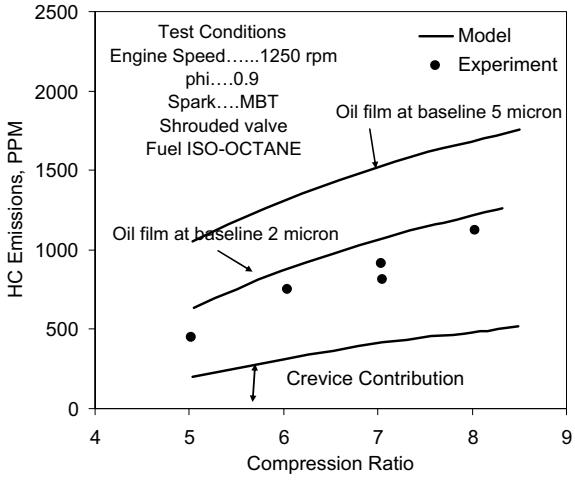

Fig. 12.18 Effect of compression ratio

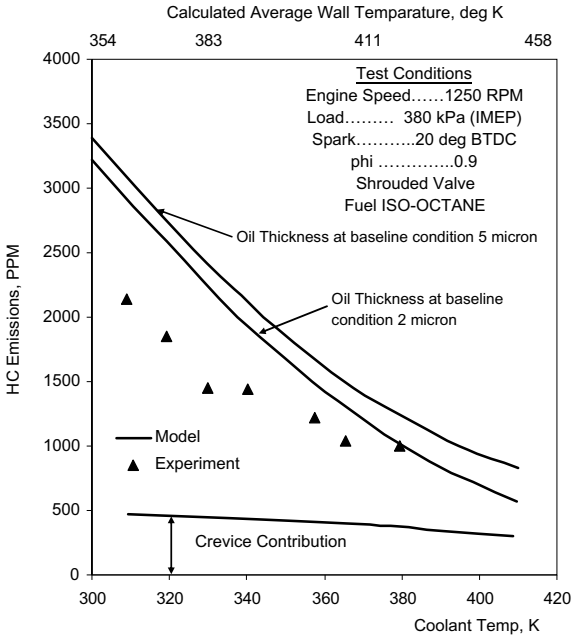

Fig. 12.19 Effect of coolant temperature on HC emissions

Effect of Oil Film Thickness

The effects of variation in wall temperature on HC emission shown in Fig. 12.19 are essentially due to the variation in the Henry constant and oil viscosity variation with temperature. The crevice mass contribution to HC emission decreases with increasing wall temperature due to reduced gas density in the crevice gap. The result of a parametric study of the effect of oil film thickness on HC emission is shown in Fig. 12.20, for the baseline condition. The emission of HC levels off at oil film thickness greater than about 5 μm, indicating that under operating conditions where the lubricating oil film thickness is greater than about 5 μm the effective penetration depth is the controlling thickness.

Effect of Increased Gas Motion

The effect of increased gas motion with a masked valve on HC emission cannot be assessed from the results of references [22, 23], because of the significant differences between the two test situations mentioned above. However, assuming a 5 um baseline oil film thickness and using the ignition and burn angle data from references [21, 23], a prediction of the HC emission variation with engine speed using a masked valve is shown plotted in Fig. 12.10 for comparison with the unmasked valve predictions

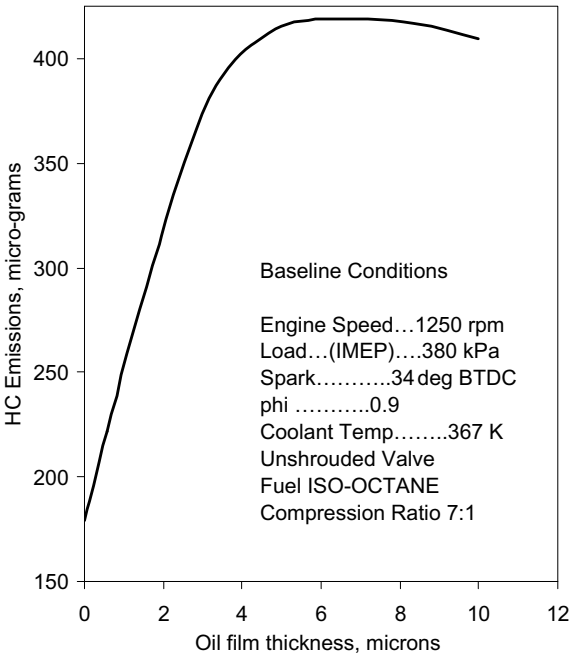

Fig. 12.20 Effect of oil thickness on HC emissions

based on reference [23]. It is seen that the differences in HC emission predicted are negligible with increased charge turbulence in the speed range 750–1250 rpm; however, at 1900 rpm a small increase is noted.

To comply with the test conditions of references [22, 23], the load (IMEP) was maintained constant over the speed range of the tests conducted with each valve type. Because of the retarded timing of the high turbulence masked valve tests, cylinder pressure levels are lower than the post-ignition pressures of the unmasked case at the same crank position. However, following the ignition, the faster combustion obtained with the masked valve results in a faster rate of pressure rise and peak pressure than with the unmasked valve [this can be seen in Fig. (12.21).

Their effects appear to balance each other with the fuel absorption process. The differences in the expansion phase of the pressure diagrams obtained with the combustion model are not significant, and therefore, the oxidation temperatures are not significantly different. The relative effects of gas-phase and oil layer conductances $g_G{}^*$ and $g_F{}^*$, and the Henry number N_{Hc} over the engine cycle can be assessed from Eq. (12.13). The magnitude of the parameter $g_G{}^* N_{\mathrm{Hc}} / g_F{}^*$ indicates whether the gas phase ($g_G{}^*$) or the oil film ($g_F{}^*$) controls the absorption and desorption processes.

When $g_G{}^* N_{\mathrm{Hc}} / g_F{}^*$ is large, Eq. (12.13) reduces to the following equation and the oil film controls.

$$\dot{m}'' = g_F^* \left[\frac{m_{m_G}}{N_{Hc}} - m_{f_F} \right] \tag{12.16}$$

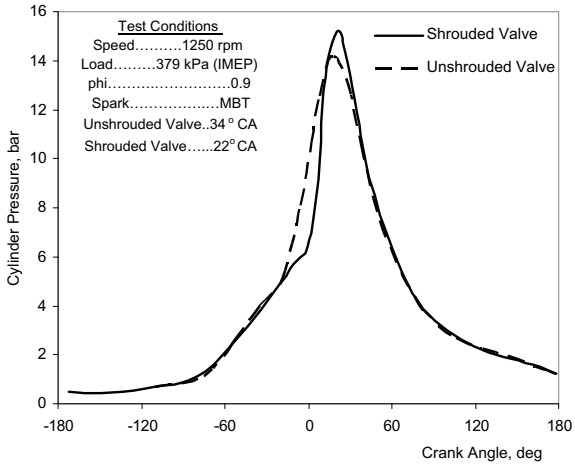

Fig. 12.21 Cylinder pressure diagram computed for shrouded and unshrouded valves

Furthermore, if N_{Hc} is itself large, the process of absorption is negligible as $m_{fG}/N_{\mathrm{Hc}} \rightarrow 0$. Conversely, when $g_G{}^* N_{\mathrm{Hc}} / g_F{}^*$ is small, Eq. (12.13) reduces to the following equation and the gas-phase controls.

$$\dot{m}'' = g_G^* \left(m_{f_F} - m_{f_F} N_{\mathrm{Hc}} \right) \tag{12.17}$$

Figure 12.22 shows the variation of $N_{\mathrm{Hc}}\ g_G{}^* / g_F{}^*$ over the engine cycle for the baseline condition and a 5 μm oil film thickness. It is seen that over most of the engine cycle, the gas and oil film conductances play an equally important role; nonetheless, around TDC, the effect of the oil film becomes dominant, but this is reduced considerably if the oil film thickness is considered to be 2 μm.

The use of Woschni's correlation for the evaluation of the convective heat transfer coefficient, h and hence $g_G{}^*$ by the Reynolds analogy is a limitation in evaluating

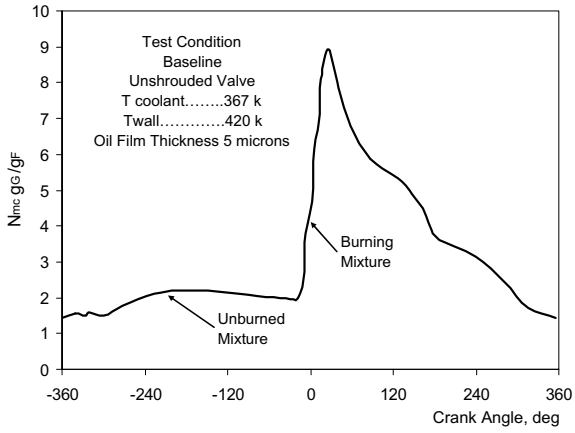

Fig. 12.22 Variation of mass transfer conductance parameter with crank angle

the effects of intake turbulence. In Woschni's correlation, effects of changes in the motion of air and turbulence will only be seen during the combustion phase of the engine cycle through their influence on the pressure diagram. Therefore, during the induction and compression periods of the engine cycle, where intake charge motion plays an important role in the process of fuel absorption into the lubricating oil film, a modification to the constant, C1 in the velocity term of Woschni's correlation would appear necessary to account for the change in valve geometry. This problem needs to be addressed before firm conclusions can be drawn as to the effects of intake charge turbulence on HC emission. See Eqs. (6.3), (17.32).

Conclusions

A model for fuel absorption and desorption by engine cylinder lubricating oil films has been presented which in general is in accord with engine experiments over a wide range of operating variables apart from EGR, where it is considered that factors such as bulk quenching and poor combustion resulting in higher cyclic variability, contribute to the higher value of exhaust hydrocarbons observed experimentally with increasing EGR.

The effects of engine geometry have not been investigated here, but it is clear from simulation studies [15] that changes in combustion chamber geometry including spark plug location result in changes in the burned and unburned gas areas in contact with cylinder wall surfaces, which result in differing fuel absorption and desorption levels.

The effect of induction generated flow and turbulence on HC absorption during the induction and compression strokes of the engine need further study.

Although precise information was not available for the lubricating oil film thickness and the Henry constant for the fuel oil film combination, it can be concluded that the minimum oil thickness compatible with adequate cylinder lubrication and an oil structure such that the Henry constant is large, contributes to reduced HC emission.

References

1. Allen DG et al (1975) Prediction of piston ring cylinder bore oil film thickness in two particular engines and correlation with experimental evidence. In: IMechE Conference on Piston Ring Scuffing, London
2. Blint RJ, Bechtel JH (1982) Hydrocarbon Combustion near a Cooled Wall. SAE 820063
3. Carrier G, Fendell F, Feldman P (1981) Cyclic absorption/desorption of gas in a liquid wall film. Combust Sci Technol 25
4. Chigashi S, Hamamoto Y, Kizima A (1971) Effects of turbulence on flame propagation in a closed vessel. Bull JSME 14
5. Daniel WA (1957) Flame quenching at the walls of an internal combustion engine. In: 6th International combustion engine

6. Daniel WA(1967) Engine variable effects on exhaust hydrocarbon composition (A single cylinder engine study with propane as the fuel). SAE 670124, SAE Transactions 76
7. Dent JC, Lakshminarayanan PA (1980) Lean burn spark ignition engine combustion modelling and experiments. In: Symposium on research in internal combustion engines in UK Universities and Polytechnics. Kings College, London
8. Dent JC, Lakshminarayanan PA (1983) A Model for absorption and desorption of fuel vapour by cylinder lubricating oil films and its contribution to hydrocarbon emissions, SAE 830652
9. Ferguson CR, Keck JC, Oforah O (1976) A theoretical investigation on the effects of mixture and flow non-uniformities on spark ignition engine combustion. US Dept of Transportation, Interim Report, June
10. Hamamoto YH, Wakisaka T, Chigashi (1976) Limits of flame propagation in spark ignition engines behaviour of flames and exhaust emissions. In: 16th FISITA congress. Tokyo
11. Hires SD, Tabaczynski R, Novak JM (1978) The prediction of ignition delay and combustion intervals for a homogeneous charge spark ignition engine. SAE 78032, SAE Transactions 87
12. Kaiser EW, Adamczyk AA, Lavoie GA (1980) The effect of oil layers on the hydrocarbon emissions generated during closed vessel combustion. In: 18th international symposium on combustion
13. Kaiser EW, Lorusso JA, Lavoie GA, Adamczyk AA (1982) The effect of oil layers on the hydrocarbon emissions from spark Ignited Engines. Combust Sci Technol 28
14. Kreith F (1960) Principles of heat transfer. International Textbook Co., Scranton
15. Lakshminarayanan PA and Dent JC (1982) Generalised procedure for flame and combustion chamber surface determination in spark ignition engines. SAE Paper 821223
16. Lakshminarayanan PA, Janakiraman PA, Gajendra Babu MK and Murthy BS (1979) An ultrasonic flowmeter for the measurement of gas velocity and temperature in intake and exhaust of an internal combustion engine. SAE Transactions, 790689
17. Lakshminarayanan PA, Janakiraman PA, Gajendra Babu MK and Murthy BS (1979) New instrumentation technique for the study of unsteady gas exchange process in engine manifolds. In: Spring meeting. Central States Section, The Combustion Institute, Apr 9–10, Columbus, Indiana
18. Lakshminarayanan PA, Janakiraman PA, Gajendra Babu MK, Murthy BS (1979) Measurement of pulsating temperature and velocity in an internal combustion engine using an ultrasonic flow meter. J Phys E: Sci Instrum 12:1053–1058
19. Lakshminarayanan PA, Janakiraman PA, Gajendra Babu MK, Murthy BS (1979) Prediction of gas exchange processes in a single cylinder internal combustion engine. SAE 790359
20. Lakshminarayanan PA, Nayak N, Dingre SV, Dani AD (2002) Predicting hydrocarbon emissions from direct injection diesel engine ASME paper
21. Lavoie GA (1982) Personal communication
22. Lavoie GA, Lorusso JA, Adamczyk AA (1980) Hydrocarbon emissions modelling for Spark-Ignition engines. In: Symposium on combustion modelling in reciprocating engines, General Motors Research Laboratories, Nov 1978. Plenum Press, London
23. Lavoie GA, Blumberg PN (1980) A fundamental model for predicting fuel consumption NO and HC emissions of the conventional spark ignition engine. Combust Sci Technol 21
24. Locusso JA, Kaiser EW, Lavoie GA (1981) Quench layer contribution to exhaust hydrocarbons from a spark ignited engine. Combust Sci Technol 25
25. Schlichting H (1955) Boundary layer theory. Pergamon Press, London
26. Sherman RH and Blumberg PN (1977) The influence of induction and exhaust processes on emission and fuel consumption in the spark ignited engine. SAE 770880, SAE Transactions 86
27. Spalding DB (1963) Convective mass transfer. Edward Arnold, London
28. Wentworth JT (1968) Piston and ring variables affect exhaust hydrocarbon emissions. SAE 680109, SAE Transactions 77
29. Woschni G (1967) A universally applicable equation for the instantaneous heat transfer coefficient in the internal combustion engine. SAE 670931, SAE Transactions 76

Chapter 13
Smoke from DI Diesel Engines

Nomenclature

A_0	Effective area of the nozzle hole (m^2)
A_h	Area of holes for the escape of soot, a function of Kolmogorov scale (m^2)
A_s	Surface area of the spray (m^2)
c	Circular surface area of spray at the wall (m^2)
$A_{s_{\text{con}}}$	Surface area of spray considering cone (m^2)
A_{s_t}	Area of Taylor microscale (m^2)
A_{sw}	Surface area of wall–spray (m^2)
Cu	Constant (0.09)
d_e	Equivalent diameter of the spray hole (m)
deg_{imp}	Degree of impingement (–)
d_o	Spray hole diameter (m)
h	Gap between adjacent flamelet (m)
η	Kolmogorov length scale (m)
k	Turbulent kinetic energy per unit mass (m^2/s^2)
l_m	Taylor's microscale (m)
N	Engine speed (rpm)
n	Number of spray holes (–)
N_f	Nozzle feature, %HE or KF, e.g. 10%, 15% (%)
n_h	Number of soot holes per unit surface area (–)
$n_{h,\text{ free}}$	Number of smoke holes for the free portion (–)
$n_{h_{\text{wall}}}$	Number of smoke holes for wall portion (–)
P_{inj}	Injection pressure (Pa)
Q	Injected quantity per stroke (kg)
q_{ip}	Duration of injection (deg CA)
ρ_f	Fuel density (kg/m^3)
ρ_s	Density of soot (2000 kg/m^3)
Soot	Soot (kg/m^3)
t_{dur}	Injection duration (s)

P. A. Lakshminarayanan and Y. V. Aghav, *Modelling Diesel Combustion*,
Mechanical Engineering Series, https://doi.org/10.1007/978-981-16-6742-8_13

t_{free}	Time for which spray is free (s)
t_{imp}	Time at which impingement starts (s)
t_{int}	Timescale for the integration of smoke passing through holes of size given by Kolmogorov scale (s)
t_{liq}	Time for which spray is liquid (s)
u_{inj}	Average velocity of sprays (m/s)
u_{wall}	Velocity of the wall jet (m/s)
V_{air}	Volume of air sucked in per cycle (m^3)
ε	Turbulent kinetic energy dissipation rate ($m^2 s^{-3}$)
ν	Kinematic viscosity of air ($m^2\ s^{-1}$)
τ	Kolmogorov timescale (s)

Khan et al. [16] first presented a model for the prediction of soot related to engine operating condition. Hiroyasu et al. [14] proposed a two-step semi-empirical model and applied it to the multi-packet combustion model. Later on, the model was extended up to a simple three-dimensional model [23]. However, this model lacked generality and required adjustment of several constants.

Fusco et al. [10] developed a phenomenological soot model consisting of an eight-step mechanism. They proposed that either pyrolysis of fuel could result in soot precursor radicals or growth species with possibilities of oxidation at intermediate stages. Although this model is more detailed, it requires tuning of as many as 21 empirical parameters.

Magnussen et al. [20] carried out an experimental investigation on steady-state free diffusion flames and developed a combustion model based on the k–ε turbulence model. Special attention was given to soot formation and combustion in turbulent flames, and it was concluded that soot was formed and contained in the turbulent eddies within the flame and that the burn-up of the soot was related to the dissipation of turbulence. Dec and Tree [7, 25] investigated interactions of combusting fuel jet free in the air and at the wall in a diesel engine using laser diagnostics. They found that soot deposition on the wall and blow-off is not the major contributors to engine-out soot emissions. In this view, Dent's work [8] was unique. The importance of turbulent energy dissipation rate on smoke in diesel engines was identified quantitatively. The turbulent mixing rate was correlated with smoke for a quiescent chamber diesel engine.

There is a principal mathematical problem in the modelling of the engine-out soot emissions by using formation and oxidation methodology [24]. Usually, at least 90% and often 99% of the formed soot becomes oxidized with a minute fraction remaining in the exhaust gas. Since the soot mass in the exhaust is the very small difference between two nearly equal quantities, i.e. between formation and oxidation, a significant error will result if only a small deviation in either the production or the formation rate.

In this chapter, the applicability of Dent's correlation [8] to explain mixing-controlled diesel combustion is explored. Finally, a model [3, 1] that clearly distinguishes the free jet and wall jet regimes of a diesel engine spray and their turbulence

structure is developed to explain the smoke. This model avoids the mathematical difficulty of finding the difference between two large and nearly equal integrals.

The Phenomenon of Soot Formation

In a conceptual sketch of a steady open turbulent flame, all the injected fuel goes through the vaporization process during ignition delay and then is converted into soot, Fig. 13.1. The simplest description for a burning spray is the model where the products of combustion exist outside a thin mantle of flame and the fuel-rich mixture remains unburned inside it. Many flamelets are formed at the peripheral mantle of the combusting spray.

Most of this soot will be oxidized at the surface of the flame depending on the level of turbulence. The average size of a flamelet could be equated to Taylor's microscale, ℓl_m. This scale defines the size of the mixing field. However, some of the soot escapes through the gaps that are scaled by viscosity and the high-frequency components of turbulence between these eddies. The Kolmogorov length scale, η, describes the gap between adjacent flamelets. This description is also applicable to the fuel spray in an engine; however, the wall impingement needs to be considered, as it results in loss of turbulent kinetic energy that is necessary for oxidation. Most of this soot will then be oxidized at the periphery of the spray. The soot escaping can be estimated by calculating flow through the holes scaled by the Kolmogorov length scale during a characteristic time as follows [3].

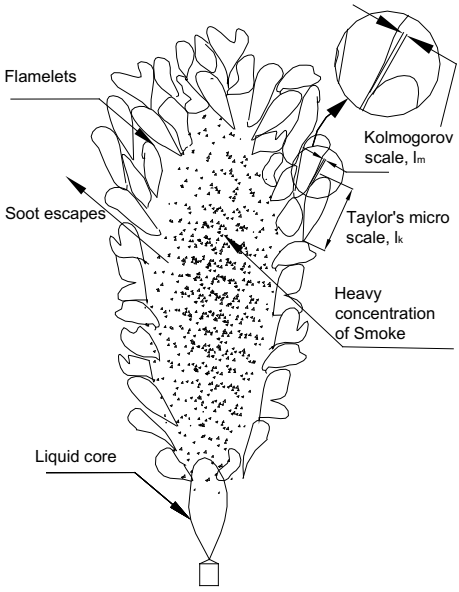

Fig. 13.1 Conceptual cross section of turbulent flame indicating the soot path

$$\text{Soot} = \frac{u_{\text{inj}} A_h n_h A_s t_{\text{int}} \rho_s}{V_{\text{air}}} \tag{13.1}$$

where

Soot	Soot in mg/m^3
A_h	Area of holes for the escape of soot, a function of Kolmogorov scale, $\eta\, \pi\, \ell_m \eta$
n_h	Number of soot holes per unit surface area
A_s	Surface area of the spray
t_{int}	Timescale for the integration of smoke passing through holes of size given by Kolmogorov scale
u_{inj}	Average velocity of sprays, $\frac{m_f}{C_d A_0 n_0 t_{\text{dur}}}$.
A_0	Effective area of nozzle hole, $\frac{\pi d_0^2 (1+N_f)}{4}$.
N_f	Nozzle feature, %HE or KF, e.g. 10%, 15%, etc.

The nozzle holes are defined as some base orifice size with %HE. The sample calculation is given in Appendixes IX and X.

d_o	Diameter of the basic nozzle hole.
t_{dur}	Injection duration.
V_{air}	Volume of air sucked in per cycle.
ρ_s	Density of soot, 2000 kg/m^3.

The features of the nozzle hole, namely hydro-erosion, HE, and k-factor, KF, used in the above equations are explained in the Appendixes IX and X [15].

Smoke is modelled to form instantaneously inside the spray, as the chemical reaction rates are too high compared to the physical rate of diffusion of the smoke at the peripheral surface of the spray. The phenomenological model, therefore, neglects chemical reactions and emphasizes the physical phenomenon.

In turbulent sprays, the liquid droplets are not only decelerated and deformed by the gas phase but an additional dispersion and some diffusion of the liquid phase can be observed that is caused by the turbulent eddies in the gas flow. On average, the random orientation of the turbulent velocity fluctuations leads to a quicker, more homogenous dispersion of the liquid droplets than in a laminar gas flow. At the same time, the momentum transfer between gas and liquid moderates the turbulent level within the gas phase. In turbulent sprays, typically a particle is assumed to interact with an eddy for a period taken as the eddy life time, t_{int} [24]. This period is also considered as the timescale of integration.

$$t_{\text{int}} = \frac{C^{\frac{3}{4}} k}{\sqrt{\frac{2}{3}\varepsilon}} \tag{13.2}$$

where

Cu	Stiesch [27] constant = 0.09.
ε	Turbulent kinetic energy dissipation rate.

$k = \frac{3}{2} u_{inj}^2$ Turbulent kinetic energy.

Though the above equation is only true for isotropic flow, which is not the case at the spray envelope, for brevity it is assumed uniform all over the surface by considering a meantime, t_{int}. It is hypothesized as the mean timescale for the two types of spray, e.g. free and wall sprays and the favourable comparison presented later validates such a bold assumption.

Application to Engine Conditions

To derive the concept Eq. (13.1), a steady open non-growing turbulent flame is considered. For simplicity, there is no liquid or wall jet considered, Fig. 13.1. Therefore, only the timescale of integration, tint, is considered. However, in the case of the engine sprays, there are a liquid phase, a free growing spray, and a growing wall jet, which are happening one after another, Fig. 13.2. Initially, the free spray would grow up to the wall with a conical shape. Then, the spray penetrates along a flat wall and is modelled to spread equally in all radial directions. The tip of the spray would form a surface of a right circular cylinder. This model simplifies the complicated combustion cavity wall to a flat plate perpendicular to the spray axis. The liquid phase is not considered to be contributing to soot. The free growing spray is considered as a frustum of cone up to the wall impingement on the wall. The soot is estimated within integration limits of t_{liq} to t_{imp}. The following equation considers the growing surface area of this free spray as time marches until wall impingement occurs.

$$\text{soot}_{\text{free}} = \int_{t_{\text{liq}}}^{t_{\text{imp}}} u_{\text{inj}} A_h n_{h_{\text{free}}} \rho_s \, \mathrm{d}t \tag{13.3}$$

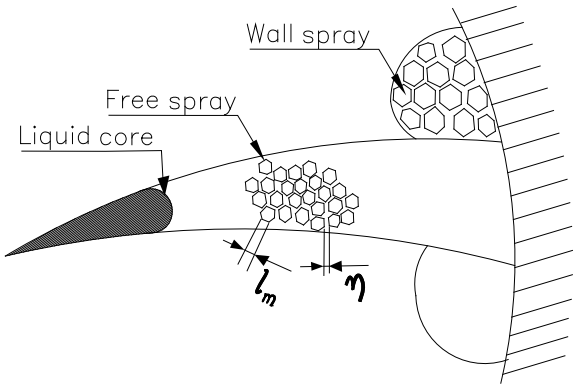

Fig. 13.2 Free jet fuel spray and subsequent wall jet under engine conditions

If wall impingement occurs, then soot is estimated from the free spray as well as the wall jet. During this period, the wall jet grows along the wall, while the free portion of the jet remains static as a cone up to the wall. The portion of the smoke from the free spray is modelled as a frustum of a static cone.

$$\text{soot}_{\text{free state}} = \int_{t_{\text{int}}}^{t_{\text{imp}}+t_{\text{int}}} u_{\text{inj}} A_h n_{h_{\text{free}}} \rho_s \, \mathrm{d}t \tag{13.4}$$

The soot emitted from the growing wall spray can be estimated as below.

$$\text{soot}_{\text{wall}} = \int_{t_{\text{imp}}}^{t_{\text{imp}}+t_{\text{int}}} u_{\text{wall}} A_h n_{h_{\text{wall}}} \rho_s \, \mathrm{d}t \tag{13.5}$$

The duration of integration, t_{int} used in Eqs. (13.4) and (13.5), is explained earlier in Eq. (13.2). After soot escapes from spray boundaries, no burnout of soot is considered to take place. Finally, the soot emitted from the free and wall portions of all the sprays is summed up to arrive at total soot in mg/m^3 by using the following equation.

$$\text{soot}_{\text{all}} = \frac{(\text{soot}_{\text{free}} + \text{soot}_{\text{free state}} + \text{soot}_{\text{wall}}) n_0}{V_{\text{air}}} \tag{13.6}$$

where

A_h	Area of soot hole.
$n_{h_{\text{free}}}$	Number of smoke holes for the free portion $= \frac{A_{s_{\text{con}}}}{A_{s_t}}$.
$A_{s_{\text{con}}}$	Surface area of spray considering cone.
A_{s_ℓ}	Area of Taylor microscale.
$n_{h_{\text{wall}}}$	Number of smoke holes for wall portion $= \frac{A_{s_{\text{cir}}}}{A_{s_t}}$.
$A_{s_{\text{cir}}}$	Circular surface area of spray at the wall.
t_{liq}	Time for which spray is liquid.
t_{free}	Time for which spray is free.
t_{imp}	Time at which impingement starts.
A_{sw}	Surface area of wall spray.
$u_{\text{wall}} = 0.75\sqrt{\frac{u_{\text{inj}} d_e}{t_{\text{imp}}}}$	Velocity of the wall jet.
d_e	Equivalent diameter of spray hole.

The total soot estimated is converted to Bosch smoke unit (BSU) by using the MIRA correlation [22] because BSU of smoke is selected for comparison with the experimental data for validation. The main inputs are the maximum injection pressure, the engine airflow, the geometry of the nozzle spray, and the cavity shape. The impingement parameters are estimated using the geometry and the equations of the spray: penetrations [3, 12, 19].

Correlating Smoke: Phenomenon with Spray Characteristics

The important engine parameters needed for smoke calculation are collected from the experimental engine under different load and speed conditions, in Table 3.2 for engines A9, B10, C12 … P12. Most of the data are related to the fuel injection system and combustion cavity, Fig. 13.3. At all these test points, smoke data are collected for analysis.

Concept of Turbulent Dissipation Rate Turbulent Mixing and Smoke

The turbulent energy dissipation rate ε can itself be used to define length, time, and velocity scales associated with the small-scale dissipative structure of turbulent motion. *Kolmogorov* defined this smallest timescale of turbulence as

$$\tau = \left(\frac{\nu}{\varepsilon}\right)^{\frac{1}{2}} \tag{13.7}$$

where

τ *Kolmogorov* timescale.
ν Kinematic viscosity of air.
ε Turbulent kinetic energy loss rate (power) per unit mass:

Dent [8] evaluated these scales in the context of a quiescent chamber engine. The turbulent energy dissipation can be expressed as

$$\varepsilon = \frac{\gamma P_{\text{inj}} 6N}{\rho_f \theta_{\text{ip}}} \tag{13.8}$$

The overall dissipative mixing rate can be written as follows.

$$\frac{1}{\tau} = \left(\frac{C}{\nu^{0.5}}\right)\left(\frac{N}{\theta_{\text{ip}}}\right)^{1.5}\left(\frac{Q}{nd_0^2}\right) \tag{13.9}$$

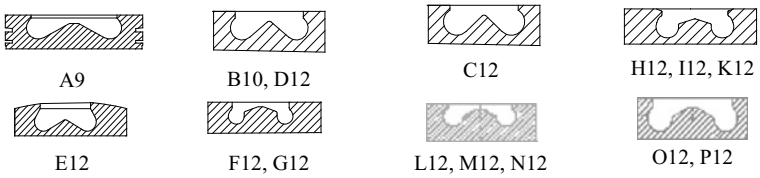

Fig. 13.3 Combustion chambers

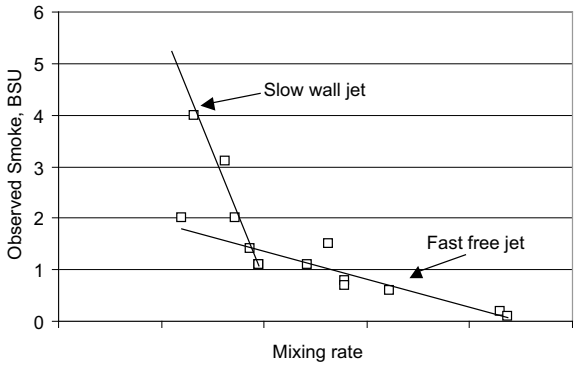

Fig. 13.4 Exhaust smoke against mixing rate

where

P_{inj} Injection pressure $= \text{const}\left(\frac{6NQ}{\theta_{ip} n d_0^2}\right)^2$.
N Engine speed, rpm.
n Number of spray holes.
d_O Spray hole diameter, m.
θ_{ip} Duration of injection, deg CA.
Q Injected quantity per stroke.
ρ_f Fuel density.

When this concept was applied for a smaller-sized experimental engine C12, then the results showed two distinct regimes, Fig. 13.4. The two regimes could be identified as a spray with and without wall impingement. Wall impingement of spray results in a slower combustion rate due to loss of turbulent kinetic energy [4].

To study the role of wall impingement, a factor, degree of impingement, is defined as

$$\deg_{imp} = \left(1 - \frac{t_{imp}}{t_{dur}}\right) \times 100 \tag{13.10}$$

where

$\deg_{imp}$ Degree of impingement,
t_{imp} Time at which impingement starts,
t_{dur} Duration of injection.

When impingement starts, the degree of impingement is 0%. There is no impingement when this value is negative, and there is impingement when this value becomes positive. The estimation of impingement time is explained in detail in Appendix VIII. Smoke values were plotted against the degree of impingement for the smoke data of the experimental engine with a bore less than 125 mm; see Fig. 13.5. This graph shows two distinct zones and relations. Before impingement starts, there is a linear correlation between smoke values and the degree of impingement. This correlation

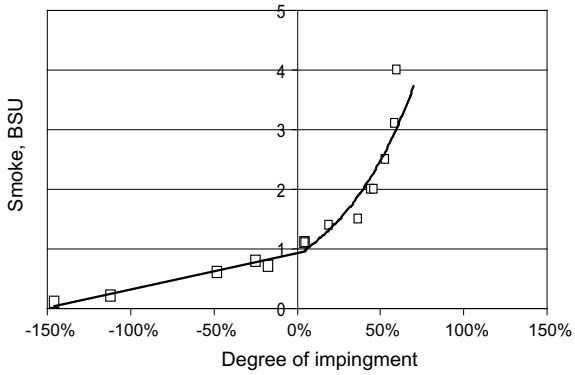

Fig. 13.5 Smoke values at different loads against the degree of impingement, engine C12

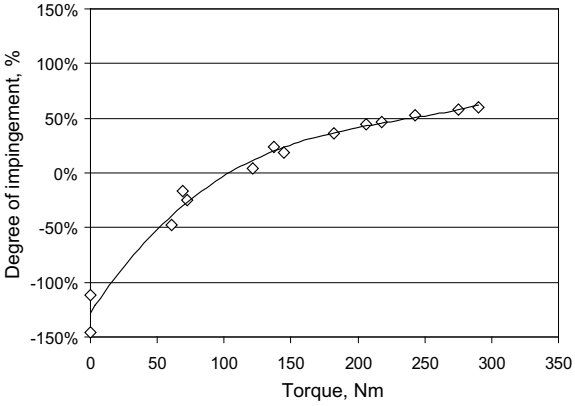

Fig. 13.6 Predicted and observed smoke, engine C12

becomes parabolic once impingement starts. This graph signifies a large contribution of impingement to the smoke emitted through the exhaust. Therefore, it is necessary to incorporate this phenomenon during the development of a new model for better predictions.

At all the experimental points, the smoke values were predicted using the new model that considers the effective turbulent energy at the spray surface for the burning of smoke generated inside the spray. The main inputs are the maximum injection pressure, the engine airflow, the geometry of the nozzle spray, and the cavity shape. The impingement parameters are estimated using the geometry and the equations of spray penetrations [18, 19].

Then, the duration of integration is evaluated using the density of turbulent energy supplied by the fuel sprays [24]. The fuel sprays were divided into free and wall jets, and the smoke is evaluated from these jets separately and added together to obtain the total smoke in the exhaust. The results of the model highlighted that above brake torque of 100 Nm, the spray impingement was predominant for the experimental

engine at all the speeds, Fig. 13.6. The predicted results are summarized in Table 13.1.

In Fig. 13.7, the observed as well as predicted smoke values for all the data points are plotted against brake torque. Although the predicted values are slightly lower than observed, both the curves indicate a similar trend rising along the torque curve. The study using the new phenomenological smoke model indicated favourable comparison over a wide range of smoke values with a regression coefficient of 0.98 with a slope near to one for one engine, Fig. 13.8.

Table 13.1 Predicted results, engine C12

Data point	Impingement time	Degree of impingement	Smoke, BSU		
	Deg CA	%	Free portion	Wall portion	Total
1	10.78	53	0.5	1.5	2.1
2	11.4	37	0.6	0.4	1
3	13.69	4	0.8	0	0.8
4	14.22	−48	0.5	0	0.5
5	14.81	−146	0.1	0	0.1
6	7.83	58	0.6	2.5	3.1
7	8.51	44	0.6	0.8	1.5
8	9.11	24	0.7	0.2	0.8
9	9.25	−17	0.7	0	0.7
10	9.4	−112	0.1	0	0.1
11	6.37	60	0.6	2.9	3.5
12	7.27	46	0.7	1.1	1.8
13	7.34	19	0.7	0.1	0.8
14	7.34	−24	0.6	0	0.6

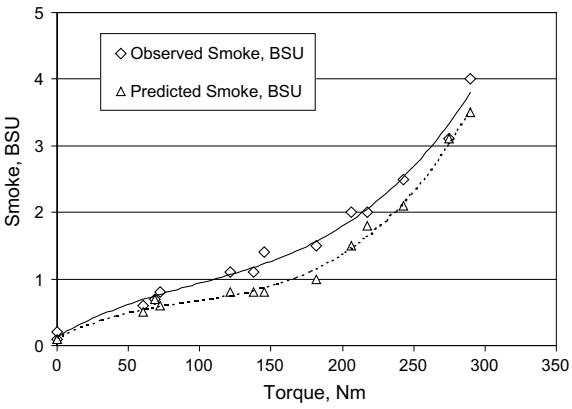

Fig. 13.7 Smoke versus torque, engine C12

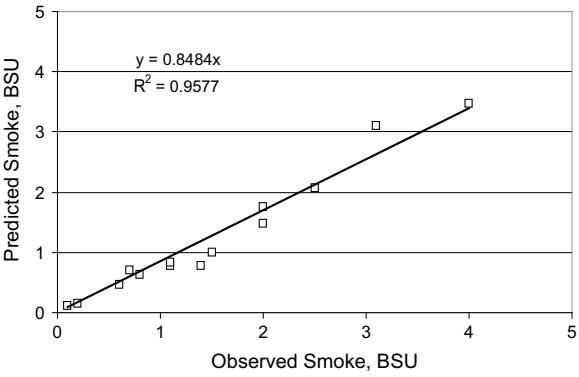

Fig. 13.8 Predicted versus observed smoke, engine C12

Then, the remaining engines were considered for model application. The investigations were limited to the operating conditions of the engines with a single injection and no exhaust gas recirculation. Parameters related to the engine performance and fuel injection system were collected simultaneously along with the smoke. In Fig. 13.9, the observed smoke was plotted against the speed, for engines of variable speed applications. Here, the rising trend of smoke is indicated as speed reduces. These engines are sufficiently fuelled at lower speeds to derive higher torque at lower speeds and hence are working at lower air–fuel ratios. Similarly, at a constant engine speed, as the load increases, the smoke increases, Fig. 13.10. The slope of the curve changes at about 50% load.

The increase in smoke with an increase in load is seen to be less significant when the engine runs at high speed, compared to the drop in smoke at the same load when the engine runs at low speeds. This can be attributed to the higher air–fuel ratio and turbulence level at higher speeds. The correlation of smoke with the method of aspiration and brake mean effective pressure met with little success, Fig. 13.11. The smoke reduces as the injection pressures and air–fuel ratio increase; however, the correlation is not satisfactory, Figs. 13.12, and 13.13.

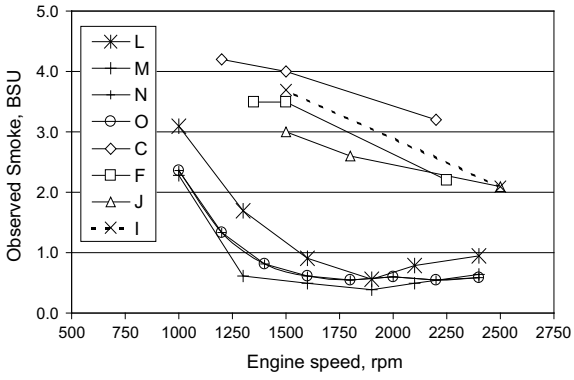

Fig. 13.9 Observed smoke along with full throttle for different engines

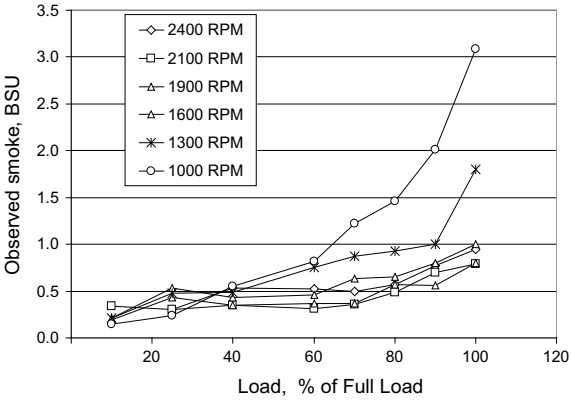

Fig. 13.10 Observed smoke at part loads at different speeds, engine L12

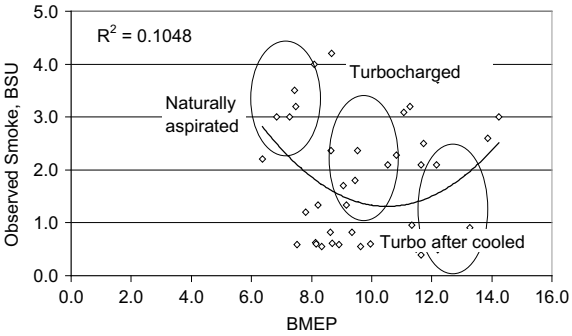

Fig. 13.11 Brake mean effective pressure and smoke

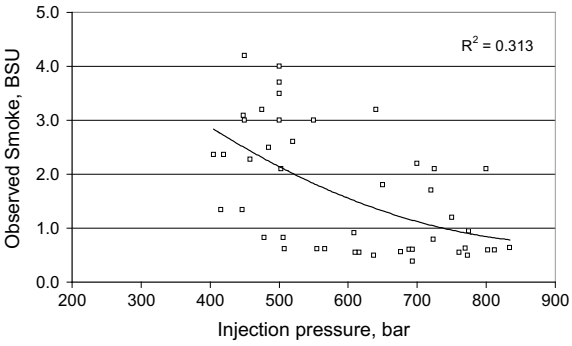

Fig. 13.12 Injection pressure and smoke

To evaluate the effect of impingement, the observed smoke was plotted against the degree of impingement, Fig. 13.14, where the degree of impingement is defined as the ratio of time after wall impingement to the total duration of injection. There is no impingement when this value is negative, and there is impingement when this value becomes positive as explained earlier in this chapter. The smoke increases as

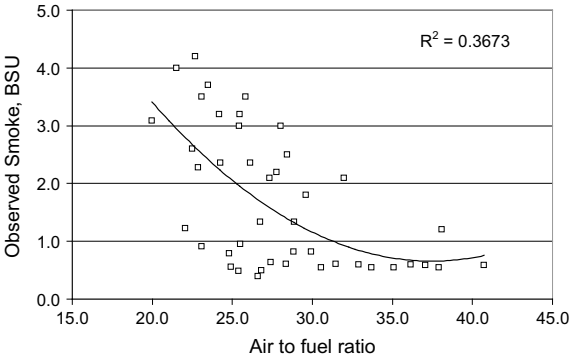

Fig. 13.13 Air-to-fuel ratio and smoke

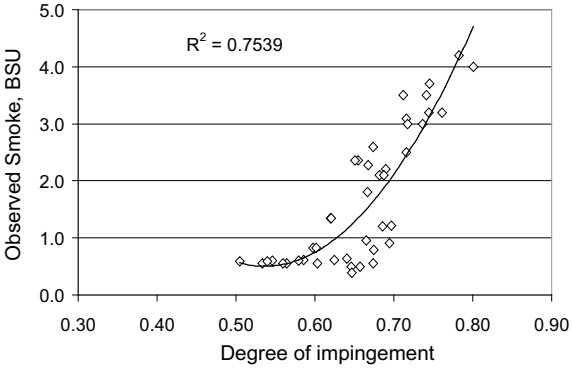

Fig. 13.14 Degree of impingement and observed smoke

the impingement increases. The effect of the wall jet on the smoke emission due to abrupt loss of turbulence at the wall, therefore, seems to be more important than that of injection pressure or air–fuel ratio. The wall effect was given less importance in phenomenological models for smoke, published earlier [8, 9, 13]. Beyond 50% load, wall impingement is the important parameter in heavy-duty DI diesel engines. Therefore, the new model presented earlier in this paper, which considers these two effects, namely wall effect and turbulence effect, has better prediction capability.

Steady-State Conditions

Initially, the model was applied at full throttle condition of the engines of variable speed application. The predicted and observed smoke values of these engines were plotted against speed, Figs. 13.15 and 13.16. For the engine types, I12, B10, F12, and L12 the predictions at full load follow both the magnitude and trend of the observed values. In the case of engines M12, N12, and O12, the model slightly over-predicts the smoke. The observed smoke was compared with predicted smoke, at all the data

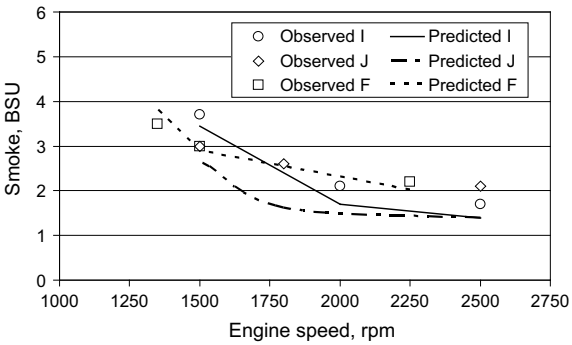

Fig. 13.15 Predicted and observed smoke, full throttle of engines I12, B10, and F12

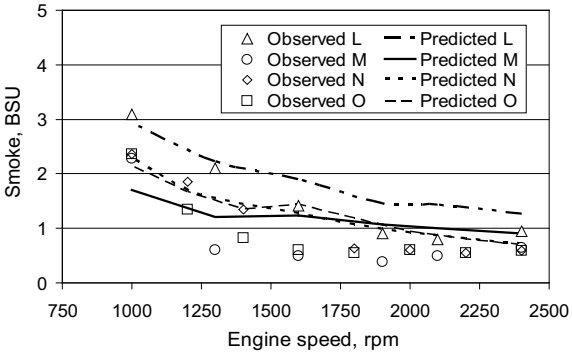

Fig. 13.16 Predicted and observed smoke, full throttle of engines L12, M12, N12, O12

points of the above engines in Fig. 13.17. Although there are some deviations, the overall regression coefficient is 0.87 for these points. These slight discrepancies are dealt with later in the discussion section. With the increase in engine speed, the turbulence increases on the spray boundaries both in free spray and at the wall due to the higher injection pressure of mechanical cam-driven injection equipment. This

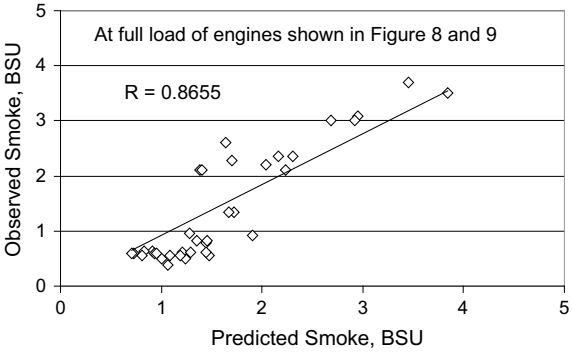

Fig. 13.17 Predicted and observed smoke, full load of I12, B10, F12, L12, M12, N12, and O12

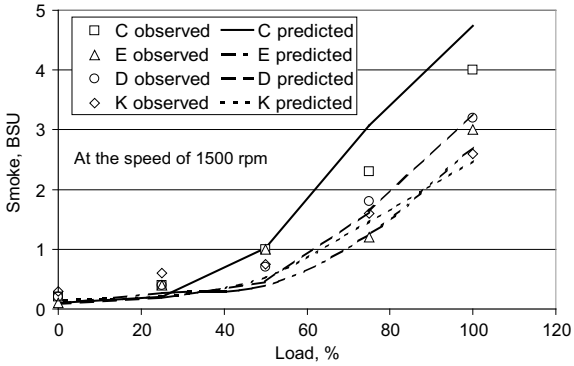

Fig. 13.18 Predicted and observed smoke, part loads of C12, E12, D12, and K12

causes more complete burnout of smoke, and hence, the smoke decreases with an increase in speed. The comparison of experiment and prediction is encouraging.

Then, the model was applied for typical part load conditions of engines at a constant speed of 1500 rpm. The predicted smoke values plotted against load are in close agreement with observed values, Fig. 13.18. The departure of the rate of increase in smoke with a load at 50% load is correctly predicted. The rate at which the smoke increases with load is very small initially corresponding to when the spray is free and increases at a high rate after the spray impinges on the wall at higher loads. The smoke was also modelled at part throttle, i.e. part load conditions for the engines of variable speed applications. The predicted values for each data point were compared favourably against the experimentally observed values, Fig. 13.19. The same trend of smoke at all speeds for different engine operating conditions could be seen in Figs. 13.20, 13.21, 13.22, 13.23, and 13.24.

Finally, the predicted values of smoke were compared with all the observed values at different speeds and loads, Fig. 13.25. The observed regression coefficient is 0.89 with a slope of 0.88 represented by a thick line. This study using the new smoke model indicated a satisfactory comparison over a wide range of smoke values.

While the correlation between the observed smoke and the calculated smoke is good for a wide variety of engines, some deviations could be observed at full load for the on-road engines, M12, N12, and O12. These points are enclosed in ellipses. If these specific few points are considered as outliers, then the slope becomes close to 1.0 with the regression coefficient tending to 0.95 represented by the dashed line in Fig. 13.25. The possible causes for the deviation of computed smoke from the observed smoke values might be the lack of consideration of the reverse squish and the complete profile of the cavity where spray impinges. The injector offset with respect to the cavity is also not considered which might change the degree of impingement and, hence, the soot produced at the wall. Also, the simplified model of a flat wall perpendicular to the spray axis is a reason for the differences observed between the experiment and the model. Thus, a better understanding of the Kolmogorov scales at the wall will improve the prediction capability of the model. The agreement between the experimental results and the theoretical results without any tuning of

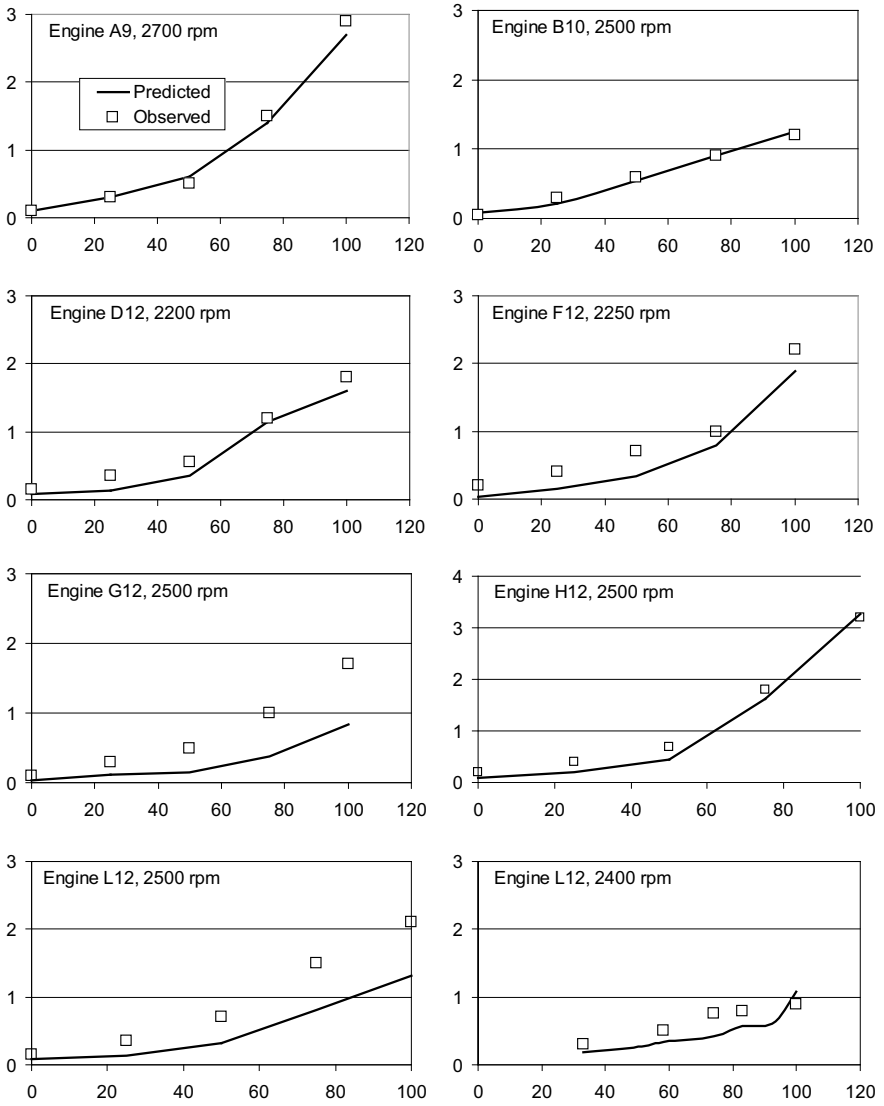

Fig. 13.19 Predicted (□) and observed (–) smoke versus % load for various engines at rated speed

model constants that are engine-specific makes the model a potentially useful tool for predicting smoke emissions.

The comparison of the experimental data over the entire engine performance map at different loads and speeds is satisfactory, even though for some engines the differences are large. The previous phenomenological models found it difficult

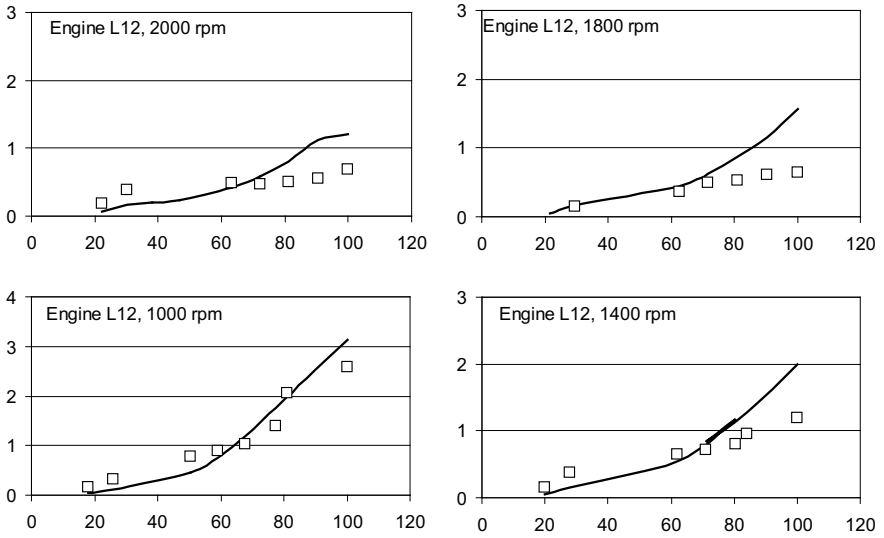

Fig. 13.20 Predicted (□) and observed (–) smoke versus % load for engine L12 at part loads

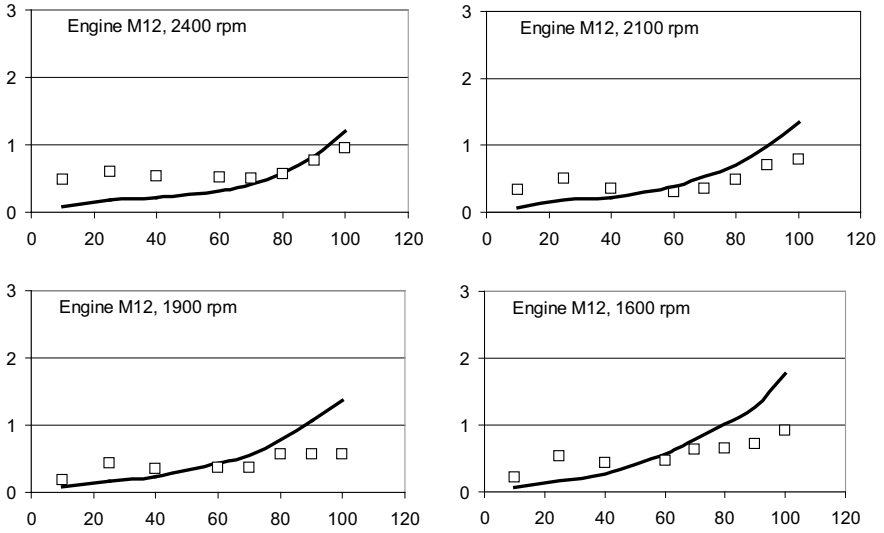

Fig. 13.21 Predicted (□) and observed (–) smoke versus % load for engine M12 at part loads

to predict even with many empirical constants adjusted for every given engine the following.

- The sudden change in the rate of increase in the smoke with an increase in load at 50% load.

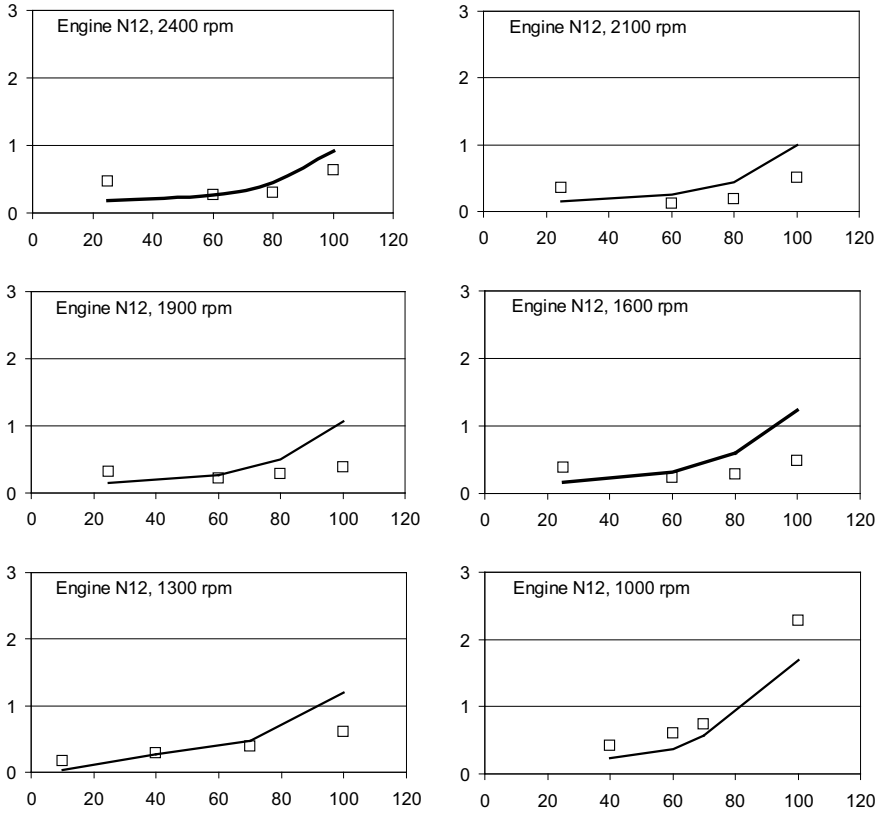

Fig. 13.22 Predicted (□) and observed (–) smoke versus % load for engine N12 at part loads

- Gradual decrease with increase in speed.

In the present attempt, no empirical constant to be fine-tuned for a given engine is used. The model rightly predicts the increase in smoke with load, due to the loss of turbulence at the wall and hence higher Kolmogorov scale that allows the escape of smoke unburnt through the spray periphery. Also, it shows the decrease in smoke with speed, due to better turbulence, i.e. lower Kolmogorov scale at higher injection pressure at higher speeds in a jerk-type injection system. There are, however, some limitations to the soot model in terms of the understanding pulsed injection, effect of squish, and fuel type.

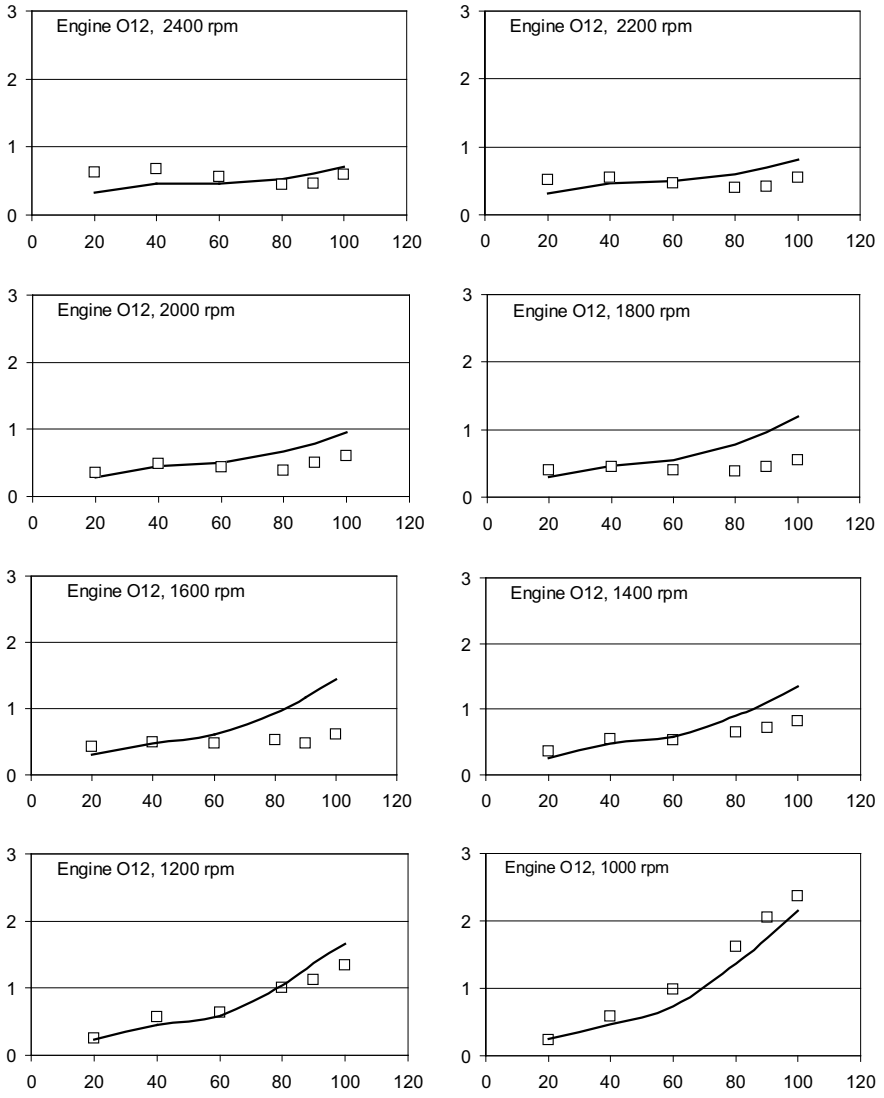

Fig. 13.23 Predicted (□) and observed (–) smoke versus % load for engine O12 at part loads

Benchmarking with Well-Known Smoke Model

Explain the boost model here! Compared to the extremely complex 3-D models or the phenomenological soot model based on mixing-controlled combustion used in advanced software like AVL Boost [5], the present model focuses on the main physical phenomenon at the surface of the spray for a brief period of the life of the

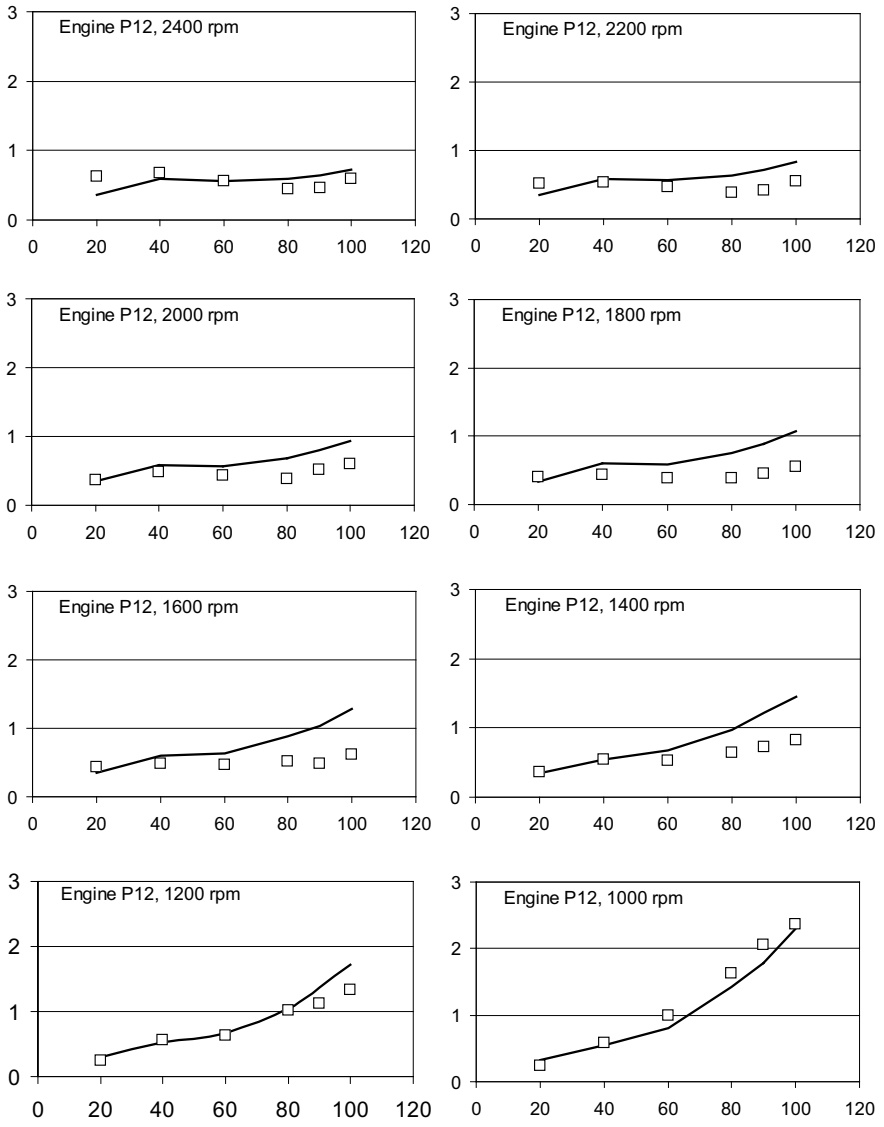

Fig. 13.24 Predicted (□) and observed (–) smoke versus % load for engine P12 at part loads

eddies. Figure 13.26 shows the comparison of observed smoke with the predicted smoke using this software and using the model described in this paper. The prediction of the trend of smoke behaviour by the present model with respect to load, especially above 50% load, is more favourable than AVL Boost. The present model could be extended to multi-jet and multiple injection common rail system, which enhances the turbulence many times at the surface area of fuel sprat. By modelling the turbulence

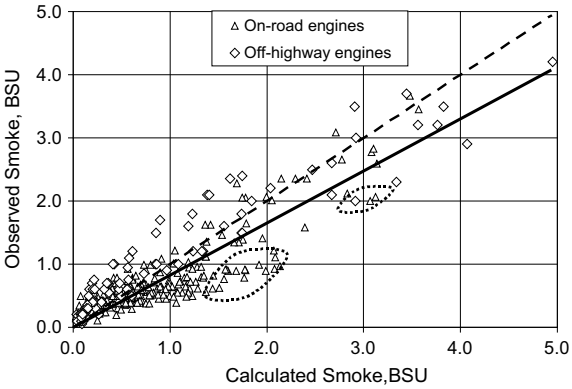

Fig. 13.25 Predicted and observed smoke for all engines, Table 4.1

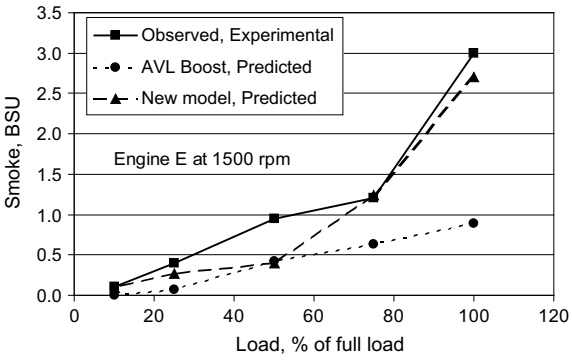

Fig. 13.26 Comparison of new model, AVL Boost and experimental data, engine E12

scale, it will be possible to predict lower smoke when such a fuel injection system is used.

Transient Conditions

As compared to steady-state working of diesel engine, the smoke emitted is more during the unsteady or transient operation mode, i.e. free acceleration, full load acceleration, etc. This is because of the lack of sufficient air for the complete combustion of the higher quantity of diesel injected to accelerate. In rapid acceleration, the engine speed increases after a time lag and remains constant. This time delay is observed for smoke opacity also. A transient cycle could be considered as a sequence of the quasi-stationary process with regard to particle formation since the combustion and injection characteristic times are short compared with the timescale for the change in engine conditions at transient running. Hence, the validity of the correlations at stationery conditions could be extrapolated to transient cycles.

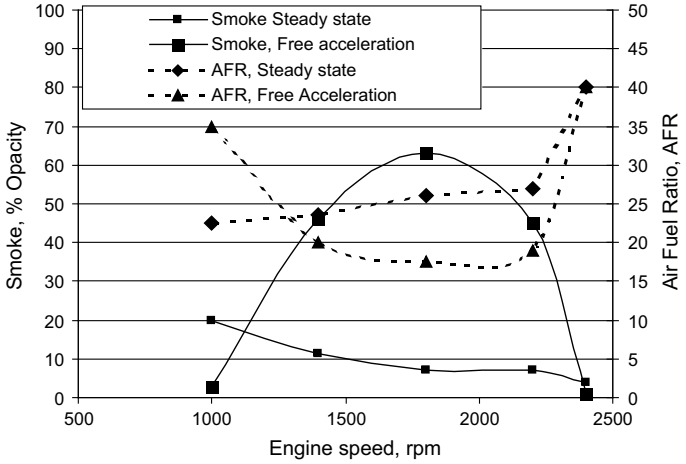

Fig. 13.27 Comparison of steady-state and free acceleration smoke and AFR at various speeds, engine B10

A "free acceleration" test is specified in few emission standards [21] where the accelerator is pressed from low idle to the high idle position and maximum smoke is recorded. Such a standard is evolved in such countries because the road infrastructure for the dense diesel vehicle traffic asks for frequent change of gears and engagement of the clutch, leading to a free acceleration of engines. A turbocharged engine was considered for this study as they suffer from higher smoke during free acceleration. The results of steady-state and free acceleration were plotted against speed, Fig. 13.27. This shows that the air–fuel ratio during free acceleration goes below steady-state operation during a certain range, which results in higher smoke values. The new model [1, 2, 3], was applied to certain points of low air–fuel ratio (AFR) to predict the maximum smoke value. The predictions at specific points are in close agreement with experimental results, Fig. 13.28. The maximum values, as

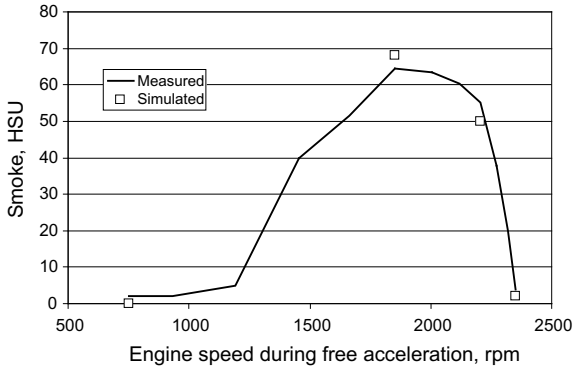

Fig. 13.28 Prediction for free acceleration smoke

well as the trend of smoke during transient conditions, are predicted satisfactorily with the new model.

References

1. Aghav YV, Lakshminarayanan PA, Babu MKG, Azim U, Dani AD (2007) Validating newly evolved smoke model at widely varying operating conditions of DI diesel engine GTP-06–1096. ASME J Eng Gas Turbines Power
2. Aghav YV, Sujeet V, Kumar MN, Thatte V, Babu MKG (2007) Simulation of turbocharged DI diesel engine during free acceleration using AVL Boost. In: AVL users international conference, Graz
3. Aghav YV, Lakshminarayanan PA, Babu MKG, Nayak NS, Dani AD (2005) Phenomenology of smoke from direct injection diesel engines. In: Paper No. 1350, Proceedings of ICEF 2005, ASME
4. Assanis DN, Filipi ZS, Fiveland SB, Syrimis M (1999) A predictive ignition delay correlation under steady-state and transient operation of a direct injection diesel engine. In: ASME-ICE fall technical conference
5. AVL Boost 4.1 Users Guide (2005)
6. De Risi A, Manieri D, Laforgia D (1999) A theoretical investigation on the effects of combustion chamber geometry and engine speed on soot and NO_x emissions. ASME-ICE 99-ICE-207, 33-1
7. Dec JE, Tree DR (2001) Diffusion-flame/wall interactions in a heavy-duty DI diesel engine. SAE 2001-01-1295
8. Dent JC (1980) Turbulent mixing rate—its effect on smoke and hydrocarbon emissions from diesel engines. SAE 800092
9. Dent JC, Mehta PS (1981) Phenomenological combustion model for a quiescent chamber diesel engine. SAE paper 811235
10. Fusco A, Knox-Kelecy AL, Foster DE (1994) Application of a phenomenological soot model to diesel engine combustion. In: Third international symposium COMODIA
11. Hulwan DB, Joshi SV, Aghav YV (2007) Smoke prediction for turbocharged DI diesel engine during free acceleration. Int Rev Mech Eng 1:N3
12. Heywood JB (1988) A text book on internal combustion engine fundamentals. McGraw-Hill, New York
13. Hiroyasu H et al (1983) Development and use of a spray combustion modeling to predict diesel engine efficiency and pollutant emissions. Bull JSME 26(214)
14. Hiroyasu K (1976) Models for combustion and formation of nitric oxide and soot in direct injection diesel engines. SAE 760129
15. Kampmann S, Dittus B, Mattes P, Kirner M (1996) The influence of hydrogrinding at VCO nozzles on the mixture preparation in a DI diesel engine. SAE 960867
16. Khan IM, Greeves G, Wang CHT (1973) Factors affecting smoke and gaseous emissions from direct injection engines and a method of calculation. SAE Transactions, 687–709
17. Kurtz EM, Foster DE (2004) Identifying a critical time for mixing in a direct injection diesel engine through the study of increased in-cylinder mixing and its effect on emissions through study of increased in-cylinder mixing and its effects on emissions. Int J Engine Res, IMechE 5
18. Lakshminarayanan PA, Dent JC (1983) Interferometric studies of vapourising and combusting sprays. SAE paper 830244
19. Lakshminarayanan PA, Aghav YV, Dani AD, Mehta PS (2002) Accurate prediction of the rate of heat release in a modern direct injection diesel engine. IMechE, 216, J Automobile
20. Magnussen BF, Hjertager HB (1977) On mathematical modeling of turbulent combustion with special emphasis on soot formation and combustion. Symposium (international) on Combustion 16(1): 719–729
21. Ministry of Road Transport, India (2004) Free acceleration test, MoRTH/**CMVR**/TAP 115/116

22. Motor Industry Research Association (MIRA) (1965) The measurement of diesel exhaust smoke. Report No. 10
23. Nishida, Keiya, and Hiroyuki Hiroyasu. "Simplified three-dimensional modeling of mixture formation and combustion in a DI diesel engine." SAE transactions (1989): 276-293.
24. Stiesch G (2003) Modelling engine spray and combustion processes. Springer
25. Tree DR, Dec JE (2001) Extinction diesel combustion: an integrated view combining laser diagnostics, chemical kinetics, and empirical validation. SAE 2001-01-1296

Chapter 14
Oxides of Nitrogen from Direct Injection Diesel Engines

Nomenclature

A_s	Surface area (m^2)
C_f	Concentration of fuel vapour (–)
δ	Virtual source = 2.3 d_e (m)
d	A distance from the nozzle tip (m)
$C_{f_{noz}}$	Vapour concentration at the nozzle (–)
$C_f(r, y)$	Vapour concentration at any position in free spray (–)
$C_{f_{wall}}$	Vapour concentration along wall–spray (–)
C_{f_x}	Vapour concentration along the axis of free spray (–)
EGR	% Of exhaust gas recirculated (%)
EOC	End of combustion for each volume (CA deg)
EOC	End of combustion (CA deg)
F	Equivalence ratio (–)
h_c	Heat transfer coefficient ($W/(m^2K)$)
N_o	Number of holes (–)
$NO_{x_{wall}}$, $NO_{x_{free}}$, $NO_{x_{cycle}}$	NO_x formed in free and wall–sprays are summed up to arrive at cycle NO_x (kg)
$NO_{x_{cycle}}$	Cycle averaged NO_x (ppm)
Q_{wall}	Heat transfer to the wall (J)
r_s	Radius of spray (m)
S	Distance from the mouth of the nozzle (m)
S_{liq}	Liquid core = 7 d_e (m)
SOC	Start of combustion for each volume (CA deg)
SOI	Start of injection (CA deg)
SWI	Start of wall impingement (CA deg)
T_{cyl}	Cylinder gas temperature (K)
t_{dur}	Combustion duration (s)
$t_{flame,}$ T_{flame}	Flame temperature (K)
$T_{fflame\ corrected}$	Corrected flame temperature (K)

P. A. Lakshminarayanan and Y. V. Aghav, *Modelling Diesel Combustion*,
Mechanical Engineering Series, https://doi.org/10.1007/978-981-16-6742-8_14

T_{wall}	Piston wall temperature (K)
V_{free}	Free spray volume (m^3)
$V_{\text{free\_corr}}$	Corrected free spray volume (m^3)
V_{spray}	Spray volume (m^3)
V_{wall}	Sectional volume of wall–spray volume (m^3)
$V_{\text{wall-corr}}$	Corrected wall–spray volume (m^3)
Φ	Equivalence ratio, the ratio of chemically correct (stoichiometric) fuel–air ratio to actual fuel–air ratio (–)
$\frac{dm_f}{d\theta}$	Rate of injection (mm^3/deg)

Most of the combustion takes place in a diffusive mode in modern DI diesel engines. In the present work, the concept of mixing-controlled combustion model is applied to NO_x formation. NO_x is formed at the spray envelope only, integrated over combustion duration, and averaged over the entire cylinder volume. The spray–wall interaction is also observed especially at higher loads. The engine spray is divided into a liquid core, a free growing spray and a growing wall jet, Fig. 14.1. The NO_x estimation is made for one spray on a volume basis and multiplied by the number of sprays to arrive at the integrated value. The concept equation for NO_x formation is as follows:

$$NO_{x_{\text{cycle}}} = \frac{\left\{\int_{\text{SOC}}^{\text{EOC}} \sum_{i=1}^{i=n} V_{\text{spray}} NO_x\right\} \frac{N_0}{\rho_f}\left(\frac{dm_f}{d\theta}\right) t_{\text{dur}}}{V_{\text{cyl}}} \tag{14.1}$$

Here,

$NO_{x_{\text{cycle}}}$	Cycle averaged NO_x, ppm
V_{spray}	Spray volume
N_o	Number of holes
SOC	Start of combustion for each volume
EOC	End of combustion for each volume
$\frac{1}{\rho_f}\frac{dm_f}{d\theta}$	Rate of injection, mm^3/deg

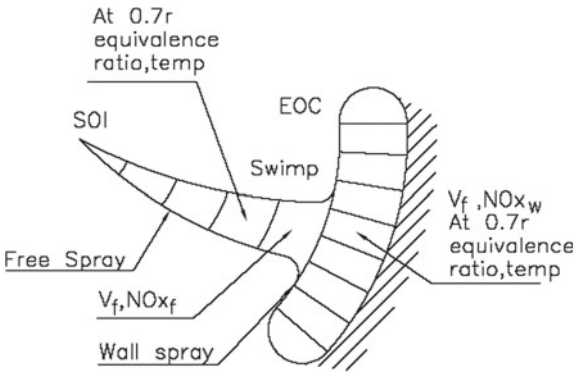

Fig. 14.1 Conceptual sketch of spray for NO_x estimation

t_{dur} Combustion duration, sec

$\sum_{i=1}^{i=n}$ Summation of n volumes of spray.

Free spray alone is formed at less than medium loads. The volume of the free spray is split into five conical regions of equal length.

$$\text{NO}_{x_{\text{free}}} = \frac{\left\{\int_{\text{SOI}}^{\text{EOC}} \sum_{i=1}^{i=5} V_{\text{free}} \text{NO}_{x_{fi}}\right\} \frac{N_0}{\rho_f} \frac{\text{d}m_f}{\text{d}\theta} t_{\text{dur}}}{V_{\text{cyl}}} \tag{14.2}$$

Here,

SOI Start of injection
EOC End of combustion.

At higher load, the interaction of the spray with the wall is observed. The wall–spray formed after impingement is also divided into five volumes of annular cylinders, Fig. 14.1.

$$\text{NO}_{x_{\text{wall}}} = \frac{\left\{\int_{\text{SOI}}^{\text{EOC}} \sum_{i=1}^{i=5} V_{\text{wall}} NO_{x_{wi}}\right\} \frac{N_0}{\rho_f} \frac{\text{d}m_f}{\text{d}\theta} t_{\text{dur}}}{V_{\text{cyl}}} \tag{14.3}$$

Here,

V_{free} Sectional volume of wall–spray volume
V_{wall} Sectional volume of wall–spray
SWI Start of wall impingement.

Finally, the NO_x formed in free and wall–sprays is summed up to arrive at cycle NO_x.

$$\text{NO}_{x_{\text{cycle}}} = \left(\text{NO}_{x_{\text{free}}} + \text{NO}_{x_{\text{wall}}}\right) \tag{14.4}$$

The equivalence ratio and flame temperature are estimated at 0.7 times radius as a representative for the different volumes of free and wall–spray. The NO_x in every volume is predicted as a function of equivalence ratio, Φ, and flame temperature, Fig. 14.2 [5].

$$\text{NO}_x = f(\Phi, t_{\text{flame}}) \tag{14.5}$$

The interactions between the spray and the wall are instrumental in rapid convective heat transfer. This heat transfer is also considered for estimation of NO_x by correcting temperature in different zones. Estimation of spray properties and heat transfer is described in Appendixes VIII and XV. In the engine environment, the fuel spray is dynamic and interactive with the wall observed especially at higher loads. Therefore, the fuel spray is divided into three sections: (a) the liquid core, (b) free

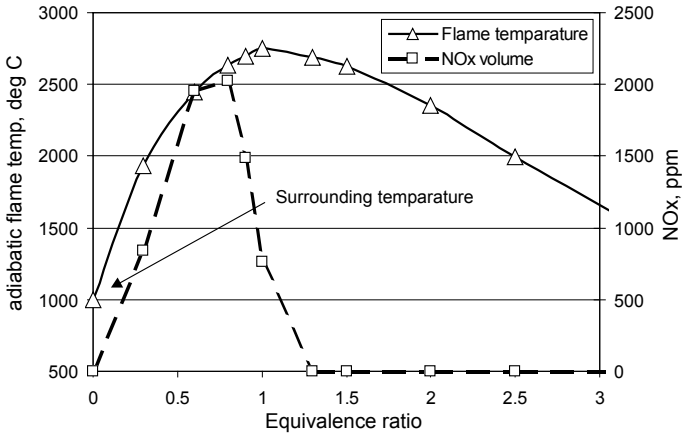

Fig. 14.2 Behaviour of NO_x and flame temperature

spray, and (c) wall jet after impingement upon the wall. The various phases of spray development are schematically shown in Fig. 14.3. In early phase, the free spray grows until the wall of the combustion chamber. Subsequently, it remains static and the wall jet develops. As soon as the injection ends, the tail of the spray starts moving and slowly the burnout of spray occurs.

Before Detachment

In Fig. 3.10, notations of the free axisymmetric spray [4] are shown, with profiles of concentration along the axis and radius. The virtual source of the evaporating jet is inside the orifice at a distance δ from the nozzle tip. Along the axis, the concentrations of fuel vapour decrease hyperbolically, Fig. 3.10, from the virtual origin where S is the distance from the mouth of the nozzle.

$$C_f(x) = 5.2C_{f_{\text{noz}}}\left[\frac{d_e}{S+\delta}\right] \tag{14.6}$$

Experiments have shown that the vapour concentration increases linearly from the virtual origin to a fixed position, S_{liq}, until the jet detaches. The distance can be considered as the length of the liquid core in the spray.

At any radius,

$$C_f(r,x) = C_{f_x}\exp\left[-203\left\{\frac{r_s}{S+\delta}\right\}^{2.5}\right] \tag{14.7}$$

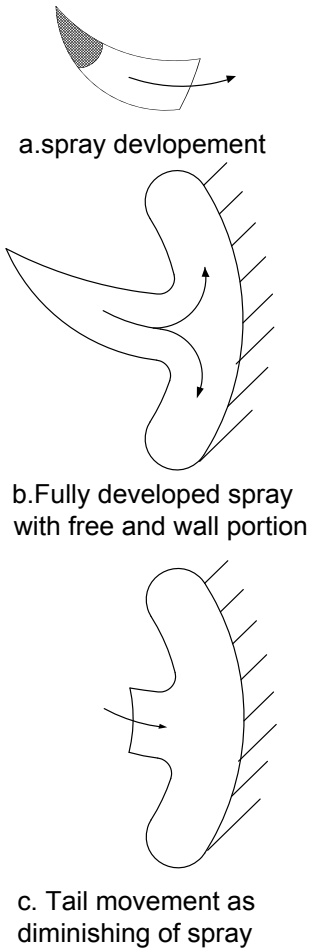

Fig. 14.3 Main events during development of engine spray

$$\Phi = 14.7 \frac{C_f(r, x)}{1 - C_f(r, x)} \tag{14.8}$$

Along the radius, the distribution of the vapour concentration is Gaussian. However, near the core of the spray, the concentration is limited to the maximum vapour concentration described above, Fig. 3.10. Along the wall–spray, the following correlation is employed.

$$C_{f_{\text{wall}}} = 0.5 \frac{d_e}{S_{\text{wall}}} \tag{14.9}$$

$$\Phi = 14.7 \frac{C_{f_{\text{wall}}}}{1 - C_{f_{\text{wall}}}} \tag{14.10}$$

where

C_{f_x} Vapour concentration along the axis of free spray
δ Virtual source, 2.3 d_e
S_{liq} Liquid core, 7 d_e
$C_{f_{noz}}$ Vapour concentration at the nozzle
$C_{f_{(r,v)}}$ Vapour concentration at any position in free spray
Φ Equivalence ratio, the ratio of chemically correct (stoichiometric) fuel–air ratio to actual fuel–air ratio
r_s Radius of spray
$C_{f_{wall}}$ Vapour concentration along wall–spray.

After Detachment

After the end of injection, the tail of the spray also penetrates similar to the tip of the jet, however slowly. The jet-like structure is still maintained, and turbulent mixing occurs entraining air into the jet-like plume, but packets of fuel are not replenished by the nozzle. Therefore, regions near the nozzle tip will be leaner than at the instant injection was complete. Sub-packets on the centreline will still move downstream at a faster rate than those near the edges of the plume. Furthermore, no appreciable increase in jet width was observed [4].

The Phenomenon of Heat Transfer

The convective mode of heat transfer plays a dominant role in modern DI diesel engines. The localized effect of this heat transfer was considered on NO_x formation. The wall–spray formed after the impingement of spray was considered instrumental in rapid convective heat transfer. The convective heat transfer rate can be described by Newton's law of cooling as:

$$Q_{\text{wall}} = h_c A_s \left(T_{\text{cyl}} - T_{\text{wall}}\right) \tag{14.11}$$

Here,

Q_{wall} Heat transfer to the wall
h_c Heat transfer coefficient
A_s Surface area
T_{cyl} Cylinder gas temperature
T_{wall} Piston wall temperature.

Exhaust Gas Recirculation (EGR)

To cope with today's stringent emission norms, various techniques are being employed by engine manufacturers to reduce the emissions from engines. EGR is the most popular method of reducing NO_x emissions. The principle of this method is the reduction of oxygen available for combustion by the introduction of a certain quantity of exhaust gas into the engine intake air. Reduced oxygen content results in lowering the peak flame temperature and hence reduced NO_x formation.

There are mainly two admission methods for EGR admission (1) internally of the engine and (2) externally using piping, Fig. 14.4. Either opening the intake can do the internal EGR during the exhaust stroke or opening the exhaust valve during the intake stroke. The external EGR can be done by tapping the fraction of exhaust gas through the exhaust pipe and recirculation it into the intake manifold. The precise control over the amount of EGR can be possible through the external EGR. The predictability of NO_x by the model is improved by taking into consideration the EGR effect. The EGR is defined by the volumetric percentage of total engine flow, i.e. incoming air plus fuel flow. The airflow will be reduced by the same percentage as that of exhaust flow recirculated. This effect is taken into consideration by introducing the correction for spray volume available for NO_x formation in free as well as wall–spray, Eqs. 14.14 and 14.15.

$$\%\ \text{EGR} = \left(1 - \frac{\text{Engine air flow with EGR}}{\text{Engine air flow without EGR}}\right) \times 100 \tag{14.12}$$

Free portion spray,

$$V_{\text{free corrected}} = V_{\text{free}}\left[1 - \frac{\text{EGR}}{100}\right] \tag{14.13}$$

Wall–spray,

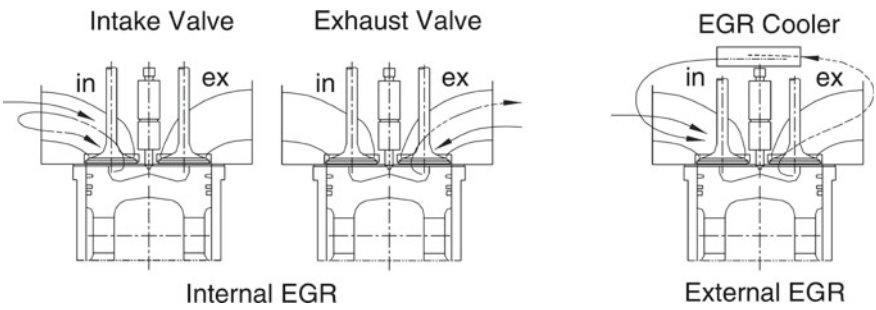

Fig. 14.4 Different EGR admission methods

$$V_{\text{wall corrected}} = V_{\text{wall}}\left[1 - \frac{\text{EGR}}{100}\right] \tag{14.14}$$

The flame temperature is also corrected using the following correlation.

$$T_{\text{flame corrected}} = T_{\text{flame}}\left[1 - \frac{\text{EGR}}{100}\right] \tag{14.15}$$

Here,

V_{free}	Free spray volume
$V_{\text{free\_corr}}$	Corrected free spray volume
V_{wall}	Wall–spray volume
$V_{\text{wall-corr}}$	Corrected wall–spray volume
T_{flame}	Flame temperature
$T_{\text{flame corrected}}$	Corrected flame temperature
EGR	% of exhaust gas recirculated.

Corrected spray volumes and temperatures are employed for NO_x predictions as in Eqs. (14.14)–(14.15).

Phenomenology of Oxides of Nitrogen

As a case study, the first data point of the engine C12 (Table 3.2) is discussed here [1]. The spray properties were estimated considering injection pressure, spray hole geometry and needle lift diagrams. The injection starts at 10° before the top dead centre, and wall impingement occurs at about 13° after the start of injection and 3-deg after the top dead centre. The estimations of penetration of free spray and wall jet against crank angle are shown in Fig. 14.5 in the graphical form.

The heat release pattern was predicted based on mixing-controlled combustion considering wall impingement. Then, the wall heat transfer is estimated considering convection between wall–spray and piston, Fig. 14.6. Finally, the NO_x emissions were predicted for free spray and wall jet portion for every crank angle using equations. The effect of heat transfer is also considered for wall jet. Then, the NO_x from the wall and free portions is summed up to arrive at the final value. Then, cumulative summation is considered as NO_x emission in the exhaust until the combustion is over, Fig. 14.7.

The experimental and predicted results for all the data points of engine C12 (Table 3.2) are given in Table 14.1. Predictions of NO_x against observations with and without heat transfer are plotted in Fig. 14.8. Consideration of heat transfer improved model predictability. The prediction and observations are plotted against percentage load for different speeds, namely rated, maximum torque, and minimum operating speed. The trends along speed and load match with experimental observations satisfactorily, Fig. 14.9.

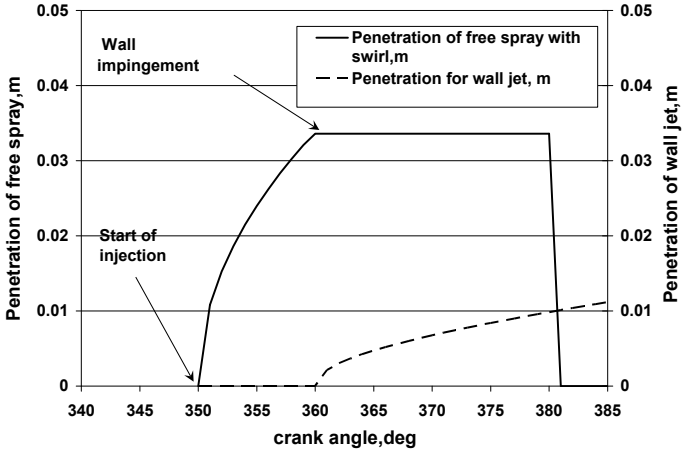

Fig. 14.5 Spray behaviour under engine environment

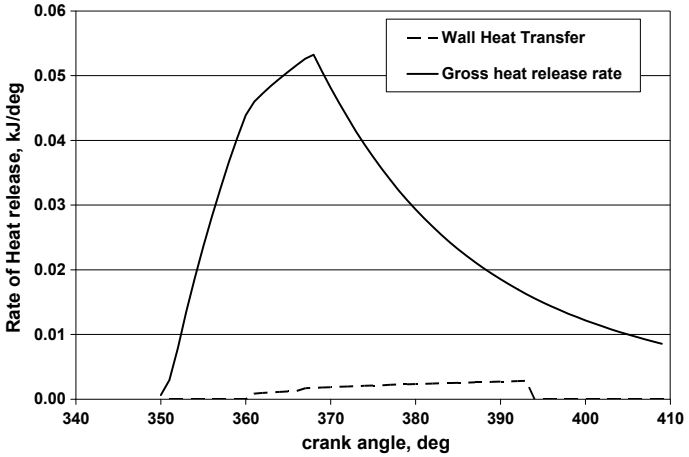

Fig. 14.6 Heat release and heat transfer

Effect of EGR

Experiments were conducted with different EGR proportions on engine C12 (Table 3.2) at 1500 rpm, Table 14.2. NO_x measurement was carried out on the engine C12 at 75% load. Exhaust gas recirculation [2, 3] is generally not recommended at 100% load as it results in the reduction of air–fuel ratio to such a low value that the smoke emissions cross acceptable limits, Fig. 14.10. In the first part, NO_x measurement was done without circulation of the exhaust gas into the engine intake air. In the second part, exhaust gas was introduced into the intake air in different percentages

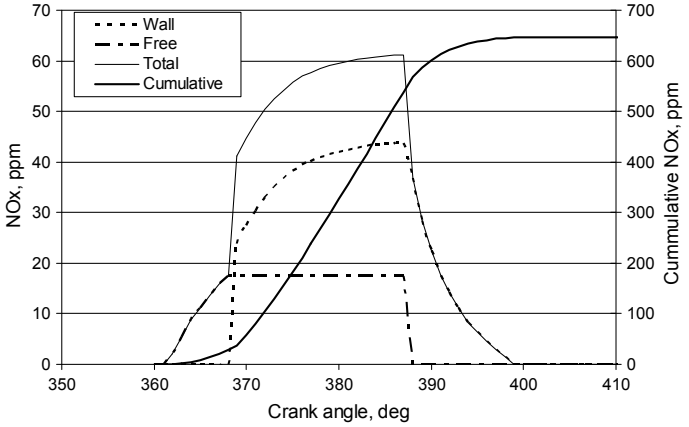

Fig. 14.7 NO_x estimation in different portions of spray

Table 14.1 Effect of heat transfer on NO_x prediction, engine C12

Data point	Torque (Nm)	Engine speed (rpm)	Injection pressure (bar)	Injected quantity (mm^3/str)	Observed NO_x (PPM)	Estimated NO_x with heat transfer (PPM)	Estimated NO_x without heat transfer (PPM)
1	242.5	2200	640	57.0	769	690	762
2	181.9	2200	560	42.8	634	528	583
3	121.3	2200	350	29.0	369	362	415
4	275.0	1500	500	65.0	1073	840	883
5	206.3	1500	400	47.3	892	658	710
6	137.5	1500	330	35.0	584	473	505
7	290.0	1200	450	64.0	1254	886	926
8	217.5	1200	310	48.0	999	636	671

using different sizes of orifices and measurement was carried out for certain EGR percentages.

Then, the newly developed model was applied to validate the NO_x predictability of the model with the EGR effect. Measured and predicted values of NO_x emissions were plotted against EGR proportions in Fig. 14.11. This plot indicated close agreement of predictions with observations for EGR application also.

The experimental and predicted values of NO_x for engine C12 (Table 3.2) agree satisfactorily (Table 14.2). Consideration of the wall heat transfer effect has improved the NO_x predictability of the model substantially. The inclusion of the EGR effect further enhances the capabilities of the model. The predicted NO_x follows the same trend of the measured with different EGR percentages, Fig. 14.11. The model showed

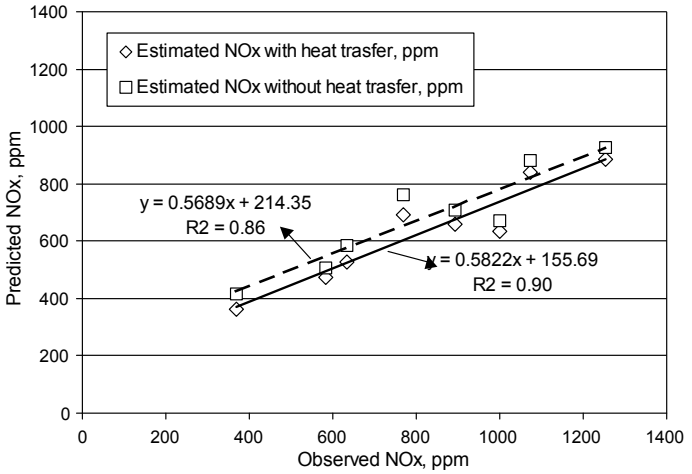

Fig. 14.8 Effect of heat transfer on NO_x prediction, engine C12

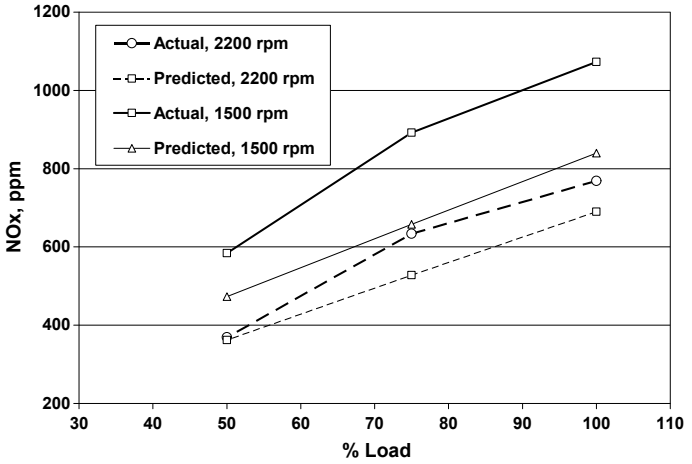

Fig. 14.9 NO_x trend lines at different speeds, engine C12

Table 14.2 Effect of EGR, engine C12

Speed (rpm)	Load (%)	Injection pressure (bar)	Injection duration (deg)	Fuelling (mm^3/str)	EGR (%)	Observed NO_x (ppm)	Estimated NO_x with heat transfer (ppm)
1500	75	500	19	48.5	0	652	614
1500	75	500	19	48.5	9	553	544
1500	75	500	19	48.5	12	519	528
1500	75	500	19	48.5	15	504	509
1500	75	500	19	48.5	18	436	474

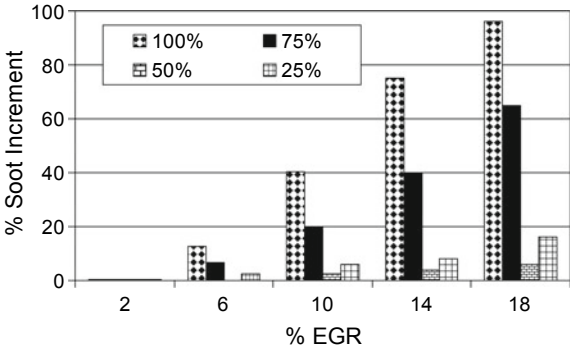

Fig. 14.10 Effect of EGR on soot, engine C12

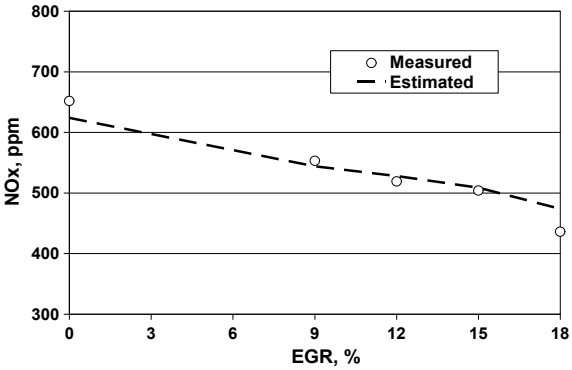

Fig. 14.11 Comparison of predicted and observed values of NO_x for different EGR percentages, engine B12

a reduction in temperature inside the engine cylinder and hence NO_x on the application of EGR as expected. Finally, the model was applied to the remaining engines described in Table 3.2 at rated and maximum torque speeds. The predicted values for all the 39 data points were plotted against observations, Fig. 14.12. The new model

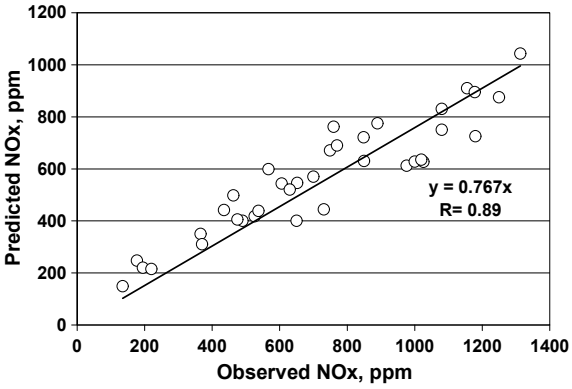

Fig. 14.12 Comparison of predictions and observed values for 6 different engines

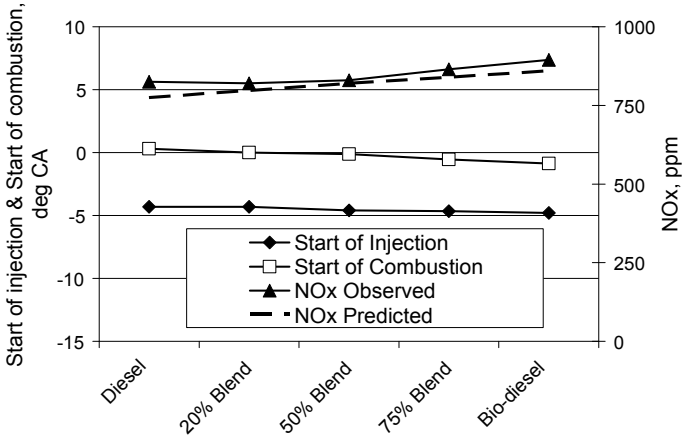

Fig. 14.13 Effect of biodiesel addition on the start of injection, combustion, and NO_x

marginally underestimates NO_x at lower operating speeds where higher NO_x was generated. This could be due to the non-consideration of the premixed phase. Even though the diffusion phase alone was considered for NO_x estimation, the correlation is satisfactory with a regression coefficient of 0.89 for all the data points.

Effect of Oxygen in the Fuel

Experiments were conducted with different proportions of biodiesel blend on engine C12 at 1500 rpm. NO_x measurement and indicator diagrams were collected simultaneously [2]. The main observation with the addition of biodiesel and NO_x emissions increased as well as injection timing as well as the start of combustion advanced. Then, this data was used as input for the NO_x model and predictions were made. The predictions followed the trend similar to observations, Fig. 14.13. The advancing effect and higher duration of injection are responsible for the increase in NO_x emissions with biodiesel.

References

1. Aghav YV, Lakshminarayanan PA, Babu MKG, Thatte V, Kumar MN (2008) Phenomenological modelling of NO_x under mixing controlled combustion in DI eiesel engines. J Therm Sci
2. Deshmukh BS, Aghav YV, Gokhale NP, Kumar MN, Ramesh A, Babu MKG (2008) An innovative EGR admission concept for heavy-duty diesel engine. In: SAE international mobility conference
3. Deshmukh BS, Aghav YV, Gokhale NP, Kumar MN, Ramesh A (2007) EGR mal-distribution analysis for DI diesel engines using AVL Boost. In: AVL users international conference, Graz

4. Lakshminarayanan PA, Dent JC (1983) Interferometric studies of vapourising and combusting sprays. SAE 830244
5. Uyehara OA (1980) Effect of burning zone A/F, fuel H/C on soot formation and thermal efficiency. SAE 800093

Chapter 15
Particulate Matter from Direct Injection Diesel Engines

Nomenclature

FSN	Filter smoke number (−)
I	Intensity of light received by the optical sensor in opacimeter with smoke in the tube (−)
I_0	Intensity of light received by the optical sensor in opacimeter with clear air in the tube (−)
k	Opacity (1/m)
L	Effective length of opacity meter, 0.430 (m)
N, T	Opacity (%)

Definitions/Abbreviations

LOC	Lubricating Oil Consumption, g/h
PM	Particulate Matter

Introduction

When fuel burns in an air deficit atmosphere, fuel cracks thermally to simpler molecules. This phenomenon is typical of heterogeneous combustion in certain zones in diesel engines. Soot forms as a result of polymerization of simple molecules like acetylene, to carbon-rich macromolecules and agglomeration [25]. With the deposit of oil and fuel on soot, a complex mixture of organic and inorganic compounds in solid and liquid phases [14] is formed. The mathematical modelling of particulate

P. A. Lakshminarayanan and Y. V. Aghav, *Modelling Diesel Combustion*,
Mechanical Engineering Series, https://doi.org/10.1007/978-981-16-6742-8_15

matter is always concentrated around soot because of its complex nature. Experimental investigations on PM emissions from used engines indicate that PM emissions are higher during transient phases of the test cycle as compared to the cold start or cruise phase [27]. Some experiments indicate a reduction in PM emissions up to 27% from engines using biodiesel in place of diesel on account of higher reactivity of soot formed from biodiesel [13]. Norton et al. [24] have studied the Fischer–Tropsch catalytic conversion process for diesel fuel and its impact on engine-out emissions. The study indicates about a 24% reduction in PM emissions from engines using diesel that has undergone Fischer–Tropsch transformation. Many studies have been carried out to establish contributions of soot, unburnt HC from fuel, and lubricating oil [4–6] to PM.

Efforts have been made for many years to correlate smoke and other contents of PM with the total PM [9]. Most of the analytical correlations consider only soot and very few deliberated unburnt HC. However, they do not account for contributions from lubricating oil and sulphur. Majewski and Jääskeläinen [19] bemoan smoke opacity readings generally do not correlate well with other PM measurement parameters, and numerous correlations between opacity or smoke readings and PM mass that have been developed can provide only approximate results.

A successful attempt has been made in this work to describe contributions of the different sources to arrive at total PM value [18].

Formation of Particulate Matter

In regions of low air–fuel ratio in the fuel sprays in a diesel combustion chamber, the evaporated fuel forms carbon from intermediate products of the reaction. The carbon in the form of soot burns subsequently at the flame front, however, insufficiently before the combustion gases leave the engine cylinder. The carbon particles are remaining in the torturous exhaust path starting from the exhaust port to the silencer, agglomerate, Fig. 15.1 [32]. On these carbon particles, unburned fuel and oil are adsorbed. Added to this are sulphates originating from fuel sulphur.

Direct Measurement of PM

Diesel particulates are of diameters below 0.04 μm and their agglomerates are of diameters up to one μm. The particulate matter (PM) is measured by sampling the gases in a full flow or partial flow tunnel. Samples are taken from the tunnel at a temperature of 47 °C ± 5 °C where the exhaust gases are diluted [17] in the range 3:1–20:1 to achieve the desired cooling effect. The gas samples are filtered and weighed using a microbalance. The two sampling methods from the full flow and partial flow are found to give equal results within experimental errors for engines emitting PM between 0.05 and 0.4 g/kWh [33] and even for ultra-low emission engines [23]. The

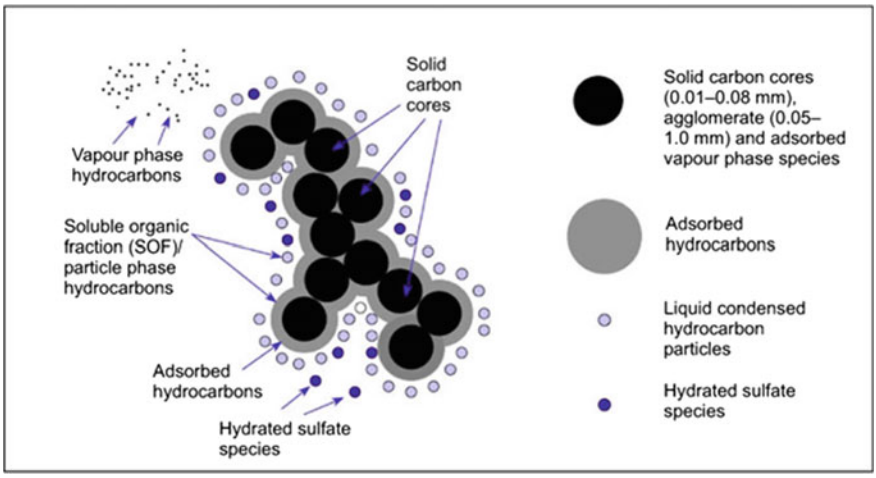

Fig. 15.1 Schematic representation of diesel particulate matter (PM) formed during the combustion of atomized fuel droplets. The resulting carbon cores agglomerate and adsorb species from the gas phase [32]

full flow tunnel is very expensive, and the partial flow tunnel is not that cost-effective both initially and to run during development trials.

Not only the infrastructure and the equipment are initially expensive, but also are maintenance intensive with high running costs.

Components of Particulate Matter (PM)

Particulate matter (PM) from a diesel engine is multifaceted. The particulate matter consists of solids like ash, sulphates, and carbon, and liquids like heavy hydrocarbons derived from fuel and oil condensing during the dilution process. The components of the PM are analysed using the sample collected on a filter. It is separated by using an extraction solvent into two fractions. One fraction is the insoluble organic fraction (IOF) made up of a solid carbon material (soot) and sulphates that cannot be dissolved by an organic solvent. The other fraction can be dissolved by the solvent and is called the soluble organic fraction (SOF), which has been adsorbed by the soot or condensed onto the filter. It is composed of unburned fuel and lubricating oil and their thermally synthesized components. The PM [17] constitutes generally 60% carbon, 5% ash from metallic additives in lubricating oil, 10% sulphate from fuel sulphur, 20% lubricating oil, and 5% liquid diesel, Fig. 15.2. These correspond to fuel containing about 350 ppm or less sulphur, common in Indian applications today. It may be noted that oils developed for engines using a DPF do not have ash forming additives and hence PM from such engines would have little or no ash. Similarly, it

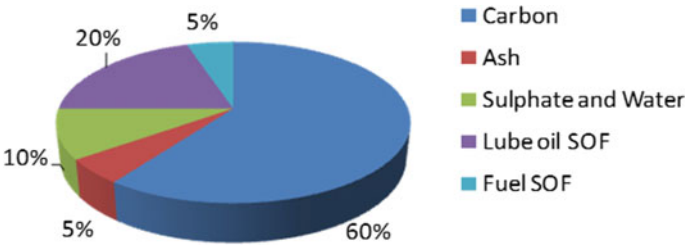

Fig. 15.2 Composition of PM Mass emissions from a conventional HD Diesel engine without DPF (SOF—soluble organic fraction) [17]

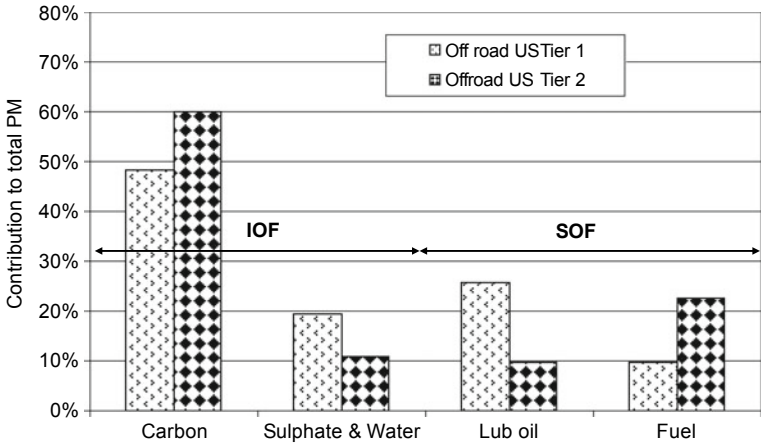

Fig. 15.3 Constituents of particulate matter at different emission norms

can be said about sulphates becoming negligible with fuels containing less than 10 ppm sulphur.

Specifically, two examples from engines satisfying US Tier-1 and Tier-2 emission norms are shown in Fig. 15.3.

Sulphur in Fuel

Sulphate is the dry sulphuric acid formed from the fuel sulphur. The intermediate product is sulphur dioxide (SO_2), a part of which forms less stable SO_3 before forming the acid when it comes in contact with condensed water of combustion. The linear dependence of SO_2 on fuel sulphur shows that the sulphate component in the total particulate matter can be correlated with the known fuel sulphur, Fig. 15.4 [8]. On the other hand, there is a negligible contribution to sulphates by the sulphur in oil. Similarly, in Fig. 15.5, the results of experiments using specially prepared (natural

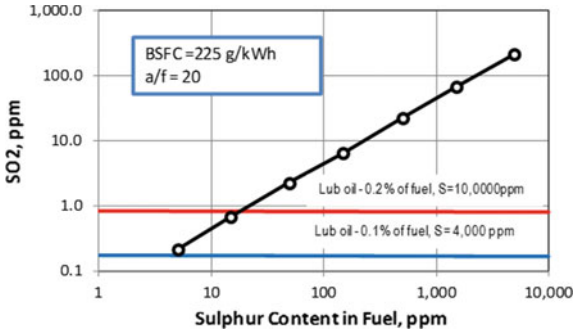

Fig. 15.4 Relationship of sulphur dioxide, a precursor for sulphates in PM with sulphur in fuel [8]

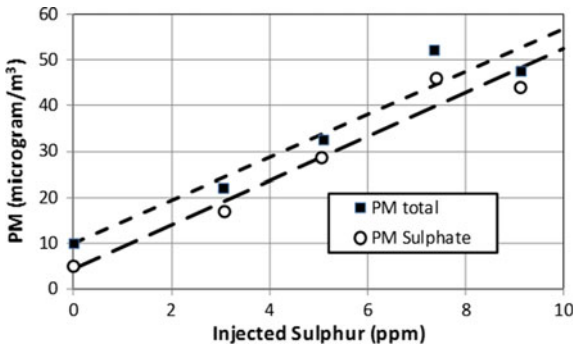

Fig. 15.5 Total particulate matter and sulphate in PM as a function of sulphur in fuel, gas turbine experiments [1]

gas) fuels in gas turbines with precisely added sulphur compound (methyl mercaptan) after completely scrubbing the native sulphur show [1] that the sulphates in PM are linearly related to the fuel sulphur.

Oil

The cylinder system is normally the largest contributor to oil-related particles, and the in-cylinder oil consumption can be categorized as (a) throw-off when oil is driven up by inertia forces, (b) reverse blow-by driven upwards by pressure, (c) evaporation from hot surfaces, and (d) top land scraping by carbon deposits on the top land (Fig. 15.6). Also, oil is consumed in diesel engines by the turbocharger and crankcase ventilation as well as when it flows past the valve stem seals and cylinder system.

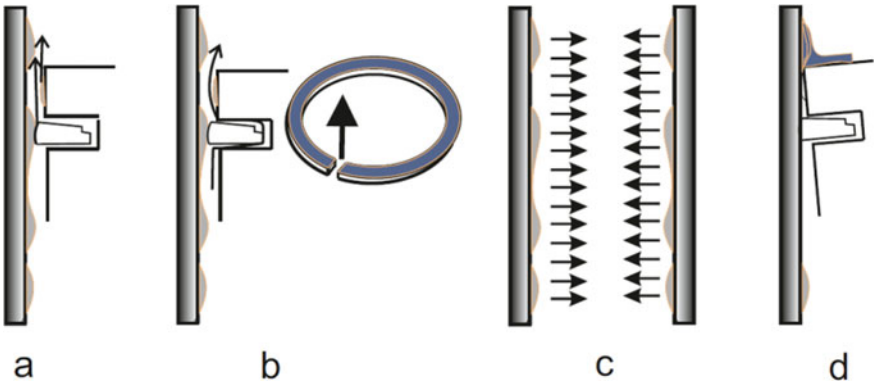

Fig. 15.6 In-cylinder oil consumption: **a** Throw-off. **b** Reverse blow-by. **c** Evaporation. and **d** Top land scraping [31]

Hydrocarbon from Fuel and Lubricating Oil

Fuel

Diesel fuel has a wide boiling range. The highest condensates partly remaining unburned are observed as hydrocarbons in the exhaust flow. A fraction of these hydrocarbons condenses on the surfaces of the soot particles on dilution at low temperatures.

Carbon Soot

Polycyclic aromatic hydrocarbons (PAH) form and grow by hydrogen abstraction and acetylene addition mechanism from the aromatic compounds of the fuel. On these nuclei, the gaseous PAHs transition to solid particles forming nuclei of soot which grow adding mass by absorption of hydrocarbons in the vapour phase. Coagulation to form spherical particles and agglomeration to form aggregate structures take place and result in the skeleton of particulate matter. Since oxygen is at a sufficiently high temperature, a majority of the soot particles may undergo oxidation during all stages of formation.

Soot is closely related to the smoke in the exhaust.

Measurement of Smoke

Two popular methods of measuring smoke are: using a filter smoke meter and an opacity meter. The two metres are highly developed in the last many years with superior control over temperature, flow, and automatic cleaning of optical parts enabling repeatability of data. They measure the concentration of carbon soot indirectly.

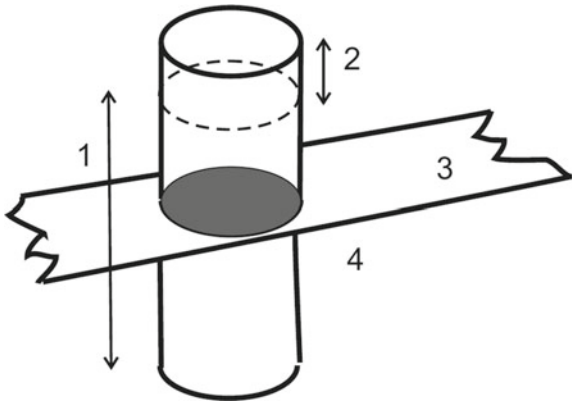

Fig. 15.7 Filter smoke meter: (1) Effective sampling length, (2) Dead volume, (3) Take-out volume, and (4) Filter area

Filter Paper Method, Filter Smoke Number (FSN)

A sample of a known volume of the exhaust gas is taken from the exhaust gas line with a probe through a pipe maintained at constant temperature and drawn through a filter paper, Fig. 15.7 [3, 7]. The blackness of the filter paper caused by the exhaust soot is quantified by measuring the light reflected by the paper when light from a controlled source is applied to it. The blackness mostly depends on the soot concentration in the gas and the volume of the sample. The filter smoke number (FSN) 0 is assigned to clean filter paper, and the "completely" black paper is assigned the value FSN 10. FSN is arrived at for a fixed sampling length of 405 mm from the observed blackness.

Opacity Meter, Opacity %

The exhaust gas is sampled into the probe by a diaphragm sampling pump into a measurement chamber, Fig. 15.8 [2]. The flow and the temperature (standard temperature 100 °C; adjustable 70–120 °C) are maintained constant to assure repeatability and high accuracy, irrespective of engine operating conditions. In the chamber, the flow is divided into two in opposing directions in a pipe. Light of intensity, $I_{0,}$ from a controlled source is sent through an orifice, and it travels through the pipe with an effective optical length of 430 mm (17 inches). The sensitivity of the detector is optimized for a low noise-to-signal ratio, and care is taken for signal stability. If the intensity sensed by the detector be I then the light extinction, the absorption coefficient, k, (m^{-1}), and opacity, N (%) are related to the measurement length, L (430 mm) as follows.

$$\frac{I}{I_0} = \text{Light Extinction} = \text{Absorption} + \text{Scattering} \tag{15.1}$$

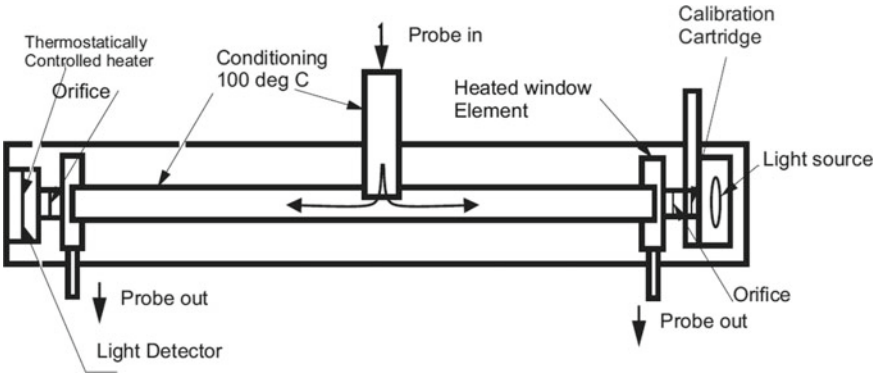

Fig. 15.8 Opacity meter probe

$$\frac{I}{I_0} = 1 - \frac{N}{100} = e^{-kL} \tag{15.2}$$

Photo-Acoustic Sensing

Photo-acoustic sensors are becoming more and more accurate to measure soot concentration and in turn particle numbers for very low emission engines using diesel particulate filters [28] for transient experiments.

Correlation of soot in PM, FSN, and Opacity

Filter smoke number, measured with a smoke meter like the AVL 415S [3, 30], represents the soot in the particulates. On the other hand, the opacity, N (%), is the attenuation of light intensity influenced mainly by the soot. Hence, a correlation between FSN and opacity exists. Experiments on many engines in five laboratories showed encouraging relationship as follows by AVL [3, 30] for a smoke number less than 4.0, Fig. 15.9.

$$N,\ \% = 0.12FSN^3 + 0.62FSN^2 + 3.96FSN \tag{15.3}$$

Mörsch and Sorsche [22] similarly showed soot separated from total particulates by thermogravimetry is strongly correlated with the opacity of the exhaust gases from 0 to 3%, Fig. 15.10. Mercer [20] showed soot concentration measured using the optical LII method is strongly related to filter smoke numbers in the range of 0–2. Thus, the use of FSN for steady-state measurement and opacity for steady and transient measurement of soot concentration is reliably established in various laboratories with a high correlation coefficient. Kirchen et al. [16] corroborated the

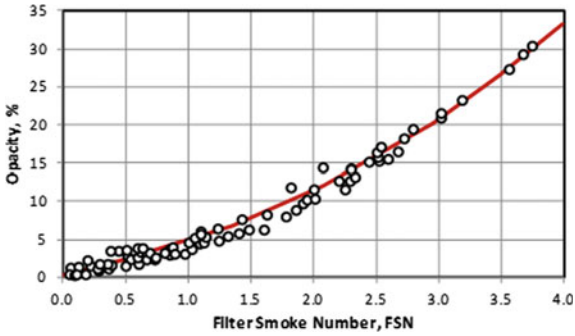

Fig. 15.9 Relationship between FSN and opacity (measured in 5 different laboratories) Ref. AVL [3, 30]

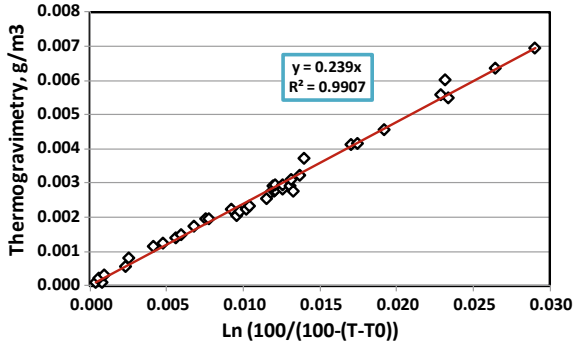

Fig. 15.10 Calibration of Opacimeter [22], T, % = opacity of exhaust; T0, % = opacity value when soot concentration is 0%

AVL correlation of FSN and soot concentration in the exhaust for two different fuels for FSN range 0–4, Fig. 15.11.

The sensitivity of the AVL415S smoke meter is down to 0.002 FSN (soot concentration of 20 $\mu g/m^3$) and is proven repeatable at steady modes up to Euro V emission standards where the PM limit is 0.02 g/kWh. The FSN to soot concentration (mg/m^3) correlation is given by Christian et al. [7] and Sluder et al. [29] as well as the AVL

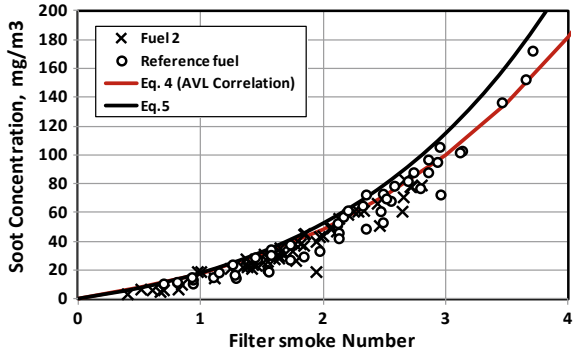

Fig. 15.11 Soot emission measured using the AVL micro-soot sensor and FSM for operation with two fuels; empirical correlations between soot concentration and FSN is shown Kirchen et al. [16]

product literature (2002) [21] as follows up to FSN of 8. Equation 15.5 is used recently in reference [15] with a pre-exponent factor of 4.95 instead of 5.32 and an exponent of 0.38 instead of 0.31. In practice, Eq. 15.5 appears to be a better fit than Eq. 15.4.

$$\text{smoke concentration} = \frac{1}{0.405} 5.32\,\text{FSN}\,e^{0.31FSN} \tag{15.4}$$

$$\text{smoke concentration} = \frac{1}{0.405} 4.95\,\text{FSN}\,e^{0.38\,\text{FSN}} \tag{15.5}$$

Calculation of Total Particulate Matter

Greeves et al. [10] showed a strong additive relationship between soot concentration derived from filter smoke meter and hydrocarbons with the PM measured in the exhaust for engines using high-pressure electronic unit injectors. Smoke and all the particulates are expressed in g/m^3. Figures 15.2 and 15.3 may be recalled here.

$$\text{Soot Particulate} = 1.0 \times \text{Smoke} \tag{15.6}$$

$$\text{HC Particulate} = 0.27 \times \text{HC} \tag{15.7}$$

$$\text{Calculated Total Particulate} = \text{Soot Particulate} + \text{HC Particulate} \tag{15.8}$$

The above calculated total particulate assumes that 27% ("yield") of the gaseous HC measured becomes soluble-organic fraction (SOF) in the particulate without any oxidation catalyst.

$$\text{yield} = \text{Contribution to particulate matter}$$

Sulphates were considered negligible because very low sulphur fuel was used. An oxidation catalyst could be used to greatly reduce the SOF part of the particulate with the requirement for a low sulphur fuel to minimize the formation of sulphate.

PM Model

Based on the many tests, an additive PM model is developed. For each mode of the cycle, e.g. 8-mode C1 cycle as per ISO 8178, the flows of soot, sulphate, and hydrocarbons are calculated.

$$\text{Exhaust flow} = \text{air flow} + \text{fuel flow} \tag{15.9}$$

If smoke is measured in opacity %, convert to FSN using Eq. (15.3) and soot concentration at NTP from Eq. (15.5),

$$\begin{aligned}\text{Soot flow} = {} & \text{Soot Concentration} \left(\text{g m}^{-3}\right) \text{at NTP} \\ & \times \text{Exhaust flow} \left(\text{m}^3\ \text{h}^{-1}\right) \text{at NTP}\end{aligned} \tag{15.10}$$

$$\text{Sulphate flow} = \left[\text{Sulphur}\right] \text{ in fuel} \times \text{fuel flow} \times 0.1 \tag{15.11}$$

$$\text{HC in PM flow} = \text{measured [HC]} \times \text{Exhaust flow} \times 0.10 \tag{15.12}$$

$$\text{Lub oil in PM flow} = \text{Lub oil consumption} \left(\text{g h}^{-1}\right) \times 0.05 \tag{15.13}$$

where 0.10, 0.10, and 0.05 are the empirical contribution factors (yields) towards the formation of sulphate, fuel-derived hydrocarbons, and oil attached to particulate matter.

Summing up Eqs. 15.10, 15.11, 15.12 and 15.13 of flows of soot, sulphate, hydrocarbon, and lubricating oil in PM, the flow rate of total particulate matter at a given mode is obtained. When the relevant weighting factors for the test cycle (e. g. C1 cycle) used to obtain the weighted PM flow, and then divided by the weighted power, the specific PM in g/kWh for the chosen cycle is obtained.

Validation of Correlation

The particulate matter is generally measured over a 5-mode, 8-mode, or 13-mode test cycle depending on application [11]. Different weighting factors are applied, and the sample is collected on a single filter to get the final cycle-averaged value. The same procedure was applied for the estimation of PM. For every mode, estimates were made, weighting factors were applied and finally summed up to get the final cycle-averaged value. The comparison of such results is done with the observed values for engines E12 and C12 (Table 3.2). These engines are of constant speed application where a 5-mode cycle was applicable and the comparison of results was satisfactory. Figure 15.12 indicates the values obtained experimentally and predicted for both the engines.

Further, Figs. 15.13 and 15.14 show that the new model accurately predicts the contributions of each of the constituents.

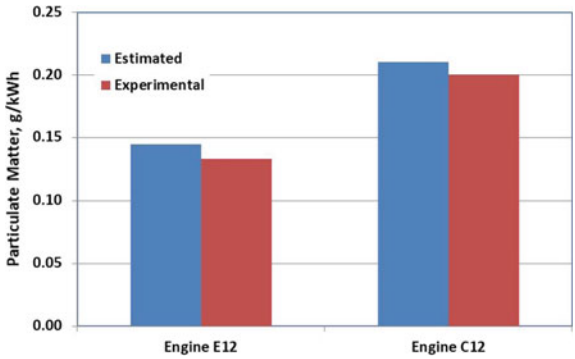

Fig. 15.12 Comparison of estimated and observed PM

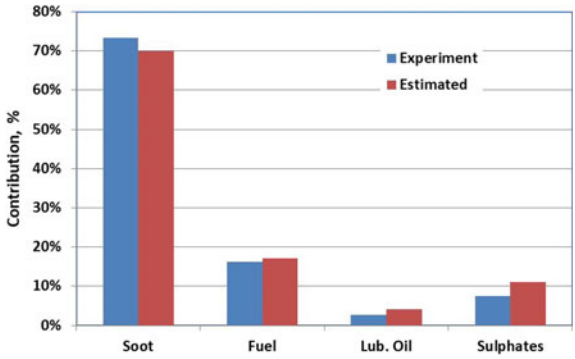

Fig. 15.13 Comparison of estimated and observed constitutes, engine E12

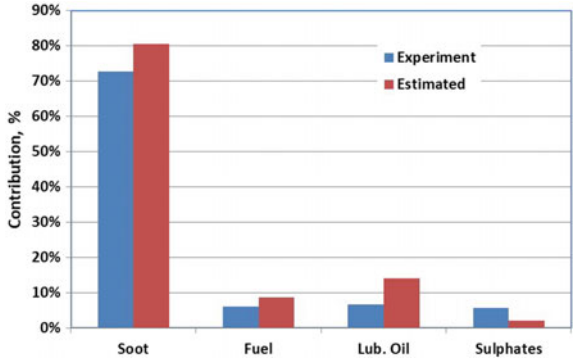

Fig. 15.14 Comparison of estimated and observed constitutes, engine C12

Experimental Validation

Various engines of swept volumes from 1.3 to 3.6 L were selected. These are naturally aspirated, turbocharged, and turbocharged after-cooled for different applications and

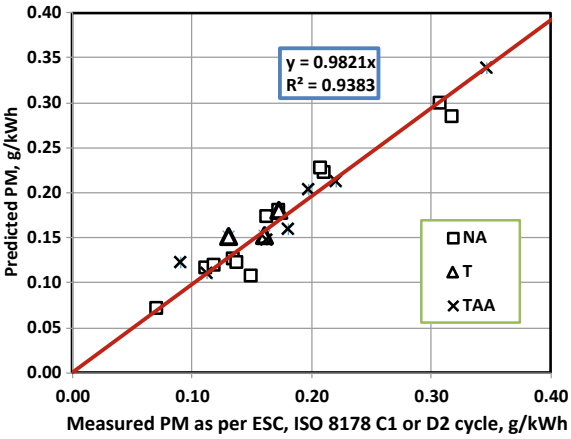

Fig. 15.15 Predicted PM and measured PM (NA-Naturally aspirated, T-Turbocharged, TAA-Turbocharged after-cooled air-to-air)

power ratings. These engines are essentially for off-road applications, namely tractors, cranes, and earthmovers as well as electric power generation satisfying Indian and European emission standards of the past and the present (Table 1 in Appendix XVI) as per C1, R49, EU steady state or D2 given in ISO8178 [12].

The PM predicted by the additive model described above and the measured using partial flow dilution tunnel is also tabulated and shown in Fig. 15.15. The correlation coefficient, R, is 97%, and the prediction on average is within 1.8% of the measured. The variation is of the order of the deviation of PM measured using different methods, e.g. using partial flow tunnel and full flow tunnel.

Discussions

Resolution and Stability of New Generation Smoke Metres

The insufficient resolution, instability, and noise plagued smoke metres and opacity metres of yore. The advent of advanced measurements and techniques to control conditions of temperature, pressure, and flow enabled highly accurate and repeatable measurement of smoke even at very low levels.

The Sensitivity of Smoke Metres

Cross-sensitivity in opacity metres due to absorption of the green light component by nitrogen dioxide could be a problem when present in large amounts especially after highly doped diesel oxidation catalysts where substantial nitric oxide is converted

into nitrogen oxides (NO_2). This is not a problem when smoke is sampled upstream of the catalysts where NO_2 is present in small quantities only, where the limits to PM are 0.02 and 0.03 g/kWh at a steady state. Such a problem does not exist in filter smoke meter, whereas it is not amenable to the transient measurement of smoke. Insensitivity of opacity meter to very small particles could be a problem in the case of ultra-low emission engines [26]. Again, a filter smoke meter could help here if the sampled volume is increased inversely proportionately to the smoke to be measured.

Cost-Effective Solution for Development

But for these minor irritants, modern opacity metres and filter smoke metres are highly cost-effective and can be used during the development of engine combustion or tuning the fuel injection system without spending a fortune on particulate samplers using either expensive partial flow tunnel or more expensive full flow tunnels.

Reliability

Also, smoke measurement by modern smoke metres is fast, reliable, and repeatable.

Measurement Noise

The plot of data of 21 different engines and ratings in Fig. 15.15 showed that except for two outliers all the points deviate from the fit by a standard deviation of 0.013 g/kWh. This deviation can be considered as noise in the measurement and hence in the prediction of PM. The minimum PM that can be predicted with reasonable confidence is about double the standard deviation which is 0.026 g/kWh.

Fit

The semi-empirical model is tested up to a PM of 0.35 g/kWh and can be reasonably extrapolated up to 0.4 g/kWh.

Conclusions

- Particulate matter, PM constitutes of soot, oil, ashes, fuel, and sulphates. Soot and oil are major constituents.
- For engine certification, a constant volume sampler in either a full flow tunnel or a partial flow tunnel is used. The equipment is accurate but costly to obtain and run, and maintenance intensive.
- For the development of engines when several experiments are planned, a cost-effective method is proposed by appreciating the constituents of PM.
- Measured oil consumption, known sulphur in fuel, and mass of soot in each mode of the steady-state emission cycles specified in ISO8178 are used to obtain the PM by a simple correlation.
- New generation opacity metres and filter paper smoke metres are well-controlled by modern computers for repeatability and sensitivity. The relationship of smoke with soot is now well-established.
- A weighted sum of the PM in different modes is compared with that obtained by certification grade constant volume samplers. Some small deviations are observed.
- The deviations are within the variation observed in the certification test itself.
- The deviations can be considered as noise in the measurement system as well as in the engine boundary conditions.
- PM can be estimated with high confidence using the correlation, in the range of 0.026–0.4 g/kWh for steady-state emission.
- This range is in the scope of the emission standards equivalent to or previous to Euro III, India TREM3A, India CEV3, USTier4f, and EU Stage 3A, 3B accepted by most of the countries in the world for the next decade, for less than 75 hp.

Acknowledgements A substantial portion of SAE paper 2017-01-7002 has been used in the chapter with copyright permission, vide Copyright Clearance Center Order Number: 1090336, Order Date: 14 Jan 2021.

References

1. Akamatsu T, Richard H, McDonell V, Samuelsen S (2014) Evaluation of the effects of carbon to hydrogen ratio and sulphur level in fuel on particulate matters from micro gas turbine engine. J Eng Gas Turbines Power 136(2):024501
2. AVL 439 Opacimeter Rev. 03 / SN 1569, SW ver. Ox1.25 and later (AVL 4210), November (2003)
3. AVL List GmbH (2005) Smoke value measurement with the filter-paper-method: application notes. Tech. rep
4. Cartillieri W, Herzog PL (1988) Swirl supported of quiescent combustion for 1990's heavy-duty DI diesel engines—an analysis. SAE 880342
5. Cartillieri W, Trittari P (1984) Particulate analysis of light-duty diesel engines [IDI and DI] with particular reference to lubricating oil particulate fraction. SAE 840418
6. Cartillieri W, Wachter WF (1987) Status report on a preliminary survey of strategies to meet US-1991 HD diesel emission standards without exhaust gas after-treatment SAE 870342
7. Christian R, Knopf F, Jaschek A, Schindler W (1993) Eine neue Meßmethodik der Boschzahl mit erhöhter Empfindlichkeit. Motortech. Z 54:16–22

8. DieselNet Technology Guide, Gaseous Emissions (2010) What Are Diesel Emissions, www.DieselNet.com. Ecopoint Inc. Revision 2010.03d
9. Ensor DS, Pilat MJ (1971) Calculation of smoke plume opacity from particulate air pollutant properties. J Air Pollut Control Assoc 21(8):496–501
10. Greeves G, Tullis S, Barker B (2003) Advanced two-actuator EUI and emission reduction for heavy-duty diesel engines. SAE Trans 112(3):914–931
11. http://www.dieselnet.com/standards/referred in 2008
12. ISO 8178–1: (2006) Reciprocating internal combustion engines—Exhaust emission measurement
13. John MES, Thomas JF, Lewis SA, Dam TQ, Dean Edwards K, DeVault GL, Retrossa DJ (2003) Particulate matter and aldehyde emissions from idling heavy-duty diesel trucks, SAE 2003–01–0289
14. Johnson JH, Bagley ST, Gratz LD, Leddy DG (1994) A review of diesel particulate control technology and emissions effects. SAE, 940233
15. Kim YJ (2008) Integrated modelling and hardware-in-the-loop study for systematic evaluation of hydraulic hybrid propulsion options. ProQuest
16. Kirchen P, Peter O, Boulouchos K, Bertola A (2010) Exhaust-stream and in-cylinder measurements and analysis of the soot emissions from a common rail diesel engine using two fuels. J Eng Gas Turbines Power 132(11):112804
17. Kittelson DB (1998) Engines and nanoparticles: a review. J Aerosol Sci 29(5):575–588
18. Lakshminarayanan PA, Aswin S (2017) Estimation of particulate matter from smoke, oil consumption, and fuel sulphur. No. 2017–01–7002. SAE Technical Paper
19. Majewski WA, Jääskeläinen H (2012) Smoke opacity: DieselNet technology guide » measurement of emissions. www.DieselNet.com. Ecopoint Inc. Revision 2013.07
20. Mercer C (ed) (2013) Optical metrology for fluids, combustion, and solids. Springer Science & Business Media
21. Model AVL (2002) 415S Smoke meter product literature. Updated October 15
22. Mörsch O, Petra S (2001) Investigation of alternative methods to determine particulate mass emissions. UNECE/WP 29
23. Particle measurement program (2010) Heavy duty inter-laboratory correlation exercise: final report world forum for harmonization of vehicle regulations. United Kingdom, Economic Commission for Europe, Inland Transport Committee. Working Party on Pollution and Energy, Sixtieth session, Geneva, 8–11 June 2010
24. Norton P, Vertin K, Bailey B, Clark NN, Lyons DW, Goguen S, Eberhardt J (1998) Emissions from trucks using fischer-tropsch diesel fuel, SAE technical series Paper no. 982526
25. Pischinger S, Backer H (2003) In: Internal combustion engines-Volume II
26. Roessler DM, Faxvog FR (1979) Opacity of black smoke: calculated variation with particle size and refractive index. Appl Opt 18(9):1399–1403
27. Shah SD, Cocker DR, Wayne Miller J, Norbeck JM (2004) Emission rates of particulate matter and elemental and organic carbon from in-use diesel engines. Environ Sci Technol
28. Schindler W, Haisch C, Beck HA, Niessner R, Jacob E, Rothe D (2004) A photoacoustic sensor system for time-resolved quantification of diesel soot emissions. SAE Trans 113(4):483–490
29. Sluder S, Wagner RM (2006) An estimate of diesel high-efficiency clean combustion impacts on FTP-75 aftertreatment requirements (SAE Paper Number 2006–01–3311). Oak Ridge National Laboratory (ORNL); Fuels, Engines, and Emissions Research Center
30. Smoke Value Measurement with the Filter Paper Method, Application Notes, AVL1007E, Rev. 02, June (2005)
31. Tornehed P (2010) Particulate emissions associated with diesel engine oil consumption
32. Twigg MV, Phillips PR (2009) Cleaning the air we breathe-controlling diesel particulate emissions from passenger cars. Platin Met Rev 53(1):27–34
33. Vojtíšek M, Pechout M, Mazač M, Dittrich A, Čihák M (2011) Particulate matter measurement with an improvised full-flow dilution tunnel. In: Slovakia University of Zilina Department of Automotive Technology, XLII international scientific conference of Czech and Slovak University departments and institutions dealing with the research of combustion engines, September, pp 8–9

Chapter 16
Multi-dimensional Modelling of Diesel Combustion: A Review

Yu Shi and Rolf D. Reitz

Nomenclature

A	A relaxation factor to smooth the process (−)
A	Pre-exponential factor (−*)
AMC	Adaptive multi-grid chemistry (−)
b	Temperature dependence factor (−*)
B_0	A constant equal to 0.61 (−*)
B_1	A constant that can have values ranging between 10 and 60 (−*)
C_2	A model constant of an order of 0.1 (−*)
C_b	An adjustable constant which is chosen such that $C_b = B1/2$ (−*)
CFD	Computational fluid dynamics (−)
ch	Number of a group is the sum of the ch number of all cells in that group (−)
CRT	Adjustable constant of the order 0.1 (−*)
C_t	Another constant usually set to unity (−*)
DOM	Discrete ordinates method (−)
E	Activation energy (kcal/mol)
E_{sf} and E_{so}	12,500 and 14,000 (kcal/mol)
g_t	Acceleration in the direction of travel (m/s^2)
k_f and k_r	Forward and reverse rate coefficients (−)
L_b	Breakup length (m)
LDEF	Lagrangian-drop and Eulerian-fluid (−)
M_{fg}	Concentration of fuel vapour, and the soot oxidation rate is a linear function (mol/L)

Y. Shi (✉) · R. D. Reitz
Engine Research Center, University of Wisconsin-Madison, Madison, USA
e-mail: yushi92@gmail.com

R. D. Reitz
e-mail: reitz@wisc.edu

P. A. Lakshminarayanan and Y. V. Aghav, *Modelling Diesel Combustion*,
Mechanical Engineering Series, https://doi.org/10.1007/978-981-16-6742-8_16

$m_{k,\text{cell}}$	Mass of species k (kg)
M_s	Mass of the net soot produced (kg)
M_{sf}	Mass of soot formed (kg)
M_{so}	Mass of soot oxidized (kg)
N_{ck}	Total number of cells required in the chemistry computation (−)
n_i' and n_i''	Stoichiometric coefficients of the reactants and products (−)
PaSR	Partially stirred reactors (−)
PO_2	Oxygen partial pressure (Pa)
r	Ratio of the amount of products to that of total reactive species (i.e. all except N_2) (−)
r_c	Droplet radius (m)
RTE	Radiation transfer equation (−)
s	Surface tension (N/m)
T	Temperature (K)
$\overline{T}$	Average in-cylinder temperature (K)
T_i	Individual temperature of each of the n cells (K)
t_{KH}	The breakup time (s)
t_l	Laminar timescale is derived from a single-droplet auto-ignition experiment of Arrhenius form (s)
t_t	Turbulence timescale related to the eddy turnover time (s)
U_r	Relative velocity between the liquid drop and the gas (m/s)
We_g	Weber number (−)
WSR	Well-stirred reactors (−)
X	Arbitrary specification of all chemical species for the M reactions (−)
$[X_j]$	Concentration of species X_j (mol/m^3)
Y_m	Mass fraction of species M (−)
Y_m*	Local and instantaneous thermodynamic equilibrium value of the mass fraction (−)
Z	Ohnesorge number (−)
z'	Proportion of fuel oxygen to fuel carbon (−)
Λ_{KH}	Wavelength corresponds to the KH (m)
ϕ	Progress equivalence ratio (−)
ρ_f	Fuel density (kg/m^3)
ρ_g	Gas density (kg/m^3

Superscript

n	Time step (−)

Subscript

i	ith processor time spent in processor P_i^{n+1} $(-)$

*These are model constants, so they do not normally have units. Some variables can have different units consistent with the context.

Fundamental concepts of fluid dynamics were substantially established in the 1800s, and more complex turbulent flows were intensively investigated in the 1900s. Models help to mathematically reveal the physics of fluid flows, and with the increasing complexity of studied problems, numerical solutions are often needed instead of analytical ones. This leads to an important branch of fluid dynamics, computational fluid dynamics (CFD). Improved CFD techniques and the exponentially increasing computational power of modern computers during the twentieth and twenty-first centuries have had a great impact on applying the sciences of fluid mechanics to design problems in engineering practice. Consequently, multi-dimensional CFD has found more and more applications in diesel engine research, design, and development since its initiation in the late 1970s. Compared to phenomenological models, multi-dimensional CFD models provide more detailed physical information about the gas exchange processes, in-cylinder flow structures, spray development, as well as combustion chemistry and pollutant formation in diesel engines.

The first part of this chapter reviews the basic approach that is used in CFD modelling of diesel engines, including the basic assumptions, equations, and numerical methods. This is followed by a description of advanced turbulence, spray and evaporation, and combustion models of in-cylinder phenomena. A detailed discussion of the historical evolution and mathematical derivation of these models is beyond the scope of the present review. Instead, the focus is placed on their applicable ranges, advantages, and disadvantages. The reader is encouraged to refer to the relevant literature cited for each model. Recent efforts for reducing the computational expense of multi-dimensional CFD modelling are also discussed. These efforts include reducing the mesh dependence of spray models and lessening the computational burden of combustion chemistry solvers by using an adaptive multi-grid chemistry (AMC) model with code parallelization. Features of popular engine CFD codes that are categorized into open-source code and commercial software are also described. The chapter concludes with a discussion of the new challenges that engine CFD modelling will be facing soon.

Basic Approach

In-cylinder flows of diesel engines are typically compressible turbulent flows. Turbulence by itself remains one of the most complex fundamental problems of fluid

dynamics. The complexity of in-cylinder flows is further increased due to the injection of a high-pressure spray and the resulting evaporation of droplets due to the multi-phase and multi-component nature of the problem. Once the combustion occurs, the additional requirement of solving reacting flows can increase the difficulty by orders of magnitude due to the vast number of participating chemical species. However, the behaviour of the fluid is still described by classical physics and is governed by several basic equations, including the continuity (mass conservation), momentum (Navier–Stokes equations), energy, and turbulence (i.e. k–ε equations) equations. These equations are supplemented by thermal and caloric equations of states (i.e. ideal gas law). Assumptions and simplifications are usually made for modelling the multi-component mixture viscosity, Fick's law of mass diffusion, and Fourier's law of enthalpy (or energy) transport, depending on the details of the models.

For the gas–liquid flows, both Eulerian–Eulerian and Eulerian–Lagrangian (i.e. discrete droplet/particle) methods can be used to solve two-phase flow problems. Due to the large dimensionality of the problem, the former method awaits "next-generation" spray and atomization models. Accordingly, the Eulerian–Lagrangian method still dominates and is widely used in current engine CFD simulations. The Eulerian–Lagrangian approach treats the gas phase as continuous and the liquid phase as consisting of discrete particles, separately. Thus, the gas-phase flow is described by the Eulerian formulation and the liquid phase is described using the Lagrangian approach, in which liquid droplets are represented as assemblages of identical particles using the discrete particle or parcel method [22]. Lagrangian spray model is based on Kelvin–Helmholtz (KH) and Rayleigh–Taylor (RT) instability analyses [15, 77] and the "blob injection concept" [78]. These numerical models are relatively efficient and can provide statistical information about the distributions of particle size, velocity, and position, which are usually in reasonable agreement with experimental measurements if the models are appropriately tuned. Mass, momentum, and heat transfer between the gas and liquid phases are accounted for through source terms in the corresponding governing equations.

The governing equations of the gas phase are partial differential equations (PDEs). Thus, numerical methods are needed to discretize the equations. The methods include (but are not restricted to) finite volume, finite difference, and finite element methods. They all use a finite difference mesh or grid to split the computational region into smaller sub-regions to approximate a continuous domain, and the discretized governing equations are then solved inside each of these portions of the domain.

Mesh generation is critical to multi-dimensional CFD engine modelling since the mesh quality has a large impact on the numerical stability of CFD solvers and the mesh density can influence the simulation results, depending on the mesh dependence of the numerical models. Distinguished by the connectivity of neighbouring grids, computational meshes are classified into structured meshes, unstructured meshes, and their hybrids. A structured mesh is characterized by regular connectivity that allows CFD solvers to see the neighbour relationships between connected cells based on their storage arrangements. Typically structured meshes are quadrilaterals and hexahedra in 2-D and 3-D space, respectively. The structured mesh saves storage space, but it is difficult to mesh complex geometries, such as the joints of manifolds, valves,

and glow plugs of diesel engines. An unstructured mesh is characterized by irregular connectivity which requires a substantially larger storage space since the neighbour connectivity also needs to be explicitly stored. But the unstructured mesh can easily deal with more complex engine geometries.

The finite volume method is the most prevalent numerical approach in engine CFD codes, such as in open-source codes such as KIVA and OpenFOAM, and other commercial CFD software. Its popularity comes from two aspects: its inherent formulation ensures the conservation of quantities such as mass, momentum, energy, and species; it is also easily formulated to allow for unstructured meshes. The finite volume method converts volume integrals in a PDE that contains a divergence term to surface integrals using the divergence theorem, and source terms can be directly volume-integrated. The surface integration then ensures that these terms are evaluated as fluxes at the surfaces of each finite volume. Because the values of the fluxes entering a control volume are identical to their leaving values, conservation can be guaranteed. The finite difference method discretizes the governing PDEs in both time and space. It replaces derivatives of PDEs with approximately equivalent difference quotients. Two sources contribute to errors of this method. The first is a round-off error due to computer rounding of decimal quantities, and the second is truncation error from using difference quotients to express derivatives when high-order terms are discarded. Using higher-order differences helps to reduce the truncation error; however, the numerical stability condition becomes stricter. Explicit differencing schemes require smaller time steps to satisfy the Courant condition to maintain convergence, and thus, implicit schemes are usually employed. The finite element method is based on converting PDEs to ordinary difference equations (ODEs) to obtain their solution by utilizing standard integration techniques. It finds more applications in structural analysis of engine bodies, and it is seldom applied to solve engine flows primarily due to the special care needed to ensure conservative solutions.

Using the aforementioned basic approaches, the complex in-cylinder physical and chemical processes of diesel engines can be solved using a series of closely coupled sub-models that describe the turbulent flow, spray injection, droplet evaporation, combustion, pollutant formation, and heat transfer. They are discussed as follows.

Turbulence Modelling

It is critical to resolving in-cylinder flow motions at both large and small scales in modelling diesel engines. The in-cylinder flows are compressible turbulent flows due to the high-speed gas exchange processes and the piston compression. Various models and methods have been proposed for solving turbulent flows, including Reynolds-averaged Navier–Stokes (RANS), large eddy simulation (LES), and probability density function (PDF) methods, and direct numerical simulation (DNS). Considering the computational expense and the solutions of interest, RANS and LES are most prevalent in engine simulations.

RANS Models

Due to their relatively high efficiency and acceptable accuracy, RANS-based turbulence models are still playing a dominant role in engine simulations nowadays, especially for engineering practices. In the context of engine simulations, RANS models are specifically referred to as the k–ε model and its variants, although other types of RANS models, such as the Reynolds stress model (RSM) ([50], can be found in very few studies [51]).

In RANS models, the Reynolds equations are solved for the mean velocity field; i.e. all turbulent fluctuations about the local mean are modelled. The closure terms, the Reynolds stresses, are determined by a turbulence model, such as the k–ε model which is based on the turbulent viscosity hypothesis [74]. The k–ε model belongs to the class of two-equation models (as compared to one-equation models in which only the turbulent kinetic energy k is solved), in which model transport equations are solved for two turbulence quantities—the turbulent kinetic energy k and its dissipation rate ε [74]. The turbulent viscosity is expressed by $\nu_t = C_\mu \, k^2/\varepsilon$ where C_μ is a model constant given as 0.09. In the standard k–ε equations, the model constants are evaluated regarding benchmark experiments.

In early studies, the standard k–ε model was widely used in engine CFD codes, such as in the KIVA II code [7, 8]. Considering the moving boundary in engines, a source term that accounts for length scale changes with velocity dilation is added to the ε equation. An additional source term is used to introduce the interaction of a spray with the turbulence in both k and ε equations.

Yakhot and Orszag [99] used the renormalization group (RNG) theory to form an improved formula for the ε equation and proposed the RNG k–ε model. Their deviation depended on the RNG theory and ε expansion [100].The RNG theory does not include any experimentally adjustable parameters. Therefore, the model constants in the deduced RNG k–ε equations are given more rigorous mathematical meanings. Since its appearance, the RNG k–ε model has been applied to model both low- and high-Reynolds number turbulent flows with great success. In IC engines, although the Mach number of the in-cylinder flow is very low, the moving piston causes the fluid to undergo large density variations. With such flow behaviour, the original RNG k–ε model cannot be directly applied. Therefore, Han and Reitz [28] further modified the ε equation to account for the effect of compressible turbulent flows in engine environments. In their analysis, in-cylinder flows were assumed to be low Mach number flows with rapid distortion and isotropic (spherical) mean strain. The effects of both the pressure dilation and dilatation dissipation that appear in the k equation were deemed to be negligible due to the assumption of isotropic distortion at a very low Mach number, and thus, the k equation remained as formulated in the original RNG k–ε model. The ε equation was similar to that of the standard one, but a focus was placed on modifying a model constant, which accounts for velocity dilation and was determined through the analysis of rapid spherical distortion. In the same study, they showed that with the modified RNG k–ε model simulated engine compressing/expanding flows agreed well with available experimental observations

and that the large-scale flow structures which are affected by the spray and the squish were consistent with endoscope combustion images. Kong et al. [45] reported that a good quantitative agreement between measured and predicted NO_x and soot emission data was obtained with the use of the modified RNG k–ε model. Since then, this RNG k–ε model has been widely adopted into many engine CFD codes and applied to various simulations [29, 41].

Large Eddy Simulation (LES)

Although the pioneering work on LES by Smagorinsky [87] and Lilly [56] appeared several decades ago, until recently (the 2000s) LES has not been widely employed in modelling engine flows. This is because, in terms of computational expense, LES lies between Reynolds stress models and DNS [74], which prevented it from being applied to engineering problems in times when computational power was very limited. Thanks to the rapid development of computer technology, LES has now found more applications in engine simulations. The basic idea of LES is to solve for large-scale eddies (i.e. those that can be resolved on the computational mesh) explicitly and to model the effect of smaller-scale motions (sub-grid scale) on large meshes through the use of a sub-grid scale (SGS) model. Early applications of LES in engine turbulent flows were reviewed by Celik et al. [19]. The review revealed that even with relatively coarse grids LES captures many more interesting features of in-cylinder flows, such as the large coherent vortical flow structures developed during the intake stroke. In more recent studies, many researchers have shown that LES offers significant advantages over RANS [52, 81, 38, 34] have shown that LES resolves more flow details, better represents a local mixing field, and can reveal engine cycle-to-cycle variations [25]. In many cases of LES in engine simulations, the same sub-models, such as wall models, spray models, and turbulent combustion models, have been retained with only the k–ε derived turbulence scales being replaced by the scales from the LES sub-grid scale model [32]. Therefore, the advantages of LES may not be fully obtained. Further improvements of the use of LES in engine simulations will depend on the corresponding development of these sub-models. To take full advantage of the power of LES, not only sound physical modelling is required but also careful numerical implementations, such as high-order numerical schemes and a high-resolution computational mesh. However, the resulted high computational cost may prevent LES from being widely used for practical engine simulations in this time and the near future. Hence, efforts are needed to compromise between reducing computational expense and benefiting from LES features. Recent research [72, 35, 39] showed that the dynamic structure LES model can give promising results on coarse meshes.

Spray and Evaporation Modelling

As briefly discussed in Sect. 16.2, the Lagrangian-drop and Eulerian-fluid (LDEF) approach is the most prevalent methodology used in multi-dimensional CFD codes to treat the interaction of gas–liquid phases that result from the high-pressure injection of fuels in diesel engines. In LDEF models, sprays are represented by discrete computational parcels. Each of these parcels represents a group of droplets that have the same characteristics, and they undergo breakup, collision, and coalescence processes whose competition determines the size and position distribution of the droplets. An evaporation model is also needed to calculate the vaporization rate of liquid droplets based on their sizes and the thermal conditions that they are subject to. Interactions due to mass, momentum, and heat transfer between the gas (described using the Eulerian method) and liquid phases are accounted for using source terms in the corresponding governing equations. Popular spray and evaporation models are reviewed in this section.

Spray Models

In the study of Reitz and Diwakar [78], atomization and drop breakup were treated as indistinguishable processes within the dense spray near the nozzle exit. Accordingly, atomization was prescribed by injecting drops ("blobs") which underwent subsequent breakup, collision, and coalescence processes. This method established a basic framework for calculating spray behaviour using CFD techniques and has been broadly adopted in engine CFD codes since it was proposed. In their study, the atomization model assumed that the injected drops had a radius equivalent to the effective nozzle hole radius and the initial axial velocity of the drops was set equal to the injection velocity. The breakup model employed two breakup regimes based on experimental measurements to determine the new drop characteristics. In Reitz's later study [77], significant improvements were made to the previous model in several aspects: a linear stability analysis was used to describe the instability at the liquid–gas interface and to predict the breakup of the liquid jet, and the method broadened to describe various regimes of a jet breakup; the product drops were distinguished from the parent drop by having different drop sizes, which had a significant effect on the fuel vapour distribution in a high-pressure spray. Since then, a variety of instability theories have been used to model the atomization and breakup processes of spray jets, and modifications to these models have been the subject of many studies. These studies include the use of the Taylor analogy breakup (TAB) model [65], Kelvin–Helmholtz (KH) instability, Rayleigh–Taylor (RT) instability models [69]; Beale and Reitz [15], and their hybrids [70]. The KH/RT hybrid model [15] is reviewed here.

In the KH/RT hybrid model, the KH theory is used to predict the initial breakup of the injected blobs or the intact liquid core. Then, the RH theory is introduced to account for the instability caused by the acceleration normal to the interface of

the liquid spray drop and its surrounding gas. Together with the KH model, the RT model is used to predict the secondary breakup of the droplets.

In the KH model, a parent parcel with radius, r, breaks up to form new droplets with radius, r_c.

$$r_c = B_0 \Lambda_{KH} \tag{16.1}$$

where B_0 is a constant equal to 0.61 and the wavelength Λ_{KH} corresponds to the KH wave with the maximum growth rate Λ_{KH} given by

$$\Lambda_{\mathrm{KH}} = \frac{9.02r\left(1 + 0.45\sqrt{Z}\right)\left(1 + 0.4T^{0.7}\right)}{\left(1 + 0.865\,\mathrm{We}_g^{1.67}\right)^{0.6}} \tag{16.2}$$

$$\Omega_{KH} = \frac{0.34 + 0.38\,\mathrm{We}_g^{1.5}}{(1+Z)\left(1 + 1.4T^{0.6}\right)}\sqrt{\frac{\sigma}{\rho_f r^3}} \tag{16.3}$$

In the equations, the gas Weber number is defined as $\mathrm{We}_g = \rho_g {U_r}^2 r/\sigma$, and the Ohnesorge number, Z, is

$$Z = \frac{\sqrt{\mathrm{We}_l}}{\mathrm{Re}_l} \tag{16.4}$$

U_r is the relative velocity between the liquid drop and the gas, σ is the surface tension, and ρ_g and ρ_f are the gas and fuel densities, respectively. The liquid Weber number is $\mathrm{We}_l = \rho_f {U_r}^2 r/\sigma$, and the liquid Reynolds number is $\mathrm{Re}_l = \rho_f U^2 r/\mu_f$, where μ_f is the liquid fuel viscosity. The Taylor number, T, is calculated

$$T = Z\sqrt{\mathrm{We}_g} \tag{16.5}$$

Due to the loss of mass during drop stripping, the parent reduces in diameter and the rate of change of the radius of the parent parcel is calculated using

$$\frac{\mathrm{d}r}{\mathrm{d}t} = \frac{r - r_c}{\tau_{\mathrm{KH}}} \tag{16.6}$$

where τ_{KH} is the breakup time given by

$$\tau_{\mathrm{KH}} = \frac{3.726 B_1 r}{\Omega_{\mathrm{KH}} \Lambda_{\mathrm{KH}}} \tag{16.7}$$

B_1 is a constant that can have values ranging between 10 and 60, and it is usually calibrated with experiments.

The RT model is only employed to influence the drops beyond the breakup length L_b, which is calculated from Levich theory as

$$L_b = C_b d_0 \sqrt{\frac{\rho_f}{\rho_g}} \tag{16.8}$$

where C_b is an adjustable constant which is chosen such that $C_b = B_1/2$ to keep the breakup length approximately equal to that calculated from the KH equations for inviscid flows.

Similar to the KH theory, the size of the new droplets is also determined by wave instability. In the RT model, the frequency of the fastest-growing wave is given by

$$\Omega_{\mathrm{RT}} = \sqrt{\frac{2}{3\sqrt{3\sigma}} \frac{\left[-g_t\left(\rho_f - \rho_a\right)\right]^{1.5}}{\rho_f + \rho_a}} \tag{16.9}$$

where g_t is the acceleration in the direction of travel. The corresponding wave number is

$$K_{\mathrm{RT}} = \sqrt{\frac{g_t\left(\rho_f - \rho_a\right)}{3\sigma}} \tag{16.10}$$

The wavelength corresponding to the fastest wave growth rate is $2\pi\ C_{\mathrm{RT}}/K_{\mathrm{RT}}$, where C_{RT} is an adjustable constant of the order 0.1. The radius of the droplet is compared to the RT wavelength, and once the wavelength is smaller than the droplet diameter, RT waves are assumed to be growing on the surface of the droplet. The wave growth time is compared to the breakup time, defined by

$$\tau_{\mathrm{RT}} = \frac{C_r}{\Omega_{\mathrm{RT}}} \tag{16.11}$$

where C_τ is another constant usually set to unity. If the wave growth time is greater than the breakup time, the drop is assumed to break up with a new radius given by

$$r_c = \frac{\pi C_{\mathrm{RT}}}{K_{\mathrm{RT}}} \tag{16.12}$$

It is noted that in both KH and RT models, the number of droplets in the computational domain is adjusted based on the mass conservation of the liquid phase once the breakup occurs. Due to its simplicity and with a lot of successful applications, this hybrid model has been adopted into many engine CFD codes, such as KIVA and STAR-CD.

The interaction between drops that result from spray atomization and breakup is crucial to decide the spatial fuel distribution in diesel combustion simulations. Inter-drop collisions are normally modelled as two-body interaction processes, and a sequence of such binary interactions can represent collisions involving three or more participating bodies. To describe the complex physical interactions of drop collision dynamics, a model is needed to solve the probability of occurrence of a collision and to predict the outcome of the collided drops.

The classic O'Rourke model [64] is one of the most widely used collision models in LDEF spray simulations. In the O'Rourke model, the possibility of collision is based on the drop number density and the relative velocity between the drops. Collisions are allowed to occur for two parcels only if they are in the same cell. The model considers two outcomes for a collision, i.e. coalescence and grazing separation. A formula for the efficiency of coalescence is defined in the model, which is derived from the argument that for coalescence to be permanent, the rotational energy of the combined mass formed by the colliding drops should be less than the surface energy required to reform the drops [18]. The collision outcome, coalescence or grazing separation, is determined stochastically by considering whether if a randomly generated number (between 0 and 1) is less or greater than the square root of the coalescence efficiency. For resulting drops, mass, momentum, and energy conservation laws are applied to calculate their sizes and velocities after the collision.

The simplicity of the O'Rourke collision model has contributed to its popularity in multi-dimensional engine CFD codes. However, the shortcomings of this model cannot be neglected. Many experiments have shown that there are more outcomes from a collision than the two that are considered in the O'Rourke model, and thus, extended models for those outcomes are needed. Also, the model assumes that only parcels within the same cell can collide, which is a further limitation. This is also the cause that the O'Rourke collision model exhibits severe dependency on mesh size. Efforts to improve the O'Rourke model have appeared in the literature. A radius of influence (ROI) method proposed by Munnannur [59] has shown a much-reduced mesh dependence, as discussed in Sect. 16.8. The dependency of the collision model on mesh size is one of the reasons that the results of LDEF spray models more or less depend on the grid size on which the models are solved. The other reason is that an inadequate mesh resolution results in under-prediction of spray momentum, which is particularly severe in the near nozzle region. This mesh dependence issue is also addressed in Sect. 16.8.

Evaporation Models

Once the fuel spray breaks up into small droplets, evaporation takes place rapidly from the surface of the droplets. In IC engine applications, the ranges of pressures and temperatures are broad, and evaporation models have to properly predict the behaviour of vaporizing droplets and sprays. These models are categorized into single-component fuel evaporation models and multi-component fuel evaporation

models that are distinguished by how they treat the fuel composition in droplets as their names suggest. The multi-component models can be further classified into two types, i.e. continuous multi-component (CMC) models and discrete multi-component (DMC) models. To simplify the complex heat and mass transfer processes of droplet evaporation, often several assumptions are used in these models; for example, the liquid droplet is treated as a perfect sphere; no absorption of the ambient gas into the liquid droplet is considered; radiation and second-order effects such as the Soret and Dufour effects are assumed to be negligible.

For simplicity, fuels are usually represented as a single-component fuel in most evaporation models in multi-dimensional engine CFD simulations. For example, tetradecane ($C_{14}H_{30}$) is normally used as a surrogate fuel for diesel, and gasoline is represented by iso-octane (C_8H_{18}) in many cases. These species are chosen because they have similar physical properties, such as density and surface tension, to diesel and gasoline. However, these similarities do not guarantee that the complex behaviour of the vaporization of multi-component fuels can be truly revealed. It has been pointed out that the preferential vaporization of light-end components in multi-component fuels affects greatly the fuel distribution near the spray and this cannot be represented by single-component fuel models [55]. Therefore, multi-component evaporation models have been of much interest in engine CFD simulations.

Zhu and Reitz [103] employed the thermodynamics of continuous systems to treat liquid mixtures and developed a continuous multi-component (CMC) model for engine applications. In their model, the liquid composition and the consequent properties were represented and described by continuous probability density functions, i.e. the Γ distribution for both liquid and vapour phases. The distribution function was only a function of the molecular weight of the studied fuel, and its shape was controlled by two parameters. The parameters were chosen so that the calculated distillation curves with the distribution reproduce best the corresponding ASTM D-86 experimental data for the fuel. Relations for the properties of the high-pressure sub- and super-critical vaporization processes were also formulated to consider droplet evaporation under a wide range of engine environments. The model was found to better characterize the characteristics of the droplet vaporization process of complex liquid mixtures.

Since there is only one additional distribution function needed to represent fuel properties, the CMC model enables a reduction of computational load while maintaining the predictability of the complex behaviour of the vaporization of multi-component fuels. However, when it is applied to combustion simulations, especially with detailed chemistry, it is difficult to model the consumption of individual components appropriately. Ra and Reitz [76] proposed a discrete multi-component (DMC) model so that the individual components of the fuel during the evaporation process can be tracked and thus can be coupled with corresponding reaction kinetics. In the DMC model, the Dirac delta function was used to represent the general distribution function for the composition of the discrete fuel mixture system. An explicit expression for the heat flux from the surrounding gas to the droplet–gas interface was also derived. The inter-diffusion of fuel vapour and the surrounding gas were taken into consideration. The model was successfully implemented into a multi-dimensional

CFD code for engine combustion simulations, and improved results of combustion characteristics and emissions were seen.

It should be noted that for simplicity in all these evaporation models, fuel vapour is assumed to be uniformly distributed in the computational cell containing the drop, and thus, a potential mesh dependency from the evaporation models is introduced. But this dependency is usually not as severe as those caused by spray and collision models in practical simulations due to a large number of drops in the cell.

Combustion Modelling

In engine environments, the combustible mixture is subject to a turbulent flow and once mixed undergoes subsequent elementary reactions which convert the fuel vapour to complete and incomplete combustion products with the accompanying release heat. So, in diesel engine simulations, combustion modelling mainly deals with two processes: low-temperature chemistry leads to auto-ignition and produces intermediate species, and second, these intermediate species trigger high-temperature reactions that contribute to the main heat release, as well as further complete and incomplete combustion products. Another important task for combustion models is to properly account for the significance of the effect of turbulence on the combustion processes. Various combustion models have been proposed for engine simulations under a variety of operating conditions. This section reviews two combustion models widely used in diesel CFD simulations, the shell/characteristic time combustion (CTC) model, and direct integration of chemical kinetics. Since the k–ε turbulence model still plays a dominant role in multi-dimensional engine CFD simulations, it is the basis of the present discussion of the combustion models. For other turbulence models, such as LES, the reader is referred to the relevant literature, such as a general diesel combustion model formulated in the context of LES, proposed by Hu [35].

Shell/CTC Model

The shell/CTC model is a widely used combustion model due to its simplicity (thus efficiency) and acceptable accuracy for conventional diesel combustion. Its tunable model constants extend its applicable range without sacrificing physical sense. This makes the model very attractive and useful for solving engineering problems. The model involves two sub-models: the shell model which simulates the auto-ignition of hydrogen fuels and the CTC model which calculates the species conversion rate and main heat release of high-temperature reactions.

Based on the theory of chemical kinetics, the reaction rate of elementary gas-phase reactions can be described in Arrhenius form. However, a single general Arrhenius expression for a single generic reaction is not able to describe the complex cool flame and two-stage ignition phenomena that are observed during the auto-ignition

of hydrocarbon fuels, and thus, multi-step reactions are normally required. The shell model [27] employs multi-step generic reactions to predict the auto-ignition of hydrocarbon fuels, and it was implemented into engine simulations with some modifications by Kong and Reitz [44].

The shell model consists of five generic species and eight generic reactions of the form

$$
\begin{aligned}
&\text{(a)}\quad \mathrm{RH} + \mathrm{O_2} \xrightarrow{K_q} 2R^* \\
&\text{(b)}\quad R^* \xrightarrow{K_p} R^* + P + \text{Heat} \\
&\text{(c)}\quad R^* \xrightarrow{f_1 K_p} R^* + B \\
&\text{(d)}\quad R^* \xrightarrow{f_4 K_p} R^* + Q \\
&\text{(e)}\quad R^* + Q \xrightarrow{f_2 K_p} R^* + B \\
&\text{(f)}\quad B \xrightarrow{K_b} 2R^* \\
&\text{(g)}\quad R^* \xrightarrow{f_3 K_p} \text{Termination} \\
&\text{(h)}\quad 2R^* \xrightarrow{K_t} \text{Termination}
\end{aligned}
\tag{16.13}
$$

The five generic species RH, R^*, B, Q, and P represent fuel, radicals formed from the fuel, branching agents, labile intermediate species, and oxidized products, respectively, and O_2 is oxygen. In the shell model, reaction (a) initializes the ignition process. The formed radicals then undergo propagation via reactions (b) to (e). Reaction (f) degenerates the branching process that converts the intermediate species B to the branching agent R^*, and R^* is terminated in reactions (g) and (h). Special care was taken to maintain the build-up of the branching agent B in Kong and Reitz's study [44], and it was shown that the reaction rate of reaction (d) limits the subsequent chain branching and it was the most influential factor on the predicted ignition delay. The model constant f_4 is therefore usually tuned to match experimental data. Although turbulence is not considered to directly affect the reaction rates in the shell model, the indirect influence of turbulence is reflected through the local concentrations of the involved species due to turbulent transport.

The shell ignition model is used only for low-temperature chemistry. Once a prespecified temperature, i.e. ~1000 K, is reached, it is deemed that the ignition stage is completed and the subsequent high-temperature reactions are then simulated using the CTC model. Extending the use of the CTC model which was originally developed for SI engine modelling [3], Kong et al. [45] combined the shell ignition model and the CTC model to simulate the overall combustion processes in a diesel engine. With this combustion model, the species conversion rate is calculated based on the thermodynamic equilibrium value of its mass fraction and the characteristic time to reach such equilibrium, expressed as

$$\frac{\mathrm{d}Y_m}{\mathrm{d}t} = -\frac{Y_m - Y_m^*}{\tau_c} \tag{16.14}$$

In the equation, Y_m is the mass fraction of species m and $Y_m{}^*$ is the local and instantaneous thermodynamic equilibrium value of the mass fraction. The characteristic time τ_c is assumed to be the same for the seven species (fuel, O_2, N_2, CO_2, CO, H_2, and H_2O) considered, and it is the sum of a laminar timescale τ_l and a turbulent timescale τ_t, given by

$$\tau_c = \tau_l + f\tau_t \tag{16.15}$$

The laminar timescale τ_l is derived from a single-droplet auto-ignition experiment of Arrhenius form, which represents the chemistry timescale of the overall reaction that converts the fuel to combustion products. In Eqs. (16.14) and (16.15), it is seen that the role of turbulence in the combustion is introduced through the timescale τ_t. In other words, turbulence mixing determines how fast a species m approaches its equilibrium state. Using the k–ε turbulence model, the turbulence timescale τ_t is related by the eddy turnover time

$$\tau_t = C_2 k/\varepsilon \tag{16.16}$$

where C_2 is a model constant of an order of 0.1, which is tunable to better match measured engine pressure traces and heat release data, as well as emissions which are determined by the species conversion rates. The progressive influence of turbulence on combustion after ignition has occurred is accounted for using a delay coefficient f of Eq. (16.15), and it is given by

$$f = \frac{1 - \mathrm{e}^{-r}}{0.632} \tag{16.17}$$

where r is the ratio of the amount of products to that of total reactive species (i.e. all except N_2), and it is an indicator of the completeness of combustion.

By tuning the aforementioned model constants against experiments, the shell/CTC model can provide satisfactory overall results (pressure trace and heat release rate) in parametric studies of diesel engines. Its relative simplicity and acceptable accuracy, particularly the high computational efficiency, have favoured its widespread use in engine optimization studies for conventional diesel combustion [82]. However, recent research [85] has shown that the performance of the shell/CTC model deteriorates when the combustion mode of a diesel engine enters the region of low-temperature premixed combustion (LTC) in which the effect of chemistry dominates. This is largely due to the oversimplified chemical kinetics, such that the shell/CTC model is not able to predict reasonable trends of unburned hydrocarbons (UHCs), carbon monoxide (CO), as well as other intermediate species of interest.

Direct Integration of Chemical Kinetics

In contrast to the shell/CTC model, direct integration of the chemical kinetics resolves the species conversion rates by considering detailed chemistry for modelling engine combustion processes. The solutions provide the combustion source terms in the energy and species transport equations. Turbulence may or may not play a role at the sub-grid scale in the model, depending on if the computational cells are treated as well-stirred reactors (WSRs) or partially stirred reactors (PaSRs).

In a combustion system, a chemical kinetics mechanism is used to define the reaction pathways and the associated reaction rates leading to the change of species concentrations and heat release. An elementary chemical reaction of arbitrary complexity can be represented by

$$\sum_{j=1}^{N} \nu'_{ji} X_j \Leftrightarrow \sum_{j=1}^{N} \nu'_{ji}{}' X_j \quad \text{for } i = 1, 2, \ldots, M \tag{16.18}$$

where ν'_j and $\nu'_j{}'$ are the stoichiometric coefficients of the reactants and products, respectively, and X is the arbitrary specification of all chemical species for the M reactions. Since a species is usually involved in multiple reactions in a chemical kinetics mechanism, its production rate is the sum of its consumption and generation rates in the associated reactions, which can be expressed by a set of ODEs, given as

$$\frac{\mathrm{d}[X_j]}{\mathrm{d}t} = \sum_{i=1}^{M} \left(\nu''_{ji} - \nu'_{ji}\right) \left(k_f \prod_{j=1}^{N} [X_j]^{\nu'_{ji}} - k_r \prod_{j=1}^{N} [X_j]^{\nu''_{ji}} \right) \quad \text{for } i = 1, 2, \ldots, M \tag{16.19}$$

where $[X_j]$ is the concentration of species X_j, and k_f and k_r are the forward and reverse rate coefficients for the ith elementary reaction, which are a function of temperature T and take the Arrhenius form as follows.

$$k = \mathrm{AT}^{-b} \exp(-E/\mathrm{RT}) \tag{16.20}$$

In the expression of the reaction rate coefficients, the constants A, b, and E are the pre-exponential factor, temperature dependence factor, and activation energy, which are determined from experiments, and R is the universal gas constant. In a chemical kinetic mechanism, the reaction rate coefficients can range over several orders of magnitude. Also due to the nonlinear Arrhenius expression, the direct integration of the chemical kinetics model usually involves solving a very stiff system of ODEs. This increases the computational effort considerably when a large number of species are included in the model.

The CHEMKIN code [43] is the most popular chemistry solver for the chemical kinetics problems described above for engine CFD codes [46], and its performance relies heavily on its ODE solver (DVODE). As compared to the shell/CTC model, the direct integration of chemical kinetics can increase the computational expense by an order of magnitude depending on the size of the chemical kinetics mechanism. A complete list of reactions that describe the chemical kinetics of even simple hydrocarbon fuels normally involves thousands of species and reactions. Solving a chemical kinetics mechanism of this size for every computational cell would make the computational time unacceptable. Thus, skeletal mechanisms (containing the order of 100 species and reactions) that are derived from their corresponding detailed mechanisms are usually employed to save computational expense while maintaining prediction accuracy. Other efforts for increasing the computational efficiency of the direct integration of the chemical kinetics approach are discussed in Sect. 16.8.

As stated above, if a computational cell is treated as a well-stirred reactor (i.e. perfectly mixed fuel–air), no turbulence effect on combustion rate is considered in the sub-grid scale. This assumption is effective in modelling homogeneous charge compression ignition (HCCI) engine combustion [46]. For conventional diesel combustion, the reaction rate coefficients of a few elementary reactions are allowed to be tuned with the justification that uncertainties of these coefficients may result from the reduction of chemical kinetics mechanism and other experimental uncertainties. It has also been shown in many studies [47] that this approach also performs very well under conventional diesel combustion conditions. To account for turbulence–chemistry interactions when the approach of direct integration of chemical kinetics is applied to study diesel combustion, the computational cells can also be assumed to be just partially stirred. The basic idea and physical meanings of the PaSR are similar to those of the CTC model. In the PaSR model, a "segregation" factor that is formulated by considering the turbulence and chemistry timescales is used to account for the imperfect, unresolved molecular diffusion processes in the reactor. The reader is referred to the studies of [63] and Tao and Chomiak [92] for more details.

Beyond the two combustion models discussed above, many other combustion models have been proposed for engine simulations. The major differences between the models are the treatment of the role of turbulence in the combustion process, the description of the flame structure, and the use of chemical kinetics. For instance, in the eddy breakup (EBU) model [89] and its variants the eddy dissipation model (EDM) [57] and the hybrid EBU/Arrhenius model (such as the CTC model), the burning rate of combustible mixture is mainly determined by the turbulent mixing rate, instead of by the rate of chemical reactions. The turbulence timescale is usually used as the control parameter of the mean chemical conversion rate in these models, which is characterized by the breakup or turnover time of turbulence eddies. However, with the direct integration of the chemical kinetics approach, it is normally assumed that the turbulent mixing rate is ultra-fast and thus the burning rate of the mixture is largely controlled by the chemical kinetics of the reactions. Using flamelet models, the structure of a turbulent flame is described as a laminar flame subject to the same

aero-thermo-chemical conditions and the primary effect of turbulence on combustion is to increase the effective flame surface area. For the non-premixed combustion in diesel engines, the representative interactive flamelet (RIF) model [71] is a very attractive approach that decouples chemical kinetics and turbulence, while maintaining tight local coupling between chemical kinetics and molecular transport [32]. Although not used widely, the conditional moment closure (CMC) model [20] and the probability density function (PDF) methods [102] have also been proposed for engine combustion simulations.

Many studies have been conducted to evaluate or compare these combustion models for engine simulations. The general conclusions are that none of them can perform equally well over the entire range of engine conditions of interest and it is necessary to tune the model constants while maintaining their physical meanings to expand the range of applicability of combustion models. For example, in a recent study by Singh et al. [85], the shell/CTC, RIF, and direct integration with detailed chemistry combustion models were compared against optical diagnostic data for multi-mode combustion in a heavy-duty DI diesel engine. They showed that all three combustion models gave reasonable predictions of the cylinder pressure and heat release rate trends for the investigated cases, and the direct integration with the detailed chemistry model performed better under low-temperature and premixed combustion modes, as expected. Since each model has its applicable ranges, it is thought that their combinations may help to extend their applicability. Efforts to develop a hybrid or universal combustion models are described in the study of Tan et al. [91]

Pollutant Emission Modelling

In-cylinder pollutant reduction by optimizing the combustion system helps the engine industry to meet more and more stringent emission standards. Therefore, reliable emission modelling in an engine CFD code is essential for its practice use in engine design and development. For a conventional diesel engine, nitric oxide (NO_x) and soot emissions are the pollutants of most concern. For advanced combustion concepts, such as HCCI, it has been demonstrated that both NO_x and soot emissions are substantially reduced, but with the price of increased carbon monoxide (CO) and unburned hydrocarbon (UHC) emissions. This section reviews the most widely used models and surveys methods for the predictions of these emissions in multi-dimensional CFD codes.

NO_x Modelling

The formation of NO_x in a diesel engine is primarily determined by the local temperature, oxygen concentration, as well as residence time. Consequently, to predict well

engine-out NO_x emissions requires that all three aspects are accurately resolved in CFD modelling and a good chemical kinetics model is also crucially necessary. With an extensive understanding of its chemical kinetics, quantitative prediction of NO_x formation becomes possible with engine CFD codes that include detailed chemistry. The thermal NO_x reactions include

$$\begin{aligned} &(1) \quad O + N_2 \Leftrightarrow NO + N \\ &(2) \quad N + O_2 \Leftrightarrow NO + O \\ &(3) \quad N + OH \Leftrightarrow NO + H \end{aligned} \tag{16.21}$$

However, four different routes, including the thermal route, the prompt (Fenimore) route, the N_2O route, and the fuel-bound nitrogen route have been identified as important in the formation of NO_x [17]. Petroleum fuels contain negligible nitrogen, and thus, the fuel-bound nitrogen route is usually not considered in engine CFD simulations. It is also noted that in engine simulations, the quantity of NO_x is normally represented by NO, and a scale factor of 1.533 (the ratio of the molecular weight of NO_2 to NO) is used to convert NO to NO_x, which is consistent with ASTM standards. The extended Zeldovich mechanism [33] for the thermal NO, as formed by the three elementary reactions in Eq. (16.21), describes the chemical kinetics of NO formation at high temperatures. The extended Zeldovich mechanism has been well adopted in engine simulations, especially for conventional diesel engines in which the in-cylinder gases are subjected to very high temperatures. However, under rich combustion conditions, the prompt (Fenimore) route of NO formation can be prominent. This is because the radical CH, which is formed as an important intermediate of rich combustion, reacts with the nitrogen to form hydrocyanic acid (HCN), which reacts further to NO [97]. Under low temperatures and lean combustion conditions, the molecular nitrogen N_2 is attacked by O atoms, and with the presence of a third-body molecule, M (which can be any molecule in the system) nitrous oxide (N_2O) is formed and subsequently reacts with O atoms to form NO.

It is obvious that to correctly predict the NO_x emissions of diesel engines operating under a wide range of conditions, the prompt and N_2O routes of NO formation are needed to supplement the thermal route. A complete list of elementary reactions for NO formation involves over a hundred reactions, such as seen in GRI 3.0 mechanism for methane combustion [88] and the extended Leeds methane oxidation mechanism [36]. The size of the detailed mechanism of NO formation is beyond the computer time limit of practical engine CFD simulations, so mechanism reduction is needed. Sun [90] extracted 12 important reactions including four species from the GRI 3.0 mechanism for the description of NO formation. They showed that the reduced NO mechanism performed similarly with the original detailed one under various conditions. In recent research by Sjöberg and Dec [86], a NO_x-induced combustion-phasing runaway phenomenon was found in HCCI engines when testing at high-load conditions. It was attributed to the fact that the combustion phasing was advanced by NO_x contained in EGR and residual gases. The authors have numerically investigated this phenomenon and found that the reaction $HO_2 + NO \Leftrightarrow NO_2 + OH$ plays a

significant role. This indicates that this reaction has to be included in reduced NO chemical kinetics mechanisms to account for its influence on fuel ignition.

Soot Modelling

Soot formation processes in a diesel engine are much more complicated than chemical-kinetic-controlled NO_x formation. It involves both chemical and physical processes, including the chemical kinetics leading to soot precursors (acetylene, benzene, and polycyclic aromatic hydrocarbons (PAHs)), particle nucleation, surface growth, surface oxidation, particle coagulation, and particle dynamics. A complete understanding of the complex phenomena of soot formation is still under experimental exploration, and thus, modelling soot formation becomes very challenging.

For engineering practice, most soot modelling in engine CFD codes usually only considers the chemical process, which directly correlates gas-phase soot precursors with engine-out soot emissions, for example, the two-step soot models. In two-step soot models, two competing processes, namely soot formation and oxidation, are considered of the form

$$\frac{\mathrm{d}M_s}{\mathrm{d}t} = \frac{\mathrm{d}M_{\mathrm{sf}}}{\mathrm{d}t} - \frac{\mathrm{d}M_{\mathrm{so}}}{\mathrm{d}t} \tag{16.22}$$

where M_s, M_{sf}, and M_{so} represent the mass of the net soot produced, soot formed, and soot oxidized, respectively. In the study of Nishida and Hiroyasu [62], two equations of Arrhenius form were used to calculate soot formation and oxidation rates following

$$\begin{aligned} \frac{\mathrm{d}M_{\mathrm{sf}}}{\mathrm{d}t} &= A_f M_{\mathrm{fg}} P^{0.5} \exp\left(-\frac{E_{\mathrm{sf}}}{\mathrm{RT}}\right) \\ \frac{\mathrm{d}M_{\mathrm{so}}}{\mathrm{d}t} &= A_0 M_s \frac{\mathrm{PO}_2}{P} P^{1.8} \exp\left(-\frac{E_{\mathrm{so}}}{\mathrm{RT}}\right) \end{aligned} \tag{16.23}$$

where E_{sf} and E_{so} are given values of 12,500 kcal/kmol and 14,000 kcal/mol. A_f and A_o are determined by calibrating with measured soot emissions.

As seen in the equation, the soot formation rate is directly linked to the concentration of fuel vapour M_{fg}, and the soot oxidation rate is a linear function of the oxygen partial pressure PO_2. This two-step soot model was found to give relatively low peak in-cylinder soot concentrations. Patterson et al. [68] attributed this to the soot oxidation rate equation and thus replaced it with a more realistic soot oxidation model adopted from Nagle and Strickland-Constable [60], in which carbon oxidation occurs by two mechanisms whose rates depend on surface chemistry involving more reactive *A* sites and the less reactive *B* sites. With more understanding of soot formation, the use of fuel vapour as the soot precursor in the formation equation also

became questionable. Also, when detailed chemistry was employed in engine simulations, the fuel vapour can no longer be used as the indicator of soot formation since it soon decomposes to other smaller intermediate hydrocarbons once low temperature occurs. In this context, Kong et al. [47] considered a more realistic soot precursor, acetylene C_2H_2, to replace the fuel vapour in their soot formation formula, and the values of activation energy were changed correspondingly. Due to this simplicity and moderate accuracy, two-step soot models have been widely used in engine CFD codes. It should not be expected to obtain quantitative predictions of soot emissions from such simplified soot models for a wide range of engine operating conditions. However, qualitative descriptions of sooting tendencies can be captured fairly well if the model constants are fine-tuned against existing measured data for the investigated engines.

To improve the soot formation models and also to broaden the range of applicability of soot models, Tao et al. [93] proposed a phenomenological soot model which is based on four global stages: particle nucleation, surface growth, surface oxidation, and particle coagulation. In the first stage, diacetylene (C_4H_2) and naphthalene were used as inception species for soot nucleation. The soot surface growth was described using an active site model proposed by Frenklach and Wang [26]. The Nagle and Strickland-Constable's O_2 oxidation model [60] and Neoh et al.'s OH oxidation model [61] were both used to describe the soot surface oxidation. Finally, soot coagulation was simulated using two empirical equations. This soot model was validated against measured data from n-heptane spray combustion under diesel-like conditions, and the spatial and temporal soot distributions were well predicted. Based on the structure of this phenomenological soot model, Tao et al. [94] further proposed a nine-step soot model for diesel engine simulations, with which successful applications were also reported in their later study for diesel engines operated over a wide range of conditions [95].

Since, as stated above, soot formation in diesel engines involves very complex chemical and physical processes, complete models for these processes in multi-dimensional engine CFD simulations would incur unacceptable computational expenses. For the foreseeable future, phenomenological models can still be very useful. Improvements to these models are needed to better predict the size distribution of engine-out soot emissions to accommodate anticipated demands of meeting stricter legislations.

CO and UHC Modelling

Modelling CO and UHC emission have received growing attention as low-temperature combustion is attracting more interest in diesel applications. CO forms in fuel-rich regions due to low oxidation rates resulting from a large amount of EGR gases needed to suppress the combustion temperature. In addition, CO is found in lean regions that are too cool for complete combustion. The kinetically controlled CO mechanism is well understood, which is fully described in skeletal or detailed

fuel oxidation mechanisms used in engine CFD simulations [67]. The key issue of predicting CO emissions is to have a correctly predicted fuel–air mixing rate. This depends on reliable turbulence and spray models, as well as adequately resolved engine geometries to account for their influence on the flow patterns that secondarily affect the mixing process. UHC is the consequence of the incomplete combustion of fuels. In diesel engines, UHC forms due to both over-mixing and under-mixing of the fuel sprays [33]. Another source to UHC is wall quenching whose influence is largely determined by the degree of spray impingement on the combustion chamber walls. Early injections, which are required to prepare a well-mixed fuel charge, may result in a portion of the injected fuel entering the crevice region from which the trapped fuel can escape the main combustion stage and then re-enter the squish region during the expansion stroke. The escaped unburned fuels finally contribute to the engine-out UHC emissions. It is obvious that to model the complex UHC formation processes, all these possible causes need to be considered. The crevice flow can be simulated using a phenomenological crevice flow model, such as the one proposed by Reitz and Kuo [79] for engine CFD modelling. The crevice flow can be also directly simulated by using an additional crevice mesh attached to the main computational domain. It has been found by the authors' study that the strength of the corner vortex (which affects the mixing rate) caused by the pushed-out crevice flow is sensitive to the width and length of the crevice mesh. This indicates that the geometry of the crevice volume needs to be carefully meshed. The spray–wall interaction model together with the heat transfer model that accounts for heat conduction through the liquid wall fuel film is crucial to model UHC formation due to the wall quenching. They are discussed in the next section.

Heat Transfer Modelling

As discussed in the previous section, heat transfer between in-cylinder flows and cylinder walls can significantly influence engine emissions, such as UHC. In addition, heat transfer also has a substantial influence on engine performance and efficiency. In most cases, convective heat transfer of the gas phase is the main contributor to the heat flux from the in-cylinder flows to cylinder walls. Therefore, convective heat transfer has been of primary interest in engine heat transfer models. However, in a high-temperature environment, especially when a large volume of soot is formed in the cylinder, the heat flux due to radiation becomes very important. Furthermore, if the spray impingement becomes severe, heat conduction due to the resulting fuel film cannot be neglected. An early review of engine heat transfer is found in Borman and Nishiwaki's study [16]. Widely used and newly developed engine heat transfer models for multi-dimensional CFD simulations are briefly reviewed here.

To resolve the details of the gas-phase convective heat transfer in engines, the very thin thermal boundary layers have to be resolved to obtain the velocity and temperature profiles in the near-wall region. This requires the use of a very fine mesh resolution, which can make CFD simulations impractical. A practical way

of removing the requirement for fine meshes while maintaining physically correct predictions of the convective heat transfer is to use velocity and temperature wall functions. The classical temperature wall function was based on assumptions of a steady and incompressible flow without source terms under which the Reynolds analogy is valid. The traditional wall function formulations also use a constant Prandtl number across the entire boundary layer. Han and Reitz [30] pointed out that these assumptions and simplifications were questionable when such wall functions were applied to engines in which the flow compressibility must be considered. A curve-fit technique was employed in Han and Reitz's [30] study to construct a simplified function of dimensionless viscosity to the turbulent Prandtl number. This enabled a direct integration to be performed of the one-dimensional energy equation so that an analytic solution of the temperature profile can be obtained and used for calculating the convective heat transfer. The proposed heat transfer model was applied to SI and DI engines, and satisfactory agreement between the predicted wall heat fluxes and measured data was obtained under both firing and motoring conditions.

As shown in the study of Abraham and Magi [6], the radiant heat loss characteristics are strongly correlated with the soot concentration and temperature in engines. Recent research by Musculus [58] has shown that radiation heat loss has a measurable influence on in-cylinder temperatures and NO_x emissions. The research demonstrates the significance of radiation heat transfer models in engine CFD simulations. The discrete ordinates method (DOM) is a well-adopted method that solves the radiation transfer equation (RTE) for the intensity of radiation in a set of ordinates, and the RTE and its boundary conditions are found in [23]. The summation of the intensity of radiation of each ordinate is substituted into the energy equation, and the effect of radiation heat transfer on the spatial temperatures is thus revealed. For applications of DOM in engine simulations, the studies of Abraham and Magi [6], Wiedenhoefer and Reitz [98], and Yoshikawa [101] are examples. It should be noted that since the in-cylinder soot acts as a blackbody in the radiation heat transfer model, the quantity of soot predicted by the emission model is influential on the calculated radiant heat loss.

With advanced injection timing required to obtain better-mixed fuel–air, an increased amount of injected fuel can impinge on the engine walls due to the low gas density and corresponding long spray penetration. When the liquid fuel films are formed, the convective heat transfer between the gas phase and the liquid phase, the heat conduction between the liquid film and the wall, as well as the energy used to vaporize the fuel must all be considered in engine CFD simulations. The geometrical dimensions of the fuel films, such as their thickness and area, depend on the dynamical characteristics of the impinging sprays and their interactions with the engine walls. The evolution of the fuel films during the engine strokes is affected by the local thermal and dynamical conditions, such as the turbulence strength and wall temperature. A good review on this topic is given by Kong [48]. Jia et al. [40] compared three widely used spray/wall interaction models, i.e. the O'Rourke and Amsden model [66], the Bai and Gosman model [14], and the Han, Xu, and Trigui model [31], for early injected sprays under HCCI-like conditions. They concluded that neither of the models outperformed the others, and all of them need to be further

improved for predictions of the film thickness and the corresponding vapour distribution. The inaccuracy of these models was attributed to the fact that the conditions under which the experiments were conducted for the model derivation and validation are usually different from the actual engine environments.

Efficient Multi-dimensional Simulation of Diesel Engine Combustion with Detailed Chemistry

This section presents three approaches that can be used in the efficient multi-dimensional simulation of diesel engine combustion. The approaches include a newly developed adaptive multi-grid chemistry (AMC) model which allows a fine mesh to be used to allow adequate resolution for the spray simulations, while dramatically reducing the number of cells that need to be computed by chemistry solvers. The second approach to improve efficiency uses recently developed spray models which reduce numerical grid size dependencies, thus enabling the simulation of DI combustion on relatively coarse meshes to save computing time. The third approach parallelizes the chemistry solver based on the computing load so that simulations can be performed on relatively coarse meshes on multiple processors.

Adaptive Multi-grid Chemistry (AMC) Model

As stated before, solving the detailed chemistry in combustion systems is essential to solving groups of extremely stiff ODEs. The numerical time step may be required to be comparable to the smallest characteristic timescale of change of chemical species for reasons of stability and/or accuracy [75]. In a practical engine, CFD simulations with directly solved chemistry by integrating the stiff ODEs, the computational time spent on the chemistry solver can be over 75% of the total running time depending on the size of the chemistry mechanism. This has motivated many efforts for reducing the computational time of chemistry solvers to increase the overall efficiency of multi-dimensional engine CFD modelling with detailed chemistry. These efforts include replacing the time-consuming direct integration by using more efficient search methods based on tabulated combustion chemistry, such as the in situ adaptive tabulations (ISATs) proposed by Pope [73], using a semi-implicit ODE solver to reduce the integration time, as proposed by Liang et al. [53], adaptively determining the size of chemical kinetic mechanism for different combustion stages [54], and multi-grid or multi-zone techniques.

The multi-grid or multi-zone techniques have achieved great success for certain classes of problems [12, 13, 24]. It was reported that an order of magnitude timing reduction was obtained for HCCI engine combustion. Shi et al. [83] extended the use

of the multi-grid technique to simulate direct injection (DI) engines and proposed an adaptive multi-grid chemistry (AMC) model which is discussed next.

The basic idea of multi-grid techniques is to group thermodynamically similar (in terms of pressure, temperature, species composition) cells in engine combustion simulations to reduce the calling frequency to the chemistry solver. Two key steps are involved: (1) mapping (grouping) eligible cells together and solving the grouped cells with the chemistry solver, and (2) redistributing the group information back onto individual cells so that the gradients can be preserved.

The Adaptive Multi-grid Mapping Technique

The key to mapping appropriate cells into a group is to find appropriate measures of similarity, as well as to establish the grouping criteria. In a computational cell assumed to be a WSR, the temperature, pressure, and species fractions describe the composition space that determines the reaction progress. Due to the temperature sensitivity of chemical reactions, it is obvious that temperature should be used as one of the grouping criteria. In the low Mach number flows typical of DI and HCCI engines, pressure gradients are small, and thus, the pressure is not needed as a grouping criterion. Strictly grouping cells with similar composition requires a search and comparison for every individual species, but this is not practical because of two concerns. Firstly, the search expense would be too large and thus would reduce the computational efficiency of the multi-grid model. Secondly, it is difficult to define an appropriate criterion of similarity for each species and thus to efficiently group as many cells as possible. Hence, it is necessary to define an indicator that represents both composition information and combustion progress. The so-called progress equivalence ratio [13] is introduced, which is defined by

$$\phi = \frac{2C^{\#}_{-CO_2} + \frac{H^{\#}_{-H_2O}}{2} - z'C^{\#}_{-CO_2}}{O^{\#}_{-CO_2-H_2O} - z'C^{\#}_{-CO_2}} \tag{16.24}$$

In this equation, the superscript # denotes the number of atoms of each species. The equivalence ratio is defined based on complete combustion, but the products CO_2 and H_2O are excluded, as indicated by the subscripts in the ϕexpression. z' defines the proportion of fuel oxygen to fuel carbon, and for hydrocarbon fuels without oxygen, z' is zero. For DI engines, because significant gradients of species mass fraction can exist, there is no guarantee that cells with similar equivalence ratios contain similar mass fractions of each species, especially for those cells that are distributed in very different physical locations. Therefore, it is necessary to limit the searching area to better group cells that have similar species composition. Due to convection and diffusion, neighbour cells can have similar thermodynamic conditions, as well as species composition. In particular, in the early stages of combustion when large gradients, for example, temperature gradients exist, the similarity may merely exist among closely adjacent cells and therefore the grouping process needs to be limited

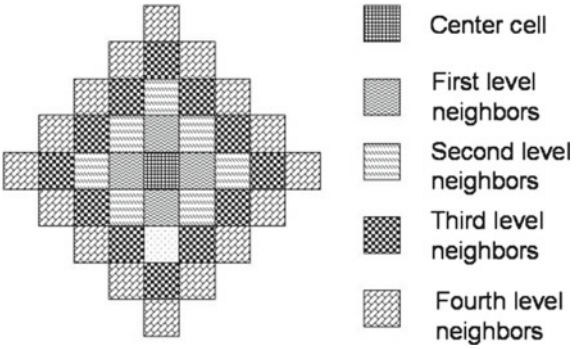

Fig. 16.1 Adaptive multi-grid grouping. Adapted from [83]

to a narrow region. However, as time progresses energy and species are transported and mixed such that there is a trend towards local uniformity. Correspondingly, the grouping process can be extended to larger and larger regions. This means that the grouping region should be determined adaptively.

Accordingly, a temperature inhomogeneity criterion was used as the indicator for assessing the grouping region adaptively, where

$$\sigma_T = \sqrt{\frac{1}{n-1}\sum_{i=1}^{n}\left(T_i - \overline{T}\right)^2} \tag{16.25}$$

In Eq. (16.25), $\overline{T}$ denotes the average in-cylinder temperature and T_i is the individual temperature of each of the n cells. The concept of adaptive neighbour search is further illustrated in Fig. 16.1 using a 2-D schematic mesh. It can be seen that the first-level search only covers the four adjacent cells (six if 3-D mesh) of the reference cell. If the in-cylinder temperature inhomogeneity is below prespecified values, the search can then be expanded to the second level or higher. The maximum search level was limited to four, where a maximum of 129 cells can be reached using the fourth-level search in 3-D block structural mesh. It should be noted that a similar treatment could also be applied to unstructured meshes. In this case, a convenient approach would be to predefine a representative search radius and to define the search level as a multiplier used to adjust the search area accordingly.

In the research of Shi et al. [83], it has been found that for HCCI engines the grouping procedure can also be applied regardless of the location of the cells as long as they are thermodynamically similar. This is to say the search can be applied to the whole computing domain. This is due to the assumption of homogeneous charge in the simulation of HCCI engines. In contrast to the neighbour mapping, it is referred to as global mapping. Similar to specifying a criterion of temperature inhomogeneity for the neighbour mapping, by defining a lower value of temperature inhomogeneity global mapping can be regarded as a fifth-level search, although in this case the location of the cells is no longer used as an additional criterion.

Remapping Technique

After the cells are mapped into a group and the group is allowed to react using the averaged conditions, it is not possible to exactly remap the mass fractions of each species back onto the original cells, because that requires solving the complete chemistry for each cell. Thus, an algorithm is needed to redistribute the species back to the cells, such that the gas properties of each cell remapped from the group would be comparable with those if the chemistry of each cell were to be solved individually.

A straightforward way of remapping the information of groups back onto their cells is to assign the mean value of the group's characteristics to each included cell. This means that all the cells in a group would have the same gas properties. This procedure would introduce artificial diffusion to the species continuity equations if significant composition gradients were present among the grouped cells. This relatively inaccurate method has proven to be inapplicable even for HCCI simulations [83].

Babajimopoulos et al. [13] proposed an improved method that attempts to preserve gradients of temperature and species composition. The method is described as follows. First, before the mapping procedure, a new quantity, ch, is defined using the number of C and H atoms of all participating species, except the combustion products, CO_2 and H_2O, where

$$\mathrm{ch} = 2\mathrm{C}^{\#}_{-\mathrm{CO}_2} + \frac{\mathrm{H}^{\#}_{-\mathrm{H}_2\mathrm{O}}}{2} \tag{16.26}$$

The ch number of a group is the sum of the ch number of all cells in that group. After the chemistry calculation, all species, except CO_2, H_2O, O_2, and N_2, are assigned back to the group's cells based on ch. In this case, the mass of species k in an individual cell is obtained from the ratio

$$m_{k,\mathrm{cell}} = m_{k,\mathrm{group}} \frac{\mathrm{ch}_{\mathrm{cell}}}{\mathrm{ch}_{\mathrm{group}}} \tag{16.27}$$

In this way, the mass of each species in the group is also conserved. Consequently, some cells can have more or fewer C or H atoms than before the mapping process, and thus, the rest of the cells in the group need to be adjusted to maintain the total number of C and H atoms in that group. After that, O_2 is distributed to maintain the total number of O atoms in each cell, and an adjustment of N_2 is used to conserve the mass of each cell. Since after the remapping process the mass fraction of each species in each cell is known, the change of the specific internal energy of each cell can be obtained from the difference between the internal energy of formation of the species present in the cell before the grouping process and that after the remapping process. The cell temperature can be computed from the updated specific internal energy and the mass fraction of species. This method is called the gradient-preserving remapping method.

Mesh-Independent Spray Models

The increased application of computational fluid dynamics to combustion problems incorporating detailed chemistry and the desire for rapid generation of results causes a need to use coarser computational meshes. Furthermore, as CFD is applied to a wider range of applications from small-bore light-duty engines to large-bore ship engines, the solutions must be able to yield accurate results over a wide range of grid sizes.

The requirement of short run-times and the resulting use of coarse computational grids pose a problem for the solution of the spray physics because the drop sizes are often orders of magnitude smaller than the size of a computational cell. Because the spray is not completely resolved on the computational mesh, sub-grid spray models are required to describe the physics associated with the injection event.

The solution to spray problems involves modelling a two-phase flow process and thus includes the complications of dealing with the interfaces between interacting fluids. In the fuel injection process, the droplets make up the liquid phase and the entrained air and vaporized fuel make up the vapour phase. Figure 16.2 shows the conceptual spray process presented by Abani et al. [2]. As discussed previously, a popular solution method is the Lagrangian-drop and Eulerian-fluid (LDEF) approach first presented by Dukowicz [22].

Severe mesh dependency has been observed in the calculation of droplet drag using the LDEF approach. In the standard LDEF implementation in engine CFD codes, such as KIVA, the particle relative velocity is defined as the difference between the particle velocity and the gas-phase velocity at the nearest node. When coarse computational grids have been used, the size of the cell is much larger than the area occupied by the spray resulting in a dampening of the momentum transfer between the droplets and the surrounding gas phase. The poor prediction of the momentum coupling results in an under-prediction of the gas-phase momentum and a resulting under-prediction of the spray penetration. This problem is most severe in the near-nozzle region where the droplets are very close together and occupy only small portions of the Eulerian mesh. Figure 16.3 from Abani et al. [2] depicts the damping of momentum transfer due to inadequate mesh resolution. Abraham [5] showed

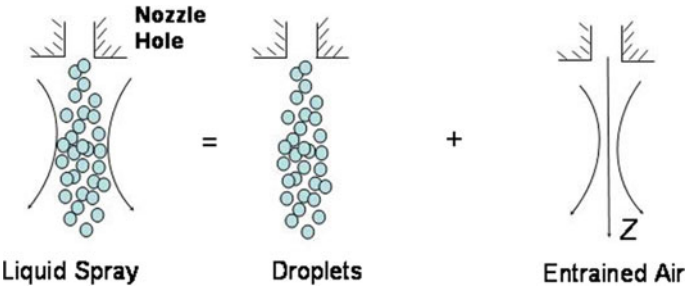

Fig. 16.2 Schematic of spray process. Adapted from [2]

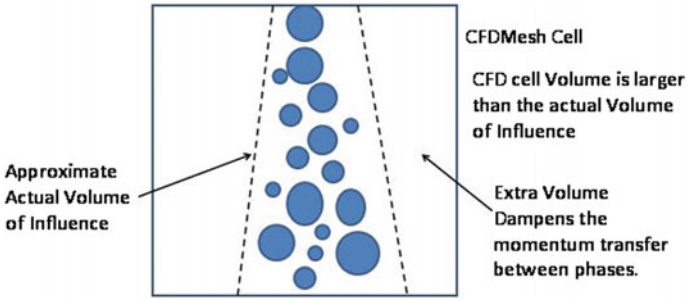

Fig. 16.3 Illustration of damping of momentum transfer due to inadequate mesh resolution. Adapted from [2]

that accurate modelling of the near-nozzle region required grid resolution on the order of the orifice diameter. However, it is not feasible from a computational time standpoint to solve engine problems on such a fine mesh. Furthermore, a fundamental assumption of the LDEF approach is that the volume fraction of droplets in each cell is small; i.e. the void fraction is near one. The use of near-droplet size meshes may violate this assumption. Therefore, it is of much interest to investigate methods that allow accurate spray simulation without using an exceedingly fine grid size. The method used in this investigation was proposed by Abani and Reitz [1] where the droplets are solved traditionally while the entrained air is modelled using turbulent gas-jet theory.

Further grid size dependency exists in LDEF spray simulation in the widely used O'Rourke collision model [64, 65]. In the O'Rourke model, collisions are only considered between droplets that are located in the same collision cell. For simplicity, the Eulerian CFD cell is often taken to be the collision cell. Thus, a change in the CFD mesh size results in a change in the possible number of collisions. Schmidt and Rutland [80] have shown that the use of a separate collision mesh greatly reduced mesh dependency in spray problems. In the present implementation, the approach of Munnannur [59], where a radius of influence (ROI) that is not based on the cell size, is adopted to assign possible collision partners for each parcel.

Gas-Jet Spray Model

Abani et al. [2] showed that mesh size dependency can be reduced by using turbulent gas-jet theory to model the air entrained by the injected fuel. Their approach was to assume that the relative velocity between a droplet and the gas phase was equal to that between the droplet and a turbulent gas jet with the same mass and momentum as that of the injected fuel. This approach imposes the axial component for the gas-phase velocity as a function of distance from the nozzle in the near-nozzle region, which is used in the droplet acceleration equation given by:

$$\frac{\mathrm{d}U}{\mathrm{d}t} = \frac{3}{8} C_D \frac{\rho_g}{\rho_l r_d} \left| U - V_{\mathrm{gas}} \right| \left(U - V_{\mathrm{gas}} \right) \tag{16.28}$$

Here, U is the droplet velocity vector, C_D is the droplet drag coefficient and is a function of Reynolds number, ρ_g and ρ_l are the gas- and liquid-phase densities, respectively, r_d is the droplet radius, and V_{gas} is the gas-phase velocity vector given as $V_{\mathrm{gas}} = (V_x, Vy, Vz)$ where V_y and V_z are components perpendicular to the spray axis and obtained from the Eulerian gas-phase solution. Finally, V_x, the axial component of the gas-phase velocity, is found from gas-jet theory [4] as:

$$V_x = \min \left\{ U_{\mathrm{inj}}, \frac{3 U_{\mathrm{inj}} d_{\mathrm{noz}} \sqrt{\frac{\rho_l}{\rho_g}}}{K_{\mathrm{entr}} x} \left[\frac{1}{\left(1 + \frac{12 r^2}{K_{\mathrm{entr}}^2 x^2} \right)^2} \right] \right\} \tag{16.29}$$

where U_{inj} is the effective injection velocity, d_{noz} is the nozzle diameter, K_{entr} is a model constant taken to be 0.7 as suggested by Abani et al. [2], x is the position downstream of the nozzle on the spray axis, and r is the radial position ($r^2 = y^2 + z^2$).

Grid-Independent Collision Model

Munnannur [59] reduced grid size dependencies of the O'Rourke collision model by employing a radius of influence (ROI) method. The ROI is a distance around a parcel that contains other possible collision partners, thus allowing mesh-independent collision calculations without the added complexity of a separate collision mesh. The droplets are then allowed to collide with any other droplet within their collision volume regardless of what CFD cell the droplet is located in.

Furthermore, Munnannur [59] implemented a method for merging parcels to reduce the computational time required in the collision calculations based on the method presented by Lapenta [49]. Simple binary merging cannot conserve mass, momentum, and energy simultaneously; however, a ternary merge followed by a binary split allows the conservation of mass, momentum, and energy. In that, implementation parcels in a collision volume are sorted by ascending mass, next the velocities of each group of three neighbouring parcels in the mass sorted list are compared using Eq. (16.30), and finally, groups of parcels having velocity errors $\varepsilon_{\mathrm{vel}\,i,j}$ less than 0.1 are merged into two parcels, where

$$\varepsilon_{\mathrm{vel}\,i,j} = \frac{\left| u_i - u_j \right|}{\left| u_i \right| + \left| u_j \right|} \tag{16.30}$$

Code Parallelization

As the cost of computers dramatically decreases, code parallelization becomes a very effective approach to saving computing times in engine CFD simulations. Traditional parallelization of CFD codes is based on domain decomposition, i.e. evenly distribute the total number of computational cells to the available processors. However, under some circumstances, cells that have to be computed using the chemistry solver are not homogeneously distributed in space. For instance, the cells that have lower temperature or lower concentration of combustible species than a specified criterion can be skipped. Even though they may be distributed evenly in space, the computing time of integrating the stiff ODEs that describe the chemical reactions might be very different because of their different stiffnesses. In some cells, the ODEs may be stiffer and thus require more iterations than other cells. This indicates that a load-balancing strategy is needed to improve the parallelization efficiency. A good load-balancing scheme has to keep the processors doing useful computations for as much of the time as possible, i.e. to minimize the waiting time of all processors. A load-balancing scheme that is based on historical uses of computing resources is described below [84].

When a detailed reaction mechanism is solved in a CFD code, most of the CPU time is spent on that part. In addition, the communication time of the input and output data of chemistry solvers is small in the overall simulations. Therefore, usually, only the chemistry computation is parallelized. In the load-balancing parallel scheme, before the chemistry solver is called, all cells that need to be computed using the chemistry solver are listed. In the initial step, those cells are evenly assigned to the available processors. Then, the time required by a processor can be defined as the ratio of the number of cells computed by this processor and the CPU time taken in the previous time step:

$$P_i^{n+1} = \frac{N_{\text{ckcell},i}^n}{t_i^n} \tag{16.31}$$

where superscript n denotes the time step and subscript i indicates the ith processor. Starting from the next time step, the cells can be assigned based on the time spent in processor P_i^{n+1}:

$$N_{\text{ckcell},i}^{n+1} = \frac{P_i^{n+1}}{\sum_{i=1}^{N_{\text{cpu}}} P_i^{n+1}} N_{ck} \tag{16.32}$$

in which N_{ck} is the total number of cells required in the chemistry computation. In this way, a dynamic balance between the processors is achieved. To smooth the process, a relaxation factor, α, is introduced in Eq. (16.33) as

$$P_i^{n+1} = \alpha P_i^n + (1-\alpha)\frac{N_{\text{ckcell},i}^n}{t_i^n} \tag{16.33}$$

The load-balancing scheme is also especially useful for heterogeneous computer clusters with a different machine hardware.

The implementation of the parallel code was tested on an HSDI engine. Figure 16.4 shows the CPU time consumed by each node at each time step in parallel computations. The left column uses 3 processors, and the right column uses 4 processors. The first row uses the conventional domain decomposition method. As aforementioned,

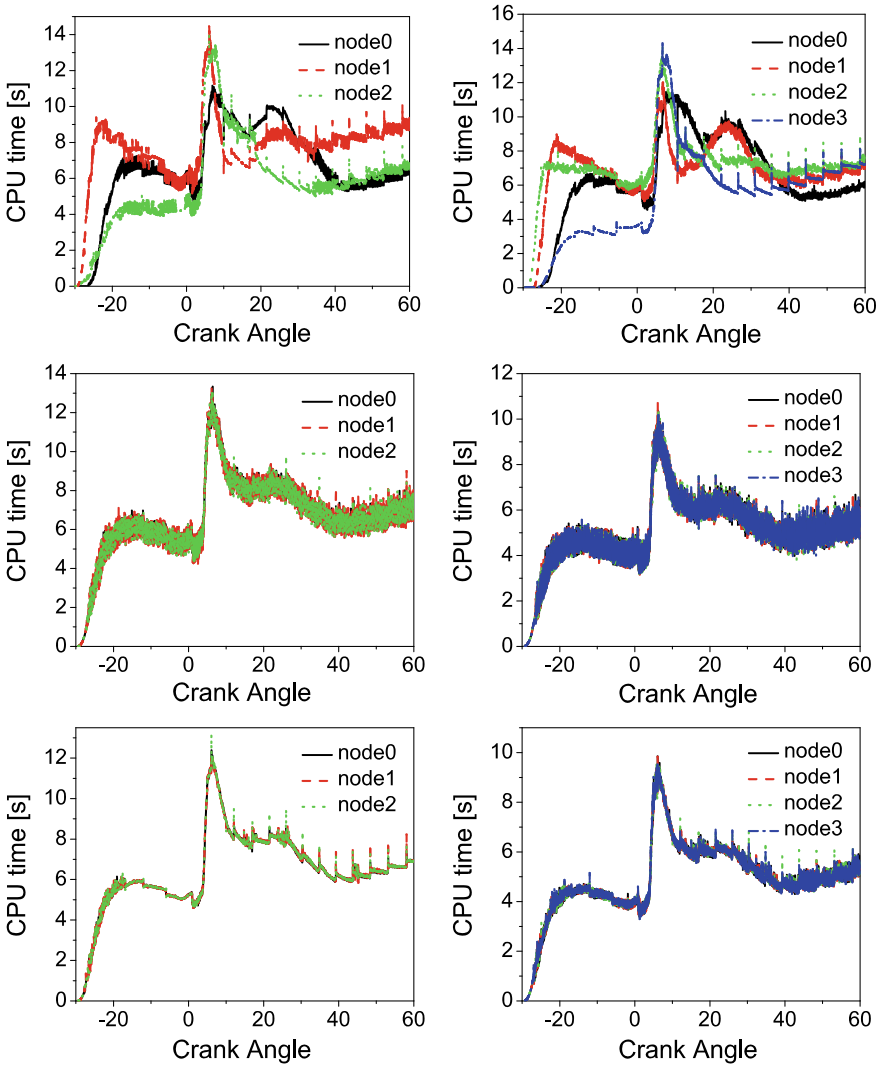

Fig. 16.4 CPU time consumed by each node with different schemes—top: domain decomposition; middle: load balancing without relaxation factor ($\alpha = 0$); bottom: load balancing with relaxation factor $\alpha = 0.5$. Left column: 3 CPUs; right column: 4 CPUs

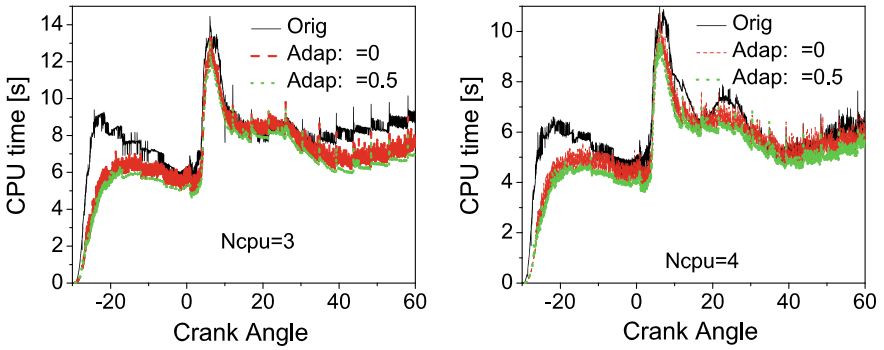

Fig. 16.5 Profile of the longest time the processors consumed (bottleneck time) at each time step

the computation load is not well scaled. In the beginning, the combustion mainly occurs in the central region of the combustion chamber. Therefore, the processor(s) in the middle array, which is the dashed line in the left column, and the dashed line and dotted line in the right column, need(s) more CPU time to complete the job(s). As the main combustion region expands, the CPU time consumed by the processors varies and is not well scaled.

The second and third rows employ the load-balancing scheme described above. The second row does not consider the relaxation factor, i.e. $\alpha = 0$. The CPU time of the processors is well scaled but subject to significant fluctuation. With the implementation of the relaxation technique, these fluctuations are successfully removed, as illustrated in the third row of Fig. 16.4. Better scalability is then achieved. Figure 16.5 summarizes the longest time that the processors consumed at each time step, and this is the bottleneck time of all the processors. The area under the curve is the total wall time of the parallel computation. Compared to the original domain decomposition method, the current load-balancing scheme greatly improves the efficiency and scalability of the parallel code. The relaxation technique works very well with the load-balancing scheme.

CFD Codes for Engine Simulation

The increasing confidence in using CFD techniques in engine designs depends on continuously improved CFD codes in terms of their fidelity and ease of use. Two pioneering works including the KIVA family of CFD codes (developed at Los Alamos National Laboratory (LANL) in the USA) and the STAR-CD family of CFD codes (developed at Imperial College in Great Britain) have made tremendous contributions in bringing CFD techniques to engine simulations. Both of these codes are being continuously developed by researchers worldwide, and their efforts have yielded many innovative models whose applications also have benefited other engineering

areas, such as turbines and ramrockets. Since its initiation, the KIVA code has been kept in an open-source form, which facilitates its further developments. Recently, another open-source CFD code, OpenFOAM, has attracted increasing interest from the engine community. STAR-CD has become commercial software offered by CD-adapco. The other main competitors in commercial engine CFD software are FIRE, FLUENT, and VECTIS. All of these CFD codes are briefly reviewed here.

Open-Source Codes

KIVA has evolved from its original release in 1985 to its latest version KIVA 4. The family contains KIVA (1985), KIVA II (1989), KIVA 3 (1993), KIVA 3 V (1997), KIVA 3 V release 2 (1999), and KIVA 4 (2006). KIVA is developed in the FORTRAN language, and the detailed description of its governing equations, numerical schemes, and the original sub-models can be found in the KIVA II report [8]. The KIVA II code enhanced its preceding versions by improving its computational accuracy and efficiency and ease of use. The KIVA II equations and numerical solution procedures are more general so that they can be applied for various studies of reaction flows. The meshing methodology of KIVA II prevented it from efficiently solving flows in complex geometries. Thus, KIVA 3 was developed to overcome this drawback by introducing a block-structured mesh with connectivity defined through indirect addressing, and a corresponding efficient storage method was introduced [9, 10]. In 1993, the KIVA 3 V code was released with a special focus on treating motions of vertical or canted valves in IC engines. In KIVA 3 V, the RNG k-turbulence model also became a standard option and other improvements were made to the wall heat transfer and soot models. The subsequent version of KIVA 3 V, KIVA 3 V release 2, added many new features to enhance the robustness, efficiency, and usefulness of the overall program for engine modelling, such as an automatic restart of the cycle with a reduced time step in case the code tends to crash, a deactivation option for a port region when it is not used in the engine cycle, an improved wall film model, etc. [11]. In all these KIVA versions, structured meshes are required to discretize engine geometries.

Many efforts have been made to enable the KIVA programs to simulate flows in complex engine geometries, but there are limitations of a structured mesh for describing detailed engine geometries. Compared to structured meshes, unstructured grids can be composed of a variety of elements including hexahedra, prisms, pyramids, and tetrahedral, and thus provide an easier route in the discretization of physical domains [96]. In this context, the newly developed KIVA 4 code employs unstructured meshes and, in response to this change, modifications and new numerical schemes have been integrated. KIVA 4 is comparable in computational efficiency to KIVA 3 V and also maintains the full generality of previous versions, in particular, in the use of the latest physics sub-models for multi-component vaporization, wall impingement, Lagrangian liquiid film movement, drop breakup, etc. [96].

KIVA provides an open platform on which researchers worldwide can implement and test their models for engine simulations. However, relatively complicated mesh generation processes and the lack of a user-friendly interface have weakened the popularity of KIVA recently. The structural programming language of KIVA, FORTRAN (mainly FORTRAN 77 and 90), is extensively used in scientific computations due to its efficiency and ease of programming. However, limited by the FORTRAN language itself, KIVA cannot adopt objective-oriented programming concepts in its structure. Thus, implementation and testing of new models, especially changes of the numerical integration scheme, can result in a large workload. Using a concurrent version control system, such as the CVS (http://www.nongnu.org/cvs/), relaxes some of these difficulties and significantly enhances the robustness of the continuously improved code.

OpenFOAM stands for Open Field Operation and Manipulation. Capabilities of this free open-source CFD toolbox are not only restricted to simulating complex fluid flows involving chemical reactions, turbulence, and heat transfer, but also able to calculate solid dynamics, electromagnetic, and even financial problems. OpenFOAM facilitates CFD research in that it is an object-oriented software toolkit, which separates the handling of physics from numerical discretization techniques. Therefore, more emphasis can be placed on developing and validating the physics of models. It employs an unstructured mesh and thus it can handle complex geometries, such as diesel engines. Its utility library provides various interfaces that can convert mesh files of popular CFD codes, such as KIVA, FLUENT, and STAR-CD. Post-processing can also be done using third-body software by converting OpenFOAM result files to corresponding formats. Recent research has pioneered the use of OpenFOAM in engine simulations [21, 37, 42]. The current OpenFOAM version 1.5 contains three solvers to deal with engine problems, including dieselFoam for simulating reacting or non-reacting diesel sprays, dieselEngineFoam for simulating reacting flows of diesel engines, as well as engineFoam mainly for SI engines. The use of OpenFOAM in solving engine problems is still in the initialization stage. Many existing physical models need to be integrated into the OpenFOAM code and to be systematically validated. Issues associated with the complicated topological changes of a moving mesh, such as moving valves in engines, still need further efforts. In addition, to appreciate the powerful functionalities of OpenFOAM needs professional skills and knowledge in objective-oriented programming and CFD fundamentals. This may limit widespread applications of OpenFOAM in engine simulations.

Commercial Software

As compared to open-source codes, commercial CFD software for engine simulations has superiority in ease of use. Their user-friendly graphic interfaces enable fast modelling and solving of engineering problems, and expertise is not necessarily required. They also provide their mesh generators or have complete functionalities of using mesh files from other popular third-body mesh software, which expedites the

mesh generating process. Technique support from software vendors or directly from software firms can help solve customers to address difficulties in a timely fashion. As a result, commercial CFD software has found more applications in engine design, development, and production in the automotive industry. STAR-CD, AVL FIRE, FLUENT, and VECTIS are the most preferred multi-dimensional CFD software in the industry. A search of the database of technical papers of SAE international (www.sae.org) reflects that the former three commercial codes have close popularity, followed by VECTIS. But the fact is that none of them exceeds the number of applications of KIVA, which somewhat indicates the role of open-source CFD codes in engine simulations in both academia and industry R&D throughout the past decades. The main reasons are that commercial CFD software is usually much more expensive to purchase, maintain, and update. They are often "black boxes" for users so that their flexibility is weak.

Future and Challenge

Engine CFD modelling has received growing attention since its initiation. As continuously improved physical models and mathematical methods are developed, the credibility of CFD modelling is also better recognized. This has made CFD modelling an indispensable tool in engine design, development, and production as a means of saving cost and time. However, there remain big challenges to quantitatively predict engine performance and emissions using CFD modelling.

The mesh generation process still requires a relatively large workload, and to describe detailed engine geometries, including features such as valve recess and glow plugs, adds additional difficulties. More advanced and user-friendly automatic mesh generation tools will favour wider applications of engine CFD modelling.

Despite the significant progress to date, spray and evaporation models need to be improved in several aspects. First, detailed nozzle flow models are needed to provide complete initial conditions for spray models to better resolve the atomization of sprays. Second, although efforts have been made as discussed in the preceding sections, the mesh dependency of spray and evaporation models may still result in inconsistent calculations for engines of different sizes. Third, to describe the different vaporizing characteristics of commercial fuels sourced from various places, improvements of evaporation models are necessary.

Inaccurate predictions of CFD models can usually be traced to the insufficient description of physical phenomena. But, in the first place, even the physics of some complex processes is not completely understood. Combustion physics in turbulent flows still challenges many modellers and experimentalists around the world. In the context of engine applications, the interaction of turbulence and chemical kinetics is of much interest to CFD modelling. Precise NO_x predictions have been seen in many modelling works thanks to well-understood NO_x formation mechanisms, but the prediction of soot emissions is relatively poor due to lack of a full understanding of its interacting physical and chemical formation processes in engine environments.

To further explore these phenomena, advanced laser diagnostic techniques are needed for model development and validation.

The speed of computers has indeed increased rapidly, but this does not necessarily mean that engine simulations using CFD tools take less computing time since CFD models are continuously improved. For instance, to capture more detailed flow structures at the sub-grid scale, LES turbulence models are preferred to perform on smaller meshes than those using RANS models. To reduce truncation errors, high-order numerical schemes are also necessary. So, methodologies that can be applied to engine CFD models to reduce computational expense, while maintaining prediction accuracy, will always be of much interest.

Demands from innovative engine techniques and advanced applications will continue to stimulate interest in developing new models. Shortly, the production of engines that feature HCCI combustion modes will likely become a reality. Biofuels will partially replace conventional fuels to ensure the sustainability of IC engines in automobiles. These will require a more fundamental understanding of fuel chemistry. To further reduce emissions from diesel engines, higher injection pressure is needed. Correspondingly, new spray models may be necessary to describe the resulting new atomization and breakup mechanisms. Stricter emission regulations may challenge CFD modelling as more detailed characteristics of engine emissions are legislated, such as the size of particulate matter.

References

1. Abani N, Reitz RD (2007) Unsteady turbulent round jets and vortex motion. Phys Fluids 19:125102.1–125102.13
2. Abani N, Kokjohn LS, Park SW et al (2008) An improved spray model for reducing numerical parameters dependencies in diesel engine CFD simulations. SAE paper 2008-01-0970
3. Abraham J, Bracco FV, Reitz RD (1985) Comparisons of computed and measured premixed charge engine combustion. Combust Flame 60:309–322
4. Abraham J (1996) Entrainment characteristics of transient jets. Numer Heat Tranf A Appl 30:347–364
5. Abraham J (1997) What is adequate resolution in the numerical computation of transient jets. SAE paper 970051
6. Abraham J, Magi V (1997) Modeling radiant heat loss characteristics in a diesel engine. SAE paper 970888
7. Amsden AA, Ramshaw JD, O'Rourke PJ, Dukowicz JK (1985) KIVA: a computer program for two- and three-dimensional fluid flows with chemical reactions and fuel sprays. Los Alamos National Lab. Report, LA-10245-MS
8. Amsden AA, O'Rourke PJ, Butler TD (1989) KIVA-II—a computer program for chemically reactive flows with sprays. Los Alamos National Laboratory Report LA-11560-MS
9. Amsden AA (1993) A KIVA program with block-structured mesh for complex geometries. Los Alamos National Laboratory Report LA-12503-MS
10. Amsden AA (1997) KIVA-3V: a block-structured KIVA program for engines with vertical or canted valves. Los Alamos National Laboratory Report LA-13313-MS
11. Amsden AA (1999) KIVA-3V, Release 2, improvements to KIVA-3V. Los Alamos National Laboratory Report LA-UR-99-915

12. Aceves SM, Flowers DL, Westbrook CK et al (2000) A multi-zone model for prediction of HCCI combustion and emissions. SAE paper 2000-01-0327
13. Babajimopoulos A, Assanis DN, Flowers DL et al (2005) A fully coupled computational fluid dynamics and multi-zone model with detailed chemical kinetics for the simulation of premixed charge compression ignition engines. Int J Engine Res 6:497–512
14. Bai C, Gosman AD (1995) Development of methodology for spray impingement simulation. SAE paper 950283
15. Beale JC, Reitz RD (1999) Modeling spray atomization with the Kelvin-Helmholtz/Rayleigh-Taylor hybrid model. Atom Sprays 9:623–650
16. Borman GL, Nishiwaki K (1987) Internal combustion engine heat transfer. Prog Energ Combust Sci 13:1–46
17. Bowman CT (1993) Control of combustion-generated nitrogen oxide emissions: technology-driven by regulation. Proc Comb Inst 24:859
18. Brazier-Smith PR, Jennings SG, Latham J (1972) The interaction of falling raindrops: coalescence. Proc R Soc London Ser A 326:393–408
19. Celik I, Yavuz I, Smirnov A (2001) Large-eddy simulations of in-cylinder turbulence in internal combustion engines: a review. Int J Engine Res 2:119–148
20. De Paola G, Mastorakos E, Wright YM, Boulouchos K (2008) Diesel engine simulations with multi-dimensional conditional moment closure. Combust Sci Tech 180:883–899
21. D'Errico G, Ettorre D, Lucchini T (2007) Comparison of combustion and pollutant emission models for DI diesel engines. SAE paper 2007-24-0045
22. Dukowicz JK (1980) A particle-fluid numerical model for liquid sprays. J Comput Phys 35:229–253
23. Fiveland WA (1988) Three-dimensional radiative heat-transfer solutions by the discrete-ordinates method. J Thermophys 2:309–316
24. Flowers DL, Aceves SM, Martinez-Frias J et al (2003) Effect of mixing on hydrocarbon and carbon monoxide emissions prediction for iso-octane HCCI engine combustion using a multi-zone detailed kinetics solver. SAE Paper 2003-01-1821
25. Fogleman M, Lumley J, Rempfer D, Haworth D (2004) Application of the proper orthogonal decomposition to datasets of IC engine flows. J Turbulence. https://doi.org/10.1088/1468-5248/5/1/023
26. Frenklach M, Wang H (1991) Detailed modeling of soot particle nucleation and growth. Proc Combust Inst 23:1559–1566
27. Halstead M, Kirsh L, Quinn C (1977) The autoignition of hydrocarbon fuels at high temperatures and pressures—fitting of a mathematical model. Combust Flame 30:45–60
28. Han Z, Reitz RD (1995) Turbulence modeling of internal combustion engines using RNG k-ε models. Comb Sci Tech 106:267–295
29. Han Z, Uludogan A, Hampson GJ, Reitz RD (1996) Mechanism of soot and NO_x emission reduction using multiple-injection in a diesel engine. SAE Paper 960633
30. Han Z, Reitz RD (1997) A temperature wall function formulation for variable-density turbulent flows with application to engine convective heat transfer modeling. Int J Heat Mass Transfer 40:613–625
31. Han Z, Xu Z, Trigui N (2000) Spray/wall interaction models for multidimensional engine simulation. Int J Engine Res 1:127–146
32. Haworth DC (2005) A Review of turbulent combustion modeling for multidimensional in-cylinder CFD. SAE paper 2005-01-0993
33. Heywood JB (1988) Internal combustion engine fundamentals. McGraw-Hill
34. Hu B, Jhavar R, Singh S et al (2007) Combustion modeling of diesel combustion with partially-premixed conditions. SAE paper 2007-01-0163
35. Hu B (2008) Development of a general diesel combustion model in the context of large eddy simulation. Ph. D. dissertation, University of Wisconsin-Madison
36. Hughes KJ, Turányi T, Pilling MJ, Tomlin AS (1999) http://www.chem.leeds.ac.uk/Combustion/Combustion.html. Accessed 20 Nov 2008

37. Jasak H, Weller H, Nordin N (2004) In-cylinder CFD simulation using a C++ object-oriented toolkit. SAE Paper 2004-01-0110
38. Jhavar R, Rutland CJ (2006) Using large-eddy simulations to study mixing effects in early injection diesel engine combustion. SAE paper 2006-01-0871
39. Jhavar R (2007) Using large-eddy simulations to study DI-HCCI diesel engine flow structure, mixing, and combustion. Ph.D. dissertation, University of Wisconsin-Madison
40. Jia M, Peng Z, Xie M et al (2008) Evaluation of spray/wall interaction models under the conditions related to diesel HCCI engines. SAE paper 2008-01-1632
41. Kaario O, Larmi M, Tanner F (2002) Relating integral length scale to turbulent time scale and comparing k-ε and RNG k-ε turbulence models in diesel combustion simulation. SAE paper 2002-01-1117
42. Kärrholm FP, Tao F, Nordin N (2008) Three-dimensional simulation of diesel spray ignition and flame lift-off using OpenFOAM and KIVA-3V CFD codes. SAE Paper 2008-01-0961
43. Kee RJ, Rupley FM, Miller JA (1991) CHEMKIN-II: a Fortran chemical kinetics package for the analysis of gas-phase chemical kinetics. Sandia National Laboratory Report SAND89-8009
44. Kong SC, Reitz RD (1993) Multidimensional modeling of diesel ignition and combustion using a multistep kinetics model. J Eng Gas Turbines Power 115:781–789
45. Kong SC, Han Z, Reitz RD (1995) The development and application of a diesel ignition and combustion model for multidimensional engine simulation. SAE Paper 950278
46. Kong SC, Marriott CD, Reitz RD, Christensen M (2001) Modeling and experiments of HCCI engine combustion using detailed chemical kinetics with multidimensional CFD. SAE paper 2001-01-1026
47. Kong SC, Sun Y, Reitz RD (2007) Modeling diesel spray flame lift-off, sooting tendency, and NO_x emissions using detailed chemistry with phenomenological soot model. J Eng Gas Turbines Power 129:245–251
48. Kong SC (2007) Drop/wall interaction criteria and their applications in diesel spray modeling. Atom Sprays 17:473–499
49. Lapenta G (2002) Particle rezoning for multidimensional kinetic particle-in-cell simulations. J Comput Phys 181:317–337
50. Launder BE, Reece GJ, Rodi W (1975) Progress in the development of a Reynolds-stress turbulent closure. J Fluid Mech 68:537–566
51. Lebrère L, Dillies B (1996) Engine flow calculations using a Reynolds stress model in the Kiva-II code. SAE Trans 105:133–155
52. Lee D, Pomraning E, Rutland CJ (2002) LES modeling of diesel engines. SAE paper 2002-01-2779
53. Liang L, Jung C, Kong S-C, Reitz RD (2007) Development of a semi-implicit solver for detailed chemistry in I.C. engine simulations. J Eng Gas Turbines Power 129:2271–2278
54. Liang L, Stevens JG, Farrell JT (2009) A dynamic adaptive chemistry scheme for reactive flow computations. Proc Combust Inst. https://doi.org/10.1016/j.proci.2008.05.073
55. Lippert AM (1999) Modeling of multi-component fuels with application to sprays and simulation of diesel engine cold start. Ph.D. dissertation, University of Wisconsin-Madison
56. Lilly DK (1967) The representation of small-scale turbulence in numerical simulation experiments. In: Goldstine HH (ed) Proceedings of IBM scientific computing symposium on environmental sciences, Yorktown Heights, NY
57. Magnussen BF, Hjertager H (1976) On mathematical modelling of turbulent combustion with special emphasis on soot formation and combustion. Proc Combust Inst 16:719–729
58. Musculus MPB (2004) On the correlation between NO_x emissions and the diesel premixed burn SAE paper 2004-01-1401
59. Munnannur A (2007) Droplet collision modeling in multi-dimensional engine spray computations. Ph.D. dissertation, University of Wisconsin-Madison
60. Nagle J, Strickland-Constable RF (1962) Oxidation of carbon between 1000 and 2000 °C. In: Proceedings of the Fifth Conference on Carbon, vol 1, pp 265–325

61. Neoh KG, Howard JB, Sarofim AF (1984) Effect of oxidation on the physical structure of soot. Proc Combust Inst 20:951–957
62. Nishida K, Hiroyasu H (1989) Simplified three-dimensional modeling of mixture formation and combustion in a D.I. diesel engine. SAE paper 890269
63. Nordin N (2001) Complex chemistry modeling of diesel spray combustion. Ph.D. dissertation, Chalmers University of Technology
64. O'Rourke PJ (1981) Collective drop effects in vaporizing liquid sprays. Ph.D. dissertation, Princeton University
65. O'Rourke PJ, Amsden AA (1987) The Tab method for numerical calculation of spray droplet break-up. SAE paper 872089
66. O'Rourke PJ, Amsden AA (2001) The spray/wall interaction submodel for the KIVA-3 wall film model. SAE paper 2001-01-0271
67. Park SW, Reitz RD (2007) Numerical study on the low emission window of homogeneous charge compression ignition diesel combustion. Combust Sci Tech 179:2279–2307
68. Patterson MA, Kong SC, Hampson GJ, Reitz RD (1994) Modeling the effects of fuel injection characteristics on diesel engine soot and NO_x emissions. SAE paper 940523
69. Patterson MA, Reitz RD (1998) Modeling the effects of fuel spray characteristics on diesel engine combustion and emissions. SAE paper 980131
70. Pelloni P, Bianchi GM (1999) Modeling the diesel fuel spray break-up by using a hybrid model. SAE paper 1999-01-0226
71. Peters N (2000) Turbulent combustion. Cambridge University Press, Cambridge, UK
72. Pomraning E, RutlandC J (2002) A dynamic one-equation non-viscosity LES model. AIAA J 44:689–701
73. Pope SB (1997) Computationally efficient implementation of combustion chemistry using *in situ* adaptive tabulation. Combust Theor Model 1:41–63
74. Pope SB (2000) Turbulent flows. Cambridge University Press, Cambridge, UK
75. Reitz RD (1980) Computations of laminar flame propagation using an explicit numerical method. In: 18th symposium (international) on combustion/the combust institute, Pittsburgh, PA, pp 433–442
76. Ra Y, Reitz RD (2008) A vaporization model for discrete multi-component fuel sprays. Int J Multiph Flow. https://doi.org/10.1016/j.ijmultiphaseflow.2008.10.006
77. Reitz RD (1987) Modeling atomization processes in high-pressure vaporizing sprays. Atom Sprays Tech 3:309–337
78. Reitz RD, Diwakar R (1987) Structure of high-pressure fuel sprays. SAE Trans 96:492–509
79. Reitz RD, Kuo TW (1989) Modeling of HC emissions due to crevice flows in premixed-charge engines. SAE paper 892085
80. Schmidt DP, Rutland CJ (2004) Reducing grid dependency in droplet collision modeling. J Eng Gas Turbines Power 126:227–233
81. Shethaji TA, Rutland CJ, Barths H et al (2005) Assessment of RANS and LES turbulence models: turbulent flow past a backward-facing step and multidimensional simulation of in-cylinder flows. SAE paper 2005-01-0202
82. Shi Y, Reitz RD (2008) Optimization study of the effects of bowl geometry, spray targeting, and swirl ratio for a heavy-duty diesel engine operated at low- and high-load. Int J Engine Res 9:325–346
83. Shi Y, Hessel RP, Reitz RD (2008) An adaptive multi-grid chemistry (AMC) model for efficient simulation of HCCI and DI engine combustion. Combust Theor Model. https://doi.org/10.1080/13647830802401101
84. Shi Y, Kokjohn SL, Ge H-W, Reitz RD (2009) Efficient multidimensional simulation of HCCI and DI engine combustion with detailed chemistry. SAE paper 09-PFL-0039
85. Singh S, Reitz RD, Musculus MPB (2006) Comparison of the characteristic time (CTC), representative interactive flamelet (RIF), and direct integration with detailed chemistry combustion models against optical diagnostic data for multi-mode combustion in a heavy-duty DI diesel engine. SAE paper 2006-01-0055

86. Sjöberg M, Dec JE (2008) Influence of fuel autoignition reactivity on the high-load limits of HCCI engines. SAE paper 2008-01-0054
87. Smagorinsky J (1963) General circulation experiments with the primitive equations: I. The basic equations. Mon Weather Rev 91:99–164
88. Smith GP, Golden DM, Frenklach M et al. http://www.me.berkeley.edu/gri_mech/. Accessed 19 Nov 2008
89. Spalding DB (1971) Mixing and chemical reaction in steady confined turbulent flames. Proc Combust Inst 13:649–657
90. Sun Y (2007) Diesel combustion optimization and emissions reduction using adaptive injection strategies (AIS) with improved numerical models. Ph.D. dissertation, University of Wisconsin-Madison
91. Tan Z, Reitz RD (2004) Development of a universal turbulent combustion model for premixed and direct injection spark/compression ignition engines. SAE paper 2004-01-0102
92. Tao F, Chomiak J (2002) Numerical investigation of reaction zone structure and flame liftoff of DI diesel sprays with complex chemistry. SAE paper 2002-01-1114
93. Tao F, Golovitchev VI, Chomiak J (2004) A phenomenological model for the prediction of soot formation in diesel spray combustion. Combust Flame 136:270–282
94. Tao F, Liu Y, Rempel, Ewert BH et al (2005) Modeling the effects of EGR and injection pressure on soot formation in a high-speed direct-injection (HSDI) diesel engine using a multi-step phenomenological soot model. SAE paper 2005-01-0121
95. Tao F, Reitz RD, Foster DE, Liu Y (2008) Nine-step phenomenological diesel soot model validated over a wide range of engine conditions. Int J Therm Sci. https://doi.org/10.1016/j.ijthermalsci.2008.08.014
96. Torres DJ, Trujillo M (2006) KIVA-4: an unstructured ALE code for compressible gas flow with sprays. J Comput Phys 219:943–975
97. Warnatz JJ, Maas U, Dibble RW, Warnatz J (2006) Combustion. Springer-Verlag, Berlin, Heidelberg
98. Wiedenhoefer JF, Reitz RD (2003) Multidimensional modeling of the effects of radiation and soot deposition in heavy-duty diesel engines. No. 2003-01-0560. SAE Technical Paper
99. Yakhot V, Orszag SA (1986) Renormalization group analysis of turbulence. I. Basic theory. J Scient Comp 1(1): 3–51
100. Yakhot V, Smith LM (1992) The renormalization group, the ε-expansion and derivation of turbulence models. J Scienti Comp 7(1): 35–61
101. Yoshikawa T, Reitz RD (2009) Effect of radiation on diesel engine combustion and heat transfer. J Thermal Sci Tech 4(1): 86–97
102. Zhang YZ, Haworth DC (2004) A general mass consistency algorithm for hybrid particle/finite-volume PDF methods. J Comp Phy 194(1): 156–193
103. Zhu G-S, Reitz RD (2002) A model for high-pressure vaporization of droplets of complex liquid mixtures using continuous thermodynamics. Int J Heat Mass Trans 45(3): 495–507

Chapter 17
Multi-dimensional Modelling of Diesel Combustion: Applications

Yu Shi and Rolf D. Reitz

Abbreviations

AMC	Adaptive Multi-grid chemistry model (–)
C	Proportionality constant (–*)
C_s, C_θ	Proportional to the reduction in axial penetration and the azimuthal deflection of the spray axis, respectively, and (–*)
d_0	Injector nozzle orifice diameter (m)
H	Lift-off length (m)
m	Mass of fuel injected (kg)
N	Engine speed (rpm)
rs	Swirl ratio (–)
s	Spray penetration tip length (m)
SOI	Start of injection (degree CA)
t	Time (s)
T_a	Ambient temperature (K)
t_{break}	Transient time from SOI to the jet breakup (s)
U	Injection velocity (m/s)
u_0	Initial fuel jet velocity (m/s)
ZST	Stoichiometric mixture fraction (–)
Δp	Pressure drop across the injector (N/m^2)
Δt	Injection duration (degree CA)
θ	Spray angle (degree)
μ_a	Dynamic viscosity of air (Pa s)
ρ_a	Air density, ambient gas density (kg/m^3)

Y. Shi (✉) · R. D. Reitz
Engine Research Center, University of Wisconsin-Madison, Madison, USA
e-mail: yushi92@gmail.com

R. D. Reitz
e-mail: reitz@wisc.edu

P. A. Lakshminarayanan and Y. V. Aghav, *Modelling Diesel Combustion*,
Mechanical Engineering Series, https://doi.org/10.1007/978-981-16-6742-8_17

ρ_l Liquid fuel density (kg/m^3)

*These are model constants, so they do not normally have units. Some variables can have different units consistent with the context.

To demonstrate the capability of engine CFD modelling in diesel engine design, development, and production, three representative case studies are discussed in this chapter. The first case investigates the UHC/CO emissions trends for a light-duty diesel engine under low-temperature combustion conditions. The CFD tool used for this study is an improved version of the KIVA-3v2 code which features the RNG turbulence model [7], the KH/RT spray model [1], a detailed chemistry solver with the newly developed PRF mechanism [21], and other improved sub-models. In addition, recently developed techniques for reducing the computational expense of multi-dimensional CFD engine simulations are also integrated into the KIVA code and are used for the first case. In the second case, engine size-scaling relationships are assessed for a light-duty and a heavy-duty diesel engine with consideration of turbulence and chemistry timescales. The last case shows how the CFD tool can optimize engine designs when coupled with optimization methodologies. In this case study, the same KIVA code is used, but with a simple combustion model, the shell/CTC model [11], to reduce the extensive computation time that is required for thousands of individual simulations.

Case Studies

The discussion about the three cases in this section shares the same structure where the problem of each case is first described together with its research background. It is followed by a list (s) of engine specifications and a description of the research approach for that case. In the last part of each case study, the simulation results are discussed in detail so that the insight gained from each type of simulation is naturally demonstrated.

Study of UHC/CO Emissions Trends

Problem description: low-temperature combustion in a light-duty diesel engine. using an efficient engine simulation code with detailed chemistry.

Recent efforts to reduce pollutant emissions and fuel consumption have resulted in the development of many advanced combustion concepts. Among them, low-temperature combustion is attracting more interest since it has been proven in many studies that low-temperature combustion helps the combustion processes avoid NOx and soot formation environments [10, 15, 19]. In practical applications, premixed charge compression ignition (PCCI) [15, 18], which realizes low-temperature combustion by injecting fuel very early to produce a premixed fuel–air charge before the ignition, and modulated kinetics (MK) [9, 10], which requires late

injection with a large amount of cooled recycled exhaust gases to delay ignition timing and thus lower the combustion temperature, are seeing a promising future. However, these approaches usually result in higher unburned hydrocarbons (UHC) and CO emissions compared to conventional diesel combustion. As discussed in section "CO and UHC Modelling" (Chap. 16), possible reasons are the cylinder wall wetting due to early injections and the low oxidation rate due to over-lean mixture and low combustion temperatures.

To achieve low-temperature combustion in a diesel engine, a highly dilute environment is usually required, namely low inhomogeneity of the in-cylinder charge and low oxygen concentration (~10%) with a large EGR rate (~60%). Experimental studies of Kook et al. [12, 13] and Opat et al. [14] found a unique behaviour of the UHC/CO emissions while performing injection sweeps for diesel engines operating in dilute environments. The unique behaviour showed that for the investigated engines, there exist injection timings that correspond to minimum values of CO emission throughout the injection sweeps, termed the CO "sweet spot". This finding provides a valuable guideline for designing PCCI diesel engines.

Advanced combustion strategies use many parameters (injection pressure, number of injection pulses, EGR rate, boost, etc.) to control the combustion process to achieve ultra-low emissions and fuel consumption. The vast number of variables in these combustion strategies necessitates a large number of iterations to achieve an optimal engine design via parametric studies. Because experimental engine design is a time-consuming process, the expense of optimizing engine designs in the laboratory is becoming more and more costly. With the increasing prediction ability of engine simulation tools, engine design aided by relatively low-cost CFD modelling is becoming more popular in both industry and academia. To quantitatively predict engine power, performance, and emissions trends, multi-dimensional CFD tools coupled with chemistry solvers, as discussed in section "Combustion Modelling" (Chap. 16), are required. However, the computational expense of the simulation may become very large if numerous cases need to be studied. Therefore, there is a need to reduce the computational expense of engine simulations using CFD tools coupled with chemistry solvers. In this section, the three approaches that were introduced in section "Efficient Multi-dimensional Simulation of Diesel Engine Combustion with Detailed Chemistry" (Chap. 16) are integrated into an improved CFD code to study the above-discussed UHC/CO emissions trends for low-temperature combustion in a light-duty diesel engine.

Engine Specifications and Investigation Approach

The studied engine in this section is a light-duty diesel engine, M16 (Table 3.2) for passenger cars, and its specifications and operating conditions are listed in Tables 17.1 and 17.2, respectively.

Before the injection sweep parametric study listed in Table 17.2, the CFD code was well-calibrated with a representative case, and thereafter, all calibrated model constants were kept the same throughout the study. An in-house code was employed to iteratively determine the engine inlet valve closing (IVC) conditions based on available measured intake temperature, pressure, and gas composition data. It was also

Table 17.1 Specifications of engine M16

Displacement (L)	0.4774
Bore (mm)	82.0
Stroke (mm)	90.4
CR	16.6:1
IVC (°ATDC)	−132
EVO (°ATDC)	112
Number of holes	7
Injection angle (°)	155

Table 17.2 Operating conditions of engine M16

Speed (rev/min)	2000
Injection pressure (bar)	860
IMEP (bar)	5.5
EGR (%)	65
Equivalence ratio	0.95
SOI (°ATDC)	−39 to −21

found that in the calibration that the start-of-injection command was 4.8° advanced from the physical SOI (start of injection, i.e. start of mass flow from injector) at the 2000 rev/min engine speed, and thus the model inputs were adjusted accordingly for all cases. The study of this section is divided into two phases: in the first phase, the study demonstrates that the current CFD code can qualitatively capture emissions trends, and the CO "sweet spot" is revealed and explained in detail; in the second phase, the effectiveness of three approaches for efficient simulation of diesel combustion (i.e. the adaptive multi-grid chemistry model, mesh-independent spray models, and code parallelization, as discussed in section "Efficient Multi-dimensional Simulation of Diesel Engine Combustion with Detailed Chemistry" (Chap. 16) is compared concerning their computational efficiency and prediction accuracy. All simulations were conducted on computers with the same configuration (Intel P4 3.0 GHz and 2G bytes memory), and the wall clock time was recorded. Due to the geometrical symmetry of the seven-hole injector, a 51.4° sector mesh was employed for the simulations. The fine mesh used in the first and second phases had 32,600 cells of the size of approximately 1.0 mm at BDC, and the coarse mesh used for the second phase had about 10,600 cells of the size of 2.5 mm. Both meshes are depicted in Fig. 17.1.

Results and Discussion

Simulations for the injection sweep were performed using the fine mesh to investigate the emissions trends. NOx, soot, CO, and UHC emissions are reported in Fig. 17.2a to d as a function of injection timings, respectively. Although UHC and soot emissions are over-predicted and under-predicted for late injection timings, the KIVA CFD code

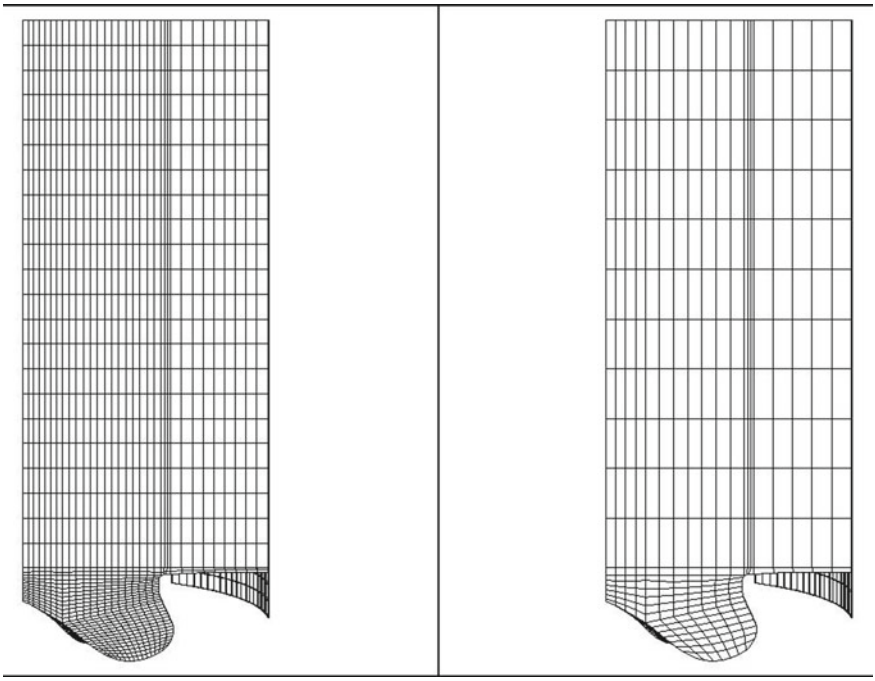

Fig. 17.1 Computational meshes (fine mesh: the left; coarse mesh: the right)

correctly predicts emissions trends over the entire range of the injection timings. More significantly, the CO "sweet spot", and especially the accompanying UHC "sweet" spot, is revealed, as seen in the experiments. This gives strong confidence in using the simulation results to further explore the formation processes of UHC/CO through in-cylinder visualization. Three cases including the boundaries of the injection sweep, namely SOI $= -21$ and SOI $= -39$, as well as the "sweet spot" timing SOI $= -33$, are studied in detail as follows.

Figure 17.3a illustrates the pressure traces and heat release rates for the three cases. Correspondingly, their combustion phasings are depicted in Fig. 17.3b expressed as the percentage of total heat release as a function of crank angle. The ignition delay (I.D.) is defined as the crank angle between ten per cent heat release and the physical injection timing. Figure 17.3b shows that it decreases as the injection timing advances. A shorter ignition delay indicates a shorter time for mixing the spray with the ambient gases before the combustion, which can deteriorate the oxidation rate of fuel and its combustion product CO during the combustion processes. However, if the mixing time alone could explain UHC/CO formation processes under the present highly dilute low-temperature combustion conditions, it would be expected to see a monotonic shape of the UHC/CO emissions trends. The phenomenon of UHC/CO emissions for low-temperature diesel combustion was investigated using a phenomenological engine spray model by Opat et al. [14] and Siewert [27] who showed that the increasing CO seen as the injection timing advanced coincided with

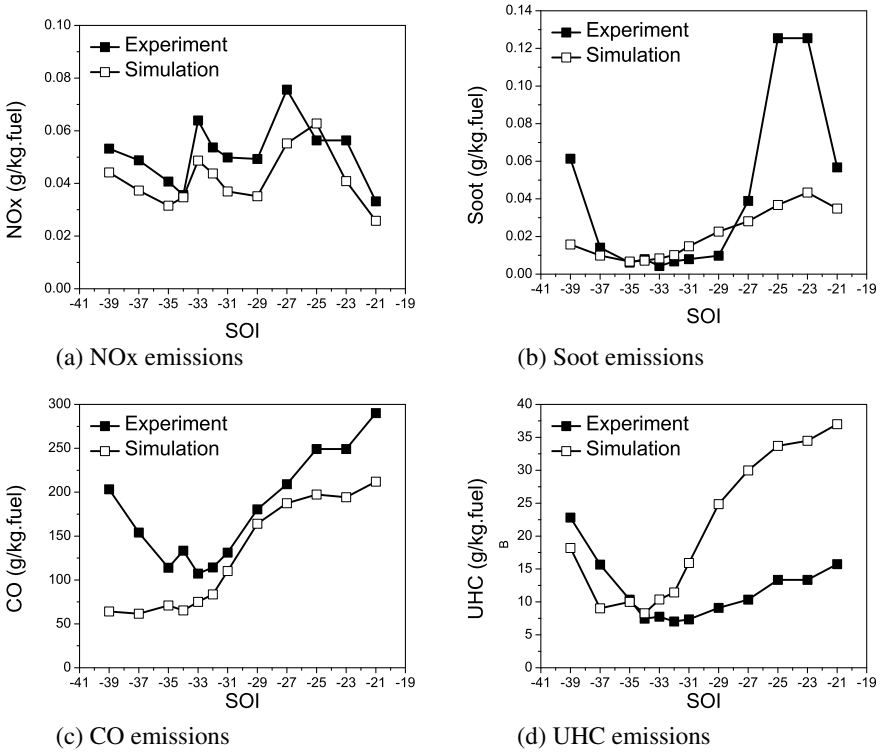

Fig. 17.2 Comparison of simulation and experimental measurement for engine-out emissions of engine M16

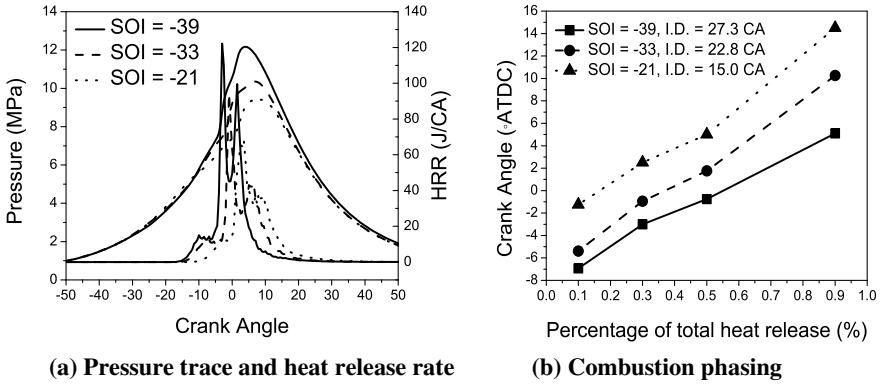

Fig. 17.3 Comparison of the three representative cases

increasing amounts of liquid fuel that missed the bowl, and the increasing CO with retarded injection timings was because less than 100% of the fuel was vaporized before fuel ignition. In light of this, in-cylinder visualizations by post-processing the simulation results were employed to investigate the mixing related phenomena, such as spray impingement, turbulence interaction, and combustion, as shown in Figs. 17.4 and 17.5.

It is observed in Fig. 17.4 that for the case of SOI $= -33$, the sprays target the piston bowl lip that splits the spray plumes into two regions, i.e. the squish and the piston bowl. Therefore, the air can be effectively used to mix the spray and thus enhance combustion in both regions. On the contrary, for the late injection case, the high-temperature zone is mainly located in the piston bowl where the combustion occurs and its peak combustion temperature is also the lowest due to the locally rich stoichiometry. These are the primary reasons that higher UHC and CO are found for this case. For the early injection case, the combustion temperature is the highest among the three cases, and thus, it benefits CO and UHC oxidation. The simulation predicts less CO than the experimental measurement, as shown in Fig. 17.2c for the early injection cases, which is attributed to complex fuel impingement events are not fully captured by the current spray impingement model. But the emission trend that UHC increases as the injection timing advances (before SOI $= -34$) are well revealed by the simulations, as shown in Fig. 17.2d. It is seen in the first and the second plot of the case of SOI $= -39$ in Fig. 17.4 that part of fuel enters the crevice region before combustion, and this trapped fuel is, therefore, the main contributor of the engine-out UHC emissions.

In-cylinder velocity fields and CO mass fraction, distributions of the three cases are also illustrated in Fig. 17.5 on vertical planes through the axis of the sprays. The tumble motion projected on the plane highly depends on the injection timing since it is seen that each case has complex and quite different flow patterns, especially near TDC. As a result, the locations of the high CO regions are also much different. For example, at the crank angle of 12 ATDC, they are located in the squish region for the early injection case, in the squish and bowl regions for the "sweet spot" case, and in the bowl region for the late injection case.

These findings from both experiments and simulations suggest that for highly dilute low-temperature combustion diesel engines, it is necessary to optimize the injection timing to match the piston bowl design to achieve low UHC/CO emissions. Extensive studies of Opat et al. [14] found that the position of the CO "sweet spot" shifts with changes of injection pressure and swirl ratio, which indicates that these are additional parameters that need to be optimized for diesel engines operated in dilute environments.

The computer time for the above cases is about 45 h. Thus, further parametric or optimization studies of the combustion system would require a huge amount of computing resources. The following section demonstrates the capability of efficient engine CFD codes for such problems.

The adaptive multi-grid chemistry (AMC) model was integrated into the KIVA code, and it was applied to study the previous cases using the fine mesh. As seen in Fig. 17.6a using the AMC model, the computational time is reduced by a factor of

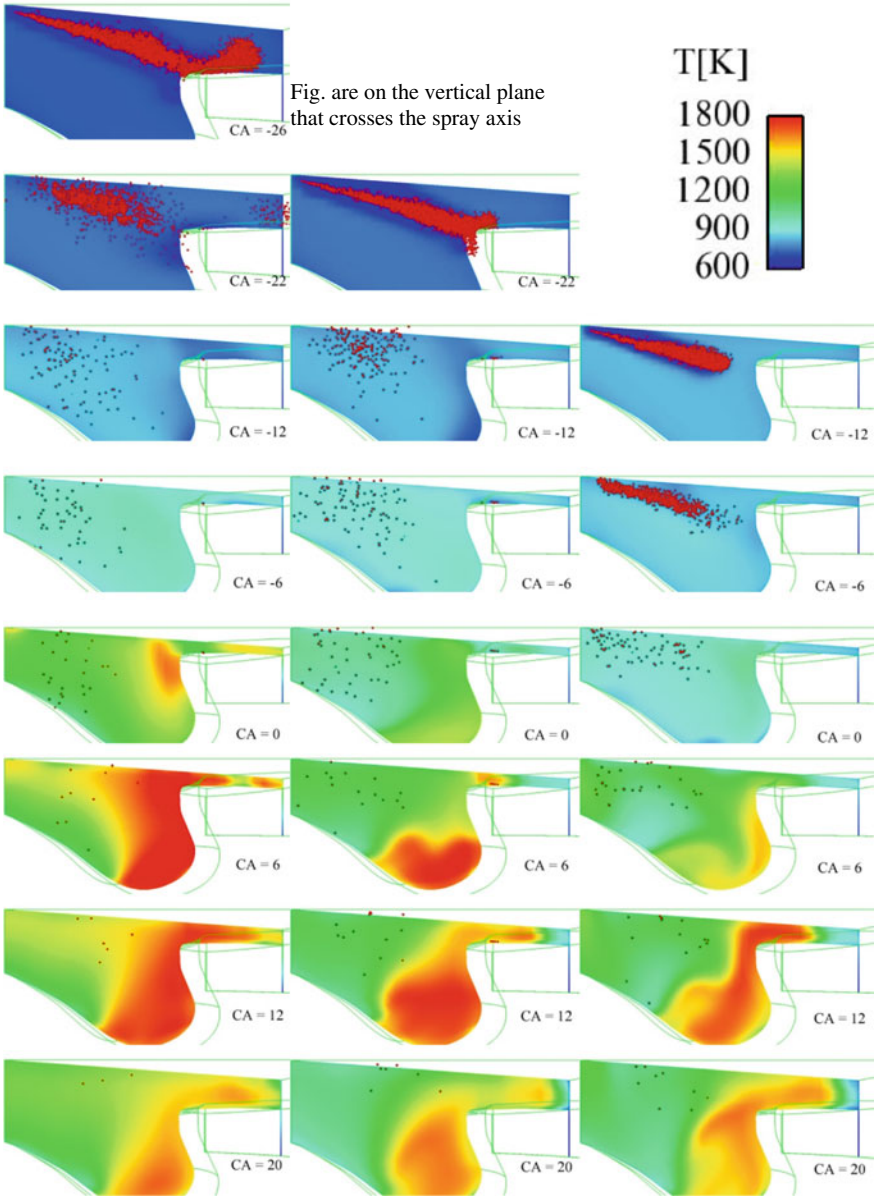

Fig. 17.4 CFD computed distributions of sprays and temperature fields for SOI $= -39$ (left), -33(middle), -21(right) cases

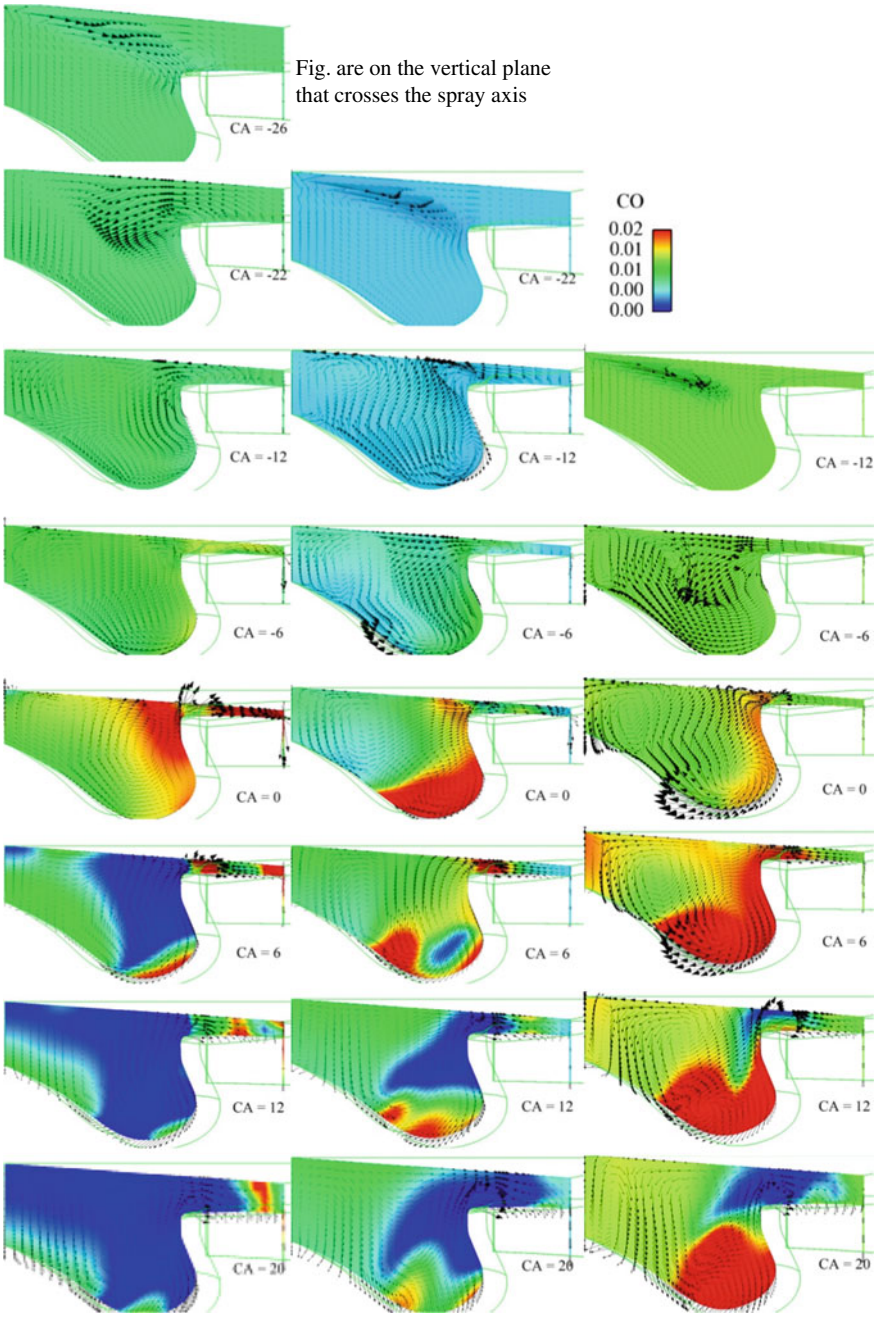

Fig. 17.5 CO mass fraction and velocity for SOI = −39 (left), −33(mid), −21(right)

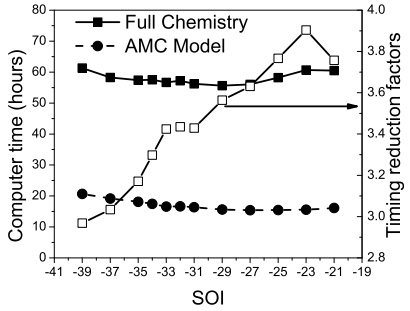

(a) Computational time

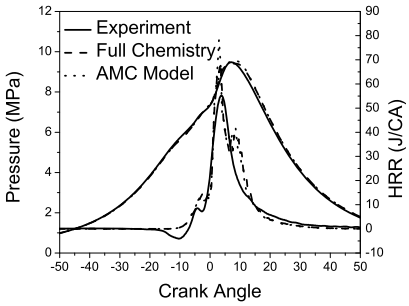

(b) Pressure trace and heat release for SOI = -21

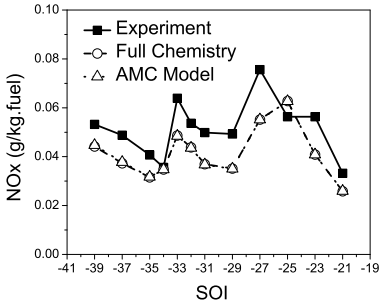

(c) NOx emissions

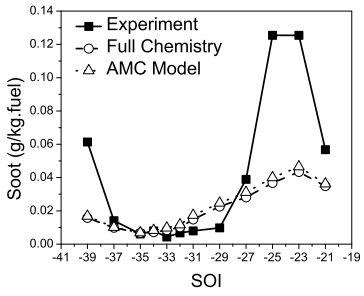

(d) Soot emissions

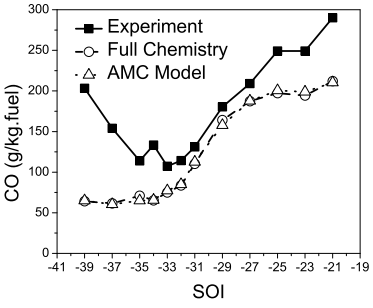

(e) CO emissions

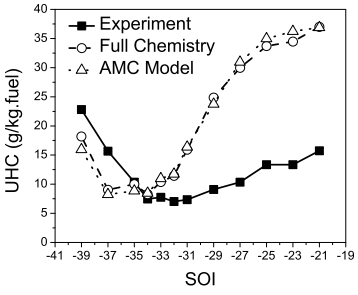

(f) UHC emissions

Fig. 17.6 Comparison of experimental results with simulated results using the fine mesh W/ and W/O the AMC model

three to four for each case, as compared to the full chemistry model. For a representative case of SOI = −21 in Fig. 17.6b, the pressure trace and heat release rate predicted by the AMC model agree excellently with the full chemistry model, and both of them match the experimental results very well. This was also true for all other cases over the entire injection timing sweep. In addition, the results of the AMC model are

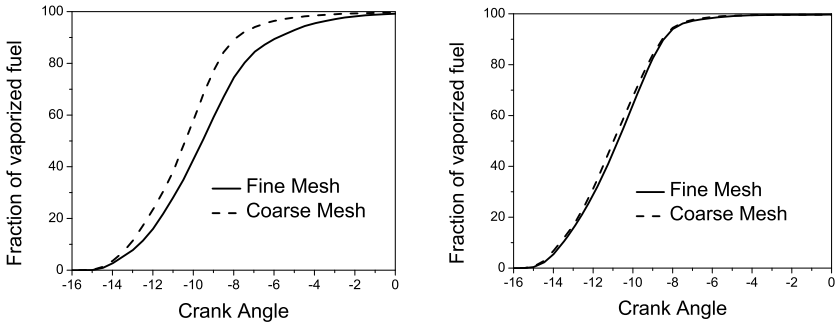

(a) The original spray model (b) The mesh-independent spray model

Fig. 17.7 Comparison of fraction of vaporized fuel using the original spray model and the mesh-independent spray model

also quantitatively consistent with those of the full chemistry simulations in terms of emissions, as shown in Fig. 17.5c–f.

The implementation of the mesh-independent spray model enables simulations of DI engine combustion on a coarse computational mesh while maintaining the relatively high accuracy of a fine mesh. Simulations on the same cases discussed in the previous section were conducted using the original spray models and the updated spray models on both coarse and fine computational meshes. To assess the performance of the spray models only, the AMC model was deactivated to isolate its effect. After verifying that the updated spray models were able to predict less mesh-dependent results, the AMC model was then activated to show the further capacity of reducing computational time using the current efficient KIVA code.

As shown in Fig. 17.7a, for the selected case of SOI $= -21$, using the original spray models produces very different results of vaporized fuel fraction between the fine mesh and the coarse mesh, and the difference is reduced significantly when updated spray models were applied (Fig. 17.7b). Therefore, it can be anticipated that the updated spray models would produce similar results of combustion characteristics and emissions when the mesh size is changed. This is proved by comparing Fig. 17.8 with Fig. 17.9, which shows that compared to the original spray model, the code with the updated spray models predicts more similar results between the coarse mesh and the fine mesh in terms of emission trends and quantities. It can be observed in Fig. 17.8 and Fig. 17.9 that the improvement is more prominent for early injection cases. Since NOx is mainly a function of temperature, the agreement in Fig. 17.8a and Fig. 17.9a is the best, as can be expected. In addition to temperature, the local concentration and gradients of species composition also play crucial roles in the formation of soot, UHC, and CO. Therefore, even though a similar distribution of fuel on a large scale can be achieved using the updated spray model on the fine and coarse meshes, the coarse mesh results in lower local concentrations and gradients and thus leads to slightly different emission results. This is further confirmed by Fig. 17.8c–d that shows that using the coarse mesh produces lower emissions in

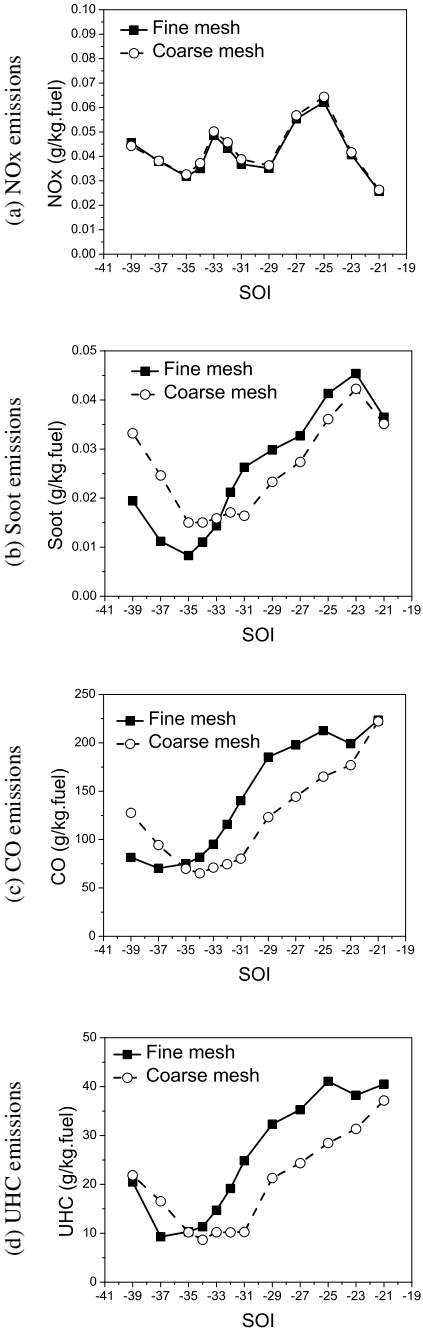

Fig. 17.8 Original spray model

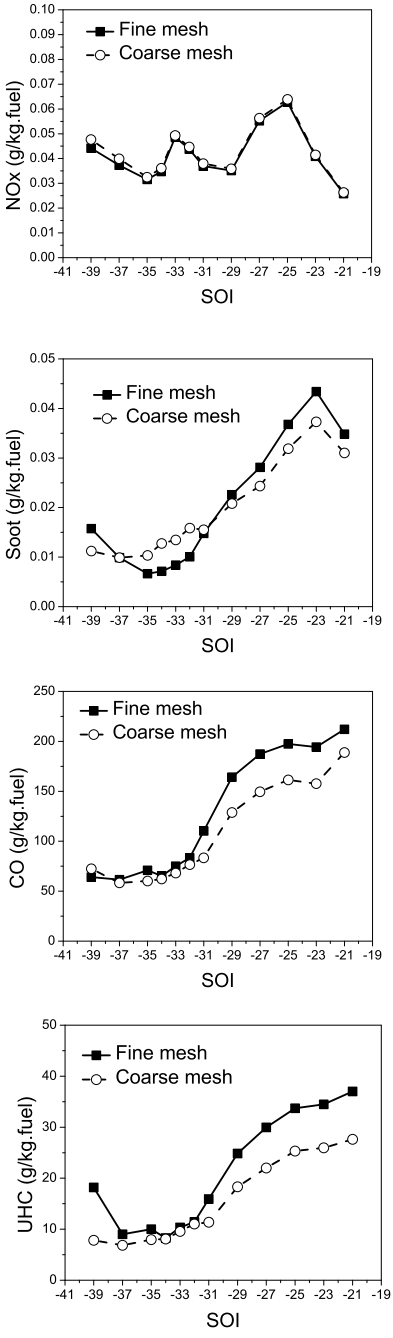

Fig. 17.9
Mesh-independent spray model

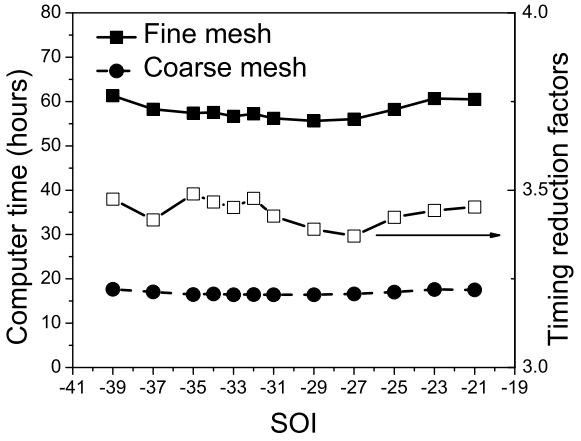

Fig. 17.10 Comparison of computational time using different meshes and the mesh-independent spray model

general. The differences are also attributed to the spray impingement model used in this study, which is not mesh independent. This suggests that to further improve the mesh independence of the current code, effort needs to be placed on developing a sub-grid evaporation model for the application of coarse meshes and reducing the mesh dependence of the current spray impingement model.

It is seen in Fig. 17.10 that the reduction of computational time roughly scales with the number of cells of the fine and coarse meshes, which is easily understood.

To further reduce computational time, the AMC model was activated for simulations using the coarse mesh. Similar to the results that were demonstrated in Fig. 17.6 for the fine mesh, the AMC model predicts very consistent results with the full chemistry model for the coarse mesh as shown in Fig. 17.11a–d. A tremendous computer time reduction (an order of magnitude) was obtained by combining these two schemes, as shown in Fig. 17.11e.

It is noted that the cost of computers has reduced dramatically in the past decades. The popularity of parallel computing in engine CFD simulations thus increases with the continuously decreasing cost of computers. Therefore, the AMC model and the mesh-independent spray model have been implemented into a parallel version of the KIVA3v2 code to explore its ability further.

The previous simulations were repeated using the coarse mesh on two and four processors, respectively. Because the parallelized code produces identical results to its series version, only the comparison of computing times is discussed. Parallelizing the simulations on two processors took an average of 3.7 h for each run, which is reduced from 5.8 h if a single processor is used (Fig. 17.12). If four processors were employed, the average computing time was further reduced to 2.6 h. As mentioned earlier, for the current code only the chemistry solver was parallelized, and the computing time spent on the master processor for the CFD calculation could not be further reduced by using more processors. Therefore, to utilize more processors while maintaining code efficiency, it would also be necessary to parallelize the CFD calculation of the KIVA code. The increasing network burden caused by more

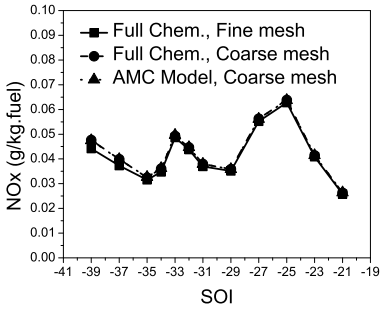

(a) NOx emissions

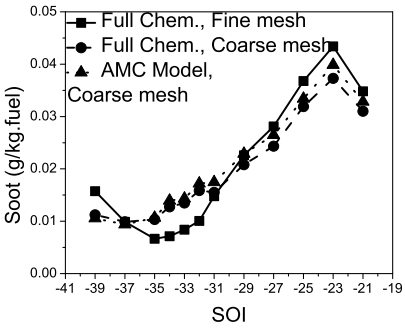

(b) Soot emissions

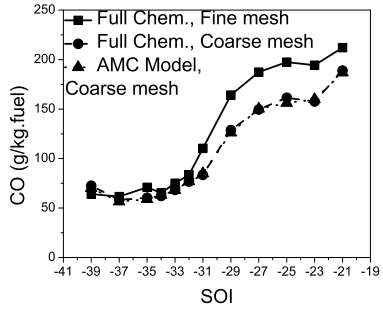

(c) CO emissions

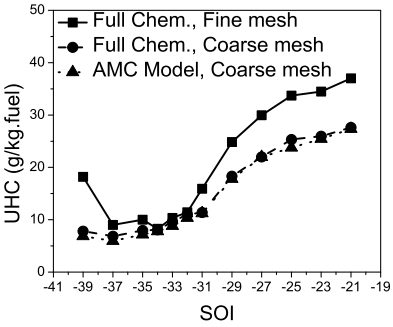

(d) UHC emissions

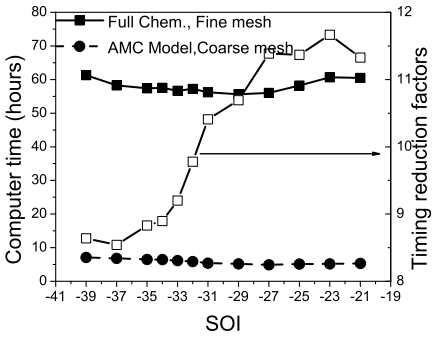

(e) Computational time

Fig. 17.11 Comparison of simulated results using the mesh-independent spray model and AMC model on fine and coarse meshes

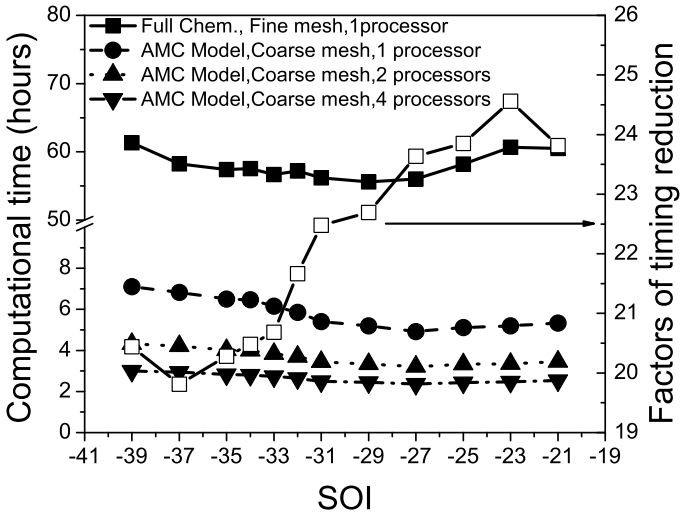

Fig. 17.12 Comparison of computational time using multiple processors, engine M16

frequent communication between processors would also reduce the efficiency of the parallelized code if more processors were used. The communication burden to the network could be reduced if the parallelization was conducted on a single CPU with multiple cores. In that case, processors exchange data through the internal high-speed bus system instead of an external network. Figure 17.12 compares the computational times.

It is seen that by combining all three approaches, it is possible to reduce the computational time by a factor of more than twenty (indicated by the open symbols in figure) for a DI engine case. The computational expense of simulating combustion using detailed chemistry is reduced to the same level as using the relatively simple shell/CTC model discussed in section "Combustion Modelling" (Chap. 16). This allows for significantly more productive engine optimizations using CFD tools with detailed chemistry.

Study of Engine Size-Scaling Relationships for a Light-Duty and a Heavy-Duty Diesel Engine

Problem Description

Currently, engine design work must be repeated for different engines that share essentially similar features. This motivates a study of the relationships between large diesel engines (such as off-road heavy-duty engines) and small engines (such as high-speed auto engines) based on CFD simulation results. Initial work was proposed by Bergin et al. [2, 3] who argued that similar combustion between different engine sizes could

be obtained by scaling a few basic engine geometry parameters, namely the engine speed and the mass of fuel injected. Later, Stager and Reitz [28] extended Bergin's work and created additional rules to scale the spray development and combustion characteristics. The scaling rules were applied to two ideally scaled engines where the small engine was obtained by halving the linear dimensions of the larger engine. They concluded that the scaling rules worked well over a range of injection timings for engines with low-temperature combustion, and the results also suggested that three regimes could be defined where turbulence and chemical kinetics timescales played different roles in influencing combustion and emissions.

This section describes scaling studies on two production diesel engines (Table 3.2)—a light-duty engine, S16 (~0.5 L displacement), and a heavy-duty engine, L16 (~2.5 L displacement). The small engine, S16, was taken as the baseline engine on which the scaling arguments were applied to obtain scaling parameters for defining a scaled large-bore engine, L16. The study also extends the applications of scaling rules to more engine operating conditions to understand the effects of turbulence and chemistry timescales over a broader range in more detail.

Engine Specifications and Investigation Approach

The investigated engines are a light-duty engine and a heavy-duty engine, which are single-cylinder experimental engines (Table 3.2) corresponding to respective production models. The original specifications of these two engines are described in Table 17.3.

The two engines S16 and L16 differ in many geometrical parameters and injection-related variables, as indicated in Table 17.3. Figure 17.13 shows a comparison of the

Table 17.3 Original engine specifications

Engine type	Small, S16	Large, L16
Bore (mm)	82.0	137.16
Stroke (mm)	90.4	165.1
Bowl diameter (mm)	51.3	98.0
Connecting rod length (mm)	145.0	261.6
Squish height (mm)	0.67	1.57
Displacement (L)	0.477	2.439
Compression ratio	16.53	16.1
Swirl ratio	2.2 ~ 5.6	0.5
IVC	-142 ATDC	-143 ATDC
EVO	142 ATDC	130 ATDC
Injection pressure (bar)	1600	1500
Number of holes	8	6
Nozzle holes diameter (·m)	133	158

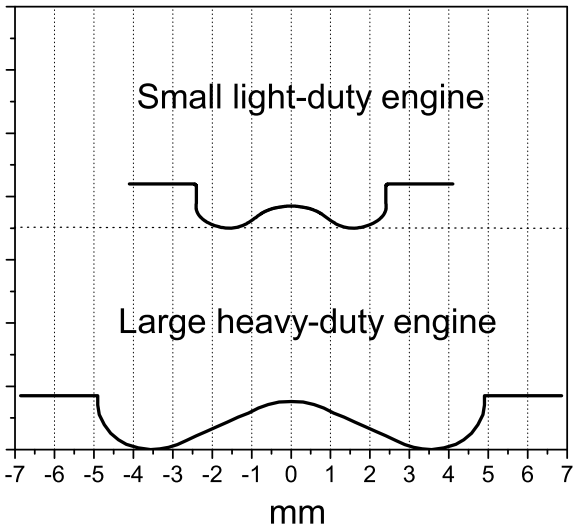

Fig. 17.13 Original piston bowl profiles. [22] Adapted from Shi and Reitz

piston profiles of the two engines, which shows that the engines also feature different bowl curves. The small engine, S16, has a deep bowl design with a vertical sidewall, but the bowl shape of the large engine, L16, is shallow, and the curved chamber wall is relatively closer to the cylinder wall.

To eliminate the differences in bowl geometrical similarity, the baseline piston bowl profile of the small engine, S16, was scaled to produce the bowl profile for a modified large engine, L16, in this study. Correspondingly, other parameters, such as the injection-related parameters and operating conditions, were scaled based on the scaling arguments, as discussed next. As is well known, the process of spray development has a primary effect on the performance and pollutant formation in diesel engines. To obtain similar spatial and temporal distributions of the vapour fuel, it is necessary to ensure that the transient spray plume trajectory scales. Here the temporal distribution of fuel represents its spatial distribution at a certain crank angle.

This at least requires the spray penetration to be scaled. The spray penetration is defined as the distance the penetrating tip of the liquid-phase fuel travels in the combustion chamber before and during vaporization. The first scaling argument about the spray penetration is based on the empirical equations derived by Hiroyasu et al. [8], which are given as

$$s = 0.39\sqrt{\frac{2\Delta p}{\rho_l}}t, \quad 0 < t < t_{\text{break}} \tag{17.1}$$

$$s = 2.95\left(\frac{\Delta p}{\rho_a}\right)^{\frac{1}{4}}\sqrt{d_0 t}, \quad t \geq t_{\text{break}} \tag{17.2}$$

$$\theta = 0.05\left(\frac{d_0^2 \rho_a \Delta p}{\mu_a^2}\right)^{\frac{1}{4}} \tag{17.3}$$

where

$$t_{\text{break}} = 28.65\frac{\rho_l d_0}{\sqrt{\rho_A \Delta p}}$$

s = Spray penetration tip length.
ρ_l = Liquid fuel density.
ρ_a = Air density.
Δp = Pressure drop across the injector.
t = Time.
d_0 = Injector nozzle orifice diameter.
t_{break} = Transient time from SOI to the jet breakup.
θ = Spray angle.
μ_a = Air dynamic viscosity.

The second scaling argument is based on the flame lift-off length of diesel fuel jets. It is defined as the distance from the injector to the reaction zone where the jet stabilizes once the initial auto-ignition phase is over. The flame lift-off has a strong effect on diesel combustion because it allows air to be entrained and premixed with the fuel jet upstream of the lift-off length, which affects the combustion and soot formation processes downstream [5, 20, 26]. Pickett et al. [20] extended Siebers' study [26] on lift-off length and studied the relationships between ignition processes and the lift-off length. A power law relationship of the lift-off length to various parameters was summarized in their paper (2005) based on an extensive database obtained using #2 diesel fuel. The expression is

$$H = \text{CT}_a^{-3.74} \rho_a^{-0.85} d_0^{0.34} U^1 Z_{\text{ST}}^{-1} \tag{17.4}$$

where:

H = Lift-off length.
C = Proportionality constant.
T_a = Ambient temperature.
ρ_{a} = Ambient gas density.
U = Injection velocity.
ZST = stoichiometric mixture fraction.

The scaling argument about the swirl ratio is based on its influence on the spray plume, which is also obtained from Hiroyasu's study [8]. Two factors were proposed to supplement the empirical equations of spray penetration and angle in quiescent air to consider the fact that the spray is bent by air swirl. These two dimensionless correlation factors are defined as follows:

$$C_s = \left(1 + \frac{\pi r_s N s}{30 u_0}\right)^{-1} \tag{17.5}$$

$$C_\theta = \left(1 + \frac{\pi r_s N s}{30 u_0}\right)^{2} = \frac{1}{C_s^2} \tag{17.6}$$

where Cs and C_θ are proportional to the reduction in axial penetration and the azimuthal deflection of the spray axis, respectively, and

r_s = Swirl ratio.
N = Engine speed.
s = Spray penetration.
$u0$ = Initial fuel jet velocity.

The correlation factors should be equal in scaled engines to obtain scaled spray penetration.

The last scaling argument is to assume that scaled engines have the same combustion and thermal efficiency, and their power output should be scaled by the mass of fuel injected into the cylinders, which is calculated from

$$m = \rho_l \frac{\pi}{4} d_0^2 U \Delta t \tag{17.7}$$

where

m = Mass of fuel injected.
ρ_l = Liquid fuel density.
d_0 = Injector nozzle orifice diameter.
U = Injection velocity (assumed constant).
Δt = Injection duration.

Scaled engines should have the same ambient conditions and fuel properties, and consequently, these parameters can be removed from the scaling arguments discussed above, such as ambient temperature and fuel density. Equations (17.2), (17.4), and (17.7) are closed for the parameters of injection velocity, nozzle orifice diameter, and injection duration in real time. Solving these equations simultaneously such that the power output is constant and the spray penetration and flame lift-off length scale directly with the scaling factor yields the scaling relations in Table 17.4.

It is well known that the thermal efficiency of a diesel engine is correlated with its compression ratio. To match the thermal efficiency of the scaled engines, it is necessary to keep the same compression ratio. This presents two options, which are either to use the relation of the displacement volume to scale the TDC volume or to use the TDC volume to scale the IVC volume. It was demonstrated in the study of Shi and Reitz [22] that the TDC volume scaling performed better than the displacement volume scaling, and thus it is discussed next. The specifications for the scaled engines are listed in Table 17.5, which is either derived from the scaling relationships shown in Table 17.4, or from the original values described in Table 17.3. It should be noted that since the stroke of the two engines S16, L16 is not scaled in proportional to their

Table 17.4 Scaling relations

Parameter	Scaling factor length	Scaling factor volume
m	L^3	V
s	L	$V^{1/3}$
H	L	$V^{1/3}$
d_0	L	$V^{1/3}$
A	L^2	$V^{2/3}$
t	$L^{1/3}$	$V^{1/9}$
U	$L^{2/3}$	$V^{2/9}$
Speed	$L^{-1/3}$	$V^{-1/9}$
Mean piston Speed	$L^{2/3}$	$V^{2/9}$
Valve-lifts	L	$V^{1/3}$

Table 17.5 Scaled parameters for the TDC volume scaled engines

Engine type	Small engine, S16 (Scaled)	Large engine, L16 (Scaled)	Scaled?
Bore (mm)	82.0	137.16	N/A
Stroke (mm)	90.4	165.1	N/A
Bowl diameter (mm)	51.3	85.9	YES
Connecting rod length (mm)	145.0	261.6	N/A
Squish height (mm)	1.33	2.23	YES
Displacement (L)	0.477	2.439	NO
TDC volume (L)	0.0359	0.1682	YES
Geometrical compression ratio	14.3	15.5	NO
Effective compression ratio	13.3	13.3	YES
Swirl ratio	1.8	1.8	YES
IVC	−142 ATDC	−126 ABTDC	YES
EVO	142 ATDC	130 ATDC	NO
Injection pressure (bar)	755	1500	YES
Number of holes	8	8	YES
Nozzle holes diameter (μm)	137	229	YES
Included spray angle	130	130	YES

piston diameter, the IVC timing of the engine must be adjusted to have the same effective compression ratios for both engines.

In addition to the scaling arguments described above, a few issues need to be addressed for numerically studying the scaled engines. First, the injection rate shape of the two engines has to be the same to deliver the scaled amount of fuel into the cylinders. Second, more heat transfer from the small engine, S16 due to its larger area/volume ratio has to be compensated for. The higher heat loss of the small engine S16 is balanced by increasing its IVC temperature. The increment of the intake temperature of the small engine S16 was determined such that the motoring pressure trace of the small engine S16 matched that of the scaled large engine under the same compression ratio, and the increment was found to be 10 K for the present study. Finally, the mesh dependency issue has to be carefully considered to minimize its influence on the simulation results for the engine of different sizes. This was accounted for by using a proper mesh size for both engines, such that either increasing or decreasing the mesh size would have consistent small changes in the simulation results. With these considerations, together with the scaling arguments, the engine operating conditions for studying the scaling relationships are shown in Table 17.6.

Results and Discussion

Simulations were conducted over an SOI sweep to investigate the effect of turbulence and chemistry timescales and their interactions. With the TDC volume scaling, the pressure, heat release rate, and the scaled spray penetration (see the inset plots) for both engines S16 and L16 at low load (Case A in Table 17.6) match very well over the SOI sweep, as shown in Fig. 17.14a–c.

As indicated in Fig. 17.14a–c, the pressure traces of the scaled large engine L16 are close to those of the small engine L16 over the broad range of injection timings, as well as its scaled heat release rates. However, because the IVC timing of the large engine, L16 needs to be altered to match the effective compression ratio, its compression processes differ slightly from those of the small engine, S16, but no noticeable influence of this discrepancy was seen on the combustion and emissions. This indicates that the current scaling argument regarding the engine power output works fairly well. The small inset plots in Fig. 17.14a–c are included to show that the scaled liquid spray penetrations in the large engine L16 also agree with those in the small engine, L16, which further supports the scaling argument for spray penetration.

The results of the TDC volume scaling at mid-load (Case B in Table 17.6) are not as good as those of the low-load cases concerning the differences in the emissions trends, which are shown in Fig. 17.15. In general, the large engine L16 produces more NOx and soot emissions. The discrepancy of soot emissions increases as the SOI timing is retarded, but the difference in NOx emissions decreases.

The injection duration of the low-load case (6.2 CA) is about half that of the mid-load case (see Tables. 17.4 and 17.6). The short injection duration reduces the time of spray jet flow interaction with the ambient turbulent flow. This leaves more

Table 17.6 Operating conditions of the TDC volume scaled engines: A, B, C low, mid, and high load, respectively

Engine type		Small engine (Scaled)	Large engine (Scaled)	Scaled?
Speed (rpm)		2000 (3000 for case C)	1685 (2502 for case C)	YES
Gross IMEP (bar)	A	4.5	4.5	YES
	B	7	7	YES
	C	10	10	YES
Equivalence ratio	A	0.25	0.25	YES
	B	0.75	0.75	YES
	C	0.75	0.75	YES
EGR rate (%)	A	55	55	YES
	B	55	55	YES
	C	25	25	YES
Oxygen (volume%)	A	17.93	17.93	YES
	B	11.97	11.97	YES
	C	17.65	17.65	YES
IVC temperature (K)	A	380	370	YES
	B	380	370	YES
	C	380	370	YES
IVC pressure (bar)	A	1.79	1.736	YES
	B	1.791	1.732	YES
	C	1.791	1.732	YES
Injected fuel (mg/cyc.)	A	11	51.5	YES
	B	22.2	104	YES
	C	32.5	151	YES
Injection duration (°CA)	A	6.2	6.2	YES
	B	12.4	12.4	YES
	C	18	18	YES

time for the transport of evaporated fuel by turbulence and bulk flow. Figure 17.14d reveals that the ignition delay is larger than the injection duration for all SOI timings, which allows time for mixing before combustion. The combustion process should be expected to scale if the chemistry timescale is more influential since the engine speeds are similar and the gas temperature was adjusted by 10 K to give similar ignition times. Therefore, the explanation of better matching of the combustion characteristics and emission trends in the two engines, S16 and L16, at low load can be understood. The longer injection duration at mid-load, thus the longer time of interaction of the jet flow with the bulk flow and the weaker effect of the chemistry on the emission formation and oxidation processes are reasons that the emissions are less scaled.

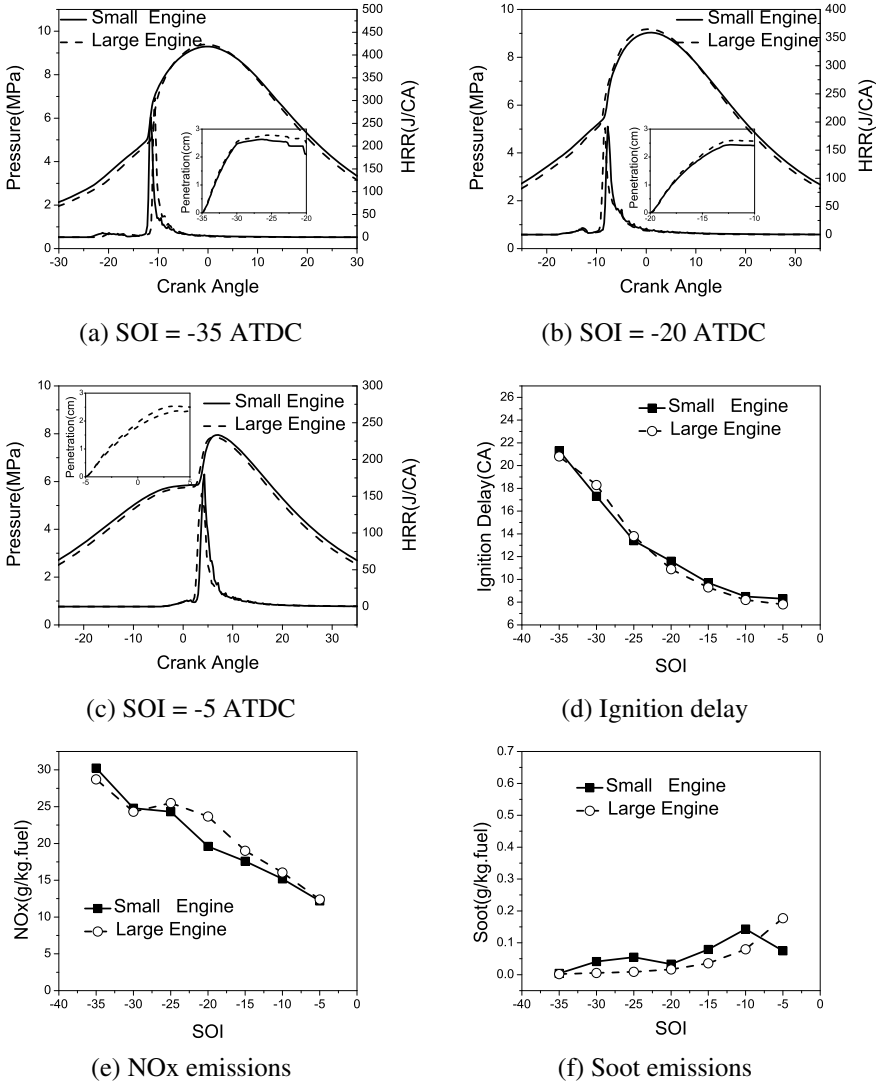

Fig. 17.14 Comparison of the TDC volume scaled engines at low load

In this study, acetylene (C_2H_2) is taken as the precursor of soot formation, and higher concentration areas of C_2H_2 correspond to more soot production propensity. Before acetylene was formed, the distributions and quantities of the local temperature, evaporated fuel, as well as oxygen concentration, were found to be very similar in the two engines. However, a comparison between Fig. 17.16a, b regarding the C_2H_2 mass fraction reveals that in the same two °CA span, more C_2H_2 is generated in the large engine (note that the large engine is shown one °CA ahead of the small

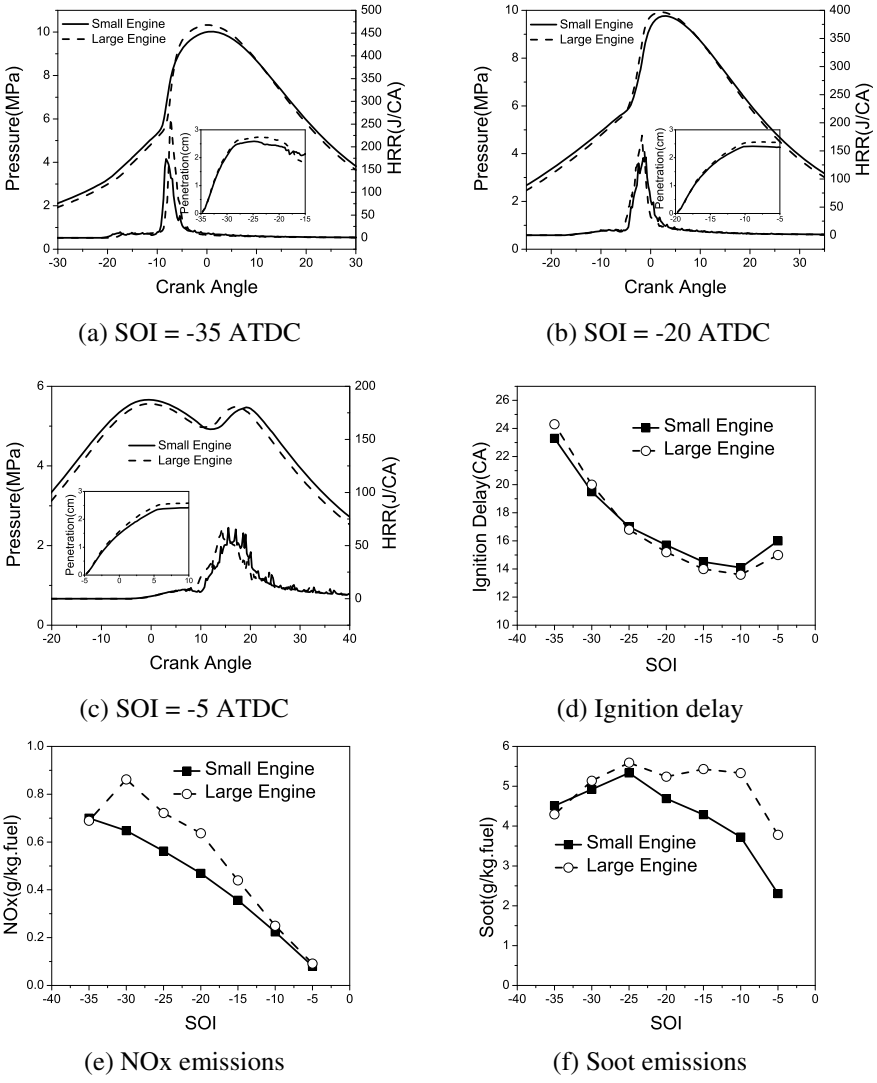

Fig. 17.15 Comparison of the TDC volume scaled engines at mid-load

engine because of its slightly earlier ignition). This directly results in more soot emissions in the large engine shown in Fig. 17.16c. The large engine has a lower speed based on the current scaling laws and therefore longer real-time for one °CA. The C_2H_2 formation reactions are fast under conditions of high temperature and low oxygen concentration, and thus the differences in C_2H_2 are due to mixing effects and oxidation. For early injection cases, the chemistry timescale of reactions of C_2H_2 is relatively large due to the lower local temperatures. The better-scaled soot emissions trend for the low-load case was primarily due to the effect of the soot oxidation

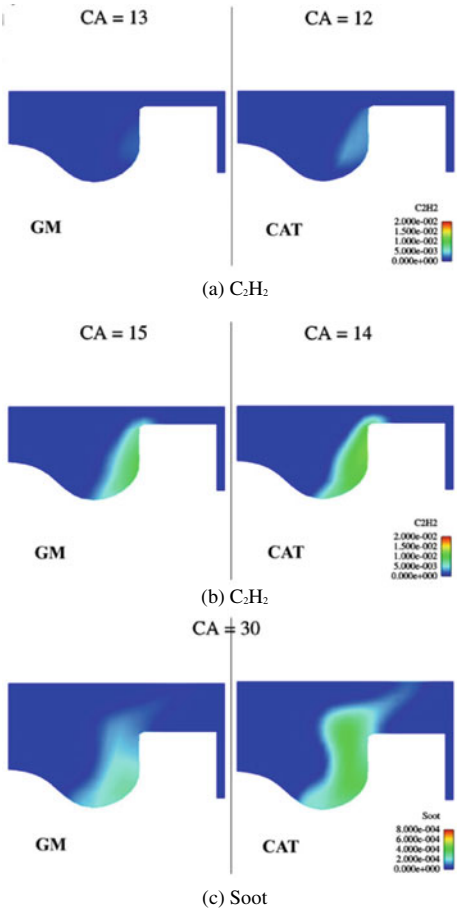

(a) C_2H_2

(b) C_2H_2

(c) Soot

Fig. 17.16 Distributions of C_2H_2 and soot mass fraction (SOI = --5 ATDC) Shi and Reitz [22]

process, whose chemistry timescale is much larger than soot formation (or C_2H_2 formation). Based on this discussion, it is expected that scaled engines operated at a higher speed would produce smaller differences in soot emissions. This is proved in Fig. 17.16 that shows less discrepancy of soot emissions between the two engines when operated at high speed for Case C listed in Table 17.6 with engine speeds of 3000 and 2502 rev/min, respectively (Fig. 17.17).

From the above study, it is seen that the engine size-scaling arguments have been validated using the KIVA CFD code. Global performance results, such as the pressure trace and heat release rates, are well-scaled based on the scaling laws. Soot emissions for the large engine L16 operated at mid- or high-load conditions do not scale well at light load. This is because the soot formation process, which is controlled by chemistry timescales, at mid- or high-load, is more significant compared to that at light load, in which the soot oxidation, which is controlled by turbulence mixing timescales, dominates. Therefore, at different engine speeds (or different real time),

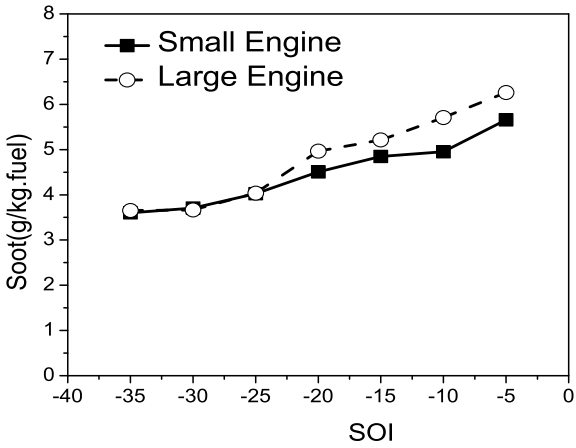

Fig. 17.17 Comparison of soot emissions of engines at high speed (engine speed 3000 and 2502 rev/min for the small S16 and large L16 engines, respectively)

the different timescales that control the net soot emissions contribute to the poor-scaled soot emissions for engines operated at mid or high load. For the low-load operating condition, better scaling of soot emissions was seen because sufficient time is available for oxidation. The large engine L16 has a longer time available for reactions compared to the higher-speed small engine. Therefore, more NO_x is produced, especially in cases with early injection timings where the gas remains at a higher temperature for larger distributions. Hence, higher EGR ratios may be needed to suppress the NO_x formation. Unscaled heat losses and NO_x can be compensated for by slightly increasing the intake temperature of the small size engine S16. Thermal management of the cooling system can be used to scale the heat losses for engines of different sizes.

Optimization of a Heavy-Duty Engine at Low and High Loads

Problem Description

Although many researchers have shown that low-temperature combustion is a very promising strategy to reduce both NOx and soot emissions in diesel engines, it has been found (as also seen in the first case study) that UHC and CO emissions are usually high. The rapid pressure rise rate occurring in PCCI engines also narrows its available operating conditions, and its application to the high-load operating condition is limited due to unacceptable engine knock. The control of the onset of combustion remains an additional challenge for the application of low-temperature combustion because the start of combustion is primarily determined by chemistry processes. Therefore, it is still of much interest to further investigate the traditional combustion regime for heavy-duty engines to improve their performance and to reduce emissions.

Genetic algorithm (GA) search techniques have become one of the mainstream optimization methods and are now increasingly used in engine design. Wickman et al. [29] conducted a study of engine combustion chamber geometry optimization for a small-bore and a large-bore engine with a single objective genetic algorithm (SOGA), and they achieved improved fuel economy and emissions for the two investigated engines. Bergin et al. [2, 3] applied SOGA to their study of large diesel engines and discovered a promising new concept called "spin-spray" combustion. 2006 nonroad emissions targets were met by optimizing the spray events without other means of emissions reduction. But SOGA demonstrates dependency on the choice of merit function, and, unfortunately, the definition of an appropriate merit function is usually unclear to the decision-maker before the optimization process of a multi-objective problem. This motivates interest in the studies and application of multi-objective genetic algorithms (MOGA). MOGA is becoming a prominent method for use in optimization and design. Genzale et al. [6] investigated a heavy-duty diesel engine operated at low load and under low-temperature combustion conditions, and a set of optimized combinations of the spray targeting, bowl geometry, and swirl ratio was revealed. Shi and Reitz [23] assessed three widely applied MOGAs for optimizing a heavy-duty diesel engine operating at a high load. In their research, the non-dominated sorting genetic algorithm II (NSGA II) [4] with a large population size was found to perform better for use in engine optimization, and an optimal injection strategy and better matching of the piston geometry with the spray plume were also identified.

For any combustion process, boundary and initial conditions are two influential aspects, and particularly the preparation of the fuel–air mixture also critically influences compression ignition combustion. Combustion and pollution formation are significantly affected by the mixing processes in diesel engines, and thus it is necessary to identify a better method to match the boundary conditions, such as matching the piston geometry with the spray plume geometry, as well as to ensure good initial conditions, such as those due to the initial flow motions like the swirl.

For a diesel engine operated at different loads, the in-cylinder thermal conditions vary considerably, which results in different spray behaviours, combustion characteristics, and pollutant formation. It can be anticipated that different injection strategies and matching of the piston geometry and spray plume are needed for engines under different operating conditions to reduce emissions and fuel consumption. This case study presents an optimization study of a heavy-duty diesel engine operated at both low load and high load for a better understanding of the effects of bowl geometry, spray targeting, and swirl ratio on engine operation. A nonparametric regression analysis tool [16, 17] is also used to post-process the optimized results to provide more visible relations between design parameters and objectives.

Engine Specifications and Investigation Approach

The geometric specifications and fuel injector parameters of the heavy-duty engine H16 (Table 3.2) are summarized in Table 17.7. The operating conditions correspond

Table 17.7 Specifications of engine H16

Combustion chamber	Quiescent, direct injection
Swirl ratio	0.5
Bore × stroke (mm)	137.16 × 165.1
Bowl width (mm)	97.8
Displacement (L)	2.44
Connection rod length (mm)	261.6
Geometric compression ratio	16.1:1
Fuel injector nozzles	8 holes, equally spaced
Spray pattern included angle	154°
Rail pressure (bar)	1600
Nozzle orifice diameter (mm)	0.217

to 20 and 95% load at high speed, respectively, Table 17.8.

The primary goal of the present study is to find optimal combustion boundary conditions, i.e. combustion chamber (bowl) shapes, for a heavy-duty engine, H16 at low load and high load. In addition, optimal combinations of spray targeting and swirl ratio levels as a function of combustion chamber shape were searched for simultaneously to further understand the effects of the initial flow conditions and the spray development on combustion, with the objectives of reducing both NO_x and soot emissions and improving fuel economy.

A total of nine parameters, including the injector spray angle, swirl ratio, SOI, and six different parameters that define the bowl geometry were studied for the high-load case. An additional parameter of injection pressure was applied to the low-load case. The compression ratio was kept fixed as 16.1, and the six bowl geometric parameters enable a search of a wide range of bowl shapes and also allow for the consideration of re-entrant-type bowls. The number of geometry parameters used gives a reasonable search space using the Kwickgrid methodology [29] although more parameters are available in the grid generator to define the bowl shapes. Figure 17.18 illustrates the six bowl geometry parameters optimized in this study.

Table 17.9 provides the ranges of the parameters, which were determined to avoid

Table 17.8 Baseline operating conditions

Conditions	High-load	Low-load
Speed (rev/min)	1672	1672
IVC temperature (K)	385	370
IVC pressure (kPa)	310	153
Load (%)	95	20
Injection quantity (mg/cyc)	229	70.9
EGR level (%)	25	20
Global equivalence ratio	0.60	0.33
O_2 concentration (vol. %)	17.65	19.52

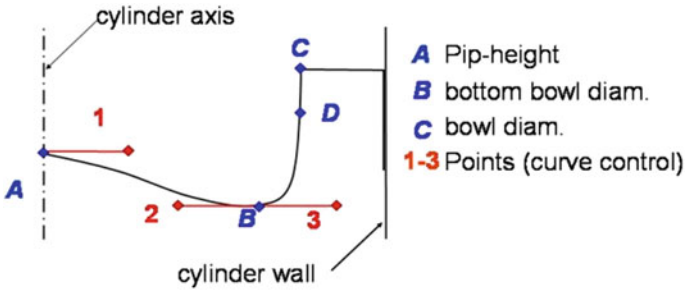

Fig. 17.18 Parameters of bowl geometry. [24] Adapted from Shi and Reitz

Table 17.9 List of optimization parameters and their ranges of engine H16

Parameters	Range	
	High-load	Low-load
A—(% bowl depth)	65–75	65–75
B—(% bowl diameter)	74–80	74–80
C—(% cylinder diameter)	71–84	71–84
1—Bezier curve control point	0.1–0.7	0.1–0.7
2—Bezier curve control point	0.3–0.9	0.3–0.9
3—Bezier curve control point	0.8–1.5	0.8–1.5
Injector spray half-angle	60–85°	60–85°
Swirl ratio	0.5–2.0	0.5–2.0
SOI (ATDC)	−15 to −13	−10 to + 10
Injection pressure (bar)	2000	850–2000

infeasible bowl designs but still to maintain diversity. The spray angles target a wide region of the piston, from the bowl floor up to the bowl lip. Considering the ability of the intake system of the experimental engine, the range of swirl ratio was restricted to a relatively narrow range. The SOI range for the high-load operation was determined based on the maximum power output of the baseline design of the engine, and for the low-load case, a broader range was considered to explore more emissions trade-offs. The injection pressure for the high-load case was fixed at 2000 bar to achieve realistic injection durations.

The optimization process is described in Fig. 17.19, which shows that the genetic algorithm is employed to generate input parameters (in the ranges listed in Table 17.9) for the KIVA CFD code. With these input parameters, the KIVA code evaluates the engine performance and emissions, which provides feedback to the genetic algorithm. The new feedback enables the genetic algorithm to search for optimum input parameters for the next KIVA evaluations. The cycle evolves until satisfactory results are obtained or the optimization process converges [25]. In this study, for each of the two cases, a total of 1272 cases were simulated.

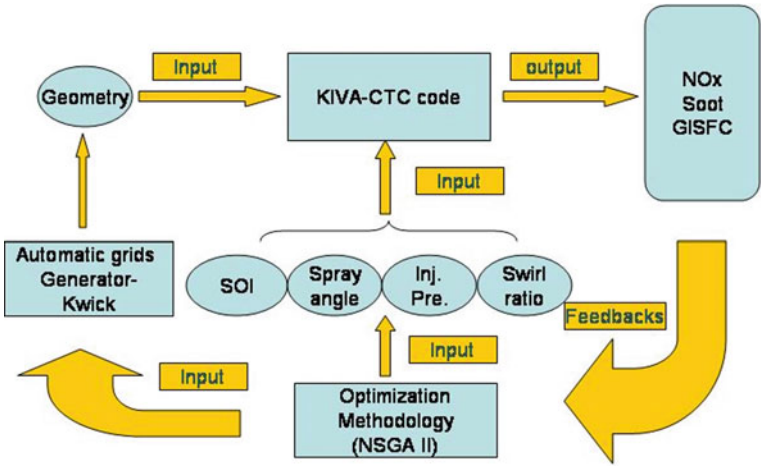

Fig. 17.19 Illustration of optimization process using genetic algorithm and the KIVA CFD code

Results and Discussion

The optimization studies on the heavy-duty engine H16 operated at high- and low-load conditions were conducted, and the Pareto solutions (representing optimal designs) with objectives of NO_x, soot, and GISFC were identified. Representative designs for each case were selected from the Pareto front (formed by all optimum solutions) as the reference designs for use with the nonparametric regression analysis. The response surfaces generated under different engine operating conditions are discussed next. The optimal designs were further explained and examined with additional parametric studies and in-cylinder visualizations to validate the present nonparametric regression technique and also to better understand the flow motions, combustion, and pollutant formation processes. Finally, a common optimal piston design was selected to show that an optimum design could be achieved for both high- and low-load operations.

All solutions from each case are plotted in the objective space, as shown by the squares in Fig. 17.20a, b for the high load and low load, respectively, and the optimal solutions are indicated by the circles. It is seen from the optimal solutions in figure that for each group, designs exist that can simultaneously reduce NOx and soot emissions while reducing the fuel consumptions, such as Design 2 in Fig. 17.20a and Design 3 in Fig. 17.20b.

A comparison of the low-load optimal designs with the high-load optimal solutions indicates that the Pareto solutions feature different aspects. Firstly, the spray included angles are no longer restricted to high values for the low-load case, although most of the optimal solutions still have flat spray targeting, as seen for the high-load case. Secondly, the effect of bowl size becomes less important compared to that of the high-load optimal designs. No small bowl design was found on the Pareto

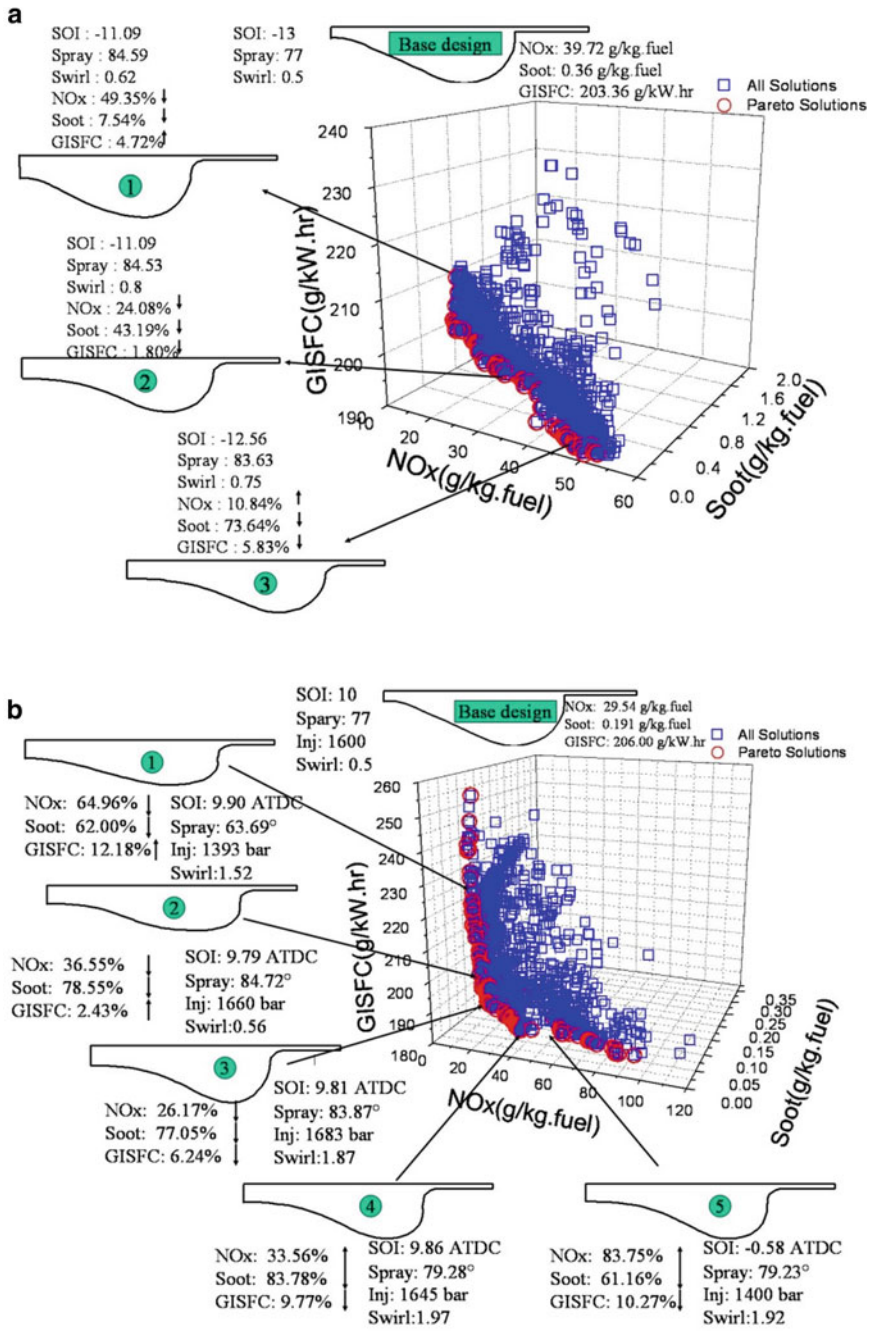

Fig. 17.20 **a** Solutions for the high-load condition. **b** Solutions for the low-load condition. Pareto front and optimal solutions. [24] Adapted from Shi and Reitz

front, and all optimal designs feature mid-range or large bowl diameters and also have a relatively large size of the bowl floor. Thirdly, the Pareto solutions seek high swirl ratios, and most of them are larger than 1.5, but for the high-load optimal solutions, almost all cases feature relatively low swirl ratios. Fourthly, for the low-load condition, high injection pressure does not certainly benefit emissions and fuel economy, and most optimal solutions have a moderate injection pressure in the range of 1400–1600 bar. All these observations imply that spray targeting and matching it with the bowl geometry, and the initial flows behave differently under high- and low-load conditions. Therefore, more details were explored with nonparametric and parametric studies as follows.

Design 2 in Fig. 17.20a for the high load and Design 3 in Fig. 17.20b for the low load were selected as reference designs for the nonparametric regression analysis since they represent optimum designs. It is also noted that for the high-load cases GISFC responded similarly with soot emissions and thus its response surfaces are not provided here. In addition, for both cases, the details of the piston geometry, such as the bowl profile curvatures were found not influential to the objectives and thus they are not further discussed.

As observed in Fig. 17.21 for the high-load condition, the spray included-angle is the most influential parameter for NOx emissions, and the peak NOx emissions are found at medium values of the spray angle. In Fig. 17.21b, reduced NO_x emissions are favoured by a low swirl condition. However, changes with swirl ratio are less than those associated with spray angle changes, so that the swirl ratio has a secondary effect on NO_x emissions. The SOI has less effect on NO_x emissions as compared to the other two. The order of parameters and how significantly they influence soot are the same as that obtained from the response surfaces of NO_x, and the spray angle is still the dominant parameter. Similar to its effect on NO_x, medium values of the spray angle contribute more soot. As shown in Fig. 17.21d, the soot emissions reduce slightly as the swirl ratio increases, for which an inverse trend is seen on NOx emissions in Fig. 17.21b.

The response surfaces of NO_x concerning SOI, spray angle, swirl ratio, and injection pressure and their interacting effects are given in Fig. 17.22a–c. It is observed that retarding SOI has the primary influence of reducing NOx emissions, which is consistent with experimental observations since the combustion temperature reduces as the SOI is retarded. But note that after 5°ATDC, the effect of SOI becomes weaker since the surface with respect to spray angle becomes flat. NOx emissions peak at about 77° spray angle, and these finding are similar to that obtained from the study of the high-load cases. Decreasing injection pressure helps reduce NOx emissions, as shown in Fig. 17.22c. Compared to the other parameters, the swirl ratio has the least effect on NOx emissions, though it can be seen that a high swirl ratio slightly promotes NOx production in Fig. 17.22b–c.

For the soot emissions, SOI is still an important parameter, but the effects of other parameters become more important than they were on NOx. As seen in Fig. 17.22d, soot emissions are minimized at about 77° spray angle, opposite to the observation on NOx. However, retarding SOI also helps to reduce soot emissions, and this is believed to be the reason that most of the Pareto designs for the low-load condition

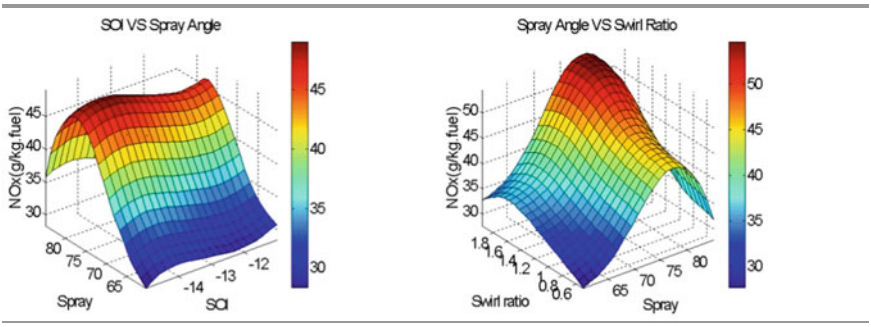

(a) Interacting of SOI and spray angle on NOx

(b) Interaction of spray angle and swirl on NOx

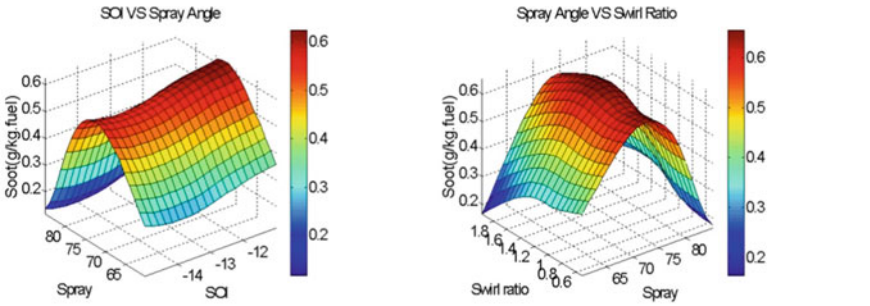

(c) Interaction of SOI and spray angle on soot

(d) Interaction of spray angle and swirl on soot

Fig. 17.21 Response surfaces for the large bowl design (Design 2 in Fig. 17.20a) under the high-load condition. [24] Adapted from Shi and Reitz

feature very late injection timings. Increasing swirl ratio or injection pressure benefits soot emissions, as seen in Fig. 17.22e–f, which also indicates the difficulty of engine design due to the trade-off between NOx and soot.

Comparison of Fig. 17.22e–f and g–i demonstrates that GISFC responds differently to the investigated parameters, which is a further challenge to engine design for low-load operation. For example, it was found above that retarding SOI helps reduce both NOx and soot emissions. However, Fig. 17.22g frustrates this finding in that the late injection timing deteriorates fuel economy significantly. However, it is also seen that if a large spray angle is employed, the effect of SOI on GISFC weakens. Therefore, to obtain both emissions reduction and fuel economy, a combination of large spray angle and late injection is needed. Figure 17.22i illustrates that GISFC decreases as the injection pressure increases. Furthermore, the effect of the swirl ratio is again seen to be the least.

For a practical engine, the combustion chamber geometry and the spray included angle cannot be varied easily. Thus, it is of interest to seek a compromise optimal design for both conditions. It is desired to achieve emissions reduction and improved fuel consumption at both high load and low load by optimizing other flexible design

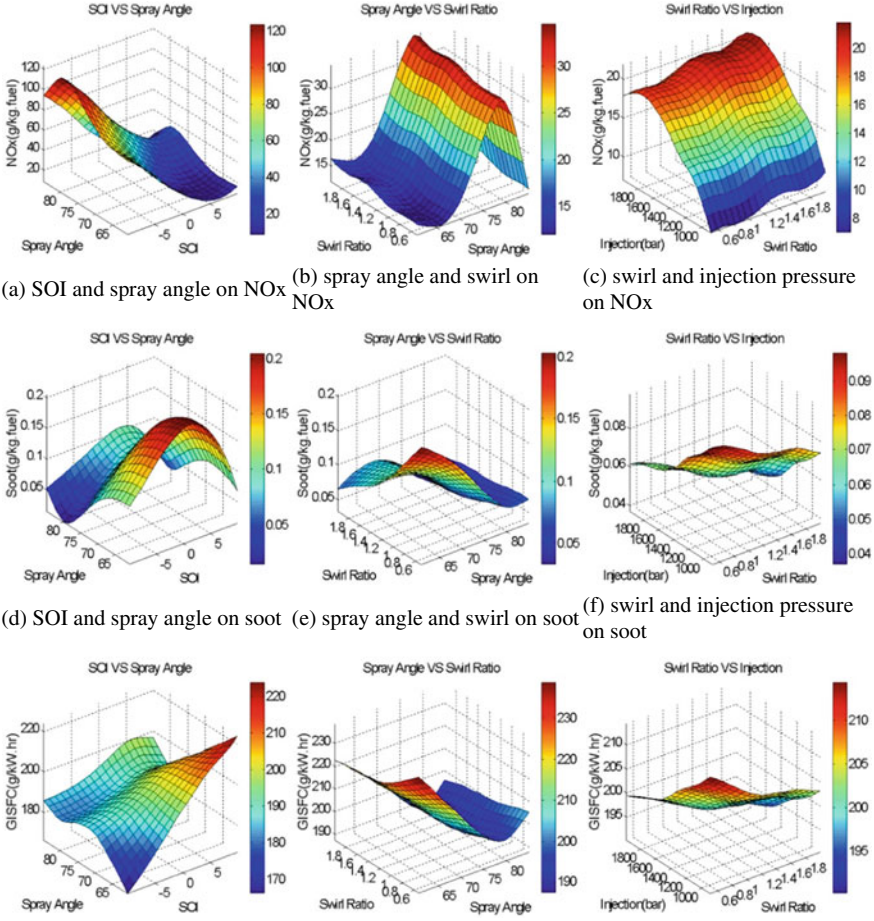

(a) SOI and spray angle on NOx (b) spray angle and swirl on NOx (c) swirl and injection pressure on NOx

(d) SOI and spray angle on soot (e) spray angle and swirl on soot (f) swirl and injection pressure on soot

(g) SOI and spray angle on GISFC (h) spray angle and swirl on GISFC (i) swirl and injection pressure on GISFC

Fig. 17.22 Response surfaces for the large bowl design (Design 3 in Fig. 17.20b) under the low-load condition. [24] Adapted from Shi and Reitz

parameters, such as the swirl ratio and the injection timing and pressure. It was shown in Fig. 17.20a that high-load Design 2 reduced emissions and fuel consumption simultaneously, compared to the baseline design. In addition, it is also observed that its combustion chamber shape shares similar features with Design 3 in Fig. 17.20b for the low-load optimization. Therefore, Design 2 and its corresponding spray angle (84.53°) were selected to conduct a study under the low-load condition. The three cases listed in Table 17.10 were studied, and the results are given in Table 17.11.

Compared to the results from the original optimized bowl design, Cases 1 and 2 are seen in Table 17.11 to reduce both NOx and soot emissions, without sacrificing fuel economy significantly. This indicates that optimal piston designs exist for both

Table 17.10 Parametric study for the low-load condition using the second high-load piston design in Fig. 17.20a

Parameters	SOI(°ATDC)	Spray(°)	Swirl	Inj. Pre. (bar)
Case 1	9.81	84.53	1.87	1683
Case 2	9.81	84.53	0.8	1683
Case 3	9.81	84.53	0.8	1200

Table 17.11 Results of parametric study for the low-load condition using the second high-load piston design in Fig. 17.20a

Objectives	NOx (g/kg.fuel)	Soot (g/kg.fuel)	GISFC (g/kW.hr)
Case 1	20.34	0.049	196.21
Case 2	17.32	0.047	201.00
Case 3	13.12	0.078	211.93

high-load and low-load conditions, but it would be necessary to provide different swirl ratios through intake system design and to employ different injection pressures and timings, for example by using a common rail injection system to accommodate the different loads to achieve clean and highly efficient combustion.

It is concluded from this case study that the use of MOGA enables an efficient search of globally optimal solutions with conflicting objectives. The use of nonparametric regression analysis together with the GA optimizations helps to quantify the influences of design parameters on the optimal objectives. The optimization showed that the high-load operating condition is more sensitive to the combustion chamber geometrical design compared to the low-load condition. This was revealed by examining the optimal solutions for the high-load optimization, in which the Pareto cases feature a broad range of bowl sizes and geometries. By choosing an optimal combustion chamber design from the high-load optimization study and varying swirl ratio, injection timing, and pressure, excellent performing designs were also found using the high-load optimal chamber geometry for the low-load condition. This suggests that engine optimization studies for all operating loads should start with an optimization study of piston geometry, spray targeting for the high-load condition. Then further optimization on the spray injection event and swirl ratio should be conducted for the low-load condition.

References

1. Beale JC, Reitz RD (1999) Modeling spray atomization with the Kelvin-Helmholtz/Rayleigh-Taylor hybrid model. Atom Sprays 9:623–650
2. Bergin MJ, Reitz RD (2005) Soot and NOx emissions reduction in diesel engines via spin-spray combustion. In: ILASS American, 18th annual conference on liquid atomization and spray systems. Irvine, CA

3. Bergin MJ, Hessel RP, Reitz RD (2005) Optimization of a large diesel engine via spin spray combustion. SAE paper 2005-01-0916
4. Deb K, Pratap A, Agarwal S, Meyarivan T (2002) A fast and elitist multiobjective genetic algorithm: NSGA-II. IEEE Trans Evol Comput 6:182–197
5. Dec JE (1997) A conceptual model of DI diesel combustion based on laser-sheet imaging. SAE Trans 106:1319–1348
6. Genzale CL, Reitz RD, Wickman DD (2007) A computational investigation into the effects of spray targeting, bowl geometry, and swirl ratio for low-temperature combustion in a heavy-duty diesel engine. SAE paper 2007-01-0119
7. Han Z, Reitz RD (1995) Turbulence modeling of internal combustion engines using RNG k-ε models. Comb Sci Tech 106:267–295
8. Hiroyasu H, Kadota T, Arai M (1978) Supplementary comments: fuel spray characterization in diesel engines. In: Combustion Modeling in reciprocating engines symposium, general motors research laboratories
9. Kimura S, Aoki O, Kitahara Y, Ogawa H et al (1999) New combustion concept for ultraclean and high-efficiency small DI diesel engines. SAE paper 1999-01-3681
10. Kimura S, Aoki O, Kitahara Y, Aiyoshizawa E (2001) Ultra-clean combustion technology combining a low-temperature and premixed combustion concept for meeting future emission standards. SAE paper 2001-01-0200
11. Kong SC, Han Z, Reitz RD (1995) The development and application of a diesel ignition and combustion model for multidimensional engine simulation. SAE Paper 950278
12. Kook S, Bae C. Miles PC et al (2005) The influence of charge dilution and injection timing on low-temperature diesel combustion and emissions. SAE paper 2005
13. Kook S, Bae C, Miles PC et al (2006) The effect of swirl ratio and fuel injection parameters on CO emission and fuel conversion efficiency for high-dilution, low-temperature combustion in an automotive diesel engine. SAE paper 2006-01-0197
14. Opat R, Ra Y, Gonzalez DMA et al (2007) Investigation of mixing and temperature effects on HC/CO emissions for highly dilute low-temperature combustion in a light-duty diesel engine. SAE paper 2007-01-0193
15. Lee S, Gonzalez MA, Reitz RD (2007) Effects of engine operating parameters on near stoichiometric diesel combustion characteristics. SAE paper 2007-01-0121
16. Lin Y, Zhang HH (2003) Component selection and smoothing in smoothing spline analysis of variance models. Institute of Statistics Mimeo Series 2556, NUCS
17. Liu Y, Lu F, Reitz RD (2006) The use of non-parametric regression to investigate the sensitivities of high-speed direct injection diesel emissions and fuel consumption to engine parameters. Int J Engine Res 7:167–180
18. Nevin RM, Sun Y, Gonzalez MA, Reitz RD (2007) PCCI investigation using variable intake valve closing in a heavy-duty diesel engine. SAE paper 2007-01-0903
19. Park SW, Reitz RD (2007) Numerical study on the low emission window of homogeneous charge compression ignition diesel combustion. Combust Sci Tech 179:2279–2307
20. Pickett LM, Siebers DL, Idicheria CA (2005) Relationship between ignition processes and the lift-off length of diesel fuel jets. SAE paper 2005-01-3843
21. Ra Y, Reitz RD (2008) A reduced chemical kinetic model for IC engine combustion simulations with primary reference fuels. Combust Flame 155:713–738
22. Shi Y, Reitz RD (2008a) Study of diesel engine size-scaling relationships based on turbulence and chemistry scales. SAE paper 2008-01-0955
23. Shi Y, Reitz RD (2008b) Assessment of optimization methodologies to study the effects of bowl geometry, spray targeting, and swirl ratio for a heavy-duty diesel engine operated at high-load. SAE paper 2008-01-0949
24. Shi Y, Reitz RD (2008) Optimization study of the effects of bowl geometry, spray targeting, and swirl ratio for a heavy-duty diesel engine operated at low- and high-Load. Int J Engine Res 9:325–346
25. Shi Y, Reitz (2009) Assessment of multi-objective genetic algorithms with different niching strategies and regression methods for engine optimization and design. ASME paper ICES2009-76015

26. Siebers DL, Higgins B, Pickett LM (2002) Flame lift-off on direct-injection diesel fuel jets: oxygen concentration effects. SAE paper 2002-01-0890
27. Siewert RM (2007) A phenomenological engine model for direct injection of liquid fuels, spray penetration, vaporization, ignition delay, and combustion. SAE paper 2007-01-0673
28. Stager LA, Reitz RD (2007) Assessment of diesel engine size-scaling relationships. SAE paper 2007-01-0127
29. Wickman DD, Senecal PK, Reitz RD (2001) Diesel engine combustion chamber geometry optimization using genetic algorithms and multi-dimensional spray and combustion modeling. SAE paper 2001-01-0547

Chapter 18
Large Eddy Simulation of Diesel Engine Combustion

Haiwen Ge

Nomenclature

a_4, b_3, b_1	Model constants (–)
C	Model constant (–)
C_k, σ_k, C_ε	Model constants (–)
C_s	Adjustable model constant (–)
$C_{s,dyn}$	Model constant (–)
C_v	Model constant in the formulation of turbulent viscosity in the SGS model (–)
Da	Damkohler number (–)
DNS	Direct numerical simulation (–)
ERC	Engine Research Center at University of Wisconsin–Madison (–)
F^b	Body force ($Nm^{-3)}$
F^s	Source term due to spray (Nm^{-3})
FTS	Flamelet timescale (–)
$G\ (x;\ y)$	Classical filters include box (top-hat) filter, Gaussian filter (–)
k	Sub-grid turbulent kinetic energy (m^2s^{-2})
K	"Grid"-level turbulent kinetic energies (m^2s^{-2})
LES	Large Eddy simulation (–)
L_{ij}	Double-filtered grid-level sub-grid stress tensor is the Leonard stress term ($m^2s^{-2)}$
l_τ	Turbulent length scale (m)
M_{ij}	Deviatory part of $L_{ij\ (}m^2s^{-2}$)
QSF	Quasi-steady flamelet mode (–)
RANS	Reynolds-averaged Navier–Stokes equations (–)
RNG	Renormalization group (–)

H. Ge (✉)
Department of Mechanical Engineering, Texas Tech University, Lubbock, United States
e-mail: haiwen.ge@ttu.edu

P. A. Lakshminarayanan and Y. V. Aghav, *Modelling Diesel Combustion*,
Mechanical Engineering Series, https://doi.org/10.1007/978-981-16-6742-8_18

SGS	Sub-grid scale (–)
S_{ij}	Strain rate tensor ($s^{-1)}$
s_l	Laminar flame speed (m/s)
s_t	Turbulent flame speed (m/s)
T_c	Cut-off temperature (K)
T_{ij}	Sub-grid stress tensor based on the test filter (m/s)
u	Turbulent velocity (m/s)
u'	Root mean square of the turbulent fluctuating velocity (m/s)
V	Local cell volume (m^3)
α	First combustion index is used to distinguish the slow-chemistry regime from the fast-chemistry regime, i.e. depending on the chemical timescale (–)
Δ	The grid filter that is computed from the local cell volume (m)
ε	Sub-grid turbulent dissipation of sub-grid kinetic energy (m^2s^{-2})
ν_t	Turbulent viscosity (m^2/s)
ρ	Density (kg/m^3)
σ_{ij}	The viscous term (Pa)
τ_{chem}	Characteristic timescale describing the duration that the current flamelet proceeds towards its steady state (s)
τ_{ij}	Sub-grid stress tensor (Pa)
τ_{ij}	"Grid"-level modelled stress tensor (Pa)
φ	Arbitrary flow variable (–)
ω	Specific turbulent dissipation rate (m^2/s^3)
$\mathcal{H}$	Heaviside function (–)
$\hat{\Delta}$	Another test filter with a length scale. Usually, this test filter is twice the grid filter (). (m)
$\hat{K}$	"Test" level turbulent kinetic energies (m^2s^{-2})
$\hat{\tau}_{ij}$	"Test" level modelled stress tensor (Pa)
$\tilde{\xi}$	Mean mixture fraction (–)
$\tau_{u_j\xi}$	Flux of the mean of mixture fraction (s^{-1})
χ_{SGS}	Sub-grid-scale scalar dissipation rate (m^2/s^3)
$\tilde{Y}_i^{\text{lib}}$	Mass fraction calculated from the flamelet library (–)
χ	Local scalar dissipation rate (m^2/s^3)
χ_c	Criterion of scalar dissipation rate between the diffusion flamelet regime and the partially premixed regime (m^2/s^3)
γ	Local mixture homogeneity, second combustion index used to distinguish the quasi-steady homogeneous regime from the quasi-steady diffusion flamelet regime (–)

Subscripts

u	An unburnt region (–)

i, j, k Component along x-, y-, and z-directions (–)

Introduction

Most of the flows in internal combustion engines are turbulent flows, which is one of the most challenging topics in the whole scientific world. The fundamental challenge is that the turbulent flow involves a wide range of timescale and length scale; i.e. the ratio of maximum scale and minimum scale is huge. To exactly model the turbulent flow (direct numerical simulation, DNS), the smallest timescale and length scale should be resolved in the numerical simulation. According to Kolmogorov's turbulence law (Kolmogorov 1991), both the smallest length and timescales, which are called the Kolmogorov scales, are proportional to $Re^{-3/4}$. For a three-dimensional case, the total grid number is proportional to $Re^{-9/4}$. Plus the total time step, the total computational cost is proportional to Re^3. The Reynolds number in engines is usually very large. Plus, the chemical reactions and multiphase flow make the situation even much complex. All of these factors prevent the DNS from engine simulations. A description of the system at a coarser level is required to make engineering simulations possible. The Reynolds-averaged numerical simulation (RANS) method (Chaps. 16 and 17) is a feasible way for engine simulations with affordable computational costs. The RANS model employs a time-averaging technique to simplify the problem so that the larger time step and grid size can be used. A lot of physics, especially unsteady behaviours, have been ignored.

An alternative is the large eddy simulation (LES), which adopts a volume averaging technique to avoid resolving the smallest scales. As it is named, LES explicitly computes the large eddies of the flows, usually whose sizes are larger than the grid size. The effects of the smaller ones are modelled using a sub-grid-scale (SGS) model. The large eddies depend more on the geometry of the system, while the small eddies are more universal. Therefore, the SGS models developed in the context of LES are more universal. By contrast, the turbulence models for RANS have different favourable flow regimes. With the increase in computational power, the application of LES in internal combustion engines becomes more feasible [52].

Comparing to the conventional Reynolds-averaged Navier–Stokes (RANS) approach, the LES usually reproduces more flow structures, eddies, and vortices. This is due to the lower dissipation nature of the SGS models and sometimes the smaller grid size. Usually, the LES is recognized as a more accurate approach. However, the accuracy of the LES is difficult to be validated, especially for the applications of engine combustion in which the results are influenced by many factors. The LES results are based on the spatially averaged quantities, while the RANS results are based on the ensemble-averaged. Special attention is required when comparing the LES results with RANS results or experimental data [52].

Usually, the computational cost of LES is much higher than the RANS simulations, which is counted as one disadvantage of the LES. This is mainly due to the much

smaller mesh size used in the LES. Given the same mesh size, the computational costs of LES are usually higher than but about the same magnitude as the ones of RANS simulations. This is particularly true when a detailed reaction mechanism is employed in the simulation of reactive flows since most of the CPU time is spent on solving the stiff ordinary differential equations of the chemical reactions. Sometimes, the RANS simulations could be slower than the LES. For instance, simulations of breathing processes using $k-\omega$ turbulence model take more CPU time than using LES with dynamic structure model, since it is more difficult for the $k-\omega$ model to get convergent in solving the transport equations [13, 14]. Thus, the computational cost of LES using moderate mesh size is acceptable for modern engineering applications.

Formulations of the LES Models

To separate the scales, the filtering technique is applied to an arbitrary flow variable defined in the space–time system:

$$\overline{\phi}(x) = \int_V G(x; y)\phi(y)\mathrm{d}y \tag{18.1}$$

Classical filters include box (top-hat) filter, Gaussian filter, and spectral (sharp cut-off) filter [53]. The flow variable is then decomposed into a resolved part $\overline{\phi}$ and an SGS part ϕ':

$$\phi = \overline{\phi} + \phi' \tag{18.2}$$

The resolved part represents the large-scale flow motion that is solved exactly, while the SGS part represents the small-scale flow motion that needs to be modelled. For the compressible flow, it will be more convenient to consider the Favre-averaged filtered quantities:

$$\tilde{\phi} = \frac{\overline{\rho\phi}}{\overline{\rho}} \tag{18.3}$$

Apply the above definition into the momentum equation, the filtered equation can be derived:

$$\frac{\partial(\overline{\rho}\tilde{u}_i)}{\partial t} + \frac{\partial\left(\overline{\rho}\tilde{u}_i\tilde{u}_j\right)}{\partial x_j} = -\frac{\partial\overline{p}}{\partial x_i} + \frac{\partial\overline{\sigma}_{ij}}{\partial x_j} - \frac{\partial\tau_{ij}}{\partial x_j} + \overline{F}_i^s + \overline{F}_i^b \tag{18.4}$$

with σ_{ij} the viscous term; F^s the source term due to spray; F^b the body force; and sub-grid stress tensor:

$$\tau_{ij} = \overline{\rho}\left(\widetilde{u_i u_j} - \tilde{u}_i \tilde{u}_j\right) \tag{18.5}$$

The sub-grid stress tensor contains the sub-grid term that is needed to be modelled, which is the focus of the LES modelling. A variety of sub-grid models have been developed. In the following sections, some representative models are introduced.

Smagorinsky Model

Using the mean gradient assumption, the Smagorinsky model [60] describes the sub-grid stress tensor as a function of strain rate tensor and cell size:

$$\tau_{ij} = -2\nu_t \overline{S}_{ij} \tag{18.6}$$

The turbulent viscosity

$$\nu_t = C_s^2 \Delta^2 \sqrt{S_{ij} S_{ij}} \tag{18.7}$$

where Δ is the grid filter that is computed from the local cell volume:

$$\Delta = V^{1/3} \tag{18.8}$$

C_s is an adjustable model constant. For different flow regimes, different values of C_s should be used, which reduces the robustness of the model. To avoid such a dilemma, a dynamic model is introduced to determine the model constant locally. The method is based on the self-similarity theory of the turbulent flow. Additional to the grid filter Δ, another test filter with a length scale $\hat{\Delta}$ is considered. Usually, this test filter is twice the grid filter ($\hat{\Delta} = 2\Delta$). The sub-grid stress tensor based on the test filter is:

$$T_{ij} = \left(\widehat{u_i u_j} - \hat{u}_i \hat{u}_j\right) \tag{18.9}$$

The difference between the test-level and double-filtered grid-level sub-grid stress tensor is the Leonard stress term [18]:

$$L_{ij} = T_{ij} - \hat{\tau}_{ij} = \widehat{\overline{u}_i \overline{u}_j} - \hat{u}_i \hat{u}_j \tag{18.10}$$

the deviatory part of L_{ij} is written as:

$$L_{ij} - \frac{1}{3} L_{kk} \delta_{ij} = C_{s,\mathrm{dyn}} M_{ij} \tag{18.11}$$

where

$$M_{ij} = 2\hat{\Delta}^2 \widehat{|\overline{S}|\overline{S}_{ij}} - 2\hat{\Delta}^2 |\overline{S}|\overline{S}_{ij} \tag{18.12}$$

Using the least square method, the model constant $C_{s,\mathrm{dyn}}$ can be determined locally:

$$C_{s,\mathrm{dyn}} = \frac{M_{ij} L_{ij}}{M_{kl} M_{kl}} \tag{18.13}$$

This is the dynamic Smagorinsky model.

One Equation Viscosity Model

The turbulent viscosity can be modelled by adopting the sub-grid kinetic energy. The sub-grid stress tensor is written as:

$$\tau_{ij} = -2\nu_t \overline{S}_{ij} + \frac{2}{3} k \delta_{ij} \tag{18.14}$$

in which the turbulent viscosity is modelled as:

$$\nu_t = C_k k^{1/2} \Delta \tag{18.15}$$

and k is the sub-grid kinetic energy that is written as:

$$k = \frac{1}{2}(\overline{u_i u_i} - \overline{u}_i \overline{u}_i) \tag{18.16}$$

The sub-grid kinetic energy k is determined by solving its transport equation. The modelled transport equation is given as:

$$\frac{\partial k}{\partial t} + \overline{u}_i \frac{\partial k}{\partial x_i} = \frac{\partial}{\partial x_i}\left(\frac{\nu_t}{\sigma_k} \frac{\partial k}{\partial x_i}\right) - \tau_{ij} \frac{\partial \overline{u}_i}{\partial x_j} - \varepsilon \tag{18.17}$$

ε is the dissipation rate of the sub-grid kinetic energy k. Its value is determined from:

$$\varepsilon = C_\varepsilon k^{3/2} \Delta^{-1} \tag{18.18}$$

C_k, σ_k, and C_ε are model constants.

Dynamic Structure Model

Similar to the dynamic Smagorinsky model, the dynamic structure model [27, 50] is based on an assumed scaling between resolved and sub-grid scales and a mathematical identity that arises. A second filtering operation that is designated the "test"-level filter is conducted. The "grid"-level (K) and "test"-level ($\hat{K}$) turbulent kinetic energies are defined by

$$K = \frac{1}{2}\left(\widetilde{u_i u_j} - \widetilde{u}_i \widetilde{u}_j\right) \tag{18.19}$$

$$\hat{K} = \frac{1}{2}\left(\widehat{u_i u_j} - \widehat{u}_i \widehat{u}_j\right) \tag{18.20}$$

respectively. The Leonard term relates the test- and grid-level kinetic energies:

$$\hat{K} = K + \frac{1}{2} L_{ii} \tag{18.21}$$

The "grid"- and "test"-level modelled stress tensor are

$$\tau_{ij} = c_{ij} K \tag{18.22}$$

$$\hat{\tau}_{ij} = c_{ij} \hat{K} \tag{18.23}$$

Substituting these models for the two stress tensors into the Germano identity yields

$$L_{ij} = c_{ij}\hat{k} - \widehat{c_{ij} k} \tag{18.24}$$

The sub-grid tensor is then written as:

$$\tau_{ij} = 2k \frac{L_{ij}}{L_{ii}} \tag{18.25}$$

Spray Models and Combustion Models for LES

Most of the current spray models and combustion models were developed in the context of RANS. When the LES is employed, some models need to be modified accordingly to keep consistent [52], especially the ones involving turbulent quantities. Currently, adjusting the spray models in the context of LES is rarely discussed. Most of the LES of engine combustion directly adopted the spray models developed in the context of RANS, with the tuning of certain model constants. Most of the adjustment

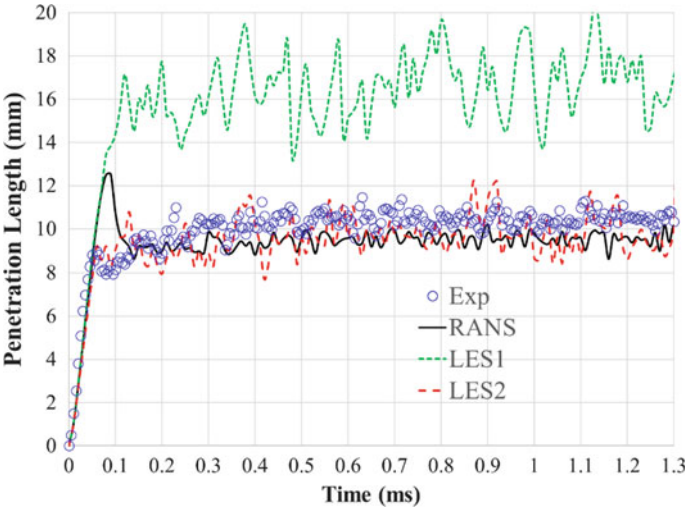

Fig. 18.1 Measured (symbol) and predicted (lines) liquid penetration length of a non-reactive spray

is to tune certain model constants in the spray models, particularly the secondary breakup model. Figure 18.1 shows the measured (symbol) and predicted (lines) liquid penetration length of a non-reactive spray in a constant volume combustion chamber (CVCC). The injector is the ECN spray A. The pressure and temperature in the CVCC at the beginning of fuel injection are 60.5 bar and 829.5 K, respectively. All the simulations use the Kelvin–Helmholtz Rayleigh–Taylor (KH-RT) breakup model, base mesh size of 2 mm, level three adaptive mesh refinement, and level three mesh embedding near the nozzle exit. With all the default model constants, the KH-RT model coupled with RANS successfully reproduces the liquid penetration length [36]. When the turbulence model is switched to LES with the dynamic structure model, the KH-RT model with all the default model constants over-predicted the liquid penetration, as indicated by the green dotted line ("LES1"). When the velocity model constant in the KH model is adjusted from the default value of 0.188 to 5.04, the results of the KH-RT model match the experimental data very well. The gas-phase velocity is utilized in the calculation of the droplet's drag force. With different turbulence model, the averaged gas-phase velocities are different. This explains why tuning the velocity model constant in the KH model has an evident impact on the spray prediction when the turbulence model is changed from RANS to LES. The liquid penetration at the end of the injector valve opening is over-predicted by the RANS, which is not shown in the results of LES. Stronger fluctuation is observed in the results of LES that is due to its transient nature. Other approaches reported in the literature used much finer mesh [46], design of experiment, and optimization to tune the model constants [39]. The fundamental ideas are the same: adjust the breakup model constants. A more rigorous physics-based approach is expected to avoid the empirical tuning of model constants.

The other aspects of the spray models also require attention. Bharadwaj et al. [5] derived the filtered equation for two-phase flow, with a focus on the spray source terms in the gas-phase transport equations. With the point source assumption, the spray source term in the transport equation of sub-grid kinetic energy is derived and modelled using a deconvolution method. Different from the RANS approach, this source term could be either sink or source of kinetic energy.

When the LES is considered, usually the turbulent combustion model that involves turbulent fluctuation should be re-developed. KIVA–CHEMKIN model and SAGE model assume that each computational cell is a perfectly stirred reactor [28, 67]. This approach assumes that the turbulence has no direct impact on the chemical kinetics. Sub-grid fluctuation is largely neglected in the formulation; i.e. the model is not dependent on the SGS model. The turbulence effects on the NOx and soot emissions are reflected through the turbulent viscosity in the LES. The same reaction mechanisms and emission models including NOx and soot can be directly applied in LES. Thus, such types of models can be directly implemented into the LES seamlessly [3, 21, 24]. However, some flamelet-based models should be adjusted. For instance, the G-equation model is a turbulent combustion model for premixed combustion, which is based on the flamelet assumption. The G-equation model tracks the flame front of the propagating flame. When a RANS model is employed, the turbulent flame speed is usually computed from Peters' model [48]:

$$s_t = s_l + u' \left[-\frac{a_4 b_3^2}{2b_1}\mathrm{Da} + \sqrt{\left(\frac{a_4 b_3^2}{2b_1}\mathrm{Da}\right)^2 + a_4 b_3 \mathrm{Da}} \right] \tag{18.26}$$

where s_l is the laminar flame speed, u' is the root mean square of the turbulent fluctuating velocity; a_4, b_3, and b_1 are model constants. Da is the Damkohler number:

$$\mathrm{Da} = \frac{s_l l_t}{u' l_F} \tag{18.27}$$

where l_t is the turbulent length scale; and

$$l_F = \frac{\lambda / c_p}{(\rho s_l)_u} \tag{18.28}$$

The subscript "u" indicates an unburnt region.

If an LES model is employed, Peters' model is no longer valid. The new formulation of turbulent flame speed is derived as [49]:

$$s_t = s_l \left[1 - \frac{b_3^2 C_\nu}{2b_1 \mathrm{Sc}_t}\frac{\Delta}{l_F} + \sqrt{\left(\frac{b_3^2 C_\nu}{2b_1 \mathrm{Sc}_t}\frac{\Delta}{l_F}\right)^2 + \frac{b_3^2 D_t}{s_l l_F}} \right] \tag{18.29}$$

with Sc_t the turbulent Schmidt number. C_v is the model constant in the formulation of turbulent viscosity in the SGS model.

In a diesel engine, the liquid fuel is injected into the gaseous charge. The bulk liquid fuel atomizes into small-size droplets. The droplets vaporize and the vapour mixes with the gaseous charge. Autoignition occurs in a premixed mixture. After the premixed burn, a turbulent diffusion flame develops, which is called diffusion burn. The laminar flamelet model can be used to model the turbulent diffusion flames. The flamelet timescale (FTS) model, which is a quasi-steady flamelet model coupled with a timescale model, was developed and applied to diesel combustion [21, 22]. The transport equation for the mean mixture fraction and the mixture fraction variance is written as:

$$\frac{\partial\left(\overline{\rho}\tilde{\xi}\right)}{\partial t}+\frac{\partial\left(\overline{\rho}\tilde{\xi}\tilde{u}_j\right)}{\partial x_j}=-\frac{\partial\tau_{u_j\tilde{\xi}}}{\partial x_j}+\frac{\partial}{\partial x_j}\left(\widetilde{\rho D\frac{\partial\xi}{\partial x_j}}\right)+\overline{\rho}\widetilde{\dot{\xi}^s} \tag{18.30}$$

$$\begin{aligned}\frac{\partial\left(\overline{\rho}\widetilde{\xi''^2}\right)}{\partial t}+\frac{\partial\left(\overline{\rho}\widetilde{\xi''^2}\tilde{u}_j\right)}{\partial x_j}=&-2\tau_{u_j\widetilde{\xi''^2}}\frac{\partial\tilde{\xi}}{\partial x_j}+\frac{\partial}{\partial x_j}\left(\overline{\rho D}\frac{\partial\tilde{\xi}}{\partial x_j}\right)\\&-2\overline{\rho}\chi_{\mathrm{sgs}}+2\left[\widetilde{\rho\xi\dot{\xi}^2}-\rho\tilde{\xi}\widetilde{\dot{\xi}^s}\right]\end{aligned} \tag{18.31}$$

The flux of the mean of mixture fraction is defined as

$$\tau_{u_j\tilde{\xi}}=\overline{\rho}\left(\widetilde{u_j\xi}-\tilde{u}_j\tilde{\xi}\right) \tag{18.32}$$

The flux of the variance of mixture fraction is defined as

$$\tau_{u_j\widetilde{\xi''^2}}=\overline{\rho}\left(\widetilde{u_j\xi''^2}-\tilde{u}_j\widetilde{\xi''^2}\right) \tag{18.33}$$

The same approach as the dynamic structure model is applied to modelling these flux terms, which are written as a function of the variance of mixture fraction and the corresponding Leonard terms:

$$\tau_{u_j\tilde{\xi}}=\widetilde{\xi''^2}\frac{L_{u_j\xi}}{L_{\xi''^2}} \tag{18.34}$$

The Leonard terms are given as

$$L_{u_j\xi}=\widetilde{\overline{\rho}\tilde{u}_j\tilde{\xi}}-\hat{\overline{\rho}}\hat{\tilde{u}}_j\hat{\tilde{\xi}} \tag{18.35}$$

$$L_{\xi''^2}=\widetilde{\overline{\rho}\tilde{\xi}\tilde{\xi}}-\hat{\overline{\rho}}\hat{\tilde{\xi}}\hat{\tilde{\xi}} \tag{18.36}$$

The sub-grid-scale scalar dissipation rate is given as

$$\chi_{\text{sgs}} = D\left(\widetilde{\frac{\partial\xi}{\partial x_i}\frac{\partial\xi}{\partial x_i}} - \frac{\partial\tilde{\xi}}{\partial x_i}\frac{\partial\tilde{\xi}}{\partial x_i}\right), \tag{18.37}$$

which is modelled using a zero-equation model:

$$\chi_{\text{sgs}} = C\frac{D}{\Delta^2}\widetilde{\xi''^2} \tag{18.38}$$

with C the model constant.

To account for the unsteady effects in diesel combustion, a characteristic timescale is introduced. The rate of change of species i is written as,

$$\frac{\partial\tilde{Y}_i}{\partial t} = \frac{\tilde{Y}_i - \tilde{Y}_i^{\text{lib}}}{\tau_{\text{chem}}} \tag{18.39}$$

$\tilde{Y}_i^{\text{lib}}$ is the mass fraction calculated from the flamelet library. τ_{chem} is the characteristic timescale describing the duration that the current flamelet proceeds towards its steady state. Its value is evaluated from a one-step irreversible reaction for diesel combustion:

$$\tau_{\text{chem}} = A^{-1}Y_{\text{fuel}}^{0.75}Y_{O_2}^{-1.5}\exp\left(\frac{E_a}{\text{RT}}\right) \tag{18.40}$$

The mixed-mode combustion model was developed for diesel combustion [23]. The model considers a flame that is consists of three modes: a kinetically controlled (KIN) mode, a quasi-steady homogenous (QSH) mode, and a quasi-steady flamelet (QSF) mode. By introducing two combustion indices α and γ that are used to identify the local combustion regimes, the final reaction rate is written as:

$$\widetilde{\omega}_i = \alpha\widetilde{\omega}_i^{\text{KIN}} + (1-\alpha)\left[\gamma\widetilde{\omega}_i^{\text{QSH}} + (1-\gamma)\frac{\left(\tilde{Y}_i - \int Y_i^{\text{FL}}p(Z)\text{d}Z\right)}{\tau_{\text{FL}}}\right] \tag{18.41}$$

The first combustion index, α, is used to distinguish the slow-chemistry regime from the fast-chemistry regime, i.e. depending on the chemical timescale. A simple criterion based on the local gas temperature is developed for α:

$$\alpha = \mathcal{H}\left(\frac{T}{T_c} - 1\right) \tag{18.42}$$

with $\mathcal{H}$ the Heaviside function and T_c the cut-off temperature. The second combustion index, γ, is used to distinguish the quasi-steady homogeneous regime from the quasi-steady diffusion flamelet regime. It is written as a function of scalar dissipation rate, which indicates the local mixture homogeneity:

$$\gamma = \min\left(1, \frac{\chi}{\chi_c}\right) \tag{18.43}$$

χ is the local scalar dissipation rate. χ_c is the criterion of scalar dissipation rate between the diffusion flamelet regime and the partially premixed regime.

Zhang and Rutland [65, 66] developed a mixing-controlled direct chemistry combustion model for LES of diesel combustion. The SGS scalar dissipation rate is modelled using a similarity term and a scaling factor estimated from the DNS data. The mixing effect is modelled by a mixing timescale based on mixture fraction variance and sub-grid scalar dissipation rate, which ranges $10^{-6} \sim 10^{-3}s$ for different engine conditions. A kinetic timescale based on the specific internal energy is introduced, which shows improvements over the conventional single-species-based timescale.

The progress variable approach coupled with the dynamic Smagorinsky model was used to simulate an HCCI engine [25, 64]. Good comparisons with experimental pressure traces were achieved. Thickened flame model is similar to the progress variable approach and G-equation model, which artificially increases the flame thickness to represent the turbulence effect on the premixed flamelet [12]. The model has been implemented into LES and applied to simulate the multiple cycles of a spark-ignited premixed charge compression ignition (PCCI) engine [61]. Coherent flamelet was adopted in LES of diesel combustion [30, 32] and spark-ignited engines [51, 63].

Applications

LES is a powerful tool to predict unsteady phenomena in a turbulent flow, which are associated with some critical phenomena in engine combustion, such as combustion instability, turbulent mixing, and turbulence-chemistry interactions. LES has been applied to engine combustion since three decades ago [3, 15, 22, 24, 25, 27, 28, 29, 37, 51, 61, 68] especially for unsteady phenomena prediction such as cyclic variation [1, 20, 62, 63] and fluctuations in spray [26]. But it is not ready for engine optimization yet due to its high computational cost, and immature physical models. A series of workshops on "LES for Internal Combustion Engine Flows" (LES4ICE) has been organized to advance LES applications for engine simulation.

In the section, the LES with dynamic structure model is applied to simulate the combustion processes of a heavy-duty diesel engine. The results are compared with the ones of the RANS with RNG (Renormalization Group) $k - \varepsilon$ model [19]. The engine is based on a Cummins N-series production, which is a single-cylinder, direct injection (DI), four-stroke diesel engine. The engine has been extensively investigated

Table 18.1 Engine configurations

Bore (mm)	139.7
Stroke (mm)	152.4
Displacement (L)	2.34
Connecting rod length (mm)	304.8
Compression ratio	11.2:1
Injector	Common rail, pilot valve actuated, mini sac
Number of holes	8
Spray included angle (degree)	152
Nozzle orifice diameter (mm)	0.196

Table 18.2 Operating conditions

Injection pressure (bar)	1200
Engine speed (rpm)	1200
Intake temperature (K)	362
Intake pressure (bar)	2.187
Start of injection (deg ATDC)	−22
Duration of injection (deg)	7
Injected fuel mass (mg)	56

experimentally [6–8, 11, 16, 17, 33–35, 40–42, 44, 45, 57, 59] and numerically [9, 16, 55, 56, 58]. Table 18.1 lists the configurations of this engine. One engine case, which features low-temperature combustion and early injection, is simulated. Table 18.2 shows the operating conditions of this case.

A commercial CFD software CONVERGE is employed in the present study. A real fluid model, the Redlich–Kwong equation of state, was employed. SAGE combustion model with ERC n-heptane mechanism [47] is used. Two different skeletal n-heptane mechanisms, the ERC mechanism [47] and Chalmers mechanism [38], are considered. The ERC reaction mechanism consists of 34 species and 74 reactions, including the mechanism of NO, N_2O, and NO_2. The Chalmers mechanism consists of 42 species and 168 reactions, including 3 reactions about N and NO. A sector mesh is used. The base mesh size is set to 2 mm. Level three adaptive mesh refinement (AMR) is activated by both temperature gradient and velocity gradient. A level three fixed embedding is applied to refine the meshes near the nozzle exit during the injection process, so that consistent mesh resolution is achieved. Thus, the minimum mesh size is 0.25 mm. Figure 18.2 shows the computational mesh coloured by the velocity magnitude during the spray injection, showing that the spray plume is covered by the fixed embedding. AMR is activated by the high-velocity gradient outside of the fixed embedding regime. The spray is represented by a collection of tetradecane droplet parcels. O'Rourke's model [43] is used to describe the turbulent dispersion. The evaporation model used is the Frossling model [2] with n-heptane

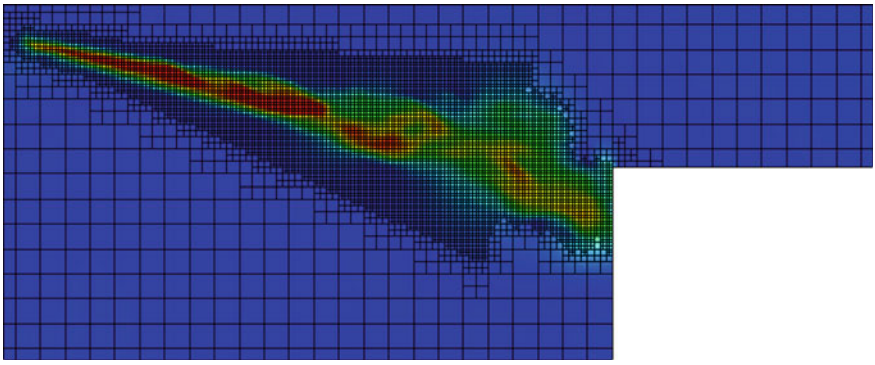

Fig. 18.2 Computational mesh

being the sourced species. To capture the droplet collision, the NTC collision with post-collision outcomes [54] is chosen. The Kelvin–Helmholtz and Rayleigh–Taylor breakup model [4] is used to model the droplet secondary breakup. A uniform droplet size that is the same as the nozzle size is set to all the droplet parcels. Except for the different turbulence models and the different velocity constant in the KH model (c.f., Fig. 18.1), all of the other models and settings in the RANS and LES are the same.

Figure 18.3 shows the comparison of measured and predicted pressure trace and heat release rate. Good agreements are achieved in all the simulations. Two-stage combustion is observed in the present case, with a cool flame followed by a diffusion

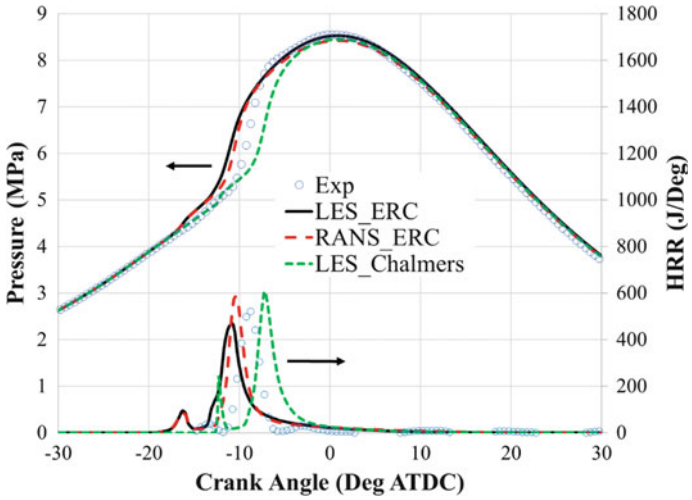

Fig. 18.3 Measured and predicted pressure trace and heat release rate

flame. This is very typical for diesel combustion with early injection [10]. Both simulations using the ERC mechanism predict the cool flame and the main combustion earlier than the experimental data, while the combustion predicted by the LES using Chalmers mechanism is later than the experimental data. Thus, the chemical kinetics is more critical for the prediction of averaged thermodynamic properties, such as pressure trace and heat release rate. Relatively, the different turbulence models have minor impacts on the predictions of these averaged quantities. The predictions of these properties mainly depend on the prediction of combustion phasing. The turbulence model influences the prediction of mixing and turbulent flame speed. With the same ERC mechanism, the LES and RANS predict almost identical timing of the cool flame, which is dominated by the chemical kinetics. The LES predicted the main combustion is earlier than the one predicted by the RANS. The peak pressure predicted by the LES matches the experimental data better.

Figure 18.4 shows the comparison of measured and predicted liquid and vapour distributions. The left column is the Planar LIF image of fuel vapour. The middle column is the results of LES. The right column is the results of RANS. The droplet parcels are indicated as blue dots in the simulation results. The contour plot indicates the concentration of the fuel vapour (C_7H_{16}). Reasonable agreements between the simulations and measurements are achieved. Overall, both LES and RANS overpredict the vapour penetration and liquid penetration after $-20°$ degrees ATDC. This may be due to the inaccurate rate of injection profile used in these simulations. As shown in Fig. 18.2, with different velocity model constant in the KH model, the LES and RANS predict similar liquid penetration. Therefore, during the early stage (before $-16°$ ATDC), the difference between LES and RANS is minor, since the spray injection and evaporation are the dominant factors for the development of the mixing and flow structure. Unstable flow phenomena are observed in both LES and RANS results. This is due to the KH instability of the spray breakup process. After $-16°$ ATDC, an evident difference in vapour distribution predicted by LES and RANS is observed. The results of RANS show a smoother distribution in space than the ones of LES, due to its time-averaged nature. The LES results are more chaotic.

Figure 18.5 shows the comparison of measured and predicted OH and temperature distributions at -11 and $-10°$ ATDC, at which the ignition occurs. The left column is the Planar LIF image of OH and temperature. The middle and right columns are the results of LES and RANS, respectively. The contour plots in blue from simulations indicate the OH mole fraction. The contour plots in green from simulations indicate the temperature. The formation of OH is well-captured by the simulations, especially the LES. According to the pressure trace shown in Fig. 18.3, the ignition events predicted by the LES and RANS are earlier than the measurement. Thus, the predicted in-cylinder temperature is higher than the experimental data. The primary distribution of OH and temperature is similar between LES and RANS. The ones predicted by LES show more complex topology and structure than the ones predicted by RANS. Comparing to the RANS results, higher OH concentration and temperature are observed in the LES results, which is consistent with the pressure trace shown in Fig. 18.3. The different turbulence models predict different gas flow fields, first

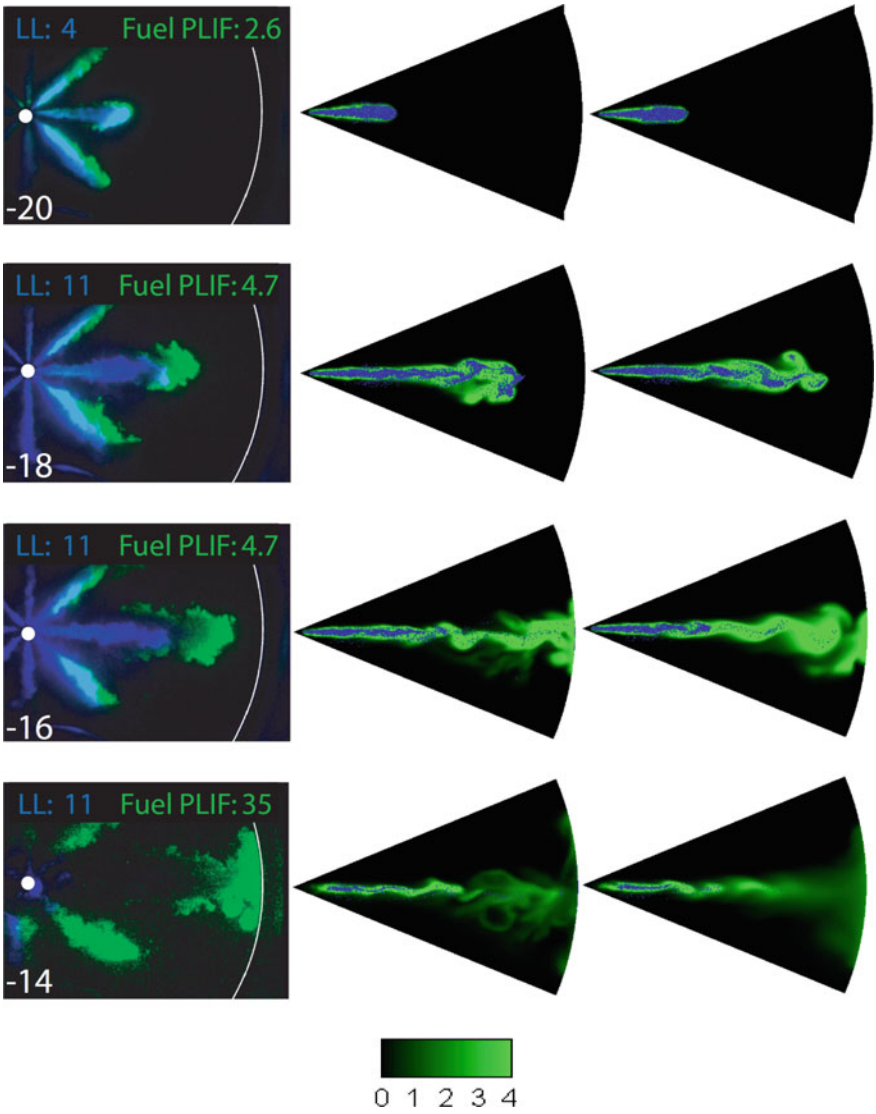

Fig. 18.4 Comparison of measured and predicted liquid and vapour distributions

the velocity and consequently the other passive scalars. Assuming the same temperature and pressure, the difference in the fuel–air mixture predicted by the different turbulence models will lead to different ignition events.

Figure 18.6 shows the scatter plot of the equivalence ratio and temperature at −14, −12, −11, and −10° ATDC. Each data point indicates one computational cell. The colour of the point indicates the mole fraction of OH. Note that the equivalence ratio is calculated from all the C, H, and O in all the components, including

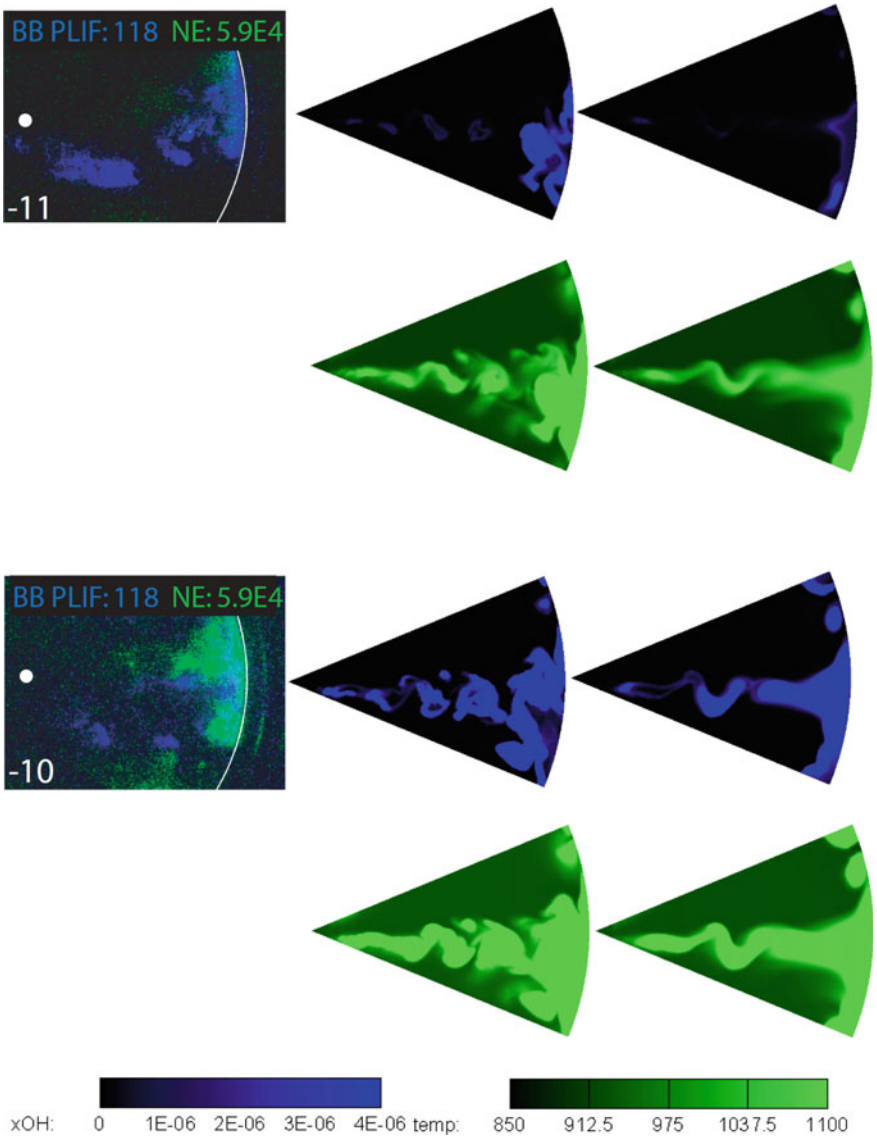

Fig. 18.5 Comparison of measured and predicted OH and temperature distributions

CO_2 and H2O. At −14° ATDC, the two simulations show very similar distributions in the spaces of equivalence ratio and temperature. At −12° ATDC, the LES results show more cells having an equivalence ratio of 0.5–2.0, which is favourable for autoignition. Additionally, some cells with an equivalence ratio of 3.0–4.0 in the LES results have a higher temperature than the RANS results, which implies that pyrolysis reactions occur earlier in the LES results than the RANS results. This

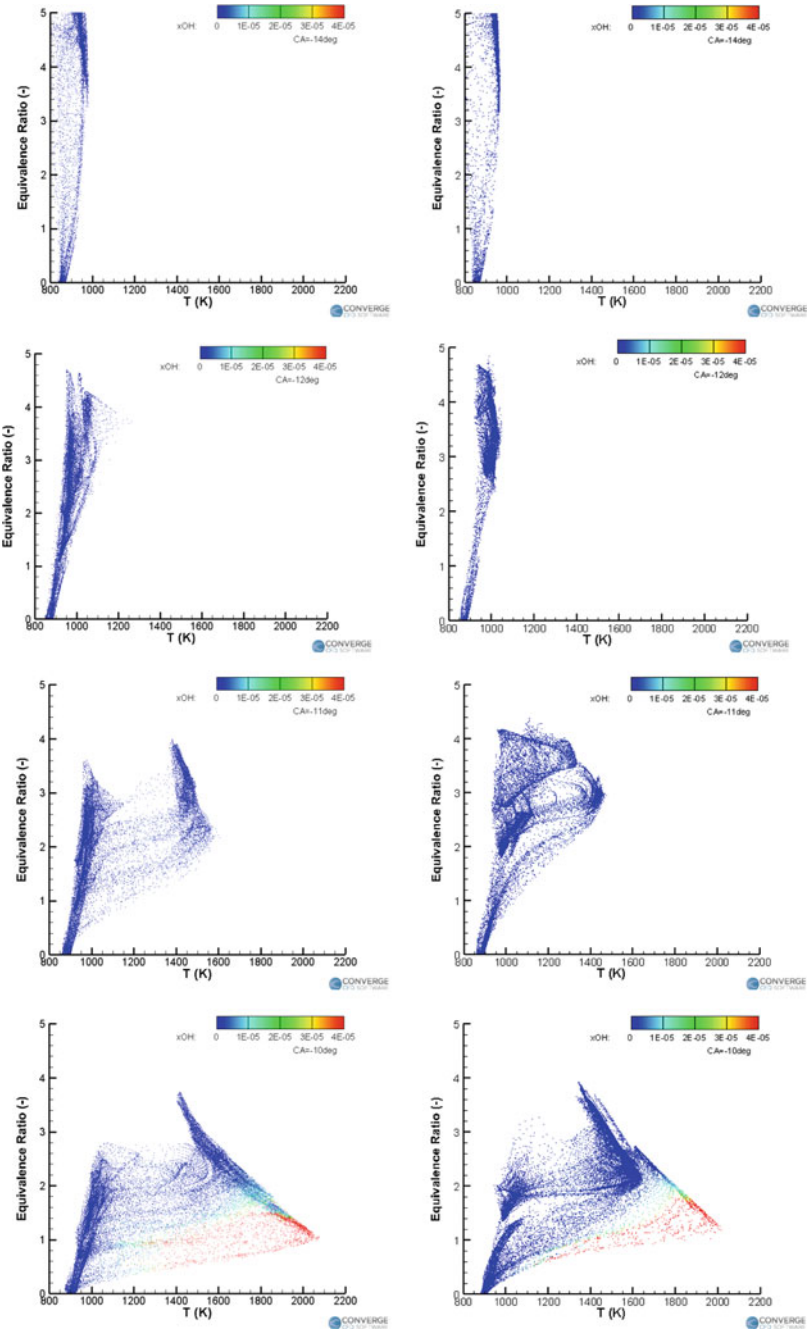

Fig. 18.6 Scatter plot of equivalence ratio and temperature at −14°, −12°, −11°, and −10° ATDC

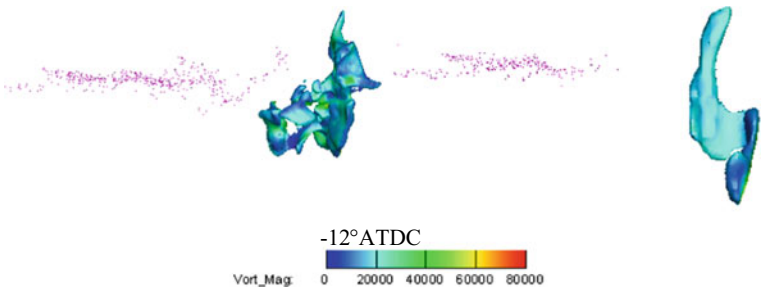

Fig. 18.7 Iso-surface of temperature (1100 K) at −12° ATDC. The iso-surface is coloured by vorticity magnitude

explains that the combustion predicted by the LES is earlier than the one predicted by RANS, as shown in Fig. 18.3. At −11° ATDC, both simulations show the ignition events. In the LES results, the high-temperature cells form a separated island from the low-temperature cells. The RANS results show a smoother and more homogeneous distribution between the low temperature and high temperature. This phenomenon can also be seen at −10° ATDC when the major combustion occurs and the flame temperature reaches more than 2000 K.

Figure 18.7 shows the iso-surface of the temperature of 1100 K at −12° ATDC, as well as the droplets. The left and right ones are the results of LES and RANS, respectively. The iso-surface is coloured by the vorticity magnitude. It shows that the flame is initialized near the liner. The flame front predicted by the RANS is much smoother than the one predicted by the LES. The vorticity magnitude on the flame front is much more homogeneous than the LES results which show many wrinkles on the iso-surface. This implies that the LES predicts a more detailed flow structure than the RANS. These wrinkles increase the total surface area of the flame front. Although the LES predicts a larger surface area, there is no evidence showing that the turbulent flame speed predicted by the LES with SAGE model is higher than the one predicted by the RANS, as shown in the profiles of pressure trace and heat release rate. This is consistent with the finding in an LES study of turbulent jet ignition [31].

Future and Challenges

Significant progress has been made in the research of LES, including fundamental research and application. Many aspects of the LES are getting mature, including sub-models, numerical schemes, numerical set-ups, and analysis. Applications of LES in engine combustions are rapidly growing. However, there are still a lot of challenges remaining. Particularly, the spray models, wall function, and combustion models should be redeveloped and evaluated in the framework of LES.

Although the LES is more sensitive to design changes [52], its unsteady nature prevents it from design evaluations. Given the same engine design, the performance

parameters of single-cycle engine combustion from LES vary. When a certain design is changed, it is very difficult to determine whether the changes in single-cycle LES results are due to the design change or its unsteady nature. To obtain meaningful LES results for the evaluation of design performance, multiple cycle LES is required. The total number of cycles should be great enough to be statistically significant, e.g. 20 cycles. This will lead to very expensive computational costs. Thus, LES is still not a good option for optimization of the engine design.

References

1. Adomeit P, Lang O, Pischinger S, Aymanns R, Graf M, Stapf G (2007) Analysis of cyclic fluctuations of charge motion and mixture formation in a DISI engine in stratified operation. SAE Trans 935–942
2. Amsden AA, O'rourke PJ, Butler TD (1989) KIVA-II: a computer program for chemically reactive flows with sprays. Los Alamos National Lab., NM (USA)
3. Banerjee S, Liang T, Rutland C, Hu B (2010) Validation of an LES multi-mode combustion model for diesel combustion. In: SAE Technical Paper 2010-01-0361. https://doi.org/10.4271/2010-01-0361
4. Beale JC, Reitz RD (1999) Modeling spray atomization with the Kelvin-Helmholtz/Rayleigh-Taylor hybrid model. Atom Sprays 9(6). https://doi.org/10.1615/AtomizSpr.v9.i6.40
5. Bharadwaj N, Rutland CJ, Chang S-M (2009) Large-eddy simulation modelling of spray-induced turbulence effects. Int J Engine Res 10(2):97–119
6. Bobba MK, Genzale CL, Musculus MPB (2009) Effect of ignition delay on in-cylinder soot characteristics of a heavy-duty diesel engine operating at low-temperature conditions. SAE Int J Engines 2(1):911–924
7. Bobba MK, Musculus MPB (2012) Laser diagnostics of soot precursors in a heavy-duty diesel engine at low-temperature combustion conditions. Combust Flame 159(2):832–843
8. Bobba M, Musculus M, Neel W (2010) Effect of post injections on in-cylinder and exhaust soot for low-temperature combustion in a heavy-duty diesel engine. SAE Int J Engines 3(1):496–516
9. Bolla M, Farrace D, Wright YM, Boulouchos K (2014) Modelling of soot formation in a heavy-duty diesel engine with conditional moment closure. Fuel 117:309–325. https://doi.org/10.1016/j.fuel.2013.09.041
10. Cantrell BA, Ge HW, Reitz RD, Rutland CJ (2009) Validation of advanced combustion models applied to two-stage combustion in a heavy-duty diesel engine. In: SAE Technical Paper 2009-01-0714. https://doi.org/10.4271/2009-01-0714
11. Chartier C, Andersson O, Johansson B, Musculus M, Bobba M (2011) Effects of post-injection strategies on near-injector over-lean mixtures and unburned hydrocarbon emission in a heavy-duty optical diesel engine. SAE Int J Engines 4(1):1978–1992
12. Colin O, Ducros F, Veynante D, Poinsot T (2000) A thickened flame model for large-eddy simulations of turbulent premixed combustion. Phys Fluids 12(7):1843–1863. https://doi.org/10.1063/1.870436
13. Cui X, Ge H, Wenwang W, Feng Y, Wang J (2021) LES study of the respiratory airflow field in a whole-lung airway model considering steady respiration. J Braz Soc Mech Sci Eng 43(3):141. https://doi.org/10.1007/s40430-021-02871-3
14. Cui X, Wenwang W, Ge H (2020) Investigation of airflow field in the upper airway under unsteady respiration pattern using large eddy simulation method. Respir Physiol Neurobiol 279:103468. https://doi.org/10.1016/j.resp.2020.103468
15. Drake MC, Haworth DC (2007) Advanced gasoline engine development using optical diagnostics and numerical modeling. Proc Combust Inst 31(1):99–124

16. Genzale CL, Reitz RD, Musculus MPB (2009) Effects of piston bowl geometry on mixture development and late-injection low-temperature combustion in a heavy-duty diesel engine. SAE Int J Engines 1(1):913–937
17. Genzale CL, Reitz RD, Musculus MPB (2009) Optical diagnostics and multi-dimensional modeling of spray targeting effects in late-injection low-temperature diesel combustion. SAE Int J Engines 2:150–172. https://doi.org/10.4271/2009-01-2699
18. Germano M, Piomelli U, Moin P, Cabot WH (1991) A dynamic subgrid-scale eddy viscosity model. Phys Fluids A 3(7):1760–1765. https://doi.org/10.1063/1.857955
19. Han Z, Reitz RD (1995) Turbulence modeling of internal combustion engines using RNG κ-ε models. Combust Sci Technol 106(4–6):267–295. https://doi.org/10.1080/00102209508907782
20. Hasse C, Sohm V, Durst B (2010) Numerical investigation of cyclic variations in gasoline engines using a hybrid URANS/LES modeling approach. Comput Fluids 39(1):25–48
21. Hu B, Jhavar R, Singh S, Reitz RD, Rutland CJ (2007) Combustion modeling of diesel combustion with partially premixed conditions. In: SAE Technical Paper 2007-01-0163. https://doi.org/10.4271/2007-01-0163
22. Hu B, Rutland CJ (2006) Flamelet modeling with LES for diesel engine simulations. In: SAE Technical Paper 2006-01-0058. https://doi.org/10.4271/2006-01-0058.
23. Hu B, Rutland CJ, Shethaji TA (2010) A mixed-mode combustion model for large-eddy simulation of diesel engines. Combust Sci Technol 182(9):1279–1320. https://doi.org/10.1080/00102201003671410
24. Jhavar R, Rutland CJ (2006) Using large eddy simulations to study mixing effects in early injection diesel engine combustion. SAE Technical Paper 2006-01-0871. https://doi.org/10.4271/2006-01-0871
25. Joelsson T, Yu R, Bai XS, Vressner A, Johansson B (2008) Large eddy simulation and experiments of the auto-ignition process of lean ethanol/air mixture in HCCI engines. SAE Int J Fuels Lubr 1(1):1110–1119. https://doi.org/10.4271/2008-01-1668
26. Johnson J, Ge HW, Naber J, Lee SY, Kurtz E, Robarge N (2013) Investigation of key mechanisms for liquid length fluctuations in transient vaporizing diesel sprays. SAE Int J Engines 6(2013):1202–1212
27. Lee D, Pomraning E, Rutland CJ (2002) LES modeling of diesel engines. SAE Trans 2566–2578
28. Li YH, Kong S-C (2008) Diesel combustion modelling using LES turbulence model with detailed chemistry. Combust Theor Model 12(2):205–219
29. Liu X, Wang H, Yao M (2020) Investigation of the chemical kinetics process of diesel combustion in a compression ignition engine using the large eddy simulation approach. Fuel 270:117544
30. Mobasheri R, Peng Z (2012) Using large eddy simulation for studying mixture formation and combustion process in a DI diesel engine. SAE Technical Paper 2012-01-1716. https://doi.org/10.4271/2012-01-1716
31. Muller M, Freeman C, Zhao P, Ge H (2018) Numerical simulation of ignition mechanism in the main chamber of turbulent jet ignition system. In: ASME ICEF2018-9587. https://doi.org/10.1115/icef2018-9587
32. Musculus MP, Rutland CJ (1995) Coherent flamelet mlodeling of diesel engine combustion. Combust Sci Technol 104(4–6):295–337
33. Musculus MPB (2005) Measurements of the influence of soot radiation on in-cylinder temperatures and exhaust NOx in a heavy-duty DI diesel engine. SAE Trans 845–866
34. Musculus MPB (2006) Multiple simultaneous optical diagnostic imaging of early-injection low-temperature combustion in a heavy-duty diesel engine. SAE Trans 83–110
35. Musculus MPB, Singh S, Reitz RD (2008) Gradient effects on two-color soot optical pyrometry in a heavy-duty DI diesel engine. Combust Flame 153(1–2):216–227
36. Muthukumar RR, Parameswaran S, Ge H (2020) Assessment of primary atomization models for spray simulation. In: ASME ICEF2020-2945:V001T05A003. https://doi.org/10.1115/ICEF2020-2945

37. Naitoh K, Itoh T, Takagi Y, Kuwahara K (1992) Large-eddy simulation of premixed-flame in the engine based on the multi-level formulation and the renormalization group theory. SAE Technical Paper 920590. https://doi.org/10.4271/920590
38. Nordin N (1998) Numerical simulations of non-steady spray combustion using a detailed chemistry approach. In: Licentiate of engineering thesis, department of thermo and fluid dynamics. Chalmers University of Technology, Goteborg, Sweden
39. Nsikane DM, Vogiatzaki K, Morgan RE, Heikal M, Mustafa K, Ward A, Winder N (2019) Novel approach for adaptive coefficient tuning for the simulation of evaporating high-speed sprays injected into a high-temperature and high-pressure environment. Int J Engine Res1468087419878911
40. O'Connor J, Musculus M (2013) Optical investigation of the reduction of unburned hydrocarbons using close-coupled post injections at LTC conditions in a heavy-duty diesel engine. SAE Int J Engines 6(1):379–399
41. O'Connor J, Musculus M (2014) In-cylinder mechanisms of soot reduction by close-coupled post-injection as revealed by imaging of soot luminosity and planar laser-induced soot incandescence in a heavy-duty diesel engine. SAE Int J Engines 7(2):673–693
42. O'Connor J, Musculus MPB, Pickett LM (2016) Effect of post injections on mixture preparation and unburned hydrocarbon emissions in a heavy-duty diesel engine. Combust Flame 170:111–123
43. O'Rourke PJ (1981) Collective drop effects on vaporizing liquid sprays. Los Alamos National Lab., NM (USA)
44. O'Connor J, Musculus M (2014a). Effect of load on close-coupled post-injection efficacy for soot reduction in an optical heavy-duty diesel research engine. J Eng Gas Turbines Power 136(10)
45. O'Connor J, Musculus M (2014) Effects of exhaust gas recirculation and load on soot in a heavy-duty optical diesel engine with close-coupled post injections for high-efficiency combustion phasing. Int J Engine Res 15(4):421–443
46. Ottenwaelder T, Pischinger S (2018) Comparing large eddy simulation of a reacting fuel spray with measured quantitative flame parameters. In: SAE Technical Paper 2018-01-1720. https://doi.org/10.4271/2018-01-1720
47. Patel A, Kong S-C, Reitz RD (2004) Development and validation of a reduced reaction mechanism for HCCI engine simulations. SAE Technical Paper 2004-01-0558. https://doi.org/10.4271/2004-01-0558
48. Peters N (1999) The turbulent burning velocity for large-scale and small-scale turbulence. J Fluid Mech 384:107–132
49. Pitsch H (2002) A G-equation formulation for large-eddy simulation of premixed turbulent combustion. Annual Res Briefs 3–14
50. Pomraning E, Rutland CJ (2002) Dynamic one-equation non viscosity large-eddy simulation model. AIAA J 40(4):689–701
51. Richard S, Colin O, Vermorel O, Benkenida A, Angelberger C, Veynante D (2007) Towards large eddy simulation of combustion in spark-ignition engines. Proc Combust Inst 31(2):3059–3066
52. Rutland CJ (2011) Large-eddy simulations for internal combustion engines—a review. Int J Engine Res 12(5):421–451. https://doi.org/10.1177/1468087411407248
53. Sagaut P (2006) Large-eddy simulation for incompressible flows: an introduction. Springer Science & Business Media
54. Schmidt DP, Rutland CJ (2000) A new droplet collision algorithm. J Comput Phys 164(1):62–80
55. Shuai S, Abani N, Yoshikawa T, Reitz RD, Park SW (2009) Simulating low-temperature diesel combustion with improved spray models. Int J Therm Sci 48(9):1786–1799. https://doi.org/10.1016/j.ijthermalsci.2009.01.011
56. Singh S, Reitz RD, Musculus MPB, Lachaux T (2007) Validation of engine combustion models against detailed in-cylinder optical diagnostics data for a heavy-duty compression-ignition engine. Int J Engine Res 8(1):97–126. https://doi.org/10.1243/14680874jer02406

57. Singh S, Musculus MPB, Reitz RD (2009) Mixing and flame structures inferred from OH-PLIF for conventional and low-temperature diesel engine combustion. Combust Flame 156(10):1898–1908
58. Singh S, Reitz RD, Musculus MPB (2006) Comparison of the characteristic time (CTC), representative interactive flamelet (RIF), and direct integration with detailed chemistry combustion models against optical diagnostic data for multi-mode combustion in a heavy-duty DI diesel engine. SAE Trans 61–82
59. Singh S, Reitz RD, Musculus MPB, Lachaux T (2007) Simultaneous optical diagnostic imaging of low-temperature, double-injection combustion in a heavy-duty DI diesel engine. Combust Sci Technol 179(11):2381–2414
60. Smagorinsky J (1963) General circulation experiments with the primitive equations: I. The basic experiment. Mon Weather Rev 91(3):99–164
61. Thobois L, Lauvergne R, Poinsot T (2007) Using LES to investigate reacting flow physics in engine design process. SAE Trans 116:165–175
62. Vermorel O, Richard S, Colin O, Angelberger C, Benkenida A, Veynante D (2007) Multi-cycle LES simulations of flow and combustion in a PFI SI 4-valve production engine. SAE Trans 152–164
63. Vermorel O, Richard S, Colin O, Angelberger C, Benkenida A, Veynante D (2009) Towards the understanding of cyclic variability in a spark-ignited engine using multi-cycle LES. Combust Flame 156(8):1525–1541
64. Yu RX, Bai XS, Vressner A, Hultqvist A. Johansson B, Olofsson J, Seyfried H, Sjöholm J, Richter M, Aldén M (2007) Effect of turbulence on HCCI combustion. In: SAE Technical Paper 2007-01-0183. https://doi.org/10.4271/2007-01-0183
65. Zhang Y, Rutland CJ (2012) A mixing controlled direct chemistry (MCDC) model for diesel engine combustion modelling using large eddy simulation. Combust Theor Model 16(3):571–588
66. Zhang Y, Rutland CJ (2013) A further evaluation of the mixing controlled direct chemistry (MCDC) combustion model for diesel engine combustion using large eddy simulation. Fuel 105:272–282. https://doi.org/10.1016/j.fuel.2012.09.050
67. Zhao D, Xia Y, Ge H, Lin Q, Wang G (2020) Large-eddy simulation of flame propagation during the ignition process in an annular multiple-injector combustor. Fuel 263:116402
68. Zhou L, Xie M-Z, Jia M, Shi J-R (2011) Large-eddy simulation of fuel injection and mixing process in a diesel engine. Acta Mech Sin 27(4):519. https://doi.org/10.1007/s10409-011-0485-1

Appendices

Appendix I: Estimation of Products of Combustion from the Interferograms

It is assumed that when the mixture fraction ($C\,(r, x)$) is greater than the concentration at the rich limit ($C_{R.L.}$), a part of the fuel vapour combines with available air according to a ratio determined by $C_{R.L}$, and the rest of the fuel remains in pure vapour form. Referring to Fig. A.1 below:

By definition of the rich limit

$$\frac{y}{y + A} = C_{R.L.} \tag{A.1}$$

Also,

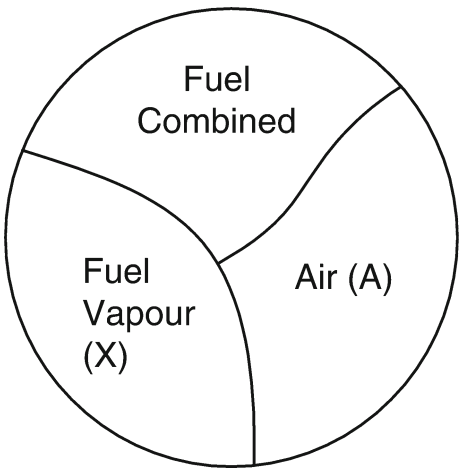

Fig. A.1. Fuel, vapour, and air in the spray

P. A. Lakshminarayanan and Y. V. Aghav, *Modelling Diesel Combustion*, Mechanical Engineering Series, https://doi.org/10.1007/978-981-16-6742-8

$$\text{Mixture fraction} = \frac{x+y}{x+y+A} \tag{A.2}$$

$$\begin{aligned} C_f =& \text{Concentration of fuel vapour} \\ =& \frac{x+y}{x+y+A} \\ =& C(r.x)\frac{C_{R.L.}}{1-C_{R.L.}} \end{aligned} \tag{A.3}$$

Appendix II: Estimation of the Concentration of Fuel Vapour in the Vapourizing and Combusting Spray from the Interferograms

Let T = Temperature.
n = Refractive index.
ρ = Density.
K = Gladstone–Dale constant.
M = Molecular weight.
and C_f = Concentration of fuel vapour.

Subscripts *f, b,* ∞*, r* refer to fuel vapour, products of combustion, the surroundings (reference, air), and the point in the jet. From Dent et al [2] for any point r in the burning jet,

$$n_r = \rho_{\text{mix}}\left[C_f K_f + \left(1 - C_f\right)K_b + 1\right] \tag{A.4}$$

Similarly,

$$n_\infty = \rho_\infty K_\infty + 1 \tag{A.5}$$

Also,

$$\rho_\infty = \frac{pM_\infty}{\text{RT}_\infty} \tag{A.6}$$

$$\rho_{\text{mix}} = \frac{p}{\text{RT}_r}\left(\frac{C_f}{M_f} + \frac{C_b}{M_b}\right) \tag{A.7}$$

Here, R is the universal gas constant and $C_b = 1 - C_f$.
Substituting Equations (v), (vi), (vii) in (iv),

$$T_r = \frac{T_\infty}{M_\infty} \frac{C_f + (1 - C_f) K_b}{\left[K_\infty - \frac{n_r - n_\infty}{\rho_\infty}\right]\left[\frac{C_f}{M_f} + \frac{1 - C_f}{M_b}\right]} \tag{A.8}$$

Appendix III: Estimation of Mass and Heat Transfer Functions

Transfer number, B [10]:

By Reynolds analogy between the mass and thermal boundary layers (Fig. 5.7)

$$\frac{m_{\text{vap},0} - m_{\text{vap},\infty}}{1 - m_{\text{vap},0}} = B_M = B_H = \frac{C_{\text{vap}}(T_\infty - T_0)}{L} \tag{A.9}$$

Here, m = Mass concentration.

T = Temperature.

L = Latent heat of vaporization + sensible heat to change liquid from sub-cooled condition to vapour at saturation temperature.

C = Specific heat.

B = Transfer number and subscripts.

vap = Vapour.

o = At the interface of liquid and vapour.

∞ = Bulk gases.

H = Heat transfer.

and M = Mass transfer.

Appendix IV: Vapour Pressure of Diesel and Fuels *A* and *B* and *B**

Vapour pressure of diesel, and fuels *A, B, B**

$$P_{\text{vap}} = 7.9 \times 10^9 \exp\left(\frac{-5400}{T_s}\right) \tag{A.10}$$

Vapour pressure of highly viscous, less volatile fuel, *G*,

$$P_{\text{vap}} = 4.1 \times 10^{11} \exp\left(\frac{-8400}{T_s}\right) \tag{A.11}$$

where T_s = Saturation temperature.

Appendix V: Calculation of Tangential Velocity of Air in the Piston Cavity from the Inlet Swirl Number

The cylinder head is assembled on the cylinder liner in a steady flow rig. The inlet of a blower is connected to the liner von Thien [11]. The air is sucked from the atmosphere through the inlet port to create a swirling flow in the liner. This is measured by a fan anemometer. The valve lift is varied in steps. The measured rate of airflow is Q m^3/s. A diesel engine of swept volume, V would inhale air at a rate of V per one stroke, (i.e.) V per half revolution, i.e. 2 V per revolution in a steady rig. If the engine speed is n rpm, the engine flow rate will be nV/30. The ratio of the speed of the air rotor to the engine speed is defined as the swirl number.

$$\text{swirl number at a valve lift} = \frac{\text{anemometer speed} \times V}{30Q} \tag{A.12}$$

A valve lift history typical of diesel engines is used to calculate the integrated swirl number at the end of the inlet stroke. This value is the characteristic swirl number of a diesel engine.

Appendix VI: Momentum of Useful Air of the Three Different Combustion Cavities Described in Kuo et al. [6]

S No.	Type	Speed	Momentum of useful air (× 1E4) kg m/s	Total fuel momentum (× 1 E4) kgm/s	ISFC g/kW hr	EIC g/kg fuel
1	*R*	1000	2.46	1.25	185	1.48
2		1300	3.36	1.165	173	0.86
3		1500	3.87	1.305	174	1.01
4		1800	4.62	1.305	169	1.35
5		2400	5.9	1.195	171	3.86
6	*S*1	1000	2.7	1.07	174	0.66
7		1300	3.36	1.165	173	1.56
8		1500	3.89	1.435	170	1.06
9		1800	4.66	1.395	174	1.81
10		2400	6.29	1.275	177	7.34
11	*S*2	1000	1.8	1.09	189	0.7
12		1300	2.01	1.27	176	0.57
13		1500	2.38	1.305	176	0.65
14		1800	3.12	1.24	173	0.63

(continued)

(continued)

S No.	Type	Speed	Momentum of useful air (× 1E4) kg m/s	Total fuel momentum (× 1 E4) kgm/s	ISFC g/kW hr	EIC g/kg fuel
15		2400	4.03	1.3	175	2.58
16	*R*	1500	3.5	2.97	219	31.6
17		1500	3.5	1.91	188	7.58
18		1500	3.82	1.07	174	0.83
19		1500	2.87	0.705	174	0.68
20	*S*1	1500	3.87	2.89	198	9.7
21		1500	3.88	2.05	185	3.62
22		1500	3.88	1.115	169	0.86
23		1500	3.31	0.675	170	0.58
24	*S*2	1500	3.39	5.84	206	6.1
25		1500	3.39	1.91	186	1.57
26		1500	1.93	1.205	186	0.61
27		1500	1.93	0.67	184	0.96

Appendix VII: Momentum of Useful Air for Engines A8, B8, C8, and D8

Type	Speed rpm	Injector hole size, mm	No of the injector holes	Average injection velocity m/s	Total fuel momentum kg m/s	Useful mass, kg	Velocity of the solid rotor at the bowl, rad m/s	ISFC g/kW h	EIC g/kg fuel
A8	2200	0.22	4	159	2.08E-03	1.40E-04	36	183	2.316
B8	1500	0.28	4	150	5.98E-03	5.00E-04	32	177	0.57
	2000			165	6.57E-03		42.5	175	0.21
	2000			171	6.98E-03		42.5	174	0.62
	2200			165	6.71E-03		46.7	173	1.66
	2500			187	7.51E-03		53.1	178	0.631
	2500			190	8.25E-03		53	180	2.436
C8	2000	0.28	4	168	7.63E-03	6.40E-04	50	174	1.629
	2050			177	6.70E-03		51	174	0.647
	1600			151	8 E-3		40	191	2.46
	1200			152	8.90E-03		30	201	4.098
D8	2013	0.25	5	180	4.31E-03	3.85E-04	30	181	0.831
	2042			177	3.98E-03		30.5	181	0.503
	2051			157	2.99E-03		30.6	175	0.442
	1800			149	3.51E-03		26.8	176	1.206
	1607			172	4.12E-03		24	182	0.718
	1200			178	4.36E-03		17.9	198	1.389

Appendix VIII: Estimation of Spray Properties and Impingement Parameters

From Lakshminarayanan and Dent [7],

Penetration of free spray

$$S = \sqrt{8C_d u_{\text{inj}} d_e t_{\text{SOI}}} \left(\frac{T_0}{T_{\text{surr}}} \right)^{\frac{1}{4}} \tag{A.13}$$

Penetration of free spray with a swirl [3],

$$\frac{S_{\text{sn}}}{S} = \left(1 + \frac{\pi n_{\text{sn}} \text{NS}}{30 u_{\text{inj}}} \right)^{-1} \tag{A.14}$$

Penetration of wall spray,

$$S_{\text{wall}} = 0.75 \sqrt{u_{\text{inj}} d_e t_{\text{imp}}} \left(\frac{T_0}{T_{\text{surr}}} \right)^{\frac{1}{4}} \tag{A.15}$$

Here, S = Penetration of spray without swirl.
u_{inj} = Velocity of fuel jet at the exit of the nozzle.
d_e = Equivalent diameter of orifice = do (ρ f /ρ a) 1/2.
d_o = Diameter of nozzle hole.
ρ_f = Density of fuel.
ρ_a = Density of charge air.
t_{SOI} = Time after start of injection.
$T0$ = Reference temperature, 294 K
T_{surr} = Surrounding temperature.
C_d = Coefficient of discharge of the nozzle.
S_{sn} = Penetration of spray with swirl.
n_{sn} = swirl number (ratio of swirl rpm to engine rpm).
N = Speed of engine.
t_{imp} = Time at which impingement occurs.

Similarly, the impingement distance available can be calculated by using a simple geometric correlation as follows (Fig. A.2),

$$S_{\text{wall}} = \frac{R_{\text{sb}}}{\sin\theta} \tag{A.16}$$

where S_{wall} = Penetration of wall spray
θ = Half spray angle

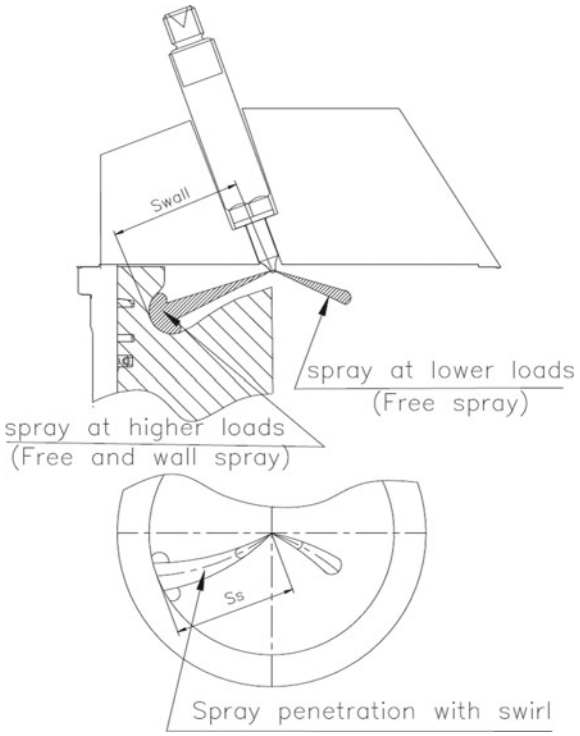

Fig. A.2 Comparison of engine sprays

The duration of injection is calculated from injection pressure diagrams. The time in crank degrees required for impingement is evaluated by comparing the spray penetration with impingement distance,

$$S_{\text{sn}} = S_{\text{wall}} \tag{A.17}$$

Differentiating Eqs. (18.13) and (18.15), we obtain the velocity of the free spray and wall jet as follows,

$$u_{\text{free}} = \sqrt{8C_d u_{\text{inj}} d_e}\frac{1}{2\sqrt{t_{\text{SOI}}}}\left(\frac{T_0}{T_{\text{surr}}}\right)^{\frac{1}{4}} \tag{A.18}$$

$$u_{\text{wall}} = 0.75\sqrt{u_{\text{inj}} d_e}\frac{1}{2\sqrt{t_{\text{im}[}}}\left(\frac{T_0}{T_{\text{surr}}}\right)^{\frac{1}{4}} \tag{A.19}$$

In other words, the kinetic energy input to the portion of the fuel in the wall jet is less by a factor, C_{wall} given by the ratio of the kinetic energy of the spray along the wall and the free spray.

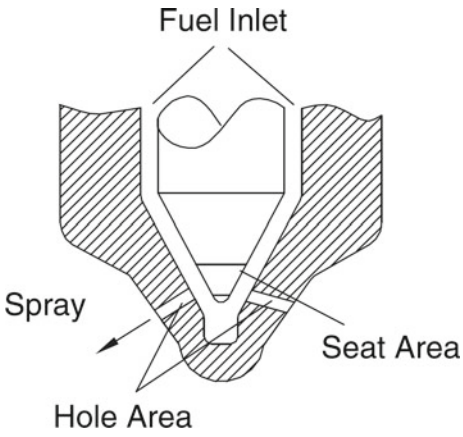

Fig. A.3 Flow area available for fuel flow

$$C_{\text{wall}} = \left(\frac{u_{\text{wall}}}{u_{\text{free}}}\right)^2 \tag{A.20}$$

Appendix IX: Calculation of Fuel Injection Rate

The rate of injection can be obtained by simulation of the fuel injection equipment or using sophisticated devices. Alternatively, it can be obtained from experimental data if available, as in the case of engines studied in the present work. The instantaneous flow area around the needle seat obtained from the measured needle lift and the total area of the spray holes are considered as two orifices in series as shown in Fig. A.3. Then fuel line pressure, cylinder pressure, and needle lift are considered as inputs for further analysis. A typical measurement of fuel pressure, cylinder pressure, and needle lift for a data point is shown in Fig. A.4.

The rate of fuel injection at any instant is calculated using the effective area of flow through the two orifices A_n, and the pressures at the injector entry, P_f, and measured in the cylinder P_{cyl}. A flow coefficient, C_d of 0.7 is reasonable for the spray holes.

The instantaneous injection rate, $\mathrm{d}m_f/\mathrm{d}\theta$

$$\frac{\mathrm{d}m_f}{\mathrm{d}\theta} = C_d \rho_f A_n \sqrt{\frac{2\left(P_f - P_{\text{cyl}}\right)}{\rho_f}} \tag{A.21}$$

In the present work, the heat release rate is modelled as a strong function of the rate of fuel injection. Therefore, the accuracy of estimation of the fuel injection rate is important, especially in the first regime of combustion.

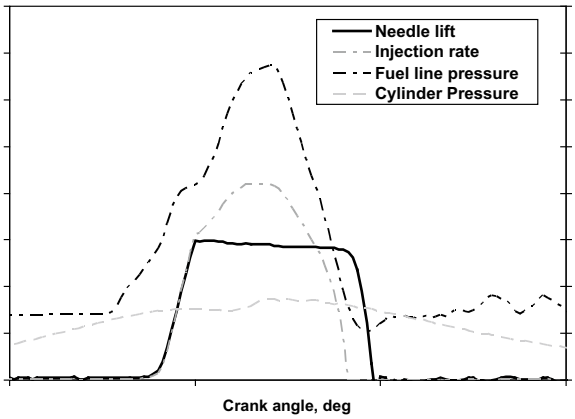

Fig. A.4 Experimental estimation of injection rate

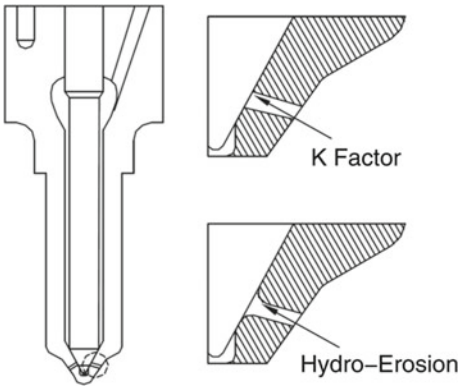

Fig. A.5 Explanation of KF and HE nozzles

Appendix X: Influence of Nozzle Features

The terms "KF" and "HE" used in this thesis refer to spray hole-manufacturing signatures of nozzles as shown in Fig. A.5. The nozzles with conical spray holes are termed as *k*-factor (KF) nozzles. Sometimes, the spray holes are finished by a hydro-grinding process, known as hydro-erosion, HE. In the case of the VCO nozzle, the spray holes are on the seat of the needle. Therefore, they have a lesser discharge coefficient and larger flow variations. The smoother entry of spray in the holes improves the discharge coefficient of the spray holes. Also, the hydro-grinding process is with close loop control that reduces nozzle-to-nozzle variation.

The nozzles hole is defined as the base orifice size with % HE or *k*-factor. This effect is considered as an enlargement of orifice diameter over base diameter.

$$N_f = \text{HE} = \frac{k\text{Factor}}{10} \tag{A.22}$$

The HE and *k*-factor are defined below:

$$\%\text{HE} = \frac{\text{flow after HE} - \text{flow before HE}}{\text{flow before HE}} \tag{A.23}$$

$$k\,\text{Factor} = \frac{d_{\text{inlet}} - d_{\text{out;et}}}{10\mu m} \tag{A.24}$$

Example 1 Base hole size is 0.19 mm with a HE of 10.5%. Then the effective area of nozzle, A_o;

$$A_0 = \frac{\pi d_0^2\left(1 + N_f\right)}{4} = \frac{\pi 0.19^2(1 + 0.105)}{4} \tag{A.25}$$

Example 2 Base hole size is 0.19 mm with a *k*-factor of 1.5. Then the effective area of nozzle, A_o;

$$A_0 = \frac{\pi d_0^2\left(1 + N_f\right)}{4} = \frac{\pi 0.19^2(1 + 0.15)}{4} \tag{A.26}$$

Appendix XI: Henry's Constant Hc for Fuel (*n*-Octane) in Oil

Following Kaiser et al. [4], the engine lubricant was assumed to be Squalane ($C_{30}H_{62}$), which closely resembled the base hydrocarbon of the SAE 5W20 oil, used by them in their bomb experiments, because of the availability of data for HC for various kinds of paraffin dissolved in Squalane over a range of temperatures [1]. Unfortunately, no values are reported for any paraffin beyond a-butane. Therefore, the following procedure was adopted for determining Hc for n-octane in Squalane. The data from reference (Table I, Chappelow and Praushnitz [1]) was plotted as $\log_e$ (Hc) against the molecular weight of the paraffin listed over the temperature range of the data. The result is shown in Fig. A.6. The data shows an approximately linear variation of Log $_{10}$ (Hc) with a molecular weight at a constant temperature. The value of HC for octane in Squalane was obtained by extrapolation.

It is recognized that the process of extrapolation is prone to error and that the use of n-octane as the fuel instead of iso-octane, which is more representative of commercial fuel, could introduce some error due to their differing solubility. However, in the absence of any more representative data, the extrapolation procedure was adopted, and Hc obtained by this procedure for n-octane in Squalane over a range of temperatures is shown plotted in Fig. A.7. It can be expressed as:

$$\log_{10}(\text{HC}) = -1.921 + 0.013\ (T - 300) \tag{A.27}$$

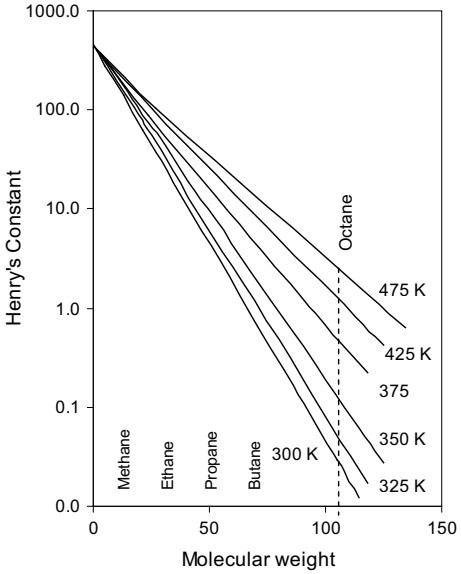

Fig. A.6 Variation of Henry's constant for a range of kinds of paraffin dissolved in Squalane (C_{30} H_{62}) data from Chappelow and Praushnitz [1]

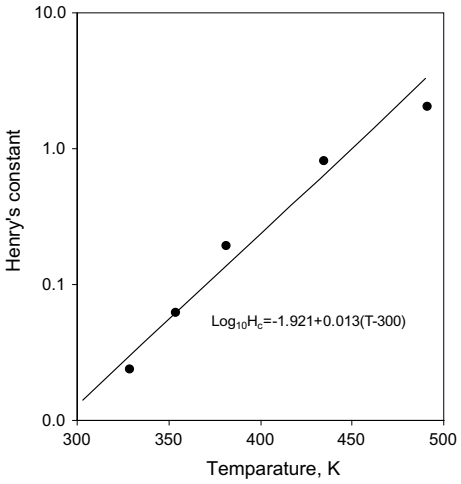

Fig. A.7 Variation of Henry's constant with temperature for octane dissolved in Squalane (C_{34} H_{62})

Appendix XII: Evaluation of g_F* and g_G*

Molecular diffusion through the effective penetration depth is assumed. Hence:

$$g_F^* = \frac{\rho\ D}{\delta} \tag{A.28}$$

where D is the mass diffusion coefficient for fuel vapour in oil and is taken from reference [5].

$$D = 7.4 \times 10^{-8} M^{0.5} \mathrm{TV}^{-0.6} \mu^{-1} \mathrm{cm}^2 \mathrm{s}^{-1} \tag{A.29}$$

Here,
M = Molar volume of fuel vapour
= 422
V = Molar volume of fuel vapour
= 176 cm^3/mole
T = Temperature,
K = Absolute viscosity of oil centipoise
Here, μ is obtained from Walther's equation [14] which can be expressed as

$$\log_{10}\left[\log_{10}\left(\frac{\mu}{\rho} + 0.6\right)\right] = 7.686 - 3.01 \log_{10} \tau \tag{A.30}$$

Evaluation of g_G* was obtained from assuming the Reynolds analogy between heat and mass transfer which implies a Levis number of unity under these conditions.

$$g_G^* = \frac{h}{C_p} \tag{A.31}$$

Here, h is the heat transfer coefficient evaluated from Woschni's correlation [13]. Of particular interest here is the velocity term in Woschni's equation:

$$C_1 U_P + C_2 \frac{V_S T_1}{P_1 V_1} (P - P_0) \mathrm{ms}^{-1} \tag{A.32}$$

Here, C_1 and $C_2$are constants: U_p is the mean piston speed; V_s the cylinder volume; P_1, V_1, and T_1 are pressure, volume, and temperature at some reference state in the engine cylinder. $(P - P_o)$ is the difference between the fired and motored cylinder pressure at any crank angle. For the same engine speed, the influence of gas motion due to the change of intake valve geometry will result in changes in h and g* through $(P - P_o)$.

Appendix XIII: In-Cylinder Oxidation of HC

The choice of a limiting temperature of 1100 K above which oxidation of fuel desorbed from the oil film can be considered complete is justified as follows. It is assumed that the fuel desorbed into the burned gas zone remains in the boundary layer at a film temperature, which is the mean of the burned gas temperature (T_b) and the wall temperature (T_w). The concentration of oxygen (m_{O2}) in the boundary layer

is assumed what remains after stoichiometric combustion in the bulk of the burned gas zone and for a lean mixture can be expressed as:

$$m_{O_2} = 0.23\frac{(A/F) - (A/F)_{\mathrm{ST}}}{1 + 1/F} \tag{A.33}$$

When the mixture is rich $m_{O2} = 0$.

A/F is the overall engine air–fuel ratio and the subscript ST refers to a stoichiometric mixture.

The net rate of increase of fuel in the boundary layer ($\mathrm{d}m_{\mathrm{net}}/\mathrm{d}t$) is the difference between rates of that desorbed ($\mathrm{d}m_D/\mathrm{d}t$) and oxidized ($\mathrm{d}m_{\mathrm{net}}/\mathrm{dt}$). The net incremental fuel mass over a time step Δt can be expressed as:

$$m_{\mathrm{nett}_{t+\Delta t}} = \left[\left(m_{D_{t+\Delta t}} - m_{D_t}\right) + m_{\mathrm{nett}_t}\right] - \frac{\mathrm{d}m_c}{\mathrm{d}t}\Delta t \tag{A.34}$$

Here,

$$\frac{\mathrm{d}m_c}{\mathrm{d}t} = \frac{\mathrm{d[HC]}}{\mathrm{d}t}(\text{Boundary layer volume} \times \text{Molecular weight of fuel}) \tag{A.35}$$

The oxidation of hydrocarbon $\mathrm{d[HC]}/\mathrm{d}t$ is considered to be represented by the rate equation used by Lavoie and Blumberg [8] for HC oxidation which has the form

$$\frac{\mathrm{d[HC]}}{\mathrm{d}t} = C_R \cdot A \cdot [O_2] \cdot \exp\left[\frac{-E}{\mathrm{RT}}\right] \text{moles cm}^{-3}s \tag{A.36}$$

Here, $C_R = 2$.

$A = 6.7 \times 1015$ cm^3 /moles.

and $E = 37{,}230$ cal/mole.

[HC] $= m_{\mathrm{net}}$/[Boundary Layer Volume $\times$ Molecular weight of Fuel] moles cm^{-3}

$[O_2]$ in moles /cm^3 is obtained from the oxygen mass fraction $\mathrm{m_{O2}}$ and the burned gas volume.

Figure A.8 shows the rates of desorption and oxidation plotted against film temperature and crank angle, for the baseline operating condition, while Fig. A.9 shows the variation in total HC against the same ordinates.

Also plotted is the net fuel (HC) present in the cylinder based on the assumption that all HC desorbed when the film temperature is above 1100 K is completely oxidized. It will be seen that this assumption is quite reasonable.

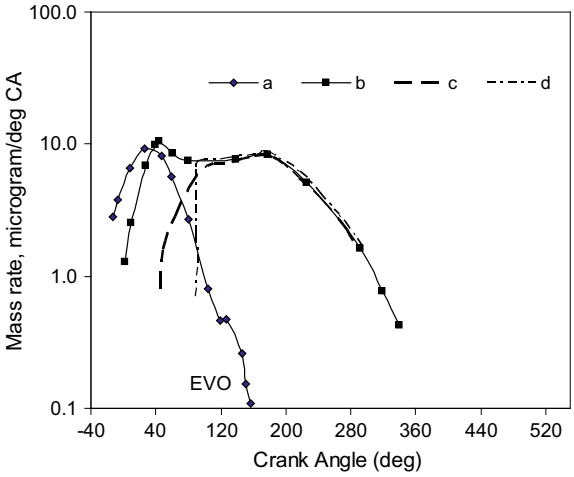

Fig. A.8 Rates of absorption and desorption, oxidation and net in-cylinder HC accumulation, $b =$ HC desorbed by oil, $c =$ HC desorbed – HC oxidized according to Arrhenius relationship, $d =$ HC desorbed – HC modelled to oxidize if the temperature is beyond 1000 K and not oxidized if the temperature is less than 1000 K

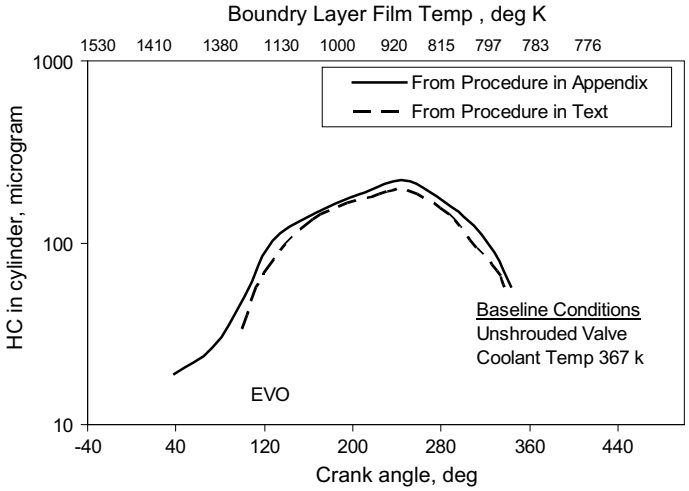

Fig. A.9 Comparison of simple HC oxidation assumption and approximate desorption oxidation model

Appendix XIV: Estimation of Wall Surface Temperature

It is known [9, 12] that cylinder wall temperature strongly affects HC emission from an engine. This effect is discussed in the paper in relationship to the Henry number,

which increases with increasing temperature, and the direct effect of temperature on oil film thickness through the kinematic viscosity of the oil.

The cylinder wall temperature is highest near the head and lowest at the crankcase. To obtain a representative cylinder wall temperature for use in the model, the cycle average of the cylinder wall area in contact with the cylinder charge (A) is computed. The total heat loss per cycle $\oint \dot{Q}\mathrm{d}t$ is computed, and the heat transfer conductance of the cylinder liner and the coolant U is taken from Lavoie et al. [9] and has a value of 1.89 kW/m^2 K.

$$\therefore \quad T_{\text{wall}} = T_{\text{coolant}} + \frac{1}{\tau}\frac{\oint \dot{Q}\mathrm{d}t}{\text{AU}} \tag{A.37}$$

Here τ = The cycle time.

$$A = \oint \sum_i A_i \mathrm{d}t \tag{A.38}$$

A_i = The instantaneous area of the sleeve in contact with zone i.

$$\dot{Q} = \sum_i \dot{q}_i'' A_i \tag{A.39}$$

Here $\dot{q}_i''$ = the instantaneous heat flux from zone i across the cylinder liner and is estimated from Woschni's correlation [13].

To compute T_{wall} instantaneous heat fluxes and dress must be available. Therefore, a wall temperature of 450 K was initially assumed to obtained values of A_{i} and $\dot{q}_i''$ to start the interaction.

Appendix XV: Experimental Data on HC emissions from DI Diesel Engines

Engine	Speed	Power	Fuel injected, mg		HC measured		Air–fuel ratio	Delay
	rpm	kW	Per cycle	During delay	ppm	mg/cycle/cylinder		ms
A10	1400	39.7	43.70	13.10	250	0.12	21.58	0.71
	1400	31.0	37.90	17.00	212	0.11	24.88	0.77
	1400	20.7	27.00	17.30	211	0.11	34.93	0.77
	1500	42.5	46.90	13.90	238	0.12	19.88	0.56
	1500	33.1	32.70	14.30	225	0.11	28.51	0.56
	1500	22.1	30.30	20.30	205	0.10	30.77	1.22

(continued)

(continued)

Engine	Speed	Power	Fuel injected, mg		HC measured		Air–fuel ratio	Delay
	rpm	kW	Per cycle	During delay	ppm	mg/cycle/cylinder		ms
	2200	55.5	43.50	14.10	307	0.15	21.13	0.45
	2200	38.8	31.00	14.90	252	0.12	29.65	0.38
	2200	26.7	16.90	10.20	263	0.13	54.39	0.53
	2200	4.9	10.40	8.50	346	0.17	88.38	0.64
	2300	56.1	45.70	16.80	206	0.10	19.88	0.54
	2300	38.0	29.60	12.30	237	0.12	30.69	0.62
	2300	25.4	16.50	9.40	266	0.13	55.05	0.36
	2300	4.9	12.20	8.30	387	0.19	74.46	0.54
	2500	56.8	40.90	12.50	208	0.10	21.95	0.47
	2500	27.6	16.70	10.20	258	0.12	53.75	0.53
	2500	5.5	11.40	10.40	384	0.18	78.74	0.73
B10	2200	48.5	47.32	5.49	190	0.13	30.30	0.53
	2200	72.8	67.28	4.32	162	0.12	24.60	0.46
	1500	60.6	72.88	3.54	121	0.10	23.20	0.56
	1500	49.6	57.80	3.96	149	0.11	28.80	0.67
	1500	33.0	40.60	6.75	168	0.11	37.70	0.78
	1500	11.0	15.92	3.40	193	0.11	59.40	0.78
C10	2210	60.6	64.10	32.20	305	0.27	22.66	1.02
	2211	46.6	49.80	34.80	383	0.31	29.17	1.13
	2207	31.6	34.90	31.00	405	0.30	41.62	1.10
	2204	0.0	16.40	16.40	646	0.40	50.24	1.21
	1508	46.1	70.20	36.50	346	0.26	19.15	1.33
	1507	35.8	53.90	38.70	374	0.26	24.94	1.38
	1500	24.3	41.60	39.10	361	0.23	32.31	1.50
	610	0.0	78.60	78.60	447	0.22	15.39	4.37
D10	2000	23.1	32.50	25.80	560	0.22	23.69	1.04
	2000	17.6	26.60	22.30	520	0.20	28.95	0.92
	2000	11.8	24.00	19.50	480	0.18	32.08	1.04
	2000	5.9	21.10	18.20	620	0.23	36.49	0.92
	1319	8.7	29.10	22.80	480	0.19	26.63	0.95
	1298	17.8	48.70	36.70	690	0.29	15.91	1.28
	1300	12.9	28.50	24.70	540	0.22	27.19	0.83
E10	1500	86.2	50.80	27.50	113	0.23	28.10	1.11
	1500	57.6	34.10	27.90	136	0.24	34.80	1.28
	1500	29.7	21.60	21.40	208	0.33	50.00	1.39

(continued)

(continued)

Engine	Speed	Power	Fuel injected, mg		HC measured		Air–fuel ratio	Delay
	rpm	kW	Per cycle	During delay	ppm	mg/cycle/cylinder		ms
	1500	8.6	12.20	12.10	232	0.34	72.50	1.44
F10	1500	39.0	27.90	23.00	565	0.24	26.70	1.28
	1500	25.8	20.30	19.50	583	0.25	38.60	1.33
	2500	78.7	39.40	26.70	214	0.09	19.02	0.53
	2500	37.7	20.70	15.80	473	0.20	37.40	0.57
	2500	9.0	8.30	8.00	470	0.20	78.20	0.60
G10	1600	90.4	65.00	14.30	65	0.05	21.61	1.33
	2500	115.4	86.00	3.10	60	0.06	13.95	0.67
H10	700	–	17.14	15.00	400	0.46	138.90	2.02
	1300	–	17.17	15.00	500	0.57	138.90	1.47
	1300	–	17.18	14.00	400	0.46	138.80	1.41
	1300	–	17.17	9.00	150	0.17	138.80	1.09
	1300	–	17.17	13.00	250	0.29	138.80	1.35
	1300	–	17.17	15.00	450	0.52	138.80	1.47
	1300	–	17.17	14.00	510	0.59	138.80	1.46
	1300	–	25.13	10.00	200	0.23	95.00	1.31

Appendix XVI: Engines List for Validating PM Model, Aspiration, Power, Smoke, and PM

Swept volume, liter	Cylinders	Aspiration	Emission standard	Power, Metric hp	Rated speed, rpm	Smoke	LOC, g/h	Predicted PM, g/kWh	Measured PM, g/kWh
1.3	2	NA	T3	24.0	3000	0.040	5	0.111	0.117
1.3	2	NA	CP2	10.8	1500	0.340	6	0.134	0.127
1.7	2	NA	CP1	21.8	1800	0.442	4.5	0.137	0.123
2.5	3	NA	CP1	23.7	1500	0.580	5	0.162	0.174
2.5	3	NA	T3	36.0	2000	0.469	5	0.307	0.300
2.7	3	NA	E3	49.3	2250	0.362	5	0.317	0.285
2.7	3	NA	T3	46.0	2250	0.379	5	0.149	0.108
3.3	4	NA	CE3	35.8	2000	0.240	5	0.210	0.223
3.3	4	NA	CP1	32.1	1500	0.300	5	0.118	0.120
3.3	4	NA	CP1	33.4	1800	0.090	5	0.070	0.072
3.6	4	NA	E3	66.3	2200	0.253	5	0.207	0.228
3.3	4	T	CP1	39.1	1500	0.210	5	0.172	0.181
3.6	4	T	CE3	60.0	2200	0.120	5	0.130	0.152
3.6	4	T	CE3	59.0	2300	0.128	5	0.160	0.153
2.6	3	TAA	T3	85.0	2200	1.218	5	0.346	0.339
2.7	3	TAA	T3	58.0	2200	0.210	5	0.197	0.204
2.7	3	TAA	CP2	30.2	1500	0.308	5	0.220	0.213
2.7	3	TAA	CP2	38.5	1500	0.513	5	0.162	0.148
3.6	4	TAA	T3	75.0	2200	0.113	5	0.090	0.123
3.6	4	TAA	T2	82.0	2200	0.098	5	0.112	0.111
3.6	4	TAA	CP2	40.5	1500	0.484	5	0.180	0.160

Notes

LOC-Lubricating Oil Consumption, g/h

T2: TIIA—India emission standard for tractor equivalent to EU Stage IIA
T3: TIIIA—India emission standard for tractor equivalent to EU Stage IIIA
E3: EU Stage IIIA
CE3: CEVBSIII-India emission standard for Construction Equipment equivalent to EU Stage IIIA
C1, C2: CPCBI, CPCBII—India Genset emission standards from the year 2005 and 2014
TAA—Turbocharged after cooled
NA—Naturally aspirated
T—Turbocharged

Nomenclature

Part			Unit
I	$C\ (r, x)$	Mixture fraction at radius r and axial distance x	–
	$C_{R \cdot L}$	Concentration at the rich limit of combustion	–
II	C_f	Concentration of fuel vapour	–
	K	Gladstone–Dale constant	m^3/kg
	M	Molecular weight	kg/kmol
	n	Refractive index	–
	R	Universal gas constant	$JK^{-1}\ mol^{-1}$
	T	Temperature	K
	ρ	Density	kg/m^3
	Subscripts		
	∞	Surroundings (reference, air),	
	b	Products of combustion	
	f	Fuel vapour	
	mix	Mixture	
	r	Any point in the jet/spray	
III	B	Spalding's mass transfer number	–
	C	Specific heat	$J\ kg^{-1}\ K^{-1}$
	L	Latent heat of vaporization + sensible heat to change liquid from sub-cooled condition to vapour at saturation temperature	$J\ kg^{-1}$
	m	Mass concentration	–
	T	Temperature	K
	Subscripts		
	H	Heat transfer	
	∞	Bulk gases	
	M	Mass transfer	
	o	Interface of liquid and vapour	
	vap	Vapour	
IV	P_{vap}	Vapour pressure of fuel	mmHg
	T_s	Saturation temperature	K
V	Q	Measured rate of airflow	m^3/s
	V	Engine of swept volume	m^3
VIII	C_d	Coefficient of discharge of the nozzle	–
VIII	C_{wall}	Ratio of the kinetic energy of the spray along the wall to the kinetic energy of the free spray	–
VIII	d_e	Equivalent diameter of orifice $= d_o\ (\rho_f / \rho_a)^{1/2}$	m
	d_o	Diameter of the nozzle hole	m
	N	Engine speed	rpm

(continued)

(continued)

Part			Unit
	θ	Half spray cone angle	degree
	R_{sb}	Radius of free spray at the impingement	m
	S	Penetration of spray without swirl	m
	S_{sn}	Penetration of free spray with a swirl	m
	S_{wall}	Penetration of wall spray	m
	T_0	Reference temperature, 294	K
	t_{imp}	Time at which impingement occurs	s
	$t_{SOI,\ tsoi}$	Time after start of injection	s
	T_{surr}	Surrounding temperature	K
	U_{free}	Velocity of the free spray tip	m/s
	U_{inj}, u_{inj}	Velocity of fuel jet at the exit of the nozzle	m/s
	U_{wall}	Velocity of the wall jet tip	m/s
	ρ_a	Density of charge air	kg/m^3
	ρ_f	Density of fuel	kg/m^3
IX	A_n	Area of the nozzle hole	m^2
	m_f	Fuel mass injected	kg
	P_{cyl}	Pressure measured in the cylinder P_{cyl}	Pa
	P_f	Pressure at the injector entry	Pa
	θ	Crank angle	degree
X	d_{inlet}	Inlet diameter of nozzle hole shaped like a cone	m
	d_{outlet}	Outlet diameter of nozzle hole shaped like a cone	m
	K-factor	Effect considered as an enlargement of orifice diameter over base diameter	–
	N_f	Factor describing hydro-erosion of nozzle orifice, a manufacturing process to achieve k-factor	–
XI	Hc	Henry's constant	–
	T	Temperature	K
XII	$(P - P_o)$	Difference between the fired and motored cylinder pressure at any crank angle	Pa
	C_1 and C_2	Constants	–
	δ	Penetration depth of fuel vapour in oil film considered as a semi-infinite slab	m
	D	Mass diffusion coefficient for fuel vapour in oil	cm^{2}s^{-1}
	g_F*	Liquid phase mass transfer conductance	kg/(m^2 s)
	h	Heat transfer coefficient evaluated from Woschni's correlation	W/(m^{2}K)
	M	Molecular weight of oil = 422	kg/kmol
	P_1	Pressure	Pa
	T	Temperature	K

(continued)

(continued)

Part			Unit
	T_1	Temperature	K
	U_p	Mean piston speed	m/s
	V	Molar volume of fuel vapour = 176	cm^3/ mole
	V_1	Volume	m^3
	V_s	Cylinder volume	m^3
	ρ	Density of fuel vapour	kg/m^3
	μ	Dynamic or absolute viscosity	cP
XIII	[HC]	Concentration of hydrocarbons	moles cm^{-3}
	$[O_2]$	Concentration of oxygen	moles/cm^3
	A	6.7×10^{15}	cm^3/moles
	A/F	Air–fuel ratio	–
	C_R	Multiplication constant for the oxidation of hydrocarbons, 2	–
	dm_D/dt	Rate of desorbed fuel	kg/s
	dm_{net}/dt	Increase of fuel in the boundary layer	kg/s
	dm_{net}/dt	Rate of oxidation	kg/s
	E	Activation energy = 37,230	cal/mole
	m_{O2}	Concentration of oxygen in the boundary layer	–
	T_b	Burned gas temperature	K
	T_w	Wall temperature	K
XIV	A_i	Instantaneous area of the sleeve in contact with zone i	m^2
XIV	τ	Cycle time	s
XIV	T_{wall}	Wall temperature	K
XIV	U	Heat transfer conductance of the cylinder liner and the coolant, 1.89	kW/m^2 K
XIV	$\oint \dot{Q} dt$	Total heat loss per cycle	J
XIV	$\dot{q}_i''$	Instantaneous heat flux from zone i across the cylinder liner and is estimated from Woschni's correlation	$W/(m^2K)$

References

1. Chappelow CC, Praushnitz JM (1974) Solubilities of gases in high boiling hydrocarbon solvents. AIChE J 20
2. Dent JC, Keightley JD, DeBoer CD (1977) Application of interferometry to air-fuel measurements. SAE Paper No. 770825
3. Heywood JB (1988) A textbook on internal combustion engine fundamentals. McGraw-Hill International edition
4. Kaiser EW, Adamczyk AA, Lavoie GA (1980) The effect of oil layers on the hydrocarbon emissions generated during closed vessel combustion. In: 18th international symposium on combustion

5. Kaiser EW, Lorusso JA, Lavoie GA, Adamczyk AA (1982) The effect of oil layers on the hydrocarbon emissions from spark ignited engines. Combust Sci Technol 28
6. Kuo TW, Henningsen S, Wu KJ (1988) Evaluation of four mixing correlations for performance and soot emission characteristic of a small open chamber diesel engine. SAE 880599
7. Lakshminarayanan PA, Dent JC (1983) Interferometric studies of vapourising and combusting sprays. SAE 830244
8. Lavoie GA, Blumberg PN (1980) A fundamental model for predicting fuel consumption NO and HC emissions of the conventional spark ignition engine. Combust Sci Technol 21
9. Lavoie GA, Lorusso JA, Adamczyk AA (1980) Hydrocarbon emissions modelling for spark ignition engines. In: Symposium on combustion modelling in reciprocating engines. General Motors Research Laboratories, Nov 1978. Plenum Press, London
10. Spalding DB (1977) Combustion and Mass transfer. Chapters 4, 6, 11, Pergamon Press, Oxford
11. von Thien (1965) Entwicklungsarbeiten an Ventilkanalen von Viertakt Dieselmotoren. Osterreichen Ingenieur Zeitschrift, Heft 9, Jg 8, Springer
12. Wentworth JT (1968) Piston and ring variables affect exhaust hydrocarbon emissions. SAE 680109, SAE Transactions 77
13. Woschni G (1967) A Universally applicable equation for the instantaneous heat transfer coefficient in the internal combustion engine. SAE 670931, SAE Transactions 76
14. Schilling A (1968) Motor oils and engine lubrication. Scientific Publications